frontiers | Research Topics

Development and novel applications of geochemical proxies in marine and terrestrial carbonate records

Edited by
Johan Schijf, Tsuyoshi Watanabe, Ed Hathorne and Hali Kilbourne

Published in
Frontiers in Marine Science

ISSN 1664-8714
ISBN 978-2-8325-5745-7
DOI 10.3389/978-2-8325-5745-7

About Frontiers

Frontiers is more than just an open access publisher of scholarly articles: it is a pioneering approach to the world of academia, radically improving the way scholarly research is managed. The grand vision of Frontiers is a world where all people have an equal opportunity to seek, share and generate knowledge. Frontiers provides immediate and permanent online open access to all its publications, but this alone is not enough to realize our grand goals.

Frontiers journal series

The Frontiers journal series is a multi-tier and interdisciplinary set of open-access, online journals, promising a paradigm shift from the current review, selection and dissemination processes in academic publishing. All Frontiers journals are driven by researchers for researchers; therefore, they constitute a service to the scholarly community. At the same time, the *Frontiers journal series* operates on a revolutionary invention, the tiered publishing system, initially addressing specific communities of scholars, and gradually climbing up to broader public understanding, thus serving the interests of the lay society, too.

Dedication to quality

Each Frontiers article is a landmark of the highest quality, thanks to genuinely collaborative interactions between authors and review editors, who include some of the world's best academicians. Research must be certified by peers before entering a stream of knowledge that may eventually reach the public - and shape society; therefore, Frontiers only applies the most rigorous and unbiased reviews. Frontiers revolutionizes research publishing by freely delivering the most outstanding research, evaluated with no bias from both the academic and social point of view. By applying the most advanced information technologies, Frontiers is catapulting scholarly publishing into a new generation.

What are Frontiers Research Topics?

Frontiers Research Topics are very popular trademarks of the *Frontiers journals series*: they are collections of at least ten articles, all centered on a particular subject. With their unique mix of varied contributions from Original Research to Review Articles, Frontiers Research Topics unify the most influential researchers, the latest key findings and historical advances in a hot research area.

Find out more on how to host your own Frontiers Research Topic or contribute to one as an author by contacting the Frontiers editorial office: frontiersin.org/about/contact

Development and novel applications of geochemical proxies in marine and terrestrial carbonate records

Topic editors

Johan Schijf — University of Maryland, College Park, United States
Tsuyoshi Watanabe — Hokkaido University, Japan
Ed Hathorne — GEOMAR Helmholtz Center for Ocean Research Kiel, Helmholtz Association of German Research Centres (HZ), Germany
Hali Kilbourne — University of Maryland Center for Environmental Science, United States

Citation

Schijf, J., Watanabe, T., Hathorne, E., Kilbourne, H., eds. (2024). *Development and novel applications of geochemical proxies in marine and terrestrial carbonate records*. Lausanne: Frontiers Media SA. doi: 10.3389/978-2-8325-5745-7

Table of contents

frontiers | Frontiers in Marine Science

TYPE Editorial
PUBLISHED 19 November 2024
DOI 10.3389/fmars.2024.1515308

OPEN ACCESS

EDITED AND REVIEWED BY
Selvaraj Kandasamy,
Central University of Tamil Nadu, India

*CORRESPONDENCE
Johan Schijf
schijf@umces.edu

RECEIVED 22 October 2024
ACCEPTED 11 November 2024
PUBLISHED 19 November 2024

CITATION
Schijf J, Hathorne EC, Kilbourne KH and Watanabe T (2024) Editorial: Development and novel applications of geochemical proxies in marine and terrestrial carbonate records. *Front. Mar. Sci.* 11:1515308. doi: 10.3389/fmars.2024.1515308

Editorial: Development and novel applications of geochemical proxies in marine and terrestrial carbonate records

Johan Schijf[1]*, Ed C. Hathorne[2], K. Halimeda Kilbourne[1] and Tsuyoshi Watanabe[3]

[1]University of Maryland Center for Environmental Science, Chesapeake Biological Laboratory, Solomons, MD, United States, [2]GEOMAR, Helmholtz Centre for Ocean Research, Kiel, Germany, [3]Department of Earth and Planetary Sciences, Graduate School of Science, Hokkaido University, Sapporo, Japan

KEYWORDS

marine carbonates, geochemical proxies, paleoclimate, seasonal cycles, elemental ratios, stable isotopes

Editorial on the Research Topic
Development and novel applications of geochemical proxies in marine and terrestrial carbonate records

Many marine and terrestrial carbonate deposits contain records of past climate and oceanographic conditions that span annual cycles to millions of years. Consisting of aragonite or (magnesian) calcite of biogenic or authigenic origin, they must accrete in regular increments to allow accurate dating of individual horizons. Advances in (micro) analytical and sampling techniques are unlocking records in new types of deposits, using novel geochemical proxies encompassing an ever-widening range of environmental variables, and going further back in time. We therefore felt that this Research Topic (RT) would be timely and informative.

In two papers, known proxies were retrieved from challenging, slow-growing organisms. Hetzinger et al. investigated specimens of high-Mg calcite coralline algae *Neogoniolithon hauckii* from the temperate Mediterranean Sea, associated with long *in situ* temperature records. High-resolution laser ablation (LA-)ICP-MS revealed Mg/Ca and Li/Ca cycles in distinctive annual banding with growth rates of 1.1–1.2 mm/y. Both display significant positive linear correlations with temperature. Hughes et al. report a 24-year isotope record from the bivalve *Astarte borealis*, a long-lived species that is difficult to drill with seasonal resolution. Secondary ion mass spectrometry (SIMS) yielded $\delta^{18}O_{shell}$ with sub-monthly resolution showing marked correlations with sea surface temperature (SST) and, after appropriate smoothing of the data, with *in situ* salinity and the North Atlantic

Oscillation (NAO) index. The authors propose that regional influences of the NAO on the Baltic temperature–$\delta^{18}O_{SW}$ correlation may render $\delta^{18}O_{shell}$ particularly sensitive to NAO variations and that SIMS analysis of long-lived bivalves may uncover such variations across the Holocene.

Four papers describe laboratory or field cultures to develop new proxies. Pacho et al. studied shell Na/Ca and K/Ca, potential proxies for seawater Ca content on geologic time scales, in laboratory cultures of benthic foraminifera *Amphistegina lessonii*, as a function of seawater K/Ca and temperature. The results suggest that K/Ca in the calcite increases with increasing $[K]_{SW}$ and does not depend on $(K/Ca)_{SW}$ at constant $[K]_{SW}$. However, due to a contrasting increase of Na/Ca in the calcite with $(Na/Ca)_{SW}$, constraining paleoceanic $[K]_{SW}$ and $[Ca]_{SW}$ may require both ratios. de Winter et al. exposed aragonitic cockles (*Cerastoderma edule*), calcitic oysters (*Ostrea edulis*), and polycrystalline mussels (*Mytilus edulis*) to a timed series of five dissolved Sr spikes in an outdoor mesocosm over a period of ~3 months. Shells were analyzed by LA-ICP-MS, to ascertain the presence of concomitant Sr/Ca peaks that could serve as recognizable time markers for use in extended growth rate experiments. All three species recorded Sr/Ca peaks that generally matched the applied spikes in dose size and timing, yielding Sr-derived growth records that were broadly consistent with growth curves based on direct size measurements. Brosset et al. analyzed Sr/Ca in the outer shell layer of *Arctica islandica* bivalves from two lab-based temperature studies (1.1–15°C) by LA-ICP-MS. The data show complicated relations between temperature, growth, and the area and elongation of biomineral units. Comparison with an earlier field-based study indicates that the Sr/Ca thermometer in lab-grown specimens is much more sensitive and that neither the calibration nor corrections for vital effects are transferable between the two. Sakata et al. grew many non-clonal colonies of Pacific massive (*Porites australiensis*) and branching (*Acropora digitifera*) corals in aquarium culture for 77 days at different temperatures (18, 21, 24, 27, 30°C). Calcification rates and photosynthetic efficiency were monitored and newly grown aragonite was analyzed for Mg/Ca, Sr/Ca, Ba/Ca, U/Ca, $\delta^{18}O$ and $\delta^{13}C$, using standard techniques. Moderate to strong negative linear correlations were found between temperature and Sr/Ca and $\delta^{18}O$ in both corals, and Ba/Ca in *A. digitifera* only, none showing a correlation with calcification rate. The authors conclude that both corals are promising targets for paleotemperature studies. Conversely, U/Ca showed a negative linear correlation with calcification rate in *A. digitifera*, but no consistent dependence on temperature. No correlation with either temperature or calcification was found for Mg/Ca and $\delta^{13}C$.

In two papers, existing proxies are applied to samples from the distant past. Ichimura et al. obtained $\delta^{18}O$ records of well-preserved fossil aragonite bivalves from the mid-latitude paleo-Pacific to investigate SST seasonality during the middle Cretaceous "supergreenhouse" climate. Assuming an invariant Cretaceous $\delta^{18}O_{SW}$ value of −1‰ (*vs.* VSMOW), the $\delta^{18}O_{shell}$ records of two species reflect temperatures of 28–35°C with a seasonal range of 7°C. These are higher than in modern mid-latitudes (e.g., 4.8–22.1°C) but with smaller seasonality, more similar to modern subtropical conditions and consistent with an ice-free Arctic and the existence of the Bering Land Bridge at that time. Jacobi et al. reconstructed SST from shallow and deeper dwelling species of planktonic foraminifera in a unique core from a North Pacific seamount above the carbonate compensation depth, to derive the position of the subarctic front (SAF) into the Pleistocene (600 ka BP). Calcite $\delta^{18}O$ and Mg/Ca reveal a sudden shift to colder SST around 280 ka BP, suggesting a southward SAF displacement that appears to be driven by a transition from sustained La Niña to El Niño-like conditions in the Pacific. Productivity, on the other hand, represented by sediment Ba/Ti ratios and by sediment Fe constraining dust input, appears to be driven by variations related to glacial–interglacial cycles.

Finally, Saenger et al. use a pseudo-proxy modeling approach, based on a large ensemble of linear inverse models, to determine whether SST distributions derived from Individual Foraminifera Analysis (IFA) is a potential proxy for Marine Heat Wave (MHW) events. With a bootstrapping algorithm, the model evaluates which MHW metric appears the most promising and then assesses what IFA sample size would be necessary to achieve a specific level of uncertainty for the MHW reconstruction, given the sedimentation rate. A case study for the Northeast Pacific indicates that cumulative MHW metrics with a 1σ threshold and 1-month duration yield the strongest transfer functions, independent of species, but that only sites with extremely high sedimentation rates allow MHW events to be predicted with uncertainties <20% for typical IFA sample sizes of 100–200 foraminifera.

We hope that readers of this RT will enjoy these papers and find inspiration for equally innovative research.

Author contributions

JS: Writing – original draft. EH: Writing – review & editing. KK: Writing – review & editing. TW: Writing – review & editing.

Acknowledgments

We are grateful to all authors and reviewers for their efforts and forbearance, and to Emily Keynton and Yunyi Zhou for logistical support. We particularly thank Lara Jacobi and co-authors for kindly agreeing to have their published paper transferred to our Research Topic. This is UMCES contribution #6396.

Conflict of interest

The authors declare that the research was conducted in the absence of any commercial or financial relationships that could be construed as a potential conflict of interest.

The author(s) declared that they were an editorial board member of Frontiers, at the time of submission. This had no impact on the peer review process and the final decision.

Publisher's note

frontiers | Frontiers in Marine Science

TYPE Original Research
PUBLISHED 30 March 2023
DOI 10.3389/fmars.2023.1074431

OPEN ACCESS

EDITED BY
Ludvig Löwemark,
National Taiwan University, Taiwan

REVIEWED BY
Li Lo,
National Taiwan University, Taiwan
Jeroen Groeneveld,
National Taiwan University, Taiwan

*CORRESPONDENCE
Lara Jacobi
ljacobi@geomar.de

SPECIALTY SECTION
This article was submitted to Marine Biogeochemistry, a section of the journal Frontiers in Marine Science

RECEIVED 19 October 2022
ACCEPTED 13 March 2023
PUBLISHED 30 March 2023

CITATION
Jacobi L, Nürnberg D, Chao W-s, Lembke-Jene L and Tiedemann R (2023) ENSO *vs* glacial-interglacial-induced changes in the Kuroshio-Oyashio transition zone during the Pleistocene. *Front. Mar. Sci.* 10:1074431. doi: 10.3389/fmars.2023.1074431

ENSO *vs* glacial-interglacial-induced changes in the Kuroshio-Oyashio transition zone during the Pleistocene

Lara Jacobi[1]*, Dirk Nürnberg[1], Weng-si Chao[2], Lester Lembke-Jene[2] and Ralf Tiedemann[2]

[1]GEOMAR, Helmholtz Centre for Ocean Research Kiel, Kiel, Germany, [2]Alfred-Wegner-Institute - Helmholtz Centre for Polar and Marine Research, Bremerhaven, Germany

The subarctic front (SAF) in the pelagic North Pacific is the northernmost front of the Kuroshio-Oyashio transition zone separating the subpolar and subtropical gyres and is marked by a strong sea surface temperature gradient. A complex interplay of e.g. variations of currents, the wind system and other forcing mechanisms causes shifts of the SAF's position on timescales from orbital to interannual. In this study, we present proxy data from the Emperor Seamount chain, which reveal a link between long-term ENSO (El Niño/Southern Oscillation) dynamics in the tropics and shifts of the SAF. Based on sediment core SO264-45-2 from Jimmu Seamount (46°33.792'N, 169°36.072'E) located close to the modern position of the SAF, we reconstruct changes in (sub)surface temperature ((sub)$SST_{Mg/Ca}$) and $\delta^{18}O_{sw\text{-}ivc}$ (approximating salinities) *via* combined Mg/Ca and $\delta^{18}O$ analyses of the shallow-dwelling foraminifera *Globigerina bulloides* and the near-thermocline-dwelling *Neogloboquadrina pachyderma*, biological productivity (XRF-based Ba/Ti ratios), and terrigenous input *via* dust (XRF-based Fe). From ~600 to ~280 ka BP we observe significantly higher $SST_{Mg/Ca}$ than after an abrupt change at 280 ka BP. We assume that during this time warmer water from the Kuroshio-Oyashio transition zone reached the core site, reflecting a shift of the SAF from a position at or even north of our study site prior to 280 ka BP to a position south of our study site after 280 ka BP. We propose that such a northward displacement of the SAF between 600-280 ka BP was induced by sustained La Niña-like conditions, which led to increased transport of tropical ocean heat into the Kuroshio-Oyashio transition zone *via* the Kuroshio Current. After ~280 ka BP, the change to more El Niño-like conditions led to less heat transfer *via* the Kuroshio Current with the SAF remaining south of the core location. In contrast, our productivity record shows a clear glacial-interglacial pattern that is common in the North Pacific. We assume that this pattern is connected to changes in nutrient supply or utilization, which are not primarily driven by changes of the Kuroshio and Oyashio Currents or the SAF.

KEYWORDS

foraminiferal geochemistry, North Pacific, Kuroshio Current, Mg/Ca SSTs, Emperor Seamount chain, subarctic front (SAF), Ba/Ti ratio

1 Introduction

The Kuroshio Current, as the northern boundary of the subtropical gyre, and the Oyashio Current, as the southern boundary of the subpolar gyre, are of significant importance for the midlatitude pelagic North Pacific (Qiu, 2019). The area between the two Currents is named the Kuroshio-Oyashio transition zone and is marked by several fronts (Figure 1). For example, the subarctic front (SAF), located close to our study site, is the northernmost front in the Kuroshio-Oyashio transition zone. Shifts of the Kuroshio and Oyashio Currents and their mixing zones have significantly affected oceanographic conditions in the North Pacific on various time scales and influence the global climate as the Kuroshio-Oyashio transition zone acts as a sink for atmospheric CO_2 (Thompson and Shackleton, 1980; Hovan et al., 1991; Kawahata et al., 2000; Yamane, 2003; Ogawa et al., 2006; Takahashi et al., 2009; Ayers and Lozier, 2012; Chiyonobu et al., 2012). Yet the timing and the causes of such shifts in the frontal system are still a matter of debate.

Some authors suggest a connection between shifts of the oceanic fronts in the North Pacific and climate changes related to glacial-interglacial cycles (Thompson and Shackleton, 1980; Kawahata and Ohshima, 2002; Harada et al., 2004; Yasudomi et al., 2014; Gallagher et al., 2015), others hypothesize a connection between El Niño-Southern Oscillation (ENSO), the Kuroshio strength and the positioning of the front system (Yamane, 2003; Chen et al., 2007). While ENSO is commonly known as the interannual oscillation between "El Niño" and "La Niña" phases, several authors suggest that there are also changes from more La Niña-like to more El Niño-like conditions on longer time scales (de Garidel-Thoron et al., 2005; Wara et al., 2005; Zheng et al., 2016; Jia et al., 2018). These authors use the paleotemperature gradient between the West Pacific Warm Pool (WPWP) and the Eastern Equatorial Pacific (EEP) ($\Delta T_{WPWP\text{-}EEP}$) as an indicator for ENSO on geological time scales. During more El Niño-like phases, there is a weak temperature gradient, whereas, during more La Niña-like phases, there is an amplified $\Delta T_{WPWP\text{-}EEP}$ (de Garidel-Thoron et al., 2005; Wara et al., 2005; Zheng et al., 2016; Jia et al., 2018). Further, the path and strength of both the Kuroshio and Oyashio Currents are affected by changes in the wind system, e.g., the westerlies or the East Asian Monsoon (Yatsu et al., 2013).

The investigation of upper ocean hydrography, particularly sea surface temperature (SST), is promising for gaining further insights into shifts of the Kuroshio-Oyashio transition zone and its frontal systems. However, in the pelagic North Pacific, variations of SSTs have little been studied beyond the availability of observational data mainly because proxy records are sparse, especially over longer time scales, beyond the last glacial (Lohmann et al., 2019; Zhong et al., 2023). One of the main causes is the limited availability of carbonate-bearing sediment records. These are restricted to, e.g., seamount areas, where the water depth does not exceed the depth of the calcite compensation depth, which lies at about ~4000 m in the open North Pacific (Chen et al., 2021). This constrains the use of foraminiferal calcite as signal carrier for paleo proxies. Our study

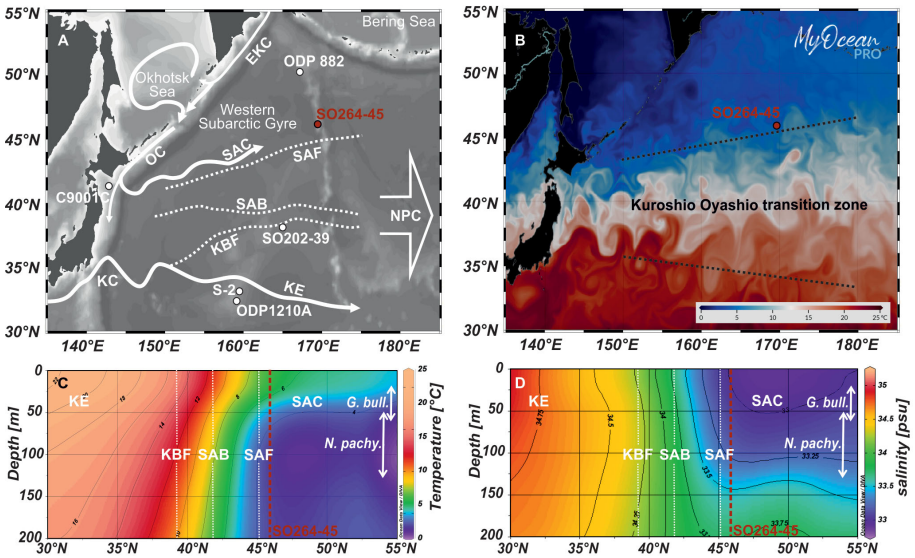

FIGURE 1
Sea surface and subsurface hydrology of the North West Pacific. **(A)** Bathymetric map indicating the locations of the study site SO264-45 and reference cores ODP Site 882 (Jaccard et al., 2010), SO202-39 (Korff et al., 2016), ODP Site 1210A (Chiyonobu et al., 2012), S-2 (Yamane, 2003), and C9001C (Matsuzaki et al., 2014). The surface current and water-mass structure in the Kuroshio-Oyashio transition area is schematically illustrated: EKC, East Kamchatka Current; KC, Kuroshio Current; KE, Kuroshio Extension; NPC, North Pacific Current; OC, Oyashio Current; SAC, Subarctic Current; KBF, Kuroshio Bifurcation Front; SAB, Subarctic Boundary; SAF, Subarctic Front. **(B)** Potential sea surface temperature of the North West Pacific from early summer 2021. The Oyashio-Kuroshio transition zone is characterized by large eddies. This figure was generated using EU Copernicus Marine Service Information with data from GLOBAL_ANALYSIS_FORECAST_PHY_001_024 (Zammit-Mangion and Wikle, 2020). **(C, D)** North-south-oriented annual temperature and salinity transects along 170°E illustrated with Ocean Data View (Schlitzer, 2019) based on data from the World Ocean Atlas 2018 (Locarnini et al., 2018; Zweng et al., 2019). The position of fronts are marked by white dotted lines; the core position by a red dotted line and depth habitats of *G. bulloides* and *N. pachyderma* by white arrows.

site, however, is located on Jimmu Seamount (water depth< 2500 m) right beneath the modern position of the SAF (Figure 1) and thus provides the rare opportunity to use foraminiferal calcite as a proxy for the reconstruction of changes in SST and $\delta^{18}O$ of seawater.

The SST variability in the mid-latitude North Pacific is dominated by the Pacific Decadal Oscillation (PDO; Mantua et al., 1997). It describes the variability between periods of warm or cool surface waters and is a highly complex system combining various forcing factors. According to Newman et al. (2016), these include: (1) changes in ocean surface heat fluxes and Ekman (wind-driven) transport related to the Aleutian low due to both local, rapidly decorrelating, unpredictable weather noise and to remote forcing from interannual to decadal tropical variability (largely El Nino) *via* the "atmospheric bridge"; (2) ocean memory, or processes determining oceanic thermal inertia including "re-emergence" and oceanic Rossby waves, that act to integrate this forcing and thus generate added PDO variability on decadal time scales; and (3) decadal changes in the Kuroshio-Oyashio current system forced by the multi-year history of basin-wide Ekman pumping, manifested as SST anomalies along the subarctic front at about 40°N in the western Pacific ocean. The whole complexity of the PDO is not yet entirely understood. Thus, it is heavily discussed in ongoing research within the meteorological and climate dynamics communities, and attempts for paleo studies on the PDO reaching back further than 500 years are rare (e.g., MacDonald and Case, 2005; Yu et al., 2015; Johnson et al., 2020; Li et al., 2020; Choi and Son, 2022). Since much of the PDO represents the oceanic response to atmospheric forcing, it is difficult to consider the PDO as a forcing function itself (Newman et al., 2016).

To further identify the influence of shifts in the frontal system on primary productivity, we also consider representative XRF-based proxy data. In the North Pacific, primary productivity is mainly described to be linked to glacial-interglacial cycles, with higher productivity during interglacials and lower productivity during glacials (Narita et al., 2002; Gorbarenko et al., 2004; Kienast et al., 2004; Jaccard et al., 2005; Brunelle et al., 2007; Shigemitsu et al., 2007; Galbraith et al., 2008; Gebhardt et al., 2008; Jaccard et al., 2010; Riethdorf et al., 2013). However, the driving mechanisms for changes in productivity over longer time scales are not yet entirely understood. For example, to what extent the productivity was influenced by the complex interplay of atmosphere and ocean and their respective circulation patterns dependent on, e.g., sea ice formation, light limitation, wind strength, nutrient supply, and stratification (Haug and Sigman, 2009; Jaccard et al., 2010; Sigman et al., 2010; Sigman et al., 2021); Kawahata et al., 2000; Matsumoto et al., 2002; Brunelle et al., 2007; Shigemitsu et al., 2007; Jaccard et al., 2010; Nishioka et al., 2011; Costa et al., 2018; Sigman et al., 2021).

Thus, our new dataset on upper ocean temperatures (based on foraminiferal Mg/Ca), marine productivity (XRF-based Ba/Ti), and terrigenous input *via* wind (XRF-based Fe) from the pelagic North Pacific provide a unique opportunity to gain further insights into upper ocean dynamics, primarily spatial and temporal shifts of the Kuroshio-Oyashio frontal systems and a possible link to productivity over the past 650 ka.

1.1 Oceanographic setting

The North Pacific is characterized by two large-scale wind-driven gyre systems: the cyclonic Subarctic Gyre in the north and the anticyclonic Subtropical Gyre in the south (Huang, 2015). The Subarctic Gyre has a strong western boundary current. The Oyashio Current originates from the East Kamchatka Current and is further fed by cold, low saline nutrient-rich water from the Okhotsk Sea. Close to the coast of northern Japan the Oyashio Current has an annual mean temperature of ~5°C and a salinity of ~33 (Locarnini et al., 2018; Zweng et al., 2019). At ~42°N the Oyashio Current splits and one path continues as the northeastward flowing Subarctic Current (SAC) (Qiu, 2019). The western limb of the North Pacific Subtropical Gyre is also formed by a strong western boundary current. The Kuroshio Current originates from the warm, saline North Equatorial Current (NEC) and transports oceanic heat from the WPWP to the northern regions (Figure 1). The location where the North Equatorial Current (NEC) bifurcates into the Kuroshio Current and the Mindanao Current (Metzger and Hurlburt, 1996; Qiu and Lukas, 1996; Ujiié et al., 2003) is located at ~15.5°N for the annual average, but varies with time and depth. The meridional migration of the NEC bifurcation is strongly influenced by ENSO (Kim et al., 2004), which is the main driver of upper ocean circulation in the tropical Pacific, (Hu et al., 2015; Joh and Di Lorenzo, 2019). In El Niño years the NEC's bifurcation point migrates to the north and the Kuroshio velocity and volume transport decrease. During La Niña years, in contrast, the NEC's bifurcation migrates to the south and the Kuroshio velocity and volume transport increase (Qiu and Lukas, 1996; Yuan et al., 2001; Kim et al., 2004). Close to the coast of southern Japan, the Kuroshio Current has an annual mean temperature of ~19°C and a salinity of ~35 (Locarnini et al., 2018; Zweng et al., 2019). After separating from the Japanese coast at ~35°N, the Kuroshio Current enters the open basin of the North Pacific and continues as Kuroshio Extension (Qiu, 2002). At Shatsky Rise (~159°E), the Kuroshio Extension bifurcates, where the main body of the Kuroshio Extension continues eastward. A secondary branch, the Kuroshio Bifurcation Front (KBF), extends northwards (Qiu, 2002).

Along the northern boundary of the Kuroshio Extension/ Kuroshio Bifurcation Front, numerous meanders and mesoscale eddies occur (Figure 1) due to the dia- and isopycnal mixing between Kuroshio and Oyashio water with vertically different temperature, salinity and velocity structures (Yasuda et al., 1996; Shimizu et al., 2001; Yasuda et al., 2002; Isoguchi et al., 2006; Mitnik et al., 2020). This mixing zone of water originating from the Kuroshio and Oyashio currents is termed the Kuroshio-Oyashio transition zone or mixed water region and is characterized by a pronounced latitudinal sea surface temperature, salinity, and nutrient gradient (Yasuda, 2003; Garcia et al., 2018; Locarnini et al., 2018; Zweng et al., 2019) (Figure 1). The northern end of the transitional zone is marked by the Subarctic Front (SAF) or Oyashio Front, which is defined as the 4°C isotherm at 100 m depth (Favorite, 1976). Subarctic surface water may drift southward across the SAF, and may cover the surface in the transition zone between

the SAF and the Subarctic Boundary (SAB). The SAB is a near surface salinity front south of the SAF (Yasuda, 2003). East of 180°W/E the distinction between the Kuroshio Extension and the Subarctic Current is no longer clear and together they form the broad eastward-moving North Pacific Current (Qiu, 2019). It has been suggested, that there is a linkage between the latitudinal displacement of the Kuroshio-Oyashio transition zone and the climatic conditions of the tropical Pacific e.g. long term ENSO-like variability (Yamamoto et al., 2005).

Intermediate water masses (~400-900 m) are dominated by North Pacific Intermediate Water (NPIW) in the Subtropical Gyre and the mixed water region (Talley, 1993), and by Pacific Subpolar Intermediate Water (PSIW) in the subarctic Gyre (Emery, 2001; Fuhr et al., 2021).

2 Material and methods

The 8.35 m long gravity core SO264-45-2 was recovered from Jimmu Seamount at 46°33.792'N and 169°36.072'E from a water depth of 2425 m during R/V SONNE cruise SO264 (SONNE-EMPEROR) in August 2018 (Nürnberg, 2018). Additionally, the sediment surface was sampled with a Multi Corer (MUC: SO264-45-1, core length: 0.15 m; 46°33.795'N and 169°36.072'E). The core site selection was based on a systematic bathymetric survey, as well as sediment echosounder profiling. The upper 4.7 m of the core presented in this study consist of foraminifera-bearing sandy silt to foraminifera-bearing calcareous ooze, in some parts containing IRD (Nürnberg, 2018) and intercalated by five tephra layers of 2-6 cm width (Figure 2).

2.1 XRF scanning

To determine the sedimentary elemental composition, the archive half of each core segment was scanned using an Avaatech X-ray Fluorescence (XRF) core scanner at the Alfred-Wegener-Institute (AWI) Bremerhaven. For preparation, the uppermost sediment layer was removed to provide a fresh and undisturbed surface, which was then covered with SPEXCerti Prep Ultralene foil. Each core segment was triple scanned at a one-centimeter resolution with a current of 0.15, 0.175 and 1 mA, tube voltages of 10, 30, and 50 kV, and acquisition times of 10, 15, and 20 sec, respectively. Element intensities were determined with the proprietory Aavatech WinAxil (Batch) software covering elements from aluminum to barium and are reported as counts per second (cps). As proxy for changes in paleoproductivity we use the barium/titanium ratio (Ba/Ti) (biogenic barium reflecting diatom productivity; e.g. Nürnberg et al., 1997). Based on the assumption that the covariance between aluminum (Al) and Ti content of terrigenous material remained constant in space and time (Galbraith et al., 2007), the XRF-derived barium counts normalized against terrigenous background elements like Al or Ti are well-established paleoproductivity proxies in the North Pacific area (Nürnberg et al., 2004; Jaccard et al., 2010; Korff et al., 2016). Al and Ti are both exclusively of detrital origin and correlate well at our study site (Supplementary Figure 6). Yet the detection of light elements like Al during XRF scanning shows a higher risk to be influenced by water trapped between the sediment and the scanning foil than heavier elements (Tjallingii et al., 2007). Thus, we use Ti for normalizing our Ba record.

Fe has been widely used to document variations in terrigenous sediment delivery and often relates to aeolian dust flux and thus wind strength (Jahn et al., 2003; Nürnberg et al., 2004; Jahn et al., 2005; Mohtadi et al., 2007; Helmke et al., 2008; Kaiser et al., 2008; Lamy et al., 2014; Abell et al., 2021). Therefore, we use the iron (Fe) record derived *via* XRF scanning as proxy for relative changes in terrigenous Fe input. Because the use of raw intensities or peak integrals of single element counts cannot be interpreted in terms of sediment composition we report our Fe-record as log-values (Weltje et al., 2008). The very good correlation of our Ti and Fe records (R^2=0.98) (Supplementary Figure 6) implies that a potential diagenetic imprint on Fe is negligible (Croudace and Rothwell, 2015).

2.2 Foraminiferal geochemistry

For geochemical studies, we use the most abundant planktic foraminiferal species foraminifera *Globigerina bulloides* (*G. bulloides*) and *Neogloboquadrina pachyderma* (*N. pachyderma*) (sinistral-coiling, Darling et al., 2006). In the Northwest Pacific, *G. bulloides* is a near-surface dweller and mainly found above the thermocline (Iwasaki et al., 2017; Schiebel et al., 2017; Taylor et al., 2018), which occurs at ~40-50 m at the study site (Locarnini et al., 2018) (Figure 1 and Supplementary Figure 1). In the study region, *G. bulloides* calcifies throughout the year (Kuroyanagi et al., 2008; Sagawa et al., 2013; Taylor et al., 2018). In the North Pacific, *N. pachyderma* is mainly found at thermocline depth (Sarnthein et al., 2004; Riethdorf, 2013; Taylor et al., 2018), thus, we assume a depth habitat of 50-130 m for our study site (Locarnini et al., 2018). *N. pachyderma* is a subpolar species and prefers water temperatures below 7°C (Reynolds and Thunell, 1986), thus in modern settings it mainly occurs from autumn to spring at our study site, which is shown by sediment trap studies from the North Pacific (Kuroyanagi et al., 2008; Sagawa et al., 2013; Taylor et al., 2018). For a detailed discussion about seasonality and habitat depth, see Supplement 1.

2.2.1 Magnesium and calcium element ratios

Mostly, ~50 visually well-preserved specimens of *G. bulloides and* ~120 of *N. pachyderma* were selected from core SO264-45-2 at 2 cm sample spacing. Due to insufficient sample material in most of the samples, specimens were selected from a rather wide size range (*G. bulloides*: 250 – 400 µm; *N. pachyderma:* 125-315 µm; potential side effects on Mg/Ca ratios are discussed in the Supplement 1). Tests were gently crushed between cleaned glass plates to open the test chambers for efficient cleaning. Chamber fillings e.g. sediment or pyrite particles were removed. The fragmented and homogenized samples were divided into one-third for stable isotope analyses and two-thirds for trace element measurements.

Cleaning of foraminiferal fragments prior to trace element analyses followed the procedures of Boyle and Keigwin (1985) and Boyle and Rosenthal (1996). These include oxidative and

reductive (with hydrazine) cleaning steps to e.g. remove oxide-rich coatings which may influence the Mg/Ca values (see Supplement 3). Samples were measured at GEOMAR - Helmholtz Centre for Ocean Research, on a VARIAN 720 ES axial ICP-OES coupled with a VARIAN SPS3 sample preparation system. The measurement strategy included regular analyses of standards and blanks to ensure analytical quality control. The data was drift-corrected and standardized to the internal consistency standard BCS-DRM 393 (ECRM 752-1) with an Mg/Ca reference value of 3.761 mmol/mol (Greaves et al., 2008). The long-term external reproducibility for the ECRM standard for Mg/Ca is ± 0.1 mmol/mol (2σ).

To monitor contamination and insufficient removal of siliciclastic material during the cleaning procedure, Al/Ca, Mn/Ca and Fe/Ca ratios were measured alongside the Mg/Ca. By assessing this data, we could not find any evidence of an influence of contamination on our Mg/Ca ratios. A detailed discussion can be found in the supporting information (Supplement 3). In addition, statistical Mg/Ca outliers were identified by applying the 1.5 interquartile method after Tukey (1977) (Supplement 3) and the two identified samples were remeasured.

2.2.2 Stable oxygen isotopes

In addition to the planktic foraminiferal species (*G. bulloides*: 250 – 400 µm; *N. pachyderma:* 125-315 µm), 3-5 tests of the benthic foraminiferal species *Uvigerina* spp. and *Cibicidoides wuellerstorfi* were selected from the size fraction 315-400 µm for oxygen isotope measurements. Planktic and benthic specimen were measured on a Thermo Fischer Scientific MAT 253 mass spectrometer equipped with an automated Kiel IV carbonate preparation device. Isotope values were calibrated to NBS-19 (National Bureau of Standards) and reported relative to the Vienna Pee Dee Belemnite (VPDB) standard. The long-term external reproducibility (n =<3,000) was monitored by the in-house Bremen standard (Solnhofen Limestone) with an analytic precision of 0.06 ‰ for $\delta^{18}O$. Applying the 1.5 interquartile method after Tukey (1977) the $\delta^{18}O$ records of both the planktic and benthic foraminifera were checked for outliers (Supplement 3).

In order to combine the $\delta^{18}O$-values of both benthic species, we follow the conventional assumption that *Uvigerina* spp. calcifies in equilibrium with surrounding seawater $\delta^{18}O$ (Shackleton, 1974; Shackleton and Hall, 1984; Labeyrie et al., 1999; Fontanier et al., 2006) and that *C. wuellerstorfi* deviates by ~0.64 ‰ from *Uvigerina* values (Shackleton and Opdyke, 1973; Labeyrie et al., 1999; Waddell et al., 2009). We hence corrected $\delta^{18}O_{C.\ wuellerstorfi}$ by adding 0.64 ‰.

2.3 Upper ocean temperature and ice volume corrected $\delta^{18}O$ seawater assessment based on foraminiferal Mg/Ca and $\delta^{18}O$

For converting Mg/Ca of foraminiferal calcite into water temperature we used well-established species-specific equations from Elderfield and Ganssen (2000) for *G. bulloides* ($Mg/Ca=0.56e^{(0.10*T)}$) and from Kozdon et al. (2009) for *N. pachyderma* ($Mg/Ca=0.13*T+0.35$) (Supplement 2). The temperature derived from *G. bulloides* is referred to as annual sea surface temperature ($SST_{Mg/Ca}$: ~20-60 m) and the temperature from *N. pachyderma* as subsurface temperature ($subSST_{Mg/Ca}$: ~50-130 m). Late Holocene temperatures of both species match the modern annual mean temperatures in the defined depth habitats (Locarnini et al., 2018; Supplementary Figure 1). For our interpretations, we assume that the foraminiferal species did not significantly change their habitat depth over time.

We are aware that changes in pH and salinity of the surrounding seawater, calcite dissolution and diagenetic effects can influence foraminiferal Mg/Ca, and hence the reconstructed absolute temperature values. Yet, we assume that these effects are either neglectable for our interpretation or lie within the assigned error range. A detailed discussion can be found in the Supplement 2–4.

Via the combined $\delta^{18}O$ and Mg/Ca measurement of the foraminiferal calcite, we calculate the $\delta^{18}O$ of seawater ($\delta^{18}O_{sw}$) by removing the temperature effect from the initial foraminiferal $\delta^{18}O$ signal. For *G. bulloides* we use the equation from Shackleton (1974) ($T=16.9-4.38*(\delta^{18}O_{calcite}-\delta^{18}O_{sw})+0.1*(\delta^{18}O_{calcite}-\delta^{18}O_{sw})^2$) and for *N. pachyderma* the species-specific equation from Mulitza et al. (2003) ($T=3.55*(\delta^{18}O_{calcite}-\delta^{18}O_{sw})+12.69$). The $\delta^{18}O_{sw}$ data is further corrected for changes in global ice volume ($\delta^{18}O_{sw\text{-}ivc}$ reported in ‰ versus SMOW; ivc = ice-volume corrected) by using a data set from De Boer et al. (2014). This was calculated based on the global LR04 stack (Lisiecki and Raymo, 2005) and simulations of continental ice sheets (De Boer et al., 2014). Modern $\delta^{18}O_{sw}$ is positively correlated to salinity (e.g. $\delta^{18}O_{sw} = 0.44*S-15.13$; LeGrande and Schmidt, 2006), yet previous studies have shown that this relationship can vary over time e.g. through changes in regional freshwater budgets, ocean circulation, and sea ice regimes (Caley and Roche, 2015; Holloway et al., 2016). Therefore, we refrain from converting the calculated $\delta^{18}O_{sw\text{-}ivc}$ into absolute salinity units. However, we interpret high values in terms of relative high saline conditions and low values in terms of relative freshening. We present $\delta^{18}O_{sw\text{-}ivc}$ as relative changes deviating from the calculated modern value.

2.4 Chronostratigraphy

Accelerated mass spectrometer radiocarbon ($AMS^{14}C$) dating provides an age estimation for the sediment surface (0–1 cm) from station SO264-45-1 (MUC). We chose the undisturbed surface sample of the MUC for this measurement, because the surface of gravity cores is often disturbed during core recovery. Approximately 90 µg C of the planktic species *G. bulloides* and the benthic species *Uvigerina peregrina* were measured at the MICADAS (Mini Carbon Dating System) facility at the AWI in Bremerhaven, Germany (AWI sample nr. 3976.1.1 and 3976.2.1). The raw ^{14}C age was converted into calendar age, using the Calib8.20 software (Stuiver et al., 2020) along with the marine calibration dataset MARINE20 (Heaton et al., 2020) and a regional reservoir age correction of ΔR = 273 +- 70 years. In this case, ΔR is the mean reservoir age of six sites from the North Pacific published by Kuzmin et al. (2001; 2007) and Yoneda et al. (2007). The

generated AMS^{14}C age range (2 sigma) for *U. peregrina* is 263-745 years BP and 1871-1301 years BP for *G. bulloides*. This age difference lies within the age range for one sample (~1500 years/sample) as discussed below.

As benthic foraminiferal $\delta^{18}O$ values from the MUC SO264-45-1 fit rather well to those of the uppermost centimeters of the gravity core SO264-45-2 (Figure 2), it is likely that both have similar surface ages. Thus, based on the ^{14}C ages from the MUC's surface we assume that the gravity core top sediments are of late Holocene age.

The stacked benthic $\delta^{18}O$ isotope record of SO264-45-2 was visually correlated to the global benthic isotope stack LR04 (Lisiecki and Raymo, 2005) by using QAnalySeries v1.5.0 (Kotov et al., 2018). Our benthic record shows smaller amplitudes than LR04, which is most likely caused by low sedimentation rates, which mute extreme values. By applying 21 tie lines and linear interpolation between the tie lines, a correlation coefficient of r = 0.82 was achieved. Further support for the age model is provided by the spectral analysis of the benthic $\delta^{18}O$ stack that reveals dominant cyclicities with a frequency of 0.01 and 0.025 as a response to the cyclic fluctuations in the Earth's orbital parameters eccentricity and obliquity (Figure 2). The spectral analysis reveals that all obliquity cycles of the past 650 ka are reflected in our benthic $\delta^{18}O$ stack. The calculated sedimentation rates are rather low with an average of 0.66 cm/ka for the discussed interval, thus one sample of 1 cm width reflects on average ~1500 years. Yet due to the observed bioturbation of the sediment (Nürnberg, 2018), the absolute age range of foraminifera in one sample might even be higher.

The ages of five tephra layers mentioned in the core description (Nürnberg, 2018) are shown in Figure 2. We assume that T4 might be the prominent Pauzhetka ash found in several records from the Northwest Pacific and Okhotsk Sea and dated to 421.2 ± 6.6 ka BP (Ponomareva et al., 2018). Yet according to our age model, the depth of T4 refers to an age of ~390 ka BP, which is likely within the range of dating uncertainty.

3 Results

3.1 Reconstruction (sub)$SST_{Mg/Ca}$ and $\delta^{18}O_{sw\text{-}ivc}$

Over the last ~650 ka BP, $\delta^{18}O$ values of *G. bulloides* fluctuate between 1.5 and 4 ‰, and those of *N. pachyderma* between 2.4 and 3.8 ‰ (Figure 3). With only few exceptions in MIS 6-8 the $\delta^{18}O$ of *N. pachyderma* are consistently heavier than those of *G. bulloides*. The $\delta^{18}O$ fluctuations of both species follow the glacial-interglacial pattern of the LR04 reference record (Lisiecki and Raymo, 2005) with heavy $\delta^{18}O$ values during glacials and light $\delta^{18}O$ values during interglacials (Figure 3). In MIS 11, however, *G. bulloides* shows lighter $\delta^{18}O$ values than in the adjacent interglacials. In MIS 7, the $\delta^{18}O$ are not light throughout the entire interglacial, yet decrease steadily. $\delta^{18}O$ of *G. bulloides* is lightest in MIS 15 and 13 compared to the other interglacials in our record, while the $\delta^{18}O$ of LR04 is heavier in MIS 15 and 13 compared to the other interglacials.

Mg/Ca ratios from *G. bulloides* vary between 0.82 and 2 mmol/mol, which leads to $SST_{Mg/Ca}$ estimates between 3.8 and 12.7°C. The $SST_{Mg/Ca}$ development of *G. bulloides* can be divided into two phases (Figures 3, 4). Between ~600 and 280 ka BP (phase B), the surface ocean temporally reached $SST_{Mg/Ca}$ of up to ~12°C (with a mean of 8.7°C), thereby being up to ~6.5°C warmer than modern annual mean SST at 30 m (Figure 3). Within this time interval, the $SST_{Mg/Ca}$ broadly follow glacial-interglacial cycles except for MIS 10, during which the $SST_{Mg/Ca}$ is high (~10°C) throughout the glacial and MIS 11, where temperatures are ~2°C lower than in the adjacent glacials. In contrast to the cold MIS 16 (min ~ 7°C), MIS 14 remains rather warm with minimum temperatures of ~9.5°C. At 480 ka BP, the $SST_{Mg/Ca}$ abruptly decreases by ~4°C (calculated as the temperature difference between three data points prior and after the decrease; the decrease itself occurs between two data points) coming close to the modern-day SST value (Figure 3). This decrease is followed by an overall increasing $SST_{Mg/Ca}$ trend for the next 200 kyrs. Phase B ends at ~ 280 ka BP after a second abrupt $SST_{Mg/Ca}$ decrease of ~3.5°C (calculated as the temperature difference between three data points prior and after the decrease; the decrease itself occurs between two data points). From here on (phase A) the $SST_{Mg/Ca}$ remain rather low with an average of ~ 6.1°C and show only minor variations (max ±2°C) around the modern annual mean temperature at 30 m of ~5.5°C (Locarnini et al., 2018). The warmest $SST_{Mg/Ca}$ occur at the beginning and end of MIS 5 and in MIS 2, while in the middle of MIS 7 and 6 the $SST_{Mg/Ca}$ are coldest.

N. pachyderma shows consistently lower Mg/Ca ratios than *G. bulloides*, which vary between 0.41 and 1.14 mmol/mol with $subSST_{Mg/Ca}$ estimates between 0.5 and 6.1°C (Figure 3). Throughout the entire record, the $subSST_{Mg/Ca}$ show amplitude variations of ±3°C around an average of ~2.9°C. This average matches the modern annual temperature at thermocline depth of ~3°C (Locarnini et al., 2018). The highest $subSST_{Mg/Ca}$ of up to ~6°C is reached at the transition to the Holocene and the lowest with ~0.5°C during MIS 12. In contrast to the $SST_{Mg/Ca}$ the $subSST_{Mg/Ca}$ do not show a shift towards warmer temperatures prior to 280 ka BP, yet rather cold subsurface conditions between MIS 13 and MIS 10. From MIS 5 to MIS 1 $subSST_{Mg/Ca}$ and $SST_{Mg/Ca}$ follow a similar low-amplitude pattern.

The $\delta^{18}O_{sw\text{-}ivc}$ records reveal a different pattern than the $SST_{Mg/Ca}$ and $subSST_{Mg/Ca}$ records (Figure 3). Both, the seasurface and subsurface $\delta^{18}O_{sw\text{-}ivc}$ records have rather similar amplitudes and fluctuations. Between ~650 and 350 ka BP *G. bulloides* shows constantly higher $\delta^{18}O_{sw\text{-}ivc}$ values than *N. pachyderma*. Between 0 and ~350 ka BP, however, both records lie within error range of each other and alternately show higher values. Prior to 280 ka BP the $\delta^{18}O_{sw\text{-}ivc}$ records of both species tend to be higher in interglacials and lower in glacials.

3.2 Productivity and terrigenous input

The XRF-based Ba/Ti record and thus the reflection of marine productivity shows a clear glacial-interglacial cyclicity. Ba/Ti values start to increase during the deglaciations and reach their maxima during the early interglacials (Figure 4). During the late interglacials and the subsequent early glacials low Ba/Ti values predominate. This pattern even holds for the period MIS 15-14, although the Ba/

Ti ratios remain on an exceptionally high level during glacial MIS 14, which even exceeds typical deglacial to early interglacial values. The deglaciation towards MIS 13 is again characterized by a continuous increase in Ba/Ti. In the late interglacial MIS 13 (~500-480 ka BP), we observe a rapid and significant decrease in Ba/Ti to typical glacial values, synchronous to significant changes in Fe and $SST_{Mg/Ca}$ (Figure 4).

The XRF-based normalized log Fe record, which is used as a proxy for terrigenous input commonly increases at the transitions from late interglacials to early glacials and decreases during the glacials. Prior to MIS 12, no distinct glacial-interglacial pattern is recognizable. Between ~560 and ~500 ka BP, Fe values are exceptionally low, which is followed by a sudden increase from ~500-480 ka BP (Figure 4). Ba/Ti and Fe appear to be anticorrelated with low Fe values in times of high Ba/Ti and vice versa. Thus, between MIS 13 and 5 Ba/Ti maxima occur on average ~30 ka earlier than Fe maxima.

4 Discussion

4.1 Influence of changes in the Kuroshio/Oyashio current system on upper ocean temperatures at Jimmu Seamount

At the study site, glacial-interglacial changes are well documented in the benthic and planktic $\delta^{18}O$ records of all species with high $\delta^{18}O$ values during glacials and low $\delta^{18}O$ values during interglacials. This indicates that climate variations did have an effect on both the upper and deep ocean. Yet in our $SST_{Mg/Ca}$ and $subSST_{Mg/Ca}$ records changes between glacial and interglacial periods are neither particularly dominant nor continuously reflected. Thus, the observed temperature variations and especially the mode shift between phases A and B, recorded in the $SST_{Mg/Ca}$ record must have been caused by different forcing mechanisms. A shift from higher $SST_{Mg/Ca}$ prior to 280 ka BP to colder $SST_{Mg/Ca}$ in more recent times, as reflected in our proxy data, does occur in few records from certain areas in the North Pacific (*cf.* 4.1.1) but it is neither a global phenomenon nor significant in the entire Pacific region (Morley and Heusser, 1997; Herbert et al., 2001; Lang and Wolff, 2011; Bordiga et al., 2013). Thus, our observed $SST_{Mg/Ca}$ shift cannot be explained by a general cooling of the (North) Pacific climate after 280 ka BP yet must be linked to changes in local hydrography, most likely the complex interplay of the Kuroshio and Oyashio Current.

4.1.1 Influences of changes in the tropical Pacific on the study region

Today the volume transport of the Kuroshio Current is linked to ENSO and the induced changes of the location of the NEC's bifurcation point (*cf.* 1.1). This way the Kuroshio velocity and volume transport is increased during La Niña years and reduced during El Niño years (Qiu and Lukas, 1996; Yuan et al., 2001; Kim et al., 2004). It is likely that such changes do not only appear on decadal timescales, but also over longer time periods. This is indicated by a study from the Ryukyu Arc region (north of the NECs bifurcation point) based on planktic foraminiferal assemblages. It shows that during the last 21 ka BP lower rates of surface transport in the Kuroshio Current occurred when more El Niño-like conditions prevailed in the Equatorial Pacific (Ujiié et al., 2003). Assuming that these mechanisms did not significantly change over the past 650 ka BP, they would also have affected the upper ocean dynamic at our study site.

To test this hypothesis, we compare our $SST_{Mg/Ca}$ record to proxy records from de Garidel-Thoron et al. (2005) and Jia et al. (2018) (Figure 5). Both studies reconstructed mean states of more La Niña-like and more El Niño-like conditions in the WPWP on millennial timescales. de Garidel-Thoron et al. (2005) used records from the WPWP (MD97-2140: SSTs generated *via* Mg/Ca from planktic foraminifera) and the EEP (ODP846: SSTs generated from alkenones) to calculate the temperature difference between the WPWP and the EEP ($\Delta T_{WPWP\text{-}EEP}$). Jia et al. (2018) calculated the $\Delta T_{WPWP\text{-}EEP}$ by using four Mg/Ca-based SST records from the WPWP as well as three SST records from the EEP generated from Mg/Ca and $U^{k'}_{37}$. The records from Jia et al. (2018) and de Garidel-Thoron et al. (2005) are not entirely concordant (Figure 5). This is likely a result of different seasonality of the proxies, regional differences, local influences on the temperature development besides ENSO, which reflects the highly dynamic development of the WPWP and EEP, and uncertainties in age models. Yet, the general trends of both records are rather similar and thus, reliably reflect major changes of ENSO dynamics on long time scales. By comparing our $SST_{Mg/Ca}$ record to these paleo-ENSO records, we focus on the long-term development and identify threshold-like events.

In phase B (~650-280 ka BP) we observe up to 6.5°C higher $SST_{Mg/Ca}$ than modern values. During this phase, the records from Jia et al. (2018) and de Garidel-Thoron et al. (2005) show several intervals of very large temperature gradients between the WPWP and the EEP pointing to prevailing La Niña-like conditions (Figure 5). From MIS 16 to MIS 15 we observe a strong increase of $SST_{Mg/Ca}$ from ~7.5 to >11°C, while both ENSO records indicate a shift from El Niño-like to 'extreme' La Niña-like conditions. This coherent shift to higher SSTs and predominant La Niña-like conditions implies an increased Kuroshio Current and thus a northward shift of the SAF through the increased amount of Kuroshio water in the Kuroshio-Oyashio transition zone. Compared to the modern SST distribution, we hypothesize that the SAF shifted at least 5° latitude northwards, so that it reached a position north of our study site (Figures 1, 6). This way surface water from the mixed water region would have reached the study site, thereby causing SSTs that were significantly higher than during times where the SAF is located south of the study site and the surface water is dominated by water from the Subarctic Current (Figures 1, 6).

At ~480 ka BP we observe an abrupt $SST_{Mg/Ca}$ decrease of ~4°C, which is accompanied by an abrupt and pronounced change from very strong La Niña-like to the strongest El Niño-like phase in the record from Jia et al. (2018). This change is also reflected in the record from de Garidel-Thoron et al. (2005) yet less pronounced (Figure 5). This change has most likely reduced the volume and

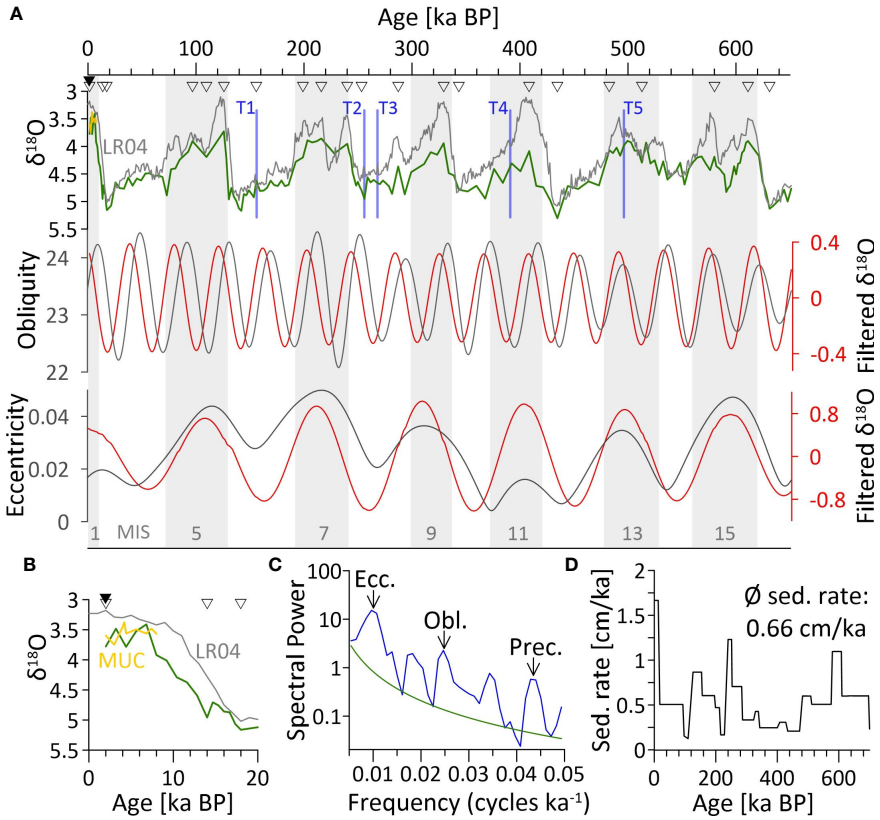

FIGURE 2
Chronostratigraphy of core SO264-45 from Jimmu Seamount (Emperor Seamount Chain). **(A)** Top: Benthic d18O stack of core SO264-45 (green line = gravity core; yellow line = multicorer) in comparison to the global benthic LR04 d18O reference stack from Lisiecki and Raymo (2005). White triangles = tie lines used for tuning the core SO264-45 d18O to LR04. Black triangle = AMS14C dating. Bottom: The filtered 41 kyr component of the benthic d18O stack of SO264-45 (red) in comparison to the orbital obliquity. Gray shadings and numbers mark Marine Isotope Stages (MIS 1-17). Tephra layers identified in core SO264-45 are indicated as blue vertical lines. **(B)** The first 20 ka of A as a close up to better indicate the MUCs d18O in correlation with the gravity core and LR04. **(C)** The frequency spectrum of the benthic d18O stack (green = 95% significance line) indicates dominant cyclicities of 100, 41 and 23 kyr as a response to cyclic fluctuations in the Earth's orbital parameters eccentricity, obliquity and precession. **(D)** Age-depth diagram for core SO264-45; the sedimentation rate is given by the curve's slope.

velocity transport of the Kuroshio Current so immensely that it induced the southward displacement of the SAF to a position south of our study site (Figure 6). Between ~470-440 ka BP both tropical ENSO records show a further increase of $\Delta T_{WPWP\text{-}EEP}$ and thus La Niña-like conditions (Figure 5). Similar to before, this change likely increased the Kuroshio Current's volume and velocity transport and thus, caused another significant northward shift of the SAF. From here until ~280 ka BP La Niña-like conditions prevailed, particularly reflected in the record from de Garidel-Thoron et al. (2005). Minor decreases of the $\Delta T_{WPWP\text{-}EEP}$ between ~600-480 ka BP and ~440-280 ka BP do not seem to have had major impact on the Kuroshio Current strength to induce a shift of the SAF to a position south of the study site. We hypothesize that there might be a tipping point in Kuroshio Current strength that needs to be reached in order to induce a shift of the SAF to a position north of the study site.

At ~280 ka BP we observe a second abrupt $SST_{Mg/Ca}$ decline by ~3.5°C (Figure 5), while the ENSO records from de Garidel-Thoron et al. (2005) and Jia et al. (2018) indicate a change from extreme La Niña-like to more El Niño-like conditions. Thus, we assume that there was another southward displacement of the SAF to a position south of our study site. From here on (phase A: 280-0 ka BP) the $SST_{Mg/Ca}$ is on average 3.6°C lower than in phase B and shows minor variations (~ ± 2°C) around the modern annual mean seasurface temperature (~5.5°C at ~30 m) (Figure 5). During this period both ENSO records indicate that El Niño-like conditions prevailed in the tropical Pacific, with almost no strong La Niña-like phases (except for ~20-5 ka BP in the Jia et al. (2018) record. Variations between El Niño-like and La Niña-like conditions within phase A are not corresponding to $SST_{Mg/Ca}$ changes, which further implies that tropical surface water entering the Kuroshio-Oyashio transition zone *via* the Kuroshio Current/Kuroshio Extension did no longer have an influence on the $SST_{Mg/Ca}$ development at the study site. The SAF likely remained south of the study site between 280-0 ka BP.

The assumption of the intensification and northward migration of the Kuroshio Current/Extension in times of more La Niña-like conditions in the tropics is supported by a study from Shatsky Rise (Yamane, 2003; core S-2; Figure 1). Shatsky Rise is located ~13° south of our core location, were the surface water is dominated by the Kuroshio Current. Yamane (2003) compared $\delta^{13}C$ values of shallow and deep-dwelling planktonic foraminifera and interpreted small $\Delta\delta^{13}C$ gradients as sustained influence of Kuroshio (Extension) water (Figure 5). This record implies that in phase B, where we observe high $SST_{Mg/Ca}$ there was a greater influence of the

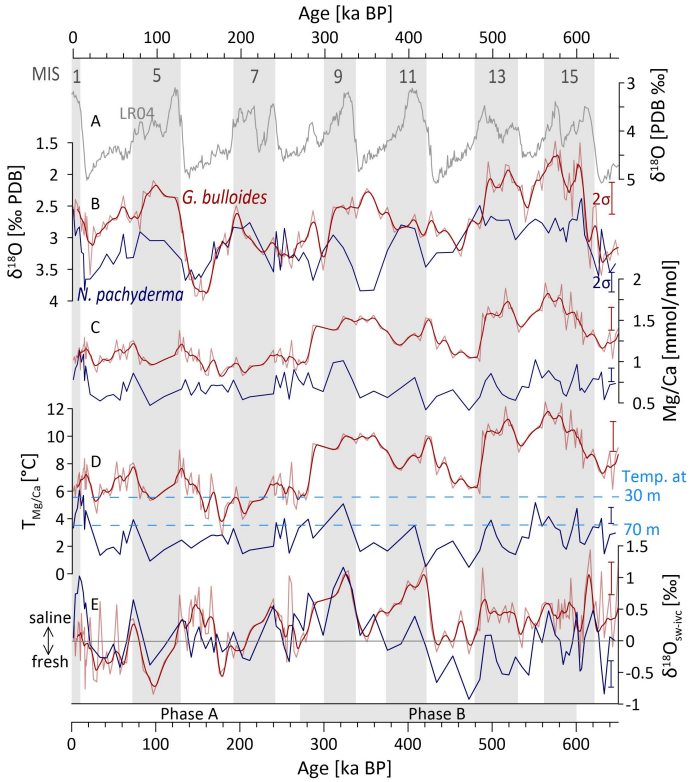

FIGURE 3
Foraminiferal sea surface (red = G. bulloides, all data (thin line) overlain by a 10 ka unweighted smooth (thick line)) and sub sea surface (dark blue = N. pachyderma) proxy data of core SO264-45 versus age. **(A)** global benthic LR04 d18O climate record (Lisiecki and Raymo, 2005) for reference. **(B)** foraminiferal d18O; **(C)** foraminiferal Mg/Ca; **(D)** reconstructed sea surface (SSTMg/Ca) and subsurface (subSSTMg/Ca) temperatures; dashed blue lines = modern annual mean water temperatures at the defined living depths of G. bulloides (~30 m) and N. pachyderma (~70 m) (Locarnini et al., 2018). **(E)** Relative changes in Ice-volume corrected d18Osw deviating from the calculated modern value (gray line). Gray shadings and numbers mark Marine Isotope Stages (MIS 1-17). Error bars mark the 95% standard deviation (2s). Phase A (0-270 ka) and B (270-600 ka) are indicated by gray boxes.

subtropical Kuroshio water at Shatsky Rise than in phase A or modern days, where we observe lower $SST_{Mg/Ca}$ (Figure 5). Moreover, the abrupt $SST_{Mg/Ca}$ decrease at ~280 ka BP (this study) goes along with Yamane's observation of a reduced influence of the Kuroshio Current at Shatsky Rise. Another study from the Shatsky Rise (ODP 1210A) by Chiyonobu et al. (2012) indicates a decrease of warm-water species of calcareous nannofossils from $5x10^9$ specimens/m^2/kyr to $2x10^9$ specimens/m^2/kyr at ~300 ka BP, while the relative abundance of the cold-water species *Coccolithus pelagicus* increased. Notably, the time difference between the abundance change and our $SST_{Mg/Ca}$ decrease could be a feature of the different resolution of age models in the study of Chiyonobu et al. (2012) and our own study and is not necessarily an indicator of a different timing between Shatsky Rise and our core location.

A similar change has also been described by Bordiga et al. (2014). They observe higher primary productivity at Shatsky Rise prior to MIS 8 and lower primary productivity in younger periods. Moreover, they detected a significant change in the faunal composition between MIS 8 and 7: While the nannofossil abundance decreases, the productivity associated with biogenic opal and foraminifera increases. Similar to our assumptions, Bordiga et al. (2014) link this change to an 'elongated state configuration' of the Kuroshio Extension with larger meanders prior to MIS 8 in connection to more La Niña-like conditions in the equatorial Pacific (Beaufort et al., 2001; Bordiga et al., 2014; Qiu, 2019). Additionally, both Bordiga et al. (2014) and Chiyonobu et al. (2012) discuss a change in the input of eolian Asian dust connected to an intensification of the East Asian Monsoon from MIS 7 onward that might have strengthened seasonality and thus, increased alternation between intensely stratified and vertically mixed surface waters that could have contributed to the change in the productivity regime.

These simultaneous changes of the Monsoon system as well as the tropical east-west temperature gradient were likely caused by physical processes (Chiyonobu et al., 2012; Bordiga et al., 2014) as this threshold-like behavior can neither be explained by orbital variations nor modulations in ice volume (Lisiecki and Raymo, 2005).

Thus, we assume that during very strong La Niña-like conditions in the tropical Pacific, as observed temporally in phase B, the high velocity transport of the Kuroshio Current and thus, the enhanced amount of tropical water in the Kuroshio-Oyashio transition zone caused a northward shift of the SAF. During times of more El Niño-like conditions, like in phase A, the SAF stayed south of the core location, which is reflected by the temporally cooler $SST_{Mg/Ca}$. Yet the temperature variations within phase A and B cannot exclusively be explained by variations in the SAF position but must have had additional influencing factors (*cf.* 4.1.2). It is likely that the connection between the observed changes

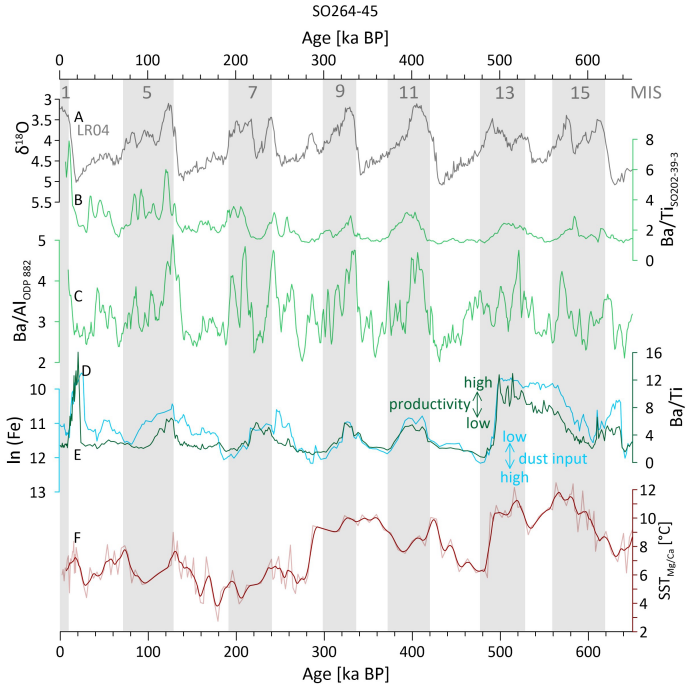

FIGURE 4
Marine productivity and eolian flux in comparison to the SSTMg/Ca development: **(A)** LR04 d18O benthic isotope stack from Lisiecki and Raymo (2005). **(B–D)** XRF-based productivity records from the North Pacific; high Ba/Al and Ba/Ti values point to a high marine productivity. **(B)** Ba/Ti record of SO202-39-3 (Korff et al., 2016). **(C)** Ba/Al record of ODP 882 (Jaccard et al., 2010). **(D)** Ba/Ti record SO264-45 (this study). **(E)** XRF-based normalized Fe record as indicator for eolian dust supply to core SO264-45 (this study); note the descending y-axis. **(F)** SSTMg/Ca record SO264-45 (thin line = raw data; thick line = 10 ka unweighted smooth). Gray shadings and numbers mark Marine Isotope Stages (MIS1-17).

in $SST_{Mg/Ca}$ at our study site and the long-term ENSO development in the tropical Pacific is not straightforward yet that it is further connected to long-term variation in the PDO and its forcing mechanisms. The PDO is connected to the tropical ENSO on shorter timescales in modern days (Newman et al., 2016); thus, changes in the long-term development could have affected these systems, which in return could have influenced the SST at our study site. Due to the high complexity of this system and missing paleo studies of the PDO, we cannot finally clarify this and instead consider a simplified model of enhanced heat transport *via* the Kuroshio Extension to our study site in times of very strong La Niña-like conditions.

4.1.2 Variations of the Oyashio/Subarctic current

Aside from changes of the Kuroshio Current/Extension, changes of the Oyashio/Subarctic Current are of major importance for the surface temperature development at our study site. Changes in the strength of the Oyashio Current are not necessarily linked to variations in the Kuroshio Current yet can have the same forcing mechanisms, e.g., changes in the intensity of the Aleutian low, mid latitude westerlies (Qiu, 2019) or glacial/interglacial climate variations (e.g. Ujiié et al., 2003; Matsuzaki et al., 2014). Therefore, a strengthening of the Kuroshio Current does neither imply that also the Oyashio Current becomes stronger nor weaker at the same time. The importance of variations in the Oyashio current for our study site becomes apparent when comparing our $SST_{Mg/Ca}$ record to the proxy record of Matsuzaki et al. (2014) (Figure 5). They investigated the radiolarian fauna east of Japan, where the Oyashio Current deviates from the coast and enters the open Pacific as Subarctic Current (core C9001C) (Figures 1, 6). Although there is no peak-to-peak correlation between increased abundances of species typical for the Oyashio Current and thus an intensification of the Oyashio and lower $SST_{Mg/Ca}$ at our study site, some parallels are apparent.

Between 600 and 480 ka BP, there are events of strong La Niña-like conditions in the tropics, and our $SST_{Mg/Ca}$ record shows its highest values while Matsuzaki et al. (2014) observes a weak Oyashio Current. At ~480 ka BP, where we observe a sudden temperature decrease at our study site there is not only a change from strong La Niña-like to strong El Niño-like conditions yet also an intensified Oyashio Current. Thus, the combination of an intensified Oyashio Current in line with the change towards strong El Niño-like conditions (and thus a weak Kuroshio Current) could have caused the a southward displacement of the SAF. Through such a southward shift of the SAF more cold subarctic water would reach our study site and could cause the observed sudden temperature decrease at ~480 ka BP.

After 480 ka BP, $SST_{Mg/Ca}$ increases again, which we link to several phases of strong La Niña-like conditions. Yet, even though the La Niña-like phases are similarly pronounced and long, as before 480 ka BP, the maximum $SST_{Mg/Ca}$ remains lower (Figure 5). We assume that this observed $SST_{Mg/Ca}$ difference is linked to the Oyashio Current. Between 480-390 ka BP and 360-340 ka BP the Oyashio Current is transiently enhanced (Figure 5; Matsuzaki et al.,

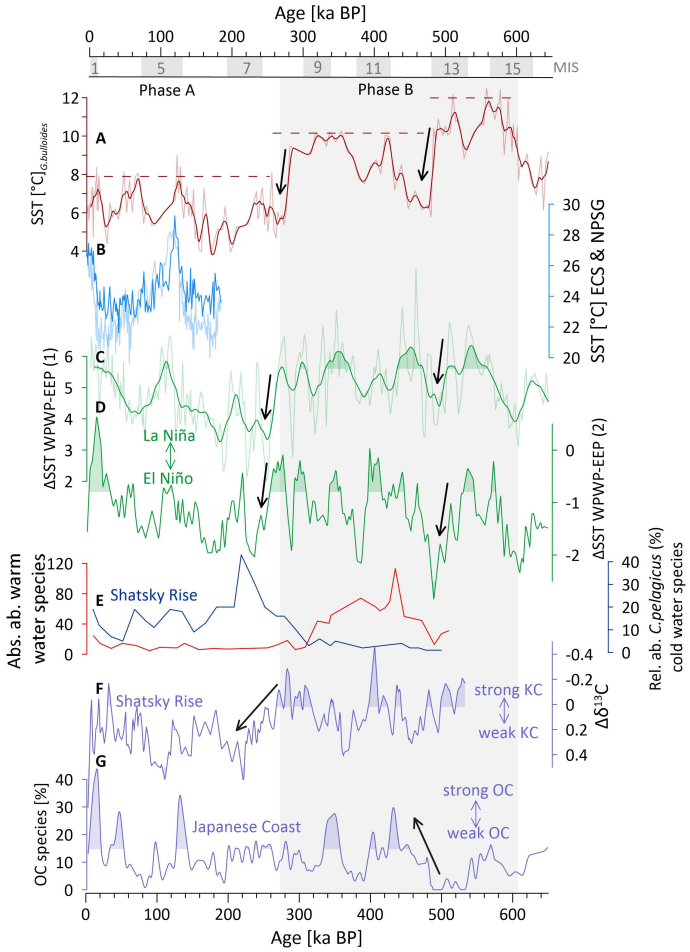

FIGURE 5
ENSO effect on the N Pacific oceanography. **(A)** SSTMg/Ca record (thin line = raw data overlain by a 10 ka unweighted smooth (thick line) at core location SO264-45. Maximum SSTMg/Ca divided into different time periods are marked as dotted lines. **(B)** Mg/Ca based SST from the East China Sea (ECS; light blue) and the North Pacific Subtropical Gyre (NPSG; dark blue) (Ujiié et al., 2016). **(C, D)** Proxy records of ENSO variability from de Garidel-Thoron et al. (2005); thin green line = complete record overlain by a 10 ka unweighted smooth = thick green line; **(B)** and Jia et al. (2018; green; **C)**. High DSSTWPWP-EEP values point to more La Niña-like conditions in the tropical W Pacific. **(E)** Relative abundance of cold water species (blue) and absolute abundances of warm water species (red) reflecting a significant change in Kuroshio influence at Shatsky Rise (Chiyonobu et al., 2012). **(F)** d13C gradient between shallow- and deepdwelling planktonic foraminifera revealing Kuroshio Current strength variations at Shatsky Rise (Yamane, 2003). **(G)** Oyashio Current strength off the Japanese coast approximated from the abundance of radiolarian fauna typical for the OC (Matsuzaki et al., 2014). Curve fillings **(B, C, E, F)** mark the upper 25% of the data. Phase A and B denote two phases of different ocean settings characterized by a mode shift between a phase of extreme La Niña-like conditions (~240-650 ka) to a phase of less strong La Niña-like and more El Niño-like like conditions (~260 ka - present). Marine Isotope Stages (MIS1-17) are marked. Black arrows mark prominent transitions between phases. Phase A (0-270 ka) and B (270-600 ka) are indicated by gray boxes.

2014). As both Currents contribute to the water of the Kuroshio-Oyashio transition zone it is likely that this enhanced influence of the Oyashio Current caused an overall lowered SST-level in the Kuroshio-Oyashio transition zone. Thus, the enhancement of the Oyashio/Subarctic Current system after 480 ka BP muted the SST-effect of the La Niña-like induced enhancement of the Kuroshio Current at our study site.

Between ~20-5 ka BP the record of Jia et al. (2018) shows another phase of very strong La Niña-like conditions in the tropical Pacific. Similar $\Delta T_{WPWP\text{-}EEP}$ values have caused a shift of the SAF in phase B. Yet, between ~20-5 ka BP our $SST_{Mg/Ca}$ record does not show any significant rise (Figure 5). In contrast to previous northward migrations of the SAF in phase B, the Oyashio Current is very strong between ~20-5 ka. We hence assume that the strong Oyashio/Subarctic Current prevented a significant northwards shift of the SAF between ~20-5 ka BP.

4.1.3 Glacial-interglacial shifts of the SAF

Several studies suggest that the frontal zones in the Kuroshio-Oyashio transition area migrated northwards during interglacials and southwards during glacials at least during the last two glacial-interglacial cycles (Thompson and Shackleton, 1980; Kawahata and Ohshima, 2002; Harada et al., 2004; Yasudomi et al., 2014; Gallagher et al., 2015). Assuming that the described changes occurred throughout our entire studied time interval, such shifts could have further contributed to changes in $SST_{Mg/Ca}$ and

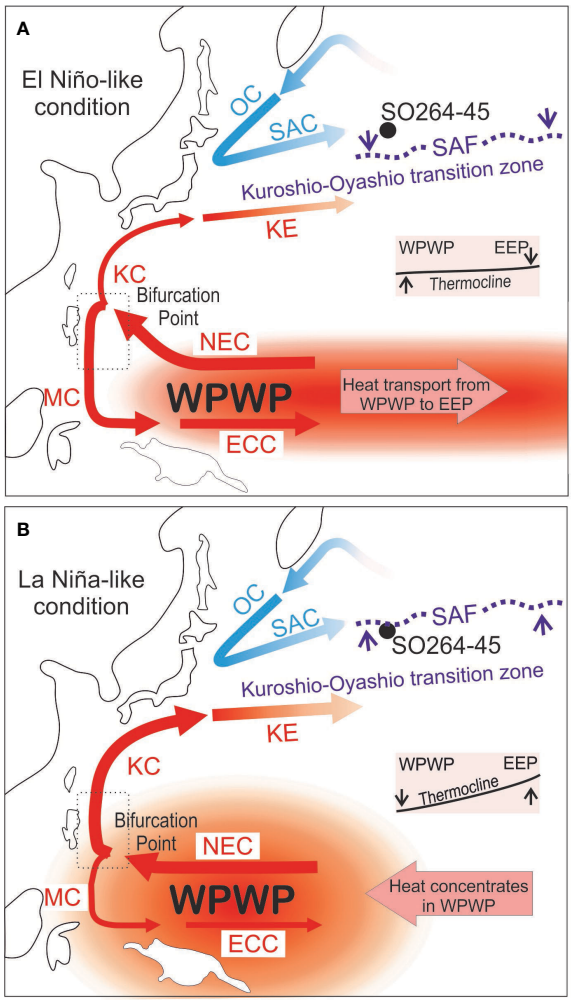

FIGURE 6
Schematic scenarios to explain the SST development and SAF positioning in the study region in terms of more La Niña-like **(B)** and more El Niño-like **(A)** climate conditions. The heat distribution and flux between the Western Pacific Warm Pool (WPWP) and the Eastern equatorial Pacific (EEP) are indicated by arrows and color shading in. Thicker (thinner) arrows indicate stronger (weaker) currents. ECC, Equatorial Counter Current; KC, Kuroshio Current; KE, Kuroshio Extension; MC, Mindanao Current; NEC, North Equatorial Current; OC, Oyashio Current; SAC, Subarctic Current; SAF, Subarctic Front. Gray boxes display thermocline variations in the tropical region.

$\delta^{18}O_{sw\text{-}ivc}$ at our study site. However, during phase A were our study site was located north of the SAF and thus dominated by subarctic water, our $SST_{Mg/Ca}$ record does not show changes that would fit to glacial-interglacial variations (Figures 3, 6). Therefore, we assume that if there had been a northward migration of the SAF during interglacials it can only have migrated to a position still south of our study site. In phase B, were we consider our study site to be located south of the SAF (Figure 6), the $SST_{Mg/Ca}$ and $\delta^{18}O_{sw\text{-}ivc}$ broadly follow glacial-interglacial cycles except for MIS 11-10. So if the SAF migrated further north during interglacials it could have caused warmer, more saline water from the Kuroshio-Oyashio transition to reach the study site, whereas southwards shift during glacials could have brought the SAF closer to the core location and thereby caused an increase of colder, less saline water from the Subarctic Current. Thus it is likely that glacial/interglacial induced shifts of the SAF contributed to our observed $SST_{Mg/Ca}$ pattern.

4.1.4 The $subSST_{Mg/Ca}$ record from *N. pachyderma*

The $subSST_{Mg/Ca}$ record derived from *N. pachyderma* is consistently lower than the $SST_{Mg/Ca}$ record derived from *G. bulloides* (Figure 3). This difference reflects firstly the deeper habitat depth of *N. pachyderma* in comparison to *G. bulloides*, where the latter inhabits water depths above the thermocline, whereas the former occurs at and below the thermocline. Thus the temperature difference between the two species indicates a stable and pronounced thermocline stratification. Secondly the seasonal bias is expressed, as *G. bulloides* reflects annual $SST_{Mg/Ca,}$ whereas *N. pachyderma* reflects $subSST_{Mg/Ca,}$ derived from the colder seasons from autumn to spring. In phase A (280-0 ka BP) our $SST_{Mg/Ca}$ and $subSST_{Mg/Ca}$ records show similar variations in amplitude in MIS 7 and 5-1, yet with an average offset of 3.5°C, while in MIS 6 the $SST_{Mg/Ca}$ and $subSST_{Mg/Ca}$ records show opposing trends.

In phase B (600-280 ka BP) the $SST_{Mg/Ca}$ record yields significantly (up to ~6.5°C) higher values than in phase A, while the $subSST_{Mg/Ca}$ record does not reflect this trend. This indicates that the dispersal of Kuroshio-Oyashio transition water in phase B was either a pure surface phenomenon, or was linked to the different temperature tolerance of both species. In the first case, water from the Kuroshio-Oyashio transition would have migrated northwards in form of a warm surface water lens, while the subsurface would have still been dominated by water from the Subarctic Current. Thus, there would have been a very pronounced shallow thermocline, as indicated in Supplementary Figure 7. However, we consider it more likely that the different temperature trends of *N. pachyderma* and *G. bulloides* are not only a phenomenon of significantly different surface and subsurface temperature evolution, but an ecological phenomenon. *N. pachyderma* is less tolerant to warmer temperatures and prefers values below 7°C (*cf.* 2.2 and Supplement 1). Therefore, it occurs less during warmer seasons than *G. bulloides*. We assume that in phase B, with an increased influence of Kuroshio-Oyashio transition water at the study site, temperatures in the preferred depth habitat of *N. pachyderma* exceeded optimal temperatures even in spring and autumn. Thus, in times of a northward displacement of the SAF *N. pachyderma* would most likely reflect a pure winter signal, which is significantly colder than the annual signal from *G. bulloides*. This change in seasonality is in accordance with plankton tow studies from the North Pacific that suggest that in modern days, *N. pachyderma* occurs from autumn to spring at colder sites (~50°N, ~165°E) while their abundance stays low until December at warmer sites (~40°N, ~165°E) (Taylor et al., 2018; Supplement 1).

4.2 Marine productivity changes

Higher marine productivity during deglaciations and interglacials and lower productivity during glacials as observed in our Ba/Ti record is common in the North Pacific and its marginal seas (Narita et al., 2002; Gorbarenko et al., 2004; Kienast et al., 2004; Nürnberg and Tiedemann, 2004; Jaccard et al., 2005; Brunelle et al., 2007; Shigemitsu et al., 2007; Galbraith et al., 2008; Gebhardt et al., 2008; Jaccard et al., 2010; Riethdorf et al., 2013). In our record we further observe, that the productivity already starts to increase during the deglaciations and decreases during the late interglacials. This is similar to observations at ODP Site 882 (Jaccard et al., 2010) located north of our site (Figure 1) which also shows productivity increases during deglaciations and its highest values in the early interglacials (Figure 4). A similar feature is observed for site SO202-39-3 (Korff et al., 2016) located south of our study site in the area of the Kuroshio Extension (Figures 1, 4). The forcing mechanisms for these productivity patterns, however, are still a matter of debate (Jaccard et al., 2010; Knudson and Ravelo, 2015; Korff et al., 2016). For the North Pacific, most authors suggest a change of nutrient supply, and in the subarctic marginal seas light limitation through sea ice cover and changes in stratification as main drivers for productivity changes (Narita et al., 2002; Gorbarenko et al., 2004; Kienast et al., 2004; Jaccard et al., 2005; Brunelle et al., 2007; Shigemitsu et al., 2007; Galbraith et al., 2008; Gebhardt et al., 2008; Jaccard et al., 2010; Riethdorf et al., 2013; Davis et al., 2020). As our site is located south of the area where sea ice would have a direct influence on productivity and the average winter SST exceeds 3°C, we exclude it as a forcing mechanism (Supplementary Figure 1). Therefore we conclude that the availability of nutrients or their utilization causes the observed glacial-interglacial productivity pattern.

Iron fertilization has been invoked as an important driver for nutrient sequestration efficiency and thus, an enhanced supply of the micronutrient Fe could increase productivity (Boyd et al., 2004; Harrison et al., 2004; Tsuda et al., 2003). One of the sources of Fe is aeolian transport (Hovan et al., 1991; Kawahata et al., 2000; Boyd et al., 2007; Shigemitsu et al., 2007). To test whether the Fe input *via* dust caused our observed productivity pattern, we compared our XRF-Fe record of core SO264-45, used as a proxy for terrigenous input *via* wind to our Ba/Ti record (Figure 4). The proxy records are apparently anticorrelated suggesting that Fe fertilization *via* dust is not the (principal) driver of marine productivity at our study site, although, we cannot say to what extent it still contributed to the observed pattern.

The amount of nutrient transport *via* water masses could have contributed to changes in productivity (Jaccard et al., 2005; Galbraith et al., 2007; Nishioka et al., 2011; Costa et al., 2018; Gray et al., 2018). Today, nutrient-rich water from the Oyashio/Subarctic Current dominates the upper ocean at our study site. The transported nutrients reach the mixed layer through vertical wintertime mixing (Nishioka et al., 2011). Our $SST_{Mg/Ca}$ record, which is linked to changes in the Kuroshio-Oyashio transition zone does not show the same fluctuations as our productivity record. Thus, although it could have contributed to changes in productivity we assume that the interplay of the Kuroshio and Oyashio Current is not the main driver for the observed productivity pattern at our study site. We do, however, consider that the amount of transported nutrients might have changed on glacial-interglacial timescales. Lembke-Jene et al. (2017) show that the export of nutrients from the Okhotsk Sea increased at the beginning of the deglacial warm phases Allerød and Preboreal, because of an enhanced input of iron and nutrient-rich terrestrial material from the Siberian hinterland *via* the Amur River caused by melting processes. They argue that such an increased export of nutrients from the Okhotsk Sea could have caused temporary nutrient-replete conditions in the Subarctic North Pacific. Riethdorf et al. (2013) also observe an enhanced input of terrestrial-derived organic matter from flooded shelf areas during early deglacial phases. As water from the Bering and Okhotsk Sea feeds the Oyashio/Subarctic Current, these nutrients could have reached the study site and caused an increase in productivity. Assuming that an enhanced terrestrial sourced nutrient supply from marginal seas like the Okhotsk Sea and the Bering Sea *via* subsurface water did not only occur on millennial- but also on glacial-interglacial timescales, this could contribute to our observed productivity pattern. Yet to further clarify on this

additional proxy records on longer time scales and in the open North Pacific would be needed.

Further it has been proposed for subarctic and Antarctic sites that strong stratification during glacials limits nutrient availability at the surface while weak stratification in interglacials enables upwelling of nutrients-rich deep water thereby enhancing productivity (Jaccard et al., 2005; Brunelle et al., 2007; Galbraith et al., 2008). Yet this topic alongside the efficiency of nutrient uptake is still a matter of debate (e.g. Knudson and Ravelo, 2015) for which further studies with detailed nutrient records and very reliable control would be needed.

5 Conclusion

Through the reconstruction of Mg/Ca and $\delta^{18}O$ based (sub) surface temperature and $\delta^{18}O_{sw\text{-}ivc}$ in the open Northwest Pacific and a comparison of XRF-based Ba/Ti and iron records we draw the following conclusions regarding the hydrological and productivity variations at the northern boundary of the Kuroshio-Oyashio transition zone:

- The $SST_{Mg/Ca}$ development at our study site is strongly related to changes in heat transport of the tropical Kuroshio Current induced by ENSO. In phases of very strong La Niña-like conditions in the tropics, the NEC bifurcation point migrates southward which enhances the velocity transport of the Kuroshio Current/Extension. This way more tropical water enters the transition zone, which causes a northward displacement of the SAF to a position north of our study site, thus a relocation of at least 5°. This way more transition water reaches our core position, which we observe as higher $SST_{Mg/Ca}$ in the time interval 280-600 ka BP. Further, we show that shifts of the SAF cause very abrupt strong temperature changes at our core position e.g. at 480 and 280 ka BP. Such shifts of the SAF have been proposed on shorter timescales and for areas closer to the coast, yet our $SST_{Mg/Ca}$ record makes it possible to track these shifts on longer time scales and into the open Pacific.
- The $SST_{Mg/Ca}$ development at our study site is further influenced by changes in the strength of the Oyashio/Subarctic Current. Both, the Kuroshio Current/Extension and the Oyashio/Subarctic Current contribute to the water in the Kuroshio-Oyashio transition zone so that an enhancement of the Oyashio Current can mute the effect of an enhancement of Kuroshio Current. We observe such an effect a) between 480-280 ka BP, where the enhanced influence of the Subarctic Current at our study site causes temperatures to stay lower than in the time interval 480-600 ka BP, even though there are similarly strong and long La Niña-like phases in both intervals and b) between ~20-5 ka BP, where a strong Oyashio Current seems to prevent a shift of the SAF up to a position north of our study site.
- Glacial-interglacial variations in the Kuroshio-Oyashio transition zone also influence the $SST_{Mg/Ca}$ development at our study site, yet they are less pronounced in our data than the mode shift between phases A and B. In phase B, where the SAF is located north of our study we observe an increase of warmer, more saline water in interglacials and colder, less saline water during glacials. We link these shifts to general glacial-interglacial variations of the Kuroshio-Oyashio transition zone and the front system.
- The productivity at our study site follows glacial-interglacial patterns with high values during the deglaciations/early interglacials and low values during glacials. Thus, we conclude that productivity is not primarily linked to the changing influences of Kuroshio/Oyashio water at our study site.
- Our Fe and Ba/Ti records are anticorrelated, thus we conclude that Fe fertilization *via* dust is not the (principal) driver of marine productivity at our study site. We further hypothesize that the observed productivity pattern might be linked to (a) glacial/interglacial variations in the subpolar marginal seas and the induced nutrient supply *via* the subarctic water masses in deglaciations because of melting processes and (b) changes in stratification that have an influence on nitrate availability and utilization.

Data availability statement

Presented data is available online at the Data Publisher for Earth and Environmental Science, PANGEA (www.pangea.de): https://doi.org/10.1594/PANGAEA.949795, https://doi.org/10.1594/PANGAEA.949771.

Author contributions

LJ, W-SC, DN and L-LJ collected the samples at sea. LJ and W-SC proceeded the XRF scanning. LJ prepared and measured the foraminiferal samples with support from DN's working group. LJ and DN developed the age model and analyzed the data. LJ made all figures and wrote the manuscript, W-SC, DN, LL-J and RT contributed with ideas and feedback throughout the whole process of designing the study and writing the manuscript. All authors contributed to the article and approved the submitted version.

Acknowledgments

We thank the German Ministry of Education and Research (BMBF) for providing funding for expedition SO264 (SONNE-EMPEROR) and subsequent works through grants 03G0264A (GEOMAR) and 03G0264B (AWI), as well as grant 03F0785A NOPAWAC "The North Pacific in Warming Climates" (AWI). We acknowledge institutional funding from AWI and GEOMAR through the research programs "PACES-II" and "Changing Earth – Sustaining Our Future".

Conflict of interest

The authors declare that the research was conducted in the absence of any commercial or financial relationships that could be construed as a potential conflict of interest.

Publisher's note

All claims expressed in this article are solely those of the authors and do not necessarily represent those of their affiliated organizations, or those of the publisher, the editors and the reviewers. Any product that may be evaluated in this article, or claim that may be made by its manufacturer, is not guaranteed or endorsed by the publisher.

Supplementary material

The Supplementary Material for this article can be found online at: https://www.frontiersin.org/articles/10.3389/fmars.2023.1074431/full#supplementary-material

References

Abell, J. T., Winckler, G., Anderson, R. F., and Herbert, T. D. (2021). Poleward and weakened westerlies during pliocene warmth. *Nature* 589, 70–75. doi: 10.1038/s41586-020-03062-1

Ayers, J. M., and Lozier, M. S. (2012). Unraveling dynamical controls on the north pacific carbon sink. *J. Geophys. Res. Ocean.* 117, 1–20. doi: 10.1029/2011JC007368

Beaufort, L., de Garidel-Thoron, T., Mix, A. C., and Pisias, N. G. (2001). ENSO-like forcing on oceanic primary production during the late pleistocene. *Science* 293, 2440–2444. doi: 10.1126/science.293.5539.2440

Bordiga, M., Beaufort, L., Cobianchi, M., Lupi, C., Mancin, N., Luciani, V., et al. (2013). Calcareous plankton and geochemistry from the ODP site 1209B in the NW pacific ocean (Shatsky rise): New data to interpret calcite dissolution and paleoproductivity changes of the last 450ka. *Palaeogeogr. Palaeoclimatol. Palaeoecol.* 371, 93–108. doi: 10.1016/j.palaeo.2012.12.021

Bordiga, M., Cobianchi, M., Lupi, C., Pelosi, N., Venti, N. L., and Ziveri, P. (2014). Coccolithophore carbonate during the last 450 ka in the NW pacific ocean (ODP site 1209B , shatsky rise). *J. Quat. Sci.* 29, 57–69. doi: 10.1002/jqs.2677

Boyd, P. W., Jickells, T., Law, C. S., Blain, S., Boyle, E. A., Buesseler, K. O., et al. (2007). Mesoscale iron enrichment experiments 1993-2005: Synthesis and future directions. *Sci. (80-.).* 315, 612–617. doi: 10.1126/science.1131669

Boyd, P. W., Law, C. S., Wong, C. S., Nojiri, Y., Tsuda, A., Levasseur, M., et al. (2004). The decline and fate of an iron-induced subarctic phytoplankton bloom. *Nature* 428, 549–553. doi: 10.1038/nature02437

Boyle, E. A., and Keigwin, L. D. (1985). Comparison of Atlantic and pacific paleochemical records for the last 215,000 years: changes in deep ocean circulation and chemical inventories. *Earth Planet. Sci. Lett.* 76, 135–150. doi: 10.1016/0012-821X(85)90154-2

Boyle, E., and Rosenthal, Y. (1996). Chemical hydrography of the south Atlantic during the last glacial maximum: Cd vs. δ13C. *South Atl.*, 423–443. doi: 10.1007/978-3-642-80353-6_23

Brunelle, B. G., Sigman, D. M., Cook, M. S., Keigwin, L. D., Haug, G. H., Plessen, B., et al. (2007). Evidence from diatom-bound nitrogen isotopes for subarctic pacific stratification during the last ice age and a link to north pacific denitrification changes. *Paleoceanography* 22, 1–17. doi: 10.1029/2005PA001205

Caley, T., and Roche, D. M. (2015). Modeling water isotopologues during the last glacial: Implications for quantitative paleosalinity reconstruction. *Paleoceanography* 30, 739–750. doi: 10.1002/2014PA002720

Chen, X. J., Zhao, X. H., and Chen, Y. (2007). Influence of El Niño/La niña on the western winter-spring cohort of neon flying squid (Ommastrephes bartramii) in the northwestern pacific ocean. *ICES. J. Mar. Sci.* 64, 1152–1160. doi: 10.1093/icesjms/fsm103

Chen, J., Zou, J., Zhu, A., Shi, X., Nürnberg, D., Lembke-Jene, L., et al. (2021). Geochemistry of surface sediments from the emperor seamount chain, north pacific. *Front. Earth Sci.* 9. doi: 10.3389/feart.2021.674842

Chiyonobu, S., Mori, Y., and Oda, M. (2012). Reconstruction of paleoceanographic conditions in the northwestern pacific ocean over the last 500kyr based on calcareous nannofossil and planktic foraminiferal assemblages. *Mar. Micropaleontol.* 96–97, 29–37. doi: 10.1016/j.marmicro.2012.07.002

Choi, J., and Son, S. W. (2022). Seasonal-to-decadal prediction of El niño–southern oscillation and pacific decadal oscillation. *NPJ Clim. Atmos. Sci.* 5, 1–8. doi: 10.1038/s41612-022-00251-9

Costa, K. M., McManus, J. F., and Anderson, R. F. (2018). Paleoproductivity and stratification across the subarctic pacific over glacial-interglacial cycles. *Paleoceanogr. Paleoclimatol.* 33, 914–933. doi: 10.1029/2018PA003363

Croudace, I. W., and Rothwell, R. G. (2015) *Micro-XRF studies of sediment cores*. Available at: http://link.springer.com/10.1007/978-94-017-9849-5.

Darling, K. F., Kucera, M., Kroon, D., and Wade, C. M. (2006). A resolution for the coiling direction paradox in neogloboquadrina pachyderma. *Paleoceanography* 21, 1–14. doi: 10.1029/2005PA001189

Davis, C. V., Myhre, S. E., Deutsch, C., Caissie, B., Praetorius, S., Borreggine, M., et al. (2020). Sea Surface temperature across the subarctic north pacific and marginal seas through the past 20,000 years: A paleoceanographic synthesis. *Quat. Sci. Rev.* 246, 106519. doi: 10.1016/j.quascirev.2020.106519

De Boer, B., Lourens, L. J., and Van De Wal, R. S. W. (2014). Persistent 400,000-year variability of antarctic ice volume and the carbon cycle is revealed throughout the plio-pleistocene. *Nat. Commun.* 5, 1–8. doi: 10.1038/ncomms3999

de Garidel-Thoron, T., Rosenthal, Y., Bassinot, F., and Beaufort, L. (2005). Stable sea surface temperatures in the western pacific warm pool over the past 1.75 million years. *Nature* 433, 294–298. doi: 10.1038/nature03189

Elderfield, H., and Ganssen, G. (2000). Past temperature and δ18O of surface ocean waters inferred from foraminiferal Mg/Ca ratios. *Nature* 405, 442–445. doi: 10.1038/35013033

Emery, W. J. (2001). Water types and water masses. *Encycl. Ocean. Sci.*, 3179–3187. doi: 10.1006/rwos.2001.0108

Favorite, F. (1976). Oceanography of the subarctic pacific region 1960-71. *Bull. Int. North Pac. Fish. Comm.* 33, 1–187.

Fontanier, C., MacKensen, A., Jorissen, F. J., Anschutz, P., Licari, L., and Griveaud, C. (2006). Stable oxygen and carbon isotopes of live benthic foraminifera from the bay of Biscay: Microhabitat impact and seasonal variability. *Mar. Micropaleontol.* 58, 159–183. doi: 10.1016/j.marmicro.2005.09.004

Fuhr, M., Laukert, G., Yu, Y., Nürnberg, D., and Frank, M. (2021). Tracing water mass mixing from the equatorial to the north pacific ocean with dissolved neodymium isotopes and concentrations. *Front. Mar. Sci.* 7. doi: 10.3389/fmars.2020.603761

Galbraith, E. D., Jaccard, S. L., Pedersen, T. F., Sigman, D. M., Haug, G. H., Cook, M., et al. (2007). Carbon dioxide release from the north pacific abyss during the last deglaciation. *Nature* 449, 890–893. doi: 10.1038/nature06227

Galbraith, E. D., Kienast, M., Jaccard, S. L., Pedersen, T. F., Brunelle, B. D., Sigman, D. M., et al. (2008). Consistent relationship between global climate and surface nitrate utilization in the western subarctic pacific throughout the last 500 ka. *Paleoceanography* 23, 1–11. doi: 10.1029/2007PA001518

Gallagher, S. J., Kitamura, A., Iryu, Y., Itaki, T., Koizumi, I., and Hoiles, P. W. (2015). The pliocene to recent history of the kuroshio and tsushima currents: a multi-proxy approach. *Prog. Earth Planet. Sci.* 2, 1–23. doi: 10.1186/s40645-015-0045-6

Garcia, H., Weathers, K. W., Paver, C. R., Smolyar, I., Boyer, T. P., Locarnini, R. A., et al. (2018). World ocean atlas 2018. volume 4: Dissolved inorganic nutrients (phosphate, nitrate and nitrate+nitrite, silicate). *NOAA. Atlas. NESDIS. 84* 84, 35.

Gebhardt, H., Sarnthein, M., Grootes, P. M., Kiefer, T., Kuehn, H., Schmieder, F., et al. (2008). Paleonutrient and productivity records from the subarctic north pacific for pleistocene glacial terminations I to V. *Paleoceanography* 23, 1–21. doi: 10.1029/2007PA001513

Gorbarenko,, Southon, J. R., Keigwin, L. D., Cherepanova, M. V., and Gvozdeva, I. G. (2004). Late pleistocene-Holocene oceanographic variability in the Okhotsk Sea: Geochemical, lithological and paleontological evidence. *Palaeogeogr. Palaeoclimatol. Palaeoecol.* 209, 281–301. doi: 10.1016/j.palaeo.2004.02.013

Gray, W. R., Rae, J. W. B., Wills, R. C. J., Shevenell, A. E., Taylor, B., Burke, A., et al. (2018). Deglacial upwelling, productivity and CO2 outgassing in the north pacific ocean. *Nat. Geosci.* 11, 340–344. doi: 10.1038/s41561-018-0108-6

Greaves, M., Caillon, N., Rebaubier, H., Bartoli, G., Bohaty, S., Cacho, I., et al. (2008). Interlaboratory comparison study of calibration standards for foraminiferal Mg/Ca thermometry. *Geochem. Geophys. Geosyst.* 9, 1–27. doi: 10.1029/2008GC001974

Harada, N., Ahagon, N., Uchida, M., and Murayama, M. (2004). Northward and southward migrations of frontal zones during the past 40 kyr in the kuroshio-oyashio transition area. *Geochem. Geophys. Geosyst.* 5, 1–16. doi: 10.1029/2004GC000740

Haug, G. H., and Sigman, D. M. (2009). Polar twins. *Nat. Geosci.* 2, 91–92. doi: 10.1038/ngeo423

Harrison, P. J., Whitney, F. A., Tsuda, A., Saito, H., and Tadokoro, K. (2004). Nutrient and plankton dynamics in the NE and NW gyres of the subarctic pacific ocean. *J. Oceanogr.* 60, 93–117. doi: 10.1023/B:JOCE.0000038321.57391.2a

Heaton, T. J., Köhler, P., Butzin, M., Bard, E., Reimer, R. W., Austin, W. E. N., et al. (2020). Marine20–the marine radiocarbon age calibration curve (0–55,000 cal BP). *Radiocarbon* 62, 779–820. doi: 10.1017/rdc.2020.68

Helmke, J. P., Bauch, H. A., Röhl, U., and Kandiano, E. S. (2008). Uniform climate development between the subtropical and subpolar northeast Atlantic across marine isotope stage 11. *Clim. Past.* 4, 181–190. doi: 10.5194/cp-4-181-2008

Herbert, T. D., Schuffert, J. D., Andreasen, D., Heusser, L., Lyle, M., Mix, A., et al. (2001). Collapse of the California current during glacial maxima linked to climate change on land. *Science* 80-.). 293, 71–76. doi: 10.1126/science.1059209

Holloway, M. D., Sime, L. C., Singarayer, J. S., Tindall, J. C., and Valdes, P. J. (2016). Reconstructing paleosalinity from δ18O: Coupled model simulations of the last glacial maximum, last interglacial and late Holocene. *Quat. Sci. Rev.* 131, 350–364. doi: 10.1016/j.quascirev.2015.07.007

Hovan, S. A., Rea, D. K., and Pisias, N. G. (1991). Late pleistocene continental climate and oceanic variability recorded in Northwest pacific sediments. *Paleoceanography* 6, 349–370. doi: 10.1029/91PA00559

Hu, D., Wu, L., Cai, W., Gupta, A.S., Ganachaud, A., Qiu, B., et al. (2015). Pacific western boundary currents and their roles in climate. *Nature* 522, 299–308. doi: 10.1038/nature14504

Huang, R. X. (2015). *Oceanographic topics: Surface/Wind driven circulation. second edi* (London: Elsevier Ltd.). doi: 10.1016/B978-0-12-382225-3.00280-2

Isoguchi, O., Kawamura, H., and Oka, E. (2006). Quasi-stationary jets transporting surface warm waters across the transition zone between the subtropical and the subarctic gyres in the north pacific. *J. Geophys. Res. Ocean.* 111, 1–17. doi: 10.1029/2005JC003402

Iwasaki, S., Kimoto, K., Kuroyanagi, A., and Kawahata, H. (2017). Horizontal and vertical distributions of planktic foraminifera in the subarctic pacific. *Mar. Micropaleontol.* 130, 1–14. doi: 10.1016/j.marmicro.2016.12.001

Jaccard, S. L., Galbraith, E. D., Sigman, D. M., and Haug, G. H. (2010). A pervasive link between Antarctic ice core and subarctic pacific sediment records over the past 800 kyrs. *Quat. Sci. Rev.* 29, 206–212. doi: 10.1016/j.quascirev.2009.10.007

Jaccard, S. L., Haug, G. H., Sigman, D. M., Pedersen, T. F., Thierstein, H. R., and Röhl, U. (2005). Glacial/interglacial changes in subarctic north pacific stratification. *Science* 80-.). 308, 1003–1006. doi: 10.1126/science.1108696

Jahn, B., Donner, B., Müller, P. J., Röhl, U., Schneider, R. R., and Wefer, G. (2003). Pleistocene variations in dust input and marine productivity in the northern benguela current: Evidence of evolution of global glacial-interglacial cycles. *Palaeogeogr. Palaeoclimatol. Palaeoecol.* 193, 515–533. doi: 10.1016/S0031-0182(03)00264-5

Jahn, B., Schneider, R. R., Müller, P. J., Donner, B., and Röhl, U. (2005). Response of tropical African and East Atlantic climates to orbital forcing over the last 1.7 ma. *Geol. Soc Spec. Publ.* 247, 65–84. doi: 10.1144/GSL.SP.2005.247.01.04

Jia, Q., Li, T., Xiong, Z., Steinke, S., Jiang, F., Chang, F., et al. (2018). Hydrological variability in the western tropical pacific over the past 700 kyr and its linkage to northern hemisphere climatic change. *Palaeogeogr. Palaeoclimatol. Palaeoecol.* 493, 44–54. doi: 10.1016/j.palaeo.2017.12.039

Joh, Y., and Di Lorenzo, E. (2019). Interactions between kuroshio extension and central tropical pacific lead to preferred decadal-timescale oscillations in pacific climate. *Sci. Rep.* 9, 1–12. doi: 10.1038/s41598-019-49927-y

Johnson, Z. F., Chikamoto, Y., Wang, S. Y. S., McPhaden, M. J., and Mochizuki, T. (2020). Pacific decadal oscillation remotely forced by the equatorial pacific and the Atlantic oceans. *Clim. Dyn.* 55, 789–811. doi: 10.1007/s00382-020-05295-2

Kaiser, J., Schefuß, E., Lamy, F., Mohtadi, M., and Hebbeln, D. (2008). Glacial to Holocene changes in sea surface temperature and coastal vegetation in north central Chile: high versus low latitude forcing. *Quat. Sci. Rev.* 27, 2064–2075. doi: 10.1016/j.quascirev.2008.08.025

Kawahata, H., and Ohshima, H. (2002). Small latitudinal shift in the kuroshio extension (Central pacific) during glacial times: Evidence from pollen transport. *Quat. Sci. Rev.* 21, 1705–1717. doi: 10.1016/S0277-3791(01)00150-0

Kawahata, H., Okamoto, T., Matsumoto, E., and Ujiie, H. (2000). Fluctuations of eolian flux and ocean productivity in the mid-latitude north pacific during the last 200 kyr. *Quat. Sci. Rev.* 19, 1279–1291. doi: 10.1016/S0277-3791(99)00096-7

Kienast, S. S., Hendy, I. L., Crusius, J., Pedersen, T. F., and Calvert, S. E. (2004). Export production in the subarctic north pacific over the last 800 kyrs: No evidence for iron fertilization? *J. Oceanogr.* 60, 189–203. doi: 10.1023/B:JOCE.0000038326.73943.aa

Kim, Y. Y., Qu, T., Jensen, T., Miyama, T., Mitsudera, H., Kang, H. W., et al. (2004). Seasonal and interannual variations of the north equatorial current bifurcation in a high-resolution OGCM. *J. Geophys. Res. Ocean.* 109, 1–19. doi: 10.1029/2003jc002013

Knudson, K. P., and Ravelo, A. C. (2015). Enhanced subarctic pacific stratification and nutrient utilization during glacials over the last 1.2 myr. *Geophys. Res. Lett.* 42, 9870–9879. doi: 10.1002/2015GL066317

Korff, L., von Dobeneck, T., Frederichs, T., Kasten, S., Kuhn, G., Gersonde, R., et al. (2016). Cyclic magnetite dissolution in pleistocene sediments of the abyssal northwest pacific ocean: Evidence for glacial oxygen depletion and carbon trapping. *Paleoceanography* 31, 600–624. doi: 10.1002/2015PA002882

Kotov, S., Paelike, H., Kotov, S., and Paelike, H. (2018)QAnalySeries - a cross-platform time series tuning and analysis tool. In: *AGUFM*. Available at: https://ui.adsabs.harvard.edu/abs/2018AGUFMPP53D1230K/abstract (Accessed April 12, 2021).

Kozdon, R., Eisenhauer, A., Weinelt, M., Meland, M. Y., and Nürnberg, D. (2009). Reassessing Mg/Ca temperature calibrations of neogloboquadrina pachyderma (sinistral) using paired δ44/40Ca and Mg/Ca measurements. *Geochem. Geophys. Geosyst.* 10, 1–14. doi: 10.1029/2008GC002169

Kuroyanagi, A., Kawahata, H., Nishi, H., and Honda, M. C. (2008). Seasonal to interannual changes in planktonic foraminiferal assemblages in the northwestern north pacific: Sediment trap results encompassing a warm period related to El niño. *Palaeogeogr. Palaeoclimatol. Palaeoecol.* 262, 107–127. doi: 10.1016/j.palaeo.2008.02.012

Kuzmin, Y. V., Burr, G. S., Gorbunov, S. V., Rakov, V. A., and Razjigaeva, N. G. (2007). A tale of two seas: Reservoir age correction values (R, ΔR) for the Sakhalin island (Sea of Japan and Okhotsk Sea). *Nucl. Instruments. Methods Phys. Res. Sect. B. Beam. Interact. Mater. Atoms.* 259, 460–462. doi: 10.1016/j.nimb.2007.01.308

Kuzmin, Y. V., Burr, G. S., and Jull, A. J. (2001). Radiocarbon reservoir correction ages in the Peter the great gulf, Sea of Japan, and Eastern coast of the kunashir, southern kuriles (Northwestern pacific). *Radiocarbon* 43, 477–481. doi: 10.1017/S0033822200038364

Labeyrie, L., Leclaire, H., Waelbroeck, C., Cortijo, E., Duplessy, J. C., Vidal, L., et al. (1999). Temporal variability of the surface and deep waters of the northwest atlantic ocean at orbital and millennial scales. *Geophys. Monogr. Ser.* 112, 77–98. doi: 10.1029/GM112p0077

Lamy, F., Gersonde, R., Winckler, G., Esper, O., Jaeschke, A., Kuhn, G., et al. (2014). Increased dust deposition in the pacific southern ocean during glacial periods. *Science* 80-.). 343, 403–407. doi: 10.1126/science.1245424

Lang, N., and Wolff, E. W. (2011). Interglacial and glacial variability from the last 800 ka in marine , ice and terrestrial archives. *Clim. Past* 7, 361–380. doi: 10.5194/cp-7-361-2011

LeGrande, A. N., and Schmidt, G. A. (2006). Global gridded data set of the oxygen isotopic composition in seawater. *Geophys. Res. Lett.* 33, 1–5. doi: 10.1029/2006GL026011

Lembke-Jene, L., Tiedemann, R., Nürnberg, D., Kokfelt, U., Kozdon, R., Max, L., et al. (2017). Deglacial variability in Okhotsk Sea intermediate water ventilation and biogeochemistry: Implications for north pacific nutrient supply and productivity. *Quat. Sci. Rev.* 160, 116–137. doi: 10.1016/j.quascirev.2017.01.016

Li, S., Wu, L., Yang, Y., Geng, T., Cai, W., Gan, B., et al. (2020). The pacific decadal oscillation less predictable under greenhouse warming. *Nat. Clim. Change* 10, 30–34. doi: 10.1038/s41558-019-0663-x

Lisiecki, L. E., and Raymo, M. E. (2005). A pliocene-pleistocene stack of 57 globally distributed benthic δ 18O records. *Paleoceanography* 20, 1–17. doi: 10.1029/2004PA001071

Locarnini, R. A., Mishonov, A. V., Baranova, O. K., Boyer, T. P., Zweng, M. M., Garcia, H. E., et al. (2018). World ocean atlas 2018, volume 1: Temperature. a. mishonov, technical Editor. *NOAA. Atlas. NESDIS.* 1, 52.

Lohmann, G., Lembke-Jene, L., Tiedemann, R., Gong, X., Scholz, P., Zou, J., et al. (2019). Challenges in the paleoclimatic evolution of the Arctic and subarctic pacific since the last glacial period–the sino–German pacific–Arctic experiment (SiGePAX). *Challenges* 10, 13. doi: 10.3390/challe10010013

MacDonald, G. M., and Case, R. A. (2005). Variations in the pacific decadal oscillation over the past millennium. *Geophys. Res. Lett.* 32, 1–4. doi: 10.1029/2005GL022478

Mantua, N. J., Hare, S. R., Zhang, Y., Wallace, J. M., and Francis, R. C. (1997). A pacific interdecadal climate oscillation with impacts on salmon production. *Bull. Am. Meteorol. Soc* 78, 1069–1079. doi: 10.1175/1520-0477(1997)078<1069:APICOW>2.0.CO;2

Matsumoto, K., Oba, T., Lynch-Stieglitz, J., and Yamamoto, H. (2002). Interior hydrography and circulation of the glacial pacific ocean. *Quat. Sci. Rev.* 21, 1693–1704. doi: 10.1016/S0277-3791(01)00142-1

Matsuzaki, K. M., Nishi, H., Suzuki, N., Cortese, G., Eynaud, F., Takashima, R., et al. (2014). Paleoceanographic history of the Northwest pacific ocean over the past 740kyr, discerned from radiolarian fauna. *Palaeogeogr. Palaeoclimatol. Palaeoecol.* 396, 26–40. doi: 10.1016/j.palaeo.2013.12.036

Metzger, E. J., and Hurlburt, H. E. (1996). Coupled dynamics of the south China Sea, the sulu Sea, and the pacific ocean. *J. Geophys. Res. C Ocean.* 101, 12331–12352. doi: 10.1029/95JC03861

Mitnik, L. M., Khazanova, E. S., and Dubina, V. A. (2020). Mesoscale and synoptic scale dynamic phenomena in the oyashio current region observed in SAR imagery. *Int. J. Remote Sens.* 41, 5861–5883. doi: 10.1080/01431161.2019.1701215

Mohtadi, M., Romero, O. E., Kaiser, J., and Hebbeln, D. (2007). Cooling of the southern high latitudes during the medieval period and its effect on ENSO. *Quat. Sci. Rev.* 26, 1055–1066. doi: 10.1016/j.quascirev.2006.12.008

Morley, J. J., and Heusser, L. E. (1997). Role of orbital forcing in east Asian monsoon climates during the last 350 kyr: Evidence from terrestrial and marine climate proxies from core RC14-99. *Paleoceanography* 12, 483–493. doi: 10.1029/97PA00213

Mulitza, S., Boltovskoy, D., Donner, B., Meggers, H., Paul, A., and Wefer, G. (2003). Temperature: δ18O relationships of planktonic foraminifera collected from surface waters. *Palaeogeogr. Palaeoclimatol. Palaeoecol.* 202, 143–152. doi: 10.1016/S0031-0182(03)00633-3

Narita, H., Sato, M., Tsunogai, S., Murayama, M., Ikehara, M., Nakatsuka, T., et al. (2002). Biogenic opal indicating less productive northwestern north pacific during the glacial ages. *Geophys. Res. Lett.* 29, 2–5. doi: 10.1029/2001GL014320

Newman, M., Alexander, M. A., Ault, T. R., Cobb, K. M., Deser, C., Di Lorenzo, E., et al. (2016). The pacific decadal oscillation, revisited. *J. Clim.* 29, 4399–4427. doi: 10.1175/JCLI-D-15-0508.1

Nishioka, J., Ono, T., Saito, H., Sakaoka, K., and Yoshimura, T. (2011). Oceanic iron supply mechanisms which support the spring diatom bloom in the oyashio region, western subarctic pacific. *J. Geophys. Res. Ocean.* 116, 1–17. doi: 10.1029/2010JC006321

Nürnberg, D. (2018). RV SONNE Fahrtbericht/Cruise report SO264 - SONNE-EMPEROR: The Plio/Pleistocene to Holocene development of the pelagic north pacific from surface to depth – assessing its role for the global carbon budget and earth ís climate, Suva (Fiji) – Yokohama (Japa. *GEOMAR report, n. ser. 046*. GEOMAR. Helmholtz-Zentrum. für. Ozeanforschung. Kiel. Ger.. *Geophys. Monogr. Ser.* 151, 1–284. doi: 10.3289/GEOMAR_REP_NS_46_2018

Nürnberg, C. C., Bohrmann, G., Schlüter, M., and Frank, M. (1997). Barium accumulation in the Atlantic sector of the southern ocean: Results from 190,000-year records. *Paleoceanography* 12, 594–603. doi: 10.1029/97PA01130

Nürnberg, D., Brughmans, N., Schönfeld, J., Ninnemann, U., and Dullo, C. (2004). Paleo-export production, terrigenous flux and Sea surface temperatures around Tasmania - implications for Glacial/Interglacial changes in the subtropical convergence zone 1–32. doi: 10.1029/151GM17

Nürnberg,, and Tiedemann, R. (2004). Environmental change in the Sea of Okhotsk during the last 1.1 million years. *Paleoceanography* 19, 1–23. doi: 10.1029/2004PA001023

Ogawa, K., Usui, T., Takatani, S., Kitao, T., Harimoto, T., Katoh, S., et al. (2006). Shipboard measurements of atmospheric and surface seawater pCO 2 in the north pacific carried out from January 1999 to October 2000 on the voluntary observation ship MS alligator liberty. *Pap. Meteorol. Geophys.* 57, 37–46. doi: 10.2467/mripapers.57.37

Ponomareva, V., Bubenshchikova, N., Portnyagin, M., Zelenin, E., Derkachev, A., Gorbarenko, S., et al. (2018). Large-Magnitude pauzhetka caldera-forming eruption in kamchatka: Astrochronologic age, composition and tephra dispersal. *J. Volcanol. Geotherm. Res.* 366, 1–12. doi: 10.1016/j.jvolgeores.2018.10.006

Qiu, B. (2002). The kuroshio extension system: Its large-scale variability and role in the midlatitude ocean-atmosphere interaction. *J. Oceanogr.* 58, 57–75. doi: 10.1023/A:1015824717293

Qiu, B. (2019). *Kuroshio and oyashio currents. 3rd ed* (Elsevier Ltd). doi: 10.1016/B978-0-12-409548-9.11295-3

Qiu, B., and Lukas, R. (1996). Seasonal and interannual variability of the north equatorial current, the Mindanao current, and the kuroshio along the pacific western boundary. *J. Geophys. Res. C Ocean.* 101, 12315–12330. doi: 10.1029/95JC03204

Reynolds, L. A., and Thunell, R. C. (1986). Seasonal production and morphologic variation of neogloboquadrina pachyderma (Ehrenberg) in the northeast pacific. *Micropaleontology* 32, 1. doi: 10.2307/1485696

Riethdorf, J. R. (2013). Deglacial development of (sub) sea surface temperature and salinity in the subarctic northwest pacific. *Paleoceanography* 28, 91–104. doi: 10.1002/palo.20014

Riethdorf, J. R., Nürnberg, D., Max, L., Tiedemann, R., Gorbarenko, S. A., and Malakhov, M. I. (2013). Millennial-scale variability of marine productivity and terrigenous matter supply in the western Bering Sea over the past 180 kyr. *Clim. Past.* 9, 1345–1373. doi: 10.1002/aur.1919

Sagawa, T., Kuroyanagi, A., Irino, T., Kuwae, M., and Kawahata, H. (2013). Seasonal variations in planktonic foraminiferal flux and oxygen isotopic composition in the western north pacific: Implications for paleoceanographic reconstruction. *Mar. Micropaleontol.* 100, 11–20. doi: 10.1016/j.marmicro.2013.03.013

Sarnthein, M., Gebhardt, H., Kiefer, T., Kucera, M., Cook, M., and Erlenkeuser, H. (2004). Mid Holocene origin of the sea-surface salinity low in the subarctic north pacific. *Quat. Sci. Rev.* 23, 2089–2099. doi: 10.1016/j.quascirev.2004.08.008

Schiebel, R., Spielhagen, R. F., Garnier, J., Hagemann, J., Howa, H., Jentzen, A., et al. (2017). Modern planktic foraminifers in the high-latitude ocean. *Mar. Micropaleontol.* 136, 1–13. doi: 10.1016/j.marmicro.2017.08.004

Schlitzer, R. (2019). *Ocean data view*. Available at: https://Https://Odv.Awi.De.

Shackleton, N. J. (1974). Attainment of isotopic equilibrium between ocean water and the benthonic foraminifera genus uvigerina: Isotopic changes in the ocean during the last glacial. *Colloq. Int. du C.N.R.S.* 219, 203–210.

Shackleton, N. J., and Hall, M. A. (1984). Oxygen and carbon isotope stratigraphy of deep Sea drilling project hole 552A: Plio-pleistocene glacial history. *Initial. Rep. DSDP. Leg. 81 Southampt. to Azores.*, 599–609. doi: 10.2973/dsdp.proc.81.116.1984

Shackleton, N. J., and Opdyke, N. D. (1973). Oxygen isotope and palaeomagnetic stratigraphy of equatorial pacific core V28-238: Oxygen isotope temperatures and ice volumes on a 10^5 year and 10^6 year scale. *Quat. Res* 3, 39–55. doi: 10.1016/0033-5894(73)90052-5

Shigemitsu, M., Narita, H., and Watanabe, Y. W. (2007). Ba, Si, U, Al, Sc, la, Th, c and 13 C/12 c in a sediment core in the western subarctic pacific as proxies of past biological production. *Mar. Chem.* 106, 442–455. doi: 10.1016/j.marchem.2007.04.004

Shimizu, Y., Yasuda, I., and Ito, S. I. (2001). Distribution and circulation of the coastal oyashio intrusion. *J. Phys. Oceanogr.* 31, 1561–1578. doi: 10.1175/1520-0485(2001)031<1561:DACOTC>2.0.CO;2

Sigman, D. M., Fripiat, F., Studer, A. S., Kemeny, P. C., Martínez-García, A., Hain, M. P., et al. (2021). The southern ocean during the ice ages: A review of the Antarctic surface isolation hypothesis, with comparison to the north pacific. *Quat. Sci. Rev.* 254. doi: 10.1016/j.quascirev.2020.106732

Sigman, D. M., Hain, M. P., and Haug, G. H. (2010). The polar ocean and glacial cycles in atmospheric CO2 concentration. *Nature* 466, 47–55. doi: 10.1038/nature09149

Stuiver, M., Reimer, P. J., and Reimer, R. W. (2020) *CALIB 8.2*. Available at: http://calib.org (Accessed 2020-10-9).

Takahashi, T., Sutherland, S. C., Wanninkhof, R., Sweeney, C., Feely, R. A., Chipman, D. W., et al. (2009). Climatological mean and decadal change in surface ocean pCO2, and net sea-air CO2 flux over the global oceans. *Deep. Res. Part II. Top. Stud. Oceanogr.* 56, 554–577. doi: 10.1016/j.dsr2.2008.12.009

Talley, L. D. (1993). Distribution and formation of north pacific intermediate water. *J. Phys. Oceanogr.* 23, 517–537. doi: 10.1175/1520-0485(1993)023<0517:DAFONP>2.0.CO;2

Taylor, B. J., Rae, J. W. B., Gray, W. R., Darling, K. F., Burke, A., Gersonde, R., et al. (2018). Distribution and ecology of planktic foraminifera in the north pacific: Implications for paleo-reconstructions. *Quat. Sci. Rev.* 191, 256–274. doi: 10.1016/j.quascirev.2018.05.006

Thompson, P. R., and Shackleton, N. J. (1980). North pacific palaeoceanography: Late quaternary coiling variations of planktonic foraminifer neogloboquadrina pachyderma. *Nature* 287, 829–833. doi: 10.1038/287829a0

Tjallingii, R., Röhl, U., Kölling, M., and Bickert, T. (2007). Influence of the water content on X-ray fluorescence corescanning measurements in soft marine sediments. *Geochem. Geophys. Geosyst.* 8, 1–12. doi: 10.1029/2006GC001393

Tsuda, A., Takeda, S., Saito, H., Nishioka, J., Nojiri, Y., Kud, I., et al (2003). A mesoscale iron enrichment in the Western subarctic Pacific induces a large centric diatom bloom. *Science (80-)* 300, 985–961. doi: 10.1126/science.1082000

Tukey, J. W. (1977). *Exploratory data analysis* (Reading, MA: Addison-Wesley).

Ujiié, Y., Asahi, H., Sagawa, T., and Bassinot, F. (2016). Evolution of the north paci fi c subtropical gyre during the past 190 kyr through the interaction of the kuroshio current with the surface and intermediate waters. *Paleoceanography* 31, 1498–1513. doi: 10.1002/2015PA002914

Ujiié, Y., Ujiié, H., Taira, A., Nakamura, T., and Oguri, K. (2003). Spatial and temporal variability of surface water in the kuroshio source region, pacific ocean, over the past 21,000 years: Evidence from planktonic foraminifera. *Mar. Micropaleontol.* 49, 335–364. doi: 10.1016/S0377-8398(03)00062-8

Waddell, L. M., Hendy, I. L., Moore, T. C., and Lyle, M. W. (2009). Ventilation of the abyssal southern ocean during the late neogene: A new perspective from the subantarctic pacific. *Paleoceanography*, 24. doi: 10.1029/2008PA001661

Wara, M. W., Ravelo, A. C., and Delaney, M. L. (2005). Climate change: Permanent El niño-like conditions during the pliocene warm period. *Science* 80-.)309, 758–761. doi: 10.1126/science.1112596

Weltje, G. J., Jan, G., and Tjallingii, R. (2008). Calibration of XRF core scanners for quantitative geochemical logging of sediment cores: Theory and application calibration of XRF core scanners for quantitative geochemical logging of sediment cores: Theory and application. *Earth Planet. Sci. Lett.* 274, 423–438. doi: 10.1016/j.epsl.2008.07.054

Yamamoto, M., Suemune, R., and Oba, T. (2005). Equatorward shift of the subarctic boundary in the northwestern pacific during the last deglaciation. *Geophys. Res. Lett.* 32, 10–13. doi: 10.1029/2004GL021903

Yamane, M. (2003). Late quaternary variations in water mass in the shatsky rise area, northwest pacific ocean. *Mar. Micropaleontol.* 48, 205–223. doi: 10.1016/S0377-8398(03)00017-3

Yasuda, I. (2003). Hydrographic structure and variability in the kuroshio- oyashio transition area. *J. Oceanogr.* 59, 389–402. doi: 10.1023/A:1025580313836

Yasuda, I., Kouketsu, S., Katsumata, K., Ohiwa, M., Kawasaki, Y., and Kusaka, A. (2002). Influence of Okhotsk Sea intermediate water on the oyashio and north pacific intermediate water. *J. Geophys. Res. Ocean.* 107, 1–11. doi: 10.1029/2001jc001037

Yasuda, I., Okuda, K., and Shimizu, Y. (1996). Distribution and modification of north pacific intermediate water in the kuroshio-oyashio interfrontal zone. *J. Phys. Oceanogr.* 26, 448–465. doi: 10.1175/1520-0485(1996)026<0448:DAMONP>2.0.CO;2

Yasudomi, Y., Motoyama, I., Oba, T., and Anma, R. (2014). Environmental fluctuations in the northwestern pacific ocean during the last interglacial period: Evidence from radiolarian assemblages. *Mar. Micropaleontol.* 108, 1–12. doi: 10.1016/j.marmicro.2014.02.001

Yatsu, A., Chiba, S., Yamanaka, Y., Ito, S. I., Shimizu, Y., Kaeriyama, M., et al. (2013). Climate forcing and the Kuroshio/Oyashio ecosystem. *ICES. J. Mar. Sci.* 70, 922–933. doi: 10.1093/icesjms/fst084

Yoneda, M., Uno, H., Shibata, Y., Suzuki, R., Kumamoto, Y., Yoshida, K., et al. (2007). Radiocarbon marine reservoir ages in the western pacific estimated by pre-bomb molluscan shells. *Nucl. Instruments. Methods Phys. Res. Sect. B. Beam. Interact. Mater. Atoms.* 259, 432–437. doi: 10.1016/j.nimb.2007.01.184

Yu, L., Furevik, T., Otterå, O. H., and Gao, Y. (2015). Modulation of the pacific decadal oscillation on the summer precipitation over East China: a comparison of

observations to 600-years control run of Bergen climate model. *Clim. Dyn.* 44, 475–494. doi: 10.1007/s00382-014-2141-5

Yuan, Y. C., Liu, Y. G., and Su, J. L. (2001). Variability of the kuroshio in the East China Sea during El-niño to la niña phenomenon of 1997 and 1998. *Acta Geophys. Sin.* 44, 199–210. doi: 10.1002/cjg2.132

Zammit-Mangion, A., and Wikle, C. K. (2020). Deep integro-difference equation models for spatio-temporal forecasting. *Spatial. Stat* 37, 100408. doi: 10.1016/j.spasta.2020.100408

Zheng, X., Li, A., Kao, S. J., Gong, X., Frank, M., Kuhn, G., et al. (2016). Synchronicity of kuroshio current and climate system variability since the last glacial maximum. *Earth Planet. Sci. Lett.* 452, 247–257. doi: 10.1016/j.epsl.2016.07.028

Zhong, Y., Lu, Z., Wilson, D. J., Zhao, D., Liu, Y., Chen, T., et al. (2023). Paleoclimate evolution of the north pacific ocean during the late quaternary: Progress and challenges. *Geosyst. Geoenvironment.* 2, 100124. doi: 10.1016/j.geogeo.2022.100124

Zweng, M. M., Reagan, J. R., Seidov, D., Boyer, T. P., Antonov, J. I., Locarnini, R. A., et al. (2019). World ocean atlas 2018, volume 2: Salinity. *NOAA. Atlas. NESDIS.* 2, 50.

frontiers | Frontiers in Marine Science

TYPE Original Research
PUBLISHED 05 April 2023
DOI 10.3389/fmars.2023.1157929

OPEN ACCESS

EDITED BY
Johan Schijf,
University of Maryland, College Park,
United States

REVIEWED BY
Donna Surge,
University of North Carolina at Chapel Hill,
United States
David Moss,
Sam Houston State University,
United States
Diana Thatcher,
Iowa State University, United States

*CORRESPONDENCE
Niels J. de Winter
n.j.de.winter@vu.nl

SPECIALTY SECTION
This article was submitted to
Marine Biogeochemistry,
a section of the journal
Frontiers in Marine Science

RECEIVED 03 February 2023
ACCEPTED 14 March 2023
PUBLISHED 05 April 2023

CITATION
de Winter NJ, van Sikkeleras S, Goudsmit-Harzevoort B, Boer W, de Nooijer L, Reichart G-J, Claeys P and Witbaard R (2023) Tracing timing of growth in cultured molluscs using strontium spiking.
Front. Mar. Sci. 10:1157929.
doi: 10.3389/fmars.2023.1157929

Tracing timing of growth in cultured molluscs using strontium spiking

Niels J. de Winter[1,2]*, Sterre van Sikkeleras[3], Barbara Goudsmit-Harzevoort[3,4], Wim Boer[5], Lennart de Nooijer[5], Gert-Jan Reichart[4,5], Philippe Claeys[2] and Rob Witbaard[3]

[1]Department of Earth Sciences, Vrije Universiteit Amsterdam, Amsterdam, Netherlands, [2]Analytical, Environmental and Geo-Chemistry Research Group, Vrije Universiteit Brussel, Brussels, Belgium, [3]Department of Estuarine and Coastal Systems, Royal Netherlands Institute for Sea Research, Texel, Netherlands, [4]Department of Earth Sciences, Utrecht University, Utrecht, Netherlands, [5]Department of Ocean Systems, Royal Netherlands Institute for Sea Research, Texel, Netherlands

Introduction: Growth experiments present a powerful tool for determining the effect of environmental parameters on growth and carbonate composition in biogenic calcifiers. For successful proxy calibration and biomineralization studies, it is vital to identify volumes of carbonate precipitated by these organisms at precise intervals during the experiment. Here, we investigate the use of strontium labelling in mollusc growth experiments.

Methods: Three bivalve species (*Cerastoderma edule*, *Mytilus edulis* and *Ostrea edulis*) were grown under monitored field conditions. The bivalves were regularly exposed to seawater with elevated concentrations of dissolved strontium chloride ($SrCl_2$). In addition, the size of their shells was determined at various stages during the experiment using calliper measurements and digital photography. Trace element profiles were measured in cross sections through the shells of these molluscs using laser ablation ICPMS and XRF techniques.

Results: Our results show that doses of dissolved strontium equivalent to 7-8 times the background marine value (~0.6 mmol/L) are sufficient to cause reproducible peaks in shell-incorporated strontium in *C. edule* and *M. edulis* shells. No negative effects were observed on shell calcification rates. Lower doses (3-5 times background values) resulted in less clearly identifiable peaks, especially in *M. edulis*. Strontium spiking labels in shells of *O. edulis* are more difficult to detect, likely due to their irregular growth.

Discussion: Strontium spiking is a useful technique for creating time marks in cultured shells and a reproducible way to monitor shell size during the growing season while limiting physical disturbance of the animals. However, accurate reconstructions of growth rates at high temporal resolution require frequent spiking with high doses of strontium.

KEYWORDS

mollusk (mollusc), growth experiment, trace element, shell, proxy development

1 Introduction

Crystalline calcium carbonate is one of the most abundant marine biominerals and is produced by organisms ranging from microbes, coccolithophores, foraminifera and molluscs to corals and fishes (Crichton, 2019). Their fossil skeletons, shells and other biostructures are common in the archaeological and geological record because they preserve relatively well and therefore play an important role as archives for past climates (Lough and Barnes, 2000; Pages 2k consortium, 2017; Henkes et al., 2018; Marchegiano et al., 2019; Moss et al., 2021; Agterhuis et al., 2022) and environments (Sampei et al., 2005; Song et al., 2014; Auderset et al., 2022). Carbonate skeletons also preserve information about life histories (Gerringer et al., 2018; Mat et al., 2020; Posenato et al., 2022), ecological relationships between organisms (Fagerstrom, 1987; Mourguiart and Carbonel, 1994; Valchev, 2003), and past human interrelations (Gutiérrez-Zugasti, 2011; Haour et al., 2016; Burchell et al., 2018). Furthermore, the contribution of calcifiers (organisms that mineralize calcium carbonate) to the rock record is of great commercial interest, for example for the extraction of building materials, as source rocks for water and hydrocarbons and as a storage rock for CO_2 (Hanshaw and Back, 1979; Izgec et al., 2008; Benavente et al., 2018; Tran et al., 2020).

Many carbonate-based reconstructions rely on analyses of their elemental or isotopic composition, the interpretation of which is anchored by modern growth experiments (Stoll et al., 2002; Sánchez-Román et al., 2008; de Winter et al., 2022a). In such experiments, calcifiers are cultured under controlled or monitored conditions with the aim to precisely study the effect of environmental changes on the composition of the precipitated carbonates. Such experiments require monitoring of the size of carbonate shells or skeletons, either by direct measurements or by a labelling approach. This ensures recognition of the parts that were deposited under specific experimental conditions or at specific times during the experiment, such that these parts can be sampled for chemical analysis. Existing labelling techniques include spiking the growth environment with (radiogenic) nuclides such as ^{14}C (Kuzyakov et al., 2006), ^{13}C (Wilmeth et al., 2018), ^{44}Ca (Nehrke et al., 2013) and ^{86}Sr (Houlbrèque et al., 2009), introducing to the growth environment fluorescent dyes which bind to the calcium carbonate formed during the experiment such as calcein (Markuszewski, 1979; Leips et al., 2001; Zhou et al., 2017; Fox et al., 2018), alizarin red S (Bashey, 2004; Zhou et al., 2017) and others (Day et al., 1995), and spiking the growth environment with elevated concentrations of trace elements (e.g. Mn or Sr; Lartaud et al., 2010; Geerken et al., 2022). The aim of these techniques is to introduce a mark or label that is clear and easy to locate in the carbonate, while avoiding interference with the process of calcification itself. For some of these methods (e.g. calcein dye) it has been demonstrated that they affect the calcification process in some organisms and therefore inadvertently influence the results of biomineralization studies (Magnabosco et al., 2018). Additionally, the differences in practical use, traceability and costs of the above-mentioned labels allow their use to be tailored to the desired experimental outcome.

In this study, we test the use of strontium (Sr) labelling in mollusc growth experiments. Strontium is a useful element for labelling in studies of marine carbonates because it is a highly soluble, conservative element in the ocean (Quinby-Hunt and Turekian, 1983). It is readily incorporated in the calcium carbonate because of its chemical similarity to Ca (Dodd, 1967). Differences in the mineral lattice cause Sr to be more readily taken up in aragonite than in calcite (Day and Henderson, 2013; Wassenburg et al., 2016). Experimental studies show that moderate incorporation of Sr does not significantly inhibit growth or affect the structural properties of calcite and aragonite (Wasylenki et al., 2005; Saito et al., 2020). In addition, the incorporation of Sr into biogenic carbonates is widely studied due to its potential as a proxy for carbonate mineralization rate or temperature (Stoll and Schrag, 2001; Lear et al., 2003; Elliot et al., 2009). It therefore presents a useful alternative to the pre-established Mn labelling technique (Lartaud et al., 2010; Geerken et al., 2022).

The bivalves *Cerastoderma edule* (common cockle), *Mytilus edulis* (blue mussel) and *Ostrea edulis* (European oyster) were selected as subjects in this study for several reasons: Firstly, these species exhibit different shell mineralogies, with the cockle shells consisting of aragonite, oyster shells predominantly of calcite and the mussels have both aragonite (inner) and calcite (outer) shell layers (Feng et al., 2014; Füllenbach et al., 2015; Nikolayev et al., 2019). This allows us to test how administered Sr peaks are taken up in these different shell minerals, which have varying affinity for the element (see above; Day and Henderson, 2013; Wassenburg et al., 2016). Secondly, all three species occur naturally in the area (Wadden Sea and North Sea), limiting risk to the success of growth experiments by ensuring optimal growing conditions as well as to the local ecosystem by not introducing invasive taxa to the Wadden Sea, which is a UNESCO World Heritage site (Beukema et al., 2001; Bennema et al., 2020). Thirdly, the species represent similar taxa from the fossil record which are used for paleoclimate and paleoenvironmental reconstructions, driving the need to better understand shell growth using growth experiments (Obelic et al., 1998; Huyghe et al., 2015; Wichern et al., 2022). Finally, all three species are (historically) commercially important, and growth experiments such as the ones described here may aid in understanding their growth to optimize aquaculture practices (Smaal and Lucas, 2000; Kraan et al., 2011; Colsoul et al., 2021). We thus investigated the potential for spiking the shells of these species with Sr to trace their growth during growth experiments.

2 Methods

2.1 Growth experiments

2.1.1 Description of growth experiments

Three bivalve species (the common cockle *Cerastoderma edule*, the blue mussel *Mytilus edulis* and the European oyster *Ostrea edulis*) were grown under monitored conditions in an outdoor growth setup in the harbour of the Royal Netherlands Institute for Sea Research

(NIOZ, Texel, the Netherlands). Juvenile (<1 year old) *O. edulis* (hereafter: "oysters") were sampled on March 2nd, 2020, from a brood stock in the Mokbaai (53°00'05.6"N, 4°45'48.5"E). Juvenile *M. edulis* (hereafter: "mussels") were collected on February 24th, 2020, from a groin along the North Sea coast of Texel (53°01'17.8"N, 4°42'32.3"E). Juvenile *C. edule* (hereafter: "cockles") were collected on March 6th, 2020, from a tidal flat located at the northern tip of the island. (53° 09'18.3"N, 4°52'54.0"E). All specimens were individually labelled with Hallprint plastic shellfish tags (Hallprint Fish Tags, Hindmarch Valley, Australia), which were glued on the shell with cyanoacrylate glue. In this way specimens could be followed individually throughout the experiment.

The NIOZ harbour (53°00'19" N, 4°47'46" E) is located at the leeside of the island of Texel with its entrance to the Marsdiep tidal inlet, which connects the Wadden Sea to the North Sea. The harbour experiences the full tidal cycle and closely follows the water properties (temperature, salinity, water contents, etc.) of the Marsdiep (Hippler et al., 2013). At approximately 600-meter distance, these properties are continuously monitored at short (<1 minute) intervals by a neighbouring measurement station operated by the NIOZ (Van Aken, 2003; de Winter et al., 2021). The harbour is shielded from most severe wave action.

Growth experiments took place in a floating setup in which open (meshed), plastic crates (600 x 400 x 400 mm) are attached to glass fibre poles, which are part of a floating mooring (see Figure 1; see also description in Hippler et al., 2013). The crates were covered by a mesh to minimize predation by crabs and birds. The growth experiments took place between February and September 2020 and involved 69 oysters, 77 mussels and 106 cockles. Oysters and mussels were suspended in 100 x 200 mm nets hung on the floating construction inside the crates. The cockles were kept in three shoebox-sized (330 x 180 x 100 mm) plastic containers filled with sand placed on the bottom of the suspended crates. The difference in housing of species allows the animals to exhibit their natural behaviour (e.g. burrowing in sediment) as well as possible within the experiment. In the floating setup, all specimens were continuously submerged roughly 20-30 cm below the water surface during the entirety of the experiment.

2.1.2 Shell measurements

Sizes of all individuals were measured four times during the experiments. For cockles, the shell height, length, and width were measured while for mussels only the maximum shell length was measured with a digital calliper which reports precision at the 0.01 mm level (average measurement interval of calliper measurements was 53 days). Considering the irregular shape of oyster shells, especially when growing together, the size of oyster shells was measured by photographing the individuals in a direction perpendicular to the plane of occlusion of the two valves using a Nikon Coolpix (Nikon Corp., Minato, Tokyo, Japan) camera fixed to a stand. The length of the axis of maximum growth (maximum distance of the ventral margin away from the hinge) was determined from these pictures by calibrating distances relative to 10 mm grid paper on which the shells were photographed using ImageJ 1.53 (Schindelin et al., 2012). Measurements were carried out in batches so that within two days all shells were measured while minimizing aerial exposure and associated growth stress.

To estimate the uncertainty on shell size measurements using the digital calliper, repeated measurements of shell size were carried out on selected specimens of each of the three bivalve species. These

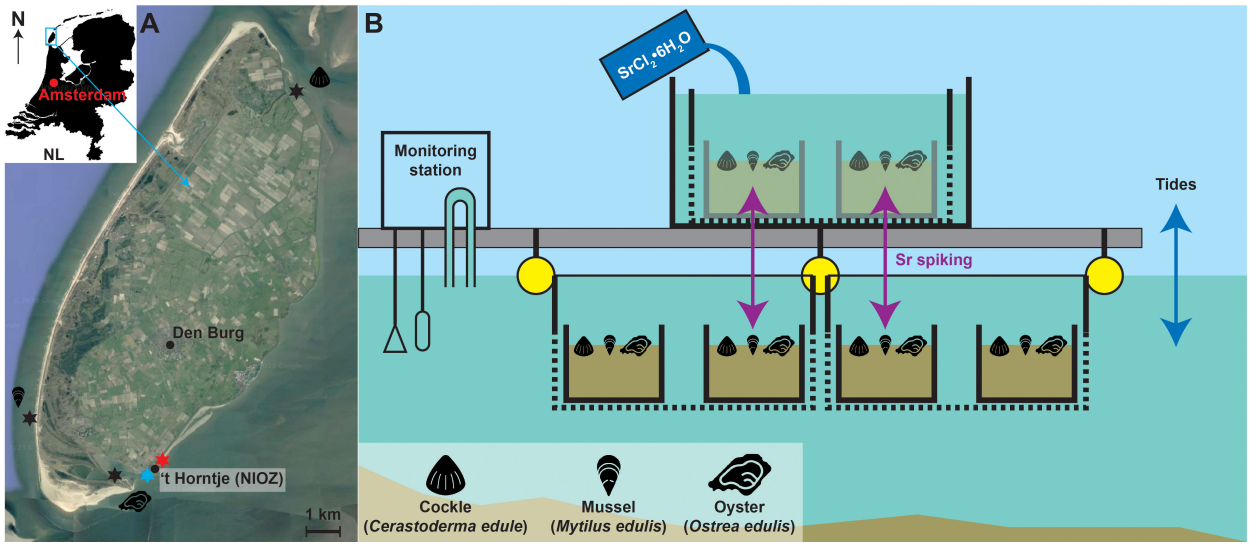

FIGURE 1
(A) Satellite image of Texel island (52°58'31"N, 4°41'05"E). Modified using Maps Data ©2023 *Alphabet Inc., Mountain View, CA, USA*. Round symbols indicate the location of named population centers. Stars indicate the origins of juvenile specimens (black; with symbols indicating the species), the location of the culture setup (red) and the location of the monitoring station (blue), ~600 meter away from the culturing locality. **(B)** Schematic overview of the experimental setup, with the floating jetty in grey, the crates in black and the buoys in yellow. Note that oysters and mussels were grown in nets attached to the side of the crates and not in the sand containers. Water depth is not to scale but was sufficient to keep the crates submerged even during the lowest tides. Purple arrows indicate the transfer of specimens to environments with elevated Sr concentrations during the spiking events.

measurements were carried out by three different persons, each measuring the length of the axis of maximum growth of each shell 10 separate times. This procedure included variability associated with the accuracy of the digital calliper as well as uncertainty associated with the personal choice of the researcher as to where the axis of maximum growth is located on the shell. Results of this test are provided in SI11. The standard deviation on separate shell size measurements using a hand-held digital calliper was 0.18 mm for *C. edule* shells and 0.21 mm for both *M. edulis* and *O. edulis* shells.

2.1.3 Strontium spiking

All individuals were spiked simultaneously with increased concentrations of Sr at multiple time intervals over the period of the experiment (see Table 1). A pre-weighed amount of hydrated strontium chloride ($SrCl_2{\cdot}6H_2O$) was dissolved in a known volume of seawater in the culture setup to obtain elevated Sr concentrations of 0.58 mmol/L, 0.33 mmol/L and 0.21 mmol/L for high, medium, and low dose spikes, respectively. These concentrations amount to an approximately 7.7-fold, 4.4-fold and 2.8-fold increase with respect to the background concentration of dissolved Sr in the environment (0.075 mmol/L when corrected for a mean salinity of 28.5 over the growth period; see de Winter et al., 2021). The concentrations of Sr in the seawater under normal conditions as well as during a high dose Sr spike event were verified using ICP-MS measurements on filtered seawater samples taken during the growth experiments (see section 2.2). All individuals were simultaneously exposed to these doses by placing the nets and containers containing the bivalves in this tank for 24h (Figure 1). The tank was suspended in the floating mooring to facilitate thermal exchange with the ambient sea water and ensure no temperature differences occurred during the Sr spiking period. After 24h, the nets and trays with specimens were taken from the Sr enriched solution and returned to the open crates, returning them to sea water with a normal marine elemental composition. This procedure was repeated every 2-3 weeks with varying Sr concentrations (Table 1).

2.1.4 Specimen selection and treatment

Three cockles (specimens G003, G511 and G600) were found dead in the experiment on June 4th and were used to test if the Sr spiking led to enriched concentrations which could be traced back in the shell carbonate. These three individuals were exposed to three Sr spikes: a high dose on April 4th and April 22nd and a medium dose on May 14th. Their shell size was measured at the start of the experiment (March 16th), on May 1st and after they were found dead (June 4th). Of the individuals which survived the entire experimental period, three specimens of each species were selected on September 24th and euthanized for further analyses (see Table 2). Over the experimental period, the size of these 9 specimens was measured 4 times and they were exposed to 5 Sr spikes.

The soft tissue was removed from all individuals, and the shells were cleaned superficially with a soft brush and left to dry overnight at room temperature. Dried shells were embedded in epoxy resin (THV 500 with THV 155 hardener; Poly-Service BV, Amsterdam, the Netherlands). Shells were sectioned through the axis of maximum growth (the same axis along which shell length was measured with callipers, see section 2.1.2) using a slow rotating (250 rpm) Buehler IsoMet 1000 precision saw (Buehler, Chicago, USA) with a wafering-thin blade. Parallel cuts were subsequently made to produce 7 mm thick sections through the shells, which were polished using a Buehler Metaserv 2000 grinder-polisher machine and finished with a polycrystalline suspension (3µm; following Ballesta-Artero et al., 2018).

TABLE 1 Overview of dates and concentrations of Sr spikes administered to the cultured molluscs.

Spike name	Date (dd/mm/yyyy)	Sr concentration (mmol/L)
Spike 1	04/04/2020	0.58
Spike 2	22/04/2020	0.58
Spike 3	14/05/2020	0.33
Spike 4	04/06/2020	0.21
Spike 5	14/07/2020	0.21

Detailed data on the concentration and timing of Sr doses is also provided in SI1.

2.2 (LA)ICPMS analyses

Laser ablation – inductively coupled plasma mass spectrometry (LAICPMS) was used to analyse Mg/Ca, Mn/Ca, Sr/Ca and Ba/Ca (using the isotopes ^{25}Mg, ^{43}Ca, ^{55}Mn, ^{88}Sr and ^{138}Ba) in all specimens. In addition, Na/Ca (based on ^{23}Na and ^{43}Ca) was analysed in shells of individuals collected at the end of the experiment on September 24th (Table 2). Measurements were carried out using an ESI NWR193UC laser system (Elemental Scientific, Omaha, NE, USA) coupled to an iCap-Q quadrupole ICP-MS (Thermo Fisher Scientific, Waltham, MA, USA) at the NIOZ. Only the shell portion mineralized during the growth experiment (easily recognized due to a difference in shell coloration; see Figure SI2) was analysed. Three parallel ablation lines were placed in the outer shell layer of the three cockle test specimens (G003, G511 and G600; found dead on June 4th) to test the repeatability of the results. Once reproducible results were obtained, single profiles were measured on representatives of all three species which survived the entire experiment. All ablation lines were placed within the outer shell layers of cockles and mussels. For the oyster shells, the lenses of chalky calcite (insofar as present) were avoided, and the ablation transects were placed exclusively on the foliated calcite.

Scan lines were ablated with a 100 * 20 µm rectangular laser spot oriented with the short side to the growth direction, resulting in an effective sampling resolution of 20 µm while ablating a large enough surface area to yield sufficient material for ICP-MS analyses (de Winter et al., 2022b). All lines were pre-ablated at high speed (40 µm/s) to remove surface contamination before being ablated a second time at 4 µm/s for final data collection.

Data were calibrated in Matlab using a modified version of the SILLS software (Signal Integration for Laboratory Laser Systems; Guillong et al., 2008), following the same protocol as de Winter et al. (2022b). Intensity ratios were calculated with ^{43}Ca as an

TABLE 2 Overview of specimens analysed in this study and the types of analyses carried out on their shells.

Specimen #	Species	Start experiment (dd/mm/yyyy)	End experiment (dd/mm/yyyy)	Type of analysis
G003	*C. edule*	16/03/2020	04/06/2020	LAICPMS (3 profiles) XRF (1 profile)
G511	*C. edule*	16/03/2020	04/06/2020	LAICPMS (3 profiles) XRF (1 profile)
G600	*C. edule*	16/03/2020	04/06/2020	LAICPMS (3 profiles) XRF (1 profile)
G457	*C. edule*	16/03/2020	24/09/2020	LAICPMS (1 profile)
G472	*C. edule*	16/03/2020	24/09/2020	LAICPMS (1 profile)
G555	*C. edule*	16/03/2020	24/09/2020	LAICPMS (1 profile)
G177	*M. edulis*	16/03/2020	24/09/2020	LAICPMS (1 profile)
G191	*M. edulis*	16/03/2020	24/09/2020	LAICPMS (1 profile)
G259	*M. edulis*	16/03/2020	24/09/2020	LAICPMS (1 profile)
G271	*O. edulis*	16/03/2020	24/09/2020	LAICPMS (1 profile)
G282	*O. edulis*	16/03/2020	24/09/2020	LAICPMS (1 profile)
G372	*O. edulis*	16/03/2020	24/09/2020	LAICPMS (1 profile)

internal standard and calibrated against NIST610 (National Institute of Standards and Technologies; Gaithersburg, MD, USA) using preferred values from the GeoReM database (Jochum et al., 2005; Jochum et al., 2011). Drift corrections were applied by measuring NHFS-2-NP (Boer et al., 2022) four times after every fourth sample and standard. The reference materials BAS752 (Bureau of Analyzed Samples, Middlesbrough, UK), RS3, coral Porites JCp-1 and giant clam Tridacna gigas JCt-1 produced by the Japanese Geological Survey (Okai et al., 2002; Inoue et al., 2004), and NHFS-2-NP, were used for quality control. RS3, JCp-1, JCt-1 and NFHS-2 were nano-particulate powder pressed pellets (Garbe-Schönberg and Müller, 2014; Jochum et al., 2019). Details on the accuracy of the LAICPMS trace element results relative to preferred values is provided in SI12. Calibrated and drift corrected elemental to calcium ratio from LAICPMS measurements is provided in the supplementary information (SI3).

The Sr concentration (measured as ^{88}Sr abundance) of filtered seawater samples taken from the culturing setup both under natural conditions and during a high dose Sr spike were analysed on the same iCap-Q quadrupole ICP-MS (Thermo Fisher Scientific, Waltham, MA, USA) at the NIOZ. The resulting seawater Sr concentrations are provided in SI3.

2.3 Micro-X-ray fluorescence analyses

As a pilot study, micro-X-ray fluorescence (μXRF) was used to analyse trace element profiles through the outer shell layers of cockle specimens G003, G511 and G600 (found dead halfway during the experiment; see Table 2). These analyses were carried out on a Bruker M4 Tornado micro-X-ray fluorescence scanner in point-by-point line scanning mode (following Vansteenberge et al., 2020), following recommendations in de Winter et al. (2017a) and standardization in Vellekoop et al. (2022). A detailed description of the μXRF setup is provided in de Winter and Claeys (2016) and details on the methodology are provided in SI4. Both the raw and calibrated XRF data for all points along the profiles are provided in the supplementary information (SI3).

2.4 Data processing

To test the utility of the Sr spiking routine to identify certain sections of shells mineralized at known time intervals, peaks in the LAICPMS and XRF Sr profiles through the shells were linked to spiked Sr doses during the experiment. The borders of Sr peaks in the profiles were visually identified as the first and last sample for which Sr concentration exceeded that of the surrounding shell material (the "background" value; see Figure 2B). The background values for Sr and other trace elements with respect to a peak were defined as the average of the 25 points before the first datapoint in the peak and the 25 points after the last datapoint in the peak in direction of measurement. Peak "height" of Sr ("[Sr_{peak}]" and similarly for other elements) was defined as the average of the highest 10 datapoints within the peak, and average peak concentration ("[Sr_{mean}]", and equivalent for other elements) was defined as the average of all datapoints within the peak (Figure 2B). The average position along the profile of the 10 datapoints with the highest Sr concentrations was used to define the position of the peak. Shell size at the time of deposition was calculated from the X and Y coordinates of the scan lines digitized on scans of cross sections through the shells after LAICPMS analyses. For each specimen, a reference point was defined at the umbo in cross section through the shell and the Euclidian distance between this point and the position on the scan line where the highest Sr value in the peak was measured was calculated as a proxy

10.3389/fmars.2023.1157929

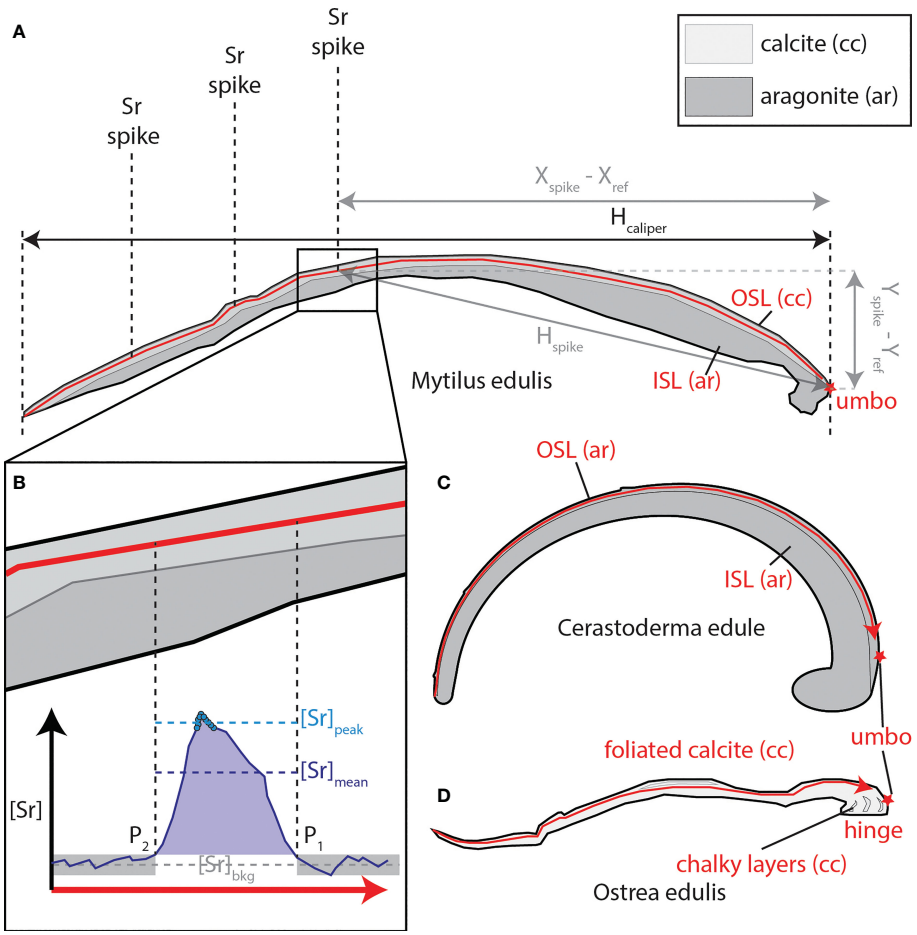

FIGURE 2
(A) Schematic representation of a cross section through a mussel shell and a LAICPMS profile measured through the calcitic outer shell layer (OSL) of this specimen (in red). Dashed lines show the locations of Sr peaks in the shell measured in the transect. Black and grey arrows indicate how shell size could be determined from the location of the Sr peaks ("H_{spike}", in grey, calculated from $X_{spike} - X_{ref}$ and $Y_{spike} - Y_{ref}$) and using calliper measurements of the entire shell ("$H_{calliper}$", in black). The red star indicates the reference position at the umbo used to determine shell size based on the position of Sr spikes. **(B)** Insert showing a typical Sr peak, with vertical dashed lines showing beginning (P_1) and end (P_2) of the peak in growth direction (note that LAICPMS scan direction is from left to right). $[Sr]_{bkg}$ = Background Sr concentration, $[Sr]_{peak}$ = peak Sr concentration (peak "height"), $[Sr]_{mean}$ = mean Sr concentration in the peak. **(C)** Schematic cross section through a cockle shell, showing aragonitic outer shell layer (OSL) and inner shell layer (ISL). Red arrowed line shows the path of a typical LAICPMS transect through this species. **(D)** Schematic cross section through oyster shell showing foliated and chalky calcite layers and the location of the hinge. Red arrowed line shows the path of a typical LAICPMS transect through this species, avoiding the chalky segments. cc, calcite, ar, aragonite.

for shell size (H_{spike}) using Pythagorean Theorem (see Figure 2B):

$$H_{spike} = \sqrt{(X_{spike} - X_{ref})^2 + (Y_{spike} - Y_{ref})^2}$$

To compare shell sizes determined from the position of Sr spikes with shell lengths measured during the experiment, shell lengths from calliper or photography measurements (section 2.1.2) were estimated at the times of administration of the Sr spike by linear interpolation between shell lengths measured before and after the Sr spike. Growth rates, defined as the increase in shell size per unit time, were calculated from the differences between successive shell size measurements and successive Sr spikes and averaged per month and per species to facilitate comparison between growth rates as determined using both methods. Note that this procedure for growth rate determination required extrapolation of growth rates before the first and after the last measurement or Sr spike for months where shell length was measured but individuals were not spiked.

3 Results

3.1 Strontium concentrations in seawater

Trace element measurements in seawater using ICP-MS (see section 2.2) reveal that the Sr concentration in ambient seawater at the culturing location was 86 ± 5 µmol/L (1σ). During a high dose Sr spike, the concentrations increased to 591 ± 36 µmol/L (1σ). These results confirm that the amount of strontium chloride added during a high dose spike indeed raises the Sr concentration by roughly 7 times, and the measured values are in close agreement with the target values for Sr concentration in the growth

10.3389/fmars.2023.1157929

environment during Sr spiking. Raw ICP-MS results of these water samples are provided in S3.

3.2 Strontium peaks in LAICPMS records

Plots of Sr/Ca ratios measured by LAICPMS (Figure 3) show that most Sr doses are recognizable in the shells of cockles, mussels, and oysters. However, there are clear differences between species. Overall, cockles show the clearest effect of the Sr spiking (Figures 3A, B), especially for the spikes with high doses, which are represented by peaks exceeding 10 mmol/mol Sr/Ca ratios in the aragonite of cockles: A 5-fold increase with respect to background ratios of ~2 mmol/mol. Medium and low dose spikes also result in concentrations exceeding 3-4 mmol/mol, well above the background variability and easily detectable. Parallel scans on specimens G003, G511 and G600 (Figure 3A) demonstrate that Sr peaks are highly reproducible within and between specimens. While the difference between high Sr doses on the one hand and medium or low doses on the other hand is clearly distinguished in the cockle records, the small difference in Sr concentration between peaks associated with medium and low doses makes it hard to distinguish between these doses from the Sr/Ca records alone (Figure 3B).

Records through the calcitic outer shell layer of the mussels (Figure 3C) and the foliated calcite of the oysters (Figure 3D) yield lower Sr/Ca ratios than those in the cockles (see also SI5). Sr peaks associated with high dose spikes (Sr/Ca of 3-5 mmol/mol in *M. edulis* and Sr/Ca 2-3 mmol/mol in oysters) generally exceed background Sr/

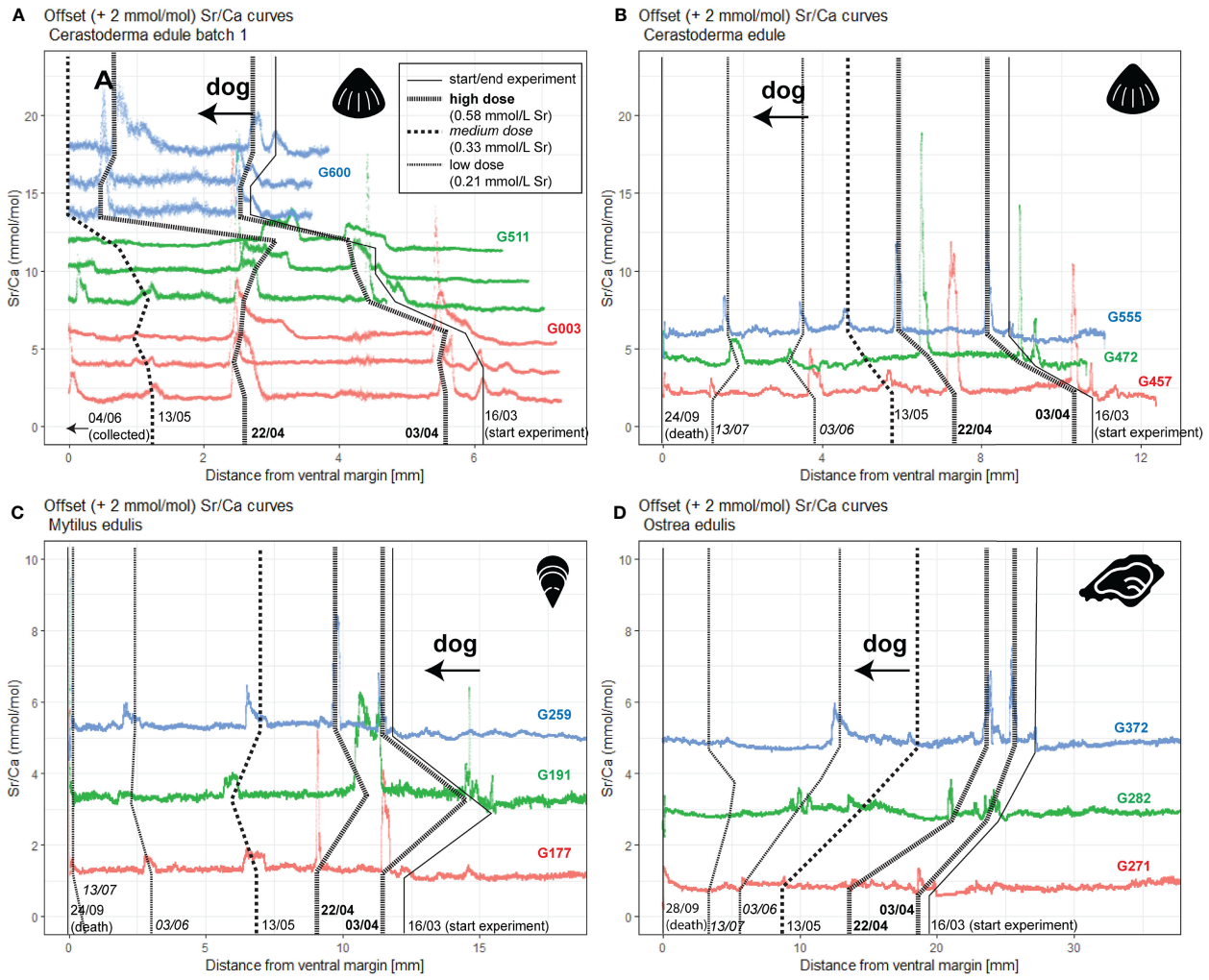

FIGURE 3
LA-ICP-MS Sr/Ca records through all aragonitic cockles **(A, B)**, calcitic outer shell layers of mussels **(C)** and foliated calcite in oysters **(D)** considered in this work. Records from subsequent specimens are indicated in different colors and offset by 2 mmol/mol from each other to promote visibility, with the lowest record showing true Sr/Ca values in agreement with axis labels. Parallel profiles within the same specimen **(A)** are also offset by 2 mmol/mol, with profiles closer to the outside of the shell plotted below profiles farther towards the inside of the outer shell layer. Lines connecting records vertically mark the beginning and end of the experimental period as recorded in the shells and the location of Sr peaks, with numbers at the bottom listing the dates (dd/mm) of the events. Doses of Sr peaks are indicated with different lengths of line dashes (see legend in **(A)**: high dose; 7.7-fold increase in $[Sr]_w$; administered at 03/04 and 22/04; medium dose; 4.4-fold increase in $[Sr]_w$; administered at 13/05; and low dose; 2.8-fold increase in $[Sr]_w$; administered at 03/06 and 13/07). Distance on horizontal axes is measured in scan direction (growth direction from right to left). "dog" = direction of growth.

10.3389/fmars.2023.1157929

Ca ratios of ~1 mmol/mol. In mussels these spikes can be recognized with confidence, but in oysters even some of the high dose spikes fail to yield clearly recognizable peaks in Sr/Ca records. Medium doses are still clearly recognized in mussels, but low dose spikes do not always produce useful peaks in Sr/Ca in this species. Interestingly, the peak height in mussels more closely reflects the size of the spiking dose than in cockles, with medium Sr doses yielding peaks that are recognizably higher than those associated with low doses and lower than those associated with high doses (Figure 3C). In oysters, the response to medium- and low-spike doses is much less predictable. Some low doses appear to produce surprisingly high Sr/Ca peaks (see e.g. the June 3 dose in specimen G372; Figure 3D), while other low doses and even medium or high dose spikes fail to produce recognizable peaks at all.

3.3 Strontium peaks in XRF profiles

X-ray fluorescence Sr/Ca profiles through the same cockle specimens G003, G511 and G600 (Figure 4) show that the high- and medium-dose peaks recorded in these shells are also detectable using µXRF (Figure 4). Background Sr/Ca values (~2 mmol/mol) are similar in µXRF profiles compared to the LAICPMS profiles through the same specimens (Figure 3A), showing that both

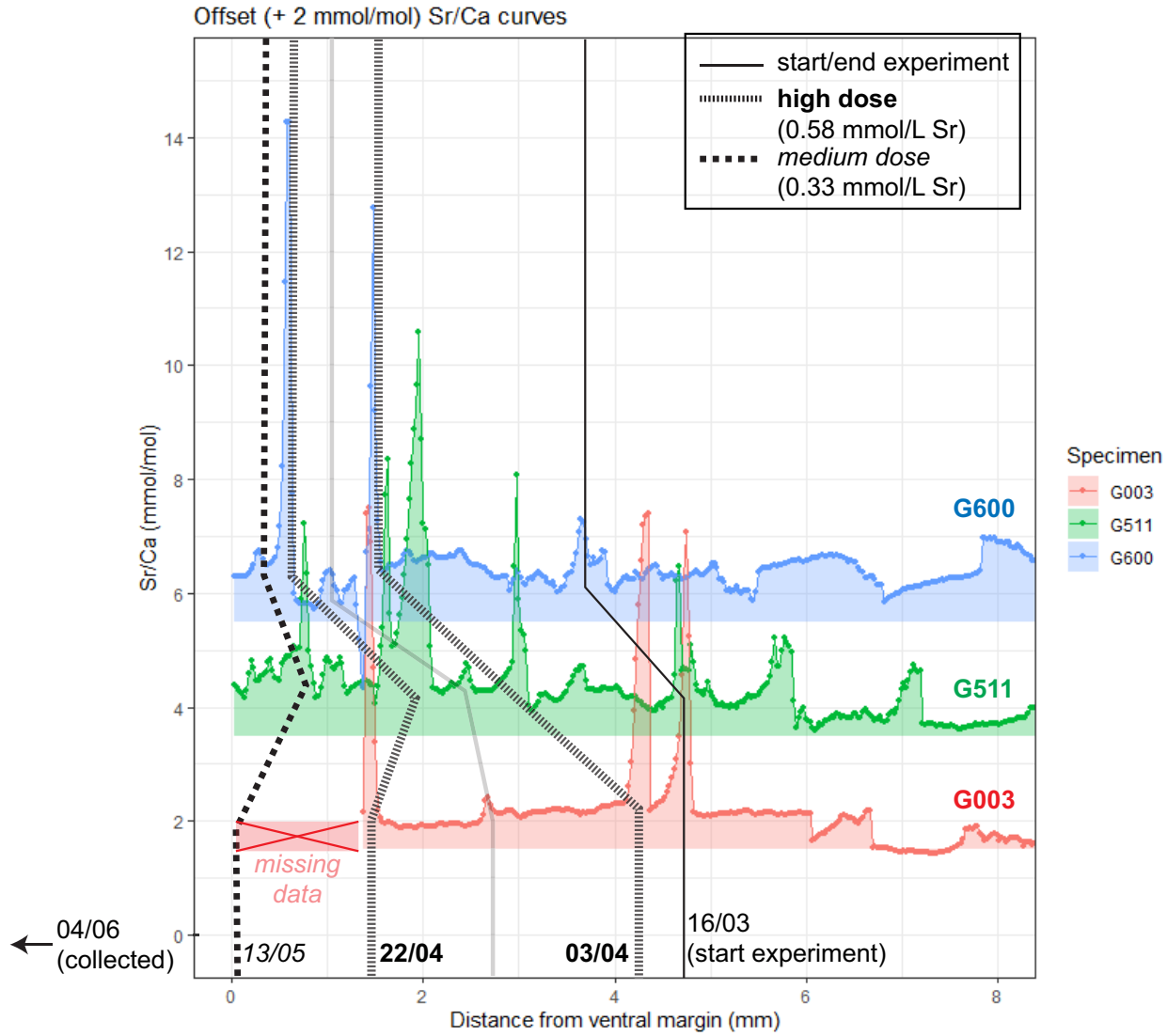

FIGURE 4
µXRF Sr/Ca records through aragonitic cockle specimens G003, G511 and G600. Records from subsequent specimens are offset by 2 mmol/mol from each other, with the lowest record showing original Sr/Ca values. Lines connecting records vertically mark the beginning of the experimental period as recorded in the shells and the location of Sr peaks, with numbers at the bottom listing the dates (dd/mm) of the events. Doses of Sr peaks are indicated with different lengths of line dashes (see legend in top right corner: high dose; 7.7-fold increase in $[Sr]_w$; administered at 03/04 and 22/04; medium dose; 4.4-fold increase in $[Sr]_w$; administered at 13/05). Distance on horizontal axis is measured in scan direction (growth direction from right to left). Note that due to issues with the cross-section surface, data from the first part of the record through specimen G003 was lost.

methods independently reproduce the same Sr/Ca values. High dose spikes are clearly recorded as peaks in Sr/Ca in the µXRF records with values generally exceeding 6 mmol/mol, similar to the values obtained through LAICPMS. The medium dose spike administered on 13/05 is more elusive, partly because the initial part of the G003 record is missing due to technical issues with the measurements. In G511, the medium dose yields a clear spike in Sr/Ca towards maximum values of ~5 mmol/mol, but in G600 the peak barely rises above the background variability. Outside the spike-associated peaks, the Sr/Ca background in µXRF profiles is more variable than in the LA-ICP-MS transects.

3.4 Shape of strontium peaks

LAICPMS data (Figure 3) reveal that the Sr peaks in all specimens exhibit a distinct shape when considered in growth direction: Sr/Ca ratios rise gradually at the onset of the peak (the point farthest away from the ventral margin to the right in Figures 3, 4), before falling sharply, resulting in a wide tail towards older parts of the shell. This asymmetry is clearest when considering the average position of the highest Sr values within the peak relative to the position within the peak, with 0 indicating the onset of the peak and 1 the end (Table 3). Mean symmetry indices, calculated as the distance between Sr/Ca peak value and the onset of the peak divided by the full width of the peak (onset to end), for all species exceed 0.5, confirming the observation that Sr peaks start gradually and end sharply. The asymmetry is largest in mussels and smallest in cockles. The average width of peaks typically increases from cockles (350 ± 190 µm; 1σ) to mussels (580 ± 300 µm; 1σ) to oysters (850 ± 390 µm; 1σ), but variability between peak heights in the same species are generally larger than variability between species (Table 3; SI6). Interestingly, some Sr/Ca peaks in the XRF profiles (Figure 4) seem to show an opposite pattern, with Sr/Ca ratios rising sharply at the onset of some Sr peaks before falling slowly in growth direction (most notably the high-dose peaks administered at 16/03 and 03/04 in specimen **G003**).

3.5 Behaviour of other trace elements during Sr spikes

Figure 5 highlights the differences between peak and background values for all measured trace elements for all specimens, showing how Sr spikes result in elevated concentrations of other elements (most notably Na and Ba). The occurrence of peaks in Sr/Ca (Figures 3, 4) coincides with peaks in other trace elements in about 70% of the Sr spikes (see Table 4 and SI7-9). This is especially visible in Na and Ba, and prevalent in oysters, where Mn and Mg also often exhibit highly elevated values compared to the background (see Table 4; Figure 5). Cockle records, showing clear Sr peaks (see sections 3.2 and 3.3) show the least covariance of other elements at Sr spiking moments. In general, concentrations of Sr and Ba are comparatively high in cockles, while mussel and oyster shells have higher relative concentrations of Na, Mg and Mn. Peak or mean values of other trace elements below the background during Sr peaks are rare (Figure 5). A summary of trace element concentrations measured in all shells during Sr spiking is provided in SI7. LAICPMS profiles showing details of the variability in other trace elements (Na, Mg, Mn and Ba) are provided in SI8.

TABLE 3 Differences in width and shape of peaks between species. St. dev, standard deviation.

Species	Mean peak width (µm)	St. dev peak width (µm)	Peak symmetry
C. edule	350	190	0.58
M. edulis	580	300	0.73
O. edulis	850	390	0.63

3.6 Effect of spike dose on peak height

There is a positive relationship between applied dose and measured peak concentrations in shell carbonate in all species. (Figure 6). This relationship is approximately linear in mussels, but non-linear in cockles and oysters. The data (Figure 6) also show that there is a large inter- and intra-species variability between the heights of Sr/Ca peaks (see also Figures 3, 4). This variability makes it hard to distinguish between peaks resulting from low and medium doses. However, in many cases the difference between high Sr doses and low or medium doses is large enough to produce significantly different peaks in the shells.

3.7 Growth curves

Shell length measurements on the outside of the shell and estimates of shell size from the position of Sr spikes were used to construct growth curves for each specimen (Figure 7). These curves demonstrate that the overall pattern of shell size over time based on actual shell size measurements is reproduced by the shell size estimates based on Sr peak positions. However, in cockles shell size based on position of Sr spike (see section 2.4) consistently underestimates shell height measured on the outside of the shell. In oysters, the shell sizes based on Sr spikes are in closer agreement with those measured on the shell pictures. In Figure 8F, shell sizes interpolated from measurements on the outside of the shell are directly compared to the shell sizes obtained from Sr peak position. In the mussels, the Sr spiking method underestimates shell size in smaller individuals, but the positive slope of the regression shows that estimates become better as the individuals grow (Figure 8F).

Monthly growth rate estimates based on limited Sr peak positions are not a good predictor of growth rates in mussels and oysters based on measurements on the outside of the shell, while the technique performs better in cockles (Figures 8C–E). Figure 7 shows that this lack of agreement might be caused by the high variability in growth between specimens and through time.

10.3389/fmars.2023.1157929

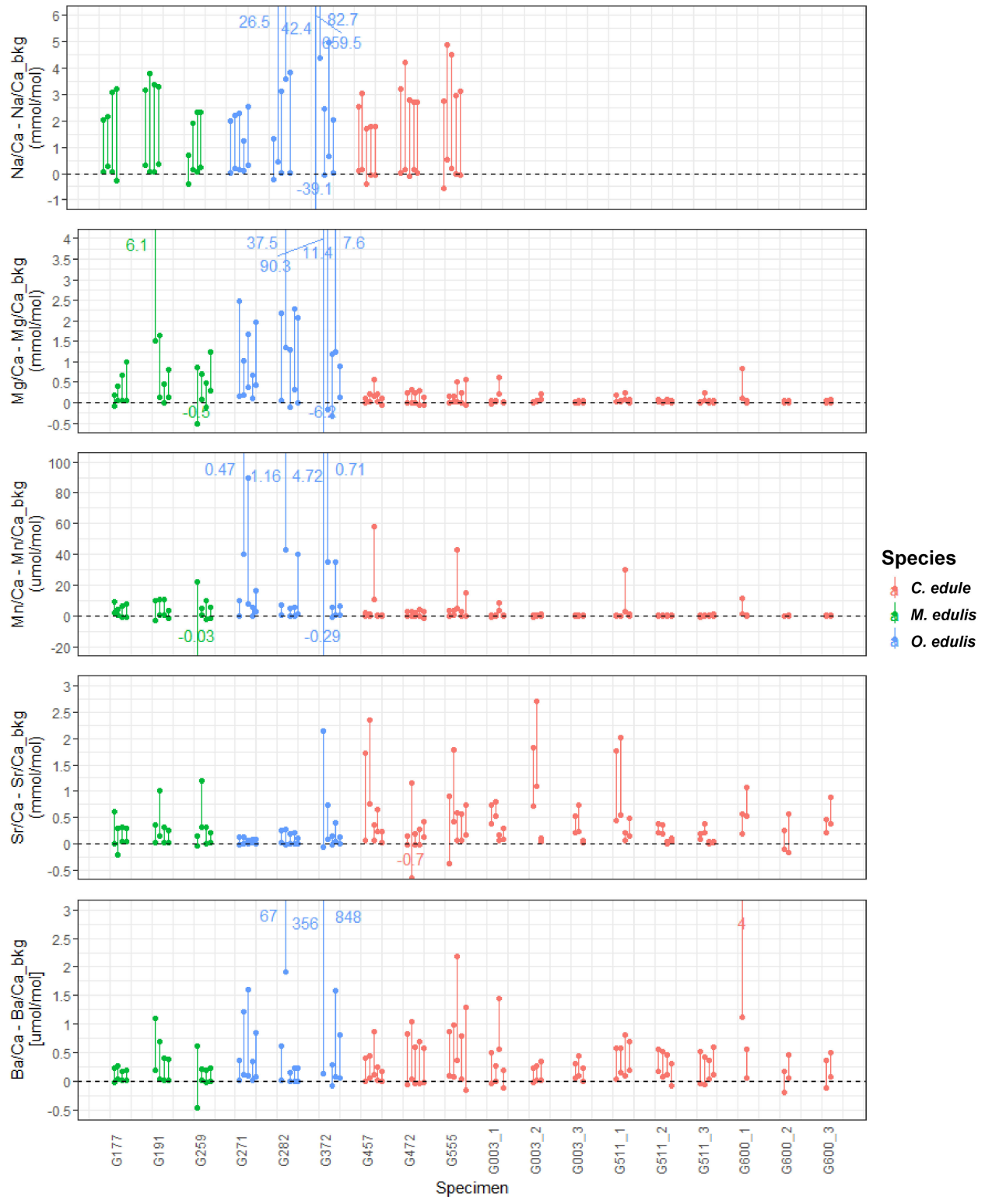

FIGURE 5
Plot showing trace element concentrations in all peaks in all specimens which lived through the entire growth experiment relative to their background values (dotted line). Lower dots show the average concentration within the peak while the higher dots (connected by a vertical line) show the average of the highest 10 measurements in the peak. Labels with subscripts (e.g. "G003_1") indicate different profiles within the same specimen. Note that for specimens G003, G511 and G600 no Na concentrations were measured. Colours indicate different species.

TABLE 4 Peak trace element ratios, mean trace element ratios within the entire peak, and background ratios of shell material mineralized before and after the peak for all specimens, organized by height of the spiking dose (high = 0.58 mmol/L, medium = 0.33 mmol/L, low = 0.21 mmol/L).

Dose	Species		Sr/Ca peak (mmol/mol)		Sr/Ca mean (mmol/mol)		Sr/Ca background (mmol/mol)		Na/Ca peak (mmol/mol)		Na/Ca mean (mmol/mol)		Na/Ca background (mmol/mol)		Mg/Ca peak (mmol/mol)		Mg/Ca mean (mmol/mol)		Mg/Ca background (mmol/mol)	
High	*M. edulis*		1.02	± 0.43	0.45	± 0.16	0.41	± 0.09	5.27	± 1.59	3.06	± 0.85	2.99	± 0.70	2.49	± 2.45	1.04	± 0.84	0.83	± 0.28
	O. edulis		0.84	± 0.86	0.23	± 0.09	0.23	± 0.08	145.15	± 291.04	10.40	± 13.38	16.11	± 29.35	28.30	± 40.84	3.37	± 3.46	4.14	± 6.10
	C. edule		1.57	± 0.81	0.81	± 0.26	0.56	± 0.31	10.26	± 2.46	6.88	± 1.90	6.83	± 1.95	0.43	± 0.23	0.30	± 0.11	0.29	± 0.11
		N	36		36		36		18		18		18		36		36		36	
		mean	1.36	± 0.81	0.65	± 0.32	0.48	± 0.28	53.56	± 171.35	6.78	± 7.97	8.64	± 16.93	5.42	± 18.64	0.94	± 1.76	1.02	± 2.72
Medium	*M. edulis*		0.62	± 0.04	0.33	± 0.02	0.30	± 0.04	6.92	± 0.83	4.06	± 0.43	4.00	± 0.42	1.45	± 0.06	0.90	± 0.03	0.92	± 0.12
	O. edulis		0.33	± 0.08	0.20	± 0.02	0.20	± 0.03	6.58	± 0.36	4.01	± 0.20	3.97	± 0.26	2.76	± 0.06	1.35	± 0.17	1.36	± 0.19
	C. edule		0.62	± 0.24	0.46	± 0.08	0.42	± 0.07	9.75	± 2.45	6.66	± 1.43	6.76	± 1.19	0.70	± 0.27	0.48	± 0.12	0.41	± 0.10
		N	15		15		15		9		9		9		15		15		15	
		mean	0.56	± 0.22	0.38	± 0.13	0.35	± 0.11	7.75	± 2.00	4.91	± 1.51	4.91	± 1.53	1.26	± 0.85	0.74	± 0.38	0.70	± 0.41
Low	*M. edulis*		0.52	± 0.02	0.29	± 0.01	0.26	± 0.02	6.53	± 0.43	3.69	± 0.29	3.59	± 0.21	2.11	± 0.42	1.26	± 0.32	1.09	± 0.21
	O. edulis		0.36	± 0.17	0.20	± 0.06	0.19	± 0.05	13.76	± 16.95	5.04	± 2.19	4.26	± 0.80	4.15	± 2.93	1.94	± 0.85	1.57	± 0.44
	C. edule		0.82	± 0.26	0.53	± 0.08	0.44	± 0.06	9.15	± 1.86	6.62	± 1.40	6.64	± 1.35	0.62	± 0.26	0.43	± 0.09	0.44	± 0.11
		N	19		19		19		15		15		15		19		19		19	
		mean	0.63	± 0.30	0.39	± 0.17	0.33	± 0.13	10.47	± 10.61	5.40	± 1.94	5.08	± 1.64	1.97	± 2.24	1.04	± 0.84	0.90	± 0.58

Dose	Species		Mn/Ca peak (µmol/mol)		Mn/Ca mean (µmol/mol)		Mn/Ca background (µmol/mol)		Ba/Ca peak (µmol/mol)		Ba/Ca mean (µmol/mol)		Ba/Ca background (µmol/mol)	
High	*M. edulis*		24.49	± 20.19	9.26	± 2.74	14.32	± 14.03	0.96	± 0.51	0.41	± 0.18	0.44	± 0.24
	O. edulis		1295	± 2043	87	± 135	116	± 262	216	± 343	7	± 10.04	4.17	± 9.77
	C. edule		3.73	± 2.46	2.17	± 0.71	2.15	± 0.74	1.48	± 1.06	0.87	± 0.50	0.81	± 0.35
		N	36		36		36		36		36		36	
		mean	222	913	± 17	60	± 23	108	± 37	153	± 2	± 4.43	1.31	± 3.93
Medium	*M. edulis*		19.10	± 3.95	9.38	± 2.10	10.03	± 1.62	0.47	± 0.12	0.21	± 0.03	0.21	± 0.04
	O. edulis		38.47	± 48.83	7.65	± 4.72	5.04	± 0.15	0.78	± 0.78	0.11	± 0.06	0.10	± 0.03

(Continued)

10.3389/fmars.2023.1157929

10.3389/fmars.2023.1157929

TABLE 4 Continued

Dose	Species		Mn/Ca peak (umol/mol)		Mn/Ca mean (umol/mol)		Mn/Ca background (umol/mol)		Ba/Ca peak (umol/mol)		Ba/Ca mean (umol/mol)		Ba/Ca background (umol/mol)	
	C. edule		19.11	± 23.55	5.53	± 5.26	3.00	± 2.25	1.48	± 0.75	0.80	± 0.38	0.66	± 0.33
		N	15		19		19		19		19		19	
		mean	22.98	± 26.91	6.72	± 4.71	4.82	± 3.35	1.14	± 0.78	0.54	± 0.44	0.46	± 0.36
Low	*M. edulis*		12.99	± 2.53	6.09	± 1.30	7.29	± 1.55	0.45	± 0.10	0.19	± 0.03	0.18	± 0.04
	O. edulis		23.51	± 16.48	6.14	± 2.22	5.28	± 2.06	0.75	± 0.53	0.11	± 0.04	0.07	± 0.04
	C. edule		5.22	± 5.37	2.10	± 1.00	2.26	± 1.23	1.23	± 0.53	0.66	± 0.37	0.67	± 0.34
		N	19		19		19		15		15		15	
		mean	12.22	± 12.66	4.01	± 2.51	4.01	± 2.50	0.95	± 0.56	0.41	± 0.38	0.40	± 0.38

Errors are presented as one standard deviation between different peaks and specimens of the same species. Values in rectangular boxes represent means and standard deviations of all peaks of all specimens for that element at that spiking dose. Definitions of peak and mean trace element ratios are explained in section 2.4 and Figure 2B.

4 Discussion

4.1 Reproducibility of Sr/Ca peaks

4.1.1 Within-specimen reproducibility

The similarity between parallel Sr/Ca profiles within the same cockle specimens (Figure 3A) demonstrate that peaks in Sr/Ca resulting from Sr spiking are reproducible within the shell. Peaks in profiles recorded farther away from the outside of the shell are generally lower (SI10). This pattern is robust when the mean Sr/Ca value within the peak is considered instead of the peak value (see Figure 2). As a result of the differences in peak shape (Figure 3A), mean Sr/Ca values belonging to the same Sr spike dose measured at different locations within the same specimen show less variability (<20% relative SD) than peak "height" values (typically >20% relative SD). Peak shape variability is more pronounced in high dose Sr spikes than medium or low dose spikes, likely because the effect of high dose spikes is detectible over a larger portion of the shells (i.e. the peaks are wider, see Figure 3). This observation places some uncertainty on the detection of the peak in labelled specimens, as the highest Sr value may be recorded at different places within the affected shell area within the same specimen. With the typical peak width of ~400 µm recorded in cockles (SI10) and a typical growth rate of 50-100 µm/d (Figure 8D) recorded in cockles in this experiment, the effect of these changes in peak shape could amount to an uncertainty of a few days in the identification of Sr peaks assuming the true peak Sr concentration can be found randomly within the affected shell area.

4.1.2 Method comparison

Our pilot measurements using µXRF scanning show that Sr/Ca peaks in cockles are detectable with this analytical method as well. The observation that peak height concentrations recorded by µXRF are similar to those measured by LAICPMS shows that these features can be retrieved from spiked shells using both methods. This is an advantage, since µXRF scanning is less destructive to the polished shell surface and would allow subsequent re-sampling or microscopic observation of the same surface without the need for repolishing (de Winter and Claeys, 2016). A disadvantage of the µXRF method is that it is sensitive to topographical differences of the scanned surface, and that the X-rays penetrate the sample further than LAICPMS ablation, causing smoothing of the peak signal (compare Figures 3, 4 and see discussion in section 4.3). Since the µXRF pilot measurements in this study were done after LAICPMS profiles were ablated on the samples, the resulting topographical features could not be avoided, and they visibly affect the Sr/Ca background in Figure 4 (see section 3.3). If µXRF scanning is used to locate trace element peaks in spiked specimens, we recommend carrying out this analysis before applying more destructive sampling methods to the shell surface.

4.1.3 Variability between species

The ease with which Sr peaks can be recognized in LAICPMS profiles decreases from cockles to mussels and oysters (Figure 3). Peaks in Sr/Ca induced by Sr spiking are much higher in cockles than in mussels and oysters, likely due to the mineralogical difference between the aragonitic outer shell layer of cockles and the calcitic layers targeted in mussels and oysters. Due to the difference in mineral

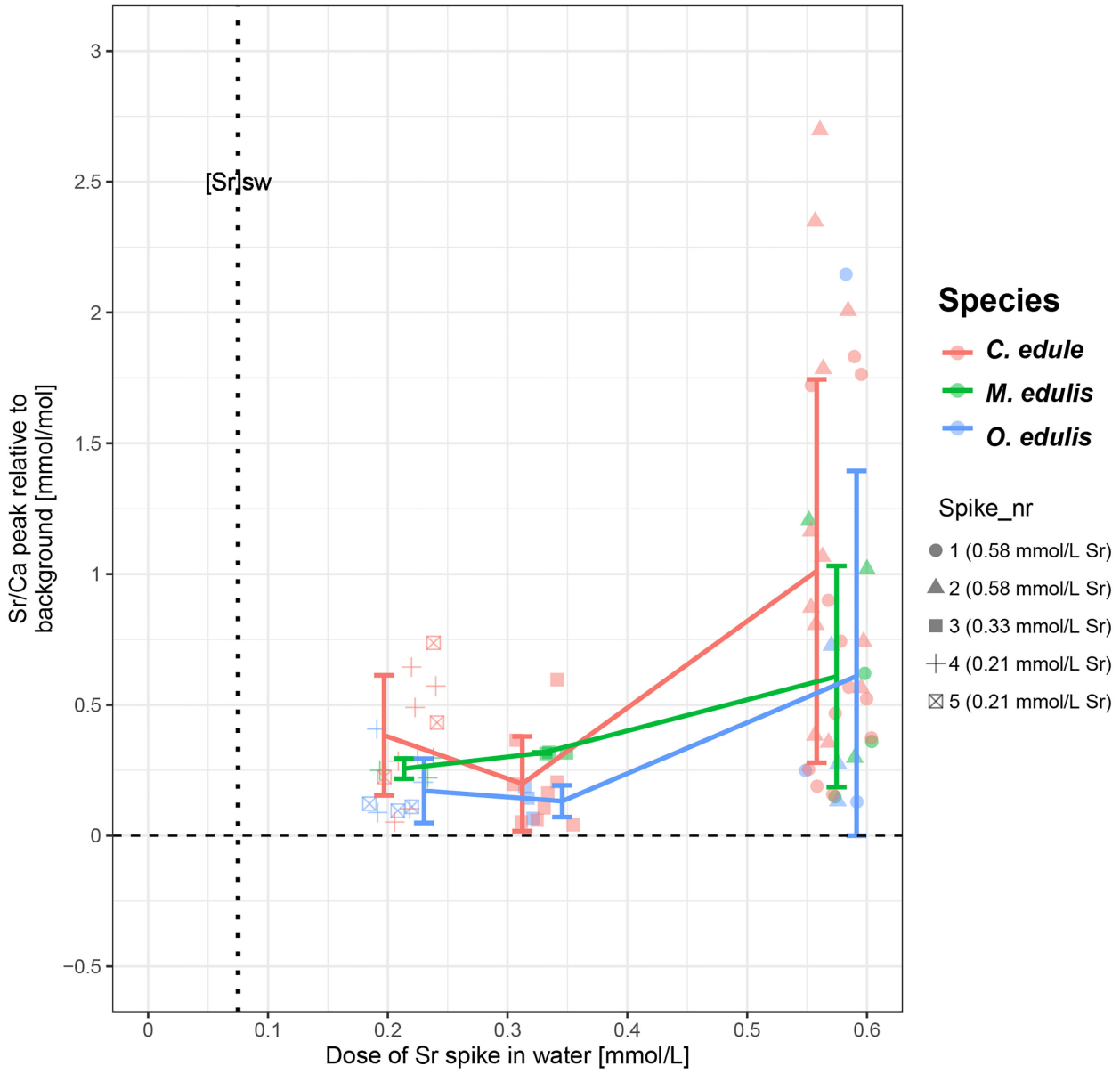

FIGURE 6
Plot showing the height of the Sr peak (in Sr/Ca ratio) relative to the background concentration ratio against the size of the elevated Sr dose for all species. Different symbols represent Sr spikes labelled in chronological order (spike 1 = 04/04/2020, spike 5 = 14/07/2020; see Table 1). Note that symbols and error bars of different species are artificially horizontally offset from each other, while the actual Sr dose was equal for all species. Detailed plots of the height of the concentration peak in other trace element plotted against spike dose are provided in SI9.

structure, the partition coefficient of elements with a high ionic radius (e.g. Sr and Ba) into aragonite is higher than into calcite, explaining higher Sr concentrations in aragonitic cockle outer shell layers than in calcitic mussel and oyster shells grown under the same environmental conditions (Day and Henderson, 2013; Wassenburg et al., 2016). This effect of different partition coefficients between aragonite and calcite is also evident from the uptake of other trace elements during the Sr peak: elements with a relatively small ionic radius (Na, Mg, Mn) show stronger enrichments relative to the background value in calcitic mussel and oyster shells while larger elements (e.g. Ba) are more enriched in the aragonite of cockle shells (Figures 5; SI5).

The increase in concentration of other elements during Sr spiking could be a result of the "closed-sum effect", which occurs because elevated Sr concentrations reduce Ca concentrations in the same shell section, thereby increasing the ratios of other trace elements to Ca (Van der Weijden, 2002). However, considering that the highest Sr/Ca peaks feature Sr/Ca ratios of at most 8 mmol/mol above a background ratio of ~2 mmol/mol in cockles (10 mmol/mol peak height, with lower peaks in mussels and oysters; Figure 3), the resulting decease in Ca concentration relative to the nominal Ca concentration in $CaCO_3$ (1 mol/mol for pure aragonite) can only explain an increase of at most 0.8% (0.008/1.0 mol/mol) relative to the background value in other

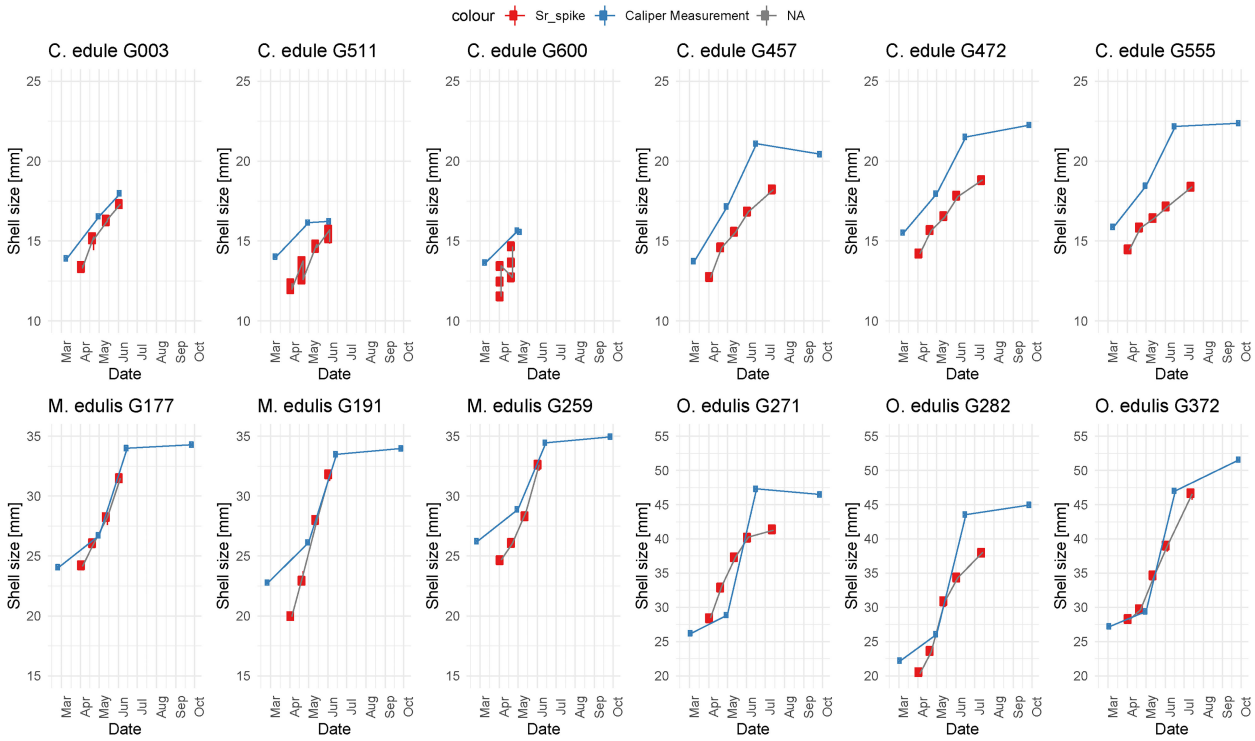

FIGURE 7
Plot showing measured shell size over time (in blue) and shell size over time inferred from the location of Sr spikes (in red) for all specimens. Vertical scales are constant between specimens of the same species, but different between species. Note that three parallel LAICPMS line scans were measured on cockle specimens G003, G511 and G600, resulting in multiple Sr spiking shell growth estimates at the same time of growth.

elemental ratios. Figure 5 shows that peaks in elemental ratios other than Sr/Ca is too large to be fully explained by the closed-sum effect.

This suggests that the uptake of different trace elements into the shells of all species studied here is linked by a common process. Differences between elemental concentrations are mainly driven by differences in the partitioning into different minerals, and increased element uptake happens simultaneously for all elements under study. This supports the hypothesis that processes affecting the concentration of trace elements in the extrapallial fluid of molluscs (e.g. through Ca-channels Hagiwara and Byerly, 1981) dominate over more element-specific processes that control the degree by which (trace) elements are built into the mineral structure (e.g. through an organic template for shell formation Gillikin et al., 2005). Our results therefore argue in favour of the biomineralization model put forward by (Carré et al., 2006).

While most Sr peaks are identified in oysters, Sr labelling produces much more easily identifiable peaks in mussels and cockles (Figure 3). This suggests that the success of Sr labelling does not depend only on shell mineralogy, but that the mode of shell growth and the location of measurement plays an important role. In contrast to cockles and mussels, oysters show highly irregular growth patterns with frequent changes in growth rate and direction (Carriker et al., 1980; Banker and Sumner, 2020). Furthermore, oysters may resorb parts of their shell to maintain pH within the extrapallial fluid during anaerobic respiration, which may affect the timeline recorded in their outer shell layers (Kent, 1992). This causes variability in growth rate along the ventral margin through cross sections of the shells (e.g. along LAICPMS; Figure 3). As a result, Sr/Ca peak height in oysters is expected to vary significantly within the shell depending on the orientation of the measured section because of these differences in local growth rate. Peak height is therefore not an ideal metric for comparing trace element compositions between shells and shell segments in oysters. For this reason, growth rates in oysters are often studied in the hinge area, which is less affected by these irregularities (e.g. Surge et al., 2001; Mouchi et al., 2013; Ullmann et al., 2013; Huyghe et al., 2019). However, the small width of oyster hinge plates, especially in young specimens, limits the temporal resolution of chemical profiles sampled in this area of the shell and therefore on the precision with which short-lived peaks in Sr concentration can be detected there. Alternative labels which can be detected at smaller scale, such as the use of fluorescent dyes or Mn labelling combined with cathodoluminescence microscopy (Huyghe et al., 2019) might be better suited for analyses in the hinge areas of oyster shells. In addition, administrating elevated concentrations of isotopically enriched strontium (e.g. ^{87}Sr or ^{86}Sr) could produce peaks with distinct isotopic signatures which would be simple to trace within the shell, albeit requiring multi-cup ICPMS or nanoSIMS techniques to detect (e.g. Houlbrèque et al., 2009). Note that a difference in the time lag of the incorporation of Sr (and other trace elements) into the shell may exist between species, or between individuals as a consequence of differences in individual growth rate

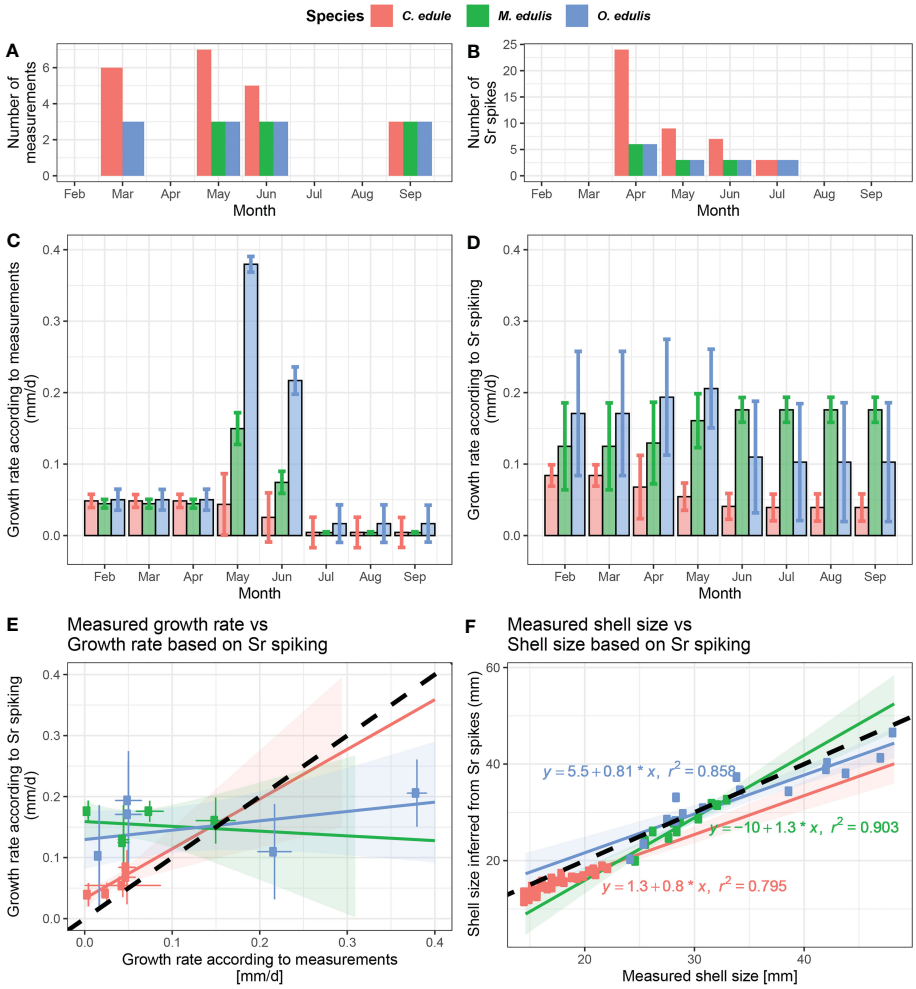

FIGURE 8
Comparison between shell sizes and growth rates calculated based on Sr spikes and shell length measurements. **(A)** Number of shell size measurements per month per species. **(B)** Number of Sr spikes per month per species. **(C)** Mean monthly growth rates calculated from shell size measurements per species. **(D)** Mean monthly growth rates calculated from positions of Sr spikes per species. **(E)** Cross plot showing growth rates calculated from shell size measurements against growth rates for the same month and the same species as calculated from the position of Sr peaks. The bold dashed line indicates equal growth rates between the two methods. **(F)** Cross plots showing measured shell size against shell size at the same time as determined from the position of Sr peaks. The bold dashed line indicates equal shell size estimates between the two methods.

or activity, which might explain part of the differences in the way Sr/Ca peaks are expressed in the shells of cockles, mussels and oysters.

4.1.4 Variability with spike timing or health

Another factor to consider when comparing the shape and height of Sr/Ca peaks is the timing of the peak relative to the growing season. Like most poikilothermic organisms, cockles, mussels, and oysters growing in temperate regions all show distinct seasonal patterns in growth rate related to changes in temperature and food availability (Bayne and Worrall, 1980; Hilbish, 1986; Richardson et al., 1993; Milano et al., 2017). Since growth rate during labelling is likely an important factor for determining the shape and height of Sr peaks (see sections 4.1.1 and 4.1.3), the timing of labelling relative to the growth season might determine whether Sr peaks can be successfully recognized, especially if growth is episodic instead of continuous. Connected to this, the health of individuals of these species is known to vary significantly over the growing season (Bayne and Worrall, 1980; Hilbish, 1986), which may affect how trace elements are taken up into the extrapallial fluid and therefore Sr concentrations in the shell (Carré et al., 2006). Comparing different Sr/Ca peaks in the same specimen associated with the same spiking dose shows that there is no clear relationship between the timing of the peak and peak height or shape (see Figures 3, 4). However, it must be noted that the period between consecutive spikes of the same dose is not very high, and experiments administering the same Sr dose at multiple different times during the growing season would be needed to fully constrain the effect of growth rate on the shape and height of Sr peaks recorded in the shells. In cockles and especially in mussels, peak height is a good indicator for Sr spiking dose (Figure 6), and Sr/Ca peaks belonging to the same dose but timed later in the growth season (e.g. high dose peaks on April 3rd and April 22nd; Figure 3) are similar in shape and size.

In addition, Sr peak shape and height in cockle specimens G003, G511 and G600 which did not survive through the full experimental

period (Figure 3A) do not seem consistently different from those in cockles that lived through the full growing season (Figure 3B). From this it seems that the decreased health (as evident from their early death) of these three specimens did not affect how Sr labels are recorded in their shells. Therefore, we do not directly observe an effect of either health or spike timing relative to the growing season on the detection of Sr spiking peaks in our specimens. The caveat of this observation is that highly dosed Sr spikes were administered early in this experiment while lower doses were used later in the season, making it hard to disentangle the effect of seasonal variability in growth rate or health from our dataset. To more thoroughly check whether seasonal variability in these conditions affects Sr labelling, an experiment could be conducted in which Sr spikes of the same doses are administered further apart in time such that the evolution of Sr peak shape and size through the season can be observed independent of the dose.

4.2 Uncertainties related to Sr peak location

Variations in peak location between different profiles through the same cockle specimen reflect the uncertainty when estimating growth rates from Sr labelling. The distance in growth direction between two Sr peaks does not scale monotonously with the position of the profiles relative to the outer margin of the shell (Figure 3A), as would be expected due to the curvature of the shells (Milano et al., 2017). Differences in growth rate reconstructed from the locations of these Sr peaks can thus not be fully explained by the shape of the shell. The location where the Sr spikes are measured in the shell matters for the estimate of the growth rate and including estimates from different places within the shell causes greater uncertainty on shell size reconstructions (Figure 6). In addition, differences in the rate or timing of trace element uptake, or (sub-)daily variations in shell growth rate, between species cannot be excluded based on our experiment (see section 4.1.3). Such differences may place additional uncertainty on the shell growth rates reconstructed from Sr spikes.

The observation that trace element profiles measured at different locations within the same specimen (Figure 3A) differ in both height and (subtly) in location in the shell cross section shows that an environmental signal (in this case an increase in Sr concentration) is not recorded uniformly within new shell material precipitated by cockles. This corroborates the results of previous studies showing that local changes in shell extension rates or differences in shell microstructure and morphology can influence the uptake of trace elements into mollusc shell carbonate (Freitas et al., 2009; Marali et al., 2017). By extension, differences in Sr peak location and height between specimens of cockles, mussels and oysters grown under the same conditions (Figure 3) demonstrate that these variations contribute to uncertainty in trace element records when comparing multiple specimens from the same environment, as hypothesized in previous studies (Schöne et al., 2006; Freitas et al., 2008). These results place additional uncertainty on paleo-environmental reconstructions from trace element profiles through (fossil) mollusc shells, even when employing a multi-specimen approach (de Winter et al., 2017b; Fröhlich et al., 2022).

4.3 Peak shape

The asymmetry in Sr peaks is consistent between species but differs between methods (Figures 3, 4). Tails in Sr/Ca peaks are hundreds of micrometers long, an order of magnitude larger than the spot sizes of LAICPMS (20 µm) and XRF (25 µm). However, while LAICPMS measurements are based on ablation of a minimum amount of surface material from the cross sections through the shells (crater depth is typically less than spot size; Holá et al., 2011; Fehrenbacher et al., 2015), while X-ray fluorescence scanning produces a depth-integrated signal of which the reach depends on the excitation energy of the X-ray photons (Jablonski and Powell, 2020). Since strontium concentrations are analysed based on the Kα1 (14.16 keV) and Kβ1 (15.82 keV), the attenuation length of Sr in calcium carbonate measured by XRF is in the order of 400-500 µm, causing the XRF Sr/Ca profiles with this method to integrate over roughly 1 mm in depth (Henke et al., 1993). Considering that the X-ray beam in the Bruker M4 setup describes an angle of 39° with respect to the true perpendicular to the sample surface (de Winter and Claeys, 2016), this attenuation length in beam direction could easily translate to an averaging of the XRF signal over a few 100 µm in lateral direction. We therefore conclude that the observation of differences in Sr/Ca peak shape between LAICPMS and XRF profiles on the scale of 100s of µm likely results from the difference in depth signal integration between the methods. This caveat of the XRF method should be considered when using the method for detecting trace element peaks in mollusk shells, since it has the potential to place significant added uncertainty on the recognition of true peak location. The observed asymmetry in LAICPMS peak shape is not a methodological artefact (depending on either spot size or the washout during LAICPMS analysis), but instead a true expression of the Sr concentration in the shells.

The fact that mussels and oysters have broader peaks with more strongly tailed Sr distributions than cockles (Table 3) is perhaps counterintuitive, given the higher total amount of Sr being taken up by cockles due to a comparatively large affinity for Sr in aragonite (see above), which could cause peak area to increase. The difference in peak width in growth direction also suggests that there is a difference in the rate or timing by which the different species record elevated Sr concentrations in their shells. However, when controlled for mean growth rate, which varies between 50-100 µm/d in cockles, 120-180 µm/d in mussels and 100-200 µm/d in oysters (Figure 8D), the estimated amount of time contained within peaks remains relatively constant between species (4 - 5.5 days; SI6), suggesting that the difference in peak width is likely caused by differences in growth rates, not by differences in response or retention time of Sr within the organisms. However, as mentioned above, delays in the incorporation of Sr in response to elevated environmental Sr concentrations may still be different between species, especially considering the differences in body mass, gill and mantle surface between the three taxa (Richardson et al., 1980; Hilbish, 1986; Richardson et al., 1993). Moreover, the asymmetric shape of Sr peaks with a slow build-up of Sr concentration and a fast drop in Sr/Ca (see **section 3.4**) suggests that the incorporation of Sr into the shell is somehow buffered or delayed relative to the onset of the spiking event in all species. This suggests

that the portion of the shell containing the peak Sr concentration might have mineralized later than the onset of the spiking event, or even after the end of the Sr spike. Unfortunately, changes in shell growth rates within the peaks cannot be reconstructed in this study, so this hypothesis cannot be tested with our dataset. Therefore, we cannot exclude the possibility that different behaviour of Sr incorporation into the shell as a function of species, shell mineralogy, physiological state or as a function of the size of the Sr dose might play a role in determining how Sr peaks are recorded in the shells and whether peak positions accurately mark the spiking event.

4.4 Estimating shell size from labelled individuals

Shell sizes determined from the umbo to the location of Sr peaks in cross sections through the shells consistently underestimate shell size measurements as taken from the outside of living individuals (Figures 7, 8). This is not surprising, because Sr spike-based distances in cross section are only measured from the umbo (reference point) to the location of the spike on the LAICPMS profile within the outer shell layer, while calliper measurements are taken along the outside of the shell (Figure 2). This effect is clear from the difference in shell size estimates based on Sr spikes for different LAICPMS transects through the same specimen, with profiles closer to the outer shell margin yielding larger shell sizes than the profile farther towards the inside of the shell (Figure 7). In addition, the curvature of the shell increases the width between the flat ends of the measurement calliper, which must move farther apart to accommodate a more curved shell. This effect of curvature is stronger in cockles than in mussels and oysters which show less curvature. Curvature also has a higher relative effect on smaller shells, explaining the trend towards closer agreement between Sr spike-based shell size estimates and calliper measurements in larger specimens (Figure 8F). Furthermore, the outside of cockle shells are ribs and grooves, causing measurements on the outside with callipers to always include the thicker ribs into the shell measurements, while cross sections may cut through grooves, reducing the measurement result. Finally, even though shell cross sections and calliper measurements were made through the axis of maximum growth, it is possible that the cross section is laterally offset from the exact direction in which the calliper measurement took place. This adds an additional offset between the measurements which should be consistent within shells of individuals.

There is also systematic uncertainty to consider in both methods of measurement: Uncertainty related to the position of Sr peaks within areas of shell affected by higher Sr concentrations is typically in the order of 0.3 mm (see sections 4.1.1 and 4.1.3). Calliper measurements are prone to human error (e.g. small variations in the way the calliper is positioned) which result in an uncertainty of ~0.2 mm (1σ; see section 2.1.2 and SI11), roughly on the same order of magnitude as variability in Sr spiking-based estimates. Together, these sources of uncertainty seem sufficient to explain most of the variability in shell size measurement within specimens, but they cannot explain the consistent offset between the two methods. Therefore, when combining labelling techniques and live measurements in growth experiments, we advise to calibrate the results of both techniques using spikes and live measurements performed at the same time during the growth experiment on the same individuals. Specimens exposed to the tidal cycle (intertidal specimens; as opposed to our subtidal setup; see Figure 1) could provide additional control on the timing of Sr spikes using tidal increment-based chronologies, removing some uncertainty related to peak width and growth rates.

4.5 Estimating growth rate from labelled individuals

Despite the offsets and uncertainties considered above, both Sr spiking and calliper measurements yield similar sigmoid-shaped shell size profiles through the growth season (Figure 7). This suggests that meaningful and reproducible information about the growth rate seasonality can be recovered from these measurements, since any consistent offsets between the methods should not affect the increase in shell size between two time intervals. However, Figures 8C–E shows that monthly averaged patterns in growth rate over time differ significantly between Sr spiking and calliper measurements. The reason for this difference is that both methods rely on a maximum of 4 or 5 datapoints per specimen which are offset from each other in time, making direct comparison of growth periods impossible. The attempt to circumvent this issue by linearly inter- and extrapolating based on shell size datapoints and aggregating results in monthly time bins did not successfully reconcile growth rate results between the methods (Figure 8E). The sparsity of shell measurements and Sr spikes (Figures 8A, B) necessitates much intra- and extrapolation to estimate average monthly growth rates. The latter likely explains deviating growth rate reconstructions, given that the growth rates calculated for cockles, for which twice the number of specimens and Sr spikes were measured, show better agreement between the methods than those of the other species.

In absence of a direct agreement between shell size estimates from the two methods, records based on our Sr spiking or calliper measurements alone clearly lack the resolution to characterize growth rate seasonality in the three species beyond a first order estimate of the months in which growth is fastest (May/June) and a reasonably accurate estimate of mean growth rates through the experimental period (see **section 4.1.3**). The overall timing of growth, shell size and growth rate found through our Sr spiking results are in good agreement with previous studies on the same species of cockles (e.g. Hilbish, 1986; Milano et al., 2017; Castrillejo et al., 2020), mussels (Page and Hubbard, 1987; Riisgaord et al., 2012) and oysters (Wilson, 1987; Richardson et al., 1993). Therefore, our data shows that detailed (monthly-scale) measurements of growth rate and shell size are possible based on Sr spiking if spikes are administered more frequently.

4.6 Outlook and recommendations

In this study, we show that, much like Mn (Mouchi et al., 2013), Sr can be used as a trace metal for spiking the shells of molluscs during growth experiments. However, our spiking experiments have varying success depending on the spike done and species. Since these issues are

not fully explained by differences in mineralogy (and the resulting Sr partition coefficients Day and Henderson, 2013; Wassenburg et al., 2016) and growth rate variability, variations between species and specimens may be related to the way molluscs take up and store elements like Sr before they end up in their shells, or to short-term changes in shell growth rate within the spiking event (~24h). To control for these, more knowledge is needed of these processes, which can be obtained by specific growth experiments with populations of a species and in which the Sr concentrations in soft tissue and new shell material as well as shell growth is traced during and after a spiking event (pulse experiment). Culturing populations with and without spiking and changing spike durations while keeping the concentrations fixed could be useful for tracing growth and concentration of the spiking agent (e.g. Sr) during spikes and the effect of spike duration, especially when shells can be internally dated and sampled on timescales beyond the pulse length (e.g. through smaller LAICPMS spots or SIMS measurements or tidal growth laminae in cockles; Evans, 1972; Sano et al., 2012). Repeating experiments like the one described here on bivalve species with very different growth characteristics, such as symbiont-bearing tridacnids, fast-growing pectinids and long-lived species like *Arctica islandica* would be very useful to gauge the response of these taxa to spiking events. Finally, experimenting with varying dose heights (concentrations of Sr in the water) could be useful. However, very high trace element concentrations must be applied with care in growth experiments, as they may inhibit the formation of carbonate by calcifying organisms (de Nooijer et al., 2009).

Conclusion and outlook

Spiking water in mollusc growth experiments with elevated concentrations of strontium of 3-8 times the background concentration produces recognizable peaks in Sr/Ca ratio in the shells of cockles, mussels, and oysters. Overall, this technique presents a simple and cost-efficient means to label mollusc shells in growth experiments with minimal disturbance of the animals. Our dataset shows that higher Sr doses (7-8 times background value; ~0.6 mmol/L) ensure the formation of clearly recognizable peaks in cockles and mussels. Spiking of oyster shells is generally less reliable due to their irregular growth and potential shell resorption. The width of Sr peaks recovered in this study's specimens (~400 μm) adds uncertainty on the exact placement of the peak which is equivalent to 3-5 days of growth if the full peak width is considered as opposed to the highest Sr values within the peak. In addition, multiple spiking events per month are necessary to accurately trace changes in growth rate through a growing season. Therefore, it seems fruitful to experiment with exposing specimens to high doses of elevated Sr concentrations frequently and for shorter time intervals (< 24 h) in an attempt to produce sharper, more easily recognizable peaks which can be used to trace shell growth in detail during experiments.

Data availability statement

The datasets presented in this study can be found in online repositories. The names of the repository/repositories and accession number(s) can be found below: https://doi.org/10.5281/zenodo.7477080. R scripts used to process data and generate figures for this study can be found in the online repository Zenodo: https://doi.org/10.5281/zenodo.7533763.

Ethical statement

Ethical review and approval was not required for the study on non-cephalopod molluscs in accordance with the local legislation in the Netherlands and institutional requirements.

Author contributions

NdW and RW designed the study. NdW, RW, and SvS carried out the growth experiments. WB, LN, GJR, and PC were responsible for the geochemical analyses. NJW, SvS, RW, and BG wrote the first draft of the manuscript. All authors contributed to the article and approved the submitted version.

Funding

This study is part of the UNBIAS project, jointly funded by a Flemish Research Foundation (FWO; 12ZB220N) post-doctoral fellowship (NdW) and a MSCA Individual Fellowship (H2020-MSCA-IF-2018; 843011 – UNBIAS; awarded to NdW). G-JR and LKD acknowledge funding from the Netherlands Earth System Science Center (NESSC; grant no. 024.002.001) from the Dutch Ministry for Education, Culture and Science (gravitation grant no. NWO 024.002.001). BG, NdW, RW and MZ acknowledge support from the Royal Netherlands Institute for Sea Research (NIOZ) and Utrecht University under a NIOZ-UU collaboration grant.

Conflict of interest

The authors declare that the research was conducted in the absence of any commercial or financial relationships that could be construed as a potential conflict of interest.

Publisher's note

Supplementary material

The Supplementary Material for this article can be found online at: https://www.frontiersin.org/articles/10.3389/fmars.2023.1157929/full#supplementary-material

References

Agterhuis, T., Ziegler, M., de Winter, N. J., and Lourens, L. J. (2022). Warm deep-sea temperatures across Eocene thermal maximum 2 from clumped isotope thermometry. *Commun. Earth Environ.* 3, 1–9. doi: 10.1038/s43247-022-00350-8

Auderset, A., Moretti, S., Taphorn, B., Ebner, P.-R., Kast, E., Wang, X. T., et al. (2022). Enhanced ocean oxygenation during Cenozoic warm periods. *Nature* 609, 77–82. doi: 10.1038/s41586-022-05017-0

Ballesta-Artero, I., Zhao, L., Milano, S., Mertz-Kraus, R., Schöne, B. R., van der Meer, J., et al. (2018). Environmental and biological factors influencing trace elemental and microstructural properties of arctica islandica shells. *Sci. Total Environ.* 645, 913–923. doi: 10.1016/j.scitotenv.2018.07.116

Banker, R. M. W., and Sumner, D. Y. (2020). Structure and distribution of chalky deposits in the pacific oyster using x-ray computed tomography (CT). *Sci. Rep.* 10, 12118. doi: 10.1038/s41598-020-68726-4

Bashey, F. (2004). A comparison of the suitability of alizarin red s and calcein for inducing a nonlethally detectable mark in juvenile guppies. *Trans. Am. Fish. Soc* 133, 1516–1523. doi: 10.1577/T03-073.1

Bayne, B., and Worrall, C. (1980). Growth and production of mussels mytilus edulis from two populations. *Mar. Ecol. Prog. Ser.* 3, 317–328. doi: 10.3354/meps003317

Benavente, D., Martinez-Martinez, J., Cueto, N., Ordoñez, S., and Garcia-del-Cura, M. A. (2018). Impact of salt and frost weathering on the physical and durability properties of travertines and carbonate tufas used as building material. *Environ. Earth Sci.* 77, 147. doi: 10.1007/s12665-018-7339-0

Bennema, F. P., Engelhard, G. H., and Lindeboom, H. (2020). Ostrea edulis beds in the central north Sea: delineation, ecology, and restoration. *ICES J. Mar. Sci.* 77, 2694–2705. doi: 10.1093/icesjms/fsaa134

Beukema, J. J., Dekker, R., Essink, K., and Michaelis, H. (2001). Synchronized reproductive success of the main bivalve species in the wadden Sea: causes and consequences. *Mar. Ecol. Prog. Ser.* 211, 143–155. doi: 10.3354/meps211143

Boer, W., Nordstad, S., Weber, M., Mertz-Kraus, R., Hönisch, B., Bijma, J., et al. (2022). New calcium carbonate nano-particulate pressed powder pellet (NFHS-2-NP) for LA-ICP-OES, LA-(MC)-ICP-MS and μXRF. *Geostand. Geoanalytical Res.* 46, 411–432. doi: 10.1111/ggr.12425

Burchell, M., Stopp, M. P., Cannon, A., Hallmann, N., and Schöne, B. R. (2018). Determining seasonality of mussel collection from an early historic Inuit site, Labrador, Canada: Comparing thin-sections with high-resolution stable oxygen isotope analysis. *J. Archaeol. Sci. Rep.* 21, 1215–1224. doi: 10.1016/j.jasrep.2018.02.016

Carré, M., Bentaleb, I., Bruguier, O., Ordinola, E., Barrett, N. T., and Fontugne, M. (2006). Calcification rate influence on trace element concentrations in aragonitic bivalve shells: Evidences and mechanisms. *Geochim. Cosmochim. Acta* 70, 4906–4920. doi: 10.1016/j.gca.2006.07.019

Carriker, M. R., Palmer, R. E., and Prezant, R. S. (1980). Functional ultramorphology of the dissoconch valves of the oyster crassostrea virginica. *Proc. Natl. Shellfisheries Assoc.* 46, 139–183. doi: 10.1016/0022-0981(80)90036-2

Castrillejo, M., Witbaard, R., Casacuberta, N., Richardson, C. A., Dekker, R., Synal, H.-A., et al. (2020). Unravelling 5 decades of anthropogenic 236U discharge from nuclear reprocessing plants. *Sci. Total Environ.* 717, 137094. doi: 10.1016/j.scitotenv.2020.137094

Colsoul, B., Boudry, P., Pérez-Parallé, M. L., Bratoš Cetinić, A., Hugh-Jones, T., Arzul, I., et al. (2021). Sustainable large-scale production of European flat oyster (Ostrea edulis) seed for ecological restoration and aquaculture: a review. *Rev. Aquac.* 13, 1423–1468. doi: 10.1111/raq.12529

Crichton, R. (2019). "Chapter 19 - biomineralization," in *Biological inorganic chemistry (Third edition)*. Ed. R. Crichton (Cambridge, Massachusetts, United States: Academic Press), 517–544. doi: 10.1016/B978-0-12-811741-5.00019-9

Day, C. C., and Henderson, G. M. (2013). Controls on trace-element partitioning in cave-analogue calcite. *Geochim. Cosmochim. Acta* 120, 612–627. doi: 10.1016/j.gca.2013.05.044

Day, R. W., Williams, M. C., and Hawkes, G. P. (1995). A comparison of fluorochromes for marking abalone shells. *Mar. Freshw. Res.* 46, 599–605. doi: 10.1071/mf9950599

de Nooijer, L. J., Toyofuku, T., and Kitazato, H. (2009). Foraminifera promote calcification by elevating their intracellular pH. *Proc. Natl. Acad. Sci.* 106, 15374–15378. doi: 10.1073/pnas.0904306106

de Winter, N. J., and Claeys, P. (2016). Micro X-ray fluorescence (μXRF) line scanning on Cretaceous rudist bivalves: A new method for reproducible trace element profiles in bivalve calcite. *Sedimentology* 64, 231–251. doi: 10.1111/sed.12299

de Winter, N. J., Dämmer, L. K., Falkenroth, M., Reichart, G.-J., Moretti, S., Martínez-García, A., et al. (2021). Multi-isotopic and trace element evidence against different formation pathways for oyster microstructures. *Geochim. Cosmochim. Acta* 308, 326–352. doi: 10.1016/j.gca.2021.06.012

de Winter, N. J., Goderis, S., Dehairs, F., Jagt, J. W., Fraaije, R. H., Van Malderen, S. J., et al. (2017b). Tropical seasonality in the late campanian (late cretaceous): Comparison between multiproxy records from three bivalve taxa from Oman. *Palaeogeogr. Palaeoclimatol. Palaeoecol.* 485, 740–760. doi: 10.1016/j.palaeo.2017.07.031

de Winter, N. J., Killam, D., Fröhlich, L., de Nooijer, L., Boer, W., Schöne, B. R., et al. (2022b). Ultradian rhythms in shell composition of photosymbiotic and non-photosymbiotic mollusks. *EGUsphere* 32, 1–61. doi: 10.5194/egusphere-2022-576

de Winter, N., Sinnesael, M., Makarona, C., Vansteenberge, S., and Claeys, P. (2017a). Trace element analyses of carbonates using portable and micro-X-ray fluorescence: Performance and optimization of measurement parameters and strategies. *J. Anal. At. Spectrom.* 32, 1211–1223. doi: 10.1039/C6JA00361C

de Winter, N. J., Witbaard, R., Kocken, I. J., Müller, I. A., Guo, J., Goudsmit, B., et al. (2022a). Temperature dependence of clumped isotopes (Δ47) in aragonite. *Geophys. Res. Lett.* 49, e2022GL099479. doi: 10.1029/2022GL099479

Dodd, J. R. (1967). Magnesium and strontium in calcareous skeletons: a review. *J. Paleontol.* 41, 1313–1329.

Elliot, M., Welsh, K., Chilcott, C., McCulloch, M., Chappell, J., and Ayling, B. (2009). Profiles of trace elements and stable isotopes derived from giant long-lived tridacna gigas bivalves: potential applications in paleoclimate studies. *Palaeogeogr. Palaeoclimatol. Palaeoecol* 280, 132–142. doi: 10.1016/j.palaeo.2009.06.007

Evans, J. W. (1972). Tidal growth increments in the cockle clinocardium nuttalli. *Science* 176, 416–417. doi: 10.1126/science.176.4033.416

Fagerstrom, J. A. (1987). *The evolution of reef communities* (New York, NY, USA: John Wiley and Sons Inc.).

Fehrenbacher, J. S., Spero, H. J., Russell, A. D., Vetter, L., and Eggins, S. (2015). Optimizing LA-ICP-MS analytical procedures for elemental depth profiling of foraminifera shells. *Chem. Geol.* 407–408, 2–9. doi: 10.1016/j.chemgeo.2015.04.007

Feng, W., Casteel, R. C., Banner, J. L., and Heinze-Fry, A. (2014). Oxygen isotope variations in rainfall, drip-water and speleothem calcite from a well-ventilated cave in Texas, USA: Assessing a new speleothem temperature proxy. *Geochim. Cosmochim. Acta* 127, 233–250. doi: 10.1016/j.gca.2013.11.039

Fox, E., Meyer, E., Panasiak, N., and Taylor, A. R. (2018). Calcein staining as a tool to investigate coccolithophore calcification. *Front. Mar. Sci.* 5. doi: 10.3389/fmars.2018.00326

Freitas, P. S., Clarke, L. J., Kennedy, H. A., and Richardson, C. A. (2008). Inter-and intra-specimen variability masks reliable temperature control on shell Mg/Ca ratios in laboratory and field cultured mytilus edulis and pecten maximus (bivalvia). *Biogeosciences* 5, 531–572. doi: 10.5194/bg-5-1245-2008

Freitas, P. S., Clarke, L. J., Kennedy, H., and Richardson, C. A. (2009). Ion microprobe assessment of the heterogeneity of Mg/Ca, Sr/Ca and Mn/Ca ratios in pecten maximus and mytilus edulis (bivalvia) shell calcite precipitated at constant temperature. *Biogeosciences* 6, 1267. doi: 10.5194/bg-6-1209-2009

Fröhlich, L., Siebert, V., Walliser, E. O., Thébault, J., Jochum, K. P., Chauvaud, L., et al. (2022). Ba/Ca profiles in shells of pecten maximus – a proxy for specific primary producers rather than bulk phytoplankton. *Chem. Geol.* 593, 120743. doi: 10.1016/j.chemgeo.2022.120743

Füllenbach, C. S., Schöne, B. R., and Mertz-Kraus, R. (2015). Strontium/lithium ratio in aragonitic shells of cerastoderma edule (Bivalvia)–a new potential temperature proxy for brackish environments. *Chem. Geol.* 417, 341–355. doi: 10.1016/j.chemgeo.2015.10.030

Garbe-Schönberg, D., and Müller, S. (2014). Nano-particulate pressed powder tablets for LA-ICP-MS. *J. Anal. At. Spectrom.* 29, 990–1000. doi: 10.1039/C4JA00007B

Geerken, E., de Nooijer, L., Toyofuku, T., Roepert, A., Middelburg, J. J., Kienhuis, M. V. M., et al. (2022). High precipitation rates characterize biomineralization in the benthic foraminifer Ammonia beccarii. *Geochim. Cosmochim. Acta* 318, 70–82. doi: 10.1016/j.gca.2021.11.026

Gerringer, M. E., Andrews, A. H., Huss, G. R., Nagashima, K., Popp, B. N., Linley, T. D., et al. (2018). Life history of abyssal and hadal fishes from otolith growth zones and oxygen isotopic compositions. *Deep Sea Res. Part Oceanogr. Res. Pap.* 132, 37–50. doi: 10.1016/j.dsr.2017.12.002

Gillikin, D. P., Lorrain, A., Navez, J., Taylor, J. W., André, L., Keppens, E., et al. (2005). Strong biological controls on Sr/Ca ratios in aragonitic marine bivalve shells. *Geochem. Geophys. Geosystems* 6, 1–16. doi: 10.1029/2004GC000874

Guillong, M., Meier, D. L., Allan, M. M., Heinrich, C. A., and Yardley, B. W. D. (2008). SILLS: A Matlab-based program for the reduction of laser ablation ICP–MS data of homogenous materials and inclusions. *Mineral. Assoc. Can. Short Course* 40, 328–333. Vancouver, B.C., Canada.

Gutiérrez-Zugasti, I. (2011). Coastal resource intensification across the pleistocene–Holocene transition in northern Spain: Evidence from shell size and age distributions of marine gastropods. *Quat. Int.* 244, 54–66. doi: 10.1016/j.quaint.2011.04.040

Hagiwara, S., and Byerly, L. (1981). Calcium channel. *Annu. Rev. Neurosci.* 4, 69–125. doi: 10.1016/0166-2236(83)90084-X

Hanshaw, B. B., and Back, W. (1979). Major geochemical processes in the evolution of carbonate–aquifer systems. *J. Hydrol.*, 43, 287–312. doi: 10.1016/0022-1694(79)90177-X

Haour, A., Christie, A., and Jaufar, S. (2016). "Tracking the cowrie shell: Excavations in the Maldives," in *Nyame akuma*, (Houston, Texas, United States) vol. 85. , 69–77. Available at: https://safa.rice.edu/Default.aspx?id=2147485729.

Henke, B. L., Gullikson, E. M., and Davis, J. C. (1993). X-Ray interactions: Photoabsorption, scattering, transmission, and reflection at e = 50-30,000 eV, z = 1-92. *At. Data Nucl. Data Tables* 54, 181–342. doi: 10.1006/adnd.1993.1013

Henkes, G. A., Passey, B. H., Grossman, E. L., Shenton, B. J., Yancey, T. E., and Pérez-Huerta, A. (2018). Temperature evolution and the oxygen isotope composition of phanerozoic oceans from carbonate clumped isotope thermometry. *Earth Planet. Sci. Lett.* 490, 40–50. doi: 10.1016/j.epsl.2018.02.001

Hilbish, T. J. (1986). Growth trajectories of shell and soft tissue in bivalves: Seasonal variation in mytilus edulis l. *J. Exp. Mar. Biol. Ecol.* 96, 103–113. doi: 10.1016/0022-0981(86)90236-4

Hippler, D., Witbaard, R., van Aken, H. M., Buhl, D., and Immenhauser, A. (2013). Exploring the calcium isotope signature of arctica islandica as an environmental proxy using laboratory- and field-cultured specimens. *Palaeogeogr. Palaeoclimatol. Palaeoecol.* 373, 75–87. doi: 10.1016/j.palaeo.2011.11.015

Holá, M., Kalvoda, J., Nováková, H., Škoda, R., and Kanický, V. (2011). Possibilities of LA-ICP-MS technique for the spatial elemental analysis of the recent fish scales: Line scan vs. depth profiling. *Appl. Surf. Sci.* 257, 1932–1940. doi: 10.1016/j.apsusc.2010.09.029

Houlbrèque, F., Meibom, A., Cuif, J.-P., Stolarski, J., Marrocchi, Y., Ferrier-Pagès, C., et al. (2009). Strontium-86 labeling experiments show spatially heterogeneous skeletal formation in the scleractinian coral porites porites. *Geophys. Res. Lett.* 36, 1–5. doi: 10.1029/2008GL036782

Huyghe, D., de Rafelis, M., Ropert, M., Mouchi, V., Emmanuel, L., Renard, M., et al. (2019). New insights into oyster high-resolution hinge growth patterns. *Mar. Biol.* 166, 48. doi: 10.1007/s00227-019-3496-2

Huyghe, D., Lartaud, F., Emmanuel, L., Merle, D., and Renard, M. (2015). Palaeogene climate evolution in the Paris basin from oxygen stable isotope (δ18O) compositions of marine molluscs. *J. Geol. Soc* 172, 576–587. doi: 10.1144/jgs2015-016

Inoue, M., Nohara, M., Okai, T., Suzuki, A., and Kawahata, H. (2004). Concentrations of trace elements in carbonate reference materials coral JCp-1 and giant clam JCt-1 by inductively coupled plasma-mass spectrometry. *Geostand. Geoanalytical Res.* 28, 411–416. doi: 10.1111/j.1751-908X.2004.tb00759.x

Izgec, O., Demiral, B., Bertin, H., and Akin, S. (2008). CO2 injection into saline carbonate aquifer formations I: laboratory investigation. *Transp. Porous Media* 72, 1–24. doi: 10.1007/s11242-007-9132-5

Jablonski, A., and Powell, C. J. (2020). Effective attenuation lengths for different quantitative applications of X-ray photoelectron spectroscopy. *J. Phys. Chem. Ref. Data* 49, 033102. doi: 10.1063/5.0008576

Jochum, K. P., Garbe-Schönberg, D., Veter, M., Stoll, B., Weis, U., Weber, M., et al. (2019). Nano-powdered calcium carbonate reference materials: Significant progress for microanalysis? *Geostand. Geoanalytical Res.* 43, 595–609. doi: 10.1111/ggr.12292

Jochum, K. P., Weis, U., Stoll, B., Kuzmin, D., Yang, Q., Raczek, I., et al. (2011). Determination of reference values for NIST SRM 610–617 glasses following ISO guidelines. *Geostand. Geoanalytical Res.* 35, 397–429. doi: 10.1111/j.1751-908X.2011.00120.x

Jochum, K. P., Willbold, M., Raczek, I., Stoll, B., and Herwig, K. (2005). Chemical characterisation of the USGS reference glasses GSA-1G, GSC-1G, GSD-1G, GSE-1G, BCR-2G, BHVO-2G and BIR-1G using EPMA, ID-TIMS, ID-ICP-MS and LA-ICP-MS. *Geostand. Geoanalytical Res.* 29, 285–302. doi: 10.1111/j.1751-908X.2005.tb00901.x

Kent, R. W. (1992). *Making dead oysters talk: Techniques for analyzing oysters from archaeological sites: Maryland historical trust, historic st. mary's city, Jefferson Patterson park and museum* (Crownsville, MD: Maryland Historical and Cultural Publications).

Kraan, C., Dekinga, A., and Piersma, T. (2011). Now an empty mudflat: past and present benthic abundances in the western Dutch wadden Sea. *Helgol. Mar. Res.* 65, 51–58. doi: 10.1007/s10152-010-0200-9

Kuzyakov, Y., Shevtzova, E., and Pustovoytov, K. (2006). Carbonate re-crystallization in soil revealed by 14C labeling: Experiment, model and significance for paleo-environmental reconstructions. *Geoderma* 131, 45–58. doi: 10.1016/j.geoderma.2005.03.002

Lartaud, F., De Rafélis, M., Ropert, M., Emmanuel, L., Geairon, P., and Renard, M. (2010). Mn Labelling of living oysters: artificial and natural cathodoluminescence analyses as a tool for age and growth rate determination of c. gigas (Thunberg 1793) shells. *Aquaculture* 300, 206–217. doi: 10.1016/j.aquaculture.2009.12.018

Lear, C. H., Elderfield, H., and Wilson, P. A. (2003). A Cenozoic seawater Sr/Ca record from benthic foraminiferal calcite and its application in determining global weathering fluxes, earth planet. *Sci. Lett.* 208, 69–84. doi: 10.1016/S0012-821X(02)01156-1

Leips, J., Baril, C. T., Rodd, F. H., Reznick, D. N., Bashey, F., Visser, G. J., et al. (2001). The suitability of calcein to mark poeciliid fish and a new method of detection. *Trans. Am. Fish. Soc* 130, 501–507. doi: 10.1577/1548-8659(2001)130<0501:TSOCTM>2.0.CO;2

Lough, J. M., and Barnes, D. J. (2000). Environmental controls on growth of the massive coral porites. *J. Exp. Mar. Biol. Ecol.* 245, 225–243. doi: 10.1016/S0022-0981(99)00168-9

Magnabosco, G., Polishchuk, I., Erez, J., Fermani, S., Pokroy, B., and Falini, G. (2018). Insights on the interaction of calcein with calcium carbonate and its implications in biomineralization studies. *CrystEngComm* 20, 4221–4224. doi: 10.1039/C8CE00853A

Marali, S., Schöne, B. R., Mertz-Kraus, R., Griffin, S. M., Wanamaker, A. D., Butler, P. G., et al. (2017). Reproducibility of trace element time-series (Na/Ca, Mg/Ca, Mn/Ca, Sr/Ca, and Ba/Ca) within and between specimens of the bivalve arctica islandica – a LA-ICP-MS line scan study. *Palaeogeogr. Palaeoclimatol. Palaeoecol.* 484, 109–128. doi: 10.1016/j.palaeo.2016.11.024

Marchegiano, M., Francke, A., Gliozzi, E., Wagner, B., and Ariztegui, D. (2019). High-resolution palaeohydrological reconstruction of central Italy during the Holocene. *Holocene* 29, 481–492. doi: 10.1177/0959683618816465

Markuszewski, R. (1979). *Structure, fluorescence, and chelating properties of calcein* (Iowa City: University of Iowa). Theses and Dissertations. doi: 10.31274/rtd-180813-2317

Mat, A. M., Sarrazin, J., Markov, G. V., Apremont, V., Dubreuil, C., Eché, C., et al. (2020). Biological rhythms in the deep-sea hydrothermal mussel bathymodiolus azoricus. *Nat. Commun.* 11, 3454. doi: 10.1038/s41467-020-17284-4

Milano, S., Schöne, B. R., and Witbaard, R. (2017). Changes of shell microstructural characteristics of cerastoderma edule (Bivalvia) — a novel proxy for water temperature. *Palaeogeogr. Palaeoclimatol. Palaeoecol.* 465, 395–406. doi: 10.1016/j.palaeo.2015.09.051

Moss, D. K., Ivany, L. C., and Jones, D. S. (2021). Fossil bivalves and the sclerochronological reawakening. *Paleobiology* 47, 551–573. doi: 10.1017/pab.2021.16

Mouchi, V., De Rafélis, M., Lartaud, F., Fialin, M., and Verrecchia, E. (2013). Chemical labelling of oyster shells used for time-calibrated high-resolution Mg/Ca ratios: a tool for estimation of past seasonal temperature variations. *Palaeogeogr. Palaeoclimatol. Palaeoecol.* 373, 66–74. doi: 10.1016/j.palaeo.2012.05.023

Mourguiart, Ph., and Carbonel, P. (1994). A quantitative method of palaeolake-level reconstruction using ostracod assemblages: an example from the Bolivian altiplano. *Hydrobiologia* 288, 183–193. doi: 10.1007/BF00006241

Nehrke, G., Keul, N., Langer, G., de Nooijer, L. J., Bijma, J., and Meibom, A. (2013). A new model for biomineralization and trace-element signatures of foraminifera tests. *Biogeosciences* 10, 6759–6767. doi: 10.5194/bg-10-6759-2013

Nikolayev, D., Lychagina, T., and Pakhnevich, A. (2019). Experimental neutron pole figures of minerals composing the bivalve mollusc shells. *SN Appl. Sci.* 1, 344. doi: 10.1007/s42452-019-0355-1

Obelic, B., Álvarez, A., Argullós, J., and Piana, E. L. (1998). "Determination of water palaeotemperature in the beagle channel (Argentina) during the last 6000 yr through stable isotope composition of mytilus edulis shells," in *Quaternary of south America and Antarctica peninsula 1998* (Abington-on-Thames, UK: Routledge, Taylor and Francis Group), ISBN: .

Okai, T., Suzuki, A., Kawahata, H., Terashima, S., and Imai, N. (2002). Preparation of a new geological survey of Japan geochemical reference material: Coral JCp-1. *Geostand. Newsl.* 26, 95–99. doi: 10.1111/j.1751-908X.2002.tb00627.x

Page, H. M., and Hubbard, D. M. (1987). Temporal and spatial patterns of growth in mussels mytilus edulis on an offshore platform: relationships to water temperature and food availability. *J. Exp. Mar. Biol. Ecol.* 111, 159–179. doi: 10.1016/0022-0981(87)90053-0

Pages 2k consortium. (2017). A global multiproxy database for temperature reconstructions of the common era. *Sci. Data* 4, 170088. doi: 10.1038/sdata.2017.88

Posenato, R., Crippa, G., de Winter, N. J., Frijia, G., and Kaskes, P. (2022). Microstructures and sclerochronology of exquisitely preserved lower Jurassic lithiotid bivalves: Paleobiological and paleoclimatic significance, palaeogeogr. *Palaeoclimatol. Palaeoecol.* 602, 111162. doi: 10.1016/j.palaeo.2022.111162

Quinby-Hunt, M. S., and Turekian, K. K. (1983). Distribution of elements in sea water. *Eos Trans. Am. Geophys. Union* 64, 130–130. doi: 10.1029/EO064i014p00130

Richardson, C. A., Collis, S. A., Ekaratne, K., Dare, P., and Key, D. (1993). The age determination and growth rate of the European flat oyster, ostrea edulis , in British waters determined from acetate peels of umbo growth lines. *ICES J. Mar. Sci.* 50, 493–500. doi: 10.1006/jmsc.1993.1052

Richardson, C. A., Crisp, D. J., Runham, N. W., and Gruffydd, L. D. (1980). The use of tidal growth bands in the shell of *Cerastoderma edule* to measure seasonal growth rates under cool temperate and sub-arctic conditions. *J. Mar. Biol. Assoc. U. K.* 60, 977–989. doi: 10.1017/S002531540004203X

Riisgaord, H. U., Boettiger, L., and Pleissner, D. (2012). Effect of salinity on growth of mussels, *Mytilus edulis*, with special reference to great belt (Denmark). *Open J. Mar. Sci.* 02, 167. doi: 10.4236/ojms.2012.24020

Saito, A., Kagi, H., Marugata, S., Komatsu, K., Enomoto, D., Maruyama, K., et al. (2020). Incorporation of incompatible strontium and barium ions into calcite (CaCO3) through amorphous calcium carbonate. *Minerals* 10, 270. doi: 10.3390/min10030270

Sampei, Y., Matsumoto, E., Dettman, D. L., Tokuoka, T., and Abe, O. (2005). Paleosalinity in a brackish lake during the Holocene based on stable oxygen and carbon isotopes of shell carbonate in nakaumi lagoon, southwest Japan. *Palaeogeogr. Palaeoclimatol. Palaeoecol.* 224, 352–366. doi: 10.1016/j.palaeo.2005.04.020

Sánchez-Román, M., Vasconcelos, C., Schmid, T., Dittrich, M., McKenzie, J. A., Zenobi, R., et al. (2008). Aerobic microbial dolomite at the nanometer scale: Implications for the geologic record. *Geology* 36, 879–882. doi: 10.1130/G25013A.1

Sano, Y., Kobayashi, S., Shirai, K., Takahata, N., Matsumoto, K., Watanabe, T., et al. (2012). Past daily light cycle recorded in the strontium/calcium ratios of giant clam shells. *Nat. Commun.* 3, 761. doi: 10.1038/ncomms1763

Schindelin, J., Arganda-Carreras, I., Frise, E., Kaynig, V., Longair, M., Pietzsch, T., et al. (2012). Fiji: an open-source platform for biological-image analysis. *Nat. Methods* 9, 676–682. doi: 10.1038/nmeth.2019

Schöne, B. R., Rodland, D. L., Fiebig, J., Oschmann, W., Goodwin, D., Flessa, K. W., et al. (2006). Reliability of multitaxon, multiproxy reconstructions of environmental conditions from accretionary biogenic skeletons. *J. Geol.* 114, 267–285. doi: 10.1086/501219

Smaal, A. C., and Lucas, L. (2000). Regulation and monitoring of marine aquaculture in the Netherlands. *J. Appl. Ichthyol.* 16, 187–191. doi: 10.1046/j.1439-0426.2000.00266.x

Song, H., Tong, J., Tian, L., Song, H., Qiu, H., Zhu, Y., et al. (2014). Paleo-redox conditions across the permian-Triassic boundary in shallow carbonate platform of the nanpanjiang basin, south China. *Sci. China Earth Sci.* 57, 1030–1038. doi: 10.1007/s11430-014-4843-2

Stoll, H. M., Klaas, C. M., Probert, I., Encinar, J. R., and Garcia Alonso, J. I. (2002). Calcification rate and temperature effects on Sr partitioning in coccoliths of multiple species of coccolithophorids in culture. *Glob. Planet. Change* 34, 153–171. doi: 10.1016/S0921-8181(02)00112-1

Stoll, H. M., and Schrag, D. P. (2001). Sr/Ca variations in Cretaceous carbonates: relation to productivity and sea level changes. *Palaeogeogr. Palaeoclimatol. Palaeoecol.* 168, 311–336. doi: 10.1016/S0031-0182(01)00205-X

Surge, D., Lohmann, K. C., and Dettman, D. L. (2001). Controls on isotopic chemistry of the American oyster, crassostrea virginica: implications for growth patterns. *Palaeogeogr. Palaeoclimatol. Palaeoecol.* 172, 283–296. doi: 10.1016/S0031-0182(01)00303-0

Tran, E. L., Reimus, P., Klein-BenDavid, O., Teutsch, N., Zavarin, M., Kersting, A. B., et al. (2020). Mobility of radionuclides in fractured carbonate rocks: Lessons from a field-scale transport experiment. *Environ. Sci. Technol.* 54, 11249–11257. doi: 10.1021/acs.est.0c03008

Ullmann, C. V., Böhm, F., Rickaby, R. E., Wiechert, U., and Korte, C. (2013). The giant pacific oyster (Crassostrea gigas) as a modern analog for fossil ostreoids: isotopic (Ca, O, c) and elemental (Mg/Ca, Sr/Ca, Mn/Ca) proxies. *Geochem. Geophys. Geosystems* 14, 4109–4120. doi: 10.1002/ggge.20257

Valchev, B. (2003). On the potential of small benthic foraminifera as paleoecological indicators: recent advances. *Ann. UMG* 46, 51–56.

Van Aken, H. M. (2003). 140 years of daily observations in a tidal inlet (Marsdiep). *ICES Mar. Sci. Symp* 219, 359–361.

Van der Weijden, C. H. (2002). Pitfalls of normalization of marine geochemical data using a common divisor. *Mar. Geol.* 184, 167–187. doi: 10.1016/S0025-3227(01)00297-3

Vansteenberge, S., de Winter, N. J., Sinnesael, M., Xueqin, Z., Verheyden, S., and Claeys, P. (2020). Benchtop μXRF as a tool for speleothem trace elemental analysis: Validation, limitations and application on an eemian to early weichselian (125–97ka) stalagmite from Belgium. *Palaeogeogr. Palaeoclimatol. Palaeoecol.* 538, 109460. doi: 10.1016/j.palaeo.2019.109460

Vellekoop, J., Kaskes, P., Sinnesael, M., Huygh, J., Déhais, T., Jagt, J. W. M., et al. (2022). A new age model and chemostratigraphic framework for the maastrichtian type area (southeastern Netherlands, northeastern Belgium). *Newsl. Stratigr.* 55, 479–501. doi: 10.1127/nos/2022/0703

Wassenburg, J. A., Scholz, D., Jochum, K. P., Cheng, H., Oster, J., Immenhauser, A., et al. (2016). Determination of aragonite trace element distribution coefficients from speleothem calcite–aragonite transitions. *Geochim. Cosmochim. Acta* 190, 347–367. doi: 10.1016/j.gca.2016.06.036

Wasylenki, L. E., Dove, P. M., Wilson, D. S., and De Yoreo, J. J. (2005). Nanoscale effects of strontium on calcite growth: An *in situ* AFM study in the absence of vital effects. *Geochim. Cosmochim. Acta* 69, 3017–3027. doi: 10.1016/j.gca.2004.12.019

Wichern, N. M. A., de Winter, N. J., Johnson, A. L. A., Goolaerts, S., Wesselingh, F., Hamers, M. F., et al. (2022). The fossil bivalve Angulus benedeni benedeni: a potential seasonally resolved stable isotope-based climate archive to investigate pliocene temperatures in the southern north Sea basin. *EGUsphere*, 1–53. doi: 10.5194/egusphere-2022-951

Wilmeth, D. T., Johnson, H. A., Stamps, B. W., Berelson, W. M., Stevenson, B. S., Nunn, H. S., et al. (2018). Environmental and biological influences on carbonate precipitation within hot spring microbial mats in little hot creek, CA. *Front. Microbiol.* 9. doi: 10.3389/fmicb.2018.01464

Wilson, J. H. (1987). Environmental parameters controlling growth of ostrea edulis l. and pecten maximus l. in suspended culture. *Aquaculture* 64, 119–131. doi: 10.1016/0044-8486(87)90348-6

Zhou, S., Zhang, X., Li, W., Li, L., and Cai, X. (2017). Experimental evaluation of fluorescent (alizarin red s and calcein) and clip-tag markers for stock assessment of ark shell, anadara broughtonii. *Chin. J. Oceanol. Limnol.* 35, 265–274. doi: 10.1007/s00343-016-5137-7

frontiers | Frontiers in Marine Science

TYPE Original Research
PUBLISHED 01 May 2023
DOI 10.3389/fmars.2023.1151592

OPEN ACCESS

EDITED BY
Travis Blake Meador,
Academy of Sciences of the Czech Republic (ASCR), Czechia

REVIEWED BY
Matthias López Correa,
National Research Council (CNR), Italy
Andres Rüggeberg,
Université de Fribourg, Switzerland

*CORRESPONDENCE
Steffen Hetzinger
steffen.hetzinger@ifg.uni-kiel.de

RECEIVED 26 January 2023
ACCEPTED 19 April 2023
PUBLISHED 01 May 2023

CITATION
Hetzinger S, Grohganz M, Halfar J, Hathorne E, Ballesteros E and Kersting DK (2023) Elemental cycles in the coralline alga *Neogoniolithon hauckii* as a recorder of temperature variability in the Mediterranean Sea.
Front. Mar. Sci. 10:1151592.
doi: 10.3389/fmars.2023.1151592

Elemental cycles in the coralline alga *Neogoniolithon hauckii* as a recorder of temperature variability in the Mediterranean Sea

Steffen Hetzinger[1]*, Madleen Grohganz[2], Jochen Halfar[3], Ed Hathorne[4], Enric Ballesteros[5] and Diego K. Kersting[6]

[1]Institut für Geowissenschaften, Christian-Albrechts-Universität zu Kiel, Kiel, Germany, [2]Palaeobiology Research Group, School of Earth Sciences, University of Bristol, Bristol, United Kingdom, [3]Chemical and Physical Sciences Department, University of Toronto Mississauga, Mississauga, ON, Canada, [4]GEOMAR Helmholtz-Zentrum für Ozeanforschung Kiel, Kiel, Germany, [5]Centre d'Estudis Avançats de Blanes (CEAB, CSIC), Girona, Spain, [6]Instituto de Acuicultura de Torre de la Sal (IATS, CSIC), Castelló, Spain

Coralline algae play important ecological roles throughout the photic zone of the world's oceans. Recent studies have shown that attached-living coralline algae can contain records of past climate variability. So far, algal-based paleo-reconstructions are mainly available from mid- to high-latitudes, while in low latitude and temperate regions only few examples exist. Here, we investigate samples from the attached-living encrusting coralline algal species *Neogoniolithon hauckii* (Rothpletz) R.A Townsend & Huisman [= *Neogoniolithon mamillosum* (Hauck) Setchell & L.R. Mason, nom illeg.] from a temperate site in the Mediterranean Sea to assess its potential as an environmental recorder. The specimens were collected at different water depths (20 and 40 m) in the Columbretes Islands (Spain). Sclerochronological analysis of sectioned samples revealed seasonal growth patterns. Mg/Ca, Li/Ca, and Ba/Ca ratios were measured in the algal skeletons using laser ablation inductively coupled mass spectrometry (LA-ICP-MS) in ultra-high resolution. We report a mean vertical extension rate of 1.1 to 1.2 mm/year (based on analysis of Mg/Ca cycles in 40 m and 20 m samples), representing the first growth rate measurement for this species. In addition, subannual banding patterns were mapped, measured, and could be linked to high frequency variability in laser-analyzed Mg/Ca ratios. Elemental ratios analyzed in *Neogoniolithon hauckii* were compared to *in situ* water temperatures measured at the water depth of sample collection. Our results show significant positive relationships between algal Mg/Ca (R=0.55) as well as Li/Ca ratios (R=0.46) and *in situ* measured temperature data (40 m specimen). Ba/Ca ratios show no significant correlation to temperature and may be influenced by other factors. These data suggest potential of this species for climate reconstructions in warm-temperate regions as *Neogoniolithon hauckii* is not only widely distributed in the Mediterranean, but also one of the few species that may be used as a temperature archive for mesophotic coralligenous assemblages that are strongly affected by the recent anthropogenic temperature rise. Further

calibration studies are needed to test the element-temperature relationships on samples with longer growth records and in different settings and water depths.

KEYWORDS

coralline algae, LA-ICP-MS, sclerochronology, temperate, Mg/Ca, Li/Ca, climate archive, subannual banding

1 Introduction

Coralline algae (Corallinophycidae, Rhodophyta) can be found worldwide in coastal ecosystems from the intertidal to mesophotic zones (Adey and Macintyre, 1973). Encrusting coralline algae build important settlement substrates for invertebrates and act as substrate binders from tropical oceans to the Arctic (Adey and Macintyre, 1973; Steneck, 1983; Steneck, 1986; Tebben et al., 2015) and are key ecosystem engineers (Schubert et al., 2020). They form rhodolith beds (free-living forms of coralline algae) in warm-temperate to Arctic regions (Foster, 2001; Hetzinger et al., 2006; Halfar et al., 2012; Teichert et al., 2014) and play an important role in coral reef growth by stabilizing and cementing reef structures in tropical oceans in modern times and on geological time scales (Kiessling, 2009; Rindi et al., 2019; Teichert et al., 2020). Coralline algae precipitate $CaCO_3$ within their cell walls (Adey et al., 2013) and are thus major carbonate producers in marine ecosystems (Canals and Ballesteros, 1997). Due to their abundance in all oceans, they are an important part of the oceanic carbon cycle (Perry et al., 2008). Corallines are well represented in the fossil record, for example in the Mediterranean region, where they have occurred for at least 140 Myr (Rindi et al., 2019), and more than 60 species of corallines have been reported from this region alone (Coll et al., 2010; Rindi et al., 2019).

Similar to tree rings and bivalve mollusks (Cook et al., 2004; Mette et al., 2016), many species of coralline algae form seasonal banding patterns during growth (Halfar et al., 2000; Kamenos et al., 2008; Halfar et al., 2011a; Williams et al., 2011). However, whether the observed growth patterns in the high-Mg calcite skeletons form annually or subannually is not clear in all species. For example, in the crustose coralline algae *Clathromorphum* sp., the calcification rate declines during seasonal decreases in temperature and light in winter periods. This translates to changes of skeletal anatomy, where a shift from narrow and elongate cells with dense walls takes place to wider and shorter cells with thinner walls, resulting in growth increment demarcations in the fall to early winter (Adey et al., 2013). These incremental growth patterns allow a clear discrimination of individual growth years. In some specimens of *Clathromorphum* sp. the yearly layering of sporangial conceptacles, i.e. cavities in which the reproductive structures develop, form in fall and early winter (Adey, 1966) and can provide an additional secondary marker for annual growth. *In situ* field monitoring experiments (Halfar et al., 2008) have confirmed that the attached-living genus *Clathromorphum* forms annual banding patterns with fastest growth during summer and reduced growth during fall and winter. This is in line with physiological considerations, which suggest that calcification and growth may slow down dramatically at reduced light intensities and temperatures (Adey, 1970). However, in some coralline algal species subseasonal growth banding patterns can make the identification of seasonal growth cycles difficult. In free-living (non-attached rhodoliths) coralline algae the episodical movement by waves, currents (Marrack, 1999), and grazing animals may lead to differences in growth rates depending on the orientation. As rhodoliths are often found on soft substrate, the bottom side of individual rhodoliths may be episodically buried in the sediment. This may influence the growth patterns in different parts of a specimen, even leading to a halt of growth in some area, while growth continues in another, potentially complicating the sclerochronological interpretation (Sletten et al., 2017b).

Coralline algae also incorporate changes in their ambient environment into the geochemistry of their skeletons (Chave and Wheeler, 1965; Moberly, 1968; Williams et al., 2011; Chan et al., 2017). Seasonality seen in trace elements in algal skeletal calcite can help to better identify annual growth banding patterns. Field calibration experiments have confirmed that algal geochemistry provides a reliable indication of ocean temperatures (Halfar et al., 2008). Comparisons between algal proxies and measured surface ocean data have shown that algal Mg/Ca ratios are temperature-dependent (Kamenos et al., 2008; Nash and Adey, 2017; Hetzinger et al., 2018). The substitution of magnesium in calcite is endothermic, favored at higher temperatures, and builds the basis for magnesium paleothermometry in different marine organisms (e.g. Lea, 2003). The direct matching of highly-resolved Mg/Ca time series measured in skeletal calcite along transects parallel to the direction of algal growth, visible in high-resolution microscope photomosaic images, can provide a valuable tool to distinguish subseasonal cyclicity from seasonal cycles and is routinely used as a method to calibrate and refine age models (e.g. Hetzinger et al., 2019). Due to the well-developed regular annual growth banding and the potential of long-lived specimens, crustose coralline algae have been established as biogenic climate archives in recent years (Svendsen et al., 2014; Hetzinger et al., 2021; Siebert et al., 2021). A number of studies have examined various aspects of the chemical and physical structure of attached-living coralline algae in order to reconstruct past changes in large-scale climate variability (Halfar et al., 2007; Gamboa et al., 2010; Williams et al., 2014; Williams et al., 2018a; Williams et al., 2018b; Leclerc et al., 2022).

Even though coralline algae are distributed worldwide the majority of algal-based paleo-reconstructions are based on cold-

water species from mid- to high-latitudes, such as *Clathromorphum* sp. and *Lithothamnion glaciale*. So far, the longest algal-based climate records have been developed from species that live attached to rocky substrate and form thick crusts with mound-like structures [e.g. *Clathromorphum compactum*, up to 650 years of continuous growth (Halfar et al., 2013)]. These records from high latitudes stem from colder waters using specimens with relatively slow growth rates (Hetzinger et al., 2019).

Tropical and subtropical coralline algal species have been less used as potential archives of climate and environmental variability [e.g. *Lithothamnion* spp. (Halfar et al., 2000; Sletten et al., 2017a); *Lithophyllum* spp. (Caragnano et al., 2014; Nash et al., 2016; Caragnano et al., 2017); *Sporolithon durum* (Darrenougue et al., 2014; Darrenougue et al., 2018)], mainly due to a lack of long-lived species. Not all coralline algal genera have the potential to be used as climate archives if their vertical growth is limited [e.g. *Phymatolithon* (Adey et al., 2018)]. In warmer tropical environments growth forms are more common to expand horizontally with only moderate thickening of the thallus, making the identification of annual growth patterns and the establishment of age chronologies difficult. Additionally, overgrowth by different algal species and by other organisms (e.g. bryozoans) is more commonly seen in tropical environments and crustal extension rates can be up to a magnitude higher than in subarctic coralline algae (e.g. Adey and Vassar, 1975). Crustose coralline algal species from warm-temperate settings have received even less attention as potential paleo-proxy archives for the reconstruction of past climate variability. Nevertheless, free-living growth forms in temperate settings have been used as paleo-sea level indicators (Aguirre et al., 2020) and for paleoecological studies (Basso, 1998; Martinuš et al., 2013).

Finding new coralline algal species potentially suitable for paleoclimate reconstructions is important in order to gain insights into past seasonal-resolution climate variability. As measured instrumental climate data, such as surface ocean temperatures, are not available before the mid-20th century for most ocean regions, it is crucial to be able to reconstruct seasonal variability before the impact of anthropogenic warming on marine ecosystems. In the Mediterranean, coralligenous assemblages and other bioconstructed habitats, like reefs and beds of the coral *Cladocora caespitosa*, are strongly affected by water temperature increase in recent decades with mass mortalities and temperature-dependent diseases occurring more frequently (Garrabou et al., 2009; Kersting et al., 2013; Hereu and Kersting, 2016; Kersting and Linares, 2019; Garrabou et al., 2022). During the past three decades the Mediterranean Sea has warmed up with a trend of 0.041 ± 0.006°C/year (Pisano et al., 2020).

Here, we have analyzed for the first time encrusting coralline alga *Neogoniolithon hauckii* (Rothpletz) R.A. Townsend & Huisman (Corallinales: Rhodophyta) samples from a temperate site in the Mediterranean Sea using high-resolution LA-ICP-MS and growth banding analysis. In this study, we assess whether this species has the potential to hold records of past environmental variability. First, we examine seasonal growth patterns and measure annual mean extension rates. Second, Mg/Ca, Li/Ca, and Ba/Ca ratios are analyzed in ultra-high resolution and elemental ratios are compared to *in situ* water temperatures in order to test their potential as paleotemperature proxies. The selection of *N. hauckii* for this study is specially suitable as it is a species whose distribution includes most of the Mediterranean Sea (Babbini and Bressan, 1997). Moreover, *Neogoniolithon hauckii* has a wide depth distribution range, that covers most of the shaded Mediterranean habitats, from 1 to 90 m depth. Although it is occasionally found in the shallows and in maërl beds (Bressan and Babbini, 2003), it is more abundant in coralligenous outcrops (Feldmann, 1937), where it is a major component of the coralline algal matrix (Ballesteros, 2006), together with *Lithophyllum stictiforme* and *Mesophyllum* spp.

2 Materials and methods

2.1 Study site and regional setting

The Columbretes Islands (NW Mediterranean Sea) are located 30 nautical miles off the nearest coast (Castelló, Spain, NW Mediterranean; Figure 1A). A marine reserve encircles the archipelago, covering an area of 5500 hectares. Illa Grossa (39° 53.825′N, 0°41.214′E), the largest of the islets in the Columbretes, is a C-shaped, drowned Quaternary volcanic caldera. A detailed description of the geographic area, including environmental and oceanographic features is available in Kersting et al. (2013).

2.1.1 Temperature measurements

High-resolution (hourly) water temperature data is provided for water depths from 5 to 40 m (in 5 m steps) at the western part of Illa Grossa (Figure 1A) by ONSET HOBO Water Temperature Pro V2 data loggers since 2007. According to the manufacturer the accuracy of the temperature loggers is ±0.2°C. The measured data is available *via* the international observation network on climate change effects in the Mediterranean marine coastal ecosystems T-MEDnet (https://t-mednet.org). Temperature data downsampled to monthly resolution are shown in Supplementary Figure 1 for water depths 5, 20, and 40 m (data in Supplementary Table 1).

2.1.2 Coralline algae collection

Attached-living crustose coralline algal samples (fruticose *Neogoniolithon hauckii*, Figure 1B) were collected alive from hard substrate at the western part of Illa Grossa Bay (Figure 1A), exactly where the temperature sensors are located, by SCUBA diving in October 2017 at 20 and 40 m water depth. Identification of the specimens collected agreed with description in Rodriguez-Prieto et al. (2013) under the name *Neogoniolithon mamillosum* (Hauck) Setchell & L.R.Masson, that according to Algaebase (https://www.algaebase.org/search/species/detail/?species_id=169942) is a heterotypic synonym of *N. hauckii*. Vouchers have been deposited in HGI Herbarium.

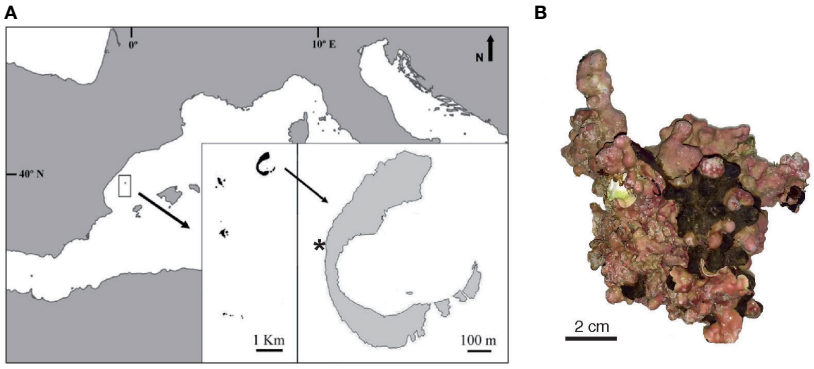

FIGURE 1
Study site and coralline algal sample. **(A)** Map of study site Columbretes Islands (Spain) in Mediterranean Sea. Inset shows crescent-shaped Illa Grossa Bay (39°53.825′N, 0°41.214′E), where coralline algae were sampled in October 2017 (by DK) and where water temperature monitoring sensors are installed (*). **(B)** Attached-living specimen of *Neogoniolithon hauckii*. Map **(A)** modified after Kersting et al. (2013).

2.2 Sample preparation and LA-ICP-MS analysis

Air-dried coralline specimens were sectioned parallel to the direction of growth using a low speed saw with diamond blades (Figure 2). Thick sections (2 mm) were cut from the slabs. Due to the delicate and fragile skeletal structure of branching growth forms and the tiny size (individual nodules often comprise only few millimeters in length/diameter), it is often difficult to section single branches/nodules exactly parallel to the growth direction. This is further complicated by the mound-like growth structure of individual nodules. In preparation for microscopic scanning, sample surfaces were polished using diamond-polishing suspensions with grit sizes of 9, 3, and 1 µm on a Struers Labopol polishing disk for 45 min per step. High-resolution digital images of the polished surface were produced using an Olympus reflected light microscope (VS-BX) attached to an automated sampling stage/imaging system equipped with the software geo.TS (Olympus Soft Imaging Systems). This setup allows two-dimensional mapping of the surfaces of polished specimens at various magnifications. The resultant high-resolution photomosaics enable the identification and lateral mapping of growth-increment patterns over the entire sample.

Polished thick sections of samples were analyzed by laser ablation inductively coupled plasma - mass spectrometry (ICP-MS) at GEOMAR Helmholtz-Centre for Ocean Research Kiel following methodology described in detail in Hetzinger et al. (2018). Li/Ca, Mg/Ca, and Ba/Ca ratios were measured using a Teledyne Photon Machines Analyte Excite 193nm ArF excimer laser ablation system coupled to a Thermo ElementXR sector field ICP-MS. Individual line transects were analyzed with a scan speed of 5 µm/s (preablation transect with 10 µm/s), a laser spot rectangular mask of 10x155 µm and a 10 Hz pulse rate. Time resolved data were blank subtracted and normalized to Ca using the iolite v3 software and calibrated using repeated analysis of NIST SRM610 and 612 glasses. As the Mg content of the coralline calcite is high and variable, the data were worked up as element/Ca ratios and calibrated with the measured element/Ca ratio of the NIST glasses. Data quality was assessed by analyses of powder pellets of the carbonate reference material JCp-1 during the same session as samples. A pellet of the original JCp-1 reference material powder was used to assess accuracy and values were the same within uncertainties to consensus values determined by solution methods in many laboratories (Hathorne et al., 2013). The exception is Li/Ca for which values are higher for the laser ablation analyses which vaporize and analyze some detrital material in the coral powder as evident in elevated Al contents compared to solution analyses. As the original powder is heterogenous for some trace metals at the small length scales of laser ablation analyses, a nano particulate pellet of the JCp-1 reference material was made (Garbe-Schönberg and Müller, 2014) and used to assess the reproducibility of the analyses. The relative standard deviation (1 sigma) of two 120 s line scans across the JCp-1 nano pellet in the same session and with the same laser conditions as the sample analyses was 41, 10 and 18% for Li/Ca, Mg/Ca and Ba/Ca, respectively. For the 10 point running average which is comparable to the smoothed data shown for the samples, the RSD was 10, 6 and 8% for Li/Ca, Mg/Ca and Ba/Ca, respectively. Detection limits defined as 3.3 times the standard deviation of the gas background intensity during the session were 0.7, 6.7, 96, and 0.04 ug/g for Li, Mg, Ca, and Ba, respectively. Sample concentrations were >>10 times detection limits except for Li which was 2-4 times the detection limit in the samples and mostly above quantification limits.

In order to test and improve the robustness of our data, we analyzed two laser transects on each specimen. We selected two samples (sampled at 20 and 40 m water depth, neo20 and neo40), which show regular banding patterns, for LA-ICP-MS measurements (Figure 2). Laser line transects were placed perpendicular to the growth lines (Figure 2B).

2.3 Age model development

Age models were generated by counting annual growth increments on the mapped and digitized image of the specimens in combination with seasonal algal Mg/Ca cycles. Our samples were

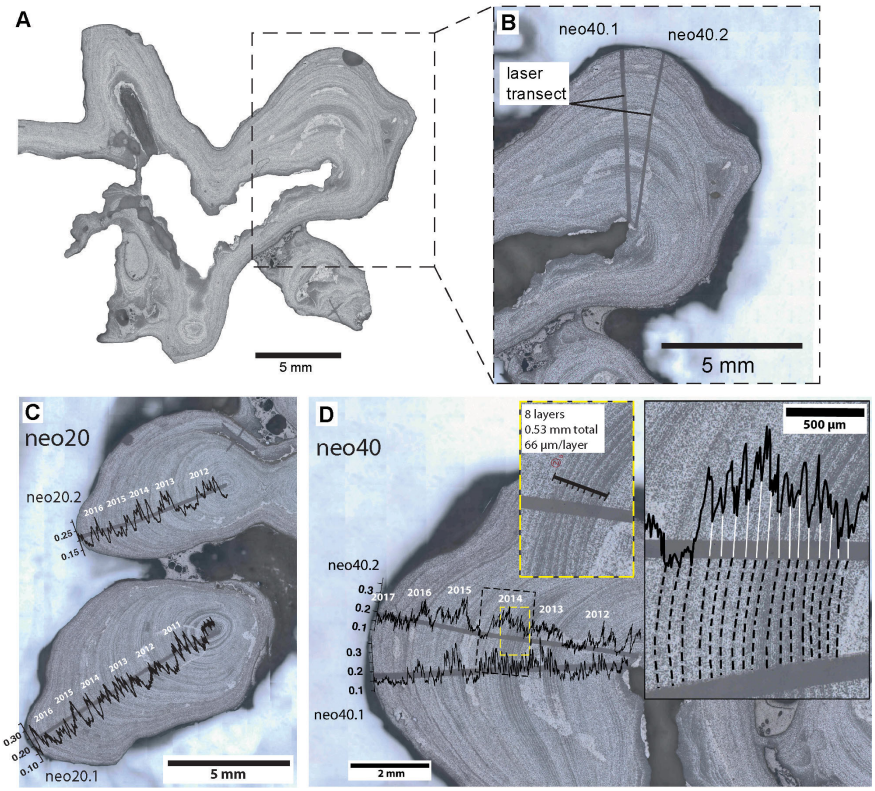

FIGURE 2
Sectioned and analyzed samples of *Neogoniolithon hauckii*. **(A)** Sectioned sample neo40, enlarged inset **(B)** shows longitudinal section of analyzed protuberance. **(B)** Magnification of sectioned protuberance with measurement transects after LA-ICP-MS analysis. Samples neo20 **(C)** and neo40 **(D)** after LA-ICP-MS analysis. Mg/Ca ratios plotted over measurement transects. Approximate year markers based on Mg/Ca age model (see Supplementary Figure 2) are placed above laser transects in order to illustrate seasonal cycles. **(D)** Two separate transects on sample neo40. Right inset shows enlarged area marked by stippled line rectangle. Mapped subannual growth lines indicated by stippled lines. White lines link minimum values of subannual cycles in Mg/Ca ratios to mapped subannual banding. Smaller inset (yellow stippled line) shows portion of the annual band 2014 where subannual band thickness was measured directly on photomosaic (8 layers marked with black bold line, total length of 0.53 mm, 66 µm per subannual layer on average, respectively). Mg/Ca ratios in **(C, D)** in (mol/mol).

collected alive; hence the top layer was assigned to the year of collection. Although yearly growth banding is clearly visible, the samples exhibit 2nd order sub-annual growth cyclicity (Figures 2C, D), which cannot always be clearly separated from annual bands. For example, sample neo20 annual cycles in Mg/Ca ratios were difficult to identify and did not consistently match the banding observed in the microscope image. Thus, the main focus of this study is the analysis of sample neo40, which exhibits clear increments and Mg/Ca ratio cyclicity. Two closely spaced laser line transects on the same protuberance of neo40 allow to test for reproducibility and enhanced matching of cycles in Mg/Ca ratios and growth increments. Sample neo20 is presented as well, although especially in the younger part (growth years 2015 and 2016) the identification of seasonal cycles in Mg/Ca ratios is difficult and cyclicity less clear in both transects (see Supplementary Figure 2, data in Supplementary Table 2), making the presumed age model less reliable than in sample neo40. High Mg values within the skeletons of high-Mg calcite coralline algae are interpreted to correspond to summer periods of growth (Chave and Wheeler, 1965; Halfar et al., 2000). Age models were established based on a combination of the pronounced seasonal cycle in algal Mg/Ca and the annual growth banding. Maximum (minimum) Mg/Ca values were tied to October (April), which is on average the warmest (coolest) month at the study site.

3 Results

3.1 Intra-sample variability

Individual transects on sample neo40, which were analyzed on the same protuberance in close proximity, were cross-matched prior to establishing an age model to check for intra-sample variability and facilitate identification of annual cycles (Figure 2D). For this purpose, a cross-correlation function (ccf) in the software R was used. Time series independent of actual age chronology of both transects on sample neo40 were generated (raw data as well as 10 point running means) and cross-correlations were performed to calculate the best fit with associated lag (Figure 3A).

The most dominant cross correlation between neo40.1 and neo40.2 occurs at a lag of -8 for the raw data and -9 for the 10-point-running mean data (Figure 3A). The results of this analysis indicate a significant similarity/overlap of both Mg/Ca ratio transects on sample neo40, when corrected for the calculated lag,

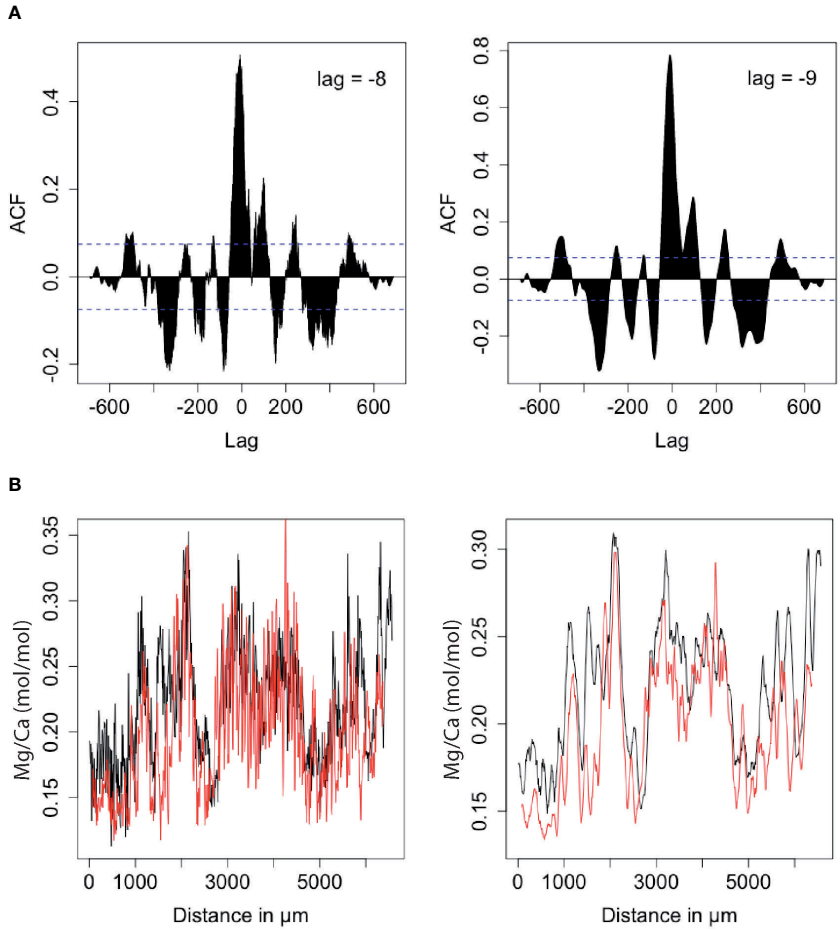

FIGURE 3
Cross-correlation of Mg/Ca transects (from left to right: 2017-2012). **(A)** Cross-correlation of Mg/Ca time series neo40.1 and neo40.2; left graph shows full resolution data, right graph 10 point running mean. **(B)** Best fit of Mg/Ca curve of neo40.2 (black curve) and Mg/Ca curve of neo40.1 (red curve) already corrected for calculated lag; left graph raw data, right graph 10 point running mean. ACF in **(A)** stands for "auto-correlation function", which displays coefficients of correlation between time series and its lagged values.

and help to identify corresponding maxima and minima (Figure 3B). Mg/Ca, Li/Ca, and Ba/Ca age models for transects samples neo20 and neo40 neo40.1 and neo40.2 transects were created using the time series software AnalySeries (Paillard et al., 1996) to obtain an equidistant proxy time series with a resolution of 12 samples/year (i.e. monthly resolution) and 52 samples/year (i.e. weekly resolution). The developed chronologies were refined and cross-checked for possible errors in the age model by comparing annual extreme values in the Mg/Ca ratios to mapped growth increment patterns for each individual year of algal growth. Sample neo40 displays a record of five years (2012-2017), sample neo20 extends to 2011 (monthly data in Supplementary Table 3).

3.2 *Neogoniolithon hauckii* annual extension rate

Annual mean extension rates (summer to summer) for the attached-living encrusting specimens of *Neogoniolithon hauckii* were calculated based on the Mg/Ca ratio age models, where maximum Mg/Ca values were tied to October, representing seasonal maximum temperatures. The distance between maxima was calculated from laser data yielding annual mean extension rates. The mean extension rates are 1.1 mm/year for sample neo40 (transect neo40.1: mean 1.08 mm, minimum 0.83 mm, maximum 1.26 mm per year; transect neo40.2: mean 1.13 mm, minimum 0.97 mm, maximum 1.43 mm per year, Figure 4). In sample neo20 transects were not averaged, since they were measured on separate protuberances (transect neo20.1: mean 1.28 mm, minimum 1.0 mm, maximum 1.42 mm per year; transect neo20.2: mean 1.2 mm, minimum 0.65 mm, maximum 1.74 mm per year). Note that the measured extension rates are based on only four annual cycles (five in transect neo20.1). Extension rates are highly variable in different parts of the specimens (Figure 2A; Supplementary Table 4).

3.3 Subannual growth banding

Subannual growth bands were mapped in a portion of sample neo40 in order to study the frequency of banding patterns and measure the banding width (Figure 2D). Approximately thirteen

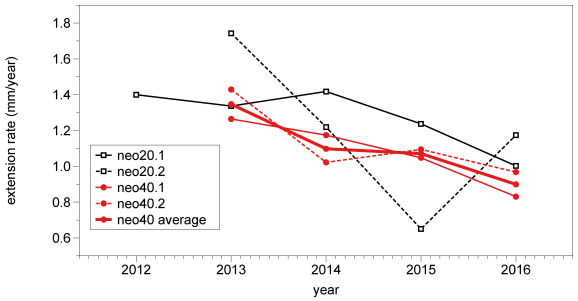

FIGURE 4
Annual extension rates of samples neo20 (black, open squares) and neo40 (red, filled circles). Sample neo20 - solid line: transect neo20.1; stippled line: transect neo20.2; sample neo40 - solid line: transect neo40.1; stippled line: transect neo40.2, bold line: average of neo40 transects.

2nd order bands were successfully linked to cycles in Mg/Ca ratios for the year 2014, indicating that high frequency variability in laser-measured Mg/Ca ratios can be tied to subannual growth patterns. Based on this comparison, an average thickness of 0.066 mm/year was directly measured from eight pronounced subannual growth bands from within one growth year on the microscope photomosaic (see inlets in Figure 2D). However, identification of a complete set of 2nd order subannual banding was only possible in some parts of sample neo40, i.e. in growth years 2014 (Figure 2D) and 2013 (not shown in detail).

3.4 Reproducibility of element/Ca ratio transects

Two laser-ablation transects (Figure 2B) on neo40 were investigated separately for each element/Ca ratio. We found a high reproducibility for Mg/Ca (R=0.62) signals and Li/Ca (R=0.47) when using ordinary least squares (OLS) regression with zero lag (Figure 5; $p<0.01$). Reproducibility is poor between individual transects for Ba/Ca (R=0.01). Reproducibility for sample neo20 is much lower for Mg/Ca (R=0.34) than in sample neo40, reproducibility is poor for Ba/Ca (R=0.1) and Li/Ca (R=0.1). In a second step, data from both transects on sample neo40 (neo40.1 and neo40.2) were averaged to calculate a sample mean (Figure 5) for each element/Ca ratio, respectively. This decreases noise caused by high intra-sample variability and establishes better comparability (Hetzinger et al., 2018). This step was not undertaken in sample neo20 due to large differences in cycles, especially in years 2015 and 2016 and the poor correlation. Variability between individual transects might also be influenced by the positioning of transects, which have been measured in close proximity to each other (Figure 2B), however, variations between different parts of the sample are expected due to microstructural differences. While transects on sample neo40 were measured in close proximity to each other (Figure 2), transects in sample neo20 were analyzed on different protuberances.

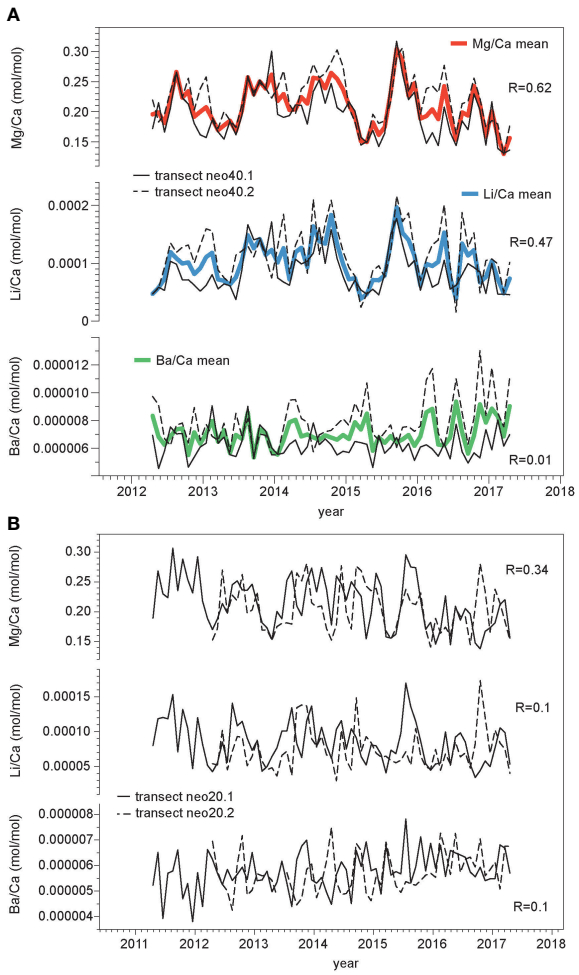

FIGURE 5
Age models for element/Ca ratios and intraspecimen variability. Changes in the Mg/Ca, Li/Ca, and Ba/Ca ratios (monthly resolution) shown over time; **(A)** sample neo40 - solid lines: transect neo40.1; stippled lines: transect neo40.2; bold lines: mean of both transects. **(B)** sample neo20 - solid lines: transect neo20.1; stippled lines: transect neo20.2. Note that due to low correlation and placement of transects on separate protuberances no means were calculated for sample neo20. Correlation coefficients are shown for comparisons between transects for each element/Ca ratio, respectively ($p<0.01$).

3.5 Comparison between element/Ca ratios

Mg/Ca and Li/Ca ratios display similar variability (Figure 5) and are significantly correlated in both samples (sample neo40: R=0.84, for sample mean; sample neo20: R=0.82 for transect neo20.1, R=0.79 for transect neo20.2; monthly means). Both, Mg/Ca and Li/Ca ratios show a cyclical seasonal pattern (Figure 6) with highest values observed during the Northern Hemisphere summer months, and vice versa. To better illustrate the cyclical variability in Mg/Ca and Li/Ca ratios, higher-resolved weekly data are plotted in comparison to local *in situ* water temperature (Figure 6). These elemental ratios have been shown to act as temperature proxies in

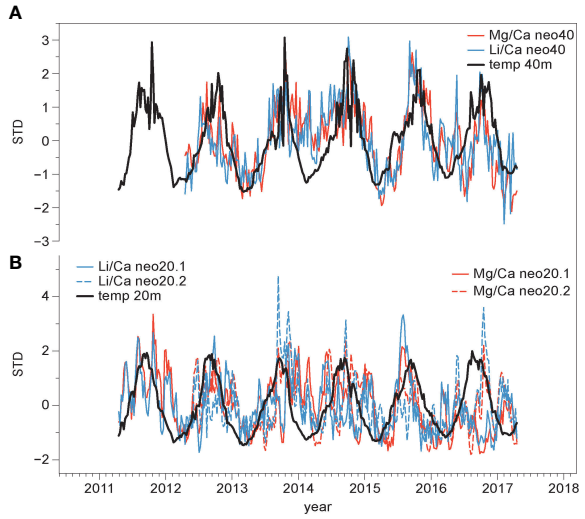

FIGURE 6
Cyclicity in element/Ca ratios in comparison to temperature (52 samples/annual cycle resolution). Changes in Mg/Ca (red) and Li/Ca (blue) ratios and *in situ* measured temperature data (black). **(A)** 40 m water depth, **(B)** 20 m water depth. Values shown are standardized by removing mean and dividing by standard deviation (STD).

other species of encrusting coralline algae (e.g. Darrenougue et al., 2014). Ba/Ca ratios do not exhibit a similar seasonal variability; Ba/Ca variability stays fairly constant until 2016, thereafter higher values are registered in the sample mean. However, this increase is mainly observed in transect neo40.2 (Figure 5), while Ba/Ca ratios in transect neo40.1 show no deviation. Ba/Ca has previously been used in coralline algae as a proxy for terrestrial input and changes in the upwelling-induced nutrient availability (Chan et al., 2011; Hetzinger et al., 2021). However, as reproducibility between transects is poor, this study concentrates on Mg/Ca and Li/Ca ratios as potential temperature proxies in further analyses.

3.6 Relationship to *in situ* temperature data

In order to study a potential link between the element/Ca ratios and water temperature, element/Ca ratios were tested against *in situ* temperature (20 and 40 m depth) using OLS regression analysis. For the April 2012 to April 2017 time period, which is covered by the coralline algal records, monthly minimum (maximum) logger-derived temperatures are on average 12.5° (25.8°C) in April (October) at 20 m depth and on average 12.6°C (22.6°C) in April (October) at 40 m. Average annual temperature is 18.1°C at 20 m and 15.9°C at 40 m depth. Note that seasonal maximum temperature peaks may occur 1-2 months earlier at 20 m depth. All monthly element/Ca ratios, except for Ba/Ca, show a significant positive correlation to *in situ* measured temperature from the study site. Mg/Ca from sample neo40 exhibits the highest correlation with temperature (Figure 7A; R=0.55 for monthly sample mean; R=0.50 for transect neo40.1; R=0.49 for transect neo40.2) followed by Li/Ca (Figure 7B; R=0.46 for monthly sample mean; R=0.47 for transect neo40.1; R=0.34 for transect neo40.2). P-values for all linear

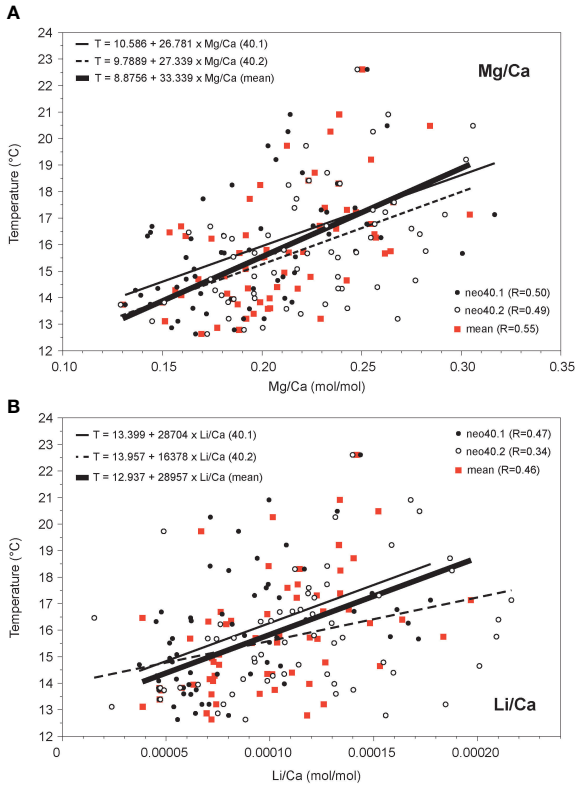

FIGURE 7
Comparison of **(A)** Mg/Ca and **(B)** Li/Ca ratios to *in situ* temperature (2012-17) for sample neo40. Linear regressions for monthly data are significant ($p<0.01$), with regression line shown in bold (sample mean), solid (transect neo40.1), and stippled (transect neo40.2). Equations and correlation coefficients (R) are shown for each regression. Both ratios are positively correlated to temperature.

regressions are smaller than 0.01. Correlations of Mg/Ca and Li/Ca ratios from sample neo20 to 20 m temperature are lower (Figure 8A, Mg/Ca: R=0.40 for transect neo20.2, R=0.24 for transect neo20.1; Figure 8B, Li/Ca: R=0.33 for transect neo20.2, R=0.29 for transect neo20.1).

4 Discussion

A main goal in this study was to assess whether the coralline alga *Neogoniolithon hauckii* holds any information on past environmental variability in its skeleton. We addressed this question by first making seasonal growth patterns visible using high-resolution photomosaics, and secondly by using ultra-high-resolution laser ablation ICP-MS to analyze trace elemental composition.

In both algal specimens 2nd order subannual cyclicity in growth banding is apparent (Figure 2). This complicates the interpretation of seasonal cycles in growth and elemental ratios. Subannual growth patterns are often difficult to discern from annual banding patterns; also changes in the life history of certain coralline algal species that have been reported from the Mediterranean (Ragazzola et al., 2020). For example, the feasibility of extracting climate records from

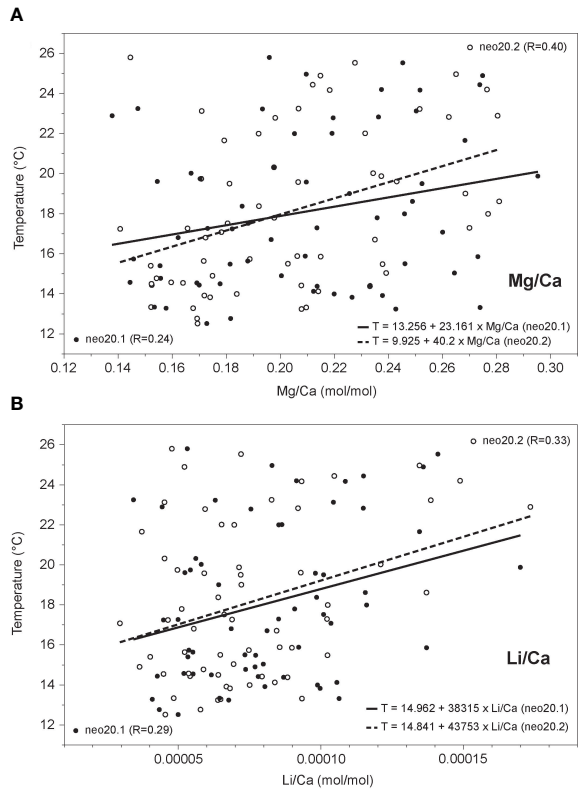

FIGURE 8
Comparison of **(A)** Mg/Ca and **(B)** Li/Ca ratios to *in situ* temperature (2011-17) for sample neo20. Linear regressions for monthly data are significant ($p<0.01$), with regression line shown in solid (transect neo20.1) and stippled (transect neo20.2). Equations and correlation coefficients (R) are shown for each regression. Both ratios are positively correlated to temperature.

attached-living encrusting Mediterranean coralline algae was recently tested using different species, such as *Lithothamnion minervae*, *Lithophyllum stictaeforme*, and *Mesophyllum philippii*. Ragazzola et al. (2020) found that *L. minervae* may be used as a recorder of temperature and its seasonality using Mg/Ca cyclicity, while irregular growth variations were observed when comparing the oldest and youngest parts of a *M. philippii* specimen, making this species less useful for climate analysis. Hence, it was noted that growth patterns need to be better understood prior to geochemical analysis as they might influence the reliability of certain species as a temperature recorder.

In our specimens, subannual growth banding is clearly visible (Figure 2) and could even be mapped and directly measured in portions of sample neo40 (Figure 2D). In addition to unclear banding patterns on sample neo20, annual cycles in Mg/Ca ratios were more difficult to identify than in sample neo40 and did not consistently match with the banding observed in the microscope image. This was observed for both measured laser transects (Figure 2C) analyzed on separate protuberances of neo20. The poor match, especially in the uppermost years of neo20, among the two adjacent protuberances may reside in different growth rates, lateral pinging-out of layers and/or the occurrence of a hiatus (Schlüter et al., 2021). However, we did not find evidence for a hiatus in sample neo20. In addition, the optimal placement of sectioning angles during sample preparation is a prerequisite for successful age model development in algal specimens, in particular in branching growth morphologies. We speculate that one reason for the deviations in sample neo20 could be that the angle of sectioning may have been chosen in a suboptimal way. The plane of sectioning crosses the inner part of both protuberances (Figure 2C), which is displayed as concentric rings in growth bands. This is not the case in sample neo40, where successful matching between well-defined seasonal cyclicity in Mg/Ca ratios and annual growth patterns was much easier in the microscope photomosaics, although subannual banding was clearly visible, too (Figure 2D). Previous studies on coralline algae have shown secondary growth banding periodicities corresponding to a monthly cycle, e.g. in *Porolithon gardineri* (Foslie) from Northwestern Hawaii (Agegian, 1981), where a link to lunar periodicity has been suggested. A lunar influence in short-term skeletal density variations has also been seen in hermatypic corals (Buddemeier, 1974). In bivalve mollusk shells a range of periodic growth patterns have been recognized, such as lunar-monthly, fortnightly, solar-daily, lunar-daily, diurnal, and semidiurnal cycles (Hallmann et al., 2009; Schöne and Surge, 2012). In free-living coralline algae (rhodoliths), subannual growth bands have been linked to growth cessations, monthly/lunar rhythms potentially superimposed on annual cycles (Freiwald and Henrich, 1994; Blake and Maggs, 2003), and second order cycles within the annual cycles (Agegian, 1981; Halfar et al., 2000; Sletten et al., 2017a). Hence, subannual banding may limit the potential for long-term climate reconstructions as these may distort or falsify age models.

In future analysis of samples from this species, optimal sample preparation and placement of laser transects will be key to allow a reliable interpretation of algal sclerochronology and geochemistry. Successful paleoclimate reconstructions can only be achieved after proper identification of annual banding patterns to allow the development of accurate age models for geochemical measurements. Eventually, only specimens which have been stained in controlled field experiments and are collected later will deliver reliable growth rates and allow a proper distinction of subannual from annual banding patterns. For example, this was shown for *Clathromorphum compactum* in a monitoring experiment in the Gulf of Maine using Alizarin-stained samples, which allowed a direct comparison between growth increments, geochemistry and *in situ* measured water temperatures in ultra-high resolution (Halfar et al., 2008). This study yielded important information on the timing of vertical growth in this species, with highest growth (= calcification) occurring between June and September at this site, when the combined influence of temperature and solar insolation is the highest. Using stained thalli from free-living *Lithothamnion glaciale*, Kamenos and Law (2010) found an effect of temperature on calcite density, but no consistent relationship with band width. However, similar to our study, they also noted the possible influence of sectioning angles in sample preparation, as individual branches in *L. glaciale* do not grow in straight lines. Thus, it is impossible to ensure that each growth band is observed parallel to its maximum axis of growth.

Using encrusting *Clathromorphum nereostratum* samples from Alaska, Halfar et al. (2011b) have shown declining growth rates with

increasing water depth as the availability of light decreases with water depth. In the temperate setting of the Columbretes Islands the observed growth rates might be influenced by reduced light intensity at higher water depths (sample collected at 40 m). *Neogoniolithon hauckii* (as *Neogoniolithon mamillosum*) has been described to be growing mainly in coralligenous outcrops, where it is a major carbonate framework builder (Ballesteros, 2006). Coralligenous outcrops develop in a wide range of depths across the Mediterranean Sea (20 to 120 m) (Ballesteros, 2006) and the 40 m sample was collected in the normal distribution range for this species in Columbretes Islands (see Kersting et al., 2021). Sea surface temperature at the study site ranges from 29.6°C in summer to 12.0°C in winter (Kersting et al., 2013). However, at 40 m depth, where sample neo40 was collected, water temperatures and seasonal variability are lower, ranging from 22.6°C maximum in summer to 12.6°C minimum in winter. This dampened seasonal cycle at greater depth, when compared to surface temperature seasonality, might potentially influence growth rates, as well as seasonal cyclicity in elemental ratios, which are related to water temperature (in particular Mg/Ca and Li/Ca).

There is no annual growth data available so far for *Neogoniolithon* sp. We report mean extension rate in specimen neo40 of 1.1 mm/year (two averaged laser measurement transects) and similar growth rates for sample neo20 at lesser depth (transect neo20.1: 1,28 mm/year; transect neo20.2: 1.2 mm/year). Hence, the difference in sampling depth may not have a significant effect on growth rates, albeit more samples are needed to investigate potential differences. The presented annual growth rates fall within the range of published annual extension rate data for other encrusting coralline algal species. Published vertical extension rates of coralline algae have a wide range, for example from around 0.1 mm/year for rhodoliths (*Lithothamnion corallioides*) from a temperate setting at the Italian coast (Piazza et al., 2022) to mean extension rates measured in rhodoliths from the NW-Indian Ocean (*Lithophyllum kotschyanum f. affine*, Gulf of Aden, temperatures between 24 and 30°C) of ca. 0.7-1.5 mm/year (Caragnano et al., 2014). Much higher growth rates of 7-20 mm/year were reported for *Porolithon gardineri* (Foslie) from NW-Hawaii (Agegian, 1981). Growth rates in rhodolith-forming coralline algae can be highly variable over time and in different parts of individual specimens, a large range between approximately 0.015-2.5 mm/year has been reported (Adey and McKibbin, 1970; Adey and Vassar, 1975; Bosence, 1983; Frantz et al., 2000; Halfar et al., 2000; Blake and Maggs, 2003; Kamenos et al., 2008; Schäfer et al., 2011; Darrenougue et al., 2013; Sletten et al., 2017a). When considering the problems in identification of banding patterns and in the differentiation of annual from subannual growth increments, the vastly different growth rates reported in the literature might in some cases be the result of a misidentification of 1st and 2nd order cycles.

In general, previous studies have reported higher annual extension rates in temperate and tropical coralline algae than in samples from colder water temperatures. Slower growth rates (< 1 mm/year) have been observed in encrusting coralline algae in high-latitude settings, where algal growth is limited by low temperatures and available light (e.g. Leclerc et al., 2022). For example, for the long-lived coralline algae *C. compactum* in the northwestern Atlantic ocean, annual growth rates range between around 100-400 µm/year with decreasing growth rates latitudinally, suggesting a direct relationship to water temperature (Adey et al., 2013). A recent study has suggested that Mg/Ca ratios from massive encrusting growth forms can yield higher correlations to temperature than transects measured on branching morphologies (i.e. individual rhodoliths) of the same species, which often only allow the generation of short uninterrupted time series due to frequent growth irregularities (Williams et al., 2018a).

Here, we report significant positive relationships between ultra-high-resolution Mg/Ca and Li/Ca ratios and water temperature. For the first time, *in situ* temperature data measured exactly at the same water depth directly at the specimen collection site allowed a temperature calibration of elemental ratios for this temperate algal species (samples were collected in distances of less than 10 meters from the sensors). Results from linear regression indicate that Mg/Ca and Li/Ca are potentially suited as a temperature proxy in the examined coralline samples. Highest correlations are found in sample neo40, correlations are lower for sample neo20, probably due to the difficulties in establishing an age model for this sample as a result of less clear seasonal Mg/Ca cycles (compare Supplementary Figure 2; Figures 7, 8). Mg/Ca shows the best fit, with around 30% of its variance explained by temperature, while 21% of variance of Li/Ca is explained by temperature in sample neo40. Similar to previous studies on other calcifying coralline algal species, we have shown for *Neogoniolithon hauckii* that Mg incorporation into the skeleton increases with temperature (Moberly, 1968; Kamenos et al., 2008; Williams et al., 2014), yielding similar relationships as shown for other coralline algal species (e.g. Caragnano et al., 2017, their table 2). Significant relationships between temperature and coralline algal Li/Ca and other element/Ca-ratios have been observed in different species (Hetzinger et al., 2011; Caragnano et al., 2014; Darrenougue et al., 2014; Darrenougue et al., 2018). The relationships to temperature may improve when using an intersample average from a larger number of sample specimens in future studies, as has previously been shown for other coralline algal species (Hetzinger et al., 2018). For a more comprehensive study the collection of a larger number of samples from different water depths is a prerequisite that will also allow quality screening to select optimally-grown and longest-lived specimens of *N. hauckii* for analysis. Ba/Ca ratios may be influenced by other factors, such as the input of sediments from land sources into the coastal ocean (Gillikin et al., 2006), upwelling processes (Lea et al., 1989), or salinity changes (Hetzinger et al., 2013). However, the open-ocean location of Columbretes Islands makes land-based influence very unlikely. Wind-driven upwelling has been observed in the Mediterranean (Bakun and Agostini, 2001), but reproducibility is poor between individual Ba/Ca transects in our sample and the time series is too short for the identification of such events.

5 Conclusion

This study represents the first assessment of *Neogoniolithon hauckii* as a potential climate archive and may function as a starting point for more detailed analyses. Our results, which suggest that

Mg/Ca and Li/Ca are suited as a temperature proxy in the examined species, indicate that *N. hauckii* may be used as a new temperature archive for mesophotic coralligenous assemblages in the Mediterranean that are strongly affected by the recent anthropogenic temperature rise. However, a better understanding of intra-annual growth patterns is critical, as well as optimal sample preparation, in order to precisely determine periods of growth and calcification in this coralline red algal species. For this task, more samples of this temperate alga from different water depths and environmental settings need to be analyzed in the future.

Data availability statement

The original contributions presented in the study are included in the article/Supplementary Material. Further inquiries can be directed to the corresponding author.

Author contributions

DK conducted the fieldwork, provided sample material and temperature data. EB identified the coralline algal species. JH prepared sample specimens and provided ultra-high-resolution photomosaics. MG, DK, and EH conducted LA-ICP-MS analyses. SH and MG analyzed and interpreted the data and wrote the original draft of the article. All coauthors provided feedback on the manuscript and have read and agreed to the submitted version of the manuscript. All authors contributed to the article.

Funding

JH was supported by a Natural Sciences and Engineering Research Council of Canada Discovery Grant (316003). DK was supported by a Ramon y Cajal postdoctoral grant funded by the Ministry of Science and Innovation (PEICTI 2021- 2023; grant no. RYC2021‐033576‐I) and by the program Beatriu de Pinós funded by the Secretary of Universities and Research (Government of Catalonia) and the Horizon 2020 program of research and innovation of the European Union under the Marie Sklodowska-Curie grant agreement No 801370. This study was partially funded by the Deutsche Forschungsgemeinschaft (DFG, German Research Foundation, project no. 401447620).

Acknowledgments

We thank the Secretaría General de Pesca and the Columbretes Islands Marine Reserve staff for logistic support. We thank two reviewers for their helpful and constructive comments.

Conflict of interest

The authors declare that the research was conducted in the absence of any commercial or financial relationships that could be construed as a potential conflict of interest.

Publisher's note

Supplementary material

The Supplementary Material for this article can be found online at: https://www.frontiersin.org/articles/10.3389/fmars.2023.1151592/full#supplementary-material

References

Adey, W. H. (1966). Distribution of saxicolous crustose corallines in the northwestern north Atlantic. *J. Phycol.* 2, 49–54. doi: 10.1111/j.1529-8817.1966.tb04593.x

Adey, W. H. (1970). The effects of light and temperature on growth rates in boreal-subarctic crustose corallines. *J. Phycol.* 6, 269–276. doi: 10.1111/j.1529-8817.1970.tb02392.x

Adey, W. H., Halfar, J., and Williams, B. (2013). Biological, physiological and ecological factors controlling high magnesium carbonate formation and producing a precision Arctic/Subarctic marine climate archive: the coralline genus *Clathromorphum* foslie emend adey. *Smithsonian Contributions to Mar. Sci.* 40, 1–48. doi: 10.5479/si.1943667X.40.1

Adey, W. H., Hernández-Kantún, J. J., Gabrielson, P. W., Nash, M. C., and Hayek, L. (2018). *Phymatolithon* (Melobesioideae, hapalidiales) in the Boreal–subarctic transition zone of the north Atlantic: a correlation of plastid DNA markers with morpho-anatomy, ecology, and biogeography. *Smithsonian Contributions to Mar. Sci* 41, 1–90. doi: 10.5479/si.1943-5667X.5441

Adey, W. H., and Macintyre, I. G. (1973). Crustose coralline algae: a re-evaluation in the geological sciences. *Geological Soc. America Bull.* 84, 883–904. doi: 10.1130/0016-7606(1973)84<883:CCAARI>2.0.CO;2

Adey, W. H., and McKibbin, D. (1970). Studies on the maerl species *Phymatolithon calcareum* (Pallas) nov. comb. and *Lithothamnium corallioides* crouan in the ria de vigo. *Botanica Marina* 13, 100–106. doi: 10.1515/botm.1970.13.2.100

Adey, W. H., and Vassar, J. M. (1975). Colonization, succession and growth rates of tropical crustose coralline algae (Rhodophyta, cryptonemiales). *Phycologia* 14 (2), 55–69. doi: 10.2216/i0031-8884-14-2-55.1

Agegian, C. R. (1981). Growth of the branched coralline alga, *Porolithon gardineri* (Foslie) in the Hawaiian archipelago. *Proc. Fourth Int. Coral Reef Symposium* 2, 420–423.

Aguirre, J., Braga, J. C., Pujalte, V., Orue-Etxebarria, X., Salazar-Ortiz, E., Rincón-Martínez, D., et al. (2020). Middle Eocene rhodoliths from tropical and mid-latitude regions. *Diversity* 12 (3), 117. doi: 10.3390/d12030117

Babbini, L., and Bressan, G. (1997). *Recensement des corallinacéies de la mer Mediterranéie et considerations phytogeographiques.* Bibliotheca Phycologica 1, 103–121.

Bakun, A., and Agostini, V. N. (2001). Seasonal patterns of wind-induced upwelling/downwelling in the Mediterranean Sea. *Scientia Marina* 65 (3), 243–257. doi: 10.3989/scimar.2001.65n3243

Ballesteros, E. (2006). Mediterranean Coralligenous assemblages: a synthesis of present knowledge. *Oceanography Mar. Biol.* 44, 123–195. doi: 10.1201/9781420006391.ch4

Basso, D. (1998). Deep rhodolith distribution in the pontian islands, Italy: a model for the paleoecology of a temperate sea. *Palaeogeography Paleoclimatol. Paleoecol.* 137, 173–187. doi: 10.1016/S0031-0182(97)00099-0

Blake, C., and Maggs, C. A. (2003). Comparative growth rates and internal banding periodicity of maerl (Corallinales, rhodophyta) from northern Europe. *Phycologia* 42 (6), 606–612. doi: 10.2216/i0031-8884-42-6-606.1

Bosence, D. W. J. (1983). "The occurrence and ecology of recent rhodoliths- a review," in *Coated grains*. Ed. T. M. Preyt (Berlin: Springer-Verlag), 225–241.

Bressan, G., and Babbini, L. (2003). *Biodiversità marine delle coste italiane: corallinales del mar mediterraneo. guida alla determinazione*. Societá italiana di biologia 10, 237.

Buddemeier, R. W. (1974). Environmental controls over annual and lunar monthly cycles in hermatypic coral calcification. *Proc. 2nd Int. Coral Reef Symp.* 259–267.

Canals, M., and Ballesteros, E. (1997). Production of carbonate particles by phytobenthic communities on the mallorca-menorca shelf, northwestern Mediterranean Sea. *Deep Sea Res. Part II: Topical Stud. Oceanography* 44 (3), 611–629. doi: 10.1016/S0967-0645(96)00095-1

Caragnano, A., Basso, D., Jacob, D. E., Storz, D., Rodondi, G., Benzoni, F., et al. (2014). The coralline red alga *Lithophyllum kotschyanum f. affine* as proxy of climate variability in the Yemen coast, gulf of Aden (NW Indian ocean). *Geochimica Et Cosmochimica Acta* 124 (0), 1–17. doi: 10.1016/j.gca.2013.09.021

Caragnano, A., Basso, D., Storz, D., Jacob, D. E., Ragazzola, F., Benzoni, F., et al. (2017). Elemental variability in the coralline alga *Lithophyllum yemenense* as an archive of past climate in the gulf of Aden (NW Indian ocean). *J. Phycology* 53 (2), 381–395. doi: 10.1111/jpy.12509

Chan, P., Halfar, J., Adey, W., Hetzinger, S., Zack, T., Moore, G. W. K., et al. (2017). Multicentennial record of Labrador Sea primary productivity and sea-ice variability archived in coralline algal barium. *Nat. Commun.* 8, 15543. doi: 10.1038/ncomms15543

Chan, P., Halfar, J., Williams, B., Hetzinger, S., Steneck, R., Zack, T., et al. (2011). Freshening of the Alaska coastal current recorded by coralline algal Ba/Ca ratios. *J. Geophysical Res.* 116 (G1), G01032. doi: 10.1029/2010JG001548

Chave, K. E., and Wheeler, B. D.Jr (1965). Mineralogic changes during growth in the red alga *Clathromorphum compactum*. *Science* 147, 621. doi: 10.1126/science.147.3658.621.a

Coll, M., Piroddi, C., Steenbeek, J., Kaschner, K., Ben Rais Lasram, F., Aguzzi, J., et al. (2010). The biodiversity of the Mediterranean Sea: estimates, patterns, and threats. *PloS One* 5 (8), e11842. doi: 10.1371/journal.pone.0011842

Cook, E. R., Woodhouse, C. A., Eakin, C. M., Meko, D. M., and Stahle, D. W. (2004). Long-term aridity changes in the Western united states. *Science* 306 (5698), 1015–1018. doi: 10.1126/science.1102586

Darrenougue, N., De Deckker, P., Eggins, S., Fallon, S., and Payri, C. (2018). A record of mining and industrial activities in new Caledonia based on trace elements in rhodolith-forming coralline red algae. *Chem. Geology* 493, 24–36. doi: 10.1016/j.chemgeo.2018.05.014

Darrenougue, N., De Deckker, P., Eggins, S., and Payri, C. (2014). Sea-Surface temperature reconstruction from trace elements variations of tropical coralline red algae. *Quaternary Sci. Rev.* 93, 34–46. doi: 10.1016/j.quascirev.2014.03.005

Darrenougue, N., De Deckker, P., Payri, C., Eggins, S., and Fallon, S. (2013). Growth and chronology of the rhodolith-forming, coralline red alga *Sporolithon durum*. *Mar. Ecol. Prog. Ser.* 474, 105–119. doi: 10.3354/meps10085

Feldmann, J. (1937). *Recherches sur la végétation marine de la méditerranée. la côte des albères* (Rouen: Imprimerie Wolf).

Foster, M. S. (2001). Rhodoliths: between rocks and soft places. *J. Phycology* 37, 659–667. doi: 10.1046/j.1529-8817.2001.00195.x

Frantz, B. R., Kashgarian, M., Coale, K. H., and Foster, M. S. (2000). Growth rate and potential climate record from a rhodolith using ^{14}C accelerator mass spectrometry. *Limnology Oceanography* 45 (8), 1773–1777. doi: 10.4319/lo.2000.45.8.1773

Freiwald, A., and Henrich, R. (1994). Reefal coralline algal build-ups within the Arctic circle: morphology and sedimentary dynamics under extreme environmental seasonality. *Sedimentology* 41, 963–984. doi: 10.1111/j.1365-3091.1994.tb01435.x

Gamboa, G., Halfar, J., Hetzinger, S., Adey, W., Zack, T., Kunz, B., et al. (2010). Mg/Ca ratios in coralline algae record northwest Atlantic temperature variations and north Atlantic oscillation relationships. *J. Geophysical Res.* 115 (C12), C12044. doi: 10.1029/2010JC006262

Garbe-Schönberg, D., and Müller, S. (2014). Nano-particulate pressed powder tablets for LA-ICP-MS. *J. Analytical Atomic Spectrometry* 29 (6), 990–1000. doi: 10.1039/C4JA00007B

Garrabou, J., Coma, R., Bensoussan, N., Bally, M., Chevaldonné, P., Cigliano, M., et al. (2009). Mass mortality in northwestern Mediterranean rocky benthic communities: effects of the 2003 heat wave. *Global Change Biol.* 15 (5), 1090–1103. doi: 10.1111/j.1365-2486.2008.01823.x

Garrabou, J., Gómez-Gras, D., Medrano, A., Cerrano, C., Ponti, M., Schlegel, R., et al. (2022). Marine heatwaves drive recurrent mass mortalities in the Mediterranean Sea. *Global Change Biol.* 28 (19), 5708–5725. doi: 10.1111/gcb.16301

Gillikin, D. P., Dehairs, F., Lorrain, A., Steenmans, D., Baeyens, W., and André, L. (2006). Barium uptake into the shells of the common mussel (Mytilus edulis) and the potential for estuarine paleo-chemistry reconstruction. *Geochimica Cosmochimica Acta* 70 (2), 395–407. doi: 10.1016/j.gca.2005.09.015

Halfar, J., Adey, W. H., Kronz, A., Hetzinger, S., Edinger, E., and Fitzhugh, W. W. (2013). Arctic Sea-ice decline archived by multicentury annual-resolution record from crustose coralline algal proxy. *Proc. Natl. Acad. Sci.* 110 (49), 19737–19741. doi: 10.1073/pnas.1313775110

Halfar, J., Eisele, M., Riegl, B., Hetzinger, S., and Godinez-Orta, L. (2012). Modern rhodolith-dominated carbonates at punta chivato, Mexico. *Geodiversitas* 34 (1), 99–113. doi: 10.5252/g2012n1a6

Halfar, J., Hetzinger, S., Adey, W., Zack, T., Gamboa, G., Kunz, B., et al. (2011a). Coralline algal growth-increment widths archive north Atlantic climate variability. *Palaeogeography Palaeoclimatol. Palaeoecol.* 302 (1-2), 71–80. doi: 10.1016/j.palaeo.2010.04.009

Halfar, J., Steneck, R. S., Joachimski, M., Kronz, A., and Wanamaker, A. D.Jr (2008). Coralline red algae as high-resolution climate recorders. *Geology* 36 (6), 463–466. doi: 10.1130/G24635A.1

Halfar, J., Steneck, R., Schöne, B. R., Moore, G. W. K., Joachimski, M. M., Kronz, A., et al. (2007). Coralline alga reveals first marine record of subarctic north pacific climate change. *Geophysical Res. Lett.* 34, L07702. doi: 10.01029/02006GL028811

Halfar, J., Williams, B., Hetzinger, S., Steneck, R. S., Lebednik, P., Winsborough, C., et al. (2011b). 225 years of Bering Sea climate and ecosystem dynamics revealed by coralline algal growth-increment widths. *Geology* 39 (6), 579–582. doi: 10.1130/G31996.1

Halfar, J., Zack, T., Kronz, A., and Zachos, J. (2000). Growth and high-resolution paleoenvironmental signals of rhodoliths (coralline red algae): a new biogenic archive. *J. Geophysical Res.* 105 (C9), 22107–22116. doi: 10.1029/1999JC000128

Hallmann, N., Burchell, M., Schöne, B. R., Irvine, G. V., and Maxwell, D. (2009). High-resolution sclerochronological analysis of the bivalve mollusk saxidomus gigantea from Alaska and British Columbia: techniques for revealing environmental archives and archaeological seasonality. *J. Archaeological Sci.* 36 (10), 2353–2364. doi: 10.1016/j.jas.2009.06.018

Hathorne, E. C., Gagnon, A., Felis, T., Adkins, J., Asami, R., Boer, W., et al. (2013). Interlaboratory study for coral Sr/Ca and other element/Ca ratio measurements. *Geochemistry Geophysics Geosystems* 14 (9), 3730–3750. doi: 10.1002/ggge.20230

Hereu, B., and Kersting, D. K. (2016). Diseases of coralline algae in the Mediterranean Sea. *Coral Reefs* 35 (2), 713–713. doi: 10.1007/s00338-016-1428-x

Hetzinger, S., Halfar, J., Kronz, A., Simon, K., Adey, W. H., and Steneck, R. S. (2018). Reproducibility of *Clathromorphum compactum* coralline algal Mg/Ca ratios and comparison to high-resolution sea surface temperature data. *Geochimica Cosmochimica Acta* 220, 96–109. doi: 10.1016/j.gca2017.09.044

Hetzinger, S., Halfar, J., Riegl, B., and Godinez-Orta, L. (2006). Sedimentology and acoustic mapping of modern rhodolith facies on a non-tropical carbonate shelf (Gulf of California, Mexico). *J. Sedimentary Res.* 76, 670–682. doi: 10.2110/jsr.2006.053

Hetzinger, S., Halfar, J., Zack, T., Gamboa, G., Jacob, D. E., Kunz, B. E., et al. (2011). High-resolution analysis of trace elements in crustose coralline algae from the north Atlantic and north pacific by laser ablation ICP-MS. *Palaeogeography Palaeoclimatology Palaeoecol.* 302 (1-2), 81–94. doi: 10.1016/j.palaeo.2010.06.004

Hetzinger, S., Halfar, J., Zack, T., Mecking, J. V., Kunz, B. E., Jacob, D. E., et al. (2013). Coralline algal barium as indicator for 20th century northwestern north Atlantic surface ocean freshwater variability. *Sci. Rep.* 3 (1761). doi: 10.1038/srep01761

Hetzinger, S., Halfar, J., Zajacz, Z., Möller, M., and Wisshak, M. (2021). Late twentieth century increase in northern spitsbergen (Svalbard) glacier-derived runoff tracked by coralline algal Ba/Ca ratios. *Climate Dynamics* 56 (9), 3295–3303. doi: 10.1007/s00382-021-05642-x

Hetzinger, S., Halfar, J., Zajacz, Z., and Wisshak, M. (2019). Early start of 20th-century Arctic sea-ice decline recorded in Svalbard coralline algae. *Geology* 47 (10), 963–967. doi: 10.1130/G46507.1

Kamenos, N., Cusack, M., and Moore, P. G. (2008). Coralline algae are global paleothermometers with bi-weekly resolution. *Geochimica Cosmochimica Acta* 72, 771–779. doi: 10.1016/j.gca.2007.11.019

Kamenos, N. A., and Law, A. (2010). Temperature controls on coralline algal skeletal growth. *J. Phycology* 46 (2), 331–335. doi: 10.1111/j.1529-8817.2009.00780.x

Kersting, D. K., Bensoussan, N., and Linares, C. (2013). Long-term responses of the endemic reef-builder *Cladocora caespitosa* to Mediterranean warming. *PloS One* 8 (8), e70820. doi: 10.1371/journal.pone.0070820

Kersting, D. K., and Linares, C. (2019). Living evidence of a fossil survival strategy raises hope for warming-affected corals. *Sci. Adv.* 5 (10), eaax2950. doi: 10.1126/sciadv.aax2950

Kersting, D. K., Mangialajo, L., and Ballesteros, E. (2021). On the edge: segregation and coexistence between epibenthic fish species in Mediterranean mesophotic habitats. *Mar. Biol.* 168 (10), 155. doi: 10.1007/s00227-021-03955-3

Kiessling, W. (2009). Geologic and biologic controls on the evolution of reefs. *Annu. Rev. Ecology Evolution Systematics* 40 (1), 173–192. doi: 10.1146/annurev.ecolsys.110308.120251

Lea, D. W. (2003). "Elemental and isotopic proxies of marine temperatures," in *The oceans and marine geochemistry*. Ed. H. Elderfield (Oxford: Elsevier-Pergamon), 365–390.

Lea, D., Shen, G. T., and Boyle, E. A. (1989). Coralline barium records temporal variability in equatorial pacific upwelling. *Nature* 340, 373–376. doi: 10.1038/340373a0

Leclerc, N., Halfar, J., Hetzinger, S., Chan, P. T. W., Adey, W., Tsay, A., et al. (2022). Suitability of the coralline alga *Clathromorphum compactum* as an Arctic archive for past sea ice cover. *Paleoceanogr. Paleoclimatol.* 37 (1), e2021PA004286. doi: 10.1029/2021PA004286

Marrack, E. C. (1999). The relationship between water motion and living rhodolith beds in the southwestern gulf of California, Mexico. *Palaios* 14, 159–171. doi: 10.2307/3515371

Martinuš, M., Fio, K., Pikelj, K., and Aščić, Š. (2013). Middle Miocene warm-temperate carbonates of central paratethys (Mt. zrinska gora, croatia): paleoenvironmental reconstruction based on bryozoans, coralline red algae, foraminifera, and calcareous nannoplankton. *Facies* 59 (3), 481–504. doi: 10.1007/s10347-012-0327-z

Mette, M. J., Wanamaker, A. D., Carroll, M. L., Ambrose, W. G., and Retelle, M. J. (2016). Linking large-scale climate variability with *Arctica islandica* shell growth and geochemistry in northern Norway. *Limnol. Oceanogr.* 61 (2), 748–764. doi: 10.1002/lno.10252

Moberly, R.Jr. (1968). Composition of magnesian calcites of algae and pelecypods by electron microprobe analysis. *Sedimentology* 11, 61–82. doi: 10.1111/j.1365-3091.1968.tb00841.x

Nash, M. C., and Adey, W. (2017). Multiple phases of mg-calcite in crustose coralline algae suggest caution for temperature proxy and ocean acidification assessment: lessons from the ultrastructure and biomineralization in *Phymatolithon* (Rhodophyta, Corallinales)1. *J. Phycology* 53 (5), 970–984. doi: 10.1111/jpy.12559

Nash, M. C., Martin, S., and Gattuso, J. P. (2016). Mineralogical response of the Mediterranean crustose coralline alga *Lithophyllum cabiochae* to near-future ocean acidification and warming. *Biogeosciences* 13 (21), 5937–5945. doi: 10.5194/bg-13-5937-2016

Paillard, D., Labeyrie, L., and Yiou, P. (1996). Macintosh program performs time-series analysis. *Eos Trans. AGU* 77, 379. doi: 10.1029/96EO00259

Perry, C. T., Spencer, T., and Kench, P. S. (2008). Carbonate budgets and reef production states: a geomorphic perspective on the ecological phase-shift concept. *Coral Reefs* 27 (4), 853–866. doi: 10.1007/s00338-008-0418-z

Piazza, G., Bracchi, V. A., Langone, A., Meroni, A. N., and Basso, D. (2022). Growth rate rather than temperature affects the B/Ca ratio in the calcareous red alga *Lithothamnion corallioides*. *Biogeosciences* 19, 1047–1065. doi: 10.5194/bg-2021-21

Pisano, A., Marullo, S., Artale, V., Falcini, F., Yang, C., Leonelli, F. E., et al. (2020). New evidence of Mediterranean climate change and variability from Sea surface temperature observations. *Remote Sens.* 12 (1), 132. doi: 10.3390/rs12010132

Ragazzola, F., Caragnano, A., Basso, D., Schmidt, D. N., and Fietzke, J. (2020). Establishing temperate crustose early Holocene coralline algae as archives for palaeoenvironmental reconstructions of the shallow water habitats of the Mediterranean Sea. *Palaeontology* 63 (1), 155–170. doi: 10.1111/pala.12447

Rindi, F., Braga, J. C., Martin, S., Peña, V., Le Gall, L., Caragnano, A., et al. (2019). Coralline algae in a changing Mediterranean Sea: how can we predict their future, if we do not know their present? *Front. Mar. Sci.* 6 (723). doi: 10.3389/fmars.2019.00723

Rodriguez-Prieto, C., Ballesteros, E., Boisset, F., and Afonso-Carrillo, J. (2013). *Guía de las macroalgas y fanerógamas marinas del mediterráneo occidental* (Spain: Ediciones OMEGA).

Schäfer, P., Fortunato, H., Bader, B., Liebetrau, V., Bauch, T., and Reijmer, J. J. G. (2011). Growth rates and carbonate production by coralline red algae in upwelling and non-upwelling settings along the pacific coast of Panama. *PALAIOS* 26 (7), 420–432. doi: 10.2110/palo.2010.p10-138r

Schlüter, M., Pyko, I., Wisshak, M., Schulbert, C., and Teichert, S. (2021). Growth interruptions in Arctic rhodoliths correspond to water depth and rhodolith morphology. *Minerals* 11 (5), 538. doi: 10.3390/min11050538

Schöne, B., and Surge, D. (2012). *Treatise Online no. 46: Part N, Revised, Volume 1, Chapter 14: Bivalve sclerochronology and geochemistry*. Treatise Online. doi: 10.17161/to.v0i0.4297

Schubert, N., Schoenrock, K. M., Aguirre, J., Kamenos, N. A., Silva, J., Horta, P. A., et al. (2020). Editorial: coralline algae: globally distributed ecosystem engineers. *Front. Mar. Sci.* 7 (352). doi: 10.3389/fmars.2020.00352

Siebert, V., Poitevin, P., Chauvaud, L., Schöne, B. R., Lazure, P., and Thébault, J. (2021). Using growth and geochemical composition of *Clathromorphum compactum* to track multiscale north Atlantic hydro-climate variability. *Palaeogeography Palaeoclimatology Palaeoecol.* 562, 110097. doi: 10.1016/j.palaeo.2020.110097

Sletten, H. R., Andrus, C. F. T., Guzmán, H. M., and Halfar, J. (2017a). Re-evaluation of using rhodolith growth patterns for paleoenvironmental reconstruction: an example from the gulf of Panama. *Palaeogeography Palaeoclimatology Palaeoecol.* 465, 264–277. doi: 10.1016/j.palaeo.2016.10.038

Sletten, H. R., Gillikin, D. P., Halfar, J., Andrus, C. F. T., and Guzmán, H. M. (2017b). Skeletal growth controls on Mg/Ca and P/Ca ratios in tropical Eastern pacific rhodoliths (coralline red algae). *Chem. Geology* 465, 1–10. doi: 10.1016/j.chemgeo.2017.05.010

Steneck, R. (1983). Escalating herbivory and resulting adaptive trends in cacareous algal crusts. *Paleobiology* 9, 44–61. doi: 10.1017/S0094837300007375

Steneck, R. (1986). The ecology of coralline algal crusts: convergent patterns and adaptive strategies. *Ann. Rev. Ecol. Syst.* 17, 273–303. doi: 10.1146/annurev.es.17.110186.001421

Svendsen, L., Hetzinger, S., Keenlyside, N., and Gao, Y. (2014). Marine-based multiproxy reconstruction of Atlantic multidecadal variability. *Geophysical Res. Lett.* 41. doi: 10.1002/2013gl059076

Tebben, J., Motti, C. A., Siboni, N., Tapiolas, D. M., Negri, A. P., Schupp, P. J., et al. (2015). Chemical mediation of coral larval settlement by crustose coralline algae. *Sci. Rep.* 5 (1), 10803. doi: 10.1038/srep10803

Teichert, S., Steinbauer, M., and Kiessling, W. (2020). A possible link between coral reef success, crustose coralline algae and the evolution of herbivory. *Sci. Rep.* 10 (1), 17748. doi: 10.1038/s41598-020-73900-9

Teichert, S., Woelkerling, W., Rüggeberg, A., Wisshak, M., Piepenburg, D., Meyerhöfer, M., et al. (2014). Arctic Rhodolith beds and their environmental controls (Spitsbergen, Norway). *Facies* 60 (1), 15–37. doi: 10.1007/s10347-013-0372-2

Williams, B., Halfar, J., DeLong, K. L., Hetzinger, S., Steneck, R. S., and Jacob, D. E. (2014). Multi-specimen and multi-site calibration of Aleutian coralline algal Mg/Ca to sea surface temperature. *Geochimica Cosmochimica Acta* 139 (0), 190–204. doi: 10.1016/j.gca.2014.04.006

Williams, B., Halfar, J., Steneck, R. S., Wortmann, U. G., Hetzinger, S., Adey, W., et al. (2011). Twentieth century δ13C variability in surface water dissolved inorganic carbon recorded by coralline algae in the northern north pacific ocean and the Bering Sea. *Biogeosciences* 8, 165–174. doi: 10.5194/bg-8-165-2011

Williams, S., Halfar, J., Zack, T., Hetzinger, S., Blicher, M., and Juul-Pedersen, T. (2018a). Comparison of climate signals obtained from encrusting and free-living rhodolith coralline algae. *Chem. Geology* 476, 418–428. doi: 10.1016/j.chemgeo.2017.11.038

Williams, S., Halfar, J., Zack, T., Hetzinger, S., Blicher, M., Juul-Pedersen, T., et al. (2018b). Coralline algae archive fjord surface water temperatures in southwest Greenland. *J. Geophysical Research: Biogeosciences* 123 (8), 2617–2626. doi: 10.1029/2018JG004385

frontiers | Frontiers in Marine Science

TYPE Original Research
PUBLISHED 26 October 2023
DOI 10.3389/fmars.2023.1279164

OPEN ACCESS

EDITED BY
Hali Kilbourne,
University of Maryland Center for Environmental Science, United States

REVIEWED BY
Madelyn Mette,
United States Department of the Interior, United States
Justin P. Dodd,
Northern Illinois University, United States

*CORRESPONDENCE
Cornélia Brosset
cornelia.brosset@uni-mainz.de
Bernd R. Schöne
bernd.schoene@uni-mainz.de

RECEIVED 17 August 2023
ACCEPTED 16 October 2023
PUBLISHED 26 October 2023

CITATION
Brosset C, Höche N, Witbaard R, Nishida K, Shirai K, Mertz-Kraus R and Schöne BR (2023) Sr/Ca in shells of laboratory-grown bivalves (*Arctica islandica*) serves as a proxy for water temperature – implications for (paleo)environmental research?. *Front. Mar. Sci.* 10:1279164. doi: 10.3389/fmars.2023.1279164

Sr/Ca in shells of laboratory-grown bivalves (*Arctica islandica*) serves as a proxy for water temperature – implications for (paleo)environmental research?

Cornélia Brosset[1]*, Nils Höche[1], Rob Witbaard[2], Kozue Nishida[3], Kotaro Shirai[4], Regina Mertz-Kraus[1] and Bernd R. Schöne[1]*

[1]Institute of Geosciences, University of Mainz, Mainz, Germany, [2]Department of Estuarine and Delta Systems, Royal Netherlands Institute for Sea Research, Yerseke, Netherlands, [3]Graduate School of Life and Environmental Sciences, University of Tsukuba, Tsukuba, Japan, [4]Atmosphere and Ocean Research Institute, The University of Tokyo, Chiba, Japan

Seawater temperature is an essential quantity for paleoclimatological and paleoecological studies. A potential archive that can provide century-long, temporally well-constrained and high-resolution temperature proxy data is available in the form of bivalve shells. However, the number of well-accepted and robust temperature proxies contained in shells is limited to stable oxygen isotopes and carbonate clumped isotopes. Many studies have therefore investigated the possibility to reconstruct temperature from element/Ca properties, specifically Sr/Ca ratios in case of aragonitic shells. As demonstrated here, in agreement with thermodynamic expectations and the lattice strain model, shell Sr/Ca of laboratory-grown *Arctica islandica* specimens is strongly positively coupled to water temperature. If ultrastructure-related bias is mathematically eliminated, up to 75% of the variability in shell Sr/Ca data can be explained by water temperature. However, in field-grown specimens, this relationship is superimposed by other environmental variables that can hardly be quantified and mathematically eliminated. The explained variability of Sr/Ca is reduced to merely 26% and the prediction uncertainty too large for reliable temperature estimates. Most likely, the equable, less biased conditions in the laboratory resulted in the production of a more uniform shell ultrastructure (with larger and more elongated biomineral units) which in turn was associated with less variable Sr/Ca values and a stronger link to water temperature. Without a detailed understanding and quantification of the factors controlling ultrastructural variations in field-grown bivalves, it remains impossible to employ shell Sr/Ca of wild *A. islandica* specimens for precise temperature estimates, merely a qualitative temperature reconstruction seems feasible.

KEYWORDS

bivalve sclerochronology, water temperature proxy, strontium-to-calcium ratio, shell ultrastructure, growth rate

1 Introduction

Ocean temperature is a crucial quantity in paleoclimatological and paleoecological research. Amongst other aspects, seasonally to annually resolved and temporally well-constrained temperature data are needed to verify and refine numerical climate models (Schmidt et al., 2014; Cauquoin et al., 2019), understand biogeographic distribution patterns (Adey and Steneck, 2001; Zacherl et al., 2003; Belanger et al., 2012) and assess the impact of short-term temperature changes on biota, specifically in coastal nearshore environments (Goberville et al., 2010; Węsławski et al., 2011). Potential archives that provide such data include shells of bivalve mollusks (Wanamaker et al., 2012; Butler et al., 2013; Lohmann and Schöne, 2013; Black et al., 2016). Bivalves are often abundant and sometimes well-preserved in the fossil record, extending their potential use back in time. They are widely distributed globally and some species such as the ocean quahog, *Arctica islandica*, can live for several hundred years (Schöne et al., 2005; Wanamaker et al., 2008a; Butler et al., 2013). More importantly, they record changes of ambient environmental conditions in their shells in precise chronological order (Jones, 1981; Witbaard et al., 1994; Schöne et al., 2005; Wanamaker et al., 2012; Wanamaker et al., 2019; Schöne et al., 2023). This environmental record is also spatially well-constrained, because bivalves are sessile organisms, compared to data extracted from mobile or migrating animals, e.g., fish (Schöne and Krause, 2016). However, extracting quantitative temperature data from bivalve shells remains a challenging task for a variety of reasons.

Due to known limitations of $\delta^{18}O$ and Δ_{47}-based temperature estimates (Witbaard et al., 1994; Eiler, 2011; De Winter et al., 2022), repeated attempts have been undertaken to explore the potential use of element/Ca ratios as paleothermometers, especially Sr/Ca values in aragonitic shells (Surge and Walker, 2006; Foster et al., 2009; Schöne et al., 2011; Schöne et al., 2013; Schöne et al., 2023) and Mg/Ca in calcitic shells (e.g., Wanamaker et al., 2008b; Tynan et al., 2017). Unlike $\delta^{18}O$, these element/Ca values are assumed to be fairly stable in marine waters (above a salinity of approx. 10; Dodd and Crisp, 1982) through time and space and can thus be assumed constant in paleothermometry equations. Furthermore, with *in-situ* analytical techniques (e.g., LA-ICP-MS), element/Ca data can be measured quickly, precisely and at very high spatial resolution. While Sr/Ca and Mg/Ca values are routinely used in many non-molluscan biogenic carbonates to reconstruct temperature histories (Beck et al., 1992; Rosenheim et al., 2004; Corrège, 2006), their use in bivalve shells (Dodd, 1965; Stecher et al., 1996; Zhao et al., 2017) is controversially debated, even in the same species. Reports on *A. islandica* range from positive (Hart and Blusztajn, 1998; Toland et al., 2000; Brosset et al., 2022) to negative (Schöne et al., 2013; Yan et al., 2013) to no correlation (Wanamaker and Gillikin, 2019) between shell Sr/Ca or Mg/Ca and temperature. Partly, these controversial findings are related to the experimental design, e.g., averaging Sr/Ca data from very slow and fast-growing shell portions, growth lines and growth increments, respectively (Schöne et al., 2013). Even if there was a relationship between shell Sr/Ca and temperature, the correlation remained low (ca. $R^2 <$ 0.30). Only a single study explored this relationship in laboratory-grown *A. islandica* specimens, but merely at two different temperature regimes and without studying the underlying shell ultrastructure (Wanamaker and Gillikin, 2019).

As with most other trace and minor elements, the incorporation of Sr and Mg into bivalve shells is reported to be strongly controlled by vital and/or kinetic effects (e.g., Foster et al., 2009), possibly to maintain certain mechanical properties of the shell. As a result, their concentration typically remains well below values observed in abiogenic aragonite and scleractinian corals (Gaetani and Cohen, 2006), and their temperature sensitivity (= the slope of the regression curve between shell Sr/Ca or Mg/Ca and temperature) often deviates from that of abiogenic aragonite (compare, e.g., Gaetani and Cohen, 2006 with Schöne et al., 2013). Furthermore, a strong coupling with growth rate (Stecher et al., 1996; Gillikin et al., 2005), ontogenetic age (Freitas et al., 2005; Schöne et al., 2011; Schöne et al., 2023) and shell ultrastructure (Shirai et al., 2008; Foster et al., 2009; Schöne et al., 2013; Füllenbach et al., 2017; Roger et al., 2017) has been reported. For example, in annual growth lines of *Arctica islandica* which consist of irregular simple/spherulitic prismatic (ISP) ultrastructure (Ropes, 1984), the Sr concentration is much higher than in the annual increments, i.e., the fast-growing portions between adjacent growth lines (Schöne et al., 2013). In the outer portion of the outer shell layer (oOSL), annual growth increments consist predominantly of homogeneous (HOM) ultrastructure, whereas in the inner portion of the outer shell layer (iOSL) crossed-acicular (CA) and fine-complex crossed-lamellar ultrastructures prevail (Ropes, 1984). As recently demonstrated (Brosset et al., 2022), the shell Sr/Ca values in annual increments (reflecting the main growing season) of juvenile field-grown *A. islandica* specimens from NE Iceland are weakly positively correlated to water temperature. After mathematical elimination of growth rate and/or ultrastructure-related bias, only a slightly stronger positive correlation was observed implying that other environmental variables exert a strong control on shell Sr/Ca (Brosset et al., 2022). Notably, the positive relationship between Sr/Ca and temperature differs from such found in synthetic aragonite and scleractinian corals (negative correlation) but agrees with thermodynamic expectations and the lattice strain model (Gaetani and Cohen, 2006).

The present study explores whether juvenile *A. islandica* specimens record water temperature in shell Sr/Ca values if grown in laboratory tanks under controlled conditions, largely devoid of environmental disturbances. Furthermore, by comparison to data of conspecific specimens grown in the field, the potential use of shell Sr/Ca as a paleothermometer is evaluated. The following hypotheses were tested. (i) After mathematical correction for shell growth rate and ultrastructural biases, shell Sr/Ca values of specimens raised under controlled conditions in laboratory tanks are more strongly correlated to water temperature and show a stronger temperature sensitivity than specimens grown in the field. (ii) The uniformity of shell ultrastructure in tank-grown specimens is expected to facilitate the analysis of the Sr/Ca-temperature relationship. Results of this study have implications for future paleotemperature estimates based on molar Sr/Ca ratios of bivalve shells.

2 Materials and methods

2.1 Sample collection and experimental conditions

For the present work, shells of twenty-one juvenile specimens of *Arctica islandica* of two laboratory growth experiments were used (Witbaard et al., 1997; Beirne et al., 2012) (Table 1). All bivalves were raised in tanks under controlled temperature regimes. Some of the material of Beirne et al. (2012) was also analyzed by Wanamaker and Gillikin (2019) for element chemical properties and growth rate, whereas specimens of Witbaard et al. (1997) were used by Höche et al. (2021) largely for the ultrastructure analysis in the hinge portion of the shells (which differs from such in the ventral margin).

Fifteen specimens employed in the studies by Witbaard et al. (1997) and Höche et al. (2021) were collected at 20 m water depth in the western Baltic Sea, Germany (Table 1). After a one-month acclimatization to fully marine conditions in laboratory tanks at Texel, The Netherlands, bivalves were allowed to grow for 95 days in a total of six tanks under stable temperatures, with aerated and filtered seawater regularly replaced. The six stable temperature regimes used for culturing were 1.1, 3.2, 6.2, 9.2, 12°C and 15°C (for details on the experimental conditions, see Witbaard et al., 1997; note that the experiment conducted at 15°C was not reported in their study, but culturing conditions were identical). Two to three bivalves were selected for this study from the nine specimens cultured in each tank with *ad libitum* food composed of a phytoplankton mixture of *Isochrysis galbana* and *Dunaliella marina*.

Six additional specimens came from 82 m water depth in the Gulf of Maine (Beirne et al., 2012). Bivalves were then transported to the Darling Marine Center (University of Maine, Orono) in Walpole, Maine and exposed to ambient temperature, food, and salinity (Beirne et al., 2012). After ca. 1.5 years, the specimens were raised in a muddy estuarine sediment with ambient seawater under stable temperature conditions of 10.3 ± 0.2°C for 47 days, followed by another 69 days at 15 ± 0.3°C (for details, see Beirne et al., 2012 and Wanamaker and Gillikin, 2019).

2.2 Sample preparation

After the experiments, all specimens were shucked, and their shells rinsed with tap water. The right valves of the Baltic Sea (BS) specimens and the left valves of the Gulf of Maine (GOM) shells were mounted on acrylic glass cubes using a plastic welder (WIKO Multi Power 3). The subsequent preparation was done in accordance with methods described in Höche et al. (2022). Briefly, a protective layer of metal epoxy resin (WIKO 05) was applied to the shell surfaces along the planned cutting axis. From each valve, two approx. 2.5 mm thick sections were cut along the maximum growth using a low-speed saw (Buehler IsoMet 1000) operated at 200 rpm. The saw was equipped with a 0.4 mm diamond-coated blade. As shells from the Baltic Sea specimens were very thin (approx. 0.5 mm), the cross-sectioned slabs were embedded in epoxy resin (Araldite 2020) to avoid damage during the cutting process. Furthermore, the epoxy was mixed with a conductive filler (Buehler 20–8500) for subsequent scanning electron microscopic (SEM) analysis. All sections were then ground with F800 and F1200 SiC suspensions on glass plates, and polished using Al_2O_3 suspension (1 µm grain size) on a Buehler MasterTex cloth. Between each grinding and polishing step specimens were ultrasonically cleaned in tap water. Once dried from air, one slab of each specimen was attached with a carbon sticker to a one-inch sample holder for SEM analysis. The mirroring section was glued to a glass slide used for *in-situ* trace element analysis by laser ablation inductively coupled plasma mass spectrometry (LA-ICP-MS).

2.3 *In-situ* chemical analysis (LA-ICP-MS)

The trace element analysis of the shells of the laboratory-grown specimens was done by LA-ICP-MS at the Institute of Geosciences, University of Mainz, following the same method and settings used in Brosset et al. (2022) for field-grown specimens. Briefly, the system consisted of a 193 nm ArF Eximer laser (ESI NWR 193; repetition rate = 10 Hz; energy density = approx. 3 J/cm²) equipped

TABLE 1 Overview of laboratory-grown specimens of *Arctica islandica* used in the present study.

Sampling locality	Duration of experiment	Temperature regime	# Specimens	# Data points	Ontogenetic age (years)	Shell height (mm)	Shell thickness (mm)
Baltic Sea (54°52′59″N, 010°08′00″E)	95 days	1.1°C	2	109	5	16.77 ± 2.29	0.47 ± 0.04
		3.2°C	2	105			
		6.2°C	3	272			
		9.2°C	3	112			
		12°C	2	78			
		15°C	3	145			
Gulf of Maine (44°26′10″ N, 067°26′18″W)	47 days	10.3°C	6	315	3	38.25 ± 0.22	1.21 ± 0.33
	69 days	15°C		273			

For a detailed description of experimental settings, see Witbaard et al. (1997) and Wanamaker and Gillikin (2019). One data point includes element chemical data obtained by LA-ICP-MS and ultrastructure analysis in scanning electron microscope images.

with a TwoVol2 ablation cell, coupled to a quadrupole inductively coupled plasma mass spectrometer (Agilent 7500ce). The laser spots (n = 1,409; 60 µm diameter) were placed 90 µm apart (center to center). In each of the two sublayers (outer, inner) of the outer shell layer (oOSL, iOSL) of the ventral margin, one transect of LA spots was placed parallel to the main growth axis (Figure 1). Strontium concentration in the shells was monitored using the ^{88}Sr intensity. Data were reduced using an in-house software program following the calculations of Longerich et al. (1996) and Jochum et al. (2011). NIST SRM 610 and NIST SRM 612 were used for calibration, and USGS MACS-3, BCR-2G, JCp-1 and JCt-1 as quality control materials, with the preferred values given in the GeoReM database (available at http://georem.mpch-mainz.gwdg.de, ver. 34, last access: 16 Dec. 2022; Jochum et al., 2005; Jochum et al., 2012; Table S1). The element concentrations determined for the quality control materials were in the range of published values, and average detection limit ($3\sigma_{background}$, Jochum et al., 2012) and element-specific Relative Standard Deviation (RSD%) values are shown in Table S1. Data from the reference materials and bivalve shells were normalized using ^{43}Ca as internal standard, and molar Sr/Ca ratios were calculated from Sr concentrations using a shell calcium content of 380,000 µg/g (Marali et al., 2017).

2.4 Ultrastructure morphometry

The other polished cross-section of each specimen was used for ultrastructural properties analysis by means of SEM, following the method reported by Höche et al. (2022). An ultrafine chemo-mechanical polishing, i.e., superficial oxidation of the inter-crystalline organics and smoothing of the carbonate phase, was performed on the cross-sections to better distinguish individual biomineral units (BMUs). Accordingly, the shell slabs were polished for ca. 10 min with a 60 nm suspension (Buehler MasterMet, pH ca. 10.1) on a Buehler MasterTex polishing cloth mounted on a rotational lap (Buehler MetaServ 2000; 50 rpm).

For direct comparison of the Sr/Ca data with the ultrastructural properties, both sections of each specimen were photographed with a digital camera under a light microscope with reflective illumination (Leica Stemi 508), and images were stitched together using the open-source software Hugin (available at https://sourceforge.net/projects/hugin/, last access: 19 Jul. 2023). In each specimen, the width of the portion grown in the laboratory was measured along the maximum growth axis, and the shell daily growth rates were approximated assuming a constant shell growth during the respective experimental intervals (for details on laboratory-grown sections identification, see Beirne et al., 2012 and Höche et al., 2021). The BigWarp tool (Fiji built-in BigDataViewer plugin available at https://imagej.net/software/fiji/, last access: 16 Dec. 2022) of the software ImageJ (Schindelin et al., 2012; Bogovic et al., 2016) was employed to align both sections of each specimen, and thus to align ultrastructure data to Sr/Ca data (Figure 1). To this avail, one SEM image (35 µm × 35 µm) was taken in corresponding shell portions in which the chemical measurements were completed. A 3rd generation Phenom Pro Desktop SEM equipped with a backscatter electron detector and a CeB_6 electron source was used to take 1,409 SEM images at 7,700× magnification and 10keV.

Prior to morphometric analyses, individual BMUs were detected in the SEM photographs following the segmentation method depicted in Höche et al. (2021). Briefly, the machine learning software Ilastik (Berg et al., 2019) was trained to recognize individual BMUs on a sample set of the studied SEM images. Subsequently, all SEM images were processed semi-automatically. The quality of the segmentations was manually

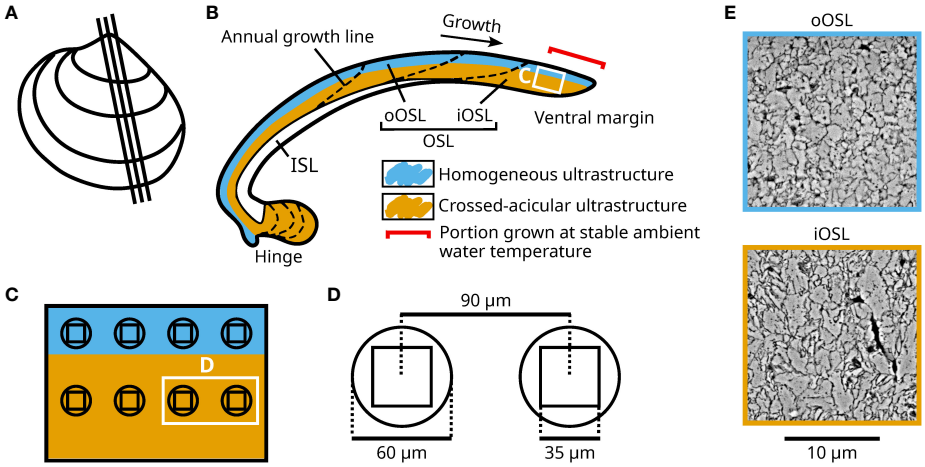

FIGURE 1
Overview of the sampling positions for ultrastructural and *in-situ* element chemical analyses in shells of *Arctica islandica* specimens cultured at 1.1, 3.2, 6.2, 9.2, 10.3, 12 and 15°C. **(A)** Depiction of a left valve from a cultured specimen illustrating the cutting axes of the studied shell. **(B)** Schematic representation of a shell slab. The shell is divided into an inner and outer shell layer (ISL, OSL), separated by the myostracum. The outer portion of the OSL (oOSL) primarily consists of homogeneous ultrastructure (blue), while crossed-acicular ultrastructure (orange) dominates in the inner portion of the OSL (iOSL). The portion of the shell grown during the experimental interval is indicated by the red bracket. **(C)** Enlargement of panel **(B)** showing the sampling positions for LA-ICP-MS and SEM for the two shell sections analyzed for every specimen. **(D)** Enlarged schematic representation of the SEM images (35 µm^2) compared to the laser spots (60 µm diameter, 90 µm between LA centers) depicted in panel **(C)**. **(E)** Example of SEM image obtained in the oOSL and the iOSL. The scale applies to both images.

assessed, and the software training refined if necessary. Morphometrical parameters, including BMU area and BMU elongation (= ratio between the minor and major axes of an ellipse fitted to the BMU), were automatically measured using the scikit-image processing library (van der Walt et al., 2014) operated through a python script (Höche et al., 2021). For each experimental temperature regime and OSL sublayers, examples of BMU segmentations are depicted in Figures S1, S2. The 15% largest BMUs of each SEM image were considered for consecutive analysis. According to previous work, this threshold value reveals the highest BMU morphology variation and provides the strongest link between the size of individual BMUs in the shell of *A. islandica* and water temperature (Höche et al., 2021).

2.5 Statistical analysis and detrending of shell Sr/Ca and ultrastructure

To assess the mathematical correlation between water temperature and shell properties, shell growth rate, Sr/Ca, BMU area and BMU elongation data were plotted against temperature (section 3.1). Kruskal-Wallis (KW) rank tests were used to compare data between all temperature regimes, and Dunn tests (generalized Bonferroni adjustment for multiple comparisons; Table S2) were used to compare data between pairs of two temperature regimes. Data from the oOSL and the iOSL were compared using Mann-Whitney *U* (MWU) two-sample rank tests. At each temperature regime and for both shell sublayers (oOSL and iOSL), median values weighted for the number of studied specimens were calculated for Sr/Ca, BMU area and BMU elongation, and were used for the subsequent analyses.

To identify potential links between shell growth rate, ultrastructure and chemical properties that could have biased the temperature sensitivity of these shell properties, crossplots were generated between (i) growth rate and Sr/Ca, (ii) Sr/Ca and ultrastructural properties, and (iii) growth rate and ultrastructural properties (BMU area and elongation). Based on these crossplots, non-linear (natural logarithm) regression models were computed and subsequently used to detrend the chemical and ultrastructural data. For this purpose, predicted values given by these regression models were subtracted from the chemical and ultrastructural data, resulting in growth rate-detrended Sr/Ca data (d_{GR}Sr/Ca), BMU area-detrended Sr/Ca data (d_{AR}Sr/Ca) as well as BMU elongation-detrended Sr/Ca data (d_{EL}Sr/Ca) i.e., residuals for each of these parameters after detrending (section 3.2). Furthermore, Sr/Ca data were mathematically corrected for combinations of growth rate and BMU area (d_{GRAR}Sr/Ca), growth rate and BMU elongation (d_{GREL}Sr/Ca), as well as growth rate, BMU area and elongation (d_{GRAREL}Sr/Ca). Also, the correlation with growth rate was eliminated from ultrastructural properties (section 3.2) to obtain growth rate-detrended BMU area data (d_{GR}AR) and growth rate-detrended BMU elongation data (d_{GR}EL).

All computations were done separately for each OSL sublayer (oOSL and iOSL; Tables 2, 3). As indicated by previous studies, *A.*

TABLE 2 Overview of the regression parameters (slope; R^2, coefficient of determination; p, probability) between shell Sr/Ca data of cultured *Arctica islandica* specimens and shell growth rate (GR; data from Baltic Sea and Gulf of Maine in regular and italic font, respectively), ultrastructural properties, i.e., area and elongation of the biomineral units (AR and EL, respectively), and temperature of the laboratory tanks (T).

Variables		Sr/Ca		d_{GR}Sr/Ca	d_{AR}Sr/Ca	d_{EL}Sr/Ca	d_{GRAR}Sr/Ca	d_{GREL}Sr/Ca	d_{GRAREL}Sr/Ca
oOSL									
ln(GR)	slope	- 0.20 ± 0.07	*0.02 ± 0.01*						
	R^2	0.40	*0.35*						
	p	< 0.05	*< 0.05*						
ln(AR)	slope	- 0.38 ± 0.72		0.08 ± 0.58					
	R^2	0		0					
	p	ns		ns					
ln(EL)	slope	- 7.96 ± 1.53		- 6.08 ± 1.30			- 11.61 ± 2.61		
	R^2	0.53		0.48			0.45		
	p	< 0.001		< 0.001			< 0.001		
T	slope	0.02 ± 0.01		0.01 ± 0.01	0.02 ± 0.01	0.03 ± 0.004	0.04 ± 0.02	0.04 ± 0.01	0.06 ± 0.01
	R^2	0.22		0.16	0.19	0.63	0.20	0.37	0.41
	p	< 0.05		< 0.05	< 0.05	< 0.001	< 0.05	< 0.001	< 0.001
iOSL									
ln(GR)	slope	- 0.11 ± 0.08	*0.10 ± 0.04*						
	R^2	0.05	*0.35*						

(Continued)

10.3389/fmars.2023.1279164

TABLE 2 Continued

Variables		Sr/Ca		d_{GR}Sr/Ca	d_{AR}Sr/Ca	d_{EL}Sr/Ca	d_{GRAR}Sr/Ca	d_{GREL}Sr/Ca	d_{GRAREL}Sr/Ca
	p	ns	*< 0.05*						
ln(AR)	slope	0.80 ± 0.15		0.88 ± 0.17					
	R^2	0.53		0.53					
	p	< 0.001		< 0.001					
ln(EL)	slope	0.36 ± 1.74		- 0.31 ± 1.91			- 1.00 ± 2.77		
	R^2	0		0			0		
	p	ns		ns			ns		
T	slope	0.03 ± 0.01		0.04 ± 0.01	0.03 ± 0.003	0.03 ± 0.01	0.06 ± 0.01	0.06 ± 0.02	0.09 ± 0.02
	R^2	0.38		0.41	0.75	0.29	0.56	0.30	0.44
	p	< 0.001		< 0.001	< 0.001	< 0.01	< 0.001	< 0.01	< 0.001

The regression curves were examined in the outer and inner portions of the outer shell layer (oOSL and iOSL, respectively) for undetrended Sr/Ca, as well as for Sr/Ca detrended (d) by GR, AR and EL, as well as combinations of GR and AR (GRAR), GR and EL (GREL), and GR, AR and EL (GRAREL). Natural logarithm models were applied for regressions between Sr/Ca and GR, AR and EL, whereas linear models were applied for relationships between Sr/Ca and T. For all regressions, ns, non-significant at $p > 0.05$.

islandica shell growth rate differs significantly between populations and sampling localities (e.g., Begum et al., 2010; Höche et al., 2022). Therefore, data detrending for shell growth-related effects was performed independently between BS and GOM specimens. All other calculations were done with data from BS and GOM combined. In order to achieve the best description of all detrended and undetrended data, linear regressions were computed between Sr/Ca and water temperature, whereas natural logarithms models were used between water temperature and shell ultrastructural properties, i.e., BMU area and elongation. Subsequently, these models were employed to compute temperature prediction intervals (1σ) based on detrended and undetrended shell Sr/Ca. These intervals were then compared with data gathered from field-grown *A. islandica* specimens from NE Iceland (Brosset et al., 2022). Alternatively, for all analyses, models using specimen-specific medians or non-weighted median values, as well as linear and/or natural logarithm detrending and regressions to water temperature for both experiments combined or

TABLE 3 Overview of the regression parameters (slope; R^2, coefficient of determination; p, probability) between shell ultrastructural properties of cultured *Arctica islandica* specimens, i.e., area and elongation of the biomineral units (AR and EL, respectively), shell growth rate (GR; data from Baltic Sea and Gulf of Maine in regular and italic font, respectively), and temperature of the laboratory tanks (T).

Variables		AR	d_{GR}AR		EL	d_{GR}EL
oOSL						
ln(GR)	slope	0.20 ± 0.07	*- 0.05 ± 0.02*		0.04 ± 0.02	*- 0.03 ± 0.01*
	R^2	0.37	*0.35*		0.13	*0.35*
	p	< 0.05	*< 0.05*		ns	*< 0.05*
ln(T)	slope	- 0.007 ± 0.03		- 0.02 ± 0.03	0.003 ± 0.01	- 0.005 ± 0.01
	R^2	0		0	0	0
	p	ns		ns	ns	ns
iOSL						
ln(GR)	slope	0.31 ± 0.12	*0.39 ± 0.15*		- 0.05 ± 0.05	*- 0.001 ± 0.0004*
	R^2	0.33	*0.35*		0	*0.35*
	p	< 0.05	*< 0.05*		ns	*< 0.05*
ln(T)	slope	0.10 ± 0.11		0.22 ± 0.08	0.05 ± 0.01	0.03 ± 0.01
	R^2	0		0.23	0.29	0.19
	p	ns		< 0.05	< 0.01	< 0.05

The regression curves were examined in the outer and inner portions of the outer shell layer (oOSL and iOSL, respectively) for undetrended AR and EL as well as growth rate (GR)-detrended AR and EL data. Natural logarithm models were applied for regressions between ultrastructural data (AR and EL), GR and T. For all regressions, ns, non-significant at $p > 0.05$.

exclusive to the Baltic Sea experiment, can be found in the online repository of the present study, i.e., in Brosset et al. (2023).

3 Results

A. islandica specimens from the Baltic Sea (BS) and the Gulf of Maine (GOM) differed in shell height, thickness and ontogenetic age (Table 1). GOM specimens were younger (3 years-old) than those originating from BS (5 years-old). However, shells from GOM were larger (average height: 38.25 ± 0.22 mm) and thicker (1.21 ± 0.33 mm) than those from BS (height = 16.77 ± 2.29 mm; thickness = 0.27 ± 0.04 mm, Table 1). Given these differences, shell growth rates were calculated separately for BS and GOM specimens (Figure 2A), and size differences were also considered when shell chemical and ultrastructural properties were compared with water temperature.

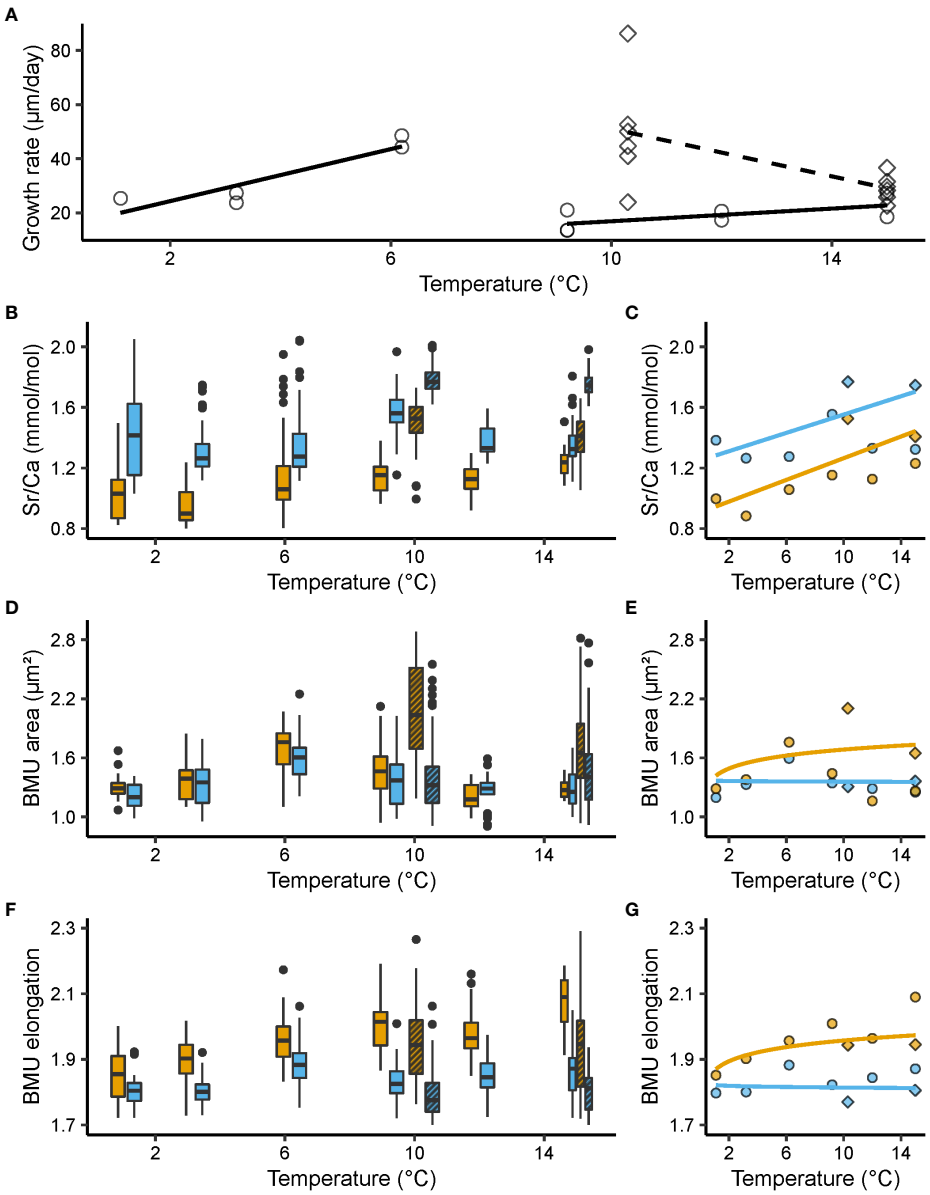

FIGURE 2
Shell growth rate (µm/day), molar Sr/Ca ratios (mmol/mol) and ultrastructural properties, i.e., biomineral unit (BMU) area (µm²) and elongation, from the outer portion of the outer shell layer (oOSL, blue) and the inner portion of the outer shell layer (iOSL, orange) of *Arctica islandica* specimens cultured at 1.1, 3.2, 6.2, 9.2, 10.3, 12 and 15°C. **(A)** Shell growth rate of studied specimens. Black solid line: linear model for Baltic Sea (BS); black dashed line: linear model for Gulf of Maine (GOM). **(B)** Shell Sr/Ca values and corresponding **(C)** median values weighted for the number of specimens (linear regression). **(D)** Area of the BMUs and corresponding **(E)** median values weighted for the number of specimens (natural logarithm regression). **(F)** Elongation of the BMUs and corresponding **(G)** median values weighted for the number of specimens (natural logarithm regression). In **(A, C, E, G)**, circles represent data from the BS experiment, while squares stand for data from the GOM experiment. In **(B, D, F)**, the bold black line represents the median, lower and upper limits of the boxes stand for the first and third quartiles, vertical lines denote the minimum and maximum values, and black dots equal outliers. Solid filled boxes = data from the Baltic Sea experiment; striped boxes = data from the Gulf of Maine experiment.

3.1 Relationship between shell properties and water temperature

3.1.1 Shell Sr/Ca and water temperature

In both sublayers of the outer shell layer, Sr/Ca was significantly ($p < 0.05$) positively linked to water temperature and differed significantly between the adjacent temperature regimes (KW, $p < 0.001$) (Figures 2B, C). When adjusted for multiple comparisons, i.e., Bonferroni correction, this relationship remained significant in more than 60% of the groups tested (Dunn, $p < 0.025$; Table S2). Noteworthy, Sr/Ca ratios of the oOSL were significantly higher than those of the iOSL, on average, by 0.28 ± 0.02 mmol/mol (MWU, $p < 0.001$), with a range of 1.26 to 1.77 and 0.88 to 1.53 mmol/mol in the oOSL and iOSL, respectively (Figures 2B, C). Sr/Ca of the iOSL was more strongly coupled to water temperature, i.e., showed a higher temperature sensitivity (slope = 0.03 ± 0.01 mmol/mol/°C, $R^2 = 0.38$, $p < 0.001$) than that of the oOSL (slope = 0.02 ± 0.01 mmol/mol/°C, $R^2 = 0.22$, $p < 0.05$) (Figure 2C, Table 2).

3.1.2 Shell ultrastructure and water temperature

At some temperature settings, ultrastructural properties differed significantly between the oOSL and iOSL (MWU, $p < 0.001$) (Figures 2D, E). For example, at 1.1, 6.2 and 15°C, BMUs were significantly larger in the iOSL than in oOSL (MWU, $p < 0.05$), whereas nearly identical sizes were observed at the remaining studied temperature regimes (MWU, $p > 0.05$). In the iOSL, the weak tendency toward larger BMUs forming in warmer water was not significant (slope = 0.10 ± 0.11 µm²/°C, $p > 0.05$). Nevertheless, in over 66% of the temperature pairs assessed, a significant difference in the area of the BMUs was obtained (Dunn, $p < 0.025$, Table S2). In contrast, irrespective on the prevailing temperature, the BMU area of the oOSL remained largely unchanged (Dunn, $p > 0.025$ for more than 70% of the tested pairs, Table S2).

The two sublayers of the OSL differed more clearly with respect to BMU elongation. BMUs were approx. 0.14 ± 0.002 more elongated in the iOSL than the oOSL (Figures 2F, G). Between adjacent temperature regimes, the BMU elongation statistically differed (KW, $p < 0.001$), but after Bonferroni adjustment only half of the paired temperature regime comparisons remained significant (Dunn, $p < 0.025$, Table S2). In the iOSL, slightly more needle-shaped BMUs were formed in warmer waters (slope = 0.05 ± 0.01, $R^2 = 0.29$, $p < 0.01$), which was not the case in the oOSL ($p > 0.05$; Table 3).

Compared with field-grown juveniles from NE Iceland (Brosset et al., 2022), the ultrastructure of the studied lab-grown specimens of *A. islandica* was more uniform. The difference cannot only be visually identified (Figure S3), but also expressed in numbers. For example, the size of BMUs varied less in shells of tank-raised bivalves than specimens grown in the field (relative 1σ variance of the mean in the oOSL: 21 vs 18%; iOSL: 20 vs 18%; Table S3). Furthermore, in tank-raised specimens, BMUs were generally much larger (oOSL: 1.47 vs 0.85 µm²; iOSL: 1.54 vs 0.97 µm²) and more elongated (oOSL: 1.85 vs 1.78; iOSL: 1.96 vs 1.77; Table S3) than in field specimens.

3.1.3 Shell growth rate and water temperature

At large, the shell growth rate of the specimens selected for this study decreased with temperature (Figure 2A). This trend was steep in GOM shells (slope = - 4.39 ± 1.83 µm/day/°C, $R^2 = 0.30$, $p < 0.01$) but non-significant in BS specimens (slope = - 0.84 ± 0.71 µm/day/°C, $p > 0.05$). The relationship between BS shell growth rate and temperature could also be described with two linear trends, which would better address the abrupt decline of shell growth rate at around 6°C (Figure 2A). Between 1.1 and 6.2°C, shell growth rate of BS specimens increased by 76% (slope = 4.81 ± 1.27 µm/day/°C, $R^2 = 0.77$, $p < 0.01$), ranging from approx. 24.23 ± 1.07 µm/day at 1.1°C to 42.71 ± 6.36 µm/day at 6.2°C. In warmer water, shell growth of BS shells declined and merely 16.60 ± 3.73 µm were added per day at 9.2°C. Between 9.2 and 15°C, daily growth rate increased slightly (slope = 1.17 ± 0.63 µm/day/°C, $R = 0.29$, $p < 0.05$), but only attained 27.53 ± 5.51 µm/day. In contrast, GOM specimens grew, on average, much faster than shells from BS, i.e., 54.79 ± 19.46 µm/day at 10.3°C and 29.88 ± 4.47 µm/day at 15°C, which translated into a gradual reduction of shell growth by nearly 10% for every degree Celsius increase. Growth at 15°C was still significantly faster (on average, 7.21 ± 1.02 µm/day faster; $p < 0.001$) in GOM specimens than in shells from BS. It should be added that the six GOM specimens showed high variability in daily growth rate at 10.3°C, ranging from 23.89 to 86.26 µm/day (Figure 2A).

3.2 Relationship between shell properties

3.2.1 Sr/Ca vs growth rate

In both OSL sublayers, Sr/Ca correlated with the shell growth rate of the specimens considered, but the signs differed between the two experiments (Figure 3A, Table 2). In BS specimens, faster shell growth was associated with lower Sr/Ca values (Table 2), specifically, in the oOSL (slope = - 0.20 ± 0.07 mmol/mol per 1 µm/day, $R^2 = 0.40$, $p < 0.05$). In contrast, shell growth rate was predominantly positively linked to Sr/Ca in GOM shells, specifically in the iOSL (slope = 0.10 ± 0.04 mmol/mol per 1 µm/day, $R^2 = 0.35$, $p < 0.05$), while the slope was less steep in the oOSL (slope = 0.02 ± 0.01, $R^2 = 0.35$, $p < 0.05$; Table 2).

3.2.2 Sr/Ca vs ultrastructure

Sr/Ca was significantly correlated to the ultrastructural properties of the shells, with a comparable Sr/Ca difference between the OSL sublayers for both experiments (Figures 3C, E and Table 2). In the iOSL, 53% of the Sr/Ca variance could be explained by the size of the BMUs, with an increase of 0.80 ± 0.15 mmol/mol/µm² ($p < 0.001$), whereas only a non-significant positive correlation was found between Sr/Ca and BMU elongation ($p > 0.05$). The link between Sr/Ca and BMU elongation was negative, significant and much stronger in the oOSL ($R^2 = 0.53$, $p < 0.001$) indicating that the strontium content was higher in rounder BMUs (Table 2). In contrast, Sr/Ca was not significantly correlated to the BMU area in the oOSL ($p > 0.05$).

3.2.3 Shell growth vs ultrastructure

Ultrastructural properties and shell growth rate were significantly correlated (Table 3). For example, in the iOSL, the

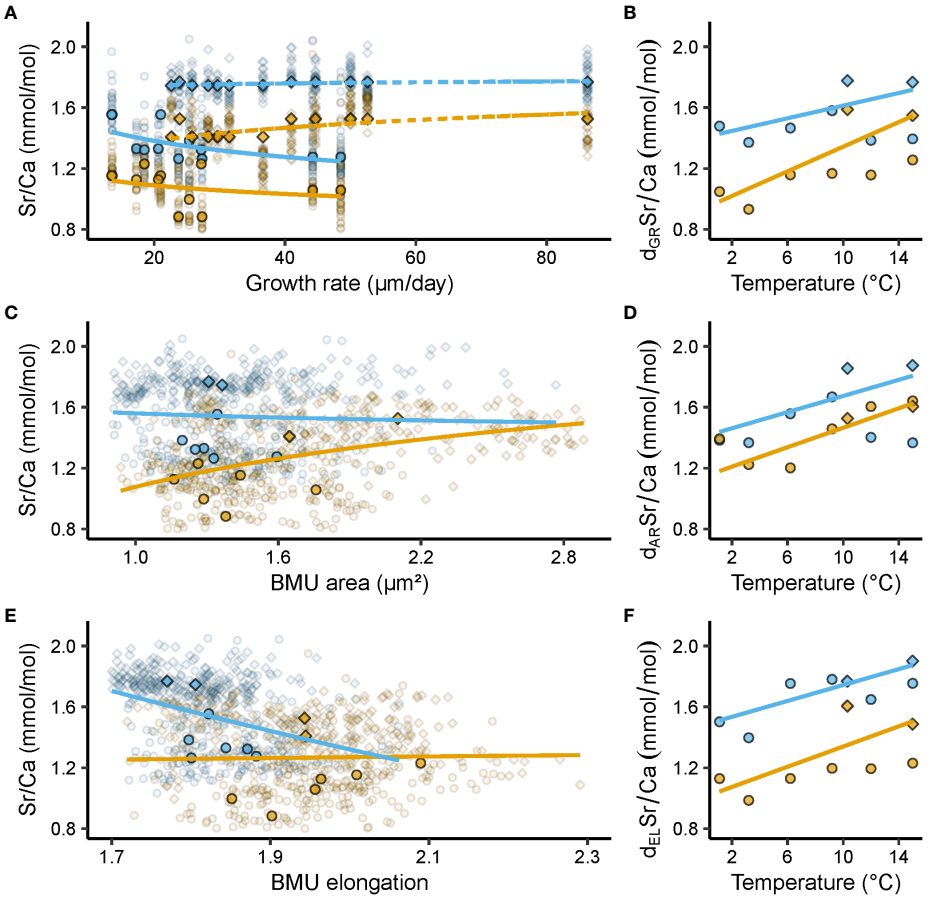

FIGURE 3
Relationships between shell Sr/Ca ratios (mmol/mol) and growth rate (µm/day), ultrastructural properties, i.e., biomineral unit (BMU) area (µm²) and elongation, and temperature (°C). Blue and orange denote data from the outer and inner portion of the outer shell layer (oOSL, iOSL), respectively, of *Arctica islandica* specimens cultured at 1.1, 3.2, 6.2, 9.2, 10.3, 12 and 15°C. **(A)** Relationship between shell Sr/Ca and growth rate (GR) (solid line = Baltic Sea specimens; dashed line = Gulf of Maine specimens). **(B)** Relationship between detrended (d) Sr/Ca and temperature (T), after removal of GR-related effects. **(C)** Relationship between Sr/Ca and BMU area (AR). **(D)** AR-detrended Sr/Ca vs T. **(E)** Relationship between Sr/Ca and BMU elongation (EL). **(F)** EL-detrended Sr/Ca vs T. Circles denote data from the Baltic Sea experiment, while squares stand for data from the Gulf of Maine experiment. In **(A, C, E)** opaque symbols = median weighted for the number of specimens, translucent symbols = raw data from which medians were calculated. All regression models were fitted to the median Sr/Ca values of a given temperature regime, weighted for the number of specimens, with a natural logarithm function for GR, AR and EL, and a linear function for T (regression parameters depicted in Table 2).

BMU area variability explained by the shell growth rate varied between 33 and 35% for BS and GOM shells, respectively ($p < 0.05$; Figure 4A, Table 3). The size of the BMUs increased between 0.31 ± 0.12 µm² (BS) and 0.39 ± 0.15 µm² (GOM) for each µm/day of shell growth (Table 3). In the oOSL of BS specimens, larger BMUs were also formed during faster shell growth (slope = 0.20 ± 0.07 µm² per µm/day; $R^2 = 0.37$, $p < 0.05$), whereas the BMU area decreased slightly with growth rate in GOM shells (slope = - 0.05 ± 0.02, $R^2 = 0.35$, $p < 0.05$, Table 3).

3.3 Relationship between detrended shell properties and water temperature

3.3.1 Ultrastructure-detrended Sr/Ca vs temperature

Once the correlation between Sr/Ca and BMU elongation was mathematically eliminated, d_{EL}Sr/Ca values of the oOSL correlated much stronger with water temperature than undetrended Sr/Ca ($R^2 = 0.63$, $p < 0.001$ vs $R^2 = 0.22$, $p < 0.05$, respectively; Figure 3E, Table 2). Likewise, mathematical elimination of BMU area-related effects from shell Sr/Ca ratios increased the correlation between Sr/Ca and water temperature. For example, 75% of d_{AR}Sr/Ca variance in the iOSL was explained by the temperature (Figure 3D, Table 2).

3.3.2 Growth rate-detrended Sr/Ca vs temperature

After elimination of growth rate-related effects, shell Sr/Ca fmars.2023.1279164data (d_{GR}Sr/Ca) were still positively correlated to water temperature (Figure 3B), but the temperature sensitivity of Sr/Ca of the oOSL was weaker than before detrending (slope = 0.01 ± 0.01 mmol/mol/°C, $R^2 = 0.16$, $p < 0.05$; compare Figures 3B, 2B). In contrast, 41% of the iOSL d_{GR}Sr/Ca variance was explained by water temperature, i.e., an increase by more than 7% compared to undetrended Sr/Ca data (Table 2).

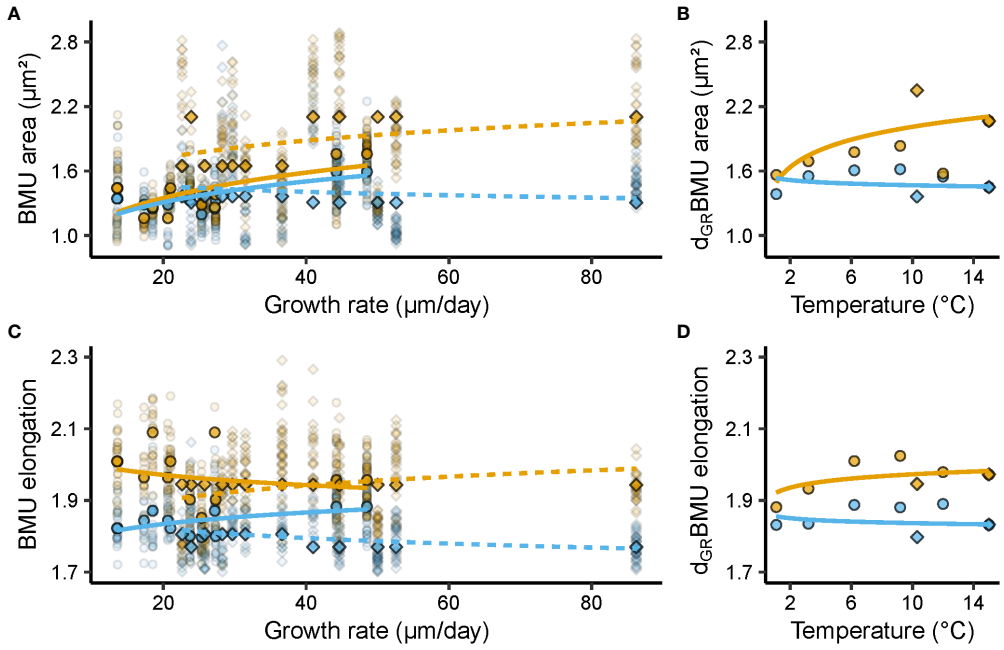

FIGURE 4
Relationships between shell ultrastructural properties, i.e., biomineral unit (BMU) area (µm²) and elongation, growth rate (µm/day), and temperature (°C). Blue and orange denote data from the outer and inner portion of the outer shell layer (oOSL, iOSL), respectively, of *Arctica islandica* specimens cultured at 1.1, 3.2, 6.2, 9.2, 10.3, 12 and 15°C. **(A)** Relationship between BMU area and shell growth rate (GR). **(B)** Relationship between GR-detrended (d) BMU area (AR) and temperature (T). **(C)** Relationship between BMU elongation (EL) and GR. **(D)** GR-detrended EL vs T. In **(A, C)** solid line = Baltic Sea specimens; dashed line = Gulf of Maine specimens. Circles denote data from the Baltic Sea experiment, while squares stand for data from the Gulf of Maine experiment. Opaque symbols = median weighted for the number of specimens; translucent symbols = raw data from which medians were calculated. All regression models were fitted to the median BMU area and elongation values of a given temperature regime, weighted for the number of specimens, with a natural logarithm function for GR and T (regression parameters depicted in Table 3).

3.3.3 Combined shell growth and ultrastructure-detrended Sr/Ca vs temperature

Similar to undetrended Sr/Ca, d_{GR}Sr/Ca was positively linked to the BMU area in the iOSL (R^2 = 0.53, $p < 0.001$; Figures 5A, C, Table 2). Therefore, the double-detrending of Sr/Ca (i.e., detrending by shell growth rate and BMU area [GRAR]), resulted in comparable results as those obtained by simple detrending (GR, AR), and no significant increase in R^2 was identified for d_{GRAR}Sr/Ca vs temperature (Table 2). However, the temperature sensitivity of d_{GRAR}Sr/Ca of the iOSL doubled compared to simple detrending (0.06 ± 0.01 vs 0.03 ± 0.01 mmol/mol/°C; Figures 5B, D). In the oOSL, the temperature sensitivity increased up to 0.04 ± 0.01 mmol/mol/°C for d_{GREL}Sr/Ca. Furthermore, a combined detrending of Sr/Ca by growth rate, BMU area and elongation (d_{GRAREL}Sr/Ca; Figure 5E) tripled the temperature sensitivity of Sr/Ca of the oOSL and increased the temperature sensitivity by 0.06 ± 0.002 mmol/mol/°C in the iOSL (Figure 5F), albeit at the expense of explained variability (Table 2). However, in both OSL sublayers, the linear models between d_{GRAREL}Sr/Ca and water temperature still showed a better fit that those obtained with undetrended Sr/Ca data (R^2 = 0.41 and 0.44 in the oOSL and iOSL, respectively; $p < 0.001$; Table 2).

3.3.4 Growth rate-detrended ultrastructural properties vs temperature

Growth rate-detrended BMU area (d_{GR}AR) data were positively correlated to water temperature in the iOSL (Figure 4B, Table 3). 23% of the d_{GR}AR variance in the iOSL could be significantly ($p < 0.05$) explained by water temperature (natural logarithm model) and sensitivity increased to 0.23 ± 0.08 µm²/°C, whereas the regression model was not significant for undetrended BMU area data (Figure 4B, Table 3). Detrending of the BMU elongation values for growth rate-related effects resulted in lower R^2 data and reduced temperature sensitivity compared to undetrended data of the iOSL (slope = 0.03 ± 0.01 per °C, R^2 = 0.19, $p < 0.05$; Figure 4D, Table 3).

4 Discussion

The present study provided new insights into the complex relationships between shell Sr/Ca of *Arctica islandica* and water temperature and confirmed previous observations and assumptions. For example, a layer-specific chemical analysis is mandatory, because the Sr content is strongly linked to the prevailing ultrastructure and is higher in the oOSL than iOSL (HOM vs CA ultrastructure). Similar findings were reported for the ocean quahog by many previous studies (e.g., Schöne et al., 2011; Karney et al., 2012; Schöne et al., 2013; Shirai et al., 2014). In addition, to properly identify relationships between shell Sr/Ca and temperature, a broad range of different experimental temperature conditions needs to be assessed (here: 1 to 15°C), specifically near the optimal growth temperature of 12 to 18°C of *A. islandica* (Witbaard et al., 1997).

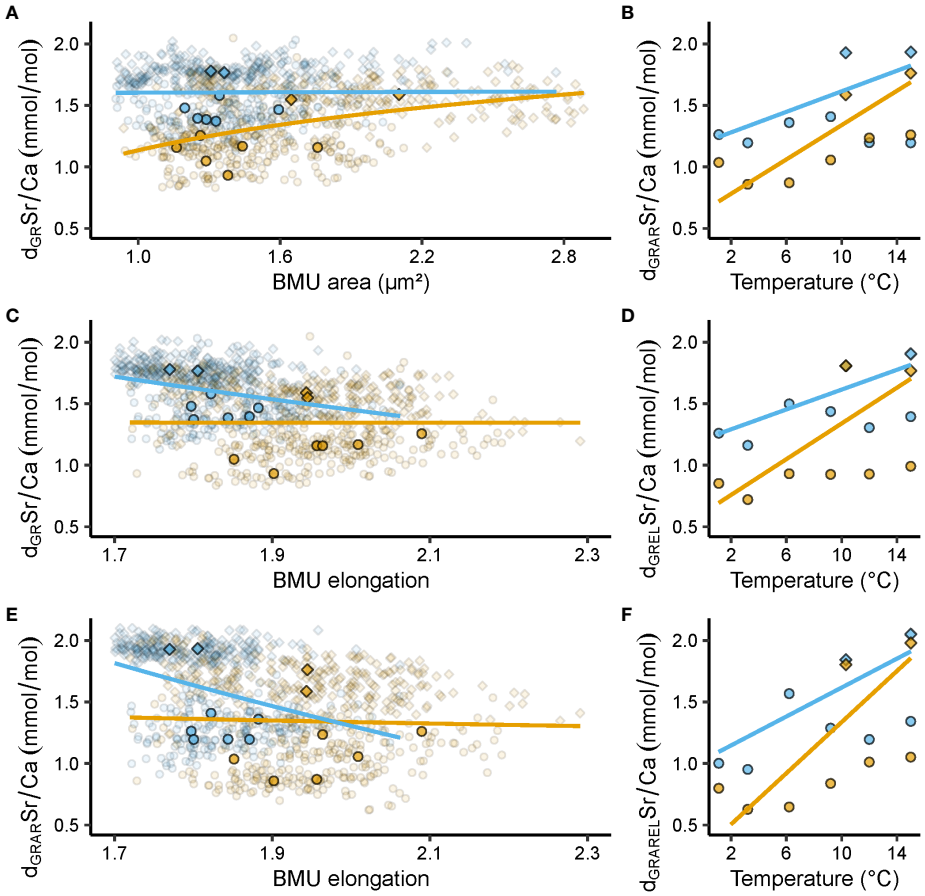

FIGURE 5
Relationships between shell Sr/Ca ratios (mmol/mol), ultrastructural properties, i.e., biomineral unit (BMU) area (µm²) and elongation, and temperature (°C). Blue and orange denote data from the outer and inner portion of the outer shell layer (oOSL, iOSL), respectively, of *Arctica islandica* specimens cultured at 1.1, 3.2, 6.2, 9.2, 10.3, 12 and 15°C. **(A)** Relationship between growth rate (GR)-detrended (d) shell Sr/Ca data and BMU area (AR). **(B)** Relationship between GR and AR-detrended Sr/Ca data and temperature (T). **(C)** Relationship between GR-detrended shell Sr/Ca data and BMU elongation (EL). **(D)** GR and EL-detrended Sr/Ca data vs T. **(E)** Relationship between GR and AR-detrended shell Sr/Ca data and EL. **(F)** GRAREL-detrended Sr/Ca data vs T. Circles denote data from the Baltic Sea experiment, while squares stand for data from the Gulf of Maine experiment. In **(A, C, E)**, opaque symbols = median weighted for the number of specimens; translucent symbols = raw data from which medians were calculated. All regression models were fitted to the median Sr/Ca values of a given temperature regime, weighted for the number of specimens, with a natural logarithm function for GR, AR and EL, and a linear function for T (regression parameters depicted in Table 2).

Most importantly, the present study confirmed the finding by Brosset et al. (2022) according to which shell Sr/Ca of field-grown *A. islandica* contains information on water temperature (positive correlation Figures 2B, C, Table 2), but is also controlled by growth rate, ultrastructure and other environmental variables. However, as shown here, shell Sr/Ca values of laboratory-raised specimens provided much more robust temperature estimates than field-grown bivalves, especially after mathematical elimination of ultrastructure-related effects from Sr/Ca data (Figures 2–5, Table 2). In tangible terms, the correlation of (ultrastructure-detrended) shell Sr/Ca with water temperature was much stronger in specimens grown in laboratory tanks (up to $R^2 = 0.75$; this study) than in nature ($R^2 = 0.26$; Brosset et al., 2022). Very likely, this can be attributed to more equable growth conditions in the laboratory minimizing environmental biases.

The present work also demonstrated that transfer functions calibrated with tank specimens cannot be used to compute temperature from Sr/Ca data of field-grown *A. islandica* specimens. This is partly due to the fact that the temperature sensitivity of Sr/Ca was stronger in tank shells than in shells of specimens from the field (oOSL: 0.03 vs 0.007 mmol/mol/°C; iOSL: 0.03 vs 0.02 mmol/mol/°C). In addition, BMUs of lab-grown specimens were larger (oOSL) and more elongated (iOSL) than in wild specimens, so that transfer functions based on ultrastructure-detrended Sr/Ca data can likewise not be applied to specimens from the field.

Overall, the findings suggested that the shell Sr/Ca thermometer of ocean quahogs merely works well under artificial laboratory conditions (temperature predicted up to ± 2.6°C in the oOSL, ± 1.0°C in the iOSL, Figure 6), but not in nature where the Sr/Ca vs temperature relationship is apparently strongly biased by environmental conditions that can hardly be quantified and corrected for. In field-grown specimens, the explained variability of shell Sr/Ca is simply too low (R^2 = 0.04 and 0.30 in the oOSL and the iOSL, respectively,

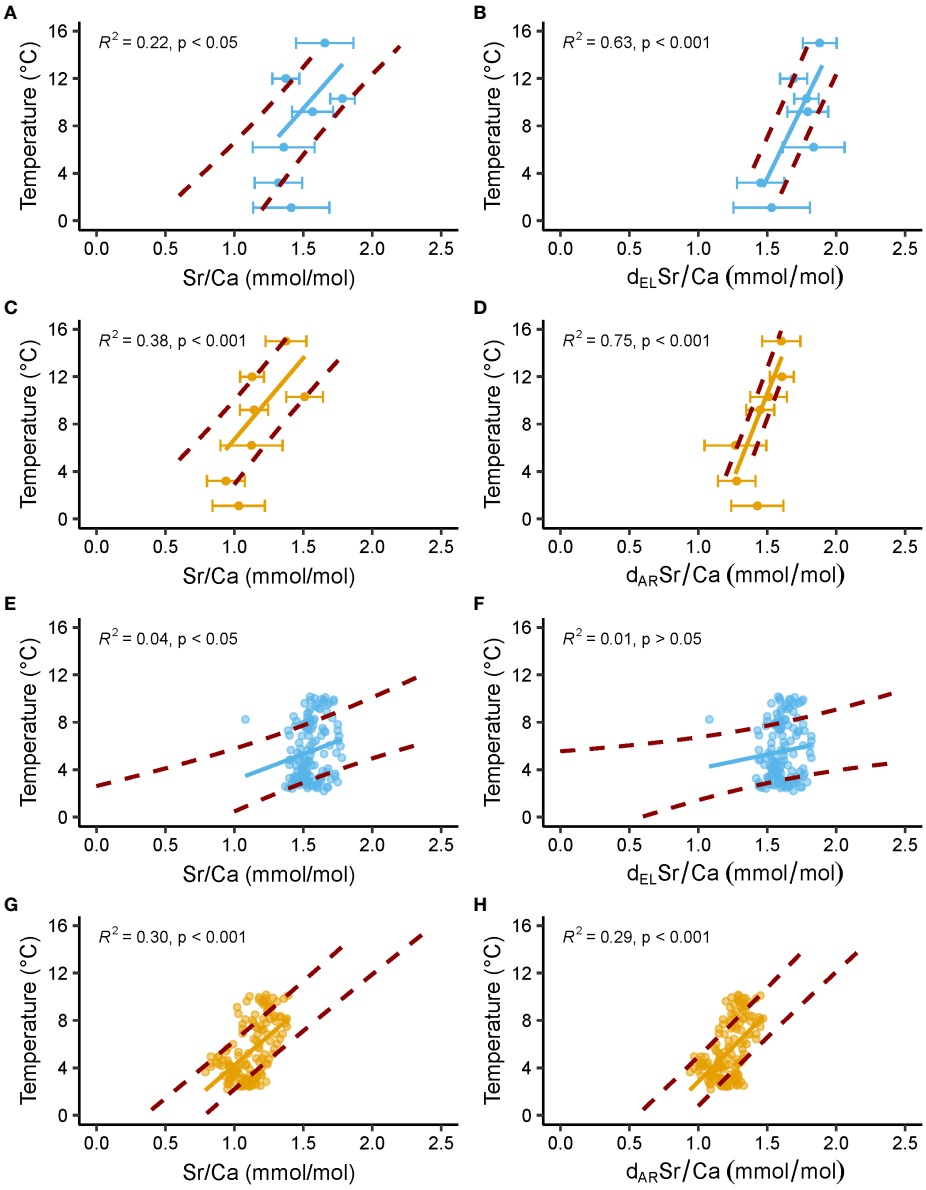

FIGURE 6
Temperature predicted from shell Sr/Ca ratios of laboratory-grown and field-grown *A. islandica* specimens. Blue and orange denote data from the outer and inner portion of the outer shell layer (oOSL, iOSL), respectively. Solid line = linear regression between predicted temperature and measured Sr/Ca; red dashed lines = upper and lower limits of the 1σ temperature interval predicted from measured Sr/Ca data. **(A–D)** Data from Baltic Sea and Gulf of Maine specimens cultured at 1.1, 3.2, 6.2, 9.2, 10.3, 12 and 15°C in laboratory tanks. Error bars = average ± 1σ. **(E–H)** Data from NE Iceland specimens grown in nature (Brosset et al., 2022). In **(B, F)** Sr/Ca data are detrended (d) for the elongation (EL) of individual biomineral units (BMUs) of the shell ultrastructure, whereas Sr/Ca data detrended for the area (AR) of the BMUs are depicted in **(D, H)**.

Figure 6) and the prediction uncertainty too large for a reliable reconstruction of water temperature (prediction interval of ± 2.1°C and ± 2.4°C in the iOSL and oOSL, respectively; Figure 6). It is important to note that Sr/Ca values in seawater can vary temporally and regionally, particularly in coastal areas (Lebrato et al., 2020; Lebrato et al., 2021; Khare et al., 2023). Assuming a constant Sr/Ca composition of the water can introduce bias in temperature estimates from bivalve shell Sr/Ca, especially when the temperature sensitivity of shell Sr/Ca is low. This underlines the need to obtain highly resolved seasonal location-specific Sr/Ca_{water} data in future studies, particularly in regions affected by riverine influx (e.g., Khare et al., 2023).

4.1 Predicted and observed relationship of Sr/Ca vs temperature

The observed positive correlation between shell Sr/Ca and temperature is in agreement with both thermodynamic expectations and the lattice strain model (Gaetani and Cohen, 2006). Note that the same trend is obtained if only the data from the Baltic Sea are used (see Brosset et al., 2023). In the crystal lattice of aragonite, Sr^{2+} can substitute for Ca^{2+} due to the same charge and similar ion size (Sr^{2+} measures 1.31 Å in 9-fold coordination, Ca^{2+} 1.18 Å, Shannon, 1976). This enables strontium ions to

occupy the same sites as calcium ions without significantly disrupting the lattice structure. With rising temperature, the lattice distortions increase and allow for more Sr^{2+} to be incorporated, resulting in higher Sr/Ca ratios (Gaetani and Cohen, 2006). The temperature sensitivity of shell Sr/Ca was nearly identical to such expected for thermodynamic equilibrium, i.e., 0.04 mmol/mol/°C (Table 2; Gaetani and Cohen, 2006). This suggests that the increase in strontium partition coefficient during moderate and rapid shell growth (HOM and CA ultrastructure) was primarily governed by thermodynamic factors.

In contrast to the temperature sensitivity, significant differences were found between predicted and observed Sr/Ca levels. For example, the Sr/Ca values of the CA ultrastructure of the iOSL (1.37 ± 0.15 mmol/mol at 15°C, Figure 2B) were almost three times higher than predicted by thermodynamics and the lattice strain model (0.51 mmol/mol at 15°C; Gaetani and Cohen, 2006). Even higher values were measured in the homogenous oOSL (1.64 ± 0.19 mmol/mol at 15°C; Figure 2B) and in particular, in the ISP ultrastructure of annual growth lines (> 3 mmol/mol, Schöne et al., 2013; Schöne et al., 2023), indicating that additional factors controlled the incorporation of strontium into the shell.

As outlined in more detail in Brosset et al. (2022), the size and shape of BMUs and ultimately, the habit of aragonite crystals could have been responsible for the Sr enrichment in the studied shells. The varying strontium concentrations in the different ultrastructure types (CA < HOM < ISP) may be explained by the amount of specific crystal faces facilitating the incorporation of trace impurities, for example, due to lattice defects (e.g., Plummer and Busenberg, 1987; Paquette and Reeder, 1995; Mavromatis et al., 2022). The substitution of Ca^{2+} by compatible ions is energetically less costly in crystals with a larger number of lattice defects. Furthermore, in aragonite, much less energy is required to substitute Ca^{2+} by Sr^{2+} ions on the surface than deeper inside of the crystal (Menadakis et al., 2008). Large exposed aragonite crystal faces thus promote the substitution of Ca^{2+} by Sr^{2+} (Menadakis et al., 2008). This may explain why the large, blocky, idiomorphic BMUs occurring at the annual growth lines contain much more strontium than xenomorphic BMUs lacking a distinct habit such as the granular HOM-BMUs of the oOSL (often irregularly shaped twinned crystallites). The highly ramified and convoluted CA-BMUs of the iOSL likely have the least developed primary crystal faces and thus come with the lowest Sr/Ca values.

An alternative or complementary explanation for the strongly varying Sr concentrations (CA < HOM < ISP) and the different relationships between Sr/Ca and temperature in the different ultrastructures (positive in HOM and CA, negative if ISP is included) may include differences in energy allocation or availability. Given that Sr/Ca values in shells of ocean quahogs remain below such observed in synthetic aragonite and above values expected for thermodynamic equilibrium, an active, energy-consumptive process seems to regulate the amount of trace impurities that end up in the shell aragonite. Such a control may be required to maintain specific mechanical properties of the shell and facilitate the formation of specific ultrastructures. It remains unclear how exactly this is achieved, e.g., by pumping undesirable ions out of the extrapallial space or by producing molecules capable to capture undesirable ions to prevent their incorporation into the shell carbonate.

It is further hypothesized that more primitive ultrastructures, i.e., ISP, are formed when less energy is available or less energy is allocated for biomineralization. In *A. islandica*, ISP ultrastructures are formed during times of strongly reduced metabolic rate during formation of annual growth lines (Schöne et al., 2023). In addition, ISP is increasingly formed during later stages of life as a result of gradually declining shell growth rate and energy-rerouting to body maintenance and gonad production, rather than biomineralization and active control over trace impurity content of the shell. As a consequence, ISP ultrastructures are then not limited to annual growth lines, but are also produced during other times of the growing season and hence, the proportion of ISP relative to CA and HOM increases gradually through lifetime. Increasingly narrower growth bands are deposited as the bivalve ages and the actual annual growth lines may be challenging to identify. Very likely, during later stages of life, shell growth with CA and HOM formation only occurs when sufficient food is available. This would be supported by the high valve gape activity and shell growth observed in *A. islandica* specimens at high [Chl-a], i.e., during phytoplankton blooms (Ballesta-Artero et al., 2017).

It is hypothesized here that during ISP formation, similar mechanisms are at work that control the incorporation of Sr into abiogenic aragonite, i.e., surface entrapment during crystal growth (Watson, 1996; Watson, 2004; Gaetani and Cohen, 2006). At lower temperatures, the rate of crystal growth is faster than the transport of Sr^{2+} to the near-surface region of the crystal and solid solution diffusion thus limited. The chemistry of the near-surface region thus becomes 'entrapped' resulting in higher Sr/Ca values in the crystal. With increasing temperature, the solid solution diffusion rate increases and the Sr/Ca values of the forming crystal decrease gradually. This mechanism has been evoked to explain the negative correlation between Sr/Ca and temperature in synthetic aragonite (Gaetani and Cohen, 2006), and may likewise be at work during ISP formation, i.e., during times when vital effects are at minimum. In contrast, when sufficient energy is available, the bivalve exerts strong control over the amount of Sr^{2+} that substitutes for Ca^{2+} in the crystal lattice and perhaps, thermodynamic processes prevail over surface entrapment so that a positive relationship establishes between shell Sr/Ca and temperature.

The positive correlation between Sr/Ca and temperature in laboratory-grown shells further increases (up to R^2 = 0.75, Table 2), if the Sr/Ca data are mathematically corrected for ultrastructure and growth rate-related effects. According to these findings, the relationship between shell Sr/Ca and temperature in laboratory-grown *A. islandica* specimens is predominantly governed by ultrastructure properties or processes related to ultrastructure formation. However, the temperature sensitivity of Sr/Ca ratios corrected for ultrastructure and growth rate-related effects (d_{GRAR}, d_{GREL} and d_{GRAREL}Sr/Ca) exceeded predictions of the lattice strain model as well as thermodynamics and reached values of up to 0.09 ± 0.02 mmol/mol/°C (d_{GRAREL}Sr/Ca of the iOSL vs T; Table 2). We currently do not have a conclusive explanation for this observation.

Noteworthy, the shell growth rate of the specimens selected for this study showed highly inconsistent trends with water temperature, both between the two experiments and across the studied temperature range (Figure 2A). It should be added that the mathematical elimination of growth rate-related effects from shell Sr/Ca data barely improved the correlation between Sr and temperature (Figure 3B, Table 2). Accordingly, for specimens grown under stable laboratory conditions selected for this study, kinetics do not seem to be the main factor regulating the incorporation of strontium into shells of *A. islandica*.

4.2 Sr/Ca thermometer only works in laboratory-grown *A. islandica*

As expected, tank-grown specimens formed shells with more uniform ultrastructure than wild specimens, possibly as a result of more equable, undisturbed growth conditions. For example, aside from HOM (oOSL) and CA (iOSL), no other ultrastructure type was formed under laboratory conditions after the acclimatization period. Specifically, fine complex cross-lamellar ultrastructure was absent, which was often reported in conjunction with stressful environmental conditions (Höche et al., 2022). Likewise, no ISP was produced, which typically occurs during annual growth line formation, i.e., during times of very slow growth (Dunca et al., 2009; Schöne et al., 2011; Karney et al., 2012; Schöne et al., 2013). Also, at a given temperature regime and within a given temperature range, BMU sizes exhibited less variability in tank-grown bivalves than specimens grown in the field (Table S3). Notably, BMUs in shells of tank specimens were 73% (oOSL) to 59% (iOSL) larger and 4% (oOSL) to 11% (iOSL) more needle-shaped than in shells of wild specimens (Table 3S).

Most likely, the more uniform ultrastructure in conjunction with larger/more elongated BMUs of laboratory-grown specimens was the main reason why shell Sr/Ca was more strongly coupled with temperature than Sr/Ca of wild *A. islandica*. As illustrated by many previous studies, some element chemical properties, specifically for Sr and Mg, are strongly tied to the prevailing shell nanoarchitecture (e.g., Schöne et al., 2011; Karney et al., 2012; Schöne et al., 2013; Shirai et al., 2014; Höche et al., 2022). Accordingly, if the shell ultrastructure properties change as the result of physiological or environmental variations (other than temperature) (compare Höche et al., 2022), the relationship between shell Sr/Ca and temperature will break down. If that assumption holds true, Sr/Ca-based temperature reconstructions are limited to ocean quahogs grown under optimum conditions in laboratory tanks, unless the factors controlling ultrastructural variations in the field are known in detail and can be quantified. It may be worthwhile to study if similar observations can be made in other species.

4.3 Considerations on tank experiments

Although the relationship between shell Sr/Ca and temperature observed in *A. islandica* specimens grown in laboratory tanks cannot be used to reconstruct temperature from field grown specimens, such experiments can provide insights into principles behind the Sr incorporation into shells. Specifically, controlled tank experiments can help to quantify the degree to which Sr/Ca values of bivalve shells are controlled by a single environmental variable, here water temperature, while other environmental disturbances are kept at minimum. In comparison with field-grown specimens this can reveal which environmental variables mask the temperature information recorded in shell Sr/Ca. Potentially, this can lead to the development of methods capable of retaining a larger proportion of the temperature signal encoded in this element/Ca ratio of wild *A. islandica* than currently possible.

To reliably identify relationships between shell properties and temperature, tank experiments should be conducted at a broad range of different thermal regimes (not just two as in Wanamaker and Gillikin, 2019) encompassing the species-specific optimum growth temperature. This is particularly relevant, if specimens exhibit large individual differences in growth rate and ultrastructure, which was the case in the GOM specimens at 10.3°C (Figures 2A, D, F). Data from the BS experiment provided a more robust insight into the temperature sensitivity of shell Sr/Ca, because specimens were exposed a broad spectrum of different temperatures ranging from 1 to 15°C, i.e., close to the lower growth temperature threshold and overlapping with the reported optimum growth temperature range (12 – 18°C, Witbaard et al., 1997). It would have been interesting to assess the extent of Sr incorporation into the shell of the GOM specimens grown below 10°C. Such an experiment would also have revealed whether individual variations in shell properties were attributable to population-specific (genotypic or epigenetic) differences or arose from ontogenetic factors such as age or size. For example, the high individual variability in growth rate observed at 10.3°C could indicate that specimens of the GOM population exhibited a broader thermal tolerance and growth response to temperature variations (Wanamaker et al., 2019) than *A. islandica* from BS (Table 2).

Slightly different results on the relationship between shell properties and water temperature may also relate to the experimental designs. In the BS experiment of Witbaard et al. (1997), all bivalves were fed *ad libitum* with a known composition of algae (*Isochrysis galbana* and *Dunaliella marina*) and experienced the exact same environmental conditions, i.e, the same water chemistry and salinity (although these were not quantified), but different water temperatures. This approach (parallel experiments) allowed to study the effect of temperature on shell properties of this species (or population) but could not unravel the response of individual specimens to changes of the thermal regime. The latter was possible with the GOM experiment (serial experiment), where the same bivalves were successively exposed to different thermal regimes. However, during the GOM experiment, food supply and salinity varied throughout the experiment (30.20 ± 0.70 at 10.3°C; 30.70 ± 0.70 at 15°C; Beirne et al., 2012; Wanamaker and Gillikin, 2019; food supply was not monitored), because laboratory aquaria were supplied with ambient seawater.

5 Summary and conclusions

As demonstrated here, shell Sr/Ca of laboratory-grown *A. islandica* specimens can be used to reconstruct water temperature with 1σ prediction uncertainty of 1°C. Shell Sr/Cr values increased with water temperature by 0.03 mmol/mol/°C which agrees with thermodynamic expectations. The explained variability was significantly higher than in field-grown specimens (Brosset et al., 2022) and attained 63% in the oOSL (homogeneous ultrastructure) and 75% in the iOSL (crossed-acicular ultrastructure). Most likely, the equable, less biased conditions in the laboratory resulted in the production of a more uniform shell ultrastructure (with larger and more elongated biomineral units) which in turn was associated with less variable Sr/Ca values and a stronger link to water temperature.

Transfer functions based on laboratory specimens cannot be used to compute temperature from Sr/Ca data of field-grown *A. islandica*. Firstly, this is impossible because the temperature sensitivity of Sr/Ca was stronger in tank-grown shells than in wild specimens (oOSL: 0.02 vs 0.007 mmol/mol/°C; iOSL: 0.03 vs 0.02 mmol/mol/°C). Secondly, BMUs of lab-grown specimens were larger (oOSL) and more elongated (iOSL) than in field-grown specimens, so that ultrastructure-detrending of Sr/Ca data leads to different results.

While the shell Sr/Ca thermometer of ocean quahogs works well under artificial laboratory conditions, the Sr/Ca vs temperature relationship is strongly biased by environmental conditions that can hardly be quantified and mathematically eliminated. In field-grown specimens, the explained variability of shell Sr/Ca is too low and the prediction uncertainty too large for a reliable reconstruction of water temperature.

Data availability statement

The datasets presented in this study can be found in online repositories. The names of the repository/repositories and accession number(s) can be found below: Brosset et al., 2023 (https://zenodo.org/record/8249992).

Ethics statement

The manuscript presents research on animals that do not require ethical approval for their study.

Author contributions

CB: Data curation, Formal Analysis, Investigation, Methodology, Validation, Visualization, Writing – original draft, Writing – review & editing. NH: Investigation, Methodology, Writing – review & editing. RW: Resources, Writing – review & editing. KN: Writing – review & editing. KS: Funding acquisition, Writing – review & editing. RM-K: Writing – review & editing. BS: Conceptualization, Data curation, Formal Analysis, Funding acquisition, Investigation, Methodology, Project administration, Supervision, Validation, Writing – original draft, Writing – review & editing.

Funding

The author(s) declare financial support was received for the research, authorship, and/or publication of this article. BRS, SCHO 793/23, German Research Foundation (DFG); KS, JPJSJRP 20181607, Japan Society for Promotion of Science (JSPS) under the Joint Research Projects-LEAD with the DFG (JRPs-LEAD with DFG). The funders had no role in study design, data collection and analysis, decision to publish, or preparation of the manuscript.

Acknowledgments

We thank Alan D. Wanamaker for providing the specimens from the Gulf of Maine experiment. We thank the two reviewers for their comments which helped to improve the clarity of this manuscript.

Conflict of interest

The authors declare that the research was conducted in the absence of any commercial or financial relationships that could be construed as a potential conflict of interest.

Publisher's note

Supplementary material

The Supplementary Material for this article can be found online at: https://www.frontiersin.org/articles/10.3389/fmars.2023.1279164/full#supplementary-material

References

Adey, W. H., and Steneck, R. S. (2001). Thermogeography over time creates biogeographic regions: a temperature/space/time-integrated model and an abundance-weighted test for benthic marine algae. *J. Phycol.* 37, 677–698. doi: 10.1046/j.1529-8817.2001.00176.x

Ballesta-Artero, I., Witbaard, R., Carroll, M. L., and van der Meer, J. (2017). Environmental factors regulating gaping activity of the bivalve *Arctica islandica* in Northern Norway. *Mar. Biol.* 164, 116. doi: 10.1007/s00227-017-3144-7

Beck, J. W., Edwards, R. L., Ito, E., Taylor, F. W., Recy, J., Rougerie, F., et al. (1992). Sea-Surface Temperature from coral skeletal Strontium/Calcium ratios. *Science* 257, 644–647. doi: 10.1126/science.257.5070.644

Begum, S., Basova, L., Heilmayer, O., Philipp, E. E. R., Abele, D., and Brey, T. (2010). Growth and energy budget models of the bivalve *Arctica islandica* at six different sites in the Northeast Atlantic realm. *J. Shellfish Res.* 29, 107–115. doi: 10.2983/035.029.0103

Beirne, E. C., Wanamaker, A. D., and Feindel, S. C. (2012). Experimental validation of environmental controls on the $\delta^{13}C$ of *Arctica islandica* (ocean quahog) shell carbonate. *Geochim. Cosmochim. Acta* 84, 395–409. doi: 10.1016/j.gca.2012.01.021

Belanger, C. L., Jablonski, D., Roy, K., Berke, S. K., Krug, A. Z., and Valentine, J. W. (2012). Global environmental predictors of benthic marine biogeographic structure. *Proc. Natl. Acad. Sci. U.S.A.* 109, 14046–14051. doi: 10.1073/pnas.1212381109

Berg, S., Kutra, D., Kroeger, T., Straehle, C. N., Kausler, B. X., Haubold, C., et al. (2019). ilastik: interactive machine learning for (bio)image analysis. *Nat. Methods* 16, 1226–1232. doi: 10.1038/s41592-019-0582-9

Black, B. A., Griffin, D., van der Sleen, P., Wanamaker, A. D., Speer, J. H., Frank, D. C., et al. (2016). The value of crossdating to retain high-frequency variability, climate signals, and extreme events in environmental proxies. *Glob. Change. Biol.* 22, 2582–2595. doi: 10.1111/gcb.13256

Bogovic, J. A., Hanslovsky, P., Wong, A., and Saalfeld, S. (2016) in *2016 IEEE 13th International Symposium on Biomedical Imaging (ISBI)*, Prague, Czech Republic: IEEE. 1123–1126. doi: 10.1109/ISBI.2016.7493463

Brosset, C., Höche, N., Shirai, K., Nishida, K., Mertz-Kraus, R., Schöne, B. R., et al. (2022). Strong coupling between biomineral morphology and Sr/Ca of *Arctica islandica* (Bivalvia)—Implications for shell Sr/Ca-based temperature estimates. *Minerals* 12, 500. doi: 10.3390/min12050500

Brosset, C., Höche, N., Witbaard, R., Nishida, K., Shirai, K., Mertz-Kraus, R., et al. (2023). Data for "Sr/Ca in shells of laboratory-grown bivalves (*Arctica islandica*) serves as a proxy for water temperature – Perspectives for (paleo)environmental research? doi: 10.5281/ZENODO.8249992

Butler, P. G., Wanamaker, A. D., Scourse, J. D., Richardson, C. A., and Reynolds, D. J. (2013). Variability of marine climate on the North Icelandic Shelf in a 1357-year proxy archive based on growth increments in the bivalve *Arctica islandica*. *Palaeogeogr. Palaeoclimatol. Palaeoecol.* 373, 141–151. doi: 10.1016/j.palaeo.2012.01.016

Cauquoin, A., Werner, M., and Lohmann, G. (2019). Water isotopes – climate relationships for the mid-Holocene and preindustrial period simulated with an isotope-enabled version of MPI-ESM. *Clim. Past* 15, 1913–1937. doi: 10.5194/cp-15-1913-2019

Corrège, T. (2006). Sea surface temperature and salinity reconstruction from coral geochemical tracers. *Palaeogeogr. Palaeoclimatol. Palaeoecol.* 232, 408–428. doi: 10.1016/j.palaeo.2005.10.014

De Winter, N. J., Witbaard, R., Kocken, I. J., Müller, I. A., Guo, J., Goudsmit, B., et al. (2022). Temperature dependence of clumped isotopes (Δ_{47}) in aragonite. *Geophys. Res. Lett.* 49, 1–12. doi: 10.1029/2022GL099479

Dodd, J. R. (1965). Environmental control of strontium and magnesium in *Mytilus*. *Geochim. Cosmochim. Acta* 29, 385–398. doi: 10.1016/0016-7037(65)90035-9

Dodd, J. R., and Crisp, E. L. (1982). Non-linear variation with salinity of Sr/Ca and Mg/Ca ratios in water and aragonitic bivalve shells and implications for paleosalinity studies. *Palaeogeogr. Palaeoclimatol. Palaeoecol.* 38, 45–56. doi: 10.1016/0031-0182(82)90063-3

Dunca, E., Mutvei, H., Göransson, P., Mörth, C.-M., Schöne, B. R., Whitehouse, M. J., et al. (2009). Using ocean quahog (*Arctica islandica*) shells to reconstruct palaeoenvironment in Öresund, Kattegat and Skagerrak, Sweden. *Int. J. Earth Sci. (Geol Rundsch)* 98, 3–17. doi: 10.1007/s00531-008-0348-6

Eiler, J. M. (2011). Paleoclimate reconstruction using carbonate clumped isotope thermometry. *Quat. Sci. Rev.* 30, 3575–3588. doi: 10.1016/j.quascirev.2011.09.001

Foster, L. C., Allison, N., Finch, A. A., and Andersson, C. (2009). Strontium distribution in the shell of the aragonite bivalve *Arctica islandica*: Sr in the shell of *Arctica islandica*. *Geochem. Geophys. Geosyst.* 10, 1–14. doi: 10.1029/2007GC001915

Freitas, P., Clarke, L. J., Kennedy, H., Richardson, C., and Abrantes, F. (2005). Mg/Ca, Sr/Ca, and stable-isotope ($\delta^{18}O$ and $\delta^{13}C$) ratio profiles from the fan mussel *Pinna nobilis*: Seasonal records and temperature relationships. *Geochem. Geophys. Geosyst.* 6, 1–16. doi: 10.1029/2004GC000872

Füllenbach, C. S., Schöne, B. R., Shirai, K., Takahata, N., Ishida, A., and Sano, Y. (2017). Minute co-variations of Sr/Ca ratios and microstructures in the aragonitic shell of *Cerastoderma edule* (Bivalvia) – Are geochemical variations at the ultra-scale masking potential environmental signals? *Geochim. Cosmochim. Acta* 205, 256–271. doi: 10.1016/j.gca.2017.02.019

Gaetani, G. A., and Cohen, A. L. (2006). Element partitioning during precipitation of aragonite from seawater: A framework for understanding paleoproxies. *Geochim. Cosmochim. Acta* 70, 4617–4634. doi: 10.1016/j.gca.2006.07.008

Gillikin, D. P., De Ridder, F., Ulens, H., Elskens, M., Keppens, E., Baeyens, W., et al. (2005). Assessing the reproducibility and reliability of estuarine bivalve shells (*Saxidomus giganteus*) for sea surface temperature reconstruction: Implications for paleoclimate studies. *Palaeogeogr. Palaeoclimatol. Palaeoecol.* 228, 70–85. doi: 10.1016/j.palaeo.2005.03.047

Goberville, E., Beaugrand, G., Sautour, B., Tréguer, P., and Somlit, T. (2010). Climate-driven changes in coastal marine systems of western Europe. *Mar. Ecol. Prog. Ser.* 408, 129–147. doi: 10.3354/meps08564

Hart, S. R., and Blusztajn, J. (1998). Clams as recorders of ocean ridge volcanism and hydrothermal vent field activity. *Science* 280, 883–886. doi: 10.1126/science.280.5365.883

Höche, N., Walliser, E. O., de Winter, N. J., Witbaard, R., and Schöne, B. R. (2021). Temperature-induced microstructural changes in shells of laboratory-grown *Arctica islandica* (Bivalvia). *PloS One* 16, e0247968. doi: 10.1371/journal.pone.0247968

Höche, N., Walliser, E. O., and Schöne, B. R. (2022). Microstructural mapping of *Arctica islandica* shells reveals environmental and physiological controls on biomineral size. *Front. Earth Sci.* 9. doi: 10.3389/feart.2021.781305

Jochum, K. P., Nohl, U., Herwig, K., Lammel, E., Stoll, B., and Hofmann, A. W. (2005). GeoReM: a new geochemical database for reference materials and isotopic standards. *Geostand Geoanalyt Res.* 29, 333–338. doi: 10.1111/j.1751-908X.2005.tb00904.x

Jochum, K. P., Scholz, D., Stoll, B., Weis, U., Wilson, S. A., Yang, Q., et al. (2012). Accurate trace element analysis of speleothems and biogenic calcium carbonates by LA-ICP-MS. *Chem. Geol.* 318-319. doi: 10.1016/j.chemgeo.2012.05.009

Jochum, K. P., Weis, U., Stoll, B., Kuzmin, D., Yang, Q., Raczek, I., et al. (2011). Determination of reference values for NIST SRM 610-617 glasses following ISO guidelines. *Geostand Geoanal Res.* 35, 397–429. doi: 10.1111/j.1751-908X.2011.00120.x

Jones, D. S. (1981). Annual growth increments in shells of *Spisula solidissima* record marine temperature variability. *Science* 211, 165–167. doi: 10.1126/science.211.4478.165

Karney, G. B., Butler, P. G., Speller, S., Scourse, J. D., Richardson, C. A., Schröder, M., et al. (2012). Characterizing the microstructure of *Arctica islandica* shells using NanoSIMS and EBSD. *Geochem. Geophys. Geosyst.* 13, Q04002. doi: 10.1029/2011GC003961

Khare, A., Hughes, H. P., Schijf, J., and Kilbourne, K. H. (2023). Apparently seasonal variations of the seawater Sr/Ca ratio across the Florida Keys Reef Tract. *Geochem Geophys Geosyst* 24, e2022GC010728. doi: 10.1029/2022GC010728

Lebrato, M., Garbe-Schönberg, D., Müller, M. N., Blanco-Ameijeiras, S., Feely, R. A., Lorenzoni, L., et al. (2020). Global variability in seawater Mg:Ca and Sr:Ca ratios in the modern ocean. *Proc. Natl. Acad. Sci. U.S.A.* 117, 22281–22292. doi: 10.1073/pnas.1918943117

Lebrato, M., Garbe-Schönberg, D., Müller, M. N., Blanco-Ameijeiras, S., Feely, R. A., Lorenzoni, L., et al. (2021). Correction for Lebrato et al., Global variability in seawater Mg:Ca and Sr:Ca ratios in the modern ocean. *Proc. Natl. Acad. Sci. U.S.A.* 118, e2119099118. doi: 10.1073/pnas.2119099118

Lohmann, G., and Schöne, B. R. (2013). Climate signatures on decadal to interdecadal time scales as obtained from mollusk shells (*Arctica islandica*) from Iceland. *Palaeogeogr. Palaeoclimatol. Palaeoecol.* 373, 152–162. doi: 10.1016/j.palaeo.2012.08.006

Longerich, H. P., Jackson, S. E., and Günther, D. (1996). Laser ablation inductively coupled plasma mass spectrometric transient signal data acquisition and analyte concentration calculation. *J. Anal. At. Spectrom.* 11, 899–904. doi: 10.1039/JA9961100899

Marali, S., Schöne, B. R., Mertz-Kraus, R., Griffin, S. M., Wanamaker, A. D., Butler, P. G., et al. (2017). Reproducibility of trace element time-series (Na/Ca, Mg/Ca, Mn/Ca, Sr/Ca, and Ba/Ca) within and between specimens of the bivalve *Arctica islandica* – A LA-ICP-MS line scan study. *Palaeogeogr. Palaeoclimatol. Palaeoecol.* 484, 109–128. doi: 10.1016/j.palaeo.2016.11.024

Mavromatis, V., Brazier, J.-M., and Goetschl, K. E. (2022). Controls of temperature and mineral growth rate on Mg incorporation in aragonite. *Geochim. Cosmochim. Acta* 317, 53–64. doi: 10.1016/j.gca.2021.10.015

Menadakis, M., Maroulis, G., and Koutsoukos, P. G. (2008). Incorporation of Mg^{2+}, Sr^{2+}, Ba^{2+} and Zn^{2+} into aragonite and comparison with calcite. *J. Math Chem.* 46, 484–491. doi: 10.1007/s10910-008-9490-4

Paquette, J., and Reeder, R. J. (1995). Relationship between surface structure, growth mechanism, and trace element incorporation in calcite. *Geochim. Cosmochim. Acta* 59, 735–749. doi: 10.1016/0016-7037(95)00004-J

Plummer, L. N., and Busenberg, E. (1987). Thermodynamics of aragonite-strontianite solid solutions: Results from stoichiometric solubility at 25 and 76°C. *Geochim. Cosmochim. Acta* 51, 1393–1411. doi: 10.1016/0016-7037(87)90324-3

Roger, L. M., George, A. D., Shaw, J., Hart, R. D., Roberts, M., Becker, T., et al. (2017). Geochemical and microstructural characterization of two species of cool-water bivalves (*Fulvia tenuicostata* and *Soletellina biradiata*) from Western Australia. *Biogeosciences* 14, 1721–1737. doi: 10.5194/bg-14-1721-2017

Ropes, J. H. (1984). Procedures for preparing acetate peels and evidence validating the annual periodicity of growth lines formed in the shells of ocean quahogs, *Arctica islandica*. *Mar. Fish. Rev.* 46, 27–35.

Rosenheim, B. E., Swart, P. K., Thorrold, S. R., Willenz, P., Berry, L., and Latkoczy, C. (2004). High-resolution Sr/Ca records in sclerosponges calibrated to temperature in situ. *Geol* 32, 145. doi: 10.1130/G20117.1

Schindelin, J., Arganda-Carreras, I., Frise, E., Kaynig, V., Longair, M., Pietzsch, T., et al. (2012). Fiji: an open-source platform for biological-image analysis. *Nat. Methods* 9, 676–682. doi: 10.1038/nmeth.2019

Schmidt, G. A., Annan, J. D., Bartlein, P. J., Cook, B. I., Guilyardi, E., Hargreaves, J. C., et al. (2014). Using palaeo-climate comparisons to constrain future projections in CMIP5. *Clim. Past* 10, 221–250. doi: 10.5194/cp-10-221-2014

Schöne, B. R., Fiebig, J., Pfeiffer, M., Gleβ, R., Hickson, J., Johnson, A. L. A., et al. (2005). Climate records from a bivalved Methuselah (*Arctica islandica*, Mollusca; Iceland). *Palaeogeogr. Palaeoclimatol. Palaeoecol.* 228, 130–148. doi: 10.1016/j.palaeo.2005.03.049

Schöne, B. R., and Krause, R. A. (2016). Retrospective environmental biomonitoring – Mussel Watch expanded. *Global Planetary Change* 144, 228–251. doi: 10.1016/j.gloplacha.2016.08.002

Schöne, B. R., Marali, S., Jantschke, A., Mertz-Kraus, R., Butler, P. G., and Fröhlich, L. (2023). Can element chemical impurities in aragonitic shells of marine bivalves serve as proxies for environmental variability? *Chem. Geol.* 616, 121215. doi: 10.1016/j.chemgeo.2022.121215

Schöne, B. R., Radermacher, P., Zhang, Z., and Jacob, D. E. (2013). Crystal fabrics and element impurities (Sr/Ca, Mg/Ca, and Ba/Ca) in shells of *Arctica islandica*—Implications for paleoclimate reconstructions. *Palaeogeogr. Palaeoclimatol. Palaeoecol.* 373, 50–59. doi: 10.1016/j.palaeo.2011.05.013

Schöne, B. R., Zhang, Z., Radermacher, P., Thébault, J., Jacob, D. E., Nunn, E. V., et al. (2011). Sr/Ca and Mg/Ca ratios of ontogenetically old, long-lived bivalve shells (*Arctica islandica*) and their function as paleotemperature proxies. *Palaeogeogr. Palaeoclimatol. Palaeoecol.* 302, 52–64. doi: 10.1016/j.palaeo.2010.03.016

Shannon, R. D. (1976). Revised effective ionic radii and systematic studies of interatomic distances in halides and chalcogenides. *Acta Cryst A* 32, 751–767. doi: 10.1107/S0567739476001551

Shirai, K., Takahata, N., Yamamoto, H., Omata, T., Sasaki, T., and Sano, Y. (2008). Novel analytical approach to bivalve shell biogeochemistry: A case study of hydrothermal mussel shell. *Geochem. J.* 42, 413–420. doi: 10.2343/geochemj.42.413

Shirai, K., Schöne, B. R., Miyaji, T., Radarmacher, P., Krause, R. A., and Tanabe, K. (2014). Assessment of the mechanism of elemental incorporation into bivalve shells (*Arctica islandica*) based on elemental distribution at the microstructural scale. *Geochim. Cosmochim. Acta* 126, 307–320. doi: 10.1016/j.gca.2013.10.050

Stecher, H. A., Krantz, D. E., Lord, C. J., Luther, G. W., and Bock, K. W. (1996). Profiles of strontium and barium in *Mercenaria mercenaria* and *Spisula solidissima* shells. *Geochim. Cosmochim. Acta* 60, 3445–3456. doi: 10.1016/0016-7037(96)00179-2

Surge, D., and Walker, K. J. (2006). Geochemical variation in microstructural shell layers of the southern quahog (*Mercenaria campechiensis*): Implications for reconstructing seasonality. *Palaeogeography Palaeoclimatology Palaeoecol.* 237, 182–190. doi: 10.1016/j.palaeo.2005.11.016

Toland, H., Perkins, B., Pearce, N., Keenan, F., and Leng, M. J. (2000). A study of sclerochronology by laser ablation ICP-MS. *J. Anal. At. Spectrom.* 15, 1143–1148. doi: 10.1039/b002014l

Tynan, S., Opdyke, B. N., Walczak, M., Eggins, S., and Dutton, A. (2017). Assessment of Mg/Ca in *Saccostrea glomerata* (the Sydney rock oyster) shell as a potential temperature record. *Palaeogeography Palaeoclimatology Palaeoecol.* 484, 79–88. doi: 10.1016/j.palaeo.2016.08.009

van der Walt, S., Schönberger, J. L., Nunez-Iglesias, J., Boulogne, F., Warner, J. D., Yager, N., et al. (2014). scikit-image: image processing in Python. *PeerJ* 2, e453. doi: 10.7717/peerj.453

Węsławski, J. M., Kendall, M. A., Włodarska-Kowalczuk, M., Iken, K., Kędra, M., Legezynska, J., et al. (2011). Climate change effects on Arctic fjord and coastal macrobenthic diversity—Observations and predictions. *Mar. Biodiv* 41, 71–85. doi: 10.1007/s12526-010-0073-9

Wanamaker, A. D., Butler, P. G., Scourse, J. D., Heinemeier, J., Eiríksson, J., Knudsen, K. L., et al. (2012). Surface changes in the North Atlantic meridional overturning circulation during the last millennium. *Nat. Commun.* 3, 1–7. doi: 10.1038/ncomms1901

Wanamaker, A. D., and Gillikin, D. P. (2019). Strontium, magnesium, and barium incorporation in aragonitic shells of juvenile *Arctica islandica*: Insights from temperature controlled experiments. *Chem. Geol.* 526, 117–129. doi: 10.1016/j.chemgeo.2018.02.012

Wanamaker, A. D., Griffin, S. M., Ummenhofer, C. C., Whitney, N. M., Black, B., Parfitt, R., et al. (2019). Pacific climate influences on ocean conditions and extreme shell growth events in the Northwestern Atlantic (Gulf of Maine). *Clim Dyn* 52, 6339–6356. doi: 10.1007/s00382-018-4513-8

Wanamaker, A. D., Heinemeier, J., Scourse, J. D., Richardson, C. A., Butler, P. G., Eiríksson, J., et al. (2008a). Very long-lived mollusks confirm 17th century AD tephra-based radiocarbon reservoir ages for north Icelandic shelf waters. *Radiocarbon* 50, 399–412. doi: 10.1017/S0033822200053510

Wanamaker, A. D. Jr., Kreutz, K. J., Wilson, T., Borns, H. W. Jr., Introne, D. S., and Feindel, S. (2008b). Experimentally determined Mg/Ca and Sr/Ca ratios in juvenile bivalve calcite for *Mytilus edulis*: implications for paleotemperature reconstructions. *Geo-Mar Lett.* 28, 359–368. doi: 10.1007/s00367-008-0112-8

Watson, E. B. (1996). Surface enrichment and trace-element uptake during crystal growth. *Geochim. Cosmochim. Acta* 60, 5013–5020. doi: 10.1016/S0016-7037(96)00299-2

Watson, E. B. (2004). A conceptual model for near-surface kinetic controls on the trace-element and stable isotope composition of abiogenic calcite crystals. *Geochim. Cosmochim. Acta* 68, 1473–1488. doi: 10.1016/j.gca.2003.10.003

Witbaard, R., Franken, R., and Visser, B. (1997). Growth of juvenile *Arctica islandica* under experimental conditions. *Helgoländer Meeresunters.* 51, 417–431. doi: 10.1007/BF02908724

Witbaard, R., Jenness, M. I., van der Borg, K., and Ganssen, G. (1994). Verification of annual growth increments in *Arctica islandica* L. from the North Sea by means of oxygen and carbon isotopes. *J. Sea Res.* 33, 91–101. doi: 10.1016/0077-7579(94)90054-X

Yan, H., Shao, D., Wang, Y., and Sun, L. (2013). Sr/Ca profile of long-lived *Tridacna gigas* bivalves from South China Sea: A new high-resolution SST proxy. *Geochim. Cosmochim. Acta* 112, 52–65. doi: 10.1016/j.gca.2013.03.007

Zacherl, D., Gaines, S. D., and Lonhart, S. I. (2003). The limits to biogeographical distributions: insights from the northward range extension of the marine snail, *Kelletia kelletii* (Forbes 1852): Northward range extension of *Kelletia kelletii*. *J. Biogeogr.* 30, 913–924. doi: 10.1046/j.1365-2699.2003.00899.x

Zhao, L., Schöne, B. R., and Mertz-Kraus, R. (2017). Controls on strontium and barium incorporation into freshwater bivalve shells (*Corbicula fluminea*). *Palaeogeogr. Palaeoclimatol. Palaeoecol.* 465, 386–394. doi: 10.1016/j.palaeo.2015.11.040

frontiers | Frontiers in Marine Science

TYPE Original Research
PUBLISHED 06 December 2023
DOI 10.3389/fmars.2023.1293823

OPEN ACCESS

EDITED BY
Tsuyoshi Watanabe,
Hokkaido University, Japan

REVIEWED BY
Kotaro Shirai,
The University of Tokyo, Japan
Benjamin Linzmeier,
University of South Alabama, United States
Steffen Hetzinger,
Christian-Albrechts-Universität zu Kiel, Germany

*CORRESPONDENCE
Hunter P. Hughes
hphughes@email.unc.edu

RECEIVED 13 September 2023
ACCEPTED 23 November 2023
PUBLISHED 06 December 2023

CITATION
Hughes HP, Surge D, Orland IJ, Zettler ML and Moss DK (2023) Seasonal SIMS $\delta^{18}O$ record in *Astarte borealis* from the Baltic Sea tracks a modern regime shift in the NAO. *Front. Mar. Sci.* 10:1293823. doi: 10.3389/fmars.2023.1293823

Seasonal SIMS $\delta^{18}O$ record in *Astarte borealis* from the Baltic Sea tracks a modern regime shift in the NAO

Hunter P. Hughes[1*], Donna Surge[1], Ian J. Orland[2,3], Michael L. Zettler[4] and David K. Moss[5]

[1]Earth, Marine and Environmental Sciences, University of North Carolina, Chapel Hill, NC, United States, [2]Department of Geoscience, University of Wisconsin-Madison, Madison, WI, United States, [3]Wisconsin Geological and Natural History Survey, University of Wisconsin-Madison, Madison, WI, United States, [4]Department of Biological Oceanography, Leibniz-Institute for Baltic Sea Research, Rostock, Germany, [5]Sam Houston State University, Environmental and Geosciences, Huntsville, TX, United States

Introduction: *Astarte borealis* holds great potential as an archive of seasonal paleoclimate, especially due to its long lifespan (several decades to more than a century) and ubiquitous distribution across high northern latitudes. Furthermore, recent work demonstrates that the isotope geochemistry of the aragonite shell is a faithful proxy of environmental conditions. However, the exceedingly slow growth rates of *A. borealis* in some locations (<0.2mm/year) make it difficult to achieve seasonal resolution using standard micromilling techniques for conventional stable isotope analysis. Moreover, oxygen isotope ($\delta^{18}O$) records from species inhabiting brackish environments are notoriously difficult to use as paleoclimate archives because of the simultaneous variation in temperature and $\delta^{18}O_{water}$ values.

Methods: Here we use secondary ion mass spectrometry (SIMS) to microsample an *A. borealis* specimen from the southern Baltic Sea, yielding 451 SIMS $\delta^{18}O_{shell}$ values at sub-monthly resolution.

Results: SIMS $\delta^{18}O_{shell}$ values exhibit a quasi-sinusoidal pattern with 24 local maxima and minima coinciding with 24 annual growth increments between March 1977 and the month before specimen collection in May 2001.

Discussion: Age-modeled SIMS $\delta^{18}O_{shell}$ values correlate significantly with both *in situ* temperature measured from shipborne CTD casts (r^2 = 0.52, p<0.001) and sea surface temperature from the ORAS5-SST global reanalysis product for the Baltic Sea region (r^2 = 0.42, p<0.001). We observe the strongest correlation between SIMS $\delta^{18}O_{shell}$ values and salinity when both datasets are run through a 36-month LOWESS function (r^2 = 0.71, p < 0.001). Similarly, we find that LOWESS-smoothed SIMS $\delta^{18}O_{shell}$ values exhibit a moderate correlation with the LOWESS-smoothed North Atlantic Oscillation (NAO) Index (r^2 = 0.46, p<0.001). Change point analysis supports that SIMS $\delta^{18}O_{shell}$ values capture a well-documented regime shift in the NAO circa 1989. We hypothesize that the correlation between the SIMS $\delta^{18}O_{shell}$ time series and the NAO is enhanced by the latter's influence on the regional covariance of water temperature and

$\delta^{18}O_{water}$ values on interannual and longer timescales in the Baltic Sea. These results showcase the potential for SIMS $\delta^{18}O_{shell}$ values in *A. borealis* shells to provide robust paleoclimate information regarding hydroclimate variability from seasonal to decadal timescales.

KEYWORDS

Bivalvia, secondary ion mass spectrometry, oxygen isotope ratios, North Atlantic oscillation, paleoclimate

1 Introduction

Over the last 30 years and starting with the work of Dettman and Lohmann (1993); Dettman and Lohmann (1995), innovations in microsampling techniques for stable isotope analysis of freshwater to marine organisms with accretionary carbonate hard parts (e.g., bivalves, gastropods, corals, and fish) have spurred discoveries in fields such as paleoclimatology, paleobiology, and archaeology (special issues Schöne and Surge, 2005; Prendergast et al., 2017 and references therein). The ability to microsample some archives at seasonal-scale resolution gave rise to the broader field of isotope sclerochronology, which combines the use of growth patterns with oxygen and stable carbon isotope ratios ($\delta^{18}O$ and $\delta^{13}C$, respectively) recorded in carbonate hard parts (Schöne and Surge, 2012; Surge and Schöne, 2015). In bivalves, shell growth patterns (growth lines and increments) are formed due to changes in the rate of carbonate deposition that is, in turn, a response to environmental and biological conditions at several periodicities: daily, tidal, fortnightly, monthly, and annual (Barker, 1964; Stanley, 1966; Pannella and MacClintock, 1968; Clark, 1974; Pannella, 1976; Jones et al., 1983; Goodwin et al., 2001). In effect, growth increments form a shell calendar that can be used to measure time. When combined with shell oxygen isotope ($\delta^{18}O$) ratios, which are a function of growth temperature and $\delta^{18}O$ values of ambient water, shell calendars are rich bioarchives of past environments and climate conditions.

The vast majority of studies using high-resolution, seasonal-scale records from fast- and slow-growing bivalves employ micromilling techniques that generate carbonate powder on the order of 10s of micrograms analyzed on conventional isotope ratio mass spectrometers (IRMS). Micromills are typically computer-aided systems equipped with cameras used to digitize sampling paths along growth lines/increments visible in the shell cross-section. Shell growth is fastest in the first few years of life, so microsampling is often restricted to the ontogenetically youngest part of the shell. This approach is easily achieved in fast growing and/or large bivalves (Weidman et al., 1994; Quitmyer et al., 1997; Surge and Walker, 2006; Schöne and Gillikin, 2013; Goodwin et al., 2021). Although this approach can achieve submonthly resolution on fast-growing shells, species that are small, slow growing, and long-lived, like those from the genus *Astarte*, are potentially untapped resources of paleoclimate information.

Astarte borealis (Schumacher, 1817) is a common constituent of many Arctic and boreal seas, and individuals are reported to live for several decades (Moss et al., 2018; Moss et al., 2021) to over a century (Torres et al., 2011; Reynolds et al., 2022). Such long lifespans are not uncommon for high-latitude species. Moss et al. (2016) document that across Bivalvia there is a tendency for lifespan to increase and growth rate to decrease from low to high latitudes. Such longevity makes this species attractive as a potential bioarchive for reconstructing changes in past and present climate. Based on previous work, *A. borealis* from the White Sea, Russia, reached 33.5 mm in length and allowed for traditional micromilling techniques (Moss et al., 2018). However, in a subsequent study, Moss et al. (2021) found that *A. borealis* from the Baltic Sea is smaller than individuals from the White Sea, precluding the use of traditional micromilling techniques. Thus, they employed secondary ion mass spectrometry (SIMS) to allow for a horizontal sampling resolution of 10 µm with a sampled mass of approximately a nanogram, orders of magnitude smaller than traditional micromilling techniques and IRMS analysis. Their study and our study of a 24-year-old *A. borealis* shell from the Baltic Sea add to the growing body of research that applies SIMS to modern marine/estuarine bivalves (e.g., Dunca et al., 2009; Olson et al., 2012; Vihtakari et al., 2016) and other modern and fossil marine organisms with accretionary carbonate hard parts (e.g., Kozdon et al., 2009; Matta et al., 2013; Linzmeier et al., 2016; Helser et al., 2018; Wycech et al., 2018).

Studies examining *A. borealis* from the Baltic Sea as paleoclimate archives can greatly improve our understanding of regional-scale climate variability across the North Atlantic. In particular, the Baltic Sea is strongly influenced by large-scale atmospheric circulation (e.g., the NAO), hydroclimate in the catchment area, and restricted water exchange with the North Sea (Lehmann et al., 2011). Although scientific research has focused on NAO decadal variability, physical mechanisms, and external forcings over the last 20-30 years, Pinto and Raible (2012) note that a dearth of long-term, high-resolution archives prior to instrumental observations contributes to uncertainties in our understanding of such regional-scale variability on longer timescales. Therefore, developing a (paleo)climate bioarchive in this region is important to improve our understanding of regional-scale climate variability on long timescales and to reduce uncertainties. Here, using SIMS, we find that $\delta^{18}O_{shell}$ values

measured from a 24-year-old *A. borealis* shell collected alive in 2001 from the Baltic Sea captures a well-documented regime shift in the NAO circa 1989 (Lehmann et al., 2011). Our study thus showcases the potential for SIMS $\delta^{18}O_{shell}$ values in this species to provide robust paleoclimate information regarding hydroclimate variability from seasonal to decadal timescales.

2 Materials and methods

2.1 Shell collection, preparation, and oxygen isotope analysis

Specimen RFP3S-47 was collected alive on 5 May 2001 from 20.9 m depth (54.7967° N, 12.38787° E) using a van Veen grab as part of an earlier benthic ecology study (Zettler, 2002). The aragonitic shell was cut along the maximum axis of growth to expose light and dark growth increments (visible under reflected light; Figure 1A) and set in a 2.5 cm-diameter and 4 mm-thick round epoxy mount alongside grains of the calcite standard UWC-3 (Kozdon et al., 2009; $\delta^{18}O$ = 12.49‰ Vienna Standard Mean Ocean Water, VSMOW). Prior to SIMS analysis, the mount was sent to Wagner Petrographic for polishing with successively finer diamond suspension grits, finishing with a 0.05 µm colloidal alumina solution. The polished sample was then sputter coated with gold to a thickness of ~60 nm.

SIMS analysis was performed at the University of Wisconsin-Madison WiscSIMS laboratory on a Cameca IMS 1280 in August 2018 during the same session as Moss et al. (2021) and following settings described in Wycech et al. (2018). Analysis pits ~10 µm in diameter and ~1 µm deep were sputtered using a 1.0 nA primary beam of $^{133}Cs^{+}$. Three Faraday detectors in the double-focusing mass spectrometer simultaneously detected secondary ions of $^{16}O^{-}$, $^{18}O^{-}$, and $^{16}OH^{-}$, with secondary $^{16}O^{-}$ count rates of ~2.4 Gcps. Values of $\delta^{18}O$ are reported in permil (‰) relative to the VPDB (Vienna Pee Dee Belemnite) standard. Precision was determined as 2 times the standard deviation (s.d.) of repeated groups of bracketing measurements on the calcite running standard UWC-3, which averaged ±0.24‰ (2 s.d.) across the analysis session. Measured (raw) $\delta^{18}O$ values were corrected to the VPDB scale for each group of 15–20 aragonite sample analyses following a 3-step procedure: 1. The instrumental bias of calcite on the VSMOW

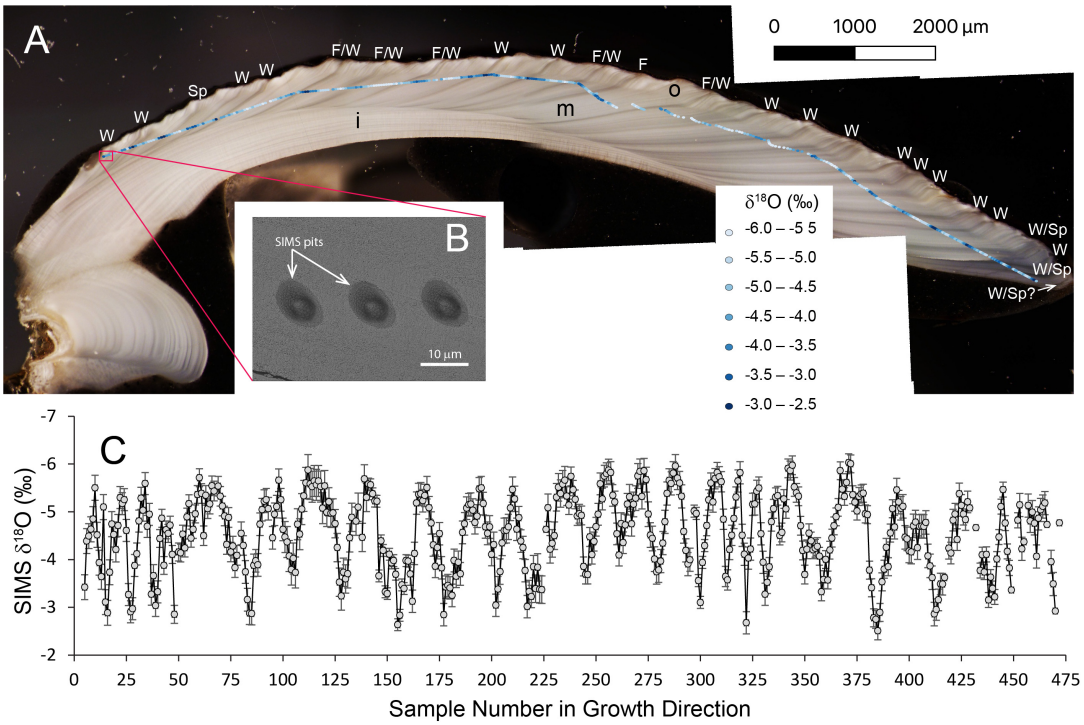

FIGURE 1
Photomicrograph of shell cross-section, location of SIMS sampling pits, SEM image of SIMS pits, and SIMS $\delta^{18}O_{shell}$ values plotted using Quantum-GIS® software (QGIS.org, 2023). **(A)** Cross-section of specimen RFP3S-47 cut along the axis of maximum growth (umbo on left, growth margin on right; growth direction from left to right), showing 3 microstructural layers (i, inner layer; m, middle layer; o, outer layer) and light/dark couplets under reflected light hypothesized to represent annual increments. Approximately 22-24 light/dark couplets are visible. Sampling pits are identified in gradational shades of blue circles (enlarged from true size of 10 µm for ease of visibility), representing 0.5‰ intervals of SIMS $\delta^{18}O_{shell}$ values where lighter blues represent lower values and darker blues are higher values. Estimated season of dark increment formation interpreted from the SIMS $\delta^{18}O_{shell}$ time series (see text for details) are labeled as follows: W, winter; Sp, spring; F, Fall. The last dark increment nearest the growth margin does not include a SIMS $\delta^{18}O_{shell}$ value; thus, the designation W/Sp? is estimated using the relative amount of shell growth from the date of harvest. Scale bar = 2000 µm. **(B)** SEM image of SIMS sampling pits at high resolution (5.5 k magnification) showing examples with no irregularities. Scale bar = 10 µm. **(C)** SIMS $\delta^{18}O_{shell}$ values sampled along direction of growth (left to right). Gray circles are individual SIMS data points. Bars are standard deviations (2σ). Gaps represent data points removed during quality control.

(Vienna Standard Mean Ocean Water) scale was calculated using the bracketing measurements of UWC-3. 2. An adjustment for the small difference in instrument bias (0.88‰) between calcite and aragonite analyses was applied based on calibration analyses of the aragonite standard UWArg-7 ($\delta^{18}O$ = 19.73‰ VSMOW, Linzmeier et al., 2016) completed at the start of the analysis session. 3. Conversion from the VSMOW to VPDB scales followed procedures outlined in Coplen (1994).

The middle microstructural layer was targeted for SIMS analysis per Moss et al. (2021). SIMS analysis started nearest the umbo and proceeded along growth direction to the growth margin, sampling nearly the entire lifespan of the specimen and yielding 482 SIMS $\delta^{18}O_{shell}$ values. Most of the shell was sampled by manual site selection along growth direction. To maximize machine time by sampling overnight, automated sampling of pre-selected points was implemented to capture the earliest ontogenetic years (40 samples) and the final ~8 light/dark couplets towards the growth margin (160 samples).

SIMS data were subjected to a quality-control protocol. First, analytical metrics of each sample measurement – including secondary ion yield, $^{16}OH^-/^{16}O^-$ ratio, and internal variability – were compared to the mean of the bracketing standards. $^{16}OH^-/^{16}O^-$ ratios ranged from 0.0129 to 0.0373, with an average of 0.0243 ± 0.0038 (1σ). Analyses were determined as outliers if they exhibited values that were above (below) the third (first) quartile by more than 1.5 times the interquartile range (Tukey, 1977), and were thus excluded from figures and interpretive discussion. This quality control removed 23 of the 482 total analyses (<5%). An additional 8 duplicate samples were removed from figures and interpretive discussion, resulting in 451 total SIMS $\delta^{18}O_{shell}$ values. Next, SIMS pits were imaged by scanning electron microscopy (SEM) to screen for irregular pit shapes, cracks, or inclusions that may bias the $\delta^{18}O$ data. For SEM imaging, the epoxy mount was loaded onto an aluminum receiver with double-sided copper tape. Images were taken using a Zeiss Supra 25 FESEM operating at 5.5 kV, using the SE2 detector, 30 µm aperture, and working distances of 12–15 mm (Carl Zeiss Microscopy, LLC, Peabody, MA). SEM images of SIMS analysis pits revealed no irregularities of either pit morphology or aragonite substrate (Figure 1B).

3 Results

3.1 SIMS $\delta^{18}O$ values in *A. borealis*

SIMS $\delta^{18}O_{shell}$ values in specimen RFP3S-47 exhibit a quasi-sinusoidal pattern (Figure 1C), with 24 cycles of local minima (−5.58 ± 0.32‰, 1σ) and maxima (−3.15 ± 0.39‰, 1σ) in agreement with the 24 light/dark couplets of annual growth increments visible under reflected light (Figure 1A). These SIMS $\delta^{18}O$ values are comparable to the SIMS $\delta^{18}O$ values measured from another Baltic Sea *A. borealis* specimen in Moss et al. (2021), where the authors noted a negative offset between their SIMS $\delta^{18}O_{shell}$ values relative to coarser resolution IRMS $\delta^{18}O$ values measured from the same specimen. Between 9 and 31 SIMS $\delta^{18}O_{shell}$ measurements comprise a full couplet in specimen RFP3S-47, averaging 19 data points per couplet. Most dark increments occur at or near the highest SIMS $\delta^{18}O_{shell}$ values (darker shades of blue circles locating SIMS pits on the shell cross-section in Figure 1A). Assuming one light/dark couplet represents an annual cycle, as is often the case in this species (Moss et al., 2018; Moss et al., 2021), our sampling interval equates to sub-monthly resolution on average (see Section 4.1 for further discussion of age modeling). However, we note that each discrete sample constitutes a 10 µm spot and a ~5 µm space between spots, and thus one-third of the shell along the sampling path is not represented by the samples presented in this study.

3.2 *In situ* temperature and salinity

Bottom water temperature (Figure 2A) and salinity (Figure 2B) were measured periodically at a location less than 2 km away from our study site (54.79169°N, 13.05831°E) using a calibrated CTD in a previous study (Zettler et al., 2017) between October 1976 and November 2017. The data span the approximate growth years of specimen RFP3S-47 based on counting couplets of light/dark growth increments (1977 to 2001). Prior to 1990, *in situ* temperature and salinity were measured at approximately seasonal resolution (n = 4 ± 1 per year). During and after 1990, the sampling frequency increased to an average of 7 ± 3 measurements per year. Throughout all years, eight months were sampled frequently, including the warmest (August) and coldest (March) months of the year (Figure 2C). However, there is a general dearth of data during the transitional months of April, June, September, and December.

On average, bottom water temperatures ranged from 11.46 ± 2.63°C (1σ) in August to 2.28 ± 1.26°C in March, equating to an

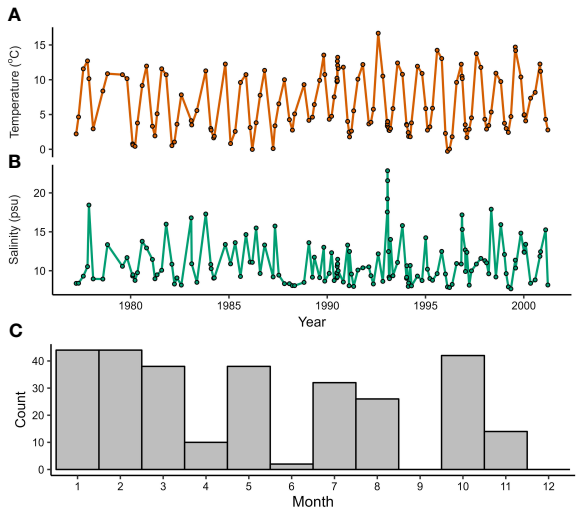

FIGURE 2
Environmental data measured less than 2 km from where specimen RFP3S-47 was collected (54°47′30.1″N, 13°03′29.9″E). **(A, B)** Bottom water temperature and salinity measured between 23-32 m depth. **(C)** Number of measurements taken in each month for all years of CTD data.

annual cycle of 9.18°C ± 3.89°C. However, we note that temperatures collected in July, August, and October are statistically indistinguishable from one another (ANOVA; n = 50, p = 0.41). The same is true for temperatures collected in February, March, and April (n = 46, p = 0.83). The highest bottom water temperature observed was 16.69°C on 5 August 1992, while the lowest temperature observed was −0.30°C on 13 February 1996. Bottom water salinity did not vary with the annual cycle. Salinity measurements exhibited a skewed-right distribution with a median value of 9.83 practical salinity units (psu). Significant deviations above average salinity occur frequently and sporadically throughout the sampling period, with a maximum value of 22.85 psu observed on 26 January 1993. Significant deviations below average salinity were lower in magnitude and frequency, with the minimum value of 7.67 psu observed on 7 May 1999.

4 Discussion

In this section, we demonstrate that the SIMS $\delta^{18}O_{shell}$ dataset from specimen RFP3S-47 yields quantitative paleoclimate information, validating SIMS $\delta^{18}O_{shell}$ values in *A. borealis* as a new climate archive for mid-to-high latitude coastal environments. First, to associate spatial changes in SIMS $\delta^{18}O_{shell}$ values to temporal changes in environmental conditions, we apply an age-model (described in the next section) to the SIMS $\delta^{18}O_{shell}$ data that aligns local $\delta^{18}O$ maxima with the coldest winter months (Figure 3). We then correlate the age-modeled SIMS $\delta^{18}O_{shell}$ dataset with *in situ* temperature and salinity data (Figure 4), as well as with the independent ORAS5 SST dataset (Zuo et al., 2019). These correlation analyses, in conjunction with the age model, show that variations in SIMS $\delta^{18}O_{shell}$ values in specimen RFP3S-47 reflect regional hydroclimate conditions. Finally, we correlate the low-frequency variance component of the SIMS $\delta^{18}O_{shell}$ dataset to interannual shifts in the NAO.

4.1 Age-modeled SIMS $\delta^{18}O_{shell}$ values

A monthly age model was applied to all $\delta^{18}O_{shell}$ samples throughout the lifespan of specimen RFP3S-47 by aligning the quasi-sinusoidal pattern to the annual cycle of temperature (as recorded by *in situ* CTD measurements) according to well-established methods (Beck et al., 1992; Klein et al., 1996; Surge et al., 2001). The age model assumes that local $\delta^{18}O_{shell}$ maxima occur during the coldest winter months (January, February, March, and April, according to the ORAS5 SST dataset), with the final data point designated as the month of collection (May 2001). All samples between local maxima were assigned months based on linear interpolation of their position between bracketing maxima, which assumes a linear growth rate within years. Counting couplets of light and dark increments backwards from the collection date provides calendar years for all SIMS $\delta^{18}O_{shell}$ samples. We thus infer relative variations in annual growth rates by examining the

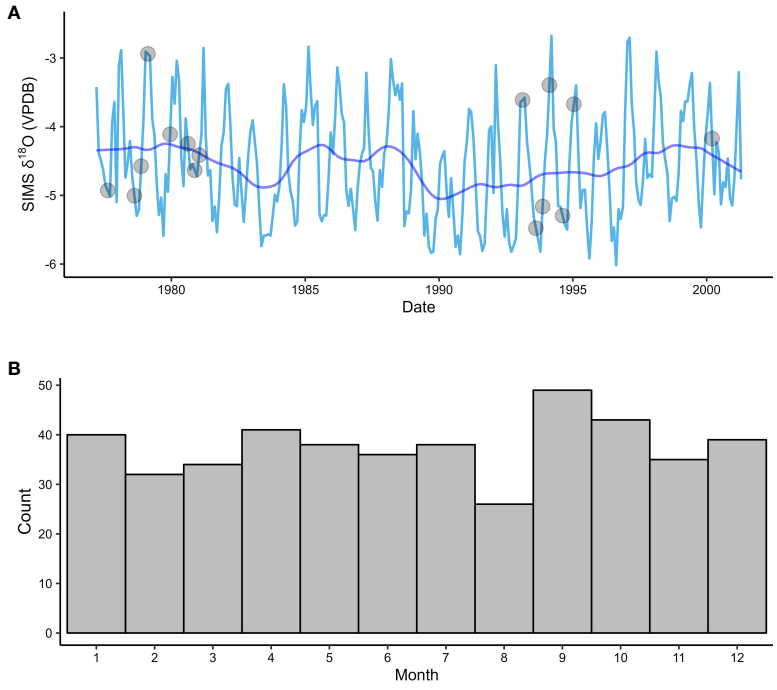

FIGURE 3
(A) Age-modeled SIMS $\delta^{18}O_{shell}$ data from the **(A)** borealis specimen. Estimated growth dates are between March 1977 and May 2001. The light blue line is monthly-averaged $\delta^{18}O_{shell}$ values, with gray dots indicating where values were linearly interpolated between bracketing months. The dark blue line represents the data passed through a 36-month LOWESS function. **(B)** Number of age-modeled growth months for SIMS $\delta^{18}O_{shell}$ data (n = 290) for all growth years (n = 24). Most months (84%) are represented by one or two data points with no bias towards any particular time of year.

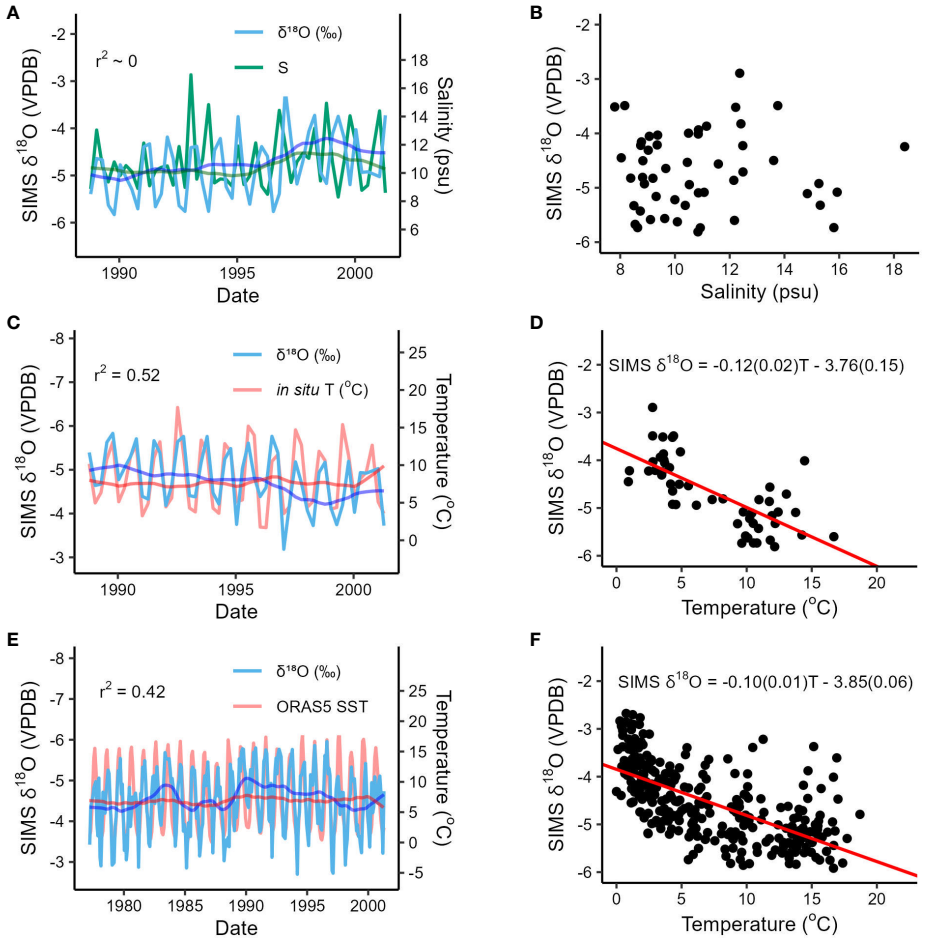

FIGURE 4
Age-modeled SIMS $\delta^{18}O_{shell}$ values compared to *in situ* salinity measurements and two independent temperature datasets from the Baltic Sea. **(A–D)** Comparison of SIMS $\delta^{18}O_{shell}$ values with *in situ* salinity **(A, B)** and temperature data **(C, D)** collected from shipboard measurements between October 1988 and May 2001 (Zettler et al., 2017), mean-averaged over seasonal intervals. **(E, F)** Comparisons of SIMS $\delta^{18}O_{shell}$ values with sea surface temperature estimates for the entire Baltic Sea region extracted from the ORAS5-SST global reanalysis product at monthly resolution (Zuo et al., 2019). The $\delta^{18}O$ axes in both **(C, E)** are inverted to better visualize variations in SIMS $\delta^{18}O_{shell}$ values due to temperature. The dark green, blue, and red lines in **(A, C, E)** show each dataset passed through a 36-month LOWESS function. The equations in **(D, F)** are displayed to assess correlation, not as proxy calibrations for absolute temperature reconstruction. Parantheticals in each equation represent the standard error of the regression coefficients.

number of samples collected in each couplet of light and dark increments (Figure 5). Excluding the year of collection and the earliest growth year (which do not constitute full light/dark increment couplets), between 9 and 31 samples were collected per year, with periods of notably slow growth in the late 1970s and early 1990s. Given each sample constitutes one 10 µm spot and a ~5 µm space between samples, we can approximate an annual growth rate in µm per year (Figure 5, secondary y-axis). However, we caution that precisely quantifying growth rates requires a specific protocol where measurements are made perpendicular to growth lines bounding growth increments along the direction of growth (Schöne et al., 2005) and often the hinge plate is used to avoid any biases imparted by the conchoidal shape of the major growth axis (e.g., Winkelstern et al., 2013; Palmer et al., 2021). Given that calculating annual growth rate was not the primary focus of this study and the sampling scheme used did not follow the necessary protocol for such an analysis, our statistical approach provides a relative estimate of growth rates that compliments the more thorough growth assessments of *A. borealis* specimens conducted by Moss et al. (2018); Moss et al. (2021).

For specimen RFP3S-47, all 24 local $\delta^{18}O_{shell}$ maxima occur at or near the dark increment, indicating formation during cold months (i.e., late fall, winter, or early spring; Figure 1A). While not a ubiquitous feature for all bivalves across all latitudes, the coincident timing of dark increment formation with $\delta^{18}O_{shell}$ maxima has been observed in other mid- to high-latitude bivalves, including *Arctica islandica* (Witbaard et al., 1994; Schöne et al., 2004) and *Mercenaria mercenaria* (Elliot et al., 2003). Fifteen local $\delta^{18}O_{shell}$ maxima occur exactly at the dark increment (i.e., winter); three occur slightly before the dark increment (i.e., late fall); and six occur slightly after the dark increment (i.e., early spring). Once all data points were age modeled, we calculated that each analysis (10 µm spot and ~5 µm space) represents on average 19.5 days.

10.3389/fmars.2023.1293823

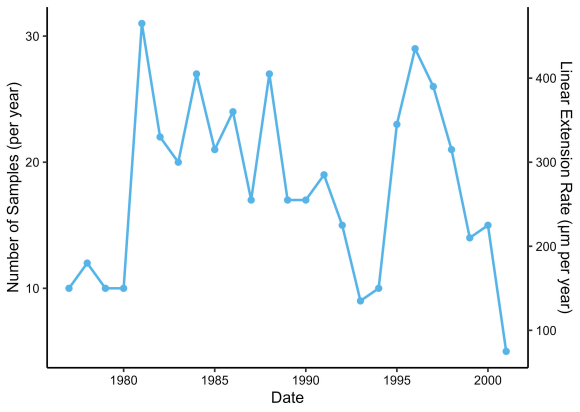

FIGURE 5
Number of data points sampled from specimen RFP3S-47 for each calendar year between the year of collection (2001) and the earliest ontogenetic year (1977). Years were assigned to each growth increment by counting couplets of light and dark increments backwards from the year of collection.

After the age model was applied, $\delta^{18}O_{shell}$ values were mean-averaged over monthly intervals between March 1977 and April 2001 (Figure 3A). Data points are distributed almost uniformly across months, which is a function of both our high sampling resolution and the inherent assumption of constant growth in our age model (Figure 3B). Out of 290 months in the time series, 141 are represented by one data point, 103 are represented by two data points, 21 are represented by three data points, 9 are represented by four data points, and one is represented by 5 data points. Only 15 months in the time series were unrepresented by any $\delta^{18}O_{shell}$ samples. For these months, $\delta^{18}O_{shell}$ values were linearly interpolated between bracketing months (gray dots, Figure 3A).

Once the data were averaged into monthly intervals, a 36-month locally weighted scatterplot smoothing (LOWESS) function was applied to highlight the low-frequency variance component (dark blue line, Figure 3A). The LOWESS function (Cleveland, 1979) is a non-parametric regression method that replaces each data point in a time series with a weighted average based on a specified window size and the values of the data points in close proximity to the central data point in that window. For the age-modeled SIMS $\delta^{18}O_{shell}$ time series, we applied a 36-point window size (i.e., a 36-month bandwidth), which is the minimum bandwidth required to mitigate any effects due to seasonality. These smoothed data accentuate interannual variability that peaks within the 3-to-4-year bandwidth over the 24-year time series. The magnitude of the interannual oscillations vary widely, with a few anomalous periods exhibiting cycles as large as 0.64 and 0.76‰ (troughs in 1984 and 1990) or as small as 0.05‰ (troughs in 1993 and 1996). Average interannual variability (0.35‰) in the age-modeled SIMS $\delta^{18}O_{shell}$ dataset is an order of magnitude lower than average seasonal variability (2.43‰). However, interannual variability appears to modulate the seasonal cycle, resulting in seasonal amplitudes as large as 3.31‰ (1997) or as low as 1.44‰ (1990).

4.2 Correlating SIMS $\delta^{18}O_{shell}$ values to temperature and salinity

To explore the mechanisms behind the apparent seasonal and interannual variability, age-modeled SIMS $\delta^{18}O_{shell}$ values were compared to salinity and two separate temperature datasets from the Baltic Sea region (Figure 4). Although we have correlated age-modeled SIMS $\delta^{18}O_{shell}$ values to two different temperature datasets, we establish this correlation strictly to assess for mechanisms of seasonal and interannual variability. As discussed in Moss et al. (2021), SIMS $\delta^{18}O_{shell}$ values cannot be used to reconstruct absolute temperatures in *A. borealis* shells. Offsets between SIMS-measured $\delta^{18}O$ and IRMS-measured $\delta^{18}O$ values, which are used in temperature calibrations, are reported in a variety of calcite and aragonite biogenic carbonates. The cause of these offsets, commonly <1‰, can be due to a variety of factors (Helser et al., 2018; Wycech et al., 2018), including possible inclusion of water or organic material in the carbonate matrix. Here, we do not attempt to characterize or calibrate the absolute $\delta^{18}O$ value from these samples, but instead use the quality-controlled analytical metrics as the basis for our assumption that SIMS faithfully measures relative changes of $\delta^{18}O$ values in specimen RFP3S-47.

Further complications associated with reconstructing temperatures from absolute SIMS $\delta^{18}O_{shell}$ values presented here arise from unconstrained $\delta^{18}O_{water}$ values at this location throughout the study period. Although studies have correlated $\delta^{18}O_{water}$ values to salinity in the Baltic Sea (Frohlich et al., 1988; Harwood et al., 2008), the strength of this correlation is likely variable in space and time. However, given that $\delta^{18}O_{shell}$ values are primarily a function of temperature and the $\delta^{18}O$ value of ambient water, we demonstrate the utility of the combined signal in assessing modes of seasonal to interannual climate variability in the Baltic Sea region. As a general rule, we define strong correlations as those with an r^2 value greater than 0.50 ($|r| > 0.70$), moderate correlations as those with an r^2 value greater than 0.1 ($0.3 < |r| < 0.7$), and weak correlations as those with an r^2 value less than 0.1 ($|r| < 0.3$).

Salinity and temperature depicted in Figure 4A through 4D were measured simultaneously via shipborne CTD measurements less than two kilometers from our study site, hereafter referred to as *in situ* salinity and temperature (Zettler et al., 2017; see Section 3.2). Although *in situ* water data extend back to the earliest estimated growth month for specimen RFP3S-47 (March 1977), the CTD sampling rate is too sparse to support analysis of subannual variance. Therefore, only *in situ* water data collected between October 1988 and May 2001 were used for comparison to age-modeled SIMS $\delta^{18}O_{shell}$ values. To facilitate comparison, age-modeled SIMS $\delta^{18}O_{shell}$ values and *in situ* salinity and temperature were mean-averaged into seasonal values (Winter = DJF, Spring = MAM, Summer = JJA, Fall = SON). The temperature dataset depicted in Figures 4E, F was compiled from the ORAS5 SST global reanalysis product (Zuo et al., 2019). The ORAS5 product was chosen above other readily available global SST products primarily for two reasons. First, it is calculated at sufficient spatiotemporal resolution (monthly; 1° x 1°) with reliable data at high latitudes, allowing us to integrate 49 grid-points into a single

regional SST estimate for the Baltic Sea (Figure 6). Second, ORAS5 is a data assimilation product that tunes the output of the European Centre for Medium-Range Weather Forecasts' OCEAN5 system to *in situ* observations. Thus, it is well-informed by remote and *in situ* observations, particularly in this dynamic high-latitude coastal region (Carton et al., 2019; Zuo et al., 2019). This is demonstrated by a strong correlation between *in situ* temperature and ORAS5 SST when both datasets are seasonally averaged (n = 51, $r^2 = 0.82$, $p < 0.001$). The correlation between SIMS $\delta^{18}O_{shell}$ values and each dataset are as follows: no correlation for *in situ* salinity ($r^2 = -0$, n = 51, p = 0.99), strong for *in situ* temperature ($r^2 = 0.52$, n = 51, $p < 0.001$), and moderate for the ORAS5 dataset ($r^2 = 0.42$, n = 290, $p < 0.001$).

Both temperature datasets exhibit a moderate-to-strong correlation with age-modeled SIMS $\delta^{18}O_{shell}$ values (Pearson's correlation coefficient, $p < 0.001$). Given the assumptions of our age model (aligning local SIMS $\delta^{18}O$ maxima to *in situ* temperature minima), this finding suggests that monthly SIMS $\delta^{18}O_{shell}$ values in specimen RFP3S-47 are varying in part with *in situ* and regional-scale temperature variability, and that temperatures at ~30m depth in the southwest corner of the Baltic Sea covary significantly with SSTs across the entire Baltic Sea. Furthermore, the standard error of the regression coefficients (parantheticals in regression equations, Figures 4D, F) overlap between the two temperature models, suggesting the relationship between SIMS $\delta^{18}O$ and both temperature datasets is similar. However, a Wilcoxon Rank Sum Test (Bauer, 1972) performed on the regression coefficeints from 10,000 bootstrapped resamples suggests that these two equations are statistically distinct ($p < 0.001$). We also note that the slopes of both SIMS $\delta^{18}O$ – temperature equations are substantially lower than those that are typically observed in other bivalves using IRMS (e.g., −0.22‰; Dettman et al., 1999). We postulate that the lower slope of the relationship between SIMS $\delta^{18}O_{shell}$ values in specimen RFP3S-47 to temperature could be attributed to ontogenetic (growth-related) effects, destructive interference of the temperature signal by $\delta^{18}O_{water}$ values, and by potential seasonal growth cessations (stops).

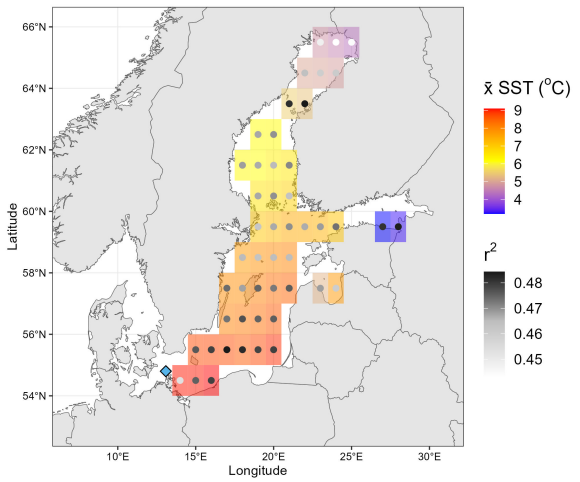

FIGURE 6
Spatial correlation analysis between the SIMS $\delta^{18}O_{shell}$ data and Baltic Sea SST estimates derived from the ORAS5 SST dataset. Mean SST ($\bar{x}$SST; shaded region) and the Pearson correlation coefficients (r^2; points) are shown for each grid point. The blue diamond marks our study site, where specimen RFP3S-47 was collected. The color of each point denotes the r^2 value between age-modeled SIMS $\delta^{18}O_{shell}$ values and SST at that specific location throughout the entire study period (March 1977 to May 2001). The shaded region behind each point indicates the $\bar{x}$SST over the entire study period.

Ontogenetic effects have been observed in many bivalve species, where the degree to which $\delta^{18}O_{shell}$ values capture the full range of seasonal variation decreases with age (Goodwin et al., 2003). However, our results are not consistent with these ontogenetic effects in specimen RFP3S-47, as neither the amplitude of $\delta^{18}O_{shell}$ couplets nor the number of SIMS $\delta^{18}O_{shell}$ measurements constituting each couplet show a secular negative trend. Therefore, we assume that SIMS $\delta^{18}O_{shell}$ values are capturing the same range of the annual cycle through all growth years and thus do not impose any artifacts on interannual variability.

Variable $\delta^{18}O_{water}$ values could reduce the apparent temperature sensitivity in age-modeled SIMS $\delta^{18}O_{shell}$ values if warmer (cooler) temperatures coincide with higher (lower) $\delta^{18}O_{water}$ values. Previous work has shown that $\delta^{18}O_{water}$ values in the Baltic Sea region are tightly coupled with salinity (Frohlich et al., 1988), and thus could be used as a proxy for $\delta^{18}O_{water}$ values. However, the poor correlation between salinity and the age-modeled SIMS $\delta^{18}O_{shell}$ dataset on seasonal timescales indicate that the relationship between the two at our site is complex. Additionally, we find that adding both temperature and salinity as predictor variables for age-modeled SIMS $\delta^{18}O_{shell}$ values does not yield better estimates than temperature alone ($r^2 = 0.52$, $p < 0.001$). Therefore, we cannot use salinity on seasonal timescales to robustly test whether variations in $\delta^{18}O_{water}$ values are diminishing the temperature sensitivity of SIMS $\delta^{18}O_{shell}$ values. Regardless, we examined the relationship between *in situ* temperature and salinity to verify if seasonal changes in salinity (used here as a proxy for $\delta^{18}O_{water}$) could influence the slope of the relationship between SIMS $\delta^{18}O_{shell}$ values and temperature (Figure S1 and Table S1). We find the correlation between *in situ* salinity and temperature is extremely weak (Figure S1; n = 146, $r^2 = 0.02$, n = 0.14), and there are no significant differences in salinities collected between summer and winter months (Table S1). While it is likely that SIMS $\delta^{18}O_{shell}$ values are influenced by variations in $\delta^{18}O_{water}$ values, the lack of seasonal variation in salinity (serving here as a proxy for $\delta^{18}O_{water}$) suggests that the influence of $\delta^{18}O_{water}$ variability on SIMS $\delta^{18}O_{shell}$ values is stochastic rather than systematic. Therefore, we find it highly unlikely that $\delta^{18}O_{water}$ variations can explain the reduced slope in the correlation between SIMS $\delta^{18}O_{shell}$ values and temperature.

Seasonal growth cessations (or stops in growth) and slow downs induced by exceeding growth temperature thresholds are a well-documented phenomena in many bivalve species (e.g., Ansell, 1968; Jones and Quitmyer, 1996; Fritz, 2001 and references therein). It is estimated that Baltic Sea *A. borealis* exhibits an upper temperature threshold between 14 – 17°C and a lower temperature threshold between 0 – 4°C (Oertzen, 1973; Oertzen and Schulz, 1973). Our *in situ* temperature dataset indicates that specimen RFP3S-47 rarely experienced summer temperatures approaching this upper

temperature threshold but regularly experienced winter temperatures in the lower threshold range. Furthermore, other environmental and physiological factors can also influence seasonal growth cessation (see Moss et al., 2018 for an overview). Moss et al. (2021) report that temperature stress during cool months could explain the growth slow downs observed in Baltic Sea *A. borealis* during that time; however, winter/spring spawning events could not be ruled out as a possibility.

Seasonal growth cessations would manifest as truncated seasonal amplitudes in $\delta^{18}O_{shell}$ values and, thus, a reduced slope in the correlation between SIMS $\delta^{18}O_{shell}$ values and temperature. To test if seasonal growth cessations were occuring, we conducted two separate statistical analyses. First, if growth cessations were occuring in the winter months, we would expect less variance in SIMS $\delta^{18}O_{shell}$ values during winter months (DJFM = December, January, February, March) than in summer months (JJAS = June, July, August, September). However, we find no significant difference in variance between winter and summer SIMS $\delta^{18}O_{shell}$ values ($n = 193$, $p = 0.58$). For the second analysis, we compared the correlation between *in situ* temperature and SIMS $\delta^{18}O_{shell}$ values collected between summer and winter months. We expect that, if growth cessations were occurring during the cold season, winter SIMS $\delta^{18}O$ values would exhibit a weaker correlation with temperature than summer values. However, results are sensitive to which temperature dataset is used. Using the seasonally averaged *in situ* temperature dataset, we find no significant correlation between SIMS $\delta^{18}O_{shell}$ values and *in situ* temperatures for neither winter months ($n = 24$, $r^2 < 0.01$, $p = 0.95$) nor summer months ($n = 24$, $r^2 = 0.08$, $p = 0.17$). Using the ORAS5 SST dataset, we find a stronger correlation between temperature and winter SIMS $\delta^{18}O_{shell}$ values ($n = 97$, $r^2 = 0.36$, $p < 0.001$) than summer values ($n = 96$, $r^2 = 0.03$, $p = 0.07$). However, we would expect this stronger correlation due to increased turnover of the Baltic Sea in the winter months, and thus specimen RFP3S-47 at ~30m depth would likely experience temperatures more similar to Baltic Sea SSTs during the cold season. The inconclusive statistical analyses conducted here, and the difficulty with determining growth cessations via visual inspection, means we cannot rule out that growth cessations are reducing the slope in the correlation between temperature and SIMS $\delta^{18}O_{shell}$ values.

Age-modeled SIMS $\delta^{18}O_{shell}$ values exhibit the greatest interannual variability of all datasets presented in this study, with apparent oscillations occurring every three to four years. Although interannual variability is an order of magnitude smaller than annual variability in the SIMS $\delta^{18}O_{shell}$ dataset, and interannual variability makes up an even smaller component of the environmental datasets, we find that correlating the interannual components of each dataset yields different results than correlating the monthly- and seasonally-averaged datasets. First, seasonal SIMS $\delta^{18}O_{shell}$ values and *in situ* salinity are strongly correlated when both datasets are passed through a 36-month LOWESS function ($r^2 = 0.71$, $n = 51$, $p < 0.001$). The correlation between seasonal SIMS $\delta^{18}O$ and *in situ* temperature actually decreases when we execute the same comparison ($r^2 = 0.05$, $n = 51$, $p = 0.13$), and this same decrease is observed to a lesser extent when comparing the smoothed monthly SIMS $\delta^{18}O$ data and ORAS5 SSTs ($r^2 = 0.29$, $n = 290$, $p < 0.001$). These analyses suggest that, while temperature imposes a strong seasonal effect on $\delta^{18}O_{shell}$ values, salinity is predominantly driving interannual variability.

4.3 SIMS $\delta^{18}O_{shell}$ values and the NAO

Given the strong influence of temperature and salinity on the SIMS $\delta^{18}O_{shell}$ values at different timescales, we suggest that $\delta^{18}O_{shell}$ values in *A. borealis* from the Baltic Sea may be used to reflect changes in the NAO. The NAO imposes a strong effect on regional temperatures and hydrology as one of the leading modes of interannual climate variability in northern Europe (Hurrell, 1995; Jones et al., 2003). The Baltic Sea is particularly sensitive to the NAO, with stronger (weaker) westerlies bringing increased (decreased) storminess and warmer (colder) winters to the region during the positive (negative) phase (Hurrell, 1995; Lehmann et al., 2011). Because the NAO exhibits a temporal periodicity of approximately 3–4 years, we hypothesize that NAO-related climate changes would work to simultaneously increase SST while decreasing $\delta^{18}O_{water}$ values (and vice versa), effects that would compound to increase the amplitude of the interannual $\delta^{18}O_{shell}$ response of *A. borealis* in the Baltic Sea.

To test this hypothesis, we compared the age-modeled SIMS $\delta^{18}O_{shell}$ dataset from specimen RFP3S-47 to the NAO index for the entire study period (Figure 7A). Here, the NAO index is defined as the normalized difference in sea level pressure between Iceland and the Azores (Rogers, 1984; Hurrell, 1995). Additionally, to determine if SIMS $\delta^{18}O_{shell}$ values could track significant changes in the NAO, we conducted a change point analysis on both monthly datasets using the pruned exact linear time (PELT) method (Killick et al., 2012), which is the optimal method for finding exact solutions in change point detection (Truong et al., 2020). These change points are shown in Figure 7A as blue diamonds on the $\delta^{18}O$ time series and black diamonds on the NAO time series. Although the two datasets are uncorrelated at monthly intervals ($r^2 = 0.002$, $p = 0.49$), they are moderately inversely correlated when each monthly dataset are passed through a 36-month LOWESS function ($r^2 = 0.46$, $n = 290$, $p < 0.001$; Figure 7A). This change in correlation between monthly and interannual timescales observed between SIMS $\delta^{18}O_{shell}$ values and the NAO is very similar to the change in correlation observed between SIMS $\delta^{18}O$ and salinity. However, we note that the correlation between SIMS $\delta^{18}O_{shell}$ values and the NAO is supported by a much larger sample size due to the higher resolution (monthly vs. seasonal) from which the smoothed data were derived.

The strength of the correlation between the smoothed SIMS $\delta^{18}O_{shell}$ dataset and the NAO is such that SIMS $\delta^{18}O_{shell}$ values track a documented regime shift in the NAO circa 1989 (Figure 7A; first black/blue diamonds), where the overall trend in the NAO shifts towards more negative values while winter NAO values remain largely positive (Lehmann et al., 2011). Moreover, the 1989 regime shift is visually striking, particularly in both LOWESS-smoothed time series. The other change point in the SIMS $\delta^{18}O$ time series (circa 1996) occurs within three years of a cluster of change points in the NAO time series, which are

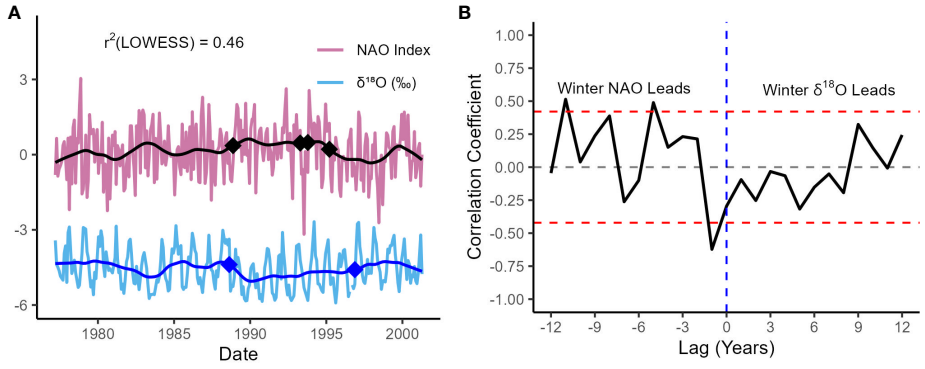

FIGURE 7
SIMS $\delta^{18}O_{shell}$ values compared to the North Atlantic Oscillation (NAO). **(A)** Age-modeled SIMS $\delta^{18}O_{shell}$ values (blue) and the NAO Index (purple), defined as the normalized difference in sea-level pressures between Iceland and the Azores. The bold blue and black lines represent each dataset passed through a 36-month LOWESS function. Diamonds indicate change points in each monthly time series, identified using a PELT change point detection method. **(B)** Lagged correlation analysis between winter (DJFM) SIMS $\delta^{18}O_{shell}$ values and the NAO Index. The x-axis values represent the number of years that the NAO lags SIMS $\delta^{18}O_{shell}$ values. The red-dotted lines ($r = \pm 0.42$) indicate the point at which the correlation becomes significant at the 95% confidence level (Hu et al., 2017).

associated with a pronounced negative excursion (1994) and an interannual shift towards more negative values (1995). All these latter change points are detected nearly within a 36-month window of each other, which lends further support to our conclusion that $\delta^{18}O_{shell}$ values covary with the NAO on interannual timescales.

The significant correlation on interannual timescales between the NAO index and the SIMS $\delta^{18}O_{shell}$ dataset suggests that positive (negative) phases of the NAO generally bring warmer (cooler) and wetter (dryer) conditions to the Baltic Sea. This finding is consistent with previous studies analyzing modeled and observed temperature and salinity data from the Baltic Sea (Hänninen et al., 2000; Lehmann et al., 2011). In summary, warmer winter SSTs are associated with positive phases of the NAO, as stronger westerly winds bring milder winters and excess precipitation to the region (Hurrell, 1995; Lehmann et al., 2011). Negative phases of the NAO are associated with weaker westerly winds, more extreme winters, and less precipitation in northern Europe (Dickson and Brander, 1993). Additionally, pulses of saline water from the North Sea through the Danish Straits are more likely to occur during a negative NAO phase (Schinke and Matthäus, 1998). Thus, opposite phases of the NAO propagate conditions where temperature and freshwater flux reinforce one another on interannual timescales, likely amplifying the environmental signal recorded in the SIMS $\delta^{18}O_{shell}$ dataset.

To evaluate the mechanisms behind the correlation between the NAO Index and the SIMS $\delta^{18}O_{shell}$ dataset, particularly during winter when the NAO exhibits the greatest regional impact, we conducted a lagged correlation analysis between winter values (DJFM) from both datasets (Figure 7B). We find that winter values from each dataset are moderately correlated when winter NAO leads winter $\delta^{18}O_{shell}$ values by one year ($r^2 = 0.39$, $n = 23$, $p = 0.002$). The significant lagged correlation between winter SIMS $\delta^{18}O_{shell}$ values and the NAO could be attributed to the stepwise hydrologic response observed across the Baltic Sea region to freshwater forcing from the NAO. Freshwater runoff into the Baltic Sea lags the NAO index by a few months, with salinity lagging further behind freshwater runoff within one year (Hänninen et al., 2000). The spread in these lag times is largely due to the broad range of residence times (hours to years) that water exhibits across the Baltic Sea region, both in the Baltic Sea itself and in its various watersheds (Ehlin, 1981; Bergström and Carlsson, 1994; Hänninen et al., 2000). Given that our site is located in the Arkona basin subregion near the mouth of the Baltic Sea, we hypothesize that the SIMS $\delta^{18}O_{shell}$ dataset is capturing an integrated signal of freshwater flux derived from melting snow and ice, the volume of which is largely controlled by the state of previous years' NAO. This hydroclimatic link between the NAO and SIMS $\delta^{18}O_{shell}$ values on interannual timescales is further supported by the significant correlation between SIMS $\delta^{18}O_{shell}$ values and *in situ* salinity when both datasets are binned annually and salinity leads by one-year (Figure S2; $n = 23$, $r^2 = 0.29$, $p = 0.007$). We observe that the lagged correlation analysis conducted specifically on winter $\delta^{18}O_{shell}$ values and the NAO index exhibits a higher coefficient of determination than the lagged correlation analysis conducted between annually binned $\delta^{18}O_{shell}$ values and salinity. We postulate this could be due to: (a) the coarser sampling resolution in the *in situ* salinity dataset precluding a winter-only comparison with SIMS $\delta^{18}O_{shell}$ values, and (b) the influence of the NAO index on both temperature and $\delta^{18}O_{water}$.

5 Conclusions

This study presents the first multidecadal $\delta^{18}O$ time series generated from an *A. borealis* shell using SIMS. At sub-monthly resolution, we find that the SIMS $\delta^{18}O_{shell}$ time series is significantly correlated to *in situ* temperatures at the mouth of the Baltic Sea ($r^2 = >0.52$), as well as regional SST across the Baltic Sea based on ORAS5 SST estimates ($r^2 = 0.42$). The strongest correlation emerges when comparing the interannual components of the SIMS $\delta^{18}O_{shell}$ dataset and salinity ($r^2 = 0.71$). We observe a moderate correlation between the interannual components of the SIMS $\delta^{18}O_{shell}$ dataset

and the NAO Index ($r^2 = 0.46$), where SIMS $\delta^{18}O_{shell}$ values capture a well-documented regime shift circa 1989 (Lehmann et al., 2011). We hypothesize that this coupling emerges as a result of NAO-related climate effects creating constructive interference between SST and $\delta^{18}O_{water}$ values at the southern margin of the Baltic Sea on interannual timescales, thereby imposing a strong environmental signal onto the SIMS $\delta^{18}O_{shell}$ dataset. The integrated hydroclimate signal captured at our site by the SIMS $\delta^{18}O_{shell}$ dataset is further supported by a significant correlation between binned DJFM winter $\delta^{18}O_{shell}$ values with the previous years' winter NAO Index ($r^2 = 0.39$). Our analyses indicate that SIMS $\delta^{18}O_{shell}$ values in *A. borealis* from the Baltic Sea are a potentially rich source of paleoclimate information, with capabilities of reconstructing the mid-to-high latitude component of the NAO during the Holocene at sub-monthly resolution over decadal timescales.

Data availability statement

The original contributions presented in the study are included in the article/Supplementary Material. Further inquiries can be directed to the corresponding author.

Author contributions

HH: Conceptualization, Formal Analysis, Visualization, Writing – original draft, Writing – review & editing. DS: Conceptualization, Funding acquisition, Investigation, Project administration, Visualization, Writing – original draft, Writing – review & editing. IO: Data curation, Investigation, Visualization, Writing – review & editing. MZ: Investigation, Writing – review & editing. DM: Investigation, Writing – review & editing.

Funding

The author(s) declare financial support was received for the research, authorship, and/or publication of this article. Funding for this study was provided by the US National Science Foundation (NSF) to Surge (#EAR-1656974). The WiscSIMS Laboratory is supported by the US NSF (Grant #EAR-1355590 and EAR-1658823). Long-term environmental data for Figures 2A, B were obtained within the framework of the German Baltic Sea Monitoring financed by the Federal Maritime and Hydrographic Agency (BSH) and carried out by the Leibniz Institute for Baltic Sea Research (IOW).

Acknowledgments

Dr. Jonathan Lees is gratefully acknowledged for his helpful suggestions towards analyzing temporal variations in the SIMS $\delta^{18}O_{shell}$ dataset. We also thank Garrett Braniecki for helpful insights into analyzing growth variations in specimen RFP3S-47. Comments from three reviewers helped improve this manuscript and were greatly appreciated.

Conflict of interest

The authors declare that the research was conducted in the absence of any commercial or financial relationships that could be construed as a potential conflict of interest.

Publisher's note

Supplementary material

The Supplementary Material for this article can be found online at: https://www.frontiersin.org/articles/10.3389/fmars.2023.1293823/full#supplementary-material

References

Ansell, A. D. (1968). The Rate of Growth of the Hard Clam Mercenaria mercenaria L) throughout the Geographical Range. *ICES J. Mar. Sci.* 31, 364–409. doi: 10.1093/icesjms/31.3.364

Barker, R. M. (1964). Microtextural variation in pelecypod shells. *Malacologia* 2, 69–86.

Bauer, D. F. (1972). Constructing confidence sets using rank statistics. *J. Am. Stat. Assoc.* 67, 687–690. doi: 10.1080/01621459.1972.10481279

Beck, J. W., Edwards, R. L., Ito, E., Taylor, F. W., Recy, J., Rougerie, F., et al. (1992). Sea-surface temperature from coral skeletal strontium/calcium ratios. *Science* 257, 644–647. doi: 10.1126/science.257.5070.644

Bergström, S., and Carlsson, B. (1994). River runoff to the Baltic Sea -1950-1990. *Ambio* 23, 280–287.

Carton, J. A., Penny, S. G., and Kalnay, E. (2019). Temperature and salinity variability in the SODA3, ECCO4r3, and ORAS5 ocean reanalyses 1993–2015. *J. Clim.* 32, 2277–2293. doi: 10.1175/JCLI-D-18-0605.1

Clark, G. R. (1974). Growth lines in invertebrate skeletons. *Ann. Rev. Earth Planet Sci.* 2, 77–99. doi: 10.1146/annurev.ea.02.050174.000453

Cleveland, W. S. (1979). Robust locally weighted regression and smoothing scatterplots. *J. Am. Stat. Assoc.* 74, 829–836. doi: 10.1080/01621459.1979.10481038

Coplen, T. B. (1994). Reporting of stable hydrogen, carbon, and oxygen isotopic abundances (Technical Report). *Pure Appl. Chem.* 66, 273–276. doi: 10.1351/pac199466020273

Dettman, D. L., and Lohmann, K. C. (1993). *Seasonal change in Paleogene surface water δ18O: Fresh-water bivalves of Western North America*. Eds. P. K. Swart, K. C. Lohmann, J. Mckenzie and S. Savin (Washington, DC: American Geophysical Union), 153–163.

Dettman, D. L., and Lohmann, K. C. (1995). Microsampling carbonates for stable isotope and minor element analysis: physical separation of samples on a 20 micrometer scale. *J. Sed. Res.* 65A, 566–569. doi: 10.1306/D426813F-2B26-11D7-8648000102C1865D

Dettman, D. L., Reische, A. K., and Lohmann, K. C. (1999). Controls on the stable isotope composition of seasonal growth bands in aragonitic fresh-water bivalves (unionidae). *Geochim. Cosmochim. Acta* 63, 1049–1057. doi: 10.1016/S0016-7037(99)00020-4

Dickson, R. R., and Brander, K. M. (1993). Effects of a changing windfield on cod stocks of the North Atlantic. *Fish. Oceanogr.* 2, 124–153. doi: 10.1111/j.1365-2419.1993.tb00130.x

Dunca, E., Mutvei, H., Göransson, P., Mörth, C.-M., Schöne, B. R., Whitehouse, M. J., et al. (2009). Using ocean quahog (Arctica islandica) shells to reconstruct palaeoenvironment in Öresund, Kattegat and Skagerrak, Sweden. *Int. J. Earth Sci.* 98, 3–17. doi: 10.1007/s00531-008-0348-6

Ehlin, U. (1981). "Hydrology of the Baltic Sea," in *Elsevier Oceanography Series*. Ed. A. Voipio (Amsterdam: Elsevier).

Elliot, M., Demenocal, P. B., Linsley, B. K., and Howe, S. S. (2003). Environmental controls on the stable isotopic composition of Mercenaria mercenaria: Potential application to paleoenvironmental studies. *Geochem. Geophys. Geosyst.* 4, 1–16. doi: 10.1029/2002GC000425

Fritz, L. W. (2001). "Chapter 2 Shell structure and age determination," in *Developments in Aquaculture and Fisheries Science*. Eds. J. N. Kraeuter and M. Castagna (Amsterdam: Elsevier).

Frohlich, K., Grabczak, J., and Rozanski, K. (1988). Deuterium and oxygen-18 in the Baltic Sea. *Chem. Geol.* 72, 77–83. doi: 10.1016/0168-9622(88)90038-3

Goodwin, D. H., Flessa, K. W., Schöne, B. R., and Dettman, D. L. (2001). Cross-calibration of daily growth increments, stable isotope variation, and temperature in the Gulf of California bivalve Mollusk Chione Cortezi: implications for paleoenvironmental analysis. *PALAIOS* 16 (4), 387–398. doi: 10.1669/0883-1351(2001)016<0387:CCODGI>2.0.CO;2

Goodwin, D. H., Gillikin, D. P., Jorn, E. N., Fratian, M. C., and Wanamaker, A. D. (2021). Comparing contemporary biogeochemical archives from Mercenaria mercenaria and Crassostrea virginica: Insights on paleoenvironmental reconstructions. *Palaeogeogr. Palaeocl.* 562, 110110. doi: 10.1016/j.palaeo.2020.110110

Goodwin, D. H., Schöne, B. R., and Dettman, D. L. (2003). Resolution and fidelity of oxygen isotopes as paleotemperature proxies in bivalve Mollusk shells: models and observations. *PALAIOS* 18, 110–125. doi: 10.1669/0883-1351(2003)18<110:RAFOOI>2.0.CO;2

Hänninen, J., Vuorinen, I., and Hjelt, P. (2000). Climatic factors in the Atlantic control the oceanographic and ecological changes in the Baltic Sea. *Limnol. Oceanogr.* 45, 703–710. doi: 10.4319/lo.2000.45.3.0703

Harwood, A. J. P., Dennis, P. F., Marca, A. D., Pilling, G. M., and Millner, R. S. (2008). The oxygen isotope composition of water masses within the North Sea. *Estuar. Coast.* 78, 353–359. doi: 10.1016/j.ecss.2007.12.010

Helser, T. E., Kastelle, C. R., Mckay, J. L., Orland, I. J., Kozdon, R., and Valley, J. W. (2018). Evaluation of micromilling/conventional isotope ratio mass spectrometry and secondary ion mass spectrometry of δ18O values in fish otoliths for sclerochronology. *Rapid Commun. Mass. Sp.* 32, 1781–1790. doi: 10.1002/rcm.8231

Hu, J., Emile-Geay, J., and Partin, J. (2017). Correlation-based interpretations of paleoclimate data–where statistics meet past climates. *Earth Planet. Sc. Lett.* 459, 362–371. doi: 10.1016/j.epsl.2016.11.048

Hurrell, J. (1995). Decadal trends in the North Atlantic oscillation: regional temperatures and precipitation. *Science* 269, 676–679. doi: 10.1126/science.269.5224.676

Jones, P. D., Osborn, T. J., and Briffa, K. R. (2003). Pressure-based measures of the north Atlantic oscillation (NAO): A comparison and an assessment of changes in the strength of the NAO and in its influence on surface climate parameters. *North Atlantic Oscillation: Climatic Significance Environ. Impact*. 134, 51–62. doi: 10.1029/134GM03

Jones, D. S., and Quitmyer, I. R. (1996). Marking time with bivalve shells: oxygen isotopes and season of annual increment formation. *PALAIOS* 11, 340–346. doi: 10.2307/3515244

Jones, D. S., Williams, D. F., and Arthur, M. A. (1983). Growth history and ecology of the Atlantic surf clam, Spisula solidissima (Dillwyn), as revealed by stable isotopes and annual shell increments. *J. Exp. Mar. Biol. Ecol.* 73, 225–242. doi: 10.1016/0022-0981(83)90049-7

Killick, R., Fearnhead, P., and Eckley, I. A. (2012). Optimal detection of changepoints with a linear computational cost. *J. Am. Stat. Assoc.* 107, 1590–1598. doi: 10.1080/01621459.2012.737745

Klein, R. T., Lohmann, K. C., and Thayer, C. W. (1996). Bivalve skeletons record sea-surface temperature and δ18O *via* Mg/Ca and 18O/16O ratios. *Geology* 24, 415–418. doi: 10.1130/0091-7613(1996)024<0415:BSRSST>2.3.CO;2

Kozdon, R., Ushikubo, T., Kita, N. T., Spicuzza, M., and Valley, J. W. (2009). Intratest oxygen isotope variability in the planktonic foraminifer N. pachyderma: Real vs. apparent vital effects by ion microprobe. *Chem. Geol.* 258, 327–337. doi: 10.1016/j.chemgeo.2008.10.032

Lehmann, A., Getzlaff, K., and Harlaß, J. (2011). Detailed assessment of climate variability in the Baltic Sea area for the period 1958 to 2009. *Clim. Res.* 46, 185–196. doi: 10.3354/cr00876

Linzmeier, B. J., Kozdon, R., Peters, S. E., and Valley, J. W. (2016). Oxygen isotope variability within nautilus shell growth bands. *PloS One* 11, e0153890. doi: 10.1371/journal.pone.0153890

Matta, M. E., Orland, I. J., Ushikubo, T., Helser, T. E., Black, B. A., and Valley, J. W. (2013). Otolith oxygen isotopes measured by high-precision secondary ion mass spectrometry reflect life history of a yellowfin sole (Limanda aspera). *Rapid Commun. Mass. Sp.* 27, 691–699. doi: 10.1002/rcm.6502

Moss, D. K., Ivany, L. C., Judd, E. J., Cummings, P. W., Bearden, C. E., Kim, W.-J., et al. (2016). Lifespan, growth rate, and body size across latitude in marine Bivalvia, with implications for Phanerozoic evolution. *Proc. R. Soc. Lond.* 283 (1836), 20161364. doi: 10.1098/rspb.2016.1364

Moss, D. K., Surge, D., and Khaitov, V. (2018). Lifespan and growth of Astarte borealis (Bivalvia) from Kandalaksha Gulf, White Sea, Russia. *Polar Biol.* 41, 1359–1369. doi: 10.1007/s00300-018-2290-9

Moss, D. K., Surge, D., Zettler, M. L., Orland, I. J., Burnette, A., and Fancher, A. (2021). Age and growth of Astarte borealis (Bivalvia) from the Southwestern Baltic Sea using secondary ion mass spectrometry. *Mar. Biol.* 168, 133. doi: 10.1007/s00227-021-03935-7

Oertzen, J. (1973). Abiotic potency and physiological resistance of shallow and deep water bivalves. *Oikos* Suppl. 15, 261–266.

Oertzen, J., and Schulz, S. (1973). Beitrag zur geographischen Verbreitung und ökologischen Rxistenz von Bivahriern der Ostsee. *Beitr. Meereskd.* 32, 75–88.

Olson, I. C., Kozdon, R., Valley, J. W., and Gilbert, P. U. P. A. (2012). Mollusk shell nacre ultrastructure correlates with environmental temperature and pressure. *J. Am. Chem. Soc* 134, 7351–7358. doi: 10.1021/ja210808s

Palmer, K. L., Moss, D. K., Surge, D., and Turek, S. (2021). Life history patterns of modern and fossil Mercenaria spp. from warm vs. cold climates. *Palaeogeogr. Palaeocl.* 566, 110227. doi: 10.1016/j.palaeo.2021.110227

Pannella, G. (1976). Tidal growth patterns in recent and fossil mollusc bivalve shells: a tool for the reconstruction of paleotides. *Sci. Nat.* 63, 539–543. doi: 10.1007/BF00622786

Pannella, G., and MacClintock, C. (1968). Biological and environmental rhythms reflected in Molluscan shell growth. *Memoir (The Paleontological Society)* 2, 64–80.

Pinto, J. G., and Raible, C. C. (2012). Past and recent changes in the North Atlantic oscillation. *WIREs Clim. Change* 3, 79–90. doi: 10.1002/wcc.150

Prendergast, A. L., Versteegh, E., and Schöne, B. R. (2017). New research on the development of high-resolution palaeoenvironmental proxies from geochemical properties of biogenic carbonates. *Palaeogeogr. Palaeocl.* 484, 1–6. doi: 10.1016/j.palaeo.2017.05.032

QGIS.org (2023). *QGIS Geographic Information System* (QGIS Association). Available at: http://www.qgis.org.

Quitmyer, I. R., Jones, D. S., and Arnold, W. S. (1997). The sclerochronology of hard clams,Mercenariaspp., from the south-Eastern U.S.A.: A method of elucidating the zooarchaeological records of seasonal resource procurement and seasonality in prehistoric shell middens. *J. Archaeol. Sci.* 24, 825–840. doi: 10.1006/jasc.1996.0163

Reynolds, D. J., Von Biela, V. R., Dunton, K. H., Douglas, D. C., and Black, B. A. (2022). Sclerochronological records of environmental variability and bivalve growth in the Pacific Arctic. *Prog. Oceanogr.* 206, 102864. doi: 10.1016/j.pocean.2022.102864

Rogers, J. C. (1984). The association between the north Atlantic oscillation and the southern oscillation in the northern hemisphere. *Mon. Weather Rev.* 112, 1999–2015. doi: 10.1175/1520-0493(1984)112<1999:TABTNA>2.0.CO;2

Schinke, H., and Matthäus, W. (1998). On the causes of major Baltic inflows —an analysis of long time series. *Cont. Shelf Res.* 18, 67–97. doi: 10.1016/S0278-4343(97)00071-X

Schöne, B. R., Fiebig, J., Pfeiffer, M., Gleβ, R., Hickson, J., Johnson, A. L. A., et al. (2005). Climate records from a Bivalved Methuselah (Arctica islandica, Mollusca; Iceland). *Palaeogeogr. Palaeocl.* 228, 130–148. doi: 10.1016/j.palaeo.2005.03.049

Schöne, B. R., Freyre Castro, A. D., Fiebig, J., Houk, S. D., Oschmann, W., and Kröncke, I. (2004). Sea surface water temperatures over the period 1884–1983 reconstructed from oxygen isotope ratios of a bivalve mollusk shell (Arctica Islandica, southern North Sea). *Paleoceanogr. Paleoclimatol.* 212, 215–232. doi: 10.1016/j.palaeo.2004.05.024

Schöne, B. R., and Gillikin, D. P. (2013). Unraveling environmental histories from skeletal diaries — Advances in sclerochronology. *Palaeogeogr. Palaeocl.* 373, 1–5. doi: 10.1016/j.palaeo.2012.11.026

Schöne, B. R., and Surge, D. (2005). Looking back over skeletal diaries — High-resolution environmental reconstructions from accretionary hard parts of aquatic organisms. *Paleoceanogr. Paleoclimatol.* 228, 1–3. doi: 10.1016/j.palaeo.2005.03.043

Schöne, B. R., and Surge, D. (2012). "Bivalve schlerochronology and geochemistry," in *Part N, Bivalvia, Revised*. Eds. P. Seldon, J. Hardesty, J. G. Carter and L. Kansas (Lawrence, Kansas: Paleontological Institute).

Schumacher, C.-F. (1817). *Essai d'un nouveau système des habitations des vers testacés: avec XXII planches* (Copenhagen: Imprimeire de M. le directeur Schultz).

Stanley, S. M. (1966). Paleoecology and diagenesis of key Largo Limestone, Florida. *AAPG Bull.* 50, 1927–1947. doi: 10.1306/5d25b6a9-16c1-11d7-8645000102c1865d

Surge, D., Lohmann, K. C., and Dettman, D. L. (2001). Controls on isotopic chemistry of the American oyster, Crassostrea virginica: implications for growth patterns. *Palaeogeogr. Palaeocl.* 172, 283–296. doi: 10.1016/S0031-0182(01)00303-0

Surge, D. M., and Schöne, B. R. (2015). "Bivalve sclerochronology," in *Encyclopedia of scientific dating methods*. Eds. W. Jack Rink and J. Thompson (Berlin-Heidelberg: SpringerNetherlands).

Surge, D., and Walker, K. J. (2006). Geochemical variation in microstructural shell layers of the southern quahog (Mercenaria campechiensis): Implications for reconstructing seasonality. *Palaeogeogr. Palaeocl.* 237, 182–190. doi: 10.1016/j.palaeo.2005.11.016

Torres, M. E., Zima, D., Falkner, K. K., Macdonald, R. W., O'brien, M., Schöne, B. R., et al. (2011). Hydrographic changes in nares strait (Canadian Arctic Archipelago) in recent decades based on δ18O profiles of bivalve shells. *Arctic* 64, 45–58. doi: 10.14430/arctic4079

Truong, C., Oudre, L., and Vayatis, N. (2020). Selective review of offline change point detection methods. *Signal Process.* 167, 107299. doi: 10.1016/j.sigpro.2019.107299

Tukey, J. W. (1977). "Exploratory data analysis," in *Reading*. Ed. M. A. Addison-Wesley (Reading: Massachusetts).

Vihtakari, M., Renaud, P. E., Clarke, L. J., Whitehouse, M. J., Hop, H., Carroll, M. L., et al. (2016). Decoding the oxygen isotope signal for seasonal growth patterns in Arctic bivalves. *Palaeogeogr. Palaeocl.* 446, 263–283. doi: 10.1016/j.palaeo.2016.01.008

Weidman, C. R., Jones, G. A., and Kyger, (1994). The long-lived mollusc Arctica islandica: A new paleoceanographic tool for the reconstruction of bottom temperatures for the continental shelves of the northern North Atlantic Ocean. *J. Geophys. Res-Oceans* 99, 18305–18314. doi: 10.1029/94JC01882

Winkelstern, I., Surge, D., and Hudley, J. W. (2013). Multiproxy sclerochronological evidence for plio-pleistocene regional warmth: United States mid-Atlantic coastal plain. *PALAIOS* 28, 649–660. doi: 10.2110/palo.2013.p13-010r

Witbaard, R., Jenness, M. I., van der Borg, K., and Ganssen, G. (1994). Verification of annual growth increments in Arctica islandica L. from the North Sea by means of oxygen and carbon isotopes. *Neth. J. Sea. Res.* 33, 91–101. doi: 10.1016/0077-7579(94)90054-X

Wycech, J. B., Kelly, D. C., Kozdon, R., Orland, I. J., Spero, H. J., and Valley, J. W. (2018). Comparison of δ18O analyses on individual planktic foraminifer (Orbulina Universa) shells by SIMS and gas-source mass spectrometry. *Chem. Geol.* 483, 119–130. doi: 10.1016/j.chemgeo.2018.02.028

Zettler, M. L. (2002). Ecological and morphological features of the bivalve Astarte borealis (Schumacher 1817) in the Baltic Sea near its geographical range. *J. Shellfish Res.* 21, 33–40.

Zettler, M. L., Friedland, R., Gogina, M., and Darr, A. (2017). Variation in benthic long-term data of transitional waters: Is interpretation more than speculation? *PLoS One* 12, e0175746. doi: 10.1371/journal.pone.0175746

Zuo, H., Balmaseda, M. A., Tietsche, S., Mogensen, K., and Mayer, M. (2019). The ECMWF operational ensemble reanalysis–analysis system for ocean and sea ice: a description of the system and assessment. *Ocean Sci.* 15, 779–808. doi: 10.5194/os-15-779-2019

frontiers | Frontiers in Marine Science

TYPE Original Research
PUBLISHED 14 February 2024
DOI 10.3389/fmars.2024.1329924

OPEN ACCESS

EDITED BY
Hali Kilbourne,
University of Maryland Center for Environmental Science, United States

REVIEWED BY
Logan Brenner,
Columbia University, United States
Allison Lawman,
Colorado College, United States

*CORRESPONDENCE
Mayuri Inoue
inouem@cc.okayama-u.ac.jp

†PRESENT ADDRESSES
Shoko Sakata,
Graduate School of Environmental, Life, Natural Science and Technology, Okayama University, Okayama, Japan
Mayuri Inoue,
Graduate School of Environmental, Life, Natural Science and Technology, Okayama University, Okayama, Japan

‡These authors have contributed equally to this work and share first authorship

RECEIVED 30 October 2023
ACCEPTED 17 January 2024
PUBLISHED 14 February 2024

CITATION
Sakata S, Inoue M, Tanaka Y, Nakamura T, Sakai K, Ikehara M and Suzuki A (2024) Assessment of chemical compositions in coral skeletons (*Acropora digitifera* and *Porites australiensis*) as temperature proxies. *Front. Mar. Sci.* 11:1329924. doi: 10.3389/fmars.2024.1329924

Assessment of chemical compositions in coral skeletons (*Acropora digitifera* and *Porites australiensis*) as temperature proxies

Shoko Sakata[1†‡], Mayuri Inoue[1*†‡], Yasuaki Tanaka[2], Takashi Nakamura[2,3], Kazuhiko Sakai[2], Minoru Ikehara[4] and Atsushi Suzuki[5]

[1]Graduate School of Natural Science and Technology, Okayama University, Okayama, Japan, [2]Sesoko Station, Tropical Biosphere Research Center, University of the Ryukyus, Okinawa, Japan, [3]Faculty of Science, University of the Ryukyus, Okinawa, Japan, [4]Marine Core Research Institute, Kochi University, Nankoku Kochi, Japan, [5]Geological Survey of Japan, National Institute of Advanced Industrial Science and Technology (AIST), Tsukuba, Japan

Although biogenic carbonates, such as foraminifera and coccolithophorids, are valuable tools for reconstructing past environments, scleractinian corals also offer environmental data from tropical to subtropical regions with a higher time resolution. For example, oxygen isotopes ($\delta^{18}O$) and strontium-calcium (Sr/Ca) ratios have been utilized to reconstruct sea surface temperatures and salinity, primarily through the use of massive-type *Porites* sp. from the Pacific, as well as corals like *Diploria* and *Montastrea* from the Atlantic. While a few types of corals other than *Porites* have been utilized in paleoclimate studies, comprehensive evaluations of their geochemical tracers as temperature proxies have not been thoroughly conducted. Therefore, in this study, we focused on branching-type *Acropora*, which are found worldwide and are often present in fossil corals. We conducted a comparison of the chemical compositions ($\delta^{18}O$, $\delta^{13}C$, Sr/Ca, U/Ca, Mg/Ca, and Ba/Ca) of *Acropora digitifera* and *Porites australiensis* through temperature-controlled culture experiments. The validity of using the chemical components of *A. digitifera* as temperature proxies was then evaluated. Three colonies of *A. digitifera* and *P. australiensis* were collected for culture experiments on Sesoko Island, Okinawa, Japan. We reared coral samples in seawater with five different temperature settings (18, 21, 24, 27, 30°). The calcification rate and photosynthesis efficiency (*Fv/Fm*) of each nubbin were measured during the experimental period. After the culture experiment for 77 days, chemical components in skeletal parts grown during the experiment were then measured. Consequently, the mean growth rates and *Fv/Fm* throughout the experiment were higher for *A. digitifera* (0.22%/d and 0.63 for growth rate and *Fv/Fm*) compared to those for *P. australiensis* (0.11%/d and 0.38 for growth rate and *Fv/Fm*). This suggests that the higher efficiency of photosynthesis in *A. digitifera* would promote greater calcification compared to *P. australiensis*. Regarding the potential use as temperature proxies, *A. digitifera* exhibited a strong negative correlation, on average, between $\delta^{18}O$ and the water temperature ($r = 0.95$, $p < 0.001$). The temperature dependency was found to be comparable to that

10.3389/fmars.2024.1329924

reported in *Porites* corals (-0.11 and -0.17 ‰/°C for *P. australiensis* and *A. digitifera*, respectively). Thus, the $\delta^{18}O$ of *A. digitifera* appeared to be a useful temperature proxy, although it was also slightly influenced by skeletal growth rate at the same temperature. A strong negative correlation was also observed between the mean Sr/Ca ratio and temperature in *A. digitifera* ($r = 0.61$, $p < 0.001$) as well as *P. australiensis* ($r = 0.56$, $p < 0.001$), without a clear influence from the skeletal growth rate. Therefore, the skeletal Sr/Ca ratio in corals may have been primarily influenced by water temperature, although large deviations in Sr/Ca were observed in *A. digitifera*, even at the same temperature settings. This deviation can be reduced by subsampling an apical part of a polyp including the axis of skeletal growth. The U/Ca ratio of *A. digitifera* appeared to be affected by internal pH variation within the corals, especially at 30°C. Similar to U/Ca ratios, metabolic and kinetic effects on corals were observed in $\delta^{13}C$ of *A. digitifera* at 18 and 30°C. In addition, considering the variation pattern of both U/Ca and $\delta^{13}C$ of *A. digitifera* at 30°C, it has been suggested that respirations may overwhelm photosynthesis for coral samples at 30°C. Therefore, the U/Ca and $\delta^{13}C$ of *A. digitifera* could potentially be used as proxies of biomineralization processes, whereas the $\delta^{18}O$ and Sr/Ca displayed a high possibility of acting as temperature proxies.

KEYWORDS

coral skeleton, culture experiment, SST proxy, geochemical tracers, calcification mechanism

1 Introduction

The chemical compositions of scleractinian corals, such as $\delta^{18}O$ and Sr/Ca, have been recognized as proxies for sea surface temperature (SST, e.g., Beck et al., 1992; Gagan et al., 2000; Cobb et al., 2003; Ramos et al., 2020). Specifically, massive corals such as *Porites* sp., which are dominated in the Pacific region, have been comprehensively used to reconstruct SST and salinity because they have clear annual bands (D'Olivo et al., 2018; Abram et al., 2020; Goodkin et al., 2021). This reconstruction method has become an indispensable tool in paleoceanography and paleoclimatology. Recently, Sr-U and Li/Mg in coral skeletons have been reported as new proxies for water temperature (Montagna et al., 2014; DeCarlo et al., 2016; Cuny-Guirriec et al., 2019). Although almost all SST records that have contributed to paleoclimate studies have been reconstructed using *Porites* corals, the genus *Isopora*, which belongs to the family Acroporidae, was successfully used in reconstructing SST during the last deglaciation, including the last glacial maximum (Felis et al., 2014). In this previous study, chemical components contained in bulk skeletal samples, rather than sub-samples collected along an annual band, were used to compare SST values. Therefore, it is important to investigate the possibility of using the chemical compositions of genera other than *Porites*, such as *Acropora*, as SST proxies, even though some of these genera grow in a branching morphology. Interestingly, Reynaud et al. (2007) found a temperature dependence of Sr/Ca in *Acropora* sp. based on the culture experiments; however, a potential colony dependence has not been investigated. In this study, we used three colonies of *Acropora digitifera* together with *Porites australiensis* for a temperature-controlled culture experiment to investigate their potential as an SST proxy and any colony dependences on its proxy.

Geochemical proxies in coral skeletons have been used to reconstruct SST as well as salinity, seawater pH, terrestrial runoff, and/or pollution (e.g., Gagan et al., 2000; McCulloch et al., 2003; Pelejero et al., 2005; Inoue et al., 2014; Wei et al., 2015; Genda et al., 2022). However, the detailed mechanisms of incorporation and variability of these proxies occurring within the corals, in addition to their skeletal growth, are not yet fully understood. Although there are studies on the biomineralization of scleractinian corals in terms of their utility as proxies, multiple species other than massive-type *Porites* have been used for this purpose (e.g., Inoue et al., 2007; Gaetani et al., 2011; Inoue et al., 2011; Gagnon et al., 2012; Ram and Erez, 2021). Furthermore, massive *Porites* reportedly show tolerance to environmental stresses, such as high temperature and turbidity, whereas branching *Acropora* seems to be more sensitive to such stresses than massive corals (Loya et al., 2001; Fitt et al., 2009; Jones et al., 2020; Afzal et al., 2023). Loya et al. (2001) reported that massive type colonies, including *Porites* sp., survived the 1998 warming incident in Okinawa, Japan, whereas branched corals, including *A. digitifera*, were heavily impacted. They suggested that this was partially attributable to tissue thickness, in which *Porites* and *Acropora* have thicker and thinner tissues,

respectively. Trophic plasticity is another cause of differences in stress tolerance among genera. Conti-Jerpe et al. (2020) defined coral trophic niches based on $\delta^{13}C$ and $\delta^{15}N$ analyses. They investigated seven genera and found that their trophic levels varied between autotrophs, mixotrophs, and heterotrophs. *Acropora* was clearly categorized as autotrophic, whereas *Porites* was mixotrophic. *Porites* corals generally transmit their symbionts directly from parents to descendants, whereas *Acropora* acquire them anew from the environment in each generation; these processes are referred to as vertical and horizontal transmissions, respectively (Lajeunesse et al., 2004). Thus, the growth strategies of corals and their responses to environmental stresses vary among genera, particularly between the massive *Porites* and the branching *Acropora*. However, direct comparisons of geochemical proxies contained in *Porites* and *Acropora* have not been made. Therefore, it is important to confirm temperature-driven patterns of the incorporation of chemical composition in the coral skeletons of different genera.

In the present study, we performed a culture experiment using both *P. australiensis* and *A. digitifera*, which are predominantly found in the shallow reefs around Okinawa, Japan, within an identical culture system. The study investigated differences in growth patterns and skeletal growth in response to temperature between the two species, as well as their potential as SST proxies. The influence of different growth patterns of two species on the variations of SST proxies is also discussed.

2 Materials and methods

2.1 Preparation of coral sub-samples (nubbins)

Corals (*Porites australiensis* and *Acropora digitifera*) were collected from a fringing reef on Sesoko Island, Okinawa, Japan, on August 12 and October 11, 2013. Three large colonies of each species were collected at intervals of approximately 10 m to avoid sampling of the clones created by fragmentation. The colonies were maintained in a tank containing running seawater from the Sesoko reef under natural light conditions at Sesoko Station, Tropical Biosphere Research Center, University of the Ryukyus, Okinawa, Japan, before the start of the experiment. Similar sized cubes (approximately 2.0 × 2.0 × 2.0 cm) and branches (approximately 2.0-3.0 cm lengths), hereafter referred to as nubbins, were cut from parent colonies of *P. australiensis* and *A. digitifera*, respectively. Prepared nubbins were combined with acrylic plates (3.0 x 3.0 cm and 4.5 x 4.5 cm for *A. digitifera* and *P. australiensis*, respectively) using superglue. Nubbins from each colony of both species were allowed to cure to recover from the stress of cutting in an outdoor aquarium for approximately one month. The skeletal growth rates were measured by buoyant weight method in which coral nubbins were suspended on the balance and underwater weight was measured (Davies, 1989). Because tissue does not contribute to the buoyant weight of the coral when weighed underwater due to its similar density with seawater, only skeletal weight can be directly weighed. For the experiment, six nubbins from each colony of both species were placed in two aquaria at each temperature setting as described in Figure 1. Since weights of all nubbins were measured during the curing period, six nubbins were arranged without significant differences in their initial weight.

2.2 Experimental settings

The seawater of Sesoko reef was filtered through a cartridge-type filter (pore size, 1 μm) and the experiment was performed using a flowthrough system. Duplicate aquaria were filled with filtered seawater adjusted to each temperature setting of 18, 21, 24, 27 and 30˚C. Filled seawater from the duplicate aquaria at each temperature was cooled from the outside by circulating the cooled water in a large tank to maintain the temperature. For seawater of 18 and 21°C, firstly seawater was cooled to approximately 23°C in separate tanks using a chiller, this cooled seawater was then distributed to the experimental aquaria and adjusted the temperature. Furthermore, for the 18°C aquaria, two chillers were externally installed in a large tank to maintain the temperature. The water temperature in each aquarium was recorded every hour using a logger (Thermocron SL, KN Laboratories, Supplementary Figure 1). Because a moderate water flow is necessary to maintain coral health (Nakamura et al., 2005), a filter pump was installed in each tank to generate gentle seawater circulation. Three nubbins from each colony of two species were placed in an aquarium. Therefore, 36 nubbins (six replicates from each colony) were cultured at each temperature with a 12:12 light/dark photoperiod (120-140 mmol/m^2/s) under metal halide lamps (Funnel 2,150 W, Kamihata, Japan). Each aquarium was cleaned by rinsing off with sponges approximately once every two weeks to remove algae attached to it. Using this system, all nubbins were cultured for 77 d, from December 2, 2013, to February 17, 2014.

2.3 Maximum quantum yield of Photosystem II of symbiotic algae

The maximum quantum yields of photosystem II (*Fv/Fm*) of symbiotic algae within all nubbins were measured using a Diving-PAM Underwater Fluorometer (Walz, Germany) after an hour of acclimation to darkness, as described by Iguchi et al. (2012). Because the surface area of the nubbins of *P. australiensis* is wide, measurements were conducted on three randomly selected parts of the colony surface, and the median value was adopted as the representative value of each nubbin. One measurement per nubbin was conducted for branching *A. digitifera*. Measurements were conducted at 14, 45, and 77 d after the start of the experiment in addition to the before the experiment.

2.4 Skeletal growth rate

Coral skeletal weights were measured 14, 35, and 63 d after the start of the experiment as buoyant weight (Davies, 1989; Anthony et al., 2008) in addition to before (day 0) and after (day 77) the

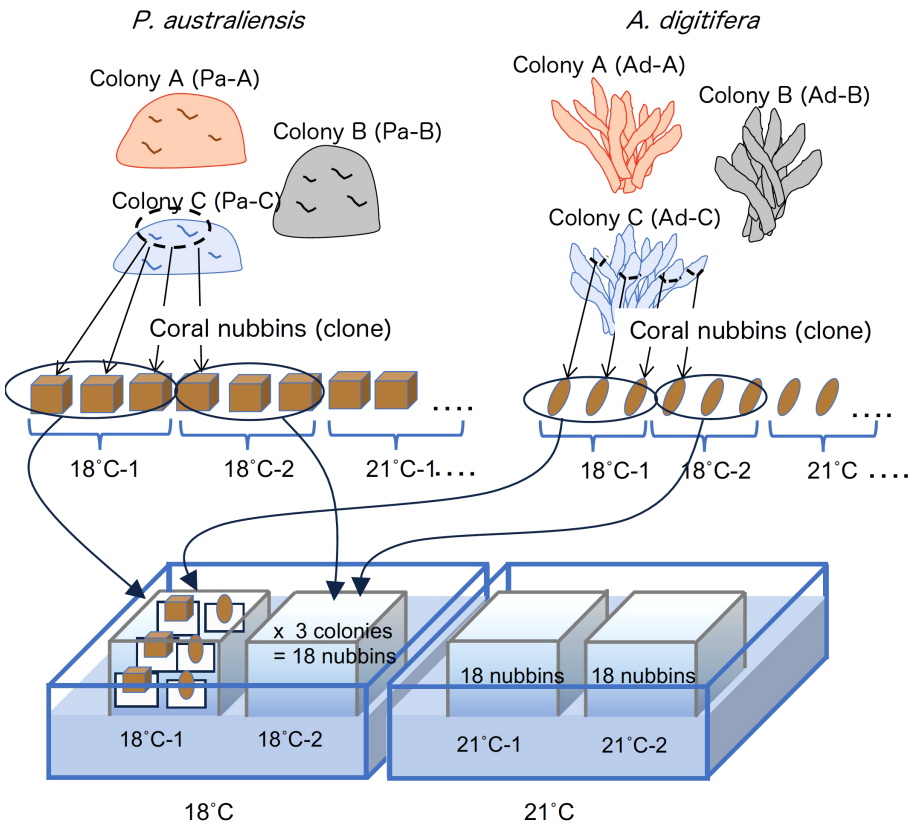

FIGURE 1
Design of the culture experiment conducted in this study.

experiment. The growth rate of coral skeleton during the experiment was calculated as the percentage change in skeletal weight during a specific period in the experiment as below:

$$\text{Growth rate}\,(\%/\text{d}) = \{(W_2 - W_1)/W_1 \times 100\}/\text{Day}$$

where W_1 and W_2 represent the skeletal weight at the beginning and end of a specific period, respectively, and Day is the number of days during the period.

2.5 Collection of skeletal samples

After the experiment was completed, coral nubbins were soaked in an H_2O_2 solution with a pH adjusted to >8 using NaOH for more than 24 h to remove tissue parts. Then, samples were rinsed several times using deionized water and dried in an oven at 40°C. In this study, marking methods, such as using alizarin red, as described by Suzuki et al. (2005), were not used to reduce stress on corals. Therefore, we visually checked the growth area of the skeletons that had grown during the experiment by comparing photographs taken before and after the experiment (Figure 2). Subsequently, the coral skeletons grown in the temperature experiment were scraped off with a spatula and stored in vials. Then collected skeletal parts were gently crushed within vials to make powder samples as bulk sample. Except for the coral samples that apparently died or did not grow large enough to collect powder samples, skeletal samples from almost all nubbins were collected from *A. digitifera*. However, skeletal samples of *P. australiensis* from the 18°C setting could not be collected because their skeletal growth was too small to visually distinguish the skeletal parts that grew during the rearing period.

2.6 Geochemical analyses of skeletal parts grown during the experiment

We measured trace element ratios (Sr/Ca, Mg/Ca, U/Ca, and Ba/Ca ratios) and isotope ratios ($\delta^{13}C$ and $\delta^{18}O$) in skeletal samples grown only during the rearing period using a method similar to that described by Inoue et al. (2018). To measure the concentrations of trace elements, 70 ± 5 μg of skeletal samples was digested in 2% HNO_3 that contained internal standards (^{45}Sc, ^{89}Y, ^{209}Bi) to correct instrumental drift. The concentrations of Sr, Ca, Mg, U, and Ba were measured at Okayama University using an inductively coupled plasma mass spectrometer (ICP-MS; Agilent Technology, 7700x). Standard solutions prepared from JCp-1, a coral (*Porites* spp.) standard material provided by the Geological Survey of Japan (Okai et al., 2002), were measured for every fifth sample for data correction. The relative standard deviations from replicate measurements of the JCp-1 standard were 0.59, 0.81, 1.5 and 3.2% for the Sr/Ca, Mg/Ca, U/Ca, and Ba/Ca ratios, respectively (n = 29). Measurements of $\delta^{18}O$ and $\delta^{13}C$ were conducted using an

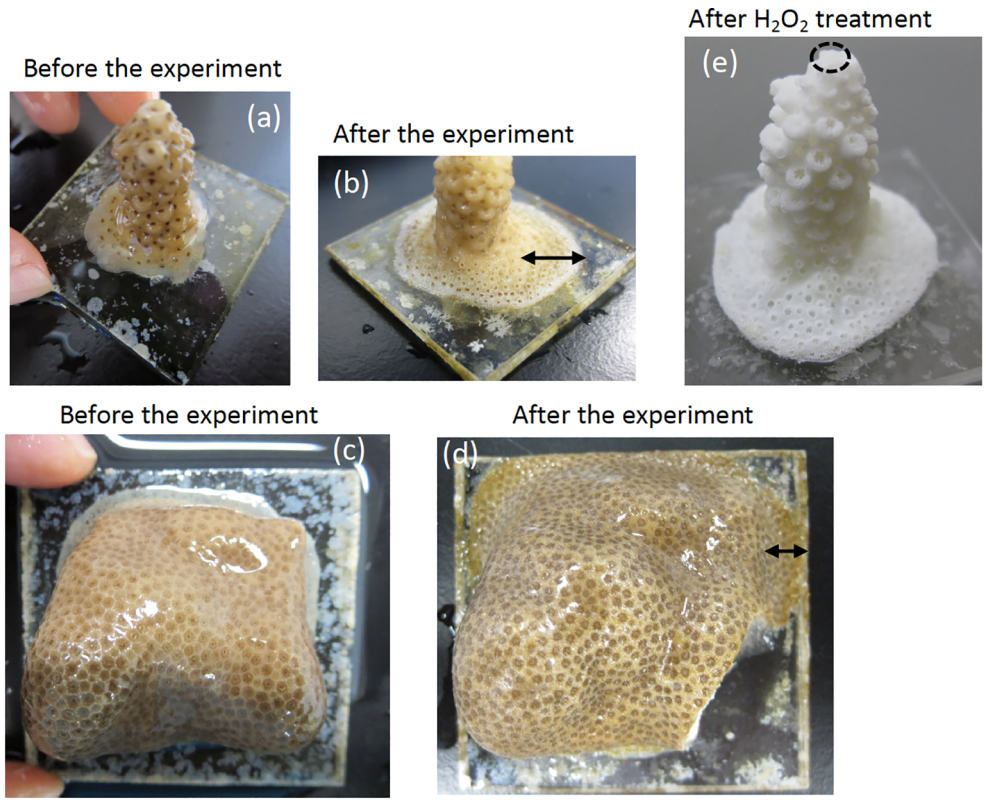

FIGURE 2
Photographs of *A. digitifera* and *P. australiensis* used in this study before **(A, C)** and after the experiment **(B, D)**, respectively. Black arrows in **(B)** and **(D)** represent skeletal parts that grew during the experiment. A photograph of *A. digitifera* following the H_2O_2 treatment to remove organic tissue parts is presented in **(E)**. An approximate place of the tip of *A. digitifera* used for an additional experiment described in the text is circled with dotted line in **(E)**. The sizes of acrylic plates prepared for *A. digitifera* and *P. australiensis* were approximately 3.0 x 3.0 and 4.5 x 4.5 cm, respectively.

online system employing an IsoPrime isotope-ratio mass spectrometer (GV Instruments Ltd.) coupled to a Multicarb automatic sample treatment system at the Center for Advanced Marine Core Research at Kochi University. Approximately 100 ± 10 μg of skeletal samples were used for the measurements and all $\delta^{18}O$ and $\delta^{13}C$ data were normalized to the Vienna Pee Dee Belemnite (V-PDB) scale using the international standard NBS-19 ($\delta^{18}O$ = -2.20‰, $\delta^{13}C$ = -1.95‰) of the National Institute of Standards and Technology. Additionally, the CO-1 ($\delta^{18}O$= -2.4 ‰, $\delta^{13}C$= 2.49 ‰) and IAEA-603 standards ($\delta^{18}O$= -2.73 ‰, $\delta^{13}C$= 2.46 ‰) of the International Atomic Energy Agency were partially used as running standards. The standard deviations for replicate measurements of $\delta^{18}O$ and $\delta^{13}C$ on NBS-19 within the mass spectrometer runs were< 0.1‰ and< 0.05‰ for $\delta^{18}O$ and $\delta^{13}C$, respectively.

2.7 Statistical analysis

The relationship between the chemical compositions of the coral skeleton and water temperature and growth rate were determined using the linear correlation of ordinary least squares. Only for the relations between Sr/Ca and $\delta^{18}O$, that have been generally used as temperature proxies, and water temperature were calibrated by the weighted least square (WLS) method. Growth rate differences among the three colonies were tested via Tukey's pairwise method using PAST (Hammer et al., 2001). Differences of measured chemical compositions between *P. australiensis* and *A. digitifera* were also tested using PAST. In this method, Bayes factor (BF), which quantifies for the hypothesis of unequal means (Hammer et al., 2001), was used to evaluate equal or unequal between two species. Practically, a BF value larger than 3 can be considered as evidence for unequal means. For this test, data at 18˚C were removed since the number of those for *P. australiensis* were very small as mentioned later. In this study, *p*-values below 0.05 were considered statistically significant and correlation coefficients above 0.5 were considered to be correlated unless otherwise noted.

3 Results

3.1 Skeletal growth and maximum quantum yield of Photosystem II of coral nubbins

The skeletal growth rates of the three colonies of *P. australiensis* (Pa-A, Pa-B, and Pa-C) and *A. digitifera* (Ad-A, Ad-B, and Ad-C) during the experiment are shown in Tables 1, 2 and Figure 3. The temporal variability of growth rates throughout the experiment is also presented in Figure 3. For *P. australiensis*, seven and 13

10.3389/fmars.2024.1329924

nubbins from the 18 and 30°C temperature settings appeared dead, respectively, as they were totally bleached and/or covered by algae at the end of the experiment (Table 1). On the other hand, eight nubbins for *A. digitifera* at only 30°C appeared dead (Table 2). Although they appeared dead at the end of the experiment, their skeletal weights were measured up to day 63 that was the last record before the end of the experiment (day 77). Then the growth rate is presented as growth per day (% per day) using weight records up to the period during skeletal growth was observed. Averaged growth rates (%/d) throughout the experiment were 0.11 ± 0.13 and 0.22 ± 0.14%/d which correspond to the skeletal growth of 13.39 ± 16.11 and 3.34 ± 2.83 mg/d, for all nubbins of *P. australiensis* and *A. digitifera*, respectively. Since the initial size and surface area, which affect skeletal growth represented by mg/d, were different between nubbins of *P. australiensis* and *A. digitifera*, hereafter we use growth rate represented by %/d for the comparison and discussion. Then, the mean growth rates were significantly different between two species ($t = 5.35$, $p < 0.001$).

The skeletons of all nubbins, except Pa-B at 30°C, grew during the first 14 out of 77 d of the experiment (Figure 3). Averaged growth rate during the first 2 weeks were higher compared to other periods in both species and 0.19 ± 0.14 and 0.42 ± 0.21%/d were

TABLE 1 Data of each parameter of all nubbins of *P. australiensis* used in the experiment.

Colony Pa-A									
Water temperature (°C)	Sample ID	Growth rate %/day	*Fv/Fm* at the day 45	Mg/Ca mmol/mol	Sr/Ca mmol/mol	Ba/Ca µmol/mol	U/Ca µmol/mol	$\delta^{13}C$ ‰	$\delta^{18}O$ ‰
18	36**	0.036	0.423	–	–	–	–	–	–
	43*	-0.005	0.404	–	–	–	–	–	–
	31*	-0.003	0.219	–	–	–	–	–	–
	40*	-0.002	0.246	–	–	–	–	–	–
	24**	0.000	0.410	–	–	–	–	–	–
	9*	0.037	0.359	–	–	–	–	–	–
21	18	0.082	0.581	5.600	8.793	59.252	1.250	-6.656	-3.927
	15**	0.202	0.565	–	–	–	–	–	–
	2	0.178	0.610	4.530	8.807	70.251	1.311	-6.142	-4.028
	8**	0.122	0.537	–	–	–	–	–	–
	28**	0.144	0.555	–	–	–	–	–	–
	42	0.214	0.498	4.950	8.834	100.856	1.383	-6.484	-3.974
24	17	0.318	0.585	5.485	8.513	31.529	1.184	-6.220	-4.190
	44	0.214	0.570	8.326	8.836	85.974	1.179	–	–
	19	0.260	0.561	5.429	8.772	43.203	1.219	-5.793	-4.039
	34	0.266	0.570	6.148	8.659	36.294	1.244	-6.113	-4.055
	16	0.259	0.579	4.360	8.783	25.535	1.291	-6.629	-5.448
	12	0.195	0.580	4.346	8.772	108.923	1.197	–	–
27	11	0.206	0.460	5.261	8.598	66.015	1.203	-4.142	-4.371
	22	0.112	0.448	7.132	8.753	73.745	1.528	-4.619	-4.307
	6	0.080	0.433	5.680	8.623	57.184	1.273	–	–
	41	0.150	0.471	5.146	8.625	64.254	1.230	–	–
	26	0.152	0.482	4.455	8.672	52.146	1.317	–	–
	25	0.210	0.492	5.444	8.715	52.423	1.453	-3.472	-3.955
30	7	0.079	0.303	5.955	8.393	52.650	1.340	–	–
	39	0.061	0.341	5.083	8.622	26.588	1.218	-5.460	-4.984

(Continued)

10.3389/fmars.2024.1329924

TABLE 1 Continued

Colony Pa-A									
Water temperature (°C)	Sample ID	Growth rate %/day	*Fv/Fm* at the day 45	Mg/Ca mmol/mol	Sr/Ca mmol/mol	Ba/Ca µmol/mol	U/Ca µmol/mol	$\delta^{13}C$ ‰	$\delta^{18}O$ ‰
	29	0.123	0.356	7.345	8.581	98.370	1.381	-5.224	-5.206
	45	0.068	0.350	6.720	–	13.024	1.591	–	–
	3	0.026	0.296	10.360	8.698	17.013	1.423	-3.911	-4.666
	23*	0.080	0.337	–	–	–	–	–	–
Colony Pa-B									
Water temperature (°C)	Sample ID	Growth rate %/day	*Fv/Fm* at the day 45	Mg/Ca mmol/mol	Sr/Ca mmol/mol	Ba/Ca µmol/mol	U/Ca µmol/mol	$\delta^{13}C$ ‰	$\delta^{18}O$ ‰
18	22*	0.037	0.339	–	–	–	–	–	–
	36*	-0.292	0.294	–	–	–	–	–	–
	1**	0.064	0.344	–	–	–	–	–	–
	3**	0.033	0.173	–	–	–	–	–	–
	11**	0.020	0.279	–	–	–	–	–	–
	27**	0.007	0.240	–	–	–	–	–	–
21	21	0.106	0.457	12.453	8.714	82.616	1.377	–	–
	18**	0.131	0.447	–	–	–	–	–	–
	43	0.135	0.436	9.938	9.093	167.242	1.852	-4.264	-3.579
	5**	0.095	0.459	–	–	–	–	–	–
	28	0.133	0.539	7.128	8.914	113.386	1.478	-6.102	-3.965
	39**	0.084	0.485	–	–	–	–	–	–
24	29	0.187	0.506	3.942	8.847	143.304	1.343	-5.518	-4.425
	4**	0.066	0.460	–	–	–	–	–	–
	32	0.164	0.525	4.827	8.718	86.721	1.418	-5.577	-4.335
	45**	0.067	0.482	–	–	–	–	–	–
	42**	0.121	0.407	–	–	–	–	–	–
	25**	0.079	0.379	–	–	–	–	–	–
27	13**	0.042	0.315	–	–	–	–	–	–
	38**	0.021	0.280	–	–	–	–	–	–
	2**	0.031	0.288	–	–	–	–	–	–
	26**	-0.002	0.284	–	–	–	–	–	–
	44**	0.046	0.309	–	–	–	–	–	–
	6**	-0.002	0.261	–	–	–	–	–	–
30	31*	-0.035	0.294	–	–	–	–	–	–
	17*	-0.063	0.155	–	–	–	–	–	–
	8*	-0.028	0.216	–	–	–	–	–	–

(Continued)

10.3389/fmars.2024.1329924

TABLE 1 Continued

Colony Pa-B									
Water temperature (°C)	Sample ID	Growth rate %/day	*Fv/Fm* at the day 45	Mg/Ca mmol/mol	Sr/Ca mmol/mol	Ba/Ca µmol/mol	U/Ca µmol/mol	$\delta^{13}C$ ‰	$\delta^{18}O$ ‰
	20*	-0.086	0.303	–	–	–	–	–	–
	23*	-0.059	0.330	–	–	–	–	–	–
	19*	-0.076	0.408	–	–	–	–	–	–
Colony Pa-C									
Water temperature (°C)	Sample ID	Growth rate %/day	*Fv/Fm* at the day 45	Mg/Ca mmol/mol	Sr/Ca mmol/mol	Ba/Ca µmol/mol	U/Ca µmol/mol	$\delta^{13}C$ ‰	$\delta^{18}O$ ‰
18	24**	-0.047	0.352	–	–	–	–	–	–
	28**	0.042	0.393	–	–	–	–	–	–
	15**	0.047	0.372	–	–	–	–	–	–
	25**	0.041	0.299	–	–	–	–	–	–
	12**	0.021	0.323	–	–	–	–	–	–
	10*	0.049	0.286	–	–	–	–	–	–
21	36	0.334	0.473	6.382	8.992	58.343	1.757	-4.533	-3.801
	16	0.381	0.488	7.762	9.082	–	1.814	-4.416	-3.503
	27	0.301	0.448	8.149	8.989	111.018	1.686	-4.615	-3.883
	19	0.309	0.484	6.349	9.039	86.018	1.727	-4.879	-3.454
	13	0.368	0.469	4.558	8.775	36.766	1.681	-5.009	-4.335
	14**	0.383	0.484	–	–	–	–	–	–
24	4	0.274	0.403	3.816	8.936	63.119	1.224	-5.709	-4.134
	2	0.311	0.386	5.313	8.412	40.542	1.130	-6.136	-4.412
	17	0.379	0.426	8.768	8.628	109.407	1.430	-4.321	-3.914
	21	0.304	0.387	13.312	8.401	104.554	1.552	-3.613	-4.113
	30	0.316	0.383	3.827	8.704	103.494	1.313	-4.450	-4.559
	39	0.308	0.375	5.203	8.768	100.186	1.586	-3.900	-4.222
27	5**	0.119	0.286	–	–	–	–	–	–
	11**	0.140	0.262	–	–	–	–	–	–
	18	0.166	0.258	8.586	8.915	118.189	1.545	-3.287	-4.473
	6**	0.155	0.278	–	–	–	–	–	–
	34	0.172	0.250	11.463	8.559	58.051	1.537	–	–
	33	0.181	0.248	7.926	8.773	55.581	1.534	-3.347	-4.300
30	1*	0.013	0.204	–	–	–	–	–	–
	20*	0.025	0.191	–	–	–	–	–	–
	37*	-0.004	0.197	9.565	8.460	88.587	1.782	-3.839	-5.047
	3*	-0.044	0.220	5.984	8.934	33.560	1.474	-4.716	-4.401

(Continued)

10.3389/fmars.2024.1329924

TABLE 1 Continued

Colony Pa-C									
Water temperature (°C)	Sample ID	Growth rate %/day	*Fv/Fm* at the day 45	Mg/Ca mmol/mol	Sr/Ca mmol/mol	Ba/Ca µmol/mol	U/Ca µmol/mol	$\delta^{13}C$ ‰	$\delta^{18}O$ ‰
	32*	0.070	0.340	6.798	8.290	76.510	–	–	–
	8*	0.005	0.279	–	–	–	–	–	–

Sample IDs with * indicate that the nubbin appeared to be dead after the experiment, and those with ** indicate that an insufficient amount of bulk skeletal samples were collected.

TABLE 2 Data of each parameter of all nubbins of *A. digitifera* used in the experiment.

Colony Ad-A									
Water temperature (°C)	Sample ID	Growth rate %/day	*Fv/Fm* at the day 45	Mg/Ca mmol/mol	Sr/Ca mmol/mol	Ba/Ca µmol/mol	U/Ca µmol/mol	$\delta^{13}C$ ‰	$\delta^{18}O$ ‰
18	16	0.016	0.574	6.821	8.997	8.878	1.533	-0.993	-2.416
	26	0.004	0.573	4.924	9.010	11.898	1.901	-0.041	-2.036
	44	-0.080	0.544	–	8.540	–	1.370	0.820	-1.990
	10**	0.002	0.419	–	–	–	–	–	–
	11	0.003	0.412	5.357	9.115	18.319	1.809	0.307	-2.121
	8	0.004	0.507	4.990	8.950	10.739	1.842	-0.296	-2.554
21	1	0.192	0.681	7.623	8.986	17.101	1.557	-2.360	-2.788
	24	0.191	0.659	5.021	9.040	15.733	1.627	-3.018	-2.996
	35	0.254	0.673	–	8.525	15.042	1.466	-2.295	-2.920
	29	0.269	0.677	7.434	8.939	15.424	1.337	-3.198	-3.063
	32	0.228	0.600	4.409	9.109	13.582	1.761	-1.651	-2.643
	5	0.280	0.674	9.351	8.956	10.874	1.609	-2.429	-2.846
24	27**	0.215	0.722	–	–	–	–	–	–
	23	0.064	0.609	6.464	8.807	7.288	1.721	-1.879	-3.330
	36	0.327	0.675	11.416	8.555	7.532	1.369	-1.546	-3.189
	43	0.341	0.700	4.684	8.941	9.480	1.530	-1.662	-3.335
	18	0.278	0.689	11.373	8.692	10.475	1.397	-1.345	-3.356
	38	0.426	0.647	–	–	12.159	1.425	-0.871	-3.020
27	37	0.149	0.665	6.133	8.822	6.382	1.505	-1.280	-3.356
	31	0.265	0.682	7.226	8.673	10.087	1.422	-0.306	-3.321
	34	0.373	0.684	11.655	8.481	17.550	1.396	-0.543	-3.708
	20	0.149	0.674	5.210	8.831	10.931	1.488	-1.106	-3.772
	39	0.183	0.687	6.166	8.809	5.697	1.685	-0.689	-3.647
	45	0.390	0.679	11.805	8.529	15.676	1.511	-1.299	-3.727
30	28*	0.168	0.644	5.481	8.855	8.399	1.695	-3.050	-4.393
	41*	0.201	0.670	5.039	8.837	9.285	1.764	-3.211	-4.608

(Continued)

10.3389/fmars.2024.1329924

TABLE 2 Continued

Colony Ad-A									
Water temperature (°C)	Sample ID	Growth rate %/day	*Fv/Fm* at the day 45	Mg/Ca mmol/mol	Sr/Ca mmol/mol	Ba/Ca µmol/mol	U/Ca µmol/mol	$\delta^{13}C$ ‰	$\delta^{18}O$ ‰
	21	0.104	0.655	7.696	8.601	6.551	1.504	-3.612	-4.506
	9	0.116	0.651	5.033	8.967	7.733	1.672	-3.063	-4.272
	17*	0.264	0.689	9.151	8.607	8.710	1.514	-2.458	-4.064
	14	0.174	0.685	6.973	8.627	5.805	1.680	-2.511	-4.190
Colony Ad-B									
Water temperature (°C)	Sample ID	Growth rate %/day	*Fv/Fm* at the day 45	Mg/Ca mmol/mol	Sr/Ca mmol/mol	Ba/Ca µmol/mol	U/Ca µmol/mol	$\delta^{13}C$ ‰	$\delta^{18}O$ ‰
18	13	0.060	0.454	6.990	9.153	10.585	1.984	-0.913	-2.367
	42	0.069	0.594	5.563	9.293	–	1.864	–	-2.661
	27	0.064	0.479	11.453	8.815	21.349	1.793	-1.129	-2.736
	4	0.036	0.419	8.430	9.036	16.973	1.830	-0.706	-2.160
	1	0.041	0.494	5.841	9.271	28.527	1.882	-1.040	-2.429
	23	0.036	0.454	5.210	9.155	11.584	1.817	-0.844	-2.605
21	20	0.391	0.604	4.506	9.080	16.541	1.500	-3.582	-3.197
	3	0.406	0.642	7.518	9.007	16.270	1.529	-3.920	-3.169
	38	0.362	0.625	5.063	9.124	16.842	1.495	-3.631	-3.075
	41	0.154	0.649	5.304	9.145	23.336	1.630	-2.648	-2.929
	15	0.120	0.648	4.593	9.205	19.434	1.900	-1.679	-2.719
	25	0.174	0.640		8.564	16.318	1.741	-1.313	-2.155
24	10	0.292	0.592	–	8.456	12.610	1.375	-1.958	-3.011
	45	0.473	0.642	4.981	9.008	10.117	1.493	-2.405	-3.451
	19	0.347	0.628	4.734	9.018	13.338	1.522	-2.301	-3.400
	14	0.262	0.616	–	8.768	–	1.357	-3.051	-3.482
	12	0.190	0.649	6.469	9.006	14.345	1.634	-2.348	-3.149
	43	0.311	0.633	6.858	8.961	12.232	1.371	-3.005	-3.478
27	11	0.353	0.595	5.495	8.833	10.662	1.432	-1.630	-3.891
	31	0.276	0.611	9.595	8.636	14.309	1.326	-1.925	-4.027
	7	0.374	0.612	8.572	8.757	7.997	1.357	–	–
	35	0.119	0.649	6.120	8.921	9.273	1.732	-1.276	-3.630
	2	0.445	0.621	7.988	8.757	11.915	1.330	-2.501	-4.238
	22	0.317	0.606	5.485	8.826	13.910	1.313	-2.204	-3.868
30	36	0.187	0.628	6.775	8.793	6.308	1.452	-3.979	-4.656
	44*	-0.018	0.562	8.127	8.700	8.728	1.806	-2.854	-4.214
	29	0.185	0.677	9.568	8.562	14.845	1.433	-3.108	-4.549

(Continued)

10.3389/fmars.2024.1329924

TABLE 2 Continued

Colony Ad-B									
Water temperature (°C)	Sample ID	Growth rate %/day	*Fv/Fm* at the day 45	Mg/Ca mmol/mol	Sr/Ca mmol/mol	Ba/Ca μmol/mol	U/Ca μmol/mol	$\delta^{13}C$ ‰	$\delta^{18}O$ ‰
	39*	0.112	0.592	5.500	8.813	5.226	1.710	-2.524	-4.294
	16*	0.109	0.674	7.648	8.741	7.422	1.574	-3.285	-4.341
	26*	0.096	0.643	–	8.436	11.578	1.463	-2.222	-3.964
Colony Ad-C									
Water temperature (°C)	Sample ID	Growth rate %/day	*Fv/Fm* at the day 45	Mg/Ca mmol/mol	Sr/Ca mmol/mol	Ba/Ca μmol/mol	U/Ca μmol/mol	$\delta^{13}C$ ‰	$\delta^{18}O$ ‰
18	43	0.054	0.600	3.993	9.271	11.616	1.720	-1.606	-2.007
	13	0.077	0.496	4.003	9.296	11.051	1.719	-1.025	-2.174
	36	0.074	0.515	6.744	9.140	9.623	1.930	-0.747	-1.725
	20	0.021	0.480	4.276	9.196	12.300	1.991	-0.487	-1.728
	39	0.043	0.452	4.879	9.271	15.450	2.057	-1.525	-2.045
	26	0.046	0.434	–	8.607	20.261	1.549	-0.563	-2.320
21	27	0.260	0.686	4.309	9.170	12.877	1.410	-3.293	-3.196
	17	0.380	0.665	6.204	9.044	14.213	1.367	-2.762	-3.022
	37	0.341	0.676	5.240	8.983	10.716	–	-3.689	-3.247
	12	0.482	0.665	6.192	8.916	17.203	1.265	-3.327	-3.156
	7	0.274	0.685	5.743	9.089	12.927	1.571	-2.170	-2.516
	41	0.300	0.650	4.444	9.110	–	1.403	-2.553	-2.842
24	16	0.294	0.698	7.403	8.805	8.270	1.262	-1.971	-3.355
	8	0.242	0.692	6.517	8.763	8.447	1.371	-1.786	-3.349
	6	0.405	0.690	5.909	8.784	8.246	1.384	-2.200	-3.476
	1	0.349	0.701	4.868	8.902	10.122	1.421	-1.691	-3.490
	18	0.460	0.692	12.363	8.434	11.146	1.371	-1.783	-3.424
	38	0.302	0.695	5.533	8.927	8.761	1.384	-1.919	-3.283
27	10	0.258	0.683	12.265	8.685	8.664	1.317	-1.166	-4.276
	28	0.365	0.707	5.839	8.815	11.048	1.229	-0.749	-3.794
	14	0.276	0.701	4.907	8.861	8.076	1.349	-1.025	-3.978
	11	0.350	0.699	5.835	8.796	10.644	1.491	-1.828	-4.104
	5	0.469	0.666	7.045	8.730	7.609	1.303	-2.557	-4.438
	23	0.411	0.697	5.412	8.822	11.468	1.290	-2.240	-4.062
30	45	0.156	0.705	10.913	8.580	15.214	1.504	-3.588	-4.784
	32*	0.216	0.693	6.766	8.631	7.908	1.515	-3.648	-4.732
	29	0.210	0.687	4.907	8.808	4.853	1.512	-2.975	-4.380
	34	0.170	0.680	4.932	8.711	6.102	1.595	-3.250	-4.554

(Continued)

10.3389/fmars.2024.1329924

TABLE 2 Continued

Colony Ad-C									
Water temperature (°C)	Sample ID	Growth rate %/day	*Fv/Fm* at the day 45	Mg/Ca mmol/mol	Sr/Ca mmol/mol	Ba/Ca µmol/mol	U/Ca µmol/mol	$\delta^{13}C$ ‰	$\delta^{18}O$ ‰
	35	0.146	0.711	5.063	8.788	8.338	1.406	-3.160	-4.282
	9	0.151	0.701	7.048	8.783	13.826	1.535	-2.508	-4.115

Sample IDs with * indicate that the nubbin appeared to be dead after the experiment, and those with ** indicate that an insufficient amount of bulk skeletal samples were collected.

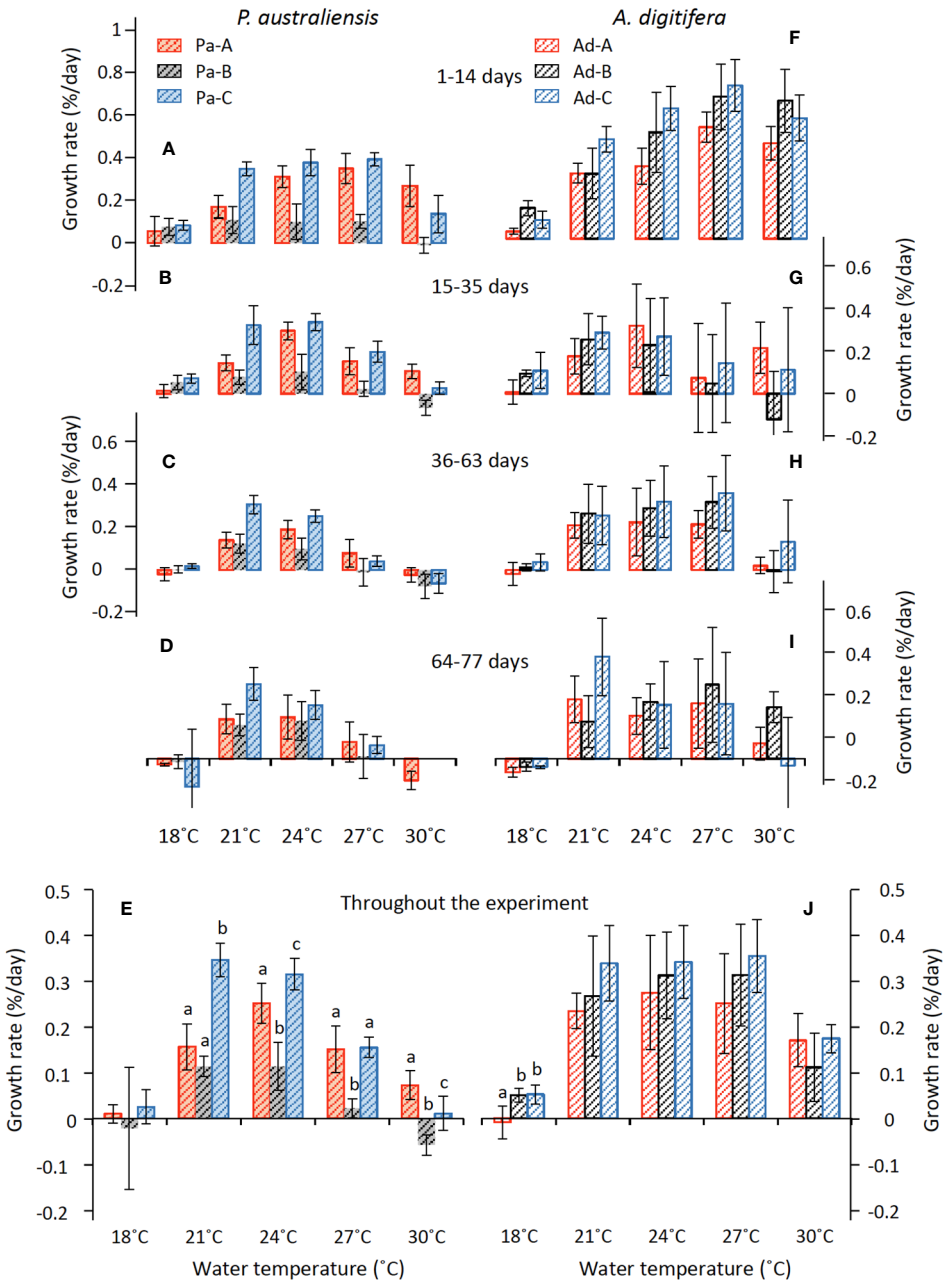

FIGURE 3
Variations in growth rate (mean ± 1sd) of *P. australiensis* **(A–E)** and *A. digitifera* **(F–J)** as a function of water temperature during the culture experiment for 77 d. The various colors indicate each colony; red, black and blue represent colonies A, B and C, respectively. Different letters (a, b, c) described on the bar indicates significant differences ($p < 0.05$) between the colonies at the same temperature. There are no colony differences in growth rate of *P. australiensis* at 18°C and *A. digitifera* from 21 to 30°C.

observed for *P. australiensis* and *A. digitifera* (Figures 3A, F). Temporal changes of mean growth rate for *P. australiensis* and *A. digitifera* for the three periods (15-35, 36-63, and 64-77 days) after the first two weeks were 0.12, 0.07, and 0.08 and 0.15, 0.18, and 0.15%/d, respectively. Deviations in the growth rate of each colony of *A. digitifera* were greater than that of *P. australiensis* throughout the experiment and at all temperature settings. Excepting the 18°C temperature, significant colony differences in the final growth rates throughout the experiment were observed for *P. australiensis*, whereas no differences were recorded for *A. digitifera* (Figures 3E, J).

Responses of the maximum photosynthetic quantum yield (*Fv*/*Fm*) against temperature were significantly higher in *A. digitifera* (0.63 ± 0.08) compared to those of *P. australiensis* throughout the experiment (0.38 ± 0.11; $t = 16.66$, $p < 0.001$; Figure 4). Temporal changes of mean *Fv*/*Fm* of *P. australiensis* and *A. digitifera* at each four measurements (before, the day 14, 45, and the end of the experiment) were 0.49, 0.42, 0.38, and 0.42 and 0.69, 0.67, 0.63, and 0.61, respectively. The values of *Fv*/*Fm* were almost the same for all three colonies of *A. digitifera*, with small deviations throughout the experiment (Figures 4E–H). In contrast, the *Fv*/*Fm* of Pa-A was higher than those of the other two colonies for *P. australiensis*, especially during the first half of the experiment (Figures 4A, B).

Because both the growth rates and *Fv*/*Fm* decreased and several nubbins were apparently dead in the last two weeks, we compared the relationships between the skeletal growth and *Fv*/*Fm* using data from days 63 and 45 for the growth rate and *Fv*/*Fm*, respectively. Consequently, strong positive relationships ($0.74 < r < 0.87$, $p < 0.001$) were observed in all three colonies of *P. australiensis*, whereas moderate to weak correlations ($0.37 < r < 0.56$, $p < 0.04$) were recorded for *A. digitifera* (Figure 5). This relation was maintained when data at 18°C was removed for *P. australiensis*, whereas it collapsed for *A. digitifera*. This suggests that the weak to moderate relationships found in *A. digitifera* were generated predominantly by data at 18°C in which *Fv*/*Fm* was lower (Figure 4G), rather than the trend found in all temperature settings.

3.2 Variations of chemical compositions

Regarding the measurements of chemical compositions, several nubbins could not be analyzed owing to an exceedingly small growth rate during the experiment, especially for the nubbins of *P. australiensis* grown under 18°C. In addition, we could not collect enough skeletal powder (> 70 and > 100 μg for trace elements and isotope measurements, respectively) from another several samples due to difficulties to distinguish the newly grown skeletal parts. On the other hand, even in nubbins that appeared to be dead at the end of the experiment, chemical compositions could be measured if they had grown sufficiently before growth stopped. Furthermore, data that were outliers based on the box plots of each Me/Ca were omitted. Therefore, the number of data obtained from each colony varied (Tables 1, 2). Correlations between each chemical composition within each species were presented in Table 3. No consistent and significant relationships were found in correlations ($r > 0.5$) between geochemical tracers for both species. However, a strong positive correlation ($r = 0.74$, $p < 0.001$) was found between Sr/Ca and $\delta^{18}O$ for *A. digitifera* although that for *P. australiensis* was moderate and not significant ($r = 0.48$, $p = 0.06$). The relationships between water temperature, growth rate, and chemical composition are shown in Figures 6, 7, and Supplementary Figure 2.

3.2.1 $\delta^{18}O$

The mean $\delta^{18}O$ of *P. australiensis* and *A. digitifera* were -4.25 ± 0.46 and -3.63 ± 0.61 ‰ (mean ± 1sd), respectively. A Bayes factor (BF) between two dataset (*A. digitifera* and *P. australiensis*) was > 100 which indicates that there is a significant difference between them. There were no colony differences in $\delta^{18}O$ within the same species (Supplementary Table 1). Since significant correlations were found between water temperature and $\delta^{18}O$ of *P. australiensis* ($r = 0.67$, $p = 0.001$) and *A. digitifera* ($r = 0.95$, $p < 0.001$, Figure 6A), calibrations were established based on the WLS method as below. We used $1/\sigma^2$ as the weight where σ is standard deviations of water temperature at each temperature setting throughout the whole period of experiments (Supplementary Figure 1).

$$P.\ australiensis: \delta^{18}O = -0.11(\pm 0.002)\,T - 1.51(\pm 0.04),\ \text{RMSR } 0.03°C\ (n = 32)$$

$$A.\ digitifera: \delta^{18}O = -0.17(\pm 0.001)\,T + 0.87(\pm 0.02),\ \text{RMSR } 0.02°C\ (n = 87)$$

where T is water temperature. On the other hand, $\delta^{18}O$ in both species showed no significant relationship against the growth rate (Figures 7A, G).

3.2.2 Sr/Ca

The mean Sr/Ca of *P. australiensis* and *A. digitifera* were 8.73 ± 0.19 and 8.82 ± 0.19 mmol/mol, respectively. A BF between two dataset was 2.15 which indicates no evidence for either equal or unequal. There were no colony differences in Sr/Ca within the same species (Supplementary Table 1). Since significant correlations were also found between water temperature and Sr/Ca of *P. australiensis* ($r = 0.56$, $p < 0.001$) and *A. difitifera* ($r = 0.61$, $p < 0.001$. Figure 6B), calibrations based on the WLS were established as below.

$$P.\ australiensis: \mathrm{Sr/Ca} = -0.040(\pm 0.001)\,T + 9.75(\pm 0.017),\ \text{RMSR } 0.01°C\ (n = 41)$$

$$A.\ digitifera: \mathrm{Sr/Ca} = -0.033(\pm 0.0005)\,T + 9.68(\pm 0.011),\ \text{RMSR } 0.02°C\ (n = 87)$$

where T is water temperature. Same as $\delta^{18}O$, Sr/Ca in both species showed no significant relationship against the growth rate (Figures 7B, H).

3.2.3 U/Ca

The mean U/Ca of *P. australiensis* and *A. digitifera* were 1.43 ± 0.20 and 1.49 ± 0.15 μmol/mol, respectively. A BF between two

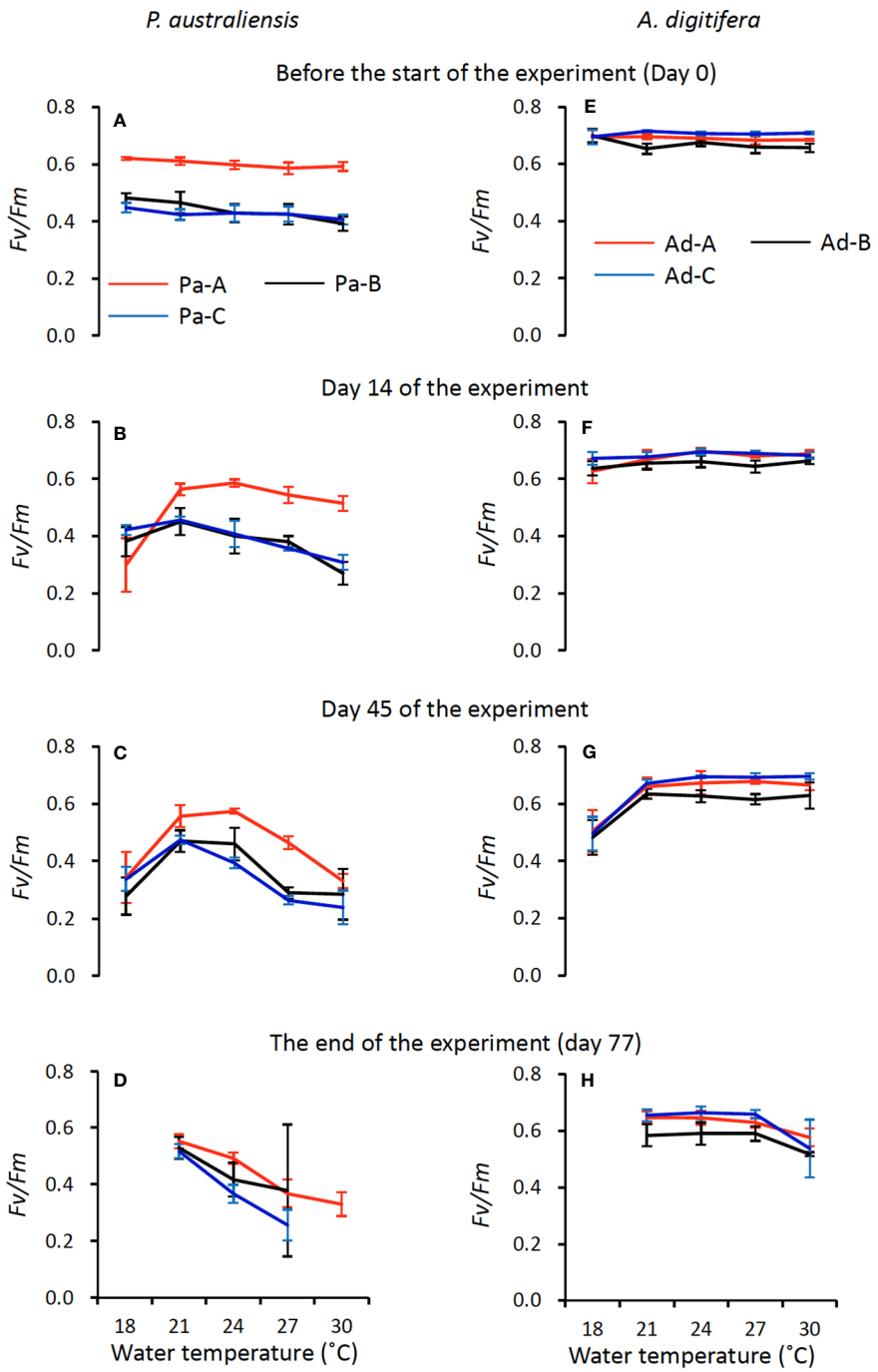

FIGURE 4
Temporal variations of maximum quantum yield of Photosystem II (*Fv/Fm*) of symbiotic algae (mean ± 1sd) in *P. australiensis* **(A-D)** and *A. digitifera* **(E-H)** as a function of water temperature.

dataset was 1.98 which indicates no evidence for either equal or unequal. Although a difference between Pa-A and Pa-C was found, no clear and consistent colony differences were found for other colonies of both species (Supplementary Table 1). Moderate correlations were found between U/Ca and water temperature for only Ad-B ($r = 0.56$, $p < 0.001$) and Ad-C ($r = 0.50$, $p < 0.001$; Supplementary Figure 2K). However no consistent relationships were observed for other colonies and non-linear relations were found in mean U/Ca as a function of water temperature as seen in Figure 6E. In contrast, significant negative correlations between U/Ca and the growth rate were found in two colonies (Ad-B and Ad-C) and all colonies combined for *A. digitifera* (Figure 7K).

3.2.4 $\delta^{13}C$

The mean $\delta^{13}C$ of *P. australiensis* and *A. digitifera* were -4.97 ± 1.03 and -2.32 ± 0.89 ‰, respectively. A BF between two dataset was > 100, indicating a significant difference between them. Similar with U/Ca, although a difference between Pa-A and Pa-C was found, no

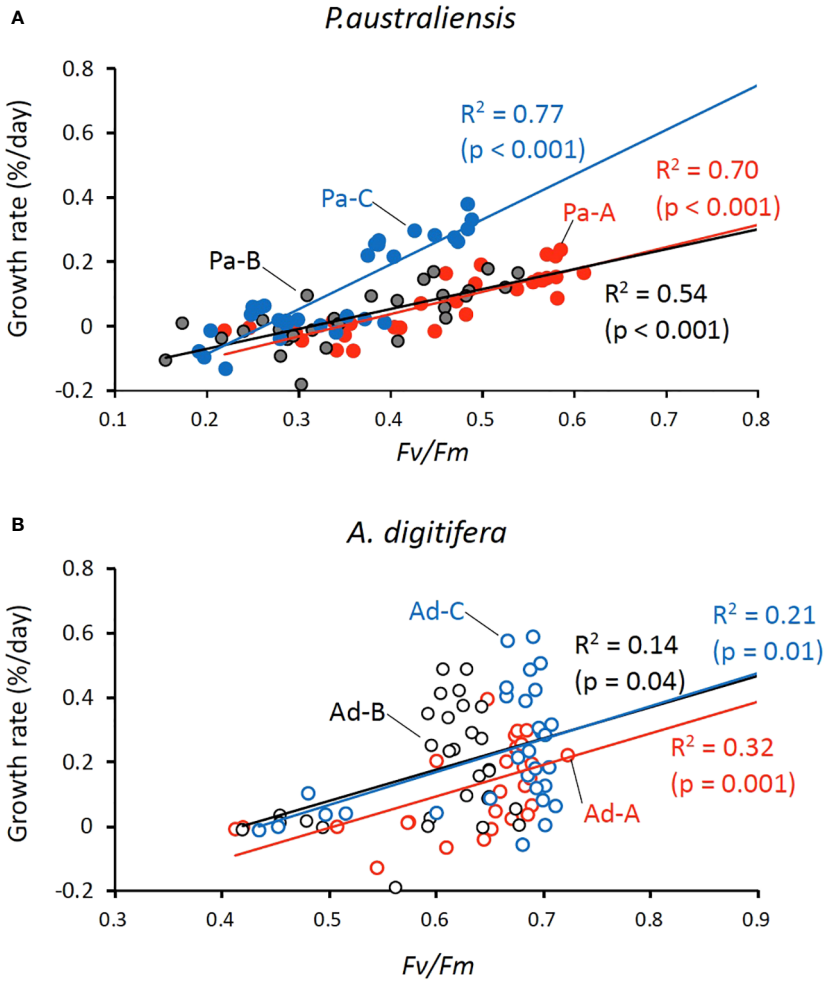

FIGURE 5
Relationships between the skeletal growth rate and *Fv/Fm* for *P. australiensis* **(A)** and *A. digitifera* **(B)** Because several coral nubbins appeared dead within the final 2 weeks of the experiment, growth rates were calculated for 63 d instead of overall period (77 d) of the experiment; values of *Fv/Fm* correspond to those at day 45 of the experiment. Note that the scale of *Fv/Fm* differs between the panel **A** and **B**.

clear and consistent colony differences were found for other colonies of both species (Supplementary Table 1). In addition, no significant correlations were found in both growth rate and water temperature and $\delta^{13}C$ of both species (Figures 6D, 7D, J).

3.2.5 Mg/Ca

The mean Mg/Ca of *P. australiensis* and *A. digitifera* were 6.66 ± 2.33 and 6.79 ± 2.16 mmol/mol, respectively. A BF between two dataset was 0.22 which indicates that there is no difference between

TABLE 3 Correlation coefficients between each chemical compositions.

	Mg/Ca	Sr/Ca	Ba/Ca	U/Ca	$\delta^{13}C$	$\delta^{18}O$	
Mg/Ca		-0.16	0.29	**0.51**	**0.57**	0.09	Mg/Ca
Sr/Ca	-0.67		0.31	0.43	-0.02	0.48	Sr/Ca
Ba/Ca	0.07	0.4		0.45	0.26	0.3	Ba/Ca
U/Ca	-0.28	**0.54**	0.19		0.58	0.28	U/Ca
$\delta^{13}C$	0.04	0.18	0.09	0.34		0.03	$\delta^{13}C$
$\delta^{18}O$	-0.23	**0.74**	0.45	**0.53**	**0.57**		$\delta^{18}O$

Blue and red numbers indicate the correlation coefficients between the chemical compositions *P. australiansis* and *A. digitifera*, respectively. Significant correlations are indicated by bold numbers ($p<0.05$).

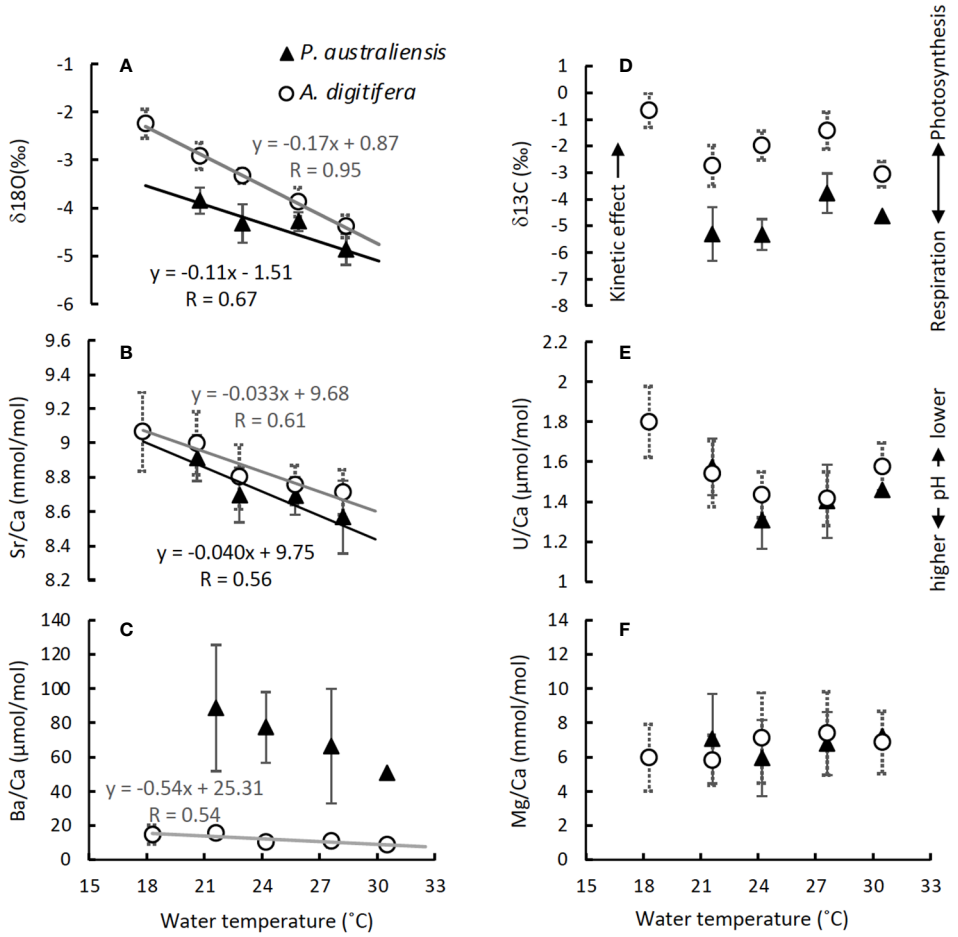

FIGURE 6
Variations in δ18O **(A)**, Sr/Ca **(B)**, Ba/Ca **(C)**, δ13C **(D)**, U/Ca **(E)** and Mg/Ca **(F)** of each colony of *P. australiensis* and *A. digitifera* as a function of water temperature. Data are presented as mean ± 1sd of all data measured on three colonies, but calibrations are performed using all individual data as seen in Supplementary Figure 2. Calibrations are presented only for those with an observed significant relationship ($r > 0.5$, $p < 0.05$).

them. In addition, there were no colony differences in both species (Supplementary Table 1). Although only one colony (Ad-A) showed a positive correlation between Mg/Ca and the growth rate (Figure 7L), no consistent correlations were found in both growth rate and water temperature and Mg/Ca of both species (Figures 6F, 7F, L).

3.2.6 Ba/Ca

Variations of Ba/Ca were very large and the mean Ba/Ca of *P. australiensis* and *A. digitifera* were 72.50 ± 34.72 and 11.27 ± 3.86 μmol/mol, respectively. Obviously, there is a difference of Ba/Ca between two species with a BF >100. Colony differences were found between Pa-A and Pa-B and Pa-B and Pa-C in addition to Ad-B and Ad-C (Supplementary Table 1). Although no correlations between Ba/Ca and growth rate were found for both species, a negative correlation was found between water temperature and mean Ba/Ca for *A. digitifera* (Figures 6C, 7C, I). In contrast to *A. digitifera*, Ba/Ca of three colonies of *P. australiensis* varies largely and showed no temperature dependences.

4 Discussion

4.1 Growth patterns of *P. australiensis* and *A. digitifera* in response to water temperature and the *Fv/Fm*

Skeletal growth rates of *P. australiensis* during the culture experiment were mostly higher (> 0.1%/d) at 24°C and lower at 18 and 30˚C (< 0.1%/d) with significant colony differences (Figure 3). Similarly, those of *A. digitifera* were higher at 21-27°C and lower at 18 and 30°C, but there were no colony differences in the skeletal growth rate at each temperature except for 18°C (Figure 3J). However, deviations in the growth rate of each colony of *P. australiensis* were small, but large for *A. digitifera*. Therefore, growth patterns, including growth variations among colonies and within a colony, differed between the two species. In addition, the average growth rate for 21-27°C of *A. digitifera* (0.30 ± 0.10%/day) was significantly higher than that of *P. australiensis* (0.18 ± 0.11%/day) which is mostly consistent to findings observed

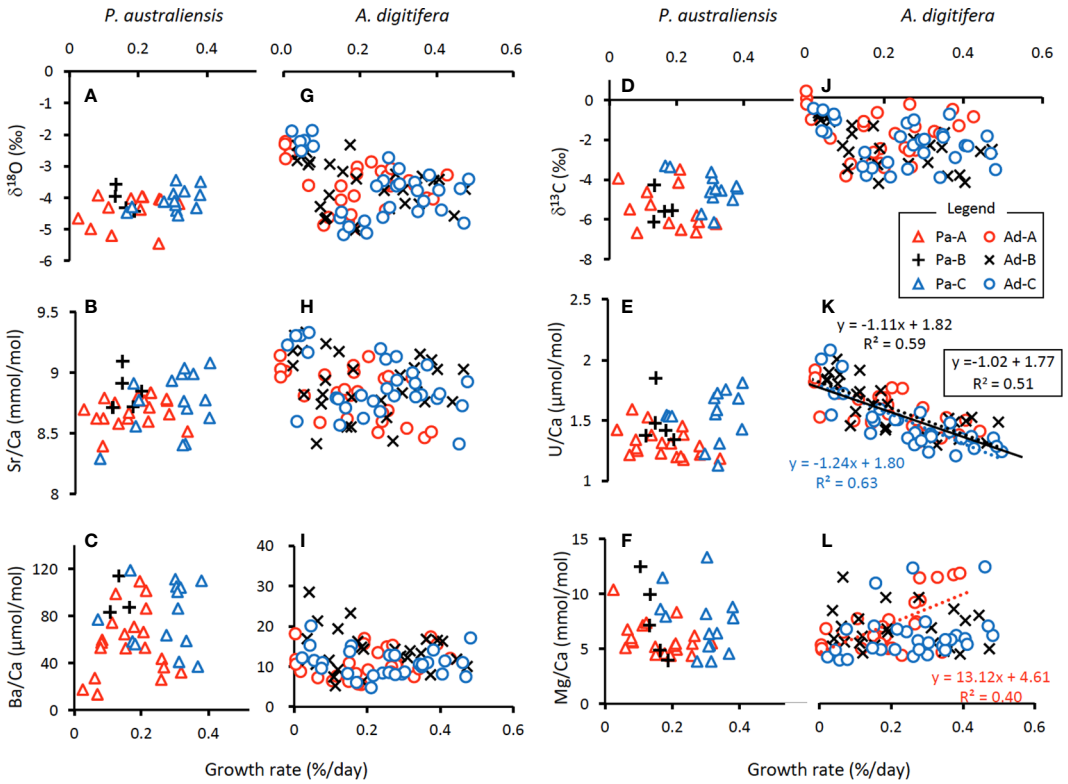

FIGURE 7
Variations in chemical compositions of each colony of *P. australiensis* **(A-F)** and *A. digitifera* **(G-L)** as a function of growth rate. Calibrations are presented only for those with an observed significant relationship ($r > 0.5$, $p < 0.05$). Colored dotted lines represent the observed relationships within a colony, while a black line in **(K)** indicates the relationship observed for data from all three colonies.

in the field. Direct comparisons of the growth rates of different species in the field were difficult because of the different depths and wave energies near the sites where corals dwell, as well as their colony size (Nakamura and Yamasaki, 2005; Pratchett et al., 2015). However, Pratchett et al. (2015) compiled the annual extension rates for 148 coral taxa measured using methods such as direct measurements following tagging or staining. As a result, most *Acropora* corals, including *A. digitifera*, had an annual extension rate greater than 30 mm/yr., whereas that of *Porites* was approximately 10 mm/yr. Although the method how to evaluate coral growth is different between our study and those conducted in the field, the results found in the present experiment seems to roughly reflect actual coral activities occurring in the coral reefs.

There have been many reports that vigorous calcification by scleractinian corals is enabled by their symbiotic relationship with photosynthesizing zooxanthellae, as referred to light enhanced calcification (LEC; reviewed by Gattuso et al., 1999; Inoue et al., 2018). However, the exact mechanism facilitating coral calcification through photosynthesis has been still unknown (reviewed by Davy et al., 2012). Therefore, the relationship between the photosynthetic efficiencies of symbiotic algae represented by *Fv/Fm* and coral growth rate in this experiment was examined. Likely to the growth rate, the *Fv/Fm* showed a colony difference for *P. australiensis* but not for *A. digitifera*, especially during the first half of the experiment (Figure 4). Although the difference in growth rate may be attributed to *Fv/Fm*, as it was higher in *A. digitifera* than in *P. australiensis* throughout the experiment, the growth pattern cannot be simply explained solely by *Fv/Fm*, particularly for *A. digitifera*. For example, the growth rate at 18°C remained the lowest throughout the experiment including the first half, when *Fv/Fm* maintained higher values (Figures 3F, G, 4E, F). Similarly, for *P. australiensis*, the *Fv/Fm* of Pa-A was higher than that of the other colonies, but the growth rate of Pa-A was similar to or lower than that of Pa-C (Figures 3A–D, 4A–C). Cohen et al. (2016) hypothesized that blue light signaling and its animal receptors may influence LEC. This suggests that a direct effect of light, rather than being mediated by the photosynthetic process, as reported previously (Gattuso et al., 1999; Al-Horani et al., 2003), may trigger the LEC. Nevertheless, in the present study, strong positive correlations between the growth rate and *Fv/Fm* were observed in all colonies of *P. australiensis* (Figure 5A). Therefore, photosynthesis appeared to have a predominant effect on skeletal growth, although other mechanisms also control it. Mallon et al. (2022) examined the interspecies relationships between photosynthesis, respiration, and calcification using photosynthesizing calcifiers in the Caribbean, including *A. cervicornis* and *P. astreoides*. Their results showed that calcification rates were linked to energy production at the organismal level and that the species-specific ratios of net calcification to photosynthesis varied with light over a diurnal cycle. This suggests

that the extent of the impact of photosynthesis on skeletal growth differed between the two species.

In fact, although only the growth response to temperature was similar, other patterns, including the average growth rate, colony differences, and relationship with photosynthesis, differed between the two species. This finding indicates that the strategies of skeletal growth would be different between genus *Porites* and *Acropora*. Also this might be attributed to a tolerance against environmental stresses, as the genus *Porites* may potentially have a greater thermal tolerance than *Acropora* (e.g., Afzal et al., 2023). However, in this study, although several nubbins stopped growing at 30°C for the latter half of the experiment for both species, the overall growth rate was higher for *A. digitifera*, even at 30°C (Figure 3). Furthermore, mortality, which was represented by the number of apparent dead nubbins in this study (13 and eight dead nubbins for *P. australiensis* and *A. digitifera*, respectively, at 30°C), was higher in *P. australiensis* despite its thermal tolerance. Xu et al. (2020) noted a higher contribution of heterotrophic predation in the coral hosts of *Porites* than *Acropora*. They also suggested that the trophic status of stress-tolerant *Porites* is more plastic than that of the vulnerable *Acropora*. In the field, *Porites* might be able to switch from photoautotrophy to heterotrophy; however, we did not feed and used filtered seawater during the experiment. This could be a cause of the suppressed growth and high mortality of nubbins of *P. australiensis* at 30°C. In contrast, *Acropora* appear to belong to the autotrophy among trophic strategies (Conti-Jerpe et al., 2020), consistent with the results that mean *Fv/Fm* and growth rate of *A. digitifera* are higher compared to those for *P. australiensis* in this study. When focusing on growth rate and *Fv/Fm* at 30˚C around the middle of the experiment period (Figures 3B, C, G, H, Figures 4B, C, F, G), *Fv/Fm* and growth rate have decreased for *P. australiensis* while high *Fv/Fm* and positive growth rate have been kept for *A. digitifera*. Under such conditions, *Porites* may shift trophic type from auto- to heterotrophic in the natural coral reef conditions.

4.2 Possible causes of variations of each geochemical compositions

Regarding the variations of chemical compositions, since consistent colony differences have not been detected within the same species (Supplementary Table 1), compiled data using those from three colonies per species are used for discussion. Among multiple chemical compositions, excepting for those at 18˚C as many data of *P. australiensis* at 18˚C were absent, in coral skeletons of two species, Sr/Ca, U/Ca and Mg/Ca were not significantly different between them. These geochemical compositions were scattered within the same range, regardless of the differences in absolute growth rate and growth patterns between the two species. This suggests that the basic mechanisms of incorporation of these chemical compositions might be consistent without large species-specific effects. For Ba/Ca, deviations at each temperature were large in all colonies of *P. australiensis*. This result may have been influenced by the tissue parts, as Ba appears to be enriched in the tissue parts (Alibert and Kinsley, 2008). In addition to Ba/Ca, differences in $\delta^{18}O$ and $\delta^{13}C$ between two species were found, as described above, suggesting the possibility of different mechanisms for incorporating these tracers.

4.2.1 $\delta^{18}O$ variations

It is well known that the $\delta^{18}O$ of coral skeletons mainly for massive *Porites* sp. can be a good proxy for sea surface temperature (SST) and salinity, which affect $\delta^{18}O$ in seawater (e.g., Gagan et al., 2000; Cobb et al., 2003; Hayashi et al., 2013; Inoue et al., 2023). In addition, a potential physiological mechanism that explains the variation of $\delta^{18}O$ based on a model of oxygen isotope fractionation in the $CaCO_3$-dissolved inorganic carbonate (DIC)-H_2O system has been proposed (Derviendt et al., 2017; Inoue et al., 2018). In the latter hypotheses, the skeletal $\delta^{18}O$ values of scleractinian corals might be influenced by the hydration reaction of metabolic CO_2 in the calcifying fluid. Since the carbonic anhydrase (CA) enzyme appears to increase the rate of CO_2 hydration in coral tissue (Hopkinson et al., 2015), differences in mean $\delta^{18}O$ between *A. digitifera* and *P. australiensis* might be attributed to variations in physiological mechanisms between the two species. However, clear temperature dependences are found in both species (Figure 6A), suggesting that activities of the CA would be independent to temperature variations.

4.2.2 Sr/Ca variations

Like $\delta^{18}O$, the Sr/Ca ratios of coral skeletons of massive *Porites* sp. has been widely used to reconstruct past SST (e.g., Corrége, 2006; Ramos et al., 2020). In contrast to the variability of $\delta^{18}O$ in seawater, which depends on the balance between evaporation and precipitation, the residence times of both Sr and Ca in seawater are generally long (>10^6 years; Drever, 1988). Then coral Sr/Ca has been considered a robust proxy for only SST. Additionally, Inoue et al. (2018) reported that the Sr/Ca of symbiotic and aposymbiotic polyps were not significantly different, while there was a difference in $\delta^{18}O$ levels between them. Although the kinetic effect on Sr/Ca through the activity of the Ca^{2+}-ATPase pump has also been reported (e.g., Cohen and McConnaughey, 2003), no Sr/Ca variations related to growth and no clear species-specific effects were found in the incorporation of strontium in this study (Figures 7B, H). However, there are relatively large variations in Sr/Ca within the same temperature settings. Given their large deviation within a specific colony (Supplementary Figures 2B, H), this may not be attributed to physiological regulations. Instead, it could be influenced by variations in nano- to micro-scale skeletal architecture as discussed below.

4.2.3 U/Ca variation

The incorporation of uranium into coral aragonite has been suggested to be controlled by SST (Min et al., 1995; Felis et al., 2009) and pH or DIC (Inoue et al., 2011; DeCarlo et al., 2015; Gothmann and Gagnon, 2021). In this study, although temperature dependencies of U/Ca were partially observed for *A. digitifera* (Supplementary Figure 2K), no clear trends as SST proxy were found (Figure 6E). Inoue et al. (2018) demonstrated distinct variations in U/Ca levels between symbiotic and aposymbiotic polyps. Changes in internal DIC and pH due to photosynthesis

have been linked to variations in pH within the calcifying fluid of these polyps. The U/Ca ratios of *A. digitifera* in this study have shown a significant negative correlation with the growth rate (Figure 7K). As coral U/Ca is negatively correlated with pH (Inoue et al., 2011), this trend might reflect variations in the internal pH probably through the photosynthesis. However, despite the differences in growth rate and *Fv/Fm*, there are no differences in the meanU/Ca between *P. australiensis* and *A. digitifera*. This suggests that other mechanisms may be involved in controlling the incorporation of uranium during skeletal growth. To thoroughly investigate the relationship between skeletal growth, internal pH and skeletal U/Ca ratios, additional data on internal pH would be necessary.

4.2.4 $\delta^{13}C$ variation

Although the mechanisms controlling $\delta^{13}C$ variation in coral skeletons are disputed (McConnaughey, 1989; Reynaud-Vaganay et al., 2001; Grottoli, 2002; Suzuki et al., 2003; Omata et al., 2008; Linsley et al., 2019), $\delta^{13}C$ values in biogenic carbonate generally depend on the photosynthetic rate. This is because ^{12}C is preferentially taken up during photosynthesis, and then ^{13}C-enriched DIC within the calcifying fluid is used to precipitate $CaCO_3$ shells or skeletal material. This leads to a positive correlation between carbonate $\delta^{13}C$ values and photosynthetic rate. In fact, the $\delta^{13}C$ values in symbiotic and aposymbiotic polyps showed differences at the control temperature of 27°C. However, the values measured from bleached symbiotic polyps at 31 and 33°C decreased to approach the values obtained from aposymbiotic polyps (Inoue et al., 2018). As mentioned above, since *Fv/Fm* level was higher in *A. digitifera* compared to *P. australiensis*, overall high values of $\delta^{13}C$ of *A. digitifera* may indicate active photosynthesis compared to *P. australiensis* (Figure 6D). However, variation patterns of $\delta^{13}C$ of both the species in response to temperature cannot be explained simply by *Fv/Fm*, suggesting that complex factors including respiration and kinetic effects would affect the isotope fractionation of carbon during the skeletal growth.

4.2.5 Mg/Ca variation

The Mg/Ca ratio in coral skeletons appears to be influenced by biological effects (Fallon et al., 2003; Meibom et al., 2004; Inoue et al., 2018), although it was initially predicted to be a proxy for SST (Mitsuguchi et al., 1996; Watanabe et al., 2001). Although previous studies have indicated that skeletal Mg/Ca ratios are primarily influenced by the skeletal growth rate from a thermodynamic perspective (Inoue et al., 2007; Brahmi et al., 2012), it appears that they are affected by biological processes rather than purely thermodynamic effects. In particular, the distribution of Mg within the coral host appears to be related to the presence of organic matrix (OM), which is an essential precursor for aragonite crystal precipitation (Cuif et al., 2003; Finch and Allison, 2008; Yoshimura et al., 2015). In fact, there are no significant differences in Mg/Ca between symbiotic and aposymbiotic polyps, despite the significant differences in growth rate (Inoue et al., 2018). In this study, no differences in Mg/Ca were observed in *A. digitifera* and *P. australiensis* (Figure 6F), suggesting that some fundamental biological processes involved in the production of OM for aragonite precipitation might be similar between the two species. Furthermore, the secretion of OM does not appear to depend on water temperature, as our study did not find any correlation between temperature and Mg/Ca (Figure 6F).

4.2.6 Ba/Ca variation

The Ba/Ca ratio in coral skeletons has been utilized for reconstructing river runoff and sediment loads (e.g., McCulloch et al., 2003; Ito et al., 2020) because barium is desorbed from fine-grained suspended particles at the estuarine mixing zone (Li and Chan, 1979). The Ba/Ca ratio in corals grown in a reef unaffected by large rivers has been used to identify indications of upwelling, which transports both dissolved seawater and marine biological barium (Alibert and Kinsley, 2008; Spreter et al., 2022). Recently, it has been used to predict the concentrations of dissolved barium in seawater (Kershaw et al., 2023) and the growth rate of aragonite (Mavromatis et al., 2018). Furthermore, there is a report Indicating that light conditions affect the Ba/Ca in coral skeletons (Yamazaki et al., 2021). However, there have been few studies examining the relationship between coral Ba/Ca and water temperature. The results obtained from this study showed very large variations of Ba/Ca, probably due to tissue parts, at the same temperature, especially for *P. australiensis*, indicating the difficulty of using coral Ba/Ca as an SST proxy. However, a negative relationship was found in *A. digitifera* (Figure 6C). Therefore, some caution might be needed for the use of Ba/Ca as environmental proxies, especially when reconstructing the upwelling, as it brings cold seawater together with dissolved barium.

4.3 Assessment of coral geochemical tracers as a temperature proxy

As reported for *Porites* spp. (Reviewed by Thompson, 2022), the $\delta^{18}O$ and Sr/Ca of all colonies of *A. digitifera* also showed clear negative correlations with temperature without consistent growth rate dependences (Figures 6, 7). Regarding the mean temperature dependences of $\delta^{18}O$ and Sr/Ca calculated using all data from three colonies of *P. australiensis* without data at 18°C, the temperature sensitivities of both tracers appeared to be lower compared to published values. Gagan et al. (2012) reported that the $\delta^{18}O$-SST sensitivities for *Porites* ranged from -0.08 to -0.22 ‰/°C. They also discovered that corals with slow growth throughout the tissue layer were less sensitive to changes in SST. The temperature sensitivity of $\delta^{18}O$ of *P. australiensis* in this study was -0.11 ‰/°C, which is applicable to slow-growing corals. Similarly, a broad range of Sr/Ca-SST sensitivities were reported for *Porites* sp., from -0.041 to -0.082 mmol/mol/°C (Gagan et al., 2012). The mean temperature sensitivity of Sr/Ca in this study (-0.040 mmol/mol/°C) was lower than the published values, and it may represent a slow-growing type, same as $\delta^{18}O$. Reynaud et al. (2007) also reported a significant negative correlation as a quadratic function between Sr/Ca of *Acropora* sp. and temperature. In addition, a strong negative

linear correlation between $\delta^{18}O$ and temperature was observed within the temperature range from 22 to 29°C in their study. Similar to *P. australiensis*, the $\delta^{18}O$ and Sr/Ca of *A. digitifera*, in this study, showed relatively lower temperature sensitivities of -0.17 ‰/°C and -0.033 mmol/mol/°C, respectively. For the $\delta^{18}O$ of *Acropora* sp., -0.30 to -0.34 ‰/°C was reported by Reynaud et al. (2007) and Juillet-Leclerc et al. (2014), which is even higher compared to that reported for *Porites* sp. However, a temperature sensitivity calculated using data obtained from the fibers precipitated during the nighttime was -0.19 ‰/°C (Juillet-Leclerc et al., 2018), which is similar to that found in the present study. In addition to $\delta^{18}O$, Juillet-Leclerc et al. (2014) demonstrated a clear Sr/Ca-temperature relationship, with a temperature range 22-29°C, for *Acropora* sp. cultured with different light intensities. Temperature sensitivities differed between high-light and low-light conditions in which higher (-0.061 mmol/mol/°C) and lower (-0.036 mmol/mol/°C) sensitivities were observed for high- and low-light conditions, respectively. In addition, Ross et al. (2019) reported -0.07 mmol/mol/˚C as temperature dependence of Sr/Ca measured from *Acropora* spp. grown under the natural reef conditions. The similarity of $\delta^{18}O$ and Sr/Ca-temperature sensitivities in this study with those obtained from skeletons precipitated under nighttime and low-light conditions suggests that the growth of *A. digitifera* was slower compared to those grown in the field and/or under more high-light conditions. This is consistent with the findings observed from *P. australiensis*. Although Mallon et al. (2022) suggested the importance of considering natural variations in light for all reef metabolism studies, light intensity in this study (120-140 mmol/m^2/s) was relatively low. This light condition would produce low calcification rates for both species, and the temperature sensitivities would differ from those obtained using corals from the field. However, a calibration study using *Isopora* collected from the Heron Island, located at the southern end of the Great Barrier Reef, demonstrated temperature dependences of -0.18 ‰/°C and -0.061 mmol/mol/˚C for $\delta^{18}O$ and Sr/Ca, respectively (Brenner et al., 2017). The former was the same as that found in this study, whereas the latter was close to that reported in a study performed under high light conditions (Juillet-Leclerc et al., 2014). Because the number of studies on calibrations using corals other than *Porites* remains small, we cannot deduce which values of temperature sensitivity are most appropriate. However, the temperature sensitivity of geochemical tracers, especially for the $\delta^{18}O$ of *Acropora*, appears to not significantly differ from that reported for *Porites*, suggesting its potential as a temperature proxy.

Gagan et al. (2012) suggested that in general, new aragonite is deposited in the calyx (within 2 mm of the growth surface), although in some cases calcification occurs throughout the depth of the tissue layer. In terms of calibration, culture experiments for a relatively short period, such as a couple of weeks to months, apparently cannot provide an elaborate analog for corals in the field because tissue parts cover the skeleton. Instead, these experiments can be used to investigate the possibility of a proxy for a specific factor, such as the growth rate, temperature, and/or pCO_2 by changing the parameter(s). Culture experiments, including those of Reynaud et al. (2007) and this study, have demonstrated a high potential for using $\delta^{18}O$ and Sr/Ca of *Acropora* sp. as temperature proxies in addition to those of *Porites*. Specifically, the $\delta^{18}O$ of *A. digitifera* seems to vary consistently as a function of temperature, without the colony dependence and deviations seen in trace elements such as Sr/Ca. The $\delta^{18}O$ variations reported by Reynaud et al. (2007) also showed a strong negative correlation (r^2 = 0.99) with very small deviations at each temperature setting. Furthermore, $\delta^{18}O$ in polyp samples of *A. digitifera* showed negative correlations with the temperature, from 27 to 33˚C, for both symbiotic and aposymbiotic polyps and even for bleached polyps of symbiotic polyps under thermal stress conditions (31 and 33˚C, Inoue et al., 2018). These findings indicate a stable behavior of $\delta^{18}O$ in response to temperature during the growth of coral skeletons, regardless of differences in growth rate, colony size, and/or photosynthesis efficiency. Nevertheless, because $\delta^{18}O$ -temperature sensitivities have differed among studies, as noted above, caution is advised when using the $\delta^{18}O$ of *Acropora* sp. as a temperature proxy. Corals grown in the field or culturing tanks for more than one year, such as in Hayashi et al. (2013), would be most useful in establishing a robust calibration.

In contrast to the $\delta^{18}O$, the Sr/Ca ratios in the nubbins of *A. digitifera* showed large deviations even at the same temperature setting (Figure 6B). Corals have small polyps in living surface and calcify skeletal corallites that are arranged in three-dimensional fans within the corallum with new corallites forming along the apex of the fan (Veron, 1986; Darke and Barnes, 1993). Comparisons of geochemical determinations using *Porites* sp. between the central and margin part of a fan of corallites which precipitated in the same year have revealed that the margin have higher coral Sr/Ca values (Alibert and McCulloch, 1997). Therefore, DeLong et al. (2013) recommended to use optimal sampling path which along the central axis of an actively extending corallite fan to reconstruct SST precisely. In addition, the distribution of magnesium is strongly correlated with the fine-scale structure of the skeleton (Meibom et al., 2004; Holcomb et al., 2009). Because skeletal parts composed of multiple polyps grown on an acrylic plate were used for the measurements in this study, differences in skeletal architecture may produce large deviations in Sr/Ca in addition to Mg/Ca. To test whether deviations in Sr/Ca and Mg/Ca become small when only the axis of corallite fan is measured, the tip of each nubbin, which is assumed to correspond to the apical parts of corallite fan, was shaved, and Sr/Ca and Mg/Ca were measured using ICP-optical emission spectrometer (ICP-OES; Agilent Technology, 720 series) via the same method described in Genda et al. (2022). Consequently, the deviations decreased, particularly for Mg/Ca, but the temperature dependence of Sr/Ca disappeared (Figure 8). Because the samples were not marked with isotope doping or alizarin red in this study (Suzuki et al., 2005; Gagnon et al., 2012), we could not confirm whether the skeletal parts used for this test grew only during the experimental period. However, this result may suggest that the skeletal growth of *A. digitifera* during the experiment in this study progressed along the acrylic plate rather than growing upward. Although the calibration of Sr/Ca-SST, using the Sr/Ca measured on apical part like performed by Ross et al. (2019), cannot be established in this study, it is important to subsample the skeletal parts along a growth axis of a specific

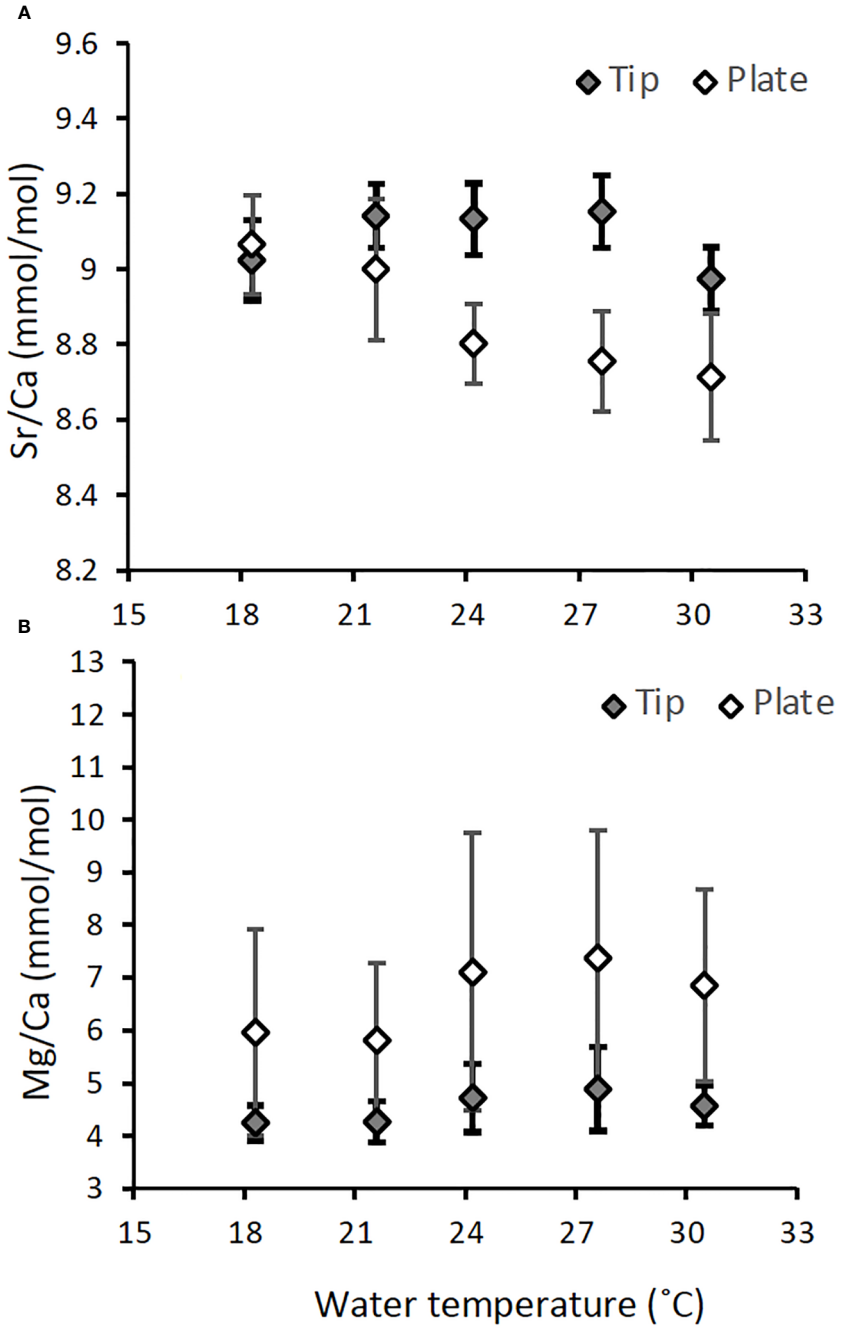

FIGURE 8
Comparison of Sr/Ca **(A)** and Mg/Ca **(B)** contained in skeletal samples collected from skeletons grown on the acrylic plate (white diamond, n = 87 and 80 for Sr/Ca and Mg/Ca, respectively) and the tips of the nubbins (filled diamond, n= 90 and 79 for Sr/Ca and Mg/Ca, respectively) for *A. digitifera*. Results are presented as mean ± 1 sd of the combined data of three colonies.

polyp of *Acropora*, like *Porites* as proposed by DeLong et al. (2013), to ensure the use of precise proxies.

4.3 Implications of biomineralization based on variations of $\delta^{13}C$ and U/Ca

As mentioned above, the systematic difference in $\delta^{13}C$ values between the two species could be explained by the difference in the photosynthesis efficiency, represented by *Fv/Fm*. Although mechanisms of $\delta^{13}C$ variations against temperature for both species were unclear, they were likely mixed with metabolic and kinetic effects on $\delta^{13}C$. For example, lowered $\delta^{13}C$ at 30°C may be attributed to the respiration since it decreased the $\delta^{13}C$ of coral skeletons (Figure 6D, Schoepf et al., 2014). On the other hand, the kinetic effect may have overwhelmed other factors changing $\delta^{13}C$ in coral skeletons at 18˚C, as the growth rate at 18°C was the lowest (McConnaughey, 1989). Accordingly, the relationship between the

$\delta^{18}O$ and $\delta^{13}C$ of *A. digitifera* at the same temperature demonstrated kinetic control, whereas *P. australiensis* did not (Figure 9). Therefore, the $\delta^{13}C$ of *A. digitifera* appears to reflect its photosynthesis, respiration, and growth rate. In contrast, water temperature was the predominant controlling factor for the $\delta^{18}O$ of *A. digitifera*, without a strong growth rate dependence. However, the existence of kinetic effects within a specific temperature should be considered when utilizing the $\delta^{18}O$ of *Acropora* corals in reconstructions of paleo-SST.

Several studies have suggested that the U/Ca ratio in coral skeletons is controlled by pH or DIC within the calcifying space (Inoue et al., 2011; DeCarlo et al., 2015; Inoue et al., 2018; Gothmann and Gagnon, 2021). Additionally, a microsensor-based determination of DIC in the extracellular calcifying medium of *Stylophora pistillata* showed that photosynthesis and respiration exerted a strong influence on chemistry, such as the pH of the calcifying space during light and dark periods (Sevilgen et al., 2019). Although the mean U/Ca values of the two species were not significantly different, a strong growth rate dependence of U/Ca was found only in *A. digitifera* (Figure 7K). Additionally, U/Ca ratios in *A. digitifera* also showed weak to moderate negative correlations with temperature, but those at higher temperature especially at 30°C shifted toward more higher values than expected from the calibration lines (Supplementary Figure 2K). A similar behavior of U/Ca in response to temperature is also found for *P. australiensis* (Figure 6E). Therefore, the U/Ca ratio of *A. digitifera*, and likely *P. australiensis* as well, at 30°C seems to reflect the growth rate, which is associated with fluctuations in pH or DIC. As seawater pH was consistent for all aquariums, the higher shift in U/Ca at 30°C may suggest that the pH of the calcifying space was lower, as U/Ca is negatively correlated to pH, than that of nubbins reared under other temperature settings. Considering the variation pattern of both U/Ca and $\delta^{13}C$ of *A. digitifera* at 30°C, respirations may overwhelm photosynthesis for coral nubbins at 30°C. Consequently, the pH at calcifying space likely decreased owing to the increased respiration rate, which is consistent with the higher shift of U/Ca at 30°C. Additionally, of the decreased pH at the calcifying space may be attributed to the decreased growth rate at 30°C, regardless of the relatively high *Fv/Fm* in *A. digitifera* (Figures 3, 4).

5 Conclusion

Various cultural experiments have been conducted using scleractinian corals, involving variations in parameters such as temperature, light, and/or pCO_2. In this study, a relatively simple culture experiment was conducted, in which only the water temperature was changed for *P. australiensis* and *A. digitifera* for 77 days. In general, the massive *Porites* sp. that grow up to 1-2 m in diameter are primarily located in the Indo-Pacific region. They are often used to reconstruct past SST based on their skeletal $\delta^{18}O$ and Sr/Ca ratios. On the other hand, *Acropora* sp. grow widespread globally and is often found as a fossil, but the potential for its geochemical tracers to serve as temperature proxies has not been thoroughly investigated. Therefore, we examined it using both *P. australiensis* and *A. digitifera*, which are commonly found in the coral reefs around Okinawa, Japan. They were cultured in the same aquaria under identical conditions, with temperatures ranging from 18 to 30°C. We used three colonies of both species to examine genetic differences in growth rate, photosynthetic efficiency (*Fv/Fm*), and variations in geochemical compositions. As a result, the overall growth rates were higher in *A. digitifera* without colony differences, whereas they were lower in *P. australiensis* compared to *A. digitifera* with colony dependences. The responses of skeletal growth to *Fv/Fm* differed between the two species, indicating that the strategies for skeletal growth vary between massive *Porites* and branching *Acropora*. Despite these differences in skeletal growth, the values of Sr/Ca, U/Ca, and Mg/Ca measured in bulk samples, including skeletal parts grown only during the experiment, showed no significant differences. However, $\delta^{18}O$, $\delta^{13}C$, and Ba/Ca exhibited significant differences between the two species. Only Sr/Ca and $\delta^{18}O$ in both species showed significant relationships to temperature, indicating that these tracers of branching *Acropora* have high potential as temperature proxies, as do those of *Porites* sp. Given that kinetic effects are also observed in the $\delta^{18}O$-$\delta^{13}C$

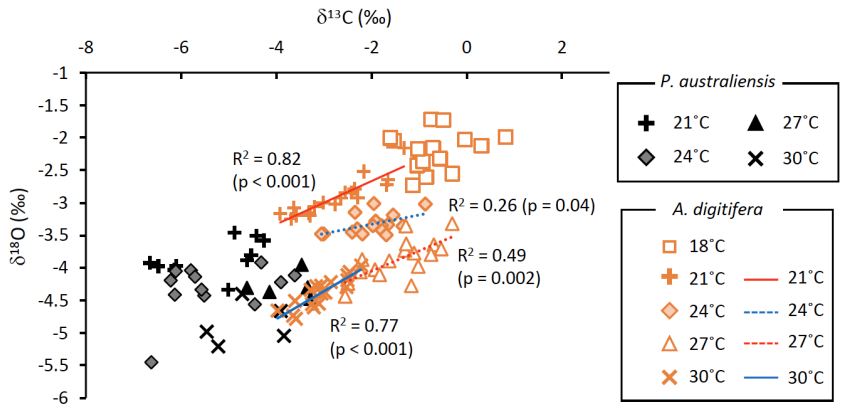

FIGURE 9
Relationships between $\delta^{13}C$ and $\delta^{18}O$ of skeletons grown under the same temperatures for *P. australiensis* (black symbols) and *A. digitifera* (orange symbols). Data are composed of three colonies.

relations at the same temperature setting, it is important to exercise caution when using $\delta^{18}O$ as a temperature proxy. In addition, it is important to sub-sample the apical parts of each polyp to reconstruct environments more precisely.

Data availability statement

The original contributions presented in the study are included in the article/Supplementary Material. Further inquiries can be directed to the corresponding author.

Ethics statement

The manuscript presents research on animals that do not require ethical approval for their study.

Author contributions

SS: Formal analysis, Methodology, Writing – review & editing. MIn: Conceptualization, Funding acquisition, Writing – original draft, Writing – review & editing. YT: Investigation, Methodology, Writing – review & editing. TN: Investigation, Methodology, Writing – review & editing. KS: Investigation, Writing – review & editing. MIk: Formal analysis, Writing – review & editing. AS: Methodology, Writing – review & editing.

Funding

The author(s) declare financial support was received for the research, authorship, and/or publication of this article. This study was supported by the Canon Foundation and JSPS KAKENHI (grant numbers 15H05329 and 26220102). Financial support for the publication of this article was supported by "Initiative for Realizing Diversity in the Research Environment" from MEXT.

Acknowledgments

We thank A. Iguchi and C. Shinzato for their help and advice regarding the culture experiments and discussion. We also thank Y. Yoshinaga and H. Kinjyo for their help and support during the experiments. This study was performed under the cooperative research program of the Center for Advanced Marine Research Core (CMCR) at Kochi University (accession numbers 14B036, 15A033, and 15B029).

Conflict of interest

The authors declare that the research was conducted in the absence of any commercial or financial relationships that could be construed as a potential conflict of interest.

Publisher's note

Supplementary material

The Supplementary Material for this article can be found online at: https://www.frontiersin.org/articles/10.3389/fmars.2024.1329924/full#supplementary-material

References

Abram, N. J., Wright, N. M., Ellis, B., Dixon, B. C., Wurtzel, J. B., England, M. H., et al. (2020). Coupling Indo-Pacific climate variability over the last millennium. *Nature* 579, 385–392. doi: 10.1038/s41586-020-2084-4

Afzal, M. S., Ikeda, K., Ueno, M., and Nakamura, T. (2023). *Dynamics of coral reef communities in Sekisei Lagoon, Japan, following the severe mass bleaching event of 2016, in the Coral Reefs of Eastern Asia under Anthropogenic Impacts*. Eds. I. Takeuchi and H. Yamashiro (Springer, Cham: Coral Reefs of the World 17), 37–52. doi: 10.1007/978-3-031-27560-9_3

Al-Horani, F. A., Al-Moghrabi, S. M., and De Beer, D. (2003). Mechanism of calcification and its relationship to photosynthesis and respiration in the scleractinian coral *Galaxea fascicularis*. *Mar. Biol.* 142, 419–426. doi: 10.1007/s00227-002-0981-8

Alibert, C., and Kinsley, L. (2008). A 170-year Sr/Ca and Ba/Ca coral record from the Western Pacific warm pool:1. What can we learn from unusual coral records? *J. Geophys. Res.* 113, C04008. doi: 10.1029/2006JC003979

Alibert, C., and McCulloch, M. T. (1997). Strontium/calcium ratios in modern *Porites* corals from the Great Barrier Reef as a proxy for sea surface temperature: Calibration of the thermometer and monitoring of ENSO. *Paleoceanogr* 12, 345–363. doi: 10.1029/97PA00318

Anthony, K. R. N., Kline, D. I., Diaz-Pulido, G., Dove, S., and Hoegh-Guldberg, O. (2008). Ocean acidification causes bleaching and productivity loss in coral reef builders. *Proc. Natl. Acad. Sci.* 105, 17442e17446. doi: 10.1073/pnas.0804478105

Beck, J. W., Edwards, R. L., Ito, E., Taylor, F. W., Récy, J., Rougerie, F., et al. (1992). Sea-surface temperature from coral skeletal strontium/calcium ratios. *Science* 257, 644–647. doi: 10.1126/science.257.5070.644

Brahmi, C., Kopp, C., Domart-Coulon, I., Stolarski, J., and Meibom, A. (2012). Skeletal growth dynamics linked to trace-element composition in the scleractinian coral *Pocillipora damicornis*. Geochim. *Cosmochim. Acta* 99, 146–158. doi: 10.1016/j.gca.2012.09.031

Brenner, L. D., Linsley, B. K., and Potts, D. C. (2017). A modern Sr/Ca-$\delta^{18}O$-sea surface temperature calibration for Isopora corals on the Great Barrier Reef. *Paleoceanography* 32, 182–194. doi: 10.1002/2016PA002973

Cobb, K. M., Charles, C. D., Cheng, H., and Edwards, R. L. (2003). El Niño–Southern oscillation and tropical Pacific climate during the last millennium. *Nature* 424, 271–276. doi: 10.1038/nature01779

Cohen, A., and McConnaughey, T. A. (2003). "Geochemical perspectives on coral mineralization," in *Biomineralization*. Eds. P. M. Dove, J. J. D. Yoreo and S. Weiner (Washington, DC: Mineral. Soc. of Am.), 151–187.

Cohen, I., Dubinsky, Z., and Erez, J. (2016). Light enhanced calcification in hermatypic corals: New insights from light spectral responses. *Front. Mar. Sci.* 2. doi: 10.3389/fmars.2015.00122

Conti-Jerpe, I. E., Thompson, P. D., Wong, C. W. M., Oliveira, N. L., Duprey, N. N., Moynihan, M. A., et al. (2020). Trophic strategies and bleaching resistance in reef-building corals. *Sci. Adv.* 6, eaaz5443. doi: 10.1126/sciadv.aaz5443

Corrége, T. (2006). Sea surface temperature and salinity reconstruction from coral geochemical tracers. *Palaeogeogr. Palaeoclimatol. Palaeoecol.* 232, 408–428. doi: 10.1016/j.palaeo.2005.10.014

Cuif, J. P., Dauphin, Y., Doucet, J., Salome, M., and Susini, J. (2003). XANES mapping of organic sulfate in three scleractinian coral skeletons. *Geochim. Cosmochim. Acta* 67, 75–83. doi: 10.1016/S0016-7037(02)01041-4

Cuny-Guirriec, K., Douville, E., Reynaud, S., Allemand, D., Bordier, L., Canesi, M., et al. (2019). Coral li/mg thermometry: caveats and constraints. *Chem. Geol.* 523, 162–178. doi: 10.1016/j.chemgeo.2019.03.038

Darke, W. M., and Barnes, D. J. (1993). Growth trajectories of corallites and ages of polyps in massive colonies of reef-building corals of the genus *Porites*. *Mar. Biol.* 117, 321–326. doi: 10.1007/BF00345677

Davies, P. S. (1989). Short-term growth measurements of corals using an accurate buoyant weighing technique. *Mar. Biol.* 101, 389–395.

Davy, S. K., Allemand, D., and Weis, V. M. (2012). Cell biology of cnidarian-dinoflagellate symbiosis. *Microbiol. Mol. Biol. Rev.* 76, 229–261. doi: 10.1128/MMBR.05014-11

DeCarlo, T. M., Gaetani, G. A., Cohen, A. L., Foster, G. L., Alpert, A. E., and Stewart, J. A. (2016). Coral sr-U thermometry. *Paleoceanography* 31, 626–638. doi: 10.1002/2015PA002908

DeCarlo, T. M., Gaetani, G. A., Holcomb, M., and Cohen, A. L. (2015). Experimental determination of factors controlling the U/Ca ratio of aragonite precipitated from seawater: implications for interpreting coral skeletons. *Geochim. Cosmochim. Acta* 162, 151–165. doi: 10.1016/j.gca.2015.04.016

DeLong, K. L., Quinn, T. M., Taylor, F. W., Shen, C.-C., and Lin, K. (2013). Improving coral-based paleoclimate reconstructions by replicating 350 years of coral Sr/Ca variation. *Palaeogeogr. Palaeoclimatol. Palaeoecol.* 373, 6–24. doi: 10.1016/j.palaeo.2012.08.019

Devriendt, L. S., Watkins, J. M., and McGregor, H. M. (2017). Oxygen isotope fractionation in the $CaCO_3$-DIC-H_2O system. *Geochim. Cosmochim. Act* 214, 115–142. doi: 10.1016/j.gca.2017.06.022

Drever, J. I. (1988). *The geochemistry of natural waters* Vol. 437 (Englewood Cliffs: Prentice hall).

D'Olivo, J. P., Sinclair, D. J., Rankenburg, K., and McCulloch, M. T. (2018). A universal multi-trace element calibration for reconstructing sea surface temperatures from long-lived porites corals: Removing 'vital-effects. ' *Geochim. Cosmochim. Acta* 239, 109–135. doi: 10.1016/j.gca.2018.07.035

Fallon, S. J., McCulloch, M. T., and Alibert, C. (2003). Examining water temperature proxies in *Porites* corals from the Great Barrier Reef: a cross-shelf comparison. *Coral Reefs* 22, 389–404. doi: 10.1007/s00338-003-0322-5

Felis, T., McGregor, H. V., Linsley, B. K., Tudhope, A. W., Gagan, M. K., Suzuki, A., et al. (2014). Intensification of meridional temperature gradient in the Great Barrier Reef following Glacial Maximum. *Nat. Commun.* 5, 4102. doi: 10.1038/ncomms5102

Felis, T., Suzuki, A., Kuhnert, H., Dima, M., Lohmann, G., and Kawahata, H. (2009). Subtropical coral reveals abrupt earlytwentieth-century freshening in the western North Pacific Ocean. *Geol* 37, 527–530. doi: 10.1130/G25581A.1

Finch, A. A., and Allison, N. (2008). Mg structural state in coral aragonite and implications for the paleoenvironmental proxy. *Geophys. Res. Lett.* 35, L08704. doi: 10.1029/2008GL033543

Fitt, W. K., Gates, R. D., Hoegh-Guldberg, O., Bythell, J. C., Jatkar, A. A., Grottoli, A. G., et al. (2009). Response of two species of Indo-Pacific corals, *Porites cylindrica* and *Stylophora pistillata*, to short-term thermal stress: The host does matter in determines the tolerance of corals to bleaching. *J. Exp. Mar. Biol. Ecol.* 373, 102–110. doi: 10.1016/j.jembe.2009.03.011

Gaetani, G. A., Cohen, A. L., Wang, Z., and Crusius, J. (2011). Rayleigh-based, multi-element coral thermometry: A biomineralization approach for developing climate proxies. *Geochim. Cosmochim. Acta* 75, 1920–1932. doi: 10.1016/j.gca.2011.01.010

Gagan, M. K., Ayliffe, L. K., Beck, J. W., Cole, J. E., Druffel, E. R. M., Dunbar, R. B., et al. (2000). New views of the tropical paleoclimate from corals. *Quat. Sci. Rev.* 19, 45–64. doi: 10.1016/S0277-3791(99)00054-2

Gagan, M. K., Dunbar, G. B., and Suzuki, A. (2012). The effect of skeletal mass accumulation in *Porites* on coral Sr/Ca and $\delta^{18}O$ paleothermometry. *Paleoceanography* 27. doi: 10.1029/2011PA002215

Gagnon, A. C., Adkins, J. F., and Erez, J. (2012). Seawater transport during coral biomineralization. *Earth Planet. Sci. Lett.* 329–330, 150–161. doi: 10.1016/j.epsl.2012.03.005

Gattuso, J. P., Allemand, D., and Frankignoulle, M. (1999). Photosynthesis and calcification at the cellular, organismal, and community levels in coral reefs: A review of interactions and control by carbonate chemistry. *Am. Zool.* 39, 160–183. doi: 10.1093/icb/39.1.160

Genda, A., Ikehara, M., Suzuki, A., Arman, A., and Inoue, M. (2022). Sea surface temperature and salinity in Lombok Strait reconstructed from coral Sr/Ca and δ^{18}–2012. *Front. Clim.* 4. doi: 10.3389/fclim.2022.918273

Goodkin, N. F., Samanta, D., Bolton, A., Ong, M. R., Hoang, P. K., Vo, S. T., et al. (2021). Natural and anthropogenic forcing of multi-decadal-to centennial-scale variability of sea surface temperature in the South China Sea. Paleoceanogr. *Paleoclimatol* 36, e2021. doi: 10.1029/2021PA004233

Gothmann, A. M., and Gagnon, A. C. (2021). The primary controls on U/Ca and minor element proxies in a cold-water coral cultured under decoupled carbonate chemistry conditions. *Geochimica Cosmochimica Acta* 315, 38–60. doi: 10.1016/j.gca.2021.09.020

Grottoli, A. G. (2002). Effect of light and brine shrimp on skeletal $\delta^{13}C$ in the Hawaiian coral Porites compressa: A tank experiment. *Geochim. Cosmochim. Acta* 66, 1955–1967. doi: 10.1016/S0016-7037(01)00901-2

Hammer, Ø., Harper, D. A. T., and Ryan, P. D. (2001). PAST: Paleontological Statistics software package for education and data analysis. *Palaeontol. Electron* 4, 9.

Hayashi, E., Suzuki, A., Nakamura, T., Iwase, A., Ishimura, T., Iguchi, A, et al. (2013). The influence of growth rate on coral climate proxies was tested using multiple colony culture experiments. *Earth Planet. Sci. Lett.* 362, 198–206. doi: 10.1016/j.epsl.2012.11.046

Holcomb, M., Cohen, A. L., Gabitov, R. I., and Hutter, J. L. (2009). The compositional and morphological features of aragonite were experimentally precipitated from seawater and biogenically precipitated from coral. *Geochim. Cosmochim. Acta* 73, 4166–4179. doi: 10.1016/j.gca.2009.04.015

Hopkinson, B. M., Tansik, A. L., and Fitt, W. K. (2015). Internal carbonic anhydrase activity in the tissue of scleractinian corals is sufficient to support proposed roles in photosynthesis and calcification. *J. Exp. Biol.* 218, 2039–2048. doi: 10.1242/jeb.118182

Iguchi, A., Ozaki, S., Nakamura, T., Inoue, M., Tanaka, Y., Suzuki, A., et al. (2012). Effects of acidified seawater on calcification and symbiotic algae in the massive coral *Porites australiensis*. *Mar. Environ. Res.* 73, 32–36. doi: 10.1016/j.marenvres.2011.10.008

Inoue, M., Fukushima, A., Chihara, M., Genda, A., Ikehara, M., Okai, T., et al. (2023). Natural and anthropogenic climate variability signals in a 237-year-long coral record from the Philippines. *Paleoceanogr. Paleoclimatol* 38, e2022PA004540. doi: 10.1029/2022PA004540

Inoue, M., Ishikawa, D., Miyaji, T., Yamazaki, A., Suzuki, A., Yamano, H., et al. (2014). Evaluation of Mn and Fe in coral skeletons (*Porites* spp.) as proxies for sediment loading and the reconstruction of 50 years of land use on Ishigaki Island, Japan. *Coral Reefs.* 33, 363–373. doi: 10.1007/s00338-014-1128-3

Inoue, M., Nakamura, T., Tanaka, Y., Suzuki, A., Yokoyama, Y., Kawahata, H., et al. (2018). The simple role of coral-algal symbiosis in coral calcification is based on multiple geochemical tracers. *Geochim. Cosmochim. Acta* 235, 76–88. doi: 10.1016/j.gca.2018.05.016

Inoue, M., Suwa, R., Suzuki, A., Sakai, K., and Kawahata, H. (2011). Effects of seawater pH on the growth and skeletal U/Ca ratios of *Acropora digitifera* coral polyps. *Geophys. Res. Lett.* 38. doi: 10.1029/2011GL047786

Inoue, M., Suzuki, A., Nohara, M., Hibino, K., and Kawahata, H. (2007). Empirical assessment of coral Sr/Ca and Mg/Ca ratios as climate proxies using colonies grown at different temperatures. *Geophys. Res. Lett.* 34, L1261. doi: 10.1029/2007GL029628

Ito, S., Watanabe, T., Yano, M., and Watanabe, T. K. (2020). Influence of local industrial changes on reef coral calcification. *Sci. Rep.* 10, 7892. doi: 10.1038/s41598-020-64877-6

Jones, R., Giofre, N., Luter, H. M., Neoh, T. L., Fisher, R., and Duckworth, A. R. (2020). Coral response to chronic turbidity. *Sci. Rep.* 10, 4762. doi: 10.1038/s41598-020-61712-w

Juillet-Leclerc, A., Reynaud, S., Dissard, D., Tisserand, G., and Ferrier-Pagès, C. (2014). Light is an active contributor to the vital effects of coral skeleton proxies. *Geochim. Cosmochim. Acta* 140, 671–690. doi: 10.1016/j.gca.2014.05.042

Juillet-Leclerc, A., Rollion-Bard, C., Reynaud, S., and Ferrier-Pagès, C. (2018). A new paradigm for $\delta^{18}O$ in coral skeleton oxygen isotope fractionation response to biological kinetic effects. *Chem. Geol.* 483, 131–140. doi: 10.1016/j.chemgeo.2018.02.035

Kershaw, J. A., Stewart, J. A., Strawson, I., de Carvalho Ferreira, M. L., Robinson, L. F., Hendry, K. R., et al. (2023). Ba/Ca of stylasterid coral skeletons records dissolved seawater barium concentrations. *Chem. Geol.* 622, 121355. doi: 10.1016/j.chemgeo.2023.121355

Lajeunesse, T. C., Thornhill, D. J., Cox, E. F., Stanton, F. G., Fitt, W. K., and Schmidt, G. W. (2004). High diversity and host specificity have been observed among the symbiotic dinoflagellates of reef coral communities in Hawaii. *Coral Reefs.* 23, 596–603. doi: 10.1007/s00338-004-0428-4

Li, Y. H., and Chan, L. H. (1979). Desorption of Ba and 226Ra from river-borne sediments in the Hudson estuary. *Earth Planet. Sci. Lett.* 43, 343–350. doi: 10.1016/0012-821X(79)90089-X

Linsley, B. K., Dunbar, R. B., Dassié, E. P., Tangri, N., Henry, W. C., Logan, D. B., et al. (2019). Coral carbon isotope sensitivity to growth rate and water depth with paleo-sea level implications. *Nat. Commun.* 10, 2056. doi: 10.1038/s41467-019-10054-x

Loya, Y., Sakai, K., Yamazato, K., Nakano, Y., Sambali, H., and van Woesik, R. (2001). Coral bleaching: winners and losers. *Ecol. Lett.* 4, 122–131. doi: 10.1046/j.1461-0248.2001.00203.x

Mallon, J., Cyronak, T. J., Hall, E. R., Banaszak, A. T., Exton, D. A., and Bass, A. M. (2022). Light-driven dynamics between the calcification and production of functionally diverse coral reef calcifiers. *Limnol. Oceanogr.* 67, 434–449. doi: 10.1002/lno.12002

Mavromatis, V., Goetschl, K. E., Grengg, C., Konrad, F., Purgstaller, B., and Dietzel, M. (2018). Barium partitioning in calcite and aragonite as a function of growth rate. *Geochim. Cosmochim. Acta* 237, 65–78. doi: 10.1016/j.gca.2018.06.018

McConnaughey, T. (1989). ^{13}C and 18O isotopic disequilibrium in biological carbonates: I. *Patterns. Geochim. Cosmochim. Acta* 53, 151–162. doi: 10.1016/0016-7037(89)90282-2

McCulloch, M. T., Fallon, S. J., Wyndham, T., Hendy, E. J., Lough, J. M., and Barnes, D. K. (2003). Coral records of increased sediment flux to the inner Great Barrier Reef since European settlement. *Nature* 421, 727–730. doi: 10.1038/nature01361

Meibom, A., Cuif, J. P., Hillion, F., Constantz, B. R., Juillet-Leclerc, A., Dauphin, Y., et al. (2004). Distribution of magnesium in coral skeletons. *Geophys. Res. Lett.* 31, L23306. doi: 10.1029/2004GL021313

Min, G. R., Edwards, R. L., Taylor, F. W., Recy, J., Gallup, C. D., and Beck, J. W. (1995). Annual cycles of U/Ca in coral skeletons and U/Ca thermometry. *Geochim. Cosmochim. Acta* 59, 2025–2042. doi: 10.1016/0016-7037(95)00124-7

Mitsuguchi, T., Matsumoto, E., Abe, O., Uchida, T., and Isdale, P. J. (1996). Mg/Ca thermometry in coral skeletons. *Science* 274, 961–963. doi: 10.1126/science.274.5289.961

Montagna, P., McCulloch, M., Douville, E., López Correa, M., Trotter, J., Rodolfo-Metalpa, R., et al. (2014). Li/Mg systematics in scleractinian corals: Calibration of the thermometer. *Geochim. Cosmochim. Acta* 132, 288–310. doi: 10.1016/j.gca.2014.02.005

Nakamura, T., and Yamasaki, H. (2005). Requirement of water flow for sustainable growth of pocilloporid corals during high-temperature periods. *Mar. pollut. Bull.* 50, 1115–1120. doi: 10.1016/j.marpolbul.2005.06.025

Nakamura, T., van Woesik, R., and Yamasaki, H. (2005). The photoinhibition of photosynthesis is reduced by water flow in the reef-building coral *Acropora digitifera*. *Mar. Ecol. Prog. Ser.* 301, 109–118. doi: 10.3354/meps301109

Okai, T., Suzuki, A., Kawahata, H., Terashima, S., and Imai, N. (2002). Preparation of new geological survey of Japan geochemical reference material: coral JCp-1. *Geostand. Geoanal. Res.* 26, 95–99. doi: 10.1111/j.1751-908X.2002.tb00627.x

Omata, T., Suzuki, A., Sato, T., Minoshima, K., Nomaru, E., Murakami, A., et al. (2008). Effect of photosynthetic light dosage on carbon isotope composition in the coral skeleton: Long-term culture of Porites spp. *J. Geophys. Res.* 113, G02014. doi: 10.1029/2007JG000431

Pelejero, C., Calvo, E., McCulloch, M. T., Marshall, J. F., Gagan, M. K., Lough, J. M., et al. (2005). Pre-industrial to modern interdecadal variability in coral reef pH. *Science* 309, 2204–2207. doi: 10.1126/science.1113692

Pratchett, M. S., Anderson, K. D., Hoogenboom, M. O., Widman, E., Baird, A. H., Pandolfi, J. M., et al. (2015). Spatial, temporal and taxonomic variation in coral growth—implications for the structure and function of coral reef ecosystems. *Oceanogr. Mar. Biol. Annu. Rev.* 53, 215–295. doi: 10.1201/b18733-7

Ram, S., and Erez, J. (2021). The distribution coefficients of major and minor elements in coral skeletons under variable calcium seawater concentrations. *Front. Earth Sci.* 9. doi: 10.3389/feart.2021.657176

Ramos, R. D., Goodkin, N. F., and Fan, T.-Y. (2020). Coral records at the northern edge of the western Pacific warm Pool reveal multiple drivers of sea surface temperature, salinity, and rainfall variability since the end of the Little Ice Age. Paleoceanogr. *Paleoclimatol* 35, e2019 doi: 10.1029/2019PA003826

Reynaud, S., Ferrier-Pagès, C., Meibom, A., Mostefaoui, S., Mortlock, R., Fairbanks, R., et al. (2007). Light and temperature effects on Sr/Ca and Mg/Ca ratios in the scleractinian coral *Acropora* sp. *Geochim. Cosmochim. Acta* 71, 354–362. doi: 10.1016/j.gca.2006.09.009

Reynaud-Vaganay, S., Juillet-Leclerc, A., Jaubert, J., and Gattuso, J. P. (2001). Effect of light on skeletal δ^{13}C and d δ^{18}O, and interaction with photosynthesis, respiration and calcification in two zooxanthellate scleractinian corals. *Palaeogeogr. Palaeoclimatol. Palaeoecol.* 175, 393–404. doi: 10.1016/S0031-0182(01)00382-0

Ross, C. L., DeCarlo, T. M., and McCulloch, M. T. (2019). Calibration of Sr/Ca, Li/Mg and Sr-U paleothermometry in branching and foliose corals. *Paleoceanogr. Paleoclimatol.* 34, 1271–1291. doi: 10.1029/2018PA003426

Schoepf, V., Levas, S. J., Rodrigues, L. J., McBride, M. O., Aschaffenburg, M. D., Matsui, Y., et al. (2014). Kinetic and metabolic isotope effects in coral skeletal carbon isotopes: A re-evaluation using experimental coral bleaching as a case study. *Geochim. Cosmochim. Acta* 146, 164–178. doi: 10.1016/j.gca.2014.09.033

Sevilgen, D. S., Venn, A. A., Hu, M. Y., Tambutté, E., De Beer, D., Planas-Bielsa, V., et al. (2019). Full in *vivo* characterization of carbonate chemistry at the site of calcification in corals. *Sci. Adv.* 5, eaau7447. doi: 10.1126/sciadv.aau7447

Spreter, P. M., Reuter, M., Mertz-Kraus, R., Taylor, O., and Brachert, T. C. (2022). Calcification response of reef corals to seasonal upwelling in the northern Arabian Sea (Masirah Island, Oman). *Biogeosci* 19, 3559–3573. doi: 10.5194/bg-19-3559-2022

Suzuki, A., Gagan, M. K., Fabricius, K., Isdale, P. J., Yukino, I., and Kawahata, H. (2003). Skeletal isotope microprofiles of growth perturbations in Porites corals during the 1997–1998 mass bleaching event. *Coral Reefs* 22, 357–369. doi: 10.1007/s00338-003-0323-4

Suzuki, A., Hibino, K., Iwase, A., and Kawahata, H. (2005). Intercolony variability of skeletal oxygen and carbon isotope signatures of cultured *Porites* corals: Temperature-controlled experiments. *Geochim. Cosmochim. Acta* 69, 4453–4462. doi: 10.1016/j.gca.2005.05.018

Thompson, D. M. (2022). Environmental records from coral skeletons: A decade of novel insights and innovation. *Wiley Interdiscip. Reviews: Climate Change* 13 (1), e745. doi: 10.1002/wcc.745

Veron, J. E. N. (1986). *Corals of Australia and the indo-pacific* (Sydney: Angus & Robertson), 644.

Watanabe, T., Winter, A., and Oba, T. (2001). Seasonal changes in sea surface temperature and salinity during the Little Ice Age in the Caribbean Sea deduced from Mg/Ca and ^{18}O/^{16}O ratios in corals. *Mar. Geol.* 173, 21–35. doi: 10.1016/S0025-3227(00)00166-3

Wei, G., Wang, Z., Ke, T., Liu, Y., Deng, W., Chen, X., et al. (2015). Decadal Variability in seawater pH in the west Pacific: Evidence from coral δ^{11}B records. *J. Geophys. Res.* 120, 7166–7181. doi: 10.1002/2015JC011066

Xu, S., Yu, K., Zhang, Z., Chen, B., Qin, Z., Huang, X., et al. (2020). Intergeneric differences in trophic status of scleractinian corals from Weizhou Island, northern South China Sea: Implication for their different environmental stress tolerance. *J. Geophys. Res.* 124, e2019JG005451. doi: 10.1029/2019JG005451

Yamazaki, A., Yano, M., Harii, S., and Watanabe, T. (2021). Effects of light on the Ba/Ca ratios in coral skeletons. *Chem. Geol.* 559, 119911. doi: 10.1016/j.chemgeo.2020.119911

Yoshimura, T., Tamenori, Y., Takahashi, O., Nguyen, L. T., Hasegawa, H., Iwasaki, N., et al. (2015). Mg coordination in biogenic carbonates constrained by theoretical and experimental XANES. *Earth Planet. Sci. Lett.* 421, 68–74. doi: 10.1016/j.epsl.2015.03.048

frontiers | Frontiers in Marine Science

TYPE Original Research
PUBLISHED 02 April 2024
DOI 10.3389/fmars.2024.1324436

OPEN ACCESS

EDITED BY
Johan Schijf,
University of Maryland, College Park,
United States

REVIEWED BY
Matthew Jones,
United States Geological Survey (USGS),
United States
N. J. De Winter,
VU Amsterdam, Netherlands
Linda Ivany,
Syracuse University, United States

*CORRESPONDENCE
Shunta Ichimura
ichimura.shunta.a4@s.mail.nagoya-u.ac.jp

RECEIVED 19 October 2023
ACCEPTED 13 March 2024
PUBLISHED 02 April 2024

CITATION
Ichimura S, Takayanagi H, Iryu Y, Takahashi S and Oji T (2024) Shallow-water temperature seasonality in the middle Cretaceous mid-latitude northwestern Pacific.
Front. Mar. Sci. 11:1324436.
doi: 10.3389/fmars.2024.1324436

Shallow-water temperature seasonality in the middle Cretaceous mid-latitude northwestern Pacific

Shunta Ichimura[1]*, Hideko Takayanagi[2,3], Yasufumi Iryu[2,3], Satoshi Takahashi[1] and Tatsuo Oji[4]

[1]Graduate School of Environmental Studies, Nagoya University, Nagoya, Japan, [2]Department of Earth Science, Graduate School of Science, Tohoku University, Sendai, Japan, [3]Advanced Institute for Marine Ecosystem Change (WPI-AIMEC), Tohoku University, Sendai, Japan, [4]Nagoya University Museum (NUM), Nagoya University, Nagoya, Japan

Temperature seasonality during the middle Cretaceous provides vital information about climate dynamics and ecological traits of organisms under the conditions of the "supergreenhouse" Earth. However, sub-annual scale paleotemperature records in the mid-latitude region remain limited. In this study, sclerochronological and stable oxygen isotope ($\delta^{18}O$) analyses of bivalve fossils from the northwestern Pacific (paleolatitude: 44°N) were used to estimate their life history and sub-annual scale temperature patterns of the middle Cretaceous. The materials studied included *Cucullaea* (*Idonearca*) *delicatostriata* and *Aphrodina pseudoplana* recovered from middle Turonian (middle Cretaceous) shallow marine deposits in Hokkaido, northern Japan. Growth increment width and shell $\delta^{18}O$ of *C.* (*I.*) *delicatostriata* revealed that the growth rate was temporally maximized and then minimized, which can be interpreted as representing spring and winter growth, respectively. Approximately 25 fortnightly growth increments occurred within that cycle, suggesting that shell formation proceeded continuously throughout the year. Based on shell $\delta^{18}O$ values, shallow-water temperatures from 28°C to 35°C with 7°C seasonality were estimated, under the assumption that seawater $\delta^{18}O$ values were annually invariant at –1‰ relative to VSMOW. This temperature seasonality in the middle Cretaceous is more than 5°C smaller than the seasonality of modern shallow-water environments at the same latitudes. These findings, taken together with previous studies of other oceanic regions, suggest that the Northern Hemisphere had low seasonal shallow-water temperature variation of up to 10°C in the middle Cretaceous.

KEYWORDS

bivalve, middle Turonian, oxygen isotope, sclerochronology, Yezo Group

1 Introduction

The middle Cretaceous "supergreenhouse" period (Aptian–Santonian; 125–83 Ma; Huber et al., 2018; Petrizzo et al., 2022) is characterized by a warm global climate (Vandermark et al., 2007; Hay, 2008); high pCO_2 levels reaching approximately 1,000 ppm (Foster et al., 2017), nearly approximating the IPCC 6th Assessment Report SSP3-7.0-lowNTCF scenario (Meinshausen et al., 2020); an absence of polar ice sheets (Moriya et al., 2007; MacLeod et al., 2013); and a much flatter equator-to-pole temperature gradient than today (Barron, 1983; Huber et al., 1995; Pucéat et al., 2007). This warm middle Cretaceous period is also associated with drastic faunal and floral transitions (Vermeij, 1977; Lidgard and Crane, 1988). Based on these characteristics, the middle Cretaceous period provides insights into a high-pCO_2 Earth, such as a possible future with accelerated anthropogenic CO_2 emissions. To properly characterize climate in the middle Cretaceous supergreenhouse period, seasonal-scale paleoenvironmental reconstruction is crucial because aspects of climate dynamics, ecology, and evolution of organisms have been controlled by seasonality throughout Earth's history (Denton et al., 2005; Marshall and Burgess, 2015).

Fossil bivalve shells are commonly used to reconstruct sub-annual scale climatic fluctuations over geological timescales (Ivany, 2012; Walliser et al., 2015; Posenato et al., 2022). Stable oxygen isotope ratios ($\delta^{18}O$ values) of marine bivalve shell carbonates (mainly aragonite and calcite) can be used for seawater temperature reconstruction because bivalve shells are precipitated in oxygen isotope equilibrium with ambient seawater (Epstein et al., 1953; Grossman and Ku, 1986). Bivalves form disconformities and translucent bands within their shells (called growth lines) when their shell growth stops or slows due to cyclic or irregular environmental or physiological changes (Kennish and Olsson, 1975; Ohno, 1989; Schöne et al., 2003). Furthermore, annual shell growth rates of bivalves ontogenetically decrease due to reductions in daily growth rates (Jones and Quitmyer, 1996), which are mainly observed in regions with small seasonality (Schöne et al., 2005; Reza Mirzaei et al., 2017) and increases in growth cessation interval, which can be observed worldwide (Hall et al., 1974; Tanabe, 1988; Jones et al., 1989; Tanabe et al., 2017, 2020). The timing of shell formation, temporal shell growth rate, and age of bivalves can be estimated by identifying the timing of growth line formation on shells and measuring the widths and numbers of these lines (Jones, 1983; Sato, 1997; Kubota et al., 2017).

Fossil bivalves with primary low-Mg calcite shells have often been used for climate reconstruction in deep time (Beard et al., 2015; de Winter et al., 2017, 2021) because low-Mg calcite is less susceptible to diagenetic alteration than aragonite. For example, $\delta^{18}O$ values of rudists with large, thick, and low-Mg calcite shells have been preferentially used for seasonal-scale paleotemperature reconstruction in the middle Cretaceous paleoenvironmental studies (Steuber et al., 2005; Walliser and Schöne, 2020; Schmitt et al., 2022). However, because rudists were reef/bioherm builders that primarily inhabited low-latitude shallow oceans, seasonal-resolution sea surface temperature (SST) records for the middle Cretaceous have mostly been reported from the low-latitude Tethys Ocean (Steuber et al., 2005; Walliser and Schöne, 2020; Huck and Heimhofer, 2021). Because seasonality varies with latitude, SST seasonality must be investigated at low latitudes, as well as middle and high latitudes, to elucidate its global seasonal climatic trends. Furthermore, the mid-latitude region is the best area for identifying maximal seasonal temperature fluctuations (Ivany, 2012; Ivany and Judd, 2022). Despite its importance, however, few middle Cretaceous studies have included reconstruction of paleo-seawater temperature and its seasonality from carbonate fossil shells in mid-latitude regions. On the other hand, aragonitic shells produced by mollusks with sufficient thickness for sclerochronological and geochemical analyses from shell cross sections (e.g., *Aphrodina*, *Cucullaea*, and *Glycymeris*) were common at low latitudes, as well as middle and high latitudes, during the middle Cretaceous (Ando and Kodama, 1998; Squires, 2010; Hoşgör and Yılmaz, 2019). The sub-annual scale paleoenvironment, including shallow-water temperature, can be reconstructed from aragonitic fossil shells in deep time if evaluation of fossil preservation shows that shell aragonite is well-preserved (Walliser et al., 2015; Hall et al., 2018; Meyer et al., 2018; Posenato et al., 2022).

The Cretaceous Aptian–Maastrichtian Yezo Group in Hokkaido (northern Japan), deposited in the middle latitudes of the northwestern Pacific, contains a variety of well-preserved marine fossils, including ammonites, bivalves, and gastropods (Suzuki et al., 1998; Hikida et al., 2003; Yabumoto et al., 2012). The Yezo Group was mainly deposited in the deep ocean. However, some parts, such as the Mikasa Formation (latest Albian–Turonian), were deposited in a shallow ocean with abundant shallow-water bivalves (Tashiro, 1995; Ando and Kodama, 1998). This study presents detailed sclerochronological and oxygen isotope records of bivalve fossils from the Mikasa Formation to reveal seasonal-scale shallow-water temperature records and their life history.

2 Geological setting

Aptian–Maastrichtian forearc (Yezo Basin) sediments of the paleo-Asian continental eastern margin (Takashima et al., 2004), called the Yezo Group, are widely distributed from Soya to Urakawa areas, central Hokkaido, northern Japan (Figure 1A). Paleomagnetic studies showed that the paleolatitude of the Yezo Basin was approximately 44° N in the Late Cretaceous (Tamaki and Itoh, 2008; Kitagawa et al., 2016). An exception is the Urakawa area, which was at approximately 16.7°N during the Campanian (Late Cretaceous) before being transported to its present position (Tamaki et al., 2008). The Cenomanian–Campanian Yezo Basin was affected by a southward shallow-water current system comparable to the modern Oyashio Current based on neodymium isotope ($^{143}Nd/^{144}Nd$ ratio) analysis of fish bone and tooth fossils from the Yezo Group (Moiroud et al., 2013). The mean annual SST in the middle–late Turonian Yezo Basin has been estimated as 26°C–29°C from planktonic foraminiferal $\delta^{18}O$ data (Moriya, 2011).

The Albian–Turonian Mikasa Formation, the Yezo Group is characterized by sandstone with hummocky cross-stratification (HCS) (Ando, 1987). The Mikasa Formation is distributed across the Sorachi–Ikushunbetsu Anticline (Figure 1B) (Ando, 1990b). The Mikasa Formation has various sedimentological facies that

10.3389/fmars.2024.1324436

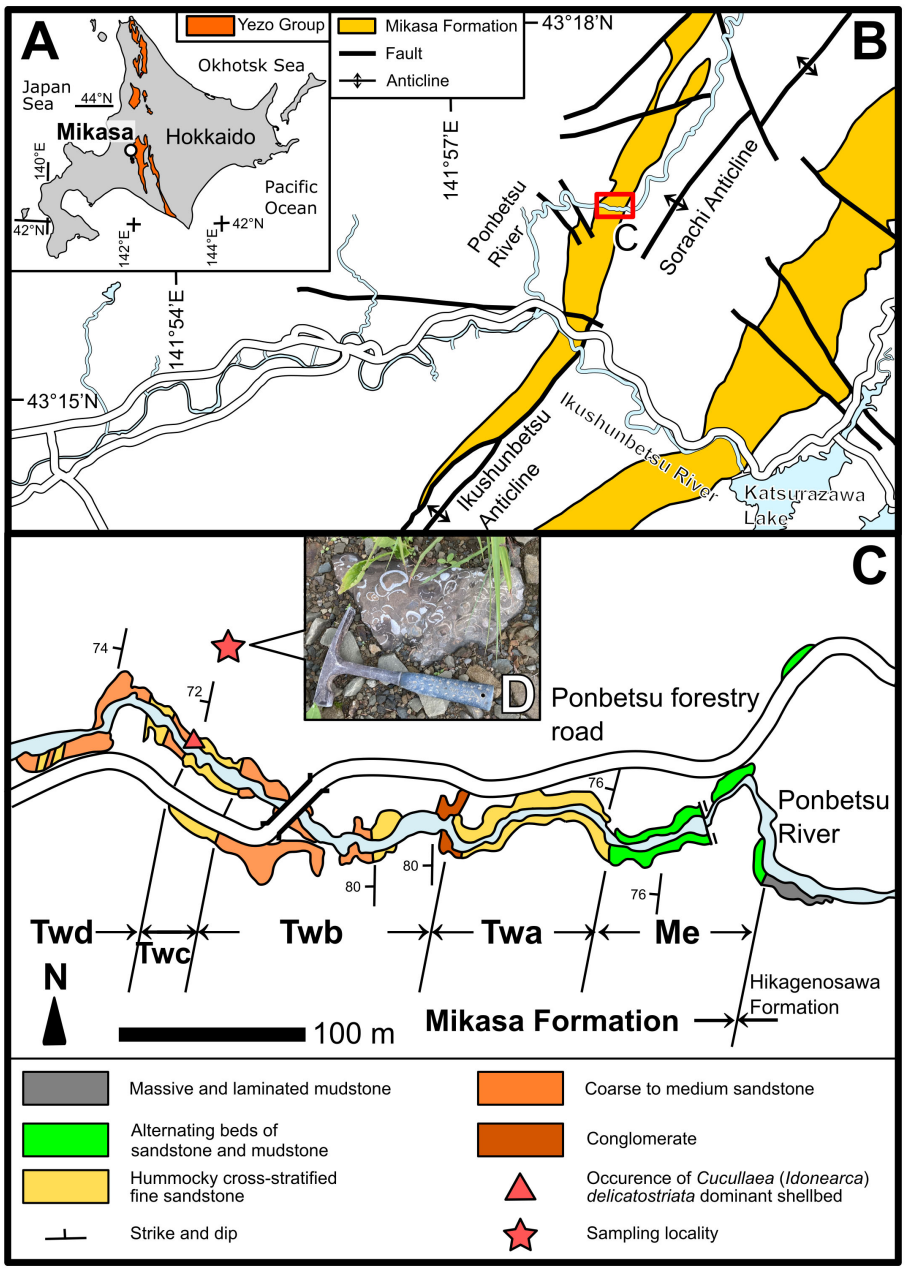

FIGURE 1
Geological map of Hokkaido modified from Takashima et al. (2004) **(A)** and the Mikasa area modified from Kikuchi (2018) **(B)**. **(C)** Map of the Ponbetsu River section modified from Ando and Kodama (1998), and details of the sampling locality. Me, Twa, Twb, Twc, and Twd in **(C)** represent sedimentary units of the Mikasa Formation in the Ponbetsu River section from Ando (1987). **(D)** Photograph of the sampled shellbed.

were deposited from the lagoon to the outer shelf, mainly under shallow-water conditions (Ando, 1990a). The Mikasa Formation is almost continuously exposed along the Ponbetsu River in Ponbetsu-cho, Mikasa City, central Hokkaido (Ponbetsu River section; Ando, 1987) (Figures 1C, 2) and is divided into five units based on sedimentary facies (Matsuno et al., 1963), designated Me (main part of the Middle Yezo Group, unit e), Twa, Twb, Twc, and Twd (Tw denotes the *Trigonia* sandstone in the western wing of the Sorachi–Ikushunbetsu Anticline) (Figures 1C, 2; Yabe, 1926; Matsumoto, 1951; Shimizu et al., 1955; Takashima et al., 2004). The Twc unit is approximately 32 m-thick and consist of fine- to very fine-grained sandstone with hummocky cross-stratification (HCS). This unit is considered to have been deposited from the lower shoreface to the shallow inner shelf, in waters tens of meters deep (Ando and Kodama, 1998). The Twc unit has been correlated with the middle Turonian based on the occurrence of an age-indicative ammonoid *Subprionocyclus neptuni* (Matsumoto, 1965) and inoceramid *Inoceramus hobetsensis* (Ando, 1987). The Twd unit is approximately 100 m-thick and mainly composed of medium- to coarse-grained sandstone with HCS (Ando and Kodama, 1998). The occurrence of *I. hobetsensis* in the lowest part and *I. teshioensis* in the uppermost part of the Twd unit

10.3389/fmars.2024.1324436

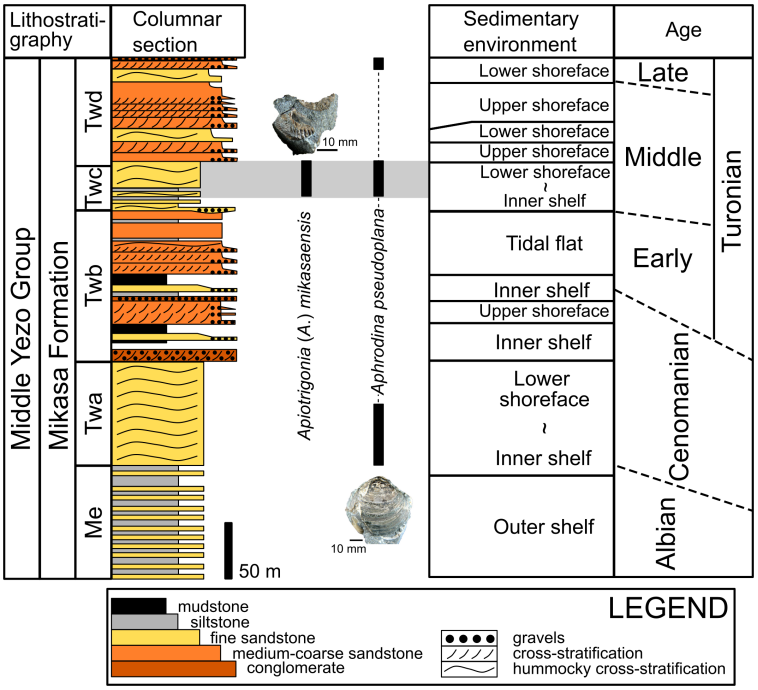

FIGURE 2
Columnar section with sedimentary setting and deposition age of the Mikasa Formation at the Ponbetsu River section modified from Ando (1987, 1990b) and Ando and Kodama (1998). Black bars with photographs of bivalve fossils represent the stratigraphic occurrences of identified bivalves in the studied shellbed according to Ando and Kodama (1998). Gray zones indicate the suggested stratigraphic ranges of our studied materials.

indicates that the Twd unit was deposited in the middle to late Turonian (Ando, 1987).

3 Materials and methods

3.1 Field sampling

A boulder of calcite-cemented fine-grained sandstone containing abundant mollusk fossils (coquina) was collected alongside a forest road near the Ponbetsu River section (Figures 1C, D). In this rock, disarticulated bivalves (*Aphrodina pseudoplana* (Figures 2, 3D), *Apiotrigonia* (*A.*) *mikasaensis* (Figure 2), *Cucullaea* (*Idonearca*) *delicatostriata* (Figures 3A–C), and possibly *Leptosolen* sp.) and gastropods (possibly naticids) were observed. Most fossils from the coquina were identified as *C.* (*I.*) *delicatostriata*, and other species were observed as only one or a few individuals.

Although this coquina was found as an isolated unrooted block, the shellbed was determined to be derived from the Twc unit or the lowermost part of the Twd unit because large boulders of fine-grained sandstone rich in *C.* (*I.*) *delicatostriata* were exclusively found near the outcrop of the Twc unit and lowermost part of the Twd unit in the Ponbetsu River section (Figure 1C); moreover, *Apiotrigonia* (*A.*) *mikasaensis*, a trigoniid bivalve restricted to the Turonian age (Tashiro, 1979), was observed in the collected coquina (Figure 2). In the studied succession, only Twc and Twd units are correlated with the Turonian, and the occurrences of *A.* (*A.*) *mikasaensis* in the Ponbetsu River section were limited to the upper Twc and lower Twd units (Ando and Kodama, 1998). These findings indicated that the studied shellbed originated from Twc or lower Twd units (Figure 2).

3.2 Sample preparation

The surfaces of the bivalve shells were carefully cleaned and exposed from the sandstone matrix. For this study, three shells of *C.* (*I.*) *delicatostriata* (Figures 3A–C; labeled PU-1, PU-2, and PU-5) and one shell of *A. pseudoplana* (Figure 3D) were selected for subsequent growth line observation and geochemical analysis, considering that these species have sufficiently thick shells for observation and geochemical sampling from cross-sections. Additionally, the abundant occurrence of *C.* (*I.*) *delicatostriata* allows intraspecific comparisons, thus improving data reliability. Shell surfaces were coated with epoxy resin to avoid mechanical damage during preparation. Shells were diagonally cut along their maximum growth direction using a diamond saw (Figures 4A, B). One side was polished with silicon carbide up to #3,000 (Figures 4A, B). Regarding *C.* (*I.*) *delicatostriata*, the other side of the cross-section was used to make a thin section (0.1 mm thickness) for growth line observation. Small pieces of shells were collected from the studied shells to evaluate the extent of diagenetic alteration and determine the diagenetic level according to preservation index (PI) (Cochran et al., 2010; Knoll et al., 2016) via scanning electron microscopy (SEM) (Figures 4A, B). The polished shell surface was etched with 5% acetic acid for 15 min prior to microstructure observation with SEM.

10.3389/fmars.2024.1324436

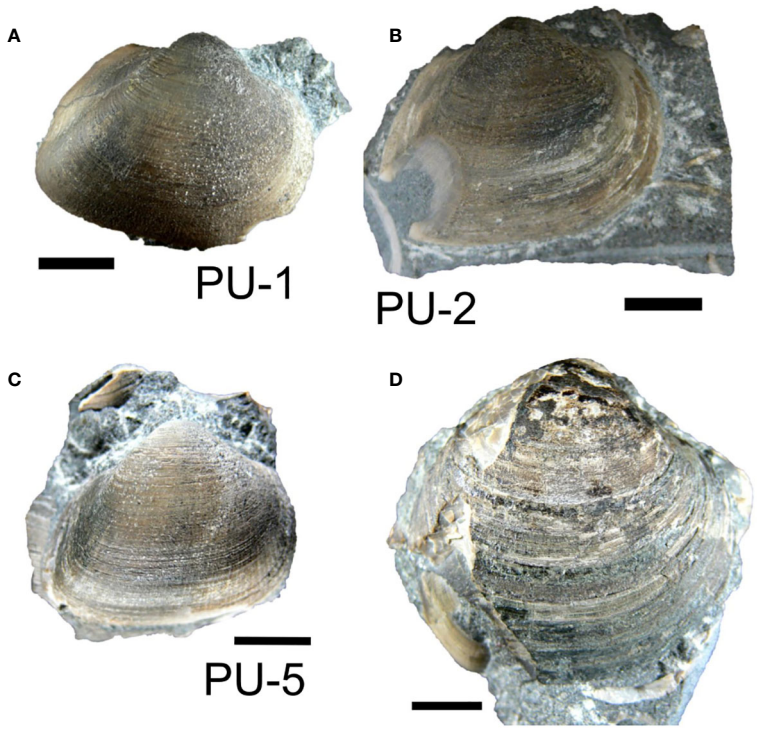

FIGURE 3
Photographs of the *Cucullaea* (*Idonearca*) *delicatostriata* (**A**: PU-1, **B**: PU-2, **C**: PU-5) and *Aphrodina pseudoplana* **(D)** shells used in this study. Scale bar = 10 mm.

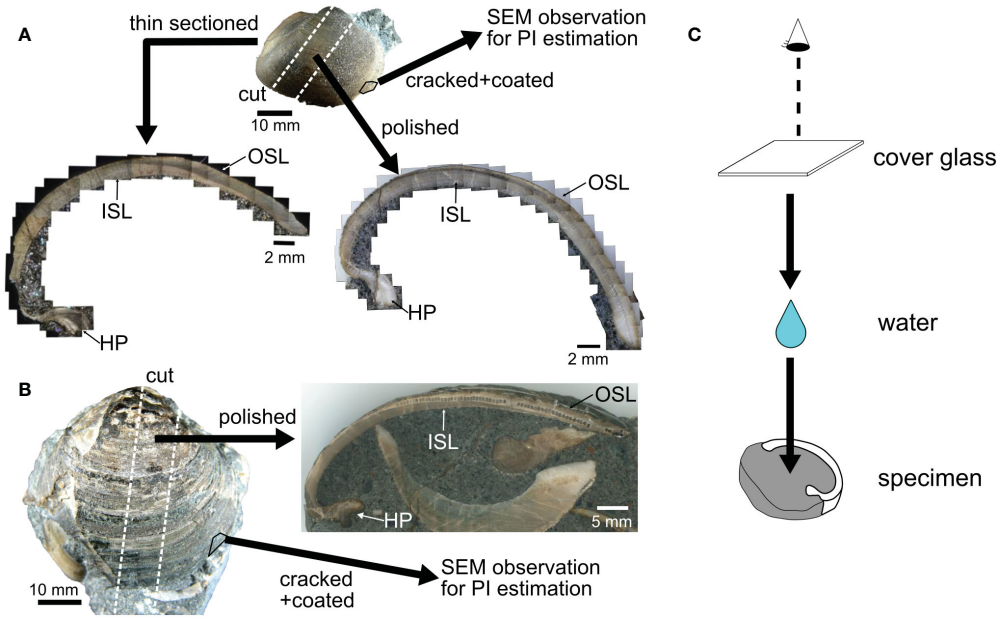

FIGURE 4
Sample preparation of *Cucullaea* (*Idonearca*) *delicatostriata* **(A)** and *Aphrodina pseudoplana* **(B)** shells. The valves were cut perpendicular to the maximum growth direction. One side of the cutting slab was polished to make a polished slab and the other side of each *C.* (*I.*) *delicatostriata* shell was thin-sectioned. Small fragments of shell were sampled by cracking each shell and then coating the cracked surface with platinum. The coated shell was used for preservation state estimation based on the PI scale (Cochran et al., 2010; Knoll et al., 2016). The surfaces of the thin section and polished shell were wetted and covered with cover glass during observation **(C)**. Small holes in the polished sections are the remains of samples used for stable isotope analysis. OSL, outer shell layer; ISL, inner shell layer; HP, hinge plate.

3.3 Evaluation of the extent of diagenetic alteration

Evaluation of diagenetic effects on shell microstructure and mineralogy is essential for reliable paleoenvironmental reconstruction because diagenesis alters the original chemical composition of the shell (Cochran et al., 2010; Pederson et al., 2019). Shell microstructure and mineralogy of the studied shells were analyzed to determine the extent of diagenetic alteration. Thin sections and polished sections of the shells were carefully observed with a binocular microscope and a petrographic microscope to identify macro-scale diagenetic products, such as mosaic calcite crystals (Maliva et al., 2000; Pederson et al., 2019).

3.3.1 Raman spectroscopic analysis

Raman spectroscopic analysis was conducted to identify the mineral composition of the studied fossils using a confocal Raman micro-spectrometer (Nicolet Almega XR; Thermo Fisher Scientific, Bremen, Germany) in the Petrology and Mineralogy Laboratory of Nagoya University, Nagoya, Japan. A 532 nm Nd-YAG laser at a power of approximately 10 mW was irradiated to the thin sections and the polished sections of studied shells through a confocal microscope (BX51; Olympus, Tokyo, Japan) with a 100× objective (Olympus Mplan-BD 100X; numerical aperture, 0.90). The scattered light was collected using backscatter geometry from a 25 μm pinhole and a holographic notch filter, dispersed using 2,400 lines/mm, and analyzed using a Peltier-cooled charge-coupled device detector composed of 256 × 1024 pixels (Andor Technology, Belfast, Ireland). Raman spectra were collected in six periods of 10 s each for point analysis. Spectra between 100 and 1,290 cm^{-1} were used to compare the spectra of calcium carbonate minerals (Parker et al., 2010; Wehrmeister et al., 2010).

3.3.2 SEM observation

The extent of diagenesis was determined using the PI, which was proposed for the evaluation of diagenetic alteration based on shell microstructure (Cochran et al., 2010; Knoll et al., 2016). First, the shell microstructure of a surface-etched polished slab coated with platinum was observed with SEM (SU6600; Hitachi High-Technologies, Tokyo, Japan) in the Laboratory of Geobiology at Nagoya University. Then, cracked shell surfaces coated with platinum were observed with SEM, and the preservation status was scored according to the PI (Cochran et al., 2010; Knoll et al., 2016).

3.4 Growth line analysis

Growth lines are observable as black-colored disconformities and translucent bands in accretionary-formed biogenic carbonates, which are caused by growth reduction or cessation. In bivalves, growth lines can be observed as concentric lines on the interior and exterior of the shells of various taxa; they were formed under environmental deterioration (e.g., tidal emersion and temperature extremes) or physical deterioration (Schöne et al., 2004; Schöne and Giere, 2005; de Winter et al., 2020). Growth lines tend to become darker with longer growth cessation. Growth lines act as records of the shell growth rate over various timescales (e.g., daily, fortnightly, and annually) (Kennish and Olsson, 1975; Ohno, 1989), indicating the timing of biological and environmental events (Kennish and Olsson, 1975; Sato, 1995). Therefore, growth lines can be used to elucidate organisms' growth strategies (Tanabe, 1988; Sugiura et al., 2014; Posenato et al., 2022).

Growth lines were observed on thin sections of each shell under crossed Nicol polarization and polished slabs of each shell under stereoscopic microscopy. To reduce diffuse reflections and obtain clear images, the surfaces of thin sections and polished slabs were immersed in water and then covered with a cover glass (Figure 4C). Enlarged images of thin sections and polished surfaces taken using microscopes were stitched into single TIFF images with Adobe Photoshop software (Adobe, San Jose, CA, USA). Throughout the study, growth lines in the outer shell layer were used for investigation because these growth lines can be observed more clearly than growth lines in the inner shell layer and hinge plate. To accurately distinguish the shell growth lines, the greyscale value of the shell cross-section was measured along the direction of shell growth, in accordance with the methods of Carré et al. (2005) and Otter et al. (2019). In fossil shells, black stains may appear in areas other than growth lines due to shell coloration or crack formation during fossilization. To remove background colors, the image of the polished section was first subjected to black and white conversion followed by a rolling ball algorithm (Sternberg, 1983) for background subtraction (10-pixel diameter). The width of growth increments (space between neighboring growth lines) was measured along the growth direction. All image processing operations were performed using ImageJ (https://imagej.nih.gov/ij/).

3.5 Stable isotope analysis

Carbonate powders (approximately 100 μg) were collected from the outer shell layers of polished shells along their growth direction using a drill bit 0.4 mm in diameter (Minitor Co., Ltd., Osaka, Japan). Stable oxygen and carbon isotope compositions of bivalve shells ($\delta^{18}O_{shell}$ and $\delta^{13}C_{shell}$, respectively) were measured with a Thermo Fisher Delta V Advantage isotope ratio mass spectrometer (Bremen, Germany) coupled to a ThermoQuest Kiel-III automated carbonate device (Bremen, Germany) at the Institute of Geology and Paleontology, Tohoku University, Sendai, Japan. Carbonate samples were reacted with 100% phosphoric acid at approximately 72°C. Both isotope ratios were expressed in conventional notation (δ, ‰) and calibrated to the NBS-19 international standard relative to Vienna Pee Dee Belemnite. The external precision (1σ) of the measured isotopic values was calculated based on repeated measurements of a laboratory reference sample (JCt-1) (Okai et al., 2004). The external precision (1σ) values of $\delta^{18}O_{shell}$ and $\delta^{13}C_{shell}$ were 0.05‰ and 0.03‰, respectively. Therefore, the error in seawater temperatures reconstructed based on the $\delta^{18}O_{shell}$ values measured in this study was approximately 0.9°C at the 95% significance level.

3.6 Paleotemperature estimation

Mollusks precipitate aragonite their shells at or near oxygen isotope equilibrium with ambient seawater (Epstein et al., 1953; Grossman and Ku, 1986; Watanabe and Oba, 1999). Seawater paleotemperature was estimated using the equation proposed by Grossman and Ku (1986) with a correlation adjustment of −0.27‰ (Dettman et al., 1999):

$$T(^\circ C) = 20.60 - 4.34\,(\delta^{18}O_{shell} - (\delta^{18}O_{seawater} - 0.27)) \quad (1)$$

where T represents seawater temperature, and $\delta^{18}O_{shell}$ and $\delta^{18}O_{seawater}$ represent oxygen isotope values of shell carbonates (relative to VPDB) and seawater where the bivalves were grown (relative to VSMOW), respectively. In this study, −1‰ was used for $\delta^{18}O_{seawater}$ according to the average $\delta^{18}O_{seawater}$ value of ocean water during the Late Cretaceous ice-free world (Shackleton and Kennett, 1975) and numerically simulated $\delta^{18}O_{seawater}$ values for the middle Cretaceous northwestern Pacific coastal region (Zhou et al., 2008). The validity of assuming a constant oxygen isotope ratio in the surrounding seawater is discussed in Section 5.3.

We reconstructed the monthly averaged paleotemperature of our study area from $\delta^{18}O_{shell}$ values using the algorithm developed by Judd et al. (2018). Input parameter values in our study are shown in Supplementary Table 1, but the following conditions were assumed when setting the parameters:

(1) The numbers of solar days within a fortnight cycle and one year were 14.7 and 365, respectively.

(2) The days of the year with the coldest and warmest temperatures (T_{pha}) within one year were regarded as January 1 and July 1, respectively, in all cases.

(3) The day of the year with maximum growth (G_{pha}) was regarded as the day in the middle of the fortnight cycle with the widest fortnightly growth increment.

We used younger age records of *C.* (*I.*) *delicatostriata* shells for the calculations because younger age records have paleotemperature and seasonal growth rate with sufficient time resolution.

4 Results

4.1 State of preservation

The studied shells showed no macro-scale diagenetic alterations in thin sections and polished sections (Figures 5A, B, E), aside from the presence of dark green needle-like chlorite in the outer part of the outer shell layer of *A. pseudoplana* (Figure 5E). These needle-like crystals extend perpendicular to the shell surface, and none straddle the growth lines.

The crossed-lamellar structure in the outer shell layer (Figure 5C) and complex crossed-lamellar structure in the inner shell layer (Figure 5D) were clearly observed in *C.* (*I.*) *delicatostriata* shells. In the *A. pseudoplana* shell, a crossed-acicular structure in the outer shell layer (Figure 5G), fine complex crossed-lamellar structures in the inner layer (Figure 5H), and irregular simple prismatic structures along the growth lines (Figure 5F) were preserved.

Raman spectroscopic analysis showed clear peaks at 153, 181, 206, 702, 706, and 1,085 cm^{-1} in all studied shells (Figure 6). The peaks at 153, 181, 206, 702, and 706 cm^{-1} together indicate the presence of aragonite (Parker et al., 2010); the peak at 1,085 cm^{-1} is the intrinsic Raman band of carbonate mineral (Wehrmeister et al., 2010). Considering that modern bivalves in the order Arcoida and the family Veneridae, which include *C.* (*I.*) *delicatostriata* and *A. pseudoplana*, respectively, produce aragonite shells (Kitamura, 2018), the two species also likely formed primarily aragonite shells. Therefore, the studied shells showed preservation of primary microstructure and mineralogy (aragonite) as indicated by SEM images and Raman spectroscopy (Figure 6).

In high-magnification SEM images, irregular thickness and fusions of crystals were observed in *C.* (*I.*) *delicatostriata* (Figures 7A–C). The PI of *C.* (*I.*) *delicatostriata* crossed-lamellar structures was 3 (good) for PU-1 (Figure 7A), 1 (poor) for PU-2 (Figure 7B), and 3 for PU-5 (Figure 7C) (Knoll et al., 2016). The PI of the *A. pseudoplana* shell could not be determined because the PI of the crossed-acicular structure has not been established (Figure 7D).

4.2 Growth line observation

Growth line visibility in the *C.* (*I.*) *delicatostriata* shell was compared between thin sections and polished sections of the same individuals (Figure 8). In the younger portion of the shells, growth lines of varying distinctness were clearly observed in both thin sections (Figure 8B) and polished sections (Figure 8D). Observation of polished sections under reflected light was more suitable for detecting faint growth lines than thin sections due to the brightness of the views. Near the ventral margin, prominent growth lines were observed in the thin sections (Figure 8C), while these lines were not clearly visible in the polished sections (Figure 8E). These results indicated that thin sections are suitable for observing growth lines throughout all ontogenetic stages, while polished sections are suitable for observing growth lines in younger portions of the shells. To monitor the shell growth pattern of *C.* (*I.*) *delicatostriata* throughout its lifetime, the most effective approach is to use thin sections and measure the width of the prominent growth increment along the growth direction.

The growth lines observed in thin sections and polished sections can be divided into two categories, prominent ("major") and faint ("minor") growth lines (Figures 5A, B, 9), according to their darkness. Major growth lines were darker than minor growth lines according to processed greyscale levels (Figure 9). The processed greyscale values more clearly reflected the blackness of growth lines than the raw greyscale values because the color inversion process and rolling ball algorithm subtracted background color heterogeneity (Figure 9). Notably, approximately 15 minor growth lines with low processed greyscale values were observed between neighboring major growth lines with high processed greyscale values in the polished sections (Figure 9).

10.3389/fmars.2024.1324436

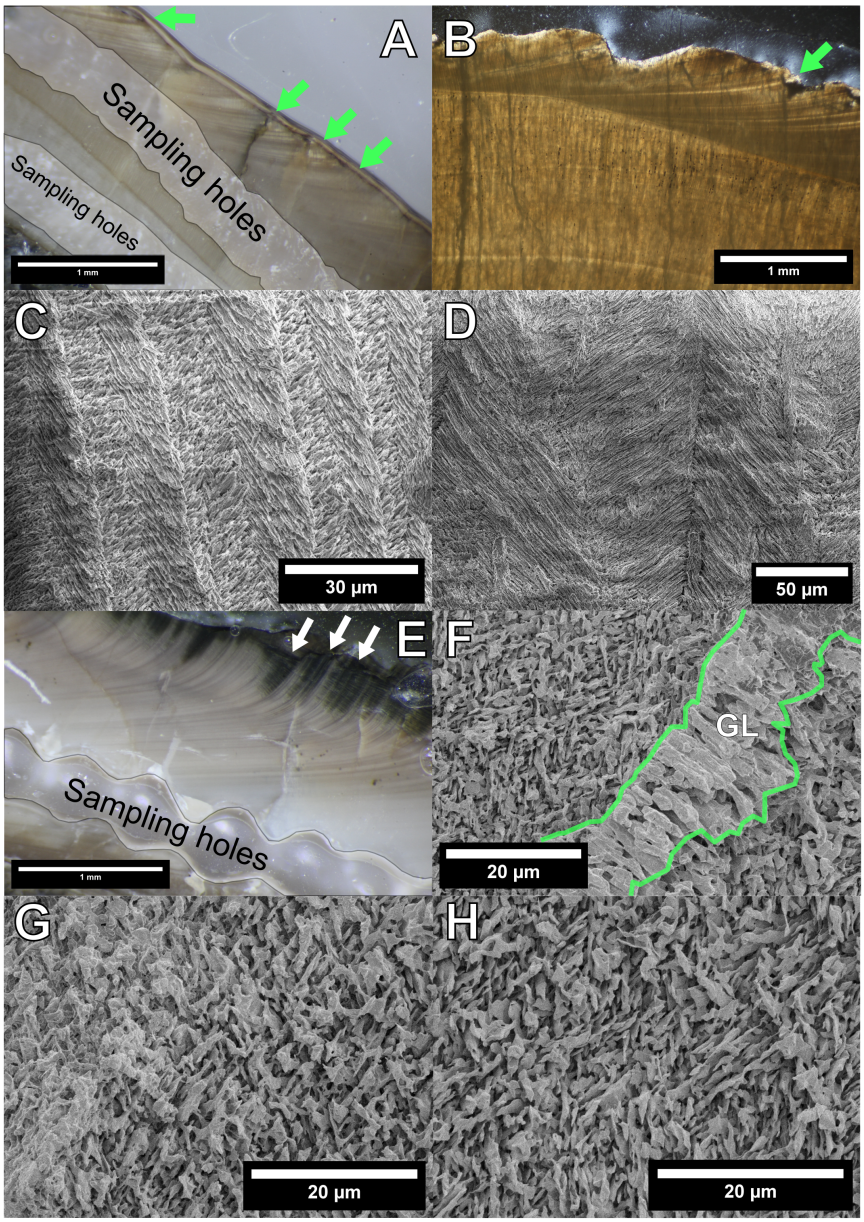

FIGURE 5
Polished section, thin section, and scanning electron microscopy (SEM) images of the studied mollusk materials. **(A)** Polished surface of *C.* (*I.*) *delicatostriata* (PU-1). **(B)** Thin section of *C.* (*I.*) *delicatostriata* (PU-2). Growth lines can be observed in both **(A, B)**. "Major" growth lines are indicated by light green arrows, and "minor" growth lines can be observed between each pair of "major" growth lines. **(C, D)** SEM images of *C.* (*I.*) *delicatostriata*. **(C)** Crossed-lamellar fabric in the outer shell layer. **(D)** Complex crossed-lamellar fabric in the inner shell layer. **(E)** Polished surface of *A. pseudoplana* showing clear growth lines. White arrows indicate chlorite-replaced parts. **(F–H)** SEM images of *A. pseudoplana*. **(F)** Irregular simple prismatic structures in the growth line (sandwiched between the light green lines); **(G)** crossed-acicular fabric in the OSL; and **(H)** fine complex crossed-lamellar fabric in the ISL.

4.3 Growth increment width

"Major" growth increment widths along the growth direction in thin sections of three *C.* (*I.*) *delicatostriata* shells are shown in Figure 10. The growth increment width varied among individuals due to intraspecific differences in growth rate and differences in the angles between the maximum growth direction and the cutting plane of each shell during thin section preparation.

4.4 $\delta^{18}O_{shell}$ and $\delta^{13}C_{shell}$ values

The $\delta^{18}O_{shell}$ profiles of the three *C.* (*I.*) *delicatostriata* shells (PU-1, 2, 5) and one *A. pseudoplana* shell showed clear cyclic variations of various amplitudes (Figure 10). The ranges of $\delta^{18}O_{shell}$ values were from −4.40‰ to −3.06‰ (average = −3.65‰, σ [standard deviation] = 0.40‰) for PU-1, from −5.12‰ to −3.31‰ (average = −4.38‰, σ = 0.43‰) for PU-2, from −5.33‰

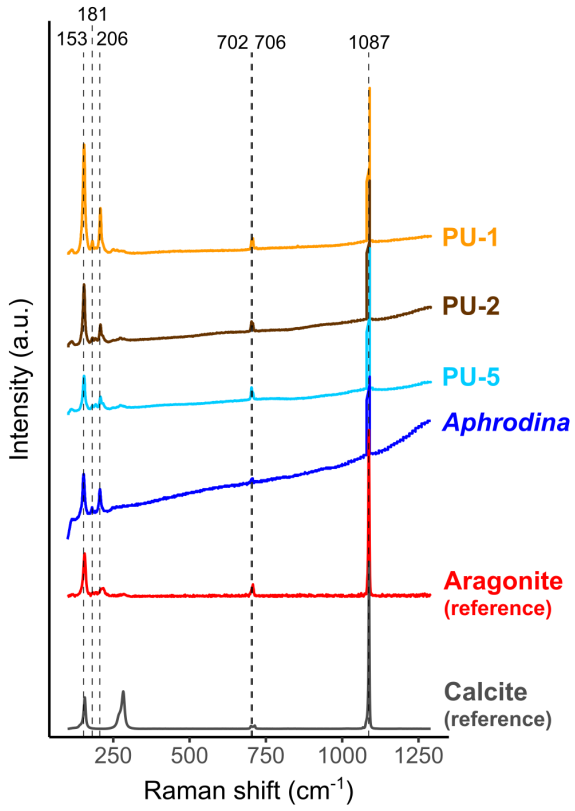

FIGURE 6
Raman spectra acquired at 100–1,290 cm^{-1} from the outer shell layer of all studied shells along with aragonite Raman spectra (aragonite R150021 with a 532 nm laser; red) and calcite Raman spectra (calcite R150075 with a 532 nm laser; gray) from RRUFF (rruff.info). Black dashed lines represent the positions of 153, 181, 206, 702, 706, and 1,085 cm^{-1}. Peaks at 153, 181, 206, 702, and 706 cm^{-1} indicate the presence of aragonite and the peak at 1,085 cm^{-1} indicates carbonate mineral.

to −2.93‰ (average = −3.70‰, σ = 0.39‰) for PU-5, and from −4.49‰ to −3.21‰ (average = −3.85‰, σ = 0.30‰) for *A. pseudoplana* (Table 1).

In contrast, the $\delta^{13}C_{shell}$ profiles of all analyzed shells did not show significant cyclicity compared with $\delta^{18}O_{shell}$ (Figure 10). The ranges of $\delta^{13}C_{shell}$ values were from −4.02‰ to 0.31‰ (average = −2.06‰, σ = 0.94‰) for PU-1, from −6.62‰ to −1.85‰ (average = −3.71‰, σ = 1.13‰) for PU-2, from −3.41‰ to −0.28‰ (average = −1.78‰, σ = 0.71‰) for PU-5, and from −2.59‰ to 0.48‰ (average = −0.78‰, σ = 0.54‰) for *A. pseudoplana* (Table 1).

5 Discussion

5.1 Evaluation of fossil preservation

5.1.1 State of preservation and shell microstructure

Shells composed primarily of aragonite are susceptible to diagenetic alteration and thus rarely retain their primary mineral composition and microstructure (Walliser et al., 2015; Posenato et al., 2022). With regard to the shell microstructure of *C.* (*I.*) *delicatostriata*, the crossed-lamellar structure in the outer shell layer (Figure 5C) and complex crossed-lamellar structure in the inner shell layer (Figure 5D) are same as those of *C. labiata*, an extant *Cucullaea* species (Taylor et al., 1969). The outermost part of the outer shell layer was absent although the shell was buried in a sandstone matrix (Figure 8C), indicating that the fossil shells were physically abraded or chemically dissolved before or during the fossilization process.

The *A. pseudoplana* shell showed a crossed-acicular structure in the outer shell layer (Figure 5G) and fine complex crossed-lamellar structure in the inner layer (Figure 5H). The needle-like crystals of chlorite present in the shell were considered pseudomorphs of biogenic aragonite produced by diagenetic alteration based on their morphology, distribution, and orientation. Silicification of biogenic carbonate with preserved microstructures has been observed in other areas (Suzuki et al., 1998; Zakhera et al., 2001; Foster et al., 2022). The arrangement of growth lines and crystals in the outermost part of the outer shell layer of *A. pseudoplana* is similar to some venerid bivalves (Chioninae and *Mercenaria stimpsoni*: Shimamoto, 1986); its shell microstructure is similar to the arcticid bivalve *Arctica islandica* (Dunca et al., 2009; Höche et al., 2021).

Dissolution traces and irregular crystal thickness were observed in high-magnification SEM images (Figure 7). A PI value of 3 was assigned for PU-1 and PU-5, whereas a value of 1 was assigned for PU-2; all of these values were lower than the best PI of 5 (classified as “excellent”; Cochran et al., 2010; Knoll et al., 2016), suggesting that the studied bivalves were affected by low-level diagenetic alteration. The partial chloritization of the surface of the *A. pseudoplana* shell is consistent with diagenetic alteration. However, chloritization of shell aragonite did not reach the parts used for stable isotope analysis in this study (Figure 5E).

The studied shells were buried in fine-grained sandstone. Biogenic carbonates in such coarse host rocks are considered highly susceptible to diagenetic alteration due to their high permeability and porosity. Nevertheless, the studied shells retained the initial shell microstructure and mineralogy although they had been slightly dissolved. The good state of preservation may be attributable to the well-cemented sandstone, which effectively limited pore water reaching the fossil sites. Well-preserved biogenic carbonate fossils buried in sediments with reduced influence of pore water are consistent with the finding that fossils of planktonic foraminifera in clay-rich sediments showed better preservation than such fossils in coarser-grained sediments (Pearson et al., 2001).

Yamamoto et al. (2017) reported a nonlinear relationship between the preservation of shell microstructure and geochemical composition, based on analyses of cathodoluminescence and SEM images, as well as measurements of the trace element concentrations and carbon and oxygen isotope compositions of Middle Pleistocene (approximately 0.8 Ma) brachiopod shells. They showed that the original isotopic composition was almost retained in many brachiopod shells that were altered due to meteoric diagenesis. Because there remains no robust criterion to assess diagenetic alteration, it is necessary to apply and cross-check multiple criteria. We suggest criteria that include assessment of whether

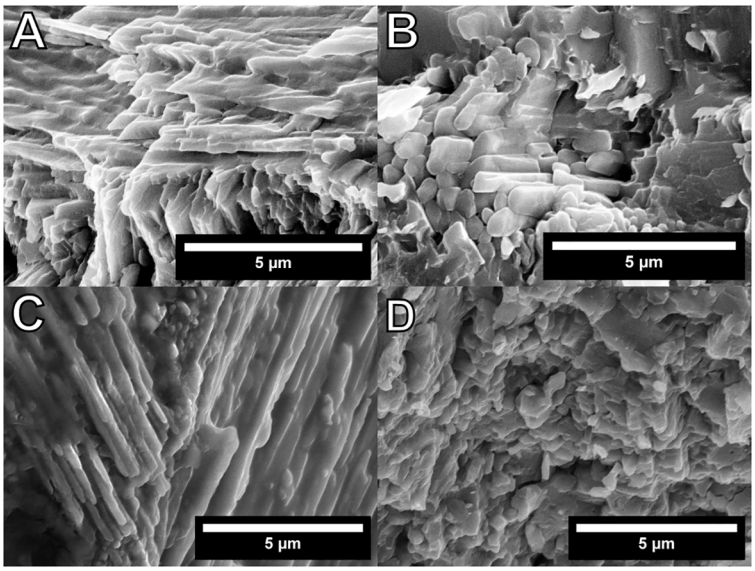

FIGURE 7
High-resolution images of the studied *Cucullaea* (*Idonearca*) *delicatostriata* (crossed-lamellar structure; PU-1, **A**; PU-2, **B**; PU-5, **C**) and *Aphrodina pseudoplana* (crossed-acicular structure; **D**) shells. Dissolution marks and irregular thickness of crystals can be observed in **(A–C)**. Preservation index values of 3 for PU-1, 1 for PU-2, and 3 for PU-5 were assigned. Indistinct structures can be observed in **(D)**, but the PI value could not be calculated because a PI for crossed-acicular structures has not been established.

the shells possess expected carbon and oxygen isotope compositions. Consequently, we concluded that the studied shells with PI of 3 retained their original carbon and oxygen isotope compositions.

5.1.2 Diagenetic effects on oxygen and carbon isotopes of the fossil shells

Previous studies suggested that geochemical and isotopic compositions of biogenic carbonate fossils with PI values > 3 are suitable as paleoenvironmental proxies (Cochran et al., 2010; Ryan et al., 2021; Tajika et al., 2023). The $\delta^{18}O_{shell}$ and $\delta^{13}C_{shell}$ values of PU-1 and PU-5, which have PI values of 3, were distributed in a similar area of the cross-plots (Figure 11). This similarity indicated that these shells have a similar preservation state and have not been affected by significant diagenetic alteration. Meanwhile, the $\delta^{18}O_{shell}$ and $\delta^{13}C_{shell}$ values of PU-2, with a low PI value of 1, were lower than the other shells (by approximately 1‰ and 2‰, respectively) (Figure 11). These results suggest that PU-2 was more diagenetically altered and affected to a greater extent by isotopic exchange of C and O between its shell aragonite and pore water with low $\delta^{18}O$ and $\delta^{13}C$ values. Pore water could supply lower $\delta^{18}O$ and $\delta^{13}C$ than contemporaneous seawater due to dissolution of decomposed organic matter (Cochran et al., 2010). Therefore, the isotopic records of PU-2 are excluded from further paleoenvironmental discussion due to diagenetic alteration. There is evidence from other areas that carbonate fossils strongly affected by diagenetic alteration have outlier $\delta^{18}O_{shell}$ and $\delta^{13}C_{shell}$ values compared with well-preserved fossils from the same locality (Cochran et al., 2010; Jones et al., 2022).

Although the isotopic composition of PU-2 was somewhat modified, its $\delta^{18}O$ values showed cyclicity similar to other studied shells (PU-1 and PU-5) with a better state of preservation, which may reflect seasonal environmental changes (Figure 10). Although Cochran et al. (2010) showed that stable isotope composition was modified in samples, they did not analyze isotopic composition along the growth axis or present any isotopic profiles. Given pristine shell microstructures, it is possible that variations in stable isotope composition, including seasonal variations, are preserved in shell carbonate even at low PI. Original seasonal $\delta^{18}O$ patterns can be preserved despite geochemical alteration. For example, heating can shift shell $\delta^{18}O$ values by 1.5‰, equivalent to 6°C–7°C in paleotemperature reconstruction, while the primary seasonal pattern is preserved (Moon et al., 2021). However, the stratigraphic horizon from which the studied shells were collected does not show any indications of exposure to high temperatures due to burial diagenesis or hydrothermal activity. Therefore, it is unlikely that the oxygen isotope profiles of the studied shells were shifted toward a smaller value while maintaining their initial seasonality.

5.2 Life history of *C.* (*I.*) *delicatostriata*

5.2.1 Timing of growth line formation in the shells of *C.* (*I.*) *delicatostriata*

The growth of carbonate shells (including bivalves) and skeletons is controlled by both tidal (Ohno, 1989; Schöne et al., 2003; Schöne and Giere, 2005) and daily rhythms (de Winter et al., 2023). In bivalves inhabiting tidally influenced areas, shell precipitation occurs during high tide; their growth is paused due to the stresses caused by tidal emersion and ebb currents during low tide, leading to the formation of growth lines (Evans, 1972; Ohno,

10.3389/fmars.2024.1324436

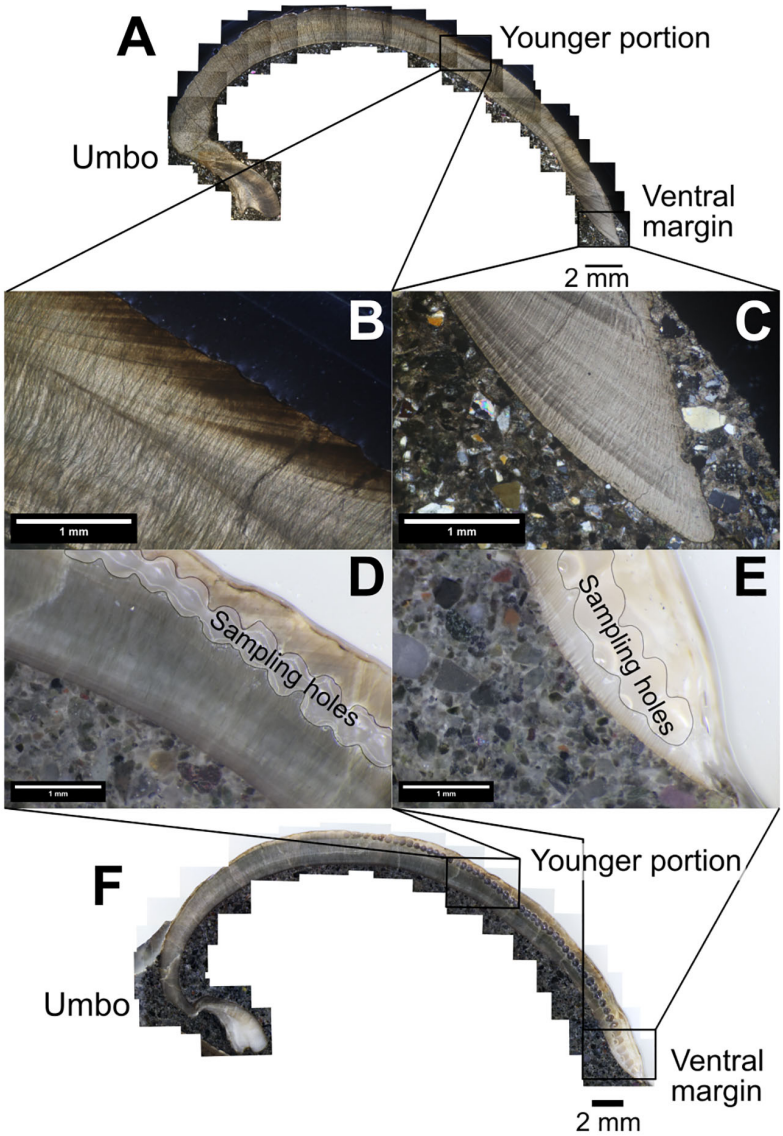

FIGURE 8
Comparison of growth line visibility in the outer shell layer between thin sections **(A–C)** and polished sections **(D–F)** of a *C.* (*I.*) *delicatostriata* shell (PU-5). The growth lines are clearly visible in the younger portions of both thin sections **(B)** and polished sections **(D)**. In the shell near the ventral margin, growth lines are clearly visible in the thin sections **(C)** but are indistinct in the polished sections **(E)**. Sampling holes in the polished sections **(D–F)** are the remains of samples taken for stable isotope analysis.

1989; Schöne et al., 2003; Reza Mirzaei et al., 2014). As tidal activity occurs twice per day, two growth lines are formed daily in the shells of bivalves inhabiting intertidal areas (Richardson, 1988; Ohno, 1989; Schöne et al., 2003). Bivalves in constantly immersed areas, such as subtidal zones, experience weaker tidal stresses and produce one growth line per day (Ohno, 1989; Reza Mirzaei et al., 2014). During spring tides, which occur on a fortnightly cycle (14.7 days), the stress at low tide is greater, which leads to more prominent growth line formation in both intertidal and subtidal bivalves (Azzoug et al., 2012; Reza Mirzaei et al., 2014). Irradiance (i.e., light intensity) is regarded as a major factor affecting bivalve shell formation controlled by daily rhythms (Ohno, 1989; Clark, 2005; Sano et al., 2012).

The most important consideration for establishing bivalve shell chronology from shell growth lines in geologic time is whether the environmental rhythms that drive modern shell growth line formation (i.e., tidal and daily rhythms) in the study periods were similar to today (Wierzbicki et al., 2023). The daily rhythm interval has lengthened at a rate of 1 s/5000 years on average (i.e., decreasing number of days per year) throughout geological time due to the decline in Earth's spin velocity (Darwin, 1880; Lantink et al., 2022). According to sclerochronological and geochemical analyses on rudist shells, day length was 23.5 h (372 days per year) in the Late Cretaceous (Campanian) (de Winter et al., 2020). The tidal rhythm in the middle Cretaceous was approximately similar to the present (14.8 days for semilunar month) because lunar-related

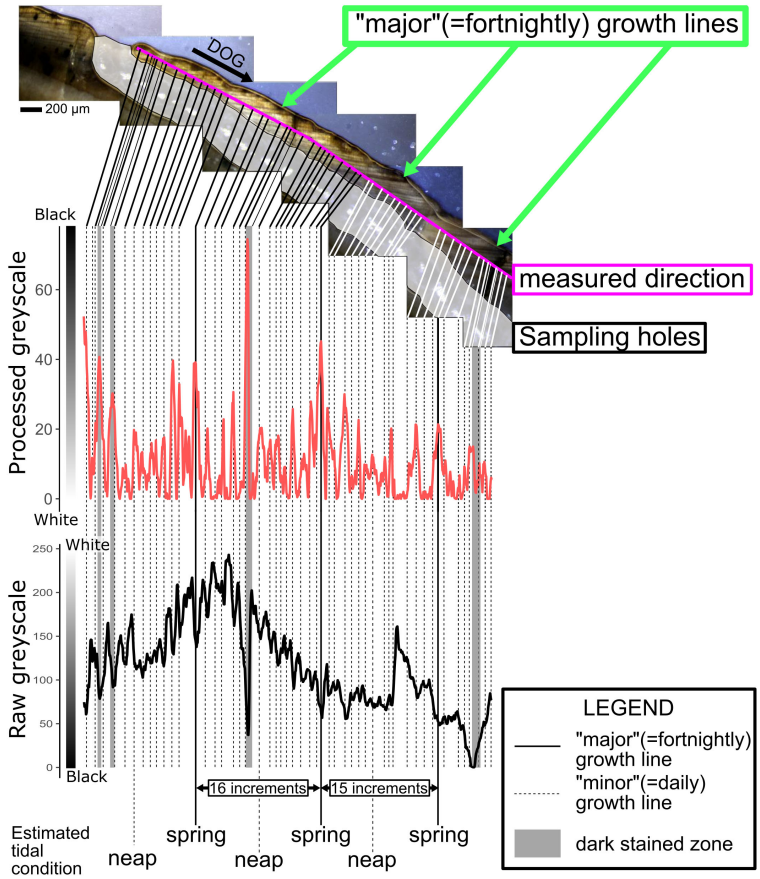

FIGURE 9
Polished section of the younger portion of a *C.* (*I.*) *delicatostriata* (PU-1) shell and greyscale values (raw and processed) along its growth direction in polished sections (pink line). Processed greyscale values were obtained by inverting the raw greyscale data and then applying the rolling ball algorithm. Raw greyscale data are shown as a black bold line and processed greyscale data are represented by red lines. Note that a high raw greyscale value is indicated by a light color, while a high processed greyscale value is represented by a dark color. The vertical black lines on the graph indicate the positions where growth lines were visually observed on the analyzed greyscale line. Solid lines indicate "major" growth lines and dashed lines indicate "minor" growth lines. The gray zones on the greyscale graph indicate the positions of dark staining. Numbers on the black arrows between lines represent the numbers of growth lines observed in the polished section. The estimated tidal condition (timing of spring tide and neap tide) is noted below the greyscale graphs.

rhythms, which are strongly related to tidal rhythm, were presumably more stable than solar rhythms throughout Earth's history (Williams, 2000; Bhattacharya and Jha, 2014; Wierzbicki et al., 2023). Calculations based on the above data indicated that the numbers of solar days, lunar days, and fortnightly growth lines per year during the middle Cretaceous were 372, 352.5, and 25.1, respectively. The numbers of growth lines according to solar days and lunar days per single fortnight cycle in the middle Cretaceous were 15.6 and 14.8, respectively.

Two different types of growth lines were recognized in the studied *C.* (*I.*) *delicatostriata* shells; specifically, distinct "major" and relatively indistinct "minor" growth lines were present, with an alternating pattern of a single "major" growth line followed by 15–16 "minor" growth lines (see Section 4.2) (Figure 9). The repeated appearance of prominent growth lines alternating with 15–16 faint growth lines can be explained as the "minor" growth lines corresponding to daily growth lines and "major" growth lines corresponding to fortnightly growth lines in modern bivalves (Carré et al., 2005; Azzoug et al., 2012). This character is consistent with the expected Cretaceous daily and fortnightly rhythm relations outlined above. Both "major" and "minor" growth lines presumably formed in response to tidal cycles; therefore, the growth lines of *C.* (*I.*) *delicatostriata* can be used for reliable inner shell chronology and as records of temporal shell growth.

5.2.2 Shell growth of *C.* (*I.*) *delicatostriata*

The $\delta^{18}O_{shell}$ values and growth lines of the studied shells can be used to delineate the life history of *C.* (*I.*) *delicatostriata*. The studied shells (PU-1, PU-2, and PU-5) exhibited distinct cyclicity of $\delta^{18}O_{shell}$ values, with an amplitude of approximately 1.5‰ over approximately 25 "major" (i.e., fortnightly) growth lines (Figure 10). Because the tidal cycle during the Cretaceous period was approximately similar to the present (Section 5.2.1 and Bhattacharya and Jha, 2014), the presence of approximately 25 fortnightly growth lines per year suggested that the bivalves continued to form shell carbonates throughout the year (Berry and Barker, 1968; Azzoug et al., 2012). The lowest and highest values of $\delta^{18}O_{shell}$ within these yearly growth line intervals represent

10.3389/fmars.2024.1324436

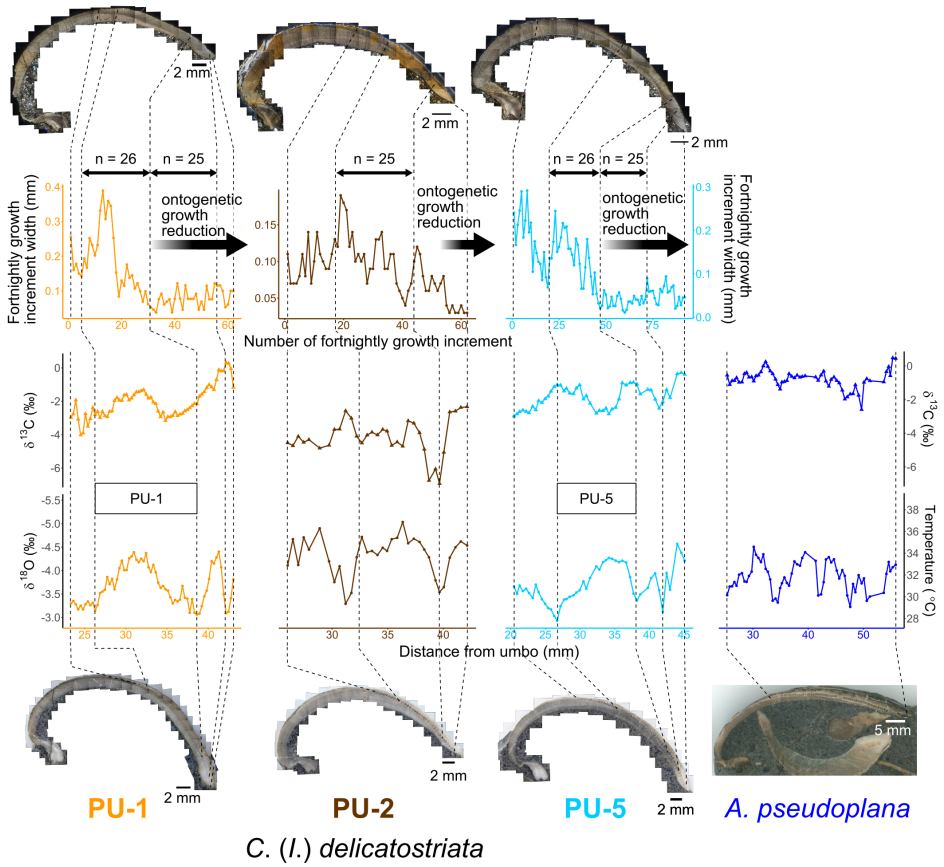

FIGURE 10
Fortnightly growth increment width of *C.* (*I.*) *delicatostriata*, $\delta^{18}O_{shell}$ and $\delta^{13}C_{shell}$ values of all studied shells with temperatures reconstructed based on Grossman and Ku (1986), and photographs of thin sections used for growth increment width measurement and polished slabs used for stable isotope analysis. Numbers above arrows indicate the number of growth lines between each pair of arrows. Approximately 25 lines are observed between the arrows, indicating a period of around 1 year. Bold black arrows on the graph of fortnightly growth increment width indicate periods of ontogenetic growth reduction. Squares on the graph of $\delta^{18}O_{shell}$ represent the positions of the annual growth increments used for monthly averaged paleotemperature calculations (Figure 13; Supplementary Table 2). For paleotemperature reconstruction from shell $\delta^{18}O$, a value of –1‰ was used for $\delta^{18}O_{seawater}$, obtained from Shackleton and Kennett (1975) and Zhou et al. (2008).

summer and winter values, respectively; the main factor controlling the $\delta^{18}O$ values is seawater temperature at the sites in which the shell grow. Therefore, the observed $\delta^{18}O_{shell}$ curves along the 25 fortnightly growth lines reflect seasonal seawater temperature variations. Bivalves that form their shell throughout the year typically inhabit the tropics (Thébault et al., 2007; Yamanashi et al., 2016) and submarine caves (Kitamura et al., 2012). Therefore, *C.* (*I.*) *delicatostriata* may have also inhabited an environment suitable for shell formation throughout the year (i.e., seasonal variation in seawater temperature).

The growth increment width and $\delta^{18}O_{shell}$ values of *C.* (*I.*) *delicatostriata* (top panels in Figure 10) represent temporal growth rate records. In younger portions of the shells, the fortnightly growth increment width shows an increase up to the maximum of 0.4 mm with a subsequent decrease (minimum = 0.05 mm) in 1 year, corresponding to 25 growth lines. The largest growth increment width was formed during the period spanning the $\delta^{18}O_{shell}$-based temperature minimum (winter) to its maximum (summer) (Figure 10), corresponding to the spring season. Conversely, the narrowest growth increments coincide with the coldest paleotemperatures and are regarded as representing winter (Figure 10). These observations suggest that the growth rate of *C.* (*I.*) *delicatostriata* reached its maximum in spring and minimum in winter. This growth pattern of bivalve shells is consistent with the patterns observed in extant bivalves inhabiting shallow-ocean areas and has been attributed to high spring phytoplankton abundance (Sato, 1997).

The "major" growth increment width and its variation significantly decreased toward the ventral shell margin (< 0.1 mm) (Figure 10), representing reductions in the shell growth rate and its seasonality during ontogeny. The presence of 25 "major" (i.e., fortnightly) growth increments within each annual growth cycle suggests that the shell was continuously precipitated throughout the year without any period of growth cessation. Although ontogenetic growth decline is common in modern bivalves (Jones and Quitmyer, 1996; Tanabe et al., 2017, 2020), ontogenetic growth characteristics in *C.* (*I.*) *delicatostriata*, which was continuous throughout the year associated with fortnightly (and daily) cycles, are similar to the characteristics of the extant tropical shallow-water bivalve *Tegillarca granosa* (Reza Mirzaei et al., 2017).

10.3389/fmars.2024.1324436

TABLE 1 Stable carbon and oxygen isotope values, paleotemperature estimated by Grossman and Ku (1986), and preservation status, as indicated by the preservation index (PI) according to Cochran et al. (2010) and Knoll et al. (2016), of the studied shells.

Bivalve taxon		*Cucullaea* (*Idonearca*) *delicatostriata*			*Aphrodina pseudoplana*
Shell name		PU-1	PU-2	PU-5	
PI score		3	1	3	undetermined
$\delta^{13}C_{shell}$ (‰)	Min	−4.02	−6.62	−3.41	−2.59
	Average	−2.06	−3.71	−1.78	−0.78
	Max	0.31	−1.85	−0.29	0.48
$\delta^{18}O_{shell}$ (‰)	Min	−4.40	−5.12	−4.57	−4.48
	Average	−3.65	−4.38	−3.70	−3.85
	Max	−3.06	−3.31	−2.93	−3.21
Temperature (°C)	Min	28.37	29.45	27.80	29.02
	Max	34.18	37.31	34.92	34.53
	Seasonal range	5.82	7.86	7.12	5.51
Number of samples		68	33	49	60

−1‰ was used as the $\delta^{18}O_{seawater}$ value.

5.3 Shallow-water temperature and its seasonality in the mid-latitude northwestern Pacific region during the Turonian

Based on the $\delta^{18}O_{shell}$ values of the two bivalve species and the relationships between temperature and aragonite $\delta^{18}O$ established by Grossman and Ku (1986; Equation 1), the annual shallow-water temperature in the middle Turonian Yezo Basin ranged from 27.8°C to 34.9°C (Figure 12; Table 1). Analysis of sedimentary facies suggested that *C.* (*I.*) *delicatostriata* and *A. pseudoplana* inhabited shallow depths less than some tens of meters (Ando and Kodama, 1998; Komatsu, 2013) (Figure 2). Because water temperature at these depths would not substantially differ from the temperature at the sea surface (Tanabe et al., 2017), the temperatures calculated in this study should reflect shallow-water temperature and its seasonality in the middle Turonian northwestern Pacific Ocean.

Seawater temperatures estimated from the shell $\delta^{18}O$ values and their seasonality can vary depending on assumed $\delta^{18}O_{seawater}$ values and their seasonal fluctuation at the site of shell growth. For example, for an actual $\delta^{18}O_{seawater}$ value 1‰ lower than the assumed value, the seawater temperature calculated based on the Equation 1 would increase by approximately 4°C. The $\delta^{18}O_{seawater}$ value varies depending on salinity because it increases with massive evaporation, whereas it decreases with strong precipitation and freshwater input due to ^{18}O depletion in the vapor and meteoric water (Craig, 1961). Based on the modern relationship of $\delta^{18}O_{seawater}$ and salinity, a salinity change of 1 causes a change of approximately 0.3‰ in $\delta^{18}O_{seawater}$ (Fairbanks et al., 1997; Abe et al., 2009; Takayanagi et al., 2015). Recent clumped isotope analysis of modern bivalve shells suggested

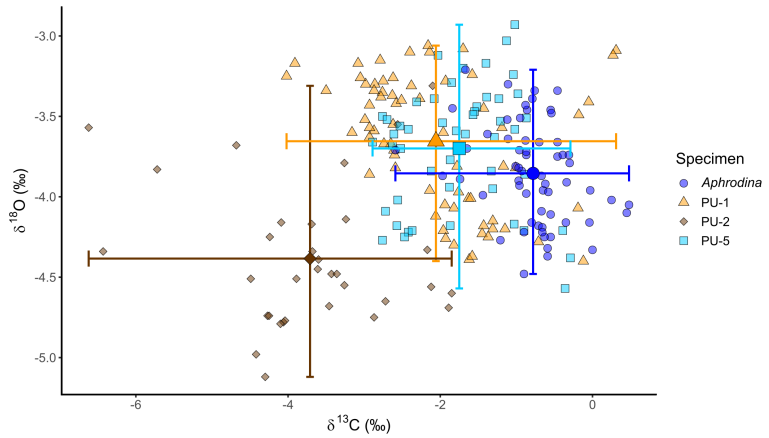

FIGURE 11
Cross-plots of $\delta^{18}O$ and $\delta^{13}C$ values of the studied *C.* (*I.*) *delicatostriata* (PU-1, 2, 5) and *A. pseudoplana* shells. Small translucent plots represent the original isotope values and large opaque plots show the average isotope ratio of each shell. Bars indicate the ranges of both isotope ratios for each shell.

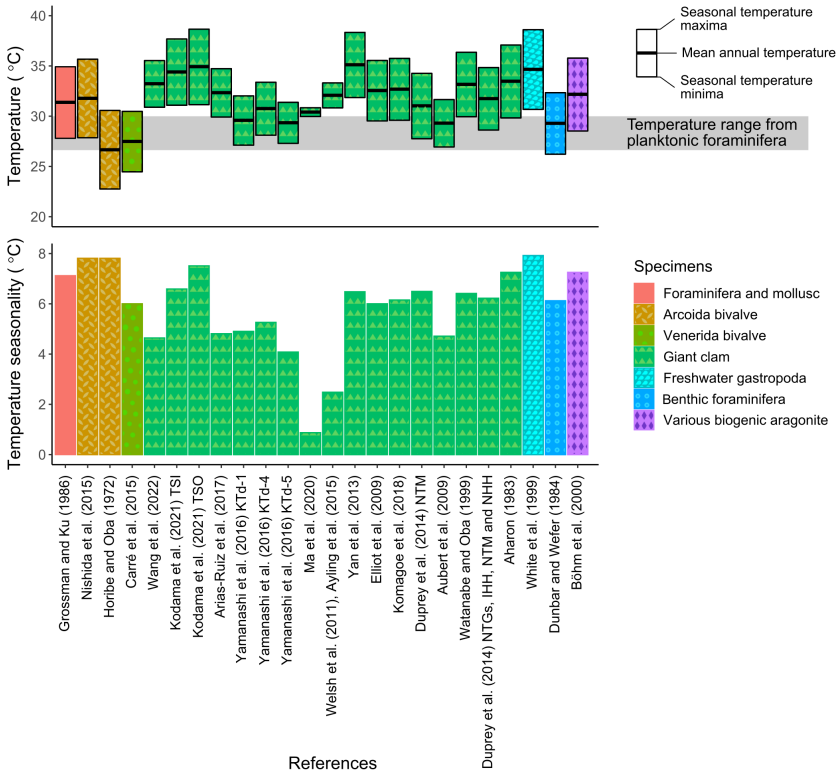

FIGURE 12
Comparison of shallow-water temperature and its seasonality calculated among various equations of temperature and aragonite $\delta^{18}O$. Aragonite $\delta^{18}O$ was derived from $\delta^{18}O_{shell}$ values of studied bivalve shells. TSI and TSO in Kodama et al. (2021), KTd-1, KTd-4, and KTd-5 in Yamanashi et al. (2016), and NTM, NTGs, IHH, and NHH in Duprey et al. (2014) represent the names of shells. Seasonal temperature maxima and minima were based on the maximum and minimum $\delta^{18}O_{shell}$ values of the studied shells. Mean annual temperature was calculated from monthly averaged $\delta^{18}O_{shell}$ values (Supplementary Table 2). The gray zone on the temperature plot represents the mean annual sea surface temperature (SST) of the middle–late Turonian Yezo Basin based on planktonic foraminiferal $\delta^{18}O$ (Moriya, 2011). The $\delta^{18}O_{seawater}$ value used for temperature estimation was –1.00‰.

that seasonal changes in $\delta^{18}O_{seawater}$ values make a significant contribution to those changes in $\delta^{18}O_{shell}$ values, thus affecting $\delta^{18}O_{shell}$-based seawater temperature estimates (Caldarescu et al., 2021). Furthermore, clumped isotope analyses of Cretaceous rudists and oysters revealed that $\delta^{18}O_{seawater}$ values at that time were not necessarily −1‰, which has been traditionally used for paleotemperature estimation from $\delta^{18}O$ values of biogenic carbonates during the Cretaceous in shallow oceans (de Winter et al., 2021; Jones et al., 2022). de Winter et al. (2021) also reported that large seasonal $\delta^{18}O_{seawater}$ fluctuations (approximately 1‰), which showed the highest values near the hottest season and lowest values near the coldest season, were present in the Campanian shallow ocean, resulting in underestimation of seawater temperature seasonality. However, it is difficult to assume that $\delta^{18}O_{seawater}$ changes over seasonal cycles.

The seasonal salinity ranges in the modern subtidal zone, especially at depths of more than 10 m, are small (salinity< 2) (Wanamaker et al., 2011; Kubota et al., 2017; Tanabe et al., 2017). This change corresponds to the $\delta^{18}O_{seawater}$ change of approximately 0.6‰, when converting salinity into $\delta^{18}O_{seawater}$; it may cause an error of< 3°C in reconstructing seawater temperatures (Grossman and Ku, 1986; Chauvaud et al., 2005). Therefore, some studies have assumed that seasonal $\delta^{18}O_{seawater}$ fluctuations were annually constant when reconstructing water temperature from $\delta^{18}O_{shell}$ values of bivalves inhabiting water with almost constant salinity (Wanamaker et al., 2011; Kubota et al., 2017; Tanabe et al., 2017). The studied species, *C.* (*I.*) *delicatostriata* and *A. pseudoplana*, presumably inhabited normal marine environments with limited freshwater influence because they are found in lower shoreface to inner shelf deposits, which likely formed at depths of 10 m to some tens of meters, and not in freshwater and estuary deposits such as oyster beds (Ando and Kodama, 1998; Komatsu, 2013) (Figure 2). The absence of neighboring prominent and faint growth lines in *C.* (*I.*) *delicatostriata* (Section 5.2.1 and Figure 9) also indicated that they did not live in the intertidal zone, which is commonly affected by freshwater input (Ohno, 1989; Tojo and Masuda, 1999; Miyaji et al., 2007; Reza Mirzaei et al., 2014). Massive freshwater inflow events, such as typhoons or heavy rains, may have occurred in the depositional area of the middle Turonian Mikasa Formation because of the humid climate conditions in the northwestern Pacific region, suggested by terrestrial organic $\delta^{13}C$ and numerical climate simulation, and the presence of HCS deposits (likely formed by storm events) in this formation (Ando, 1987; Hasegawa, 2003; Hasegawa et al., 2012; Higuchi et al., 2021). However, such short-term precipitation events are unlikely to be recorded in the $\delta^{18}O$ profiles of the studied shells due to their temporal resolution (more than one week), which is not sufficiently high for detection. Therefore, our seasonal $\delta^{18}O_{shell}$ variations likely

reflect shallow-water temperature seasonality at the time the shells inhabited.

The reconstructed paleotemperature in our study was consistent with shallow-water paleotemperature records (28°C–34°C) from the late Cenomanian mid-latitude (36°–45°N paleolatitude) North American Interior Seaway, derived from clumped isotope analysis on oyster fossil species (*Pycnodonte newberryi* shells from the Mancos Shale Formation at 36°N paleolatitude, *P. newberryi* shells from the Tropic Shale Formation at 37°N paleolatitude, *P. kellumi* shells from the Frontier Formation at 43°–45°N paleolatitude, and *P. kellumi* shells from the Greenhorn Formation at 44°N paleolatitude) using the temperature calculation formula of Petersen et al. (2019) (Jones et al., 2022). In contrast, planktonic foraminiferal $\delta^{18}O$ from the western extension of the Mikasa Formation indicated that the mean annual sea surface water temperature of the middle to late Turonian Yezo Basin ranged from 26°C to 29°C (Moriya, 2011). These temperatures are lower than temperatures determined from the studied shells (Figure 12). Such differences may have been due to variations in seawater temperatures during the Turonian and differences in growth site environments (e.g., depths) between benthic bivalves and planktonic foraminifera. Furthermore, the planktonic foraminiferal temperatures reported by Moriya (2011) do not necessarily reflect sea surface temperatures because planktonic foraminifera inhabit areas close to the sea surface and areas within the mixed layer. However, considering that Moriya (2011) did not provide detailed geological or paleontological data on the studied samples or information about the oxygen isotope thermometer used, it is not possible to identify the factors responsible for these discrepancies.

Differences in reconstructed temperatures between bivalves and foraminifera could have been partly due to differences in the equations representing the relationships between ($\delta^{18}O_{shell}$ – $\delta^{18}O_{seawater}$) and seawater temperature (i.e., oxygen isotope thermometers). The equations proposed in previous studies differ among taxa and environmental settings (Nishida, 2020; Kodama et al., 2021). We calculated and compared shallow-water temperatures and their seasonality in the Turonian Yezo basin using 24 equations established for aragonite $\delta^{18}O$ in various modern marine calcifiers (Figure 12). These equations were derived from the arcid bivalve *Scapharca broughtonii* (Horibe and Oba, 1972; Nishida et al., 2015), venerid bivalve *Mesodesma donacium* (Carré et al., 2005), giant clam *Tridacna squamosa* (Arias-Ruiz et al., 2017; Kodama et al., 2021; Wang et al., 2022), *T. derasa* (Yamanashi et al., 2016), *T. gigas* (Elliot et al., 2009; Welsh et al., 2011; Yan et al., 2013; Ayling et al., 2015; Ma et al., 2020), *T. maxima* (Duprey et al., 2014; Komagoe et al., 2018), *Hippopus hippopus* (Watanabe and Oba, 1999; Aubert et al., 2009), a combination of giant clam species (Aharon, 1983; Duprey et al., 2014), the freshwater gastropod *Peregriana peregra* (White et al., 1999), various benthic foraminifera (Dunbar and Wefer, 1984), and various biogenic aragonites (Böhm et al., 2000).

Although the reconstructed seawater temperatures differed according to the equations used, they fell within a range from 22°C to 39°C, with seasonality of <8°C (Figure 12). In some cases (e.g., Dunbar and Wefer, 1984), the reconstructed temperatures were consistent with temperatures estimated from planktonic foraminifera for the same time period (Moriya, 2011), but more commonly, the reconstructed temperatures were higher than temperatures from planktonic foraminifera (e.g., Grossman and Ku, 1986 and Yan et al., 2013). The seawater temperatures reconstructed using equations derived from bivalves taxonomically close to *C.* (*I.*) *delicatostriata* (*Scapharca broughtonii*: Horibe and Oba, 1972) and *A. pseudoplana* (*Mesodesma donacium*: Carré et al., 2005) were slightly lower but roughly similar to temperatures derived from the studied bivalves, suggesting that the two fossil species precipitated their shells under physiological conditions similar to the conditions experienced by closely related extant species. The reconstructed seawater temperature of the middle Turonian Yezo Basin was significantly higher than the temperatures of the modern mid-latitude ocean (Figure 13). For example, the modern eastern Pacific Ishikari area of Hokkaido, Japan (44°N), has a surface seawater temperature of 4.8°C–22.1°C (monthly averaged data from Japan Meteorological Agency, 2024a). These findings suggest that extremely warm shallow water was present in the mid-latitude region during the middle Cretaceous "supergreenhouse" Earth.

Monthly averaged sub-annual scale $\delta^{18}O_{shell}$ data along the growth direction of two *C.* (*I.*) *delicatostriata* specimens (PU-1 and PU-5) (Figure 10) indicated that seasonal shallow-water temperature variation was approximately 6°C in the middle Turonian mid-latitude northwestern Pacific Ocean (Figure 13; Supplementary Table 2). This value is substantially smaller than temperature ranges in modern mid-latitude regions, such as Hokkaido, where the monthly averaged sea surface temperature changes by approximately 17°C throughout the year (Japan Meteorological Agency, 2024a) (Figure 13). Low seasonal variability of SST is typically observed in modern low-latitude tropical ocean areas, such as 22.7°C–29.3°C (6.6°C seasonality) derived from eastern Pacific data collected around southern Okinawa Island, the Ryukyu Islands, Japan (26°N; Japan Meteorological Agency, 2024b) (Figure 13). This finding is consistent with previous studies arguing that paleo-Hokkaido was located in a subtropical climate during the middle Cretaceous (e.g., Hay and Floegel, 2012).

5.4 Shallow-water temperatures during the Turonian greenhouse Earth

Shallow-water temperatures and their seasonal variations during the Turonian were estimated based on $\delta^{18}O_{shell}$ values (Figure 14) of rudist shells from the low-latitude Tethys Ocean (2–10 m water depth, < 30°N paleolatitude) in some previous studies. *Distefanella* sp. from the middle Turonian sediments in Zakynthos Island, Greece (91.1 Ma, 16.5°N paleolatitude) indicated one year seawater temperatures of 28.5°C–34.4°C with a seasonal variation of 5.9°C (Steuber et al., 2005). *Hippurites resectus* from the Gosau Group (the upper Turonian to the lower Coniacian, 89–91 Ma, 27.4°–27.5°N paleolatitude) and *Vaccinites inequicostatus* from the same group and Theresienstein, Austria, indicate seawater temperatures of 24.1°C–29.7°C (five years) and 25.9°C–35.0°C (1.5–2 years), respectively (Steuber et al., 2005; Walliser and Schöne, 2020). These temperatures were estimated using the equation of Anderson and Arthur (1983), assuming a constant $\delta^{18}O_{seawater}$ value of −1‰ throughout the year.

10.3389/fmars.2024.1324436

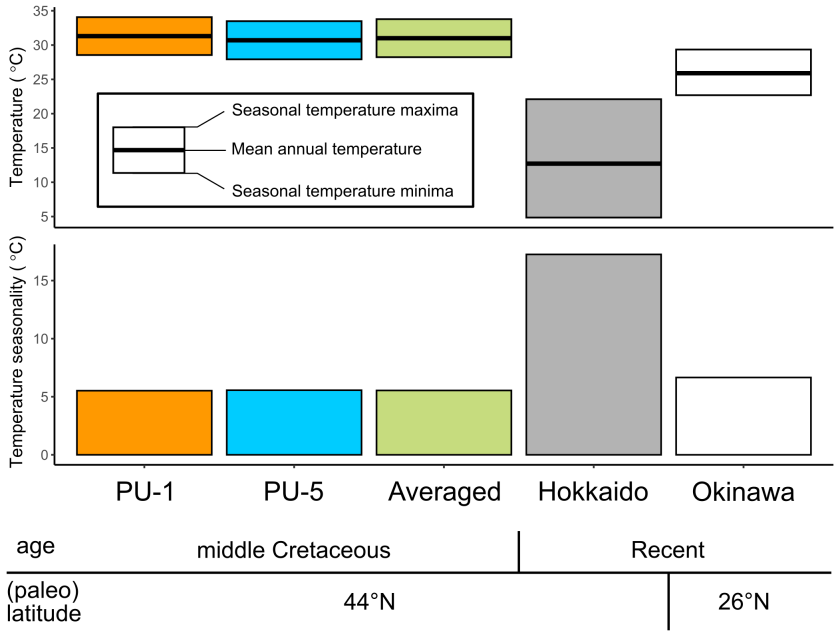

FIGURE 13
Comparison of monthly averaged shallow-ocean temperature and its seasonality in the western to northwestern Pacific regions among the middle Turonian, middle Cretaceous derived from this study (PU-1, PU-5, Averaged), and recent ocean derived from Japan Meteorological Agency (2024a) (Hokkaido) and Japan Meteorological Agency (2024b) (Okinawa). PU-1 and PU-5 refer to *Cucullaea* (*Idonearca*) *delicatostriata* shells examined in this study and averaged indicates averaged temperatures of PU-1 and PU-5. Mean annual temperature was calculated from monthly averaged temperature values (Supplementary Table 2).

The shallow-water temperature estimated in this study roughly coincided with the previous estimations; the common range was 28°C–35°C (Figure 14). One exception to this trend was the minimum temperature recorded in the Gosau Group (24.1°C), which was lower than the temperatures in the Mikasa Formation, although the Mikasa Formation was deposited in a higher latitude setting than the Gosau Group.

There are multiple possible explanations for the temperature differences outlined above, such as differences in $\delta^{18}O_{seawater}$ values between Tethys and Pacific Oceans. According to a numerical climate model of the global $\delta^{18}O_{seawater}$ value distributions, $\delta^{18}O_{seawater}$ values in the middle Cretaceous Tethys Ocean were approximately +0.5‰. This value is approximately 1.5‰ higher than the northwestern Pacific region at the same time (Zhou et al., 2008), as noted by Walliser and Schöne (2020). Consistent with the results of Zhou et al. (2008), the estimated shallow-water temperatures of the Gosau Group and Theresienstein depositional area were 31°C–43°C, higher than results for the Pacific derived in the present study. Warmer temperatures in the Tethys Ocean than the Pacific Ocean are consistent with planktonic foraminiferal biogeography of the middle Turonian Yezo Group with loss of frequent Tethyan type (tropical–subtropical) foraminifera and transitions to Transition type (warm–temperate) foraminifera bioprovinces (Nishi et al., 2003).

The effects of shallow-ocean currents can also explain the lower minimum seawater temperatures observed in the low-latitude Tethys Ocean (Walliser and Schöne, 2020) compared with the mid-latitude northwestern Pacific (this study). Cold currents flowed from the Arctic to the western Tethys Ocean, including the depositional area of the Gosau Group (Walliser and Schöne, 2020). In contrast, during the Turonian, the Pacific Ocean was separated from the Arctic Ocean by the Bering Land Bridge (Herman and Spicer, 1996, 2010; Herman et al., 2019). In this ocean–land configuration, the cold Arctic water could not flow into the Pacific Ocean, leading to warm shallow-water temperatures in the mid-latitude Pacific Ocean. The seasonal variations of shallow-water temperatures were commonly smaller than 7°C in the low-latitude Tethys (including the Gosau Group and Theresienstein area) and the mid-latitude Pacific (Figure 12).

Ivany (2012) noted that the seasonality of SST in the modern Northern Hemisphere is greatest at 40°–45°N. Our study site (44°N) exhibited good alignment with this maximal SST (or shallow-water temperature) seasonality zone of the Turonian Northern Hemisphere, indicating that maximum SST (or shallow-water temperature) seasonality in the mid-Cretaceous was similar to seasonality in the modern tropics. Additionally, the meridional temperature gradients and seasonal SST (or shallow-water temperature) ranges in the Northern Hemisphere were flatter and smaller in the mid-Cretaceous than at present. Low-temperature seasonality in the Northern Hemisphere during the Turonian is consistent with paleontological evidence from high-latitude plant and vertebrate fossils. Herman et al. (2019) reported conifer- and angiosperm-dominant floras from the Derevyannye Gory Formation (Turonian–Coniacian) of the New Siberia Island, Russia (70°N paleolatitude) and they concluded that low-temperature seasonality was present in the Turonian–Coniacian Arctic. Vandermark et al. (2007) reported that the extinct diapsid reptile *Champsosaurus* fossils from the Turonian–Coniacian sediments in Axel Heiberg Island, northern Canada (79°N, paleolatitude), was dominated by subadult-stage individuals, suggesting that temperatures suitable for

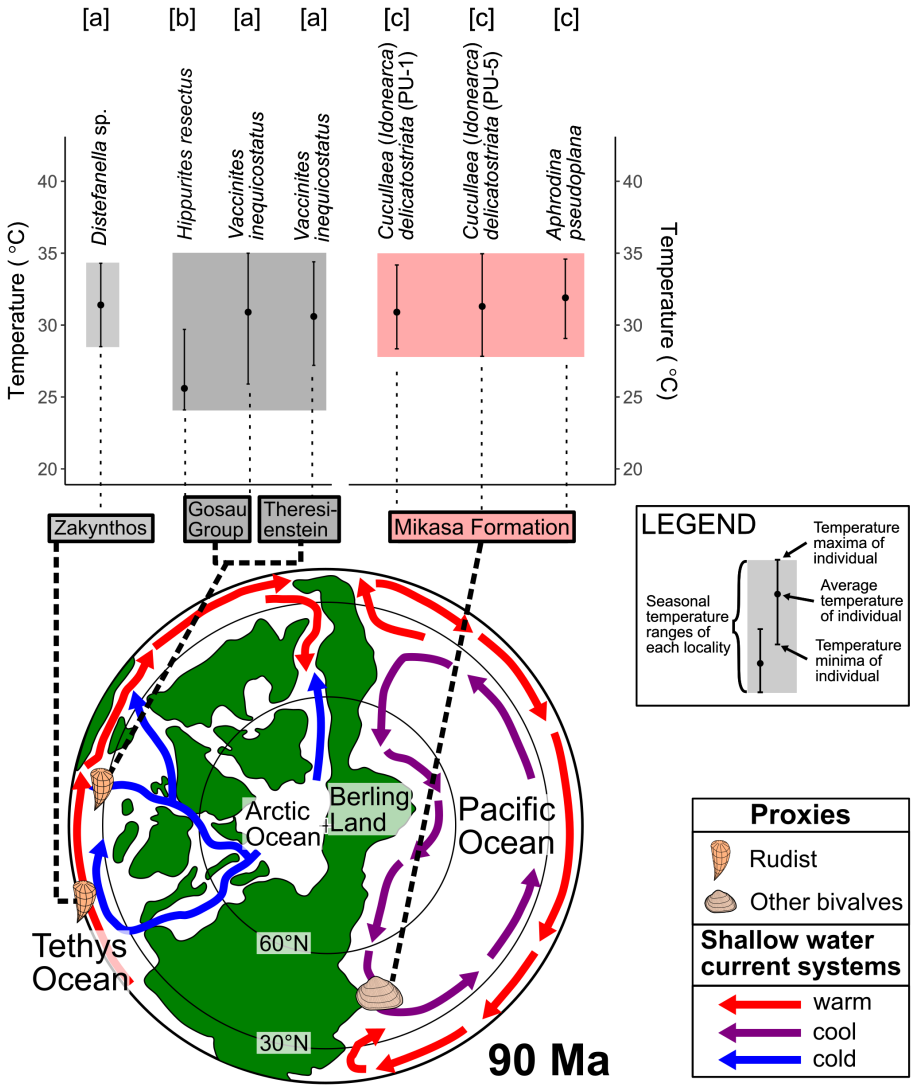

FIGURE 14
Shallow-water temperature records including seasonality during the Turonian compiled from this and previous studies ([a] Steuber et al. (2005); [b] Walliser and Schöne (2020); [c] this study), along with a paleogeographic map of the late Turonian (90 Ma) Northern Hemisphere modified from Nakajima et al. (2017) and Herman et al. (2019) with shallow-water current systems from Moiroud et al. (2013) and Mansour and Wagreich (2022). Shallow-water temperature data for individuals from the same region are grouped together as local shallow-water temperatures, with the Gosau Group and Theresienstein combined due to their close localities (Walliser and Schöne, 2020). The paleogeographic position of each locality is based on previous studies (Steuber et al., 2005; Walliser and Schöne, 2020) and paleomagnetic records for this study (Tamaki and Itoh, 2008). The $\delta^{18}O_{seawater}$ value for temperature estimation from shell carbonate $\delta^{18}O$ was –1.00‰ for all data according to the original article (Steuber et al., 2005; Walliser and Schöne, 2020).

reproduction and growth of reptiles were present during the Turonian–Coniacian at high latitudes due to a warm mean annual temperature with small temperature seasonality. The absence of ice sheets was presumably responsible for the reduced seasonal temperature variations on a global scale in the mid-Cretaceous (Steuber et al., 2005; Ivany, 2012). Under ice-free Earth conditions, the positive feedback of ice albedo becomes absent or is greatly weakened compared with today. In this case, the ice-free climate maintains warm shallow-water temperatures even in winter, resulting in slight temperature seasonality. Conversely, during the Eocene when the Antarctic ice sheet was ice-free, as in the Cretaceous, the annual SST range was greater than during the icehouse period in Antarctica (Buick and Ivany, 2004). There is a need for further data acquisition and numerical modeling of the latitudinal gradients and annual ranges of SST and air temperature during the middle Cretaceous and other greenhouse periods.

6 Conclusions

Growth increment and stable isotope analyses were performed on newly obtained bivalve fossils with preserved biogenic aragonite and shell microstructures from the middle Turonian Mikasa Formation, Yezo Group, in Hokkaido, Japan, to reveal the life history characteristics of the bivalves and sub-annual scale paleotemperature variations of mid-latitude shallow-water areas in the northwestern Pacific region during the Turonian. In *Cucullaea* (*Idonearca*) *delicatostriata*, approximately 25

fortnightly growth lines were observed per year, indicated by $\delta^{18}O_{shell}$, demonstrating that the annual cycles obtained from growth line analysis are consistent with those obtained from $\delta^{18}O_{shell}$ ratios. Growth increment width and $\delta^{18}O_{shell}$ values of *C.* (*I.*) *delicatostriata* revealed that they continuously produced their shells throughout the year, with the seasonal growth rate maximized in spring and minimized in winter. Reconstructed temperatures from bivalve $\delta^{18}O_{shell}$ values ranged from 28°C to 35°C and showed significantly smaller seasonality compared with temperatures in modern Hokkaido. The $\delta^{18}O_{seawater}$ value was assumed to be −1‰ without seasonal variations due to the limited influence of freshwater in the studied section. A comparison of temperature seasonality records with the same period from the Tethys Ocean showed similar values, indicating that tropical ocean conditions with low seasonality in mid-latitude regions were not limited to the Tethys Ocean but also occurred in the northwestern Pacific Ocean. Low shallow-water temperature seasonality in the mid-latitudes suggests that seasonal temperature fluctuations in the Northern Hemisphere were small in the middle Turonian "supergreenhouse" period.

Data availability statement

The original contributions presented in the study are included in the article/Supplementary Material. Further inquiries can be directed to the corresponding author.

Author contributions

SI: Writing – original draft, Conceptualization, Investigation, Methodology, Visualization, Data curation. HT: Investigation, Writing – review & editing, Data curation, Funding acquisition. YI: Writing – review & editing, Data curation, Funding acquisition. ST: Supervision, Writing – review & editing, Conceptualization, Funding acquisition. TO: Supervision, Writing – review & editing, Conceptualization, Funding acquisition, Investigation.

Funding

The author(s) declare financial support was received for the research, authorship, and/or publication of this article. This research was supported by Grant-in-Aid for Scientific Research (B: No. 19H02014 to TO, 23H01287to ST, 21K18642 and 23H01263 to YI).

Acknowledgments

We express our appreciation to the editor and three reviewers for their time and valuable comments. We would like to thank Y. Koketsu (Nagoya University) for assistant of Raman spectroscopic analysis. We also thank T. Miyaji (National Ainu Museum) for useful advice about growth line analysis. We gratefully acknowledge the Sorachi Forest Management Office for permitting us to conduct field survey. We thank S. Hayashi (Nagoya University) and Y. Ando (Mizunami Fossil Museum) for helping SEM observation. We also thank H. Oda (Tohoku University) for helping stable isotope analysis. We like to thank D. Nakai (Nagoya University) for advice about improving growth line observation. This work was partly supported by World Premier International Research Center Initiative (WPI), MEXT, Japan.

Conflict of interest

The authors declare that the research was conducted in the absence of any commercial or financial relationships that could be construed as a potential conflict of interest.

Publisher's note

Supplementary material

The Supplementary Material for this article can be found online at: https://www.frontiersin.org/articles/10.3389/fmars.2024.1324436/full#supplementary-material

References

Abe, O., Agata, S., Morimoto, M., Abe, M., Yoshimura, K., Hiyama, T., et al. (2009). A 6.5-year continuous record of sea surface salinity and seawater isotopic composition at Harbour of Ishigaki Island, southwest Japan. *Isotopes Environ. Health Stud.* 45, 247–258. doi: 10.1080/10256010903083847

Aharon, P. (1983). 140,000-yr isotope climatic record from raised coral reefs in New Guinea. *Nature* 304, 720–723. doi: 10.1038/304720a0

Anderson, T. F., and Arthur, M. A. (1983). Stable isotopes of oxygen and carbon and their application to sedimentologic and paleoenvironmental problems. *Stable Isot. Sediment. Geol.* 10, 1–151. doi: 10.2110/SCN.83.01.0000

Ando, H. (1987). Shallow marine deposits in the Mikasa Formation of the Middle Yezo Group in Central Hokkaido — with special reference to hummocky cross stratification. *Acad. Stud. Biol. Geol. Sch. Educ. Waseda Univ.* 36, 21–32. (in Japanese with English abstract)

Ando, H. (1990a). Shallow-marine sedimentary facies distribution and progradational sequences of the Mikasa Formation, Middle Yezo Group (Upper Cretaceous). *Jour. Geol. Soc Japan* 96, 453–469. doi: 10.5575/GEOSOC.96.453 (in Japanese with English abstract)

Ando, H. (1990b). Stratigraphy and shallow marine sedimentary facies of the Mikasa Formation, Middle Yezo Group (Upper Cretaceous). *Jour. Geol. Soc Japan* 96, 279–295_4. doi: 10.5575/GEOSOC.96.279 (in Japanese with English abstract)

Ando, H., and Kodama, T. (1998). Shallow-marine bivalvian faunal change during Cenomanian to Turonian, Late Cretaceous —Ponbetsu River section in the Mikasa Formation, Middle Yezo Group, Hokkaido, Japan—. *Bull. Mikasa City Museum* 2, 1–15. (in Japanese with English abstract)

Arias-Ruiz, C., Elliot, M., Bézos, A., Pedoja, K., Husson, L., Cahyarini, S. Y., et al. (2017). Geochemical fingerprints of climate variation and the extreme La Niña 2010–11 as recorded in a *Tridacna squamosa* shell from Sulawesi, Indonesia. *Palaeogeogr. Palaeoclimatol. Palaeoecol.* 487, 216–228. doi: 10.1016/J.PALAEO.2017.08.037

Aubert, A., Lazareth, C. E., Cabioch, G., Boucher, H., Yamada, T., Iryu, Y., et al. (2009). The tropical giant clam *Hippopus hippopus* shell, a new archive of environmental conditions as revealed by sclerochronological and $\delta^{18}O$ profiles. *Coral Reefs* 28, 989–998. doi: 10.1007/S00338-009-0538-0/FIGURES/7

Ayling, B. F., Chappell, J., Gagan, M. K., and McCulloch, M. T. (2015). ENSO variability during MIS 11 (424–374 ka) from *Tridacna gigas* at Huon Peninsula, Papua New Guinea. *Earth Planet. Sci. Lett.* 431, 236–246. doi: 10.1016/J.EPSL.2015.09.037

Azzoug, M., Carré, M., and Schauer, A. J. (2012). Reconstructing the duration of the West African Monsoon season from growth patterns and isotopic signals of shells of *Anadara senilis* (Saloum Delta, Senegal). *Palaeogeogr. Palaeoclimatol. Palaeoecol.* 346–347, 145–152. doi: 10.1016/J.PALAEO.2012.06.001

Barron, E. J. (1983). A warm, equable Cretaceous: The nature of the problem. *Earth Sci. Rev.* 19, 305–338. doi: 10.1016/0012-8252(83)90001-6

Beard, J. A., Ivany, L. C., and Runnegar, B. (2015). Gradients in seasonality and seawater oxygen isotopic composition along the early Permian Gondwanan coast, SE Australia. *Earth Planet. Sci. Lett.* 425, 219–231. doi: 10.1016/J.EPSL.2015.06.004

Berry, W. B. N., and Barker, R. M. (1968). Fossil Bivalve Shells indicate Longer Month and Year in Cretaceous than Present. *Nature* 217, 938–939. doi: 10.1038/217938b0

Bhattacharya, B., and Jha, S. (2014). Late cretaceous diurnal tidal system: A study from Nimar sandstone, Bagh group, Narmada Valley, Central India. *Curr. Sci.* 107, 1032–1037.

Böhm, F., Joachimski, M. M., Dullo, W. C., Eisenhauer, A., Lehnert, H., Reitner, J., et al. (2000). Oxygen isotope fractionation in marine aragonite of coralline sponges. *Geochim. Cosmochim. Acta* 64, 1695–1703. doi: 10.1016/S0016-7037(99)00408-1

Buick, D. P., and Ivany, L. C. (2004). 100 years in the dark: Extreme longevity of Eocene bivalves from Antarctica. *Geology* 32, 921–924. doi: 10.1130/G20796.1

Caldarescu, D. E., Sadatzki, H., Andersson, C., Schäfer, P., Fortunato, H., and Meckler, A. N. (2021). Clumped isotope thermometry in bivalve shells: A tool for reconstructing seasonal upwelling. *Geochim. Cosmochim. Acta* 294, 174–191. doi: 10.1016/J.GCA.2020.11.019

Carré, M., Bentaleb, I., Blamart, D., Ogle, N., Cardenas, F., Zevallos, S., et al. (2005). Stable isotopes and sclerochronology of the bivalve *Mesodesma donacium*: Potential application to Peruvian paleoceanographic reconstructions. *Palaeogeogr. Palaeoclimatol. Palaeoecol.* 228, 4–25. doi: 10.1016/J.PALAEO.2005.03.045

Chauvaud, L., Lorrain, A., Dunbar, R. B., Paulet, Y.-M., rard Thouzeau, G., ric Jean, F., et al. (2005). Shell of the Great Scallop *Pecten maximus* as a high-frequency archive of paleoenvironmental changes. *Geochemistry Geophys. Geosystems* 6. doi: 10.1029/2004GC000890

Clark, G. R. (2005). Daily growth lines in some living Pectens (Mollusca: Bivalvia), and some applications in a fossil relative: Time and tide will tell. *Palaeogeogr. Palaeoclimatol. Palaeoecol.* 228, 26–42. doi: 10.1016/j.palaeo.2005.03.044

Cochran, J. K., Kallenberg, K., Landman, N. H., Harries, P. J., Weinreb, D., Turekian, K. K., et al. (2010). Effect of diagenesis on the Sr, O, and C isotope composition of Late Cretaceous mollusks from the Western Interior Seaway of North America. *Am. J. Sci.* 310, 69–88. doi: 10.2475/02.2010.01

Craig, H. (1961). Isotopic variations in meteoric waters. *Sci.* 133, 1702–1703. doi: 10.1126/SCIENCE.133.3465.1702

Darwin, G. H. (1880). XX. On the secular changes in the elements of the orbit of a satellite revolving about a tidally distorted planet. *Philos. Trans. R. Soc London* 171, 713–891. doi: 10.1098/RSTL.1880.0020

Denton, G. H., Alley, R. B., Comer, G. C., and Broecker, W. S. (2005). The role of seasonality in abrupt climate change. *Quat. Sci. Rev.* 24, 1159–1182. doi: 10.1016/J.QUASCIREV.2004.12.002

Dettman, D. L., Reische, A. K., and Lohmann, K. C. (1999). Controls on the stable isotope composition of seasonal growth bands in aragonitic fresh-water bivalves (unionidae). *Geochim. Cosmochim. Acta* 63, 1049–1057. doi: 10.1016/S0016-7037(99)00020-4

de Winter, N. J., Goderis, S., Dehairs, F., Jagt, J. W. M., Fraaije, R. H. B., Van Malderen, S. J. M., et al. (2017). Tropical seasonality in the late Campanian (Late Cretaceous): Comparison between multiproxy records from three bivalve taxa from Oman. *Palaeogeogr. Palaeoclimatol. Palaeoecol.* 485, 740–760. doi: 10.1016/j.palaeo.2017.07.031

de Winter, N. J., Goderis, S., Van Malderen, S. J. M., Sinnesael, M., Vansteenberge, S., Snoeck, C., et al. (2020). Subdaily-scale chemical variability in a *Torreites sanchezi* rudist shell: implications for rudist paleobiology and the cretaceous day-night cycle. *Paleoceanogr. Paleoclimatol.* 35, e2019PA003723. doi: 10.1029/2019PA003723

de Winter, N. J., Killam, D., Fröhlich, L., De Nooijer, L., Boer, W., Schöne, B. R., et al. (2023). Ultradian rhythms in shell composition of photosymbiotic and non-photosymbiotic mollusks. *Biogeosciences* 20, 3027–3052. doi: 10.5194/bg-20-3027-2023

de Winter, N. J., Müller, I. A., Kocken, I. J., Thibault, N., Ullmann, C. V., Farnsworth, A., et al. (2021). Absolute seasonal temperature estimates from clumped isotopes in bivalve shells suggest warm and variable greenhouse climate. *Commun. Earth Environ.* 2, 1–8. doi: 10.1038/s43247-021-00193-9

Dunbar, R. B., and Wefer, G. (1984). Stable isotope fractionation in benthic foraminifera from the Peruvian continental margin. *Mar. Geol.* 59, 215–225. doi: 10.1016/0025-3227(84)90094-X

Dunca, E., Mutvei, H., Göransson, P., Mörth, C. M., Schöne, B. R., Whitehouse, M. J., et al. (2009). Using ocean quahog (*Arctica islandica*) shells to reconstruct palaeoenvironment in Öresund, Kattegat and Skagerrak, Sweden. *Int. J. Earth Sci.* 98, 3–17. doi: 10.1007/s00531-008-0348-6

Duprey, N., Lazareth, C. E., Dupouy, C., Butscher, J., Farman, R., Maes, C., et al. (2014). Calibration of seawater temperature and $\delta^{18}O$ seawater signals in *Tridacna maxima*'s $\delta^{18}O$ shell record based on in *situ* data. *Coral Reefs* 34, 437–450. doi: 10.1007/s00338-014-1245-z

Elliot, M., Welsh, K., Chilcott, C., McCulloch, M., Chappell, J., and Ayling, B. (2009). Profiles of trace elements and stable isotopes derived from giant long-lived *Tridacna gigas* bivalves: Potential applications in paleoclimate studies. *Palaeogeogr. Palaeoclimatol. Palaeoecol.* 280, 132–142. doi: 10.1016/J.PALAEO.2009.06.007

Epstein, S., Buchsbaum, R., Lowenstam, H. A., and Urey, H. C. (1953). Revised carbonate-water isotopic temperature scale. *Bull. Geol. Soc Am.* 54, 1315–1326. doi: 10.1130/0016-7606(1953)64[1315:RCITS]2.0.CO;2

Evans, J. W. (1972). Tidal growth increments in the cockle *Clinocardium nuttalli*. *Sci.* 176, 416–417. doi: 10.1126/SCIENCE.176.4033.416

Fairbanks, R. G., Evans, M. N., Rubenstone, J. L., Mortlock, R. A., Broad, K., Moore, M. D., et al. (1997). Evaluating climate indices and their geochemical proxies measured in corals. *Coral Reefs* 16, 93–100. doi: 10.1007/s003380050245

Foster, W. J., Hirtz, J. A., Farrell, C., Reistroffer, M., Twitchett, R. J., and Martindale, R. C. (2022). Bioindicators of severe ocean acidification are absent from the end-Permian mass extinction. *Sci. Rep.* 12, 1–9. doi: 10.1038/s41598-022-04991-9

Foster, G. L., Royer, D. L., and Lunt, D. J. (2017). Future climate forcing potentially without precedent in the last 420 million years. *Nat. Commun.* 8, 1–8. doi: 10.1038/ncomms14845

Grossman, E. L., and Ku, T. L. (1986). Oxygen and carbon isotope fractionation in biogenic aragonite: Temperature effects. *Chem. Geol. Isot. Geosci. Sect.* 59, 59–74. doi: 10.1016/0168-9622(86)90057-6

Hall, C. A., Dollase, W. A., and Corbató, C. E. (1974). Shell growth in Tivela stultorum (Mawe 1823) and *Callista chione* (Linnaeus 1758) (Bivalvia): annual periodicity, latitudinal differences, and diminution with age. *Palaeogeogr. Palaeoclimatol. Palaeoecol.* 15, 33–61. doi: 10.1016/0031-0182(74)90036-4

Hall, J. L. O., Newton, R. J., Witts, J. D., Francis, J. E., Hunter, S. J., Jamieson, R. A., et al. (2018). High benthic methane flux in low sulfate oceans: Evidence from carbon isotopes in Late Cretaceous Antarctic bivalves. *Earth Planet. Sci. Lett.* 497, 113–122. doi: 10.1016/J.EPSL.2018.06.014

Hasegawa, T. (2003). Cretaceous terrestrial paleoenvironments of northeastern Asia suggested from carbon isotope stratigraphy: Increased atmospheric pCO_2-induced climate. *J. Asian Earth Sci.* 21, 849–859. doi: 10.1016/S1367-9120(02)00109-8

Hasegawa, H., Tada, R., Jiang, X., Suganuma, Y., Imsamut, S., Charusiri, P., et al. (2012). Drastic shrinking of the Hadley circulation during the mid-Cretaceous Supergreenhouse. *Clim. Past* 8, 1323–1337. doi: 10.5194/cp-8-1323-2012

Hay, W. W. (2008). Evolving ideas about the Cretaceous climate and ocean circulation. *Cretac. Res.* 29, 725–753. doi: 10.1016/J.CRETRES.2008.05.025

Hay, W. W., and Floegel, S. (2012). New thoughts about the Cretaceous climate and oceans. *Earth-Science Rev.* 115, 262–272. doi: 10.1016/J.EARSCIREV.2012.09.008

Herman, A. B., Kostyleva, V. V., Nikolskii, P. A., Basilyan, A. E., and Kotel'nikov, A. E. (2019). New data on the Late Cretaceous flora of the New Siberia Island, New Siberian Islands. *Stratigr. Geol. Correl.* 27, 323–338. doi: 10.1134/S0869593819030031/FIGURES/7

Herman, A. B., and Spicer, R. A. (1996). Palaeobotanical evidence for a warm Cretaceous Arctic Ocean. *Nat. 1996 3806572* 380, 330–333. doi: 10.1038/380330a0

Herman, A. B., and Spicer, R. A. (2010). Mid-Cretaceous floras and climate of the Russian high Arctic (Novosibirsk Islands, Northern Yakutiya). *Palaeogeogr. Palaeoclimatol. Palaeoecol.* 295, 409–422. doi: 10.1016/J.PALAEO.2010.02.034

Higuchi, T., Abe-Ouchi, A., and Chan, W. (2021). Differences between present-day and cretaceous hydrological cycle responses to rising CO_2 concentration. *Geophys. Res. Lett.* 48, e2021GL094341. doi: 10.1029/2021GL094341

Hikida, Y., Suzuki, S., Togo, Y., and Ijiri, A. (2003). An exceptionally well-preserved fossil seep community from the Cretaceous Yezo Group in the Nakagawa area, Hokkaido, northern Japan. *Paleontol. Res.* 7, 329–342. doi: 10.2517/PRPSJ.7.329

Höche, N., Walliser, E. O., de Winter, N. J., Witbaard, R., and Schöne, B. R. (2021). Temperature-induced microstructural changes in shells of laboratory-grown *Arctica islandica* (Bivalvia). *PloS One* 16, e0247968. doi: 10.1371/JOURNAL.PONE.0247968

Horibe, S., and Oba, T. (1972). Temperature scales of aragonite-water and calcite-water systems. *Kaseki (Fossils)* 23, 69–74. (in Japanese with English abstract)

Hoşgör, İ., and Yılmaz, İ. (2019). Paleogeographic northeastern limits of *Aphrodina dutrugei* (Cocquand 1862)(Heterodonta, Bivalvia) from the Cenomanian of the Arabian Platform. *Riv. It. Paleontol. Strat.* 125, 421–431. doi: 10.13130/2039-4942/11773

Huber, B. T., Hodell, D. A., and Hamilton, C. P. (1995). Middle-Late Cretaceous climate of the southern high latitudes: stable isotopic evidence for minimal equator-to-pole thermal gradients. *Geol. Soc Am. Bull.* 107, 1164–1191. doi: 10.1130/0016-7606(1995)107<1164:MLCCOT>2.3.CO;2

Huber, B. T., MacLeod, K. G., Watkins, D. K., and Coffin, M. F. (2018). The rise and fall of the Cretaceous Hot Greenhouse climate. *Glob. Planet. Change* 167, 1–23. doi: 10.1016/j.gloplacha.2018.04.004

Huck, S., and Heimhofer, U. (2021). Early Cretaceous sea surface temperature evolution in subtropical shallow seas. *Sci. Rep.* 11, 1–9. doi: 10.1038/s41598-021-99094-2

Ivany, L. C. (2012). Reconstructing paleoseasonality from accretionary skeletal carbonates – challenges and opportunities. *Paleontol. Soc. Pap.* 18, 133–166.

Ivany, L. C., and Judd, E. J. (2022). Deciphering temperature seasonality in Earth's ancient oceans. *Annu. Rev. Earth Planet. Sci.* 50, 123–152. doi: 10.1146/annurev-earth-032320-095156

Japan Meteorological Agency (2024a) *Coastal sea-surface temperature information in coastal Ishikari area* (Hokkaido). Available online at: https://www.data.jma.go.jp/kaiyou/data/db/kaikyo/series/engan/engan109.html (Accessed 11, Mar, 2024).

Japan Meteorological Agency (2024b) *Coastal sea-surface temperature information in southern Okinawa island* (Ryukyu Islands). Available online at: https://www.data.jma.go.jp/kaiyou/data/db/kaikyo/series/engan/engan704.html (Accessed 11, Mar, 2024).

Jones, D. S. (1983). Sclerochronology: Reading the Record of the Molluscan Shell: Annual growth increments in the shells of bivalve molluscs record marine climatic changes and reveal surprising longevity. *Am. Sci.* 71, 384–391.

Jones, D. S., Arthur, M. A., and Allard, D. J. (1989). Sclerochronological records of temperature and growth from shells of *Mercenaria mercenaria* from Narragansett Bay, Rhode Island. *Mar. Biol.* 102, 225–234. doi: 10.1007/BF00428284

Jones, M. M., Petersen, S. V., and Curley, A. N. (2022). A tropically hot mid-Cretaceous North American Western Interior Seaway. *Geology* 50, 954–958. doi: 10.1130/G49998.1

Jones, D. S., and Quitmyer, I. R. (1996). Marking time with bivalve shells: oxygen isotopes and season of annual increment formation. *Palaios* 11, 340–346. doi: 10.2307/3515244

Judd, E. J., Wilkinson, B. H., and Ivany, L. C. (2018). The life and time of clams: Derivation of intra-annual growth rates from high-resolution oxygen isotope profiles. *Palaeogeogr. Palaeoclimatol. Palaeoecol.* 490, 70–83. doi: 10.1016/J.PALAEO.2017.09.034

Kennish, M. J., and Olsson, R. K. (1975). Effects of thermal discharges on the microstructural growth of *Mercenaria mercenaria*. *Environ. Geol.* 1, 41–64. doi: 10.1007/BF02426940

Kikuchi, K. (2018). The occurrence of *Paleodictyon* in shallow-marine deposits of the Upper Cretaceous Mikasa Formation, Hokkaido Island, northern Japan: Implications for spatiotemporal variation of the *Nereites* ichnofacies. *Palaeogeogr. Palaeoclimatol. Palaeoecol.* 503, 81–89. doi: 10.1016/J.PALAEO.2018.04.016

Kitagawa, Y., Takashima, R., and Itoh, Y. (2016). Paleomagnetism of the Sorachi and Yezo Group in the Ashibetsu area , central Hokkaido, Japan. *Bull. Tohoku Univ. Museum* 15, 109–125. (in Japanese with English abstract)

Kitamura, A. (2018). Combined sclerochronological and oxygen isotope analyses of marine bivalve shells to examine high-resolution Holocene environmental changes. *Quat. Res.* 57, 19–29. doi: 10.4116/jaqua.57.19 (in Japanese)

Kitamura, A., Yamamoto, N., and Kobayashi, K. (2012). Growth of the submarine cave-dwelling micro-bivalve *Carditella iejimensis*. *Venus (Japanese J. Malacol.* 70, 41–45. doi: 10.18941/venus.70.1-4_41

Knoll, K., Landman, N. H., Cochran, J. K., MacLeod, K. G., and Sessa, J. A. (2016). Microstructural preservation and the effects of diagenesis on the carbon and oxygen isotope composition of Late Cretaceous aragonitic mollusks from the Gulf Coastal Plain and the Western Interior Seaway. *Am. J. Sci.* 316, 591–613. doi: 10.2475/07.2016.01

Kodama, S., Takayanagi, H., Yoshii, K., Nhu Ha, T. T., Asami, R., Abe, O., et al. (2021). Carbon and oxygen isotope records of *Tridacna squamosa* shells from two different latitudes in the Ryukyu Islands. *Paleontol. Res.* 25, 79–92. doi: 10.2517/2020PR003

Komagoe, T., Watanabe, T., Shirai, K., Yamazaki, A., and Uematu, M. (2018). Geochemical and Microstructural Signals in Giant Clam *Tridacna maxima* Recorded Typhoon Events at Okinotori Island, Japan. *J. Geophys. Res. Biogeosciences* 123, 1460–1474. doi: 10.1029/2017JG004082

Komatsu, T. (2013). Palaeoecology of the mid-Cretaceous siphonate bivalve genus *Goshoraia* (Mollusca, Veneridae) from Japan. *Palaeontology* 56, 381–397. doi: 10.1111/J.1475-4983.2012.01206.X

Kubota, K., Shirai, K., Murakami-Sugihara, N., Seike, K., Hori, M., and Tanabe, K. (2017). Annual shell growth pattern of the Stimpson's hard clam *Mercenaria stimpsoni* as revealed by sclerochronological and oxygen stable isotope measurements. *Palaeogeogr. Palaeoclimatol. Palaeoecol.* 465, 307–315. doi: 10.1016/J.PALAEO.2016.05.016

Lantink, M. L., Davies, J. H. F. L., Ovtcharov, M., and Hilgen, F. J. (2022). Milankovitch cycles in banded iron formations constrain the Earth–Moon system 2.46 billion years ago. *EARTH Atmos. Planet. Sci.* 119, 1–10. doi: 10.1073/pnas.2117146119

Lidgard, S., and Crane, P. R. (1988). Quantitative analyses of the early angiosperm radiation. *Nature* 331, 344–346. doi: 10.1038/331344a0

Ma, X., Yan, H., Fei, H., Liu, C., Shi, G., Huang, E., et al. (2020). A high-resolution $\delta^{18}O$ record of modern *Tridacna gigas* bivalve and its paleoenvironmental implications. *Palaeogeogr. Palaeoclimatol. Palaeoecol.* 554, 109800. doi: 10.1016/J.PALAEO.2020.109800

MacLeod, K. G., Huber, B. T., Berrocoso, Á. J., and Wendler, I. (2013). A stable and hot Turonian without glacial $\delta^{18}O$ excursions is indicated by exquisitely preserved Tanzanian foraminifera. *Geology* 41, 1083–1086. doi: 10.1130/G34510.1

Maliva, R. G., Missimer, T. M., and Dickson, J. A. D. (2000). Skeletal aragonite neomorphism in Plio-Pleistocene sandy limestones and sandstones, Hollywood, Florida, USA. *Sediment. Geol.* 136, 147–154. doi: 10.1016/S0037-0738(00)00102-0

Mansour, A., and Wagreich, M. (2022). Earth system changes during the cooling greenhouse phase of the Late Cretaceous: Coniacian-Santonian OAE3 subevents and fundamental variations in organic carbon deposition. *Earth-Science Rev.* 229, 104022. doi: 10.1016/J.EARSCIREV.2022.104022

Marshall, D. J., and Burgess, S. C. (2015). Deconstructing environmental predictability: seasonality, environmental colour and the biogeography of marine life histories. *Ecol. Lett.* 18, 174–181. doi: 10.1111/ELE.12402

Matsumoto, T. (1951). The Yezo group and the Kwanmon group. *J. Geol. Soc Japan* 57, 95–98. doi: 10.5575/GEOSOC.57.95 (in Japanese)

Matsumoto, T. (1965). A monograph of the collignoniceratidae from Hokkaido part I: studies of the Cretaceous ammonites from Hokkaido and Saghalien-XIV. *Mem. Fac. Sci. Kyūsyū Univ. Ser. D Geol.* 16, 1–80. doi: 10.5109/1543624

Matsuno, K., Tanaka, K., and Mizuno, A. (1963). *Explainatory text of the geological map of Japan, Scale 1:50000* Vol. 179 (Iwamizawa: Geological Survey of Japan).

Meinshausen, M., Nicholls, Z. R. J., Lewis, J., Gidden, M. J., Vogel, E., Freund, M., et al. (2020). The shared socio-economic pathway (SSP) greenhouse gas concentrations and their extensions to 2500. *Geosci. Model. Dev.* 13, 3571–3605. doi: 10.5194/gmd-13-3571-2020

Meyer, K. W., Petersen, S. V., Lohmann, K. C., and Winkelstern, I. Z. (2018). Climate of the Late Cretaceous North American Gulf and Atlantic Coasts. *Cretac. Res.* 89, 160–173. doi: 10.1016/J.CRETRES.2018.03.017

Miyaji, T., Tanabe, K., and Schöne, B. R. (2007). Environmental controls on daily shell growth of *Phacosoma japonicum* (Bivalvia: Veneridae) from Japan. *Mar. Ecol. Prog. Ser.* 336, 141–150. doi: 10.3354/MEPS336141

Moiroud, M., Pucéat, E., Donnadieu, Y., Bayon, G., Moriya, K., Deconinck, J. F., et al. (2013). Evolution of the neodymium isotopic signature of neritic seawater on a northwestern Pacific margin: new constrains on possible end-members for the composition of deep-water masses in the Late Cretaceous ocean. *Chem. Geol.* 356, 160–170. doi: 10.1016/J.CHEMGEO.2013.08.008

Moon, L. R., Judd, E. J., Thomas, J., and Ivany, L. C. (2021). Out of the oven and into the fire: Unexpected preservation of the seasonal $\delta^{18}O$ cycle following heating experiments on shell carbonate. *Palaeogeogr. Palaeoclimatol. Palaeoecol.* 562, 110115. doi: 10.1016/J.PALAEO.2020.110115

Moriya, K. (2011). Development of the Cretaceous greenhouse climate and the oceanic thermal structure. *Paleontol. Res.* 15, 77–88. doi: 10.2517/1342-8144-15.2.077

Moriya, K., Wilson, P. A., Friedrich, O., Erbacher, J., and Kawahata, H. (2007). Testing for ice sheets during the mid-Cretaceous greenhouse using glassy foraminiferal calcite from the mid-Cenomanian tropics on Demerara Rise. *Geology* 35, 615–618. doi: 10.1130/G23589A.1

Nakajima, Y., Danilov, I. G., Hirayama, R., Sonoda, T., and Scheyer, T. M. (2017). Morphological and histological evidence for the oldest known softshell turtles from Japan. *J. Vertebr. Paleontol.* 37, e1278606. doi: 10.1080/02724634.2017.1278606

Nishi, H., Takashima, R., Hatsugai, T., Saito, T., Moriya, K., Ennyu, A., et al. (2003). Planktonic foraminiferal zonation in the Cretaceous Yezo Group, Central Hokkaido, Japan. *J. Asian Earth Sci.* 21, 867–886. doi: 10.1016/S1367-9120(02)00138-4

Nishida, K. (2020). Stable carbon and oxygen isotopes of molluscan shells: Implications to paleontological studies on biological carbonates. *Fossils* 107, 5–20. doi: 10.14825/kaseki.107.0_5 (in Japanese with English abstract)

Nishida, K., Suzuki, A., Isono, R., Hayashi, M., Watanabe, Y., Yamamoto, Y., et al. (2015). Thermal dependency of shell growth, microstructure, and stable isotopes in laboratory-reared *Scapharca broughtonii* (Mollusca: Bivalvia). *Geochemistry Geophys. Geosystems* 16, 2395–2408. doi: 10.1002/2014GC005634

Ohno, T. (1989). Variable rhythms of micro-growth striation formation in bivalve shells (Review). *Benthos Res.* 37, 35–48. doi: 10.5179/BENTHOS1981.1989.37_35 (in Japanese with English abstract)

Okai, T., Suzuki, A., Terashima, S., Inoue, M., Nohara, M., Kawahata, H., et al. (2004). Collaborative analysis of GSJ/AIST geochemieal reference materials JCp-1 (Coral) and JCt-1 (Giant Clam). *Chikyukagaku (Geochemistry)* 38, 281–286. doi: 10.14934/CHIKYUKAGAKU.38.281 (in Japanese with English abstract)

Otter, L. M., Agbaje, O. B. A., Kilburn, M. R., Lenz, C., Henry, H., Trimby, P., et al. (2019). Insights into architecture, growth dynamics, and biomineralization from pulsed Sr-labelled *Katelysia rhytiphora* shells (Mollusca, Bivalvia). *Biogeosciences* 16, 3439–3455. doi: 10.5194/BG-16-3439-2019

Parker, J. E., Thompson, S. P., Lennie, A. R., Potter, J., and Tang, C. C. (2010). A study of the aragonite-calcite transformation using Raman spectroscopy, synchrotron powder diffraction and scanning electron microscopy. *CrystEngComm* 12, 1590–1599. doi: 10.1039/B921487A

Pearson, P. N., Ditchfield, P. W., Singano, J., Harcourt-Brown, K. G., Nicholas, C. J., Olsson, R. K., et al. (2001). Warm tropical sea surface temperatures in the Late Cretaceous and Eocene epochs. *Nature* 413, 481–487. doi: 10.1038/35097000

Pederson, C., Mavromatis, V., Dietzel, M., Rollion-Bard, C., Nehrke, G., Jöns, N., et al. (2019). Diagenesis of mollusc aragonite and the role of fluid reservoirs. *Earth Planet. Sci. Lett.* 514, 130–142. doi: 10.1016/J.EPSL.2019.02.038

Petersen, S. V., Defliese, W. F., Saenger, C., Daëron, M., Huntington, K. W., John, C. M., et al. (2019). Effects of improved ^{17}O correction on interlaboratory agreement in clumped isotope calibrations, estimates of mineral-specific offsets, and temperature dependence of acid digestion fractionation. *Geochemistry Geophys. Geosystems* 20, 3495–3519. doi: 10.1029/2018GC008127

Petrizzo, M. R., Amaglio, G., Watkins, D. K., MacLeod, K. G., Huber, B. T., Hasegawa, T., et al. (2022). Biotic and paleoceanographic changes across the Late Cretaceous oceanic anoxic event 2 in the southern high latitudes (IODP sites U1513 and U1516, SE Indian Ocean). *Paleoceanogr. Paleoclimatol.* 37, e2022PA004474. doi: 10.1029/2022PA004474

Posenato, R., Crippa, G., de Winter, N. J., Frijia, G., and Kaskes, P. (2022). Microstructures and sclerochronology of exquisitely preserved Lower Jurassic lithiotid bivalves: Paleobiological and paleoclimatic significance. *Palaeogeogr. Palaeoclimatol. Palaeoecol.* 602, 111162. doi: 10.1016/J.PALAEO.2022.111162

Pucéat, E., Lécuyer, C., Donnadieu, Y., Naveau, P., Cappetta, H., Ramstein, G., et al. (2007). Fish tooth $\delta^{18}O$ revising Late Cretaceous meridional upper ocean water temperature gradients. *Geology* 35, 107–110. doi: 10.1130/G23103A.1

Reza Mirzaei, M., Hwai, A. T. S., and Khalil, M. (2017). Temporal Variation in Shell Growth Rate of Cockle *Anadara granosa* in Relation with its Reproductive Cycle. *J. Shellfish Res.* 36, 69–78. doi: 10.2983/035.036.0109

Reza Mirzaei, M., Yasin, Z., and Shau Hwai, A. T. (2014). Periodicity and shell microgrowth pattern formation in intertidal and subtidal areas using shell cross sections of the blood cockle, *Anadara granosa*. *Egypt. J. Aquat. Res.* 40, 459–468. doi: 10.1016/J.EJAR.2014.11.008

Richardson, C. A. (1988). Tidally produced growth bands in the subtidal bivalve *Spisula subtruncata* (Da Costa). *J. Molluscan Stud.* 54, 71–82. doi: 10.1093/MOLLUS/54.1.71

Ryan, D. R., Witts, J. D., and Landman, N. H. (2021). Palaeoecological analysis of a methane seep deposit from the Upper Cretaceous (Maastrichtian) of the U.S. Western Interior. *Lethaia* 54, 185–203. doi: 10.1111/let.12396

Sano, Y., Kobayashi, S., Shirai, K., Takahata, N., Matsumoto, K., Watanabe, T., et al. (2012). Past daily light cycle recorded in the strontium/calcium ratios of giant clam shells. *Nat. Commun.* 3, 761. doi: 10.1038/ncomms1763

Sato, S. (1995). Spawning periodicity and shell microgrowth patterns of the venerid bivalve *Phacosoma japonicum* (Reeve 1850). *Veliger* 38, 61–72. doi: 10.3800/PBR.2.77

Sato, S. (1997). Shell microgrowth patterns of bivalves reflecting seasonal change of phytoplankton abundance. *Paleontol. Res.* 1, 260–266. doi: 10.2517/prpsj.1.260

Schmitt, K. E., Huck, S., Krummacker, M., De Winter, N. J., Godet, A., Claeys, P., et al. (2022). Radiolitid rudists: an underestimated archive for Cretaceous climate reconstruction? *Lethaia* 55, 1–21. doi: 10.18261/let.55.4.4

Schöne, B. R., Dunca, E., Mutvei, H., and Norlund, U. (2004). A 217-year record of summer air temperature reconstructed from freshwater pearl mussels (*M. margarifitera*, Sweden). *Quat. Sci. Rev.* 23, 1803–1816. doi: 10.1016/J.QUASCIREV.2004.02.017

Schöne, B. R., Fiebig, J., Pfeiffer, M., Gleß, R., Hickson, J., Johnson, A. L. A., et al. (2005). Climate records from a bivalved Methuselah (*Arctica islandica*, Mollusca; Iceland). *Palaeogeogr. Palaeoclimatol. Palaeoecol.* 228, 130–148. doi: 10.1016/J.PALAEO.2005.03.049

Schöne, B. R., and Giere, O. (2005). Growth increments and stable isotope variation in shells of the deep-sea hydrothermal vent bivalve mollusk *Bathymodiolus brevior* from the North Fiji Basin, Pacific Ocean. *Deep Sea Res. Part I Oceanogr. Res. Pap.* 52, 1896–1910. doi: 10.1016/J.DSR.2005.06.003

Schöne, B. R., Tanabe, K., Dettman, D. L., and Sato, S. (2003). Environmental controls on shell growth rates and $\delta^{18}O$ of the shallow-marine bivalve mollusk *Phacosoma japonicum* in Japan. *Mar. Biol.* 142, 473–485. doi: 10.1007/s00227-002-0970-y

Shackleton, N. J., and Kennett, J. P. (1975). Paleotemperature history of the Cenozoic and the initiation of Antarctic glaciation: oxygen and carbon isotope analyses in DSDP Sites 277, 279 and 281. *Rep. Deep Sea Drill Pr* 29, 743–755. doi: 10.2973/dsdp.proc.29.117.1975

Shimamoto, M. (1986). Shell microstructure of the veneridae (Bivalvia) and its phylogenetic implications. *Sci. Rep. Tohoku Univ. Second Ser. Geol.* 56, 1–A40.

Shimizu, I., Tanaka, K., and Imai, I. (1955). *Explainatory text of the geological map of Japan, Scale 1:50000* (Kami-Ashibetsu: Geological Survey of Japan).

Squires, R. L. (2010). Northeast Pacific upper Cretaceous and paleocene glycymeridid bivalves. *J. Paleontol.* 84, 895–917. doi: 10.1666/09-130.1

Sternberg, S. R. (1983). Biomedical image processing. *Comput. (Long. Beach. Calif).* 16, 22–34. doi: 10.1109/MC.1983.1654163

Steuber, T., Rauch, M., Masse, J. P., Graaf, J., and Malkoč, M. (2005). Low-latitude seasonality of Cretaceous temperatures in warm and cold episodes. *Nat. 2005 4377063* 437, 1341–1344. doi: 10.1038/nature04096

Sugiura, D., Katayama, S., Sasa, S., and Sasaki, K. (2014). Age and growth of the ark shell *Scapharca broughtonii* (Bivalvia, arcidae) in Japanese waters. *J. Shellfish Res.* 33, 315–324. doi: 10.2983/035.033.0130

Suzuki, S., Togo, Y., and Hikida, Y. (1998). Preliminary report on the preservation of some molluscan fossils from Nakagawa-cho, Hokkaido, Japan. *Bull. Nakagawa Museum Nat. Hist.* 1, 81–94. (in Japanese with English abstract)

Tajika, A., Landman, N. H., Cochran, J. K., Nishida, K., Shirai, K., Ishimura, T., et al. (2023). Ammonoid extinction versus nautiloid survival: Is metabolism responsible? *Geology* 51 (7), 621–625. doi: 10.1130/G51116.1

Takashima, R., Kawabe, F., Nishi, H., Moriya, K., Wani, R., and Ando, H. (2004). Geology and stratigraphy of forearc basin sediments in Hokkaido, Japan: Cretaceous environmental events on the north-west Pacific margin. *Cretac. Res.* 25, 365–390. doi: 10.1016/J.CRETRES.2004.02.004

Takayanagi, H., Asami, R., Otake, T., Abe, O., Miyajima, T., Kitagawa, H., et al. (2015). Quantitative analysis of intraspecific variations in the carbon and oxygen isotope compositions of the modern cool-temperate brachiopod *Terebratulina crossei*. *Geochim. Cosmochim. Acta* 170, 301–320. doi: 10.1016/J.GCA.2015.08.006

Tamaki, M., and Itoh, Y. (2008). Tectonic implications of paleomagnetic data from upper Cretaceous sediments in the Oyubari area, central Hokkaido, Japan. *Isl. Arc* 17, 270–284. doi: 10.1111/J.1440-1738.2008.00617.X

Tamaki, M., Oshimbe, S., and Itoh, Y. (2008). A large latitudinal displacement of a part of Cretaceous forearc basin in Hokkaido, Japan: paleomagnetism of the Yezo Supergroup in the Urakawa area. *J. Geol. Soc Japan* 114, 207–217. doi: 10.5575/GEOSOC.114.207

Tanabe, K. (1988). An attempt for age estimation of bivalves using shell growth lines. *Benthos Res.* 32, 12–17. doi: 10.5179/BENTHOS1981.1988.12

Tanabe, K., Mimura, T., Miyaji, T., Shirai, K., Kubota, K., Murakami-Sugihara, N., et al. (2017). Interannual to decadal variability of summer sea surface temperature in the Sea of Okhotsk recorded in the shell growth history of Stimpson's hard clams (*Mercenaria stimpsoni*). *Glob. Planet. Change* 157, 35–47. doi: 10.1016/J.GLOPLACHA.2017.08.010

Tanabe, K., Miyaji, T., Murakami-Sugihara, N., Shirai, K., and Moriya, K. (2020). Annual shell growth patterns of three venerid bivalve mollusk species in the subtropical northwestern Pacific as revealed by sclerochronological and stable oxygen isotope analyses. *Mar. Biol.* 167, 1–15. doi: 10.1007/S00227-019-3637-7/FIGURES/8

Tashiro, M. (1979).). A STUDY OF THE "PENNATAE TRIGONIIDS" FROM JAPAN. *Trans. Proc. Paleontol. Soc Japan. New Ser.* 116, 179–222. doi: 10.14825/prpsj1951.1979.116_179

Tashiro, M. (1995). Stratigraphical occurrence of the Cenomanian bivalves from Hokkaido. *Mem. Fac. Sci. Kochi Univ. E Ser. Geol* 16, 15–31.

Taylor, J. D., Kennedy, W. J., and Hall, A. (1969). The shell structure and mineralogy of the Bivalvia. I. Introduction. Nuculacea-trigonacea. *Bull. Br. Museum (Natural Hist.) Zool* supplement, 1–125. doi: 10.5962/p.312694

Thébault, J., Chauvaud, L., Clavier, J., Guarini, J., Dunbar, R. B., Fichez, R., et al. (2007). Reconstruction of seasonal temperature variability in the tropical Pacific Ocean from the shell of the scallop, *Comptopallium radula*. *Geochim. Cosmochim. Acta* 71, 918–928. doi: 10.1016/J.GCA.2006.10.017

Tojo, B., and Masuda, F. (1999). Tidal growth patterns and growth curves of the Miocene potamidid gastropod *Vicarya yokoyamai*. *Paleontol. Res.* 3, 193–201. doi: 10.2517/prpsj.3.193

Vandermark, D., Tarduno, J. A., and Brinkman, D. B. (2007). A fossil champsosaur population from the high Arctic: Implications for Late Cretaceous paleotemperatures. *Palaeogeogr. Palaeoclimatol. Palaeoecol.* 248, 49–59. doi: 10.1016/J.PALAEO.2006.11.008

Vermeij, G. J. (1977). The Mesozoic marine revolution: evidence from snails, predators and grazers. *Paleobiology* 3, 245–258. doi: 10.1017/S0094837300005352

Walliser, E. O., and Schöne, B. R. (2020). Paleoceanography of the Late Cretaceous northwestern Tethys Ocean: Seasonal upwelling or steady thermocline? *PloS One* 15, e0238040. doi: 10.1371/JOURNAL.PONE.0238040

Walliser, E. O., Schöne, B. R., Tütken, T., Zirkel, J., Grimm, K. I., and Pross, J. (2015). The bivalve *Glycymeris planicostalis* as a high-resolution paleoclimate archive for the Rupelian (Early Oligocene) of central Europe. *Clim. Past* 11, 653–668. doi: 10.5194/cp-11-653-2015

Wanamaker, A. D., Kreutz, K. J., Schöne, B. R., and Introne, D. S. (2011). Gulf of Maine shells reveal changes in seawater temperature seasonality during the Medieval Climate Anomaly and the Little Ice Age. *Palaeogeogr. Palaeoclimatol. Palaeoecol.* 302, 43–51. doi: 10.1016/j.palaeo.2010.06.005

Wang, G., Yan, H., Liu, C., Han, T., Zhou, P., Zhao, N., et al. (2022). Oxygen isotope temperature calibrations for modern *Tridacna* shells in western Pacific. *Coral Reefs* 41, 113–130. doi: 10.1007/S00338-021-02208-5/TABLES/3

Watanabe, T., and Oba, T. (1999). Daily reconstruction of water temperature from oxygen isotopic ratios of a modern *Tridacna* shell using a freezing microtome sampling technique. *J. Geophys. Res. Ocean.* 104, 20667–20674. doi: 10.1029/1999JC900097

Wehrmeister, U., Soldati, A. L., Jacob, D. E., Häger, T., and Hofmeister, W. (2010). Raman spectroscopy of synthetic, geological and biological vaterite: a Raman spectroscopic study. *J. Raman Spectrosc.* 41, 193–201. doi: 10.1002/JRS.2438

Welsh, K., Elliot, M., Tudhope, A., Ayling, B., and Chappell, J. (2011). Giant bivalves (*Tridacna gigas*) as recorders of ENSO variability. *Earth Planet. Sci. Lett.* 307, 266–270. doi: 10.1016/J.EPSL.2011.05.032

White, R. M. P., Dennis, P. F., and Atkinson, T. C. (1999). Experimental calibration and field investigation of the oxygen isotopic fractionation between biogenic aragonite and water. *Rapid Commun. Mass Spectrom.* 13, 1242–1247. doi: 10.1002/(SICI)1097-0231(19990715)13:13

Wierzbicki, A., Wolfgring, E., Wagreich, M., Kędzierski, M., and Mertz-Kraus, R. (2023). Astronomically controlled deep-sea life in the Late Cretaceous reconstructed from ultra-high-resolution inoceramid shell archives. *Geobiology* 21, 474–490. doi: 10.1111/GBI.12548

Williams, G. E. (2000). Geological constraints on the Precambrian history of earth's rotation and the moon's orbit. *Rev. Geophys.* 38, 37–59. doi: 10.1029/1999RG900016

Yabe, H. (1926). A new scheme of the stratigraphical subdivision of the Cretaceous deposits of Hokkaidô. *Proc. Imp. Acad.* 2, 214–218. doi: 10.2183/PJAB1912.2.214

Yabumoto, Y., Hikida, Y., and Nishino, T. (2012). *Apsopelix miyazakii*, a new species of crossognathid fish (Teleostei) from the upper Cretaceous of Hokkaido, Japan. *Paleontol. Res.* 16, 37–46. doi: 10.2517/1342-8144-16.1.037

Yamamoto, K., Takizawa, M., Takayanagi, H., Asami, R., and Iryu, Y. (2017). Nonlinear relationship between preservation of microstructure and geochemical composition of Pleistocene brachiopod shells from the Ryukyu Islands, southwestern Japan. *Isl. Arc* 26, e12217. doi: 10.1111/iar.12217

Yamanashi, J., Takayanagi, H., Isaji, A., Asami, R., and Iryu, Y. (2016). Carbon and oxygen isotope records from *Tridacna derasa* shells: toward establishing a reliable proxy for sea surface environments. *PloS One* 11, e0157659. doi: 10.1371/JOURNAL.PONE.0157659

Yan, H., Shao, D., Wang, Y., and Sun, L. (2013). Sr/Ca profile of long-lived *Tridacna gigas* bivalves from South China Sea: A new high-resolution SST proxy. *Geochim. Cosmochim. Acta* 112, 52–65. doi: 10.1016/J.GCA.2013.03.007

Zakhera, M., Kassab, A., and Chinzei, K. (2001). *Hyotissocameleo*, a new Cretaceous oyster subgenus and its shell microstructure, from Wadi Tarfa, Easthern Desert of Egypt. *Paleontol. Res.* 5, 77–86. doi: 10.2517/prpsj.5.77

Zhou, J., Poulsen, C. J., Pollard, D., and White, T. S. (2008). Simulation of modern and middle Cretaceous marine $\delta^{18}O$ with an ocean-atmosphere general circulation model. *Paleoceanography* 23, PA3223. doi: 10.1029/2008PA001596

frontiers | Frontiers in Marine Science

TYPE Original Research
PUBLISHED 01 August 2024
DOI 10.3389/fmars.2024.1385347

OPEN ACCESS

EDITED BY
Ed Hathorne,
Helmholtz Association of German Research Centres (HZ), Germany

REVIEWED BY
Sambuddha Misra,
Indian Institute of Science (IISc), India
Toshihiro Yoshimura,
Japan Agency for Marine-Earth Science and Technology (JAMSTEC), Japan

*CORRESPONDENCE
Laura Pacho
laura.pacho.sampedro@nioz.nl
Lennart Jan De Nooijer
lennart.de.nooijer@nioz.nl

RECEIVED 12 February 2024
ACCEPTED 16 July 2024
PUBLISHED 01 August 2024

CITATION
Pacho L, De Nooijer LJ, Boer W and Reichart G-J (2024) Differences between potassium and sodium incorporation in foraminiferal shell carbonate.
Front. Mar. Sci. 11:1385347.
doi: 10.3389/fmars.2024.1385347

Differences between potassium and sodium incorporation in foraminiferal shell carbonate

Laura Pacho[1]*, Lennart Jan De Nooijer[1]*, Wim Boer[1] and Gert-Jan Reichart[1,2]

[1]Royal Netherlands Institute for Sea Research (NIOZ), Ocean Systems, Texel, Netherlands, [2]Department of Geosciences, Utrecht University, Utrecht, Netherlands

The isotopic and elemental composition of the fossil shells of foraminifera are often used for reconstructing past environments and climates. These so-called proxy relations are based on the effect of environmental conditions (e.g. seawater temperature, pH) on the isotopic ratio (e.g. $\delta^{11}B$ or $\delta^{18}O$) or partitioning of elements (commonly expressed as El/Ca or D_{El}) during calcification. Whereas many studies focused on proxy-calibrations of divalent cations, incorporation of monovalent cations are less well constrained. Here we calibrate shell potassium content (K/Ca_{cc}) as a function of 1) seawater K^+ concentration, 2) the ratio of potassium and calcium in seawater (K/Ca_{sw}) and 3) temperature. Moreover, we analyze Na^+ incorporation into the calcite as a function of seawater K^+ and Ca^{2+} concentrations. First, we cultured specimens of the larger benthic foraminifer *Amphistegina lessonii* at four different seawater $[Ca^{2+}]$ and constant $[K^+]$, resulting in a range of K/Ca_{sw}. Secondly, we cultured specimens of the same species at four different $[Ca^{2+}]_{sw}$ and $[K^+]_{sw}$ while keeping the ratio between these two ions constant. Finally, we tested the effect of temperature (from 18 to 28°C) on K-incorporation in this species. Measured K/Ca_{cc} values are not notably affected by $[Ca^{2+}]_{sw}$, while seawater $[K^+]$ positively influences potassium incorporation, resulting in a positive correlation between seawater K/Ca values and K/Ca_{cc}. Although the $[Na^+]$ in the culture media was constant throughout both experiments, incorporated Na responded positively to decreasing $[Ca^{2+}]_{sw}$, resulting in a positive correlation between sea water Na/Ca and Na/Ca_{cc}. The difference in the controls on K- and Na-incorporation suggests that the (biological) control on these ions differs. Part of the observed variability in element partitioning may be explained by differences in chemical speciation and crystallographic coordination in the calcite lattice.

KEYWORDS

foraminifera, biomineralization, K/Ca, Na/Ca, proxy, culture experiment

1 Introduction

Our climate is rapidly changing as a consequence of anthropogenic greenhouse gas emissions to the atmosphere. Predicting the effects of increases in atmospheric CO_2 levels are greatly helped by reconstructions of past climate change. Such reconstructions, in turn, can be derived from the chemical composition of the shells of foraminifera: the boron isotopic composition of their calcite reflects primarily seawater pH (Sanyal et al., 1995), while for example the Mg/Ca can be used to reconstruct past seawater temperature (Nürnberget al., 1996; Holland et al., 2020). Incorporation of elements is usually also affected by biological control during calcification. This is apparent from the large deviation in El/Ca between species (Bentov and Erez, 2006; De Nooijer et al., 2023), within species (De Nooijer et al., 2014; Sadekov et al., 2016) and even within single chamber walls (Kunioka et al., 2006; Fehrenbacher et al., 2017; Levi et al., 2019). These observations have prompted investigating the physiological controls acting on ion uptake by foraminifera during calcification (Erez, 2003; De Nooijer et al., 2014; Schmidt et al., 2016; Evans et al., 2018; Tyszka et al., 2019). The active proton pumping (Bentov et al., 2009; De Nooijer et al., 2009) and calcium uptake (Toyofuku et al., 2017) may be the key in understanding divalent cation uptake and incorporation and at the same time may affect reconstruction of such elements' concentrations.

Concentrations of the major ions in seawater (Na^+, Mg^{2+}, Ca^{2+}, K^+) are not constant on geological time scales with residence times of 1.1 to 100 Myrs (Horibe et al., 1974; Hardie, 1996; Lécuyer, 2016; Zeebe and Tyrrell, 2018; Hauzer et al., 2021). The changes of $[Ca^{2+}]_{sw}$ result in changes in the incorporation of other elements into the calcite of foraminifera, likely as a result of competition of these ions with Ca^{2+} for a place in the crystal lattice (Dueñas-Bohórquez et al., 2011; Mewes et al., 2015a; Hauzer et al., 2018). In theory, past concentrations of calcium in seawater may be estimated from foraminiferal El/Ca ratios of elements that have a higher residence time than calcium (Na; (Hauzer et al., 2018). This, however, requires calibration of El/Ca as a function of $[Ca^{2+}]$. For Mg^{2+} incorporation, a non-linear response to $[Ca^{2+}]$ is described (Segev and Erez, 2006; Hauzer et al., 2018), It has been described linear correlations for Li/Ca_{cc} versus Li/Ca_{sw}, Sr/Ca_{cc} versus Sr/Ca_{sw} (Mewes et al., 2015b; Hauzer et al., 2018) and Na/Ca_{cc} versus Na/Ca_{sw} (Hauzer et al., 2018).

One of the major elements in seawater is K^+ with an average concentration of 380 mg/L (Wang et al., 2020) and a residence time of ~12 Myrs (Culkin and Cox, 1966). The 2 main sources for potassium in seawater are continental runoff and hydrothermal fluxes, while K is removed from seawater by pore-water entrapment or adsorption into clay minerals (Kronberg, 1985; Sun et al., 2016). However, K^+ incorporation into foraminiferal calcite and its potential dependency on environmental parameters are at the first steps with only a few publications. Culturing experiments with benthic foraminifera suggested both foraminiferal K/Ca_{cc} and Na/Ca_{cc} as a potential proxy for seawater $[Ca^{2+}]$ (Hauzer et al., 2018; Nambiar et al., 2023). Such reconstructions are important as they can reveal long-term changes in the oceans' major ion composition and thereby allow studying changes in the rates of geological processes including weathering, seafloor spreading and authigenic mineral formation (Horita et al., 2002; Fantle and DePaolo, 2005).

Compared to other major elements in seawater, K^+ has a large ionic radius and can interfere with the structure of proteins, requiring cells to regulate the concentration of this ion. Studies looking at the impact of temperature showed no apparent effect on K/Ca in a variety of organisms (Li et al., 2021) and suggest that K-incorporation is correlated only to the concentration of K^+ in the medium during inorganic precipitation experiments (Ishikawa and Ichikuni, 1984). Another very well-known monovalent ion in seawater is Na^+, with an average concentration of 10.6 g/L (Duxbury et al., 2024). Na/Ca_{cc} has being studied as a proxy before for changes in salinity in the past (Wit et al., 2013; Geerken et al., 2018), although this was debated to be the case by Hauzer et al. (2021). In addition, there is no effect of temperature on Na-incorporation (Allen et al., 2016).

Incorporation of monovalent cations and whether these elements are affected by the so-called vital effects of foraminifera remain largely unknown. Incorporation of K^+ by skeleton of corals has been shown to be related to incorporation of Na^+ and explains the similarity in the way they are incorporated (Mitsuguchi and Kawakami, 2012). Moreover, using the incorporation of divalent cations such as Mg^{2+} and Sr^{2+} as proxies also requires known sea water element to calcium ratios, which is on geological time scales can rely on changes in seawater $[Ca^{2+}]$. It is also vital to understand the inter-species' effect of environmental parameters on element incorporation. Finally, it is necessary to quantify the interaction between incorporated ions, for example Na^+ and K^+, to correct fossil El/Ca for changes in the composition of the seawater's major ion inventory.

In this study, we report the results of a set of experiments to calibrate K^+ incorporation in the benthic foraminifer *Amphistegina lessonii* as a function of $[Ca^{2+}]$, $[K^+]$and $[Ca^{2+}]$ and temperature. We set up controlled growth experiments to decouple the effect of these variables on calcitic K/Ca, which are inherently correlated in nature to deconvolve the underlying processes involved in K^+ and Na^+ uptake. Hence, grown specimens were also used to analyze their Na/Ca to test potential impacts of $[Ca^{2+}]$, $[K^+]$ and temperature on sodium incorporation. Accordingly, we aim to evaluate the potential of foraminiferal K/Ca and Na/Ca values as a proxy for $[Ca^{2+}]_{sw}$ and seawater chemistry in general.

2 Materials and methods

Three sets of controlled growth experiments were performed (Table 1). In the first set only the seawater's calcium concentration (i.e. $[Ca^{2+}]_{sw}$) was varied. In the second set of experiments, we varied both $[K^+]_{sw}$ and $[Ca^{2+}]_{sw}$, while keeping K/Ca_{sw} constant. These two sets of experiments were done under identical, constant temperature, salinity, and inorganic carbon chemistry. Finally, a set of experiments was conducted with varying temperatures, while keeping element concentrations, salinity and inorganic carbon chemistry constant.

10.3389/fmars.2024.1385347

TABLE 1 Three different culture experiments with *A. lessonii*.

Manipulated parameter	Temperature °C	$[Ca^{2+}]_{sw}$ (mmol/kg)	$[K^{+}]_{sw}$ (mmol/kg)	K/Ca_{sw} (mol/mol)	$Na/Ca_{sw} * 10^{-3}$ (mol/mol)
$[Ca^{2+}]_{sw}$	24 (constant)	7.63 - 19.93	8.4 (constant)	0.44 - 1.01	23.8 - 58.52
$[K^{+}]_{sw}$, $[Ca^{2+}]_{sw}$	24 (constant)	7.84 - 15.36	6.78 - 13.86	0.87 (constant)	33.25 - 67.47
Temperature °C	18, 22, 26 and 28	9.97 (constant)	9.72 (constant)	0.95 (constant)	26 (constant)

2.1 Culture set-up: $[Ca^{2+}]_{sw}$, and $[K^{+}]_{sw}$ and $[Ca^{2+}]_{sw}$

For the two experiments in which Ca- and/or K-concentrations were varied, specimens of *A. lessonii* were isolated from coral rubble retrieved from the tropical aquarium of Burgers' Zoo [Arnhem, the Netherlands; (Ernst et al., 2011)]. Approximately 100 living specimens were selected and transferred to Petri dishes and placed at 26°C with a light/dark cycle of 12h/12h to stimulate asexual reproduction. Within 2 weeks, between 80 and 90 juveniles were released from several adults that were incubated in pre-made culture media.

For these two sets of experiments, the amounts of salts were added following the recipes of (Kester, 1967) and (Wit et al., 2013), however changing the concentrations of $CaCl_2$ and KCl (Supplementary Tables S4, S5). We mixed the artificial seawater with filtered (< 2 µm) North Sea Water, using a ratio of 1 to 5 (20% North Sea Water and 80% artificial seawater) and we measured and controlled the salinity (within +/-0.1 salinity units) at the start and at the end of the experiment using a conductometer.

The prepared media were divided over culture flasks (De Goeyse et al., 2021) that were placed in a cabinet with a controlled atmospheric pCO_2 of 600 ppm and a light/dark cycle of 12h/12h. Evaporation of the culture media was minimized by saturating the atmosphere inside the cabinet with water vapor. The culture media were subsampled for DIC and TA by filling replicate 5mL vials, pre-poisoned with $HgCl_2$, and storage at 4°C until analyses using a Continuous Segmented Flow Analyzer (QuAAtro). For DIC the method was the same as the one used in the temperature experiment (2.1.1) but for TA an adapted method from (Sarazin et al., 1999) was used, changing the organic acid from formic acid to Phthalic acid, keeping the same indicator Bromo Phenol Blue which is blue at a pH of 3.7 and giving a green color at more alkaline phases having an absorbance at 590nm (Supplementary Tables S1, S2). *A. lessonii* was grown under these pre-set conditions for six weeks. Almost all replicates had sufficient material to have one or two analysis per replicate for K/Ca_{cc} using ICP-MS (Supplementary Tables S1, S2). Every batch of foraminifera measured contained between 10-25 individuals per condition. The specimens that were selected for analysis were fully grown (i.e. consisted of more than 15 chambers) to minimize the contribution to the chemical signal by the first 1 or 2 chambers that were built before the experimental incubation a correlation with weight of Ca against K/Ca_{cc} was plotted to ensure there was no correlation and hence no effect of growth rate when K and Na incorporated into the calcite (Supplementary Table S12, Supplementary Figure S2) The mortality rate during the experiments was derived from the temperature experiment and equaled 22% (i.e. 78% of the incubated specimens were alive at the end of the experiment).

2.2 Culture set-up: temperature experiment

The procedure for selecting specimens, feeding, and subsampling of the culture media were identical to that in the first two sets of experiments. Juveniles derived from asexual reproduction events were divided into 4 equal groups, with at least 20 juveniles per group, which were transferred to Petri dishes with filtered (< 2 µm) North Sea water. At this stage, the juveniles had not more than seven chambers. Three or four replicates (depending on the number of juveniles available per condition) were subsequently incubated at each of the four different temperatures: 18°C, 22°C, 26°C, and 28°C (Table 1). All incubations used a light/dark cycle of 12h/12h and a light intensity of approximately 180 µmol photons m^{-2} s^{-1} for a total of eight weeks. During the experiment, the foraminifera were observed weekly to monitor how many of the incubated specimens were alive. Every week, culture media were replaced and the foraminifera were fed freeze-dried algae *Dunialiella salina* (Van Dijk et al., 2017a) suspended in precleaned water (cleaned by rinsing the Falcon tubes with Milli-Q water three times).

To monitor potential changes in inorganic carbon chemistry, culture media were subsampled for dissolved inorganic carbon (DIC) and total alkalinity (TA) (Supplementary Table S3). Vials for these sub-samples were pre-poisoned with $HgCl_2$ and stored at 4°C until they were analyzed. DIC samples were acidified, and the CO_2 was dialyzed to reduce the phenolphthalein indicator and spectrophotometrically measured at 550nm using Continuous Segmented Flow Analyzer (QuAAtro); TA was measured by using an acid buffered solution of formic acid and was measured spectrophotometrically (Sarazin et al., 1999) using a QuAAtro. For the temperature experiments salinity of the culture media was monitored using a refractometer and was always 36 +/- 0.5. Because we used the same culture water for the different temperature experiments, we do not expect offsets between these experiments. Measured values for DIC and TA together with the temperature and salinity were used to calculate pH, pCO_2, $[HCO_3^-]$, $[CO_3^{2-}]$ and the saturation state with respect to calcium (Ω_{Ca}) using PyCO2SYS (Humphreys et al., 2022) (Supplementary Table S3).

2.3 Element/Ca ratios

2.3.1 Element/Ca in seawater

To analyze the El/Ca values of the culture media, we sub-sampled the culture media from every replicate of the two experiments (2.1.1). Samples were diluted 900 times in 2 steps using a 30x dilution with 1M HNO_3 sub boiled distilled quality acid, with a standard element mix containing Sc, Rh and In added to it. Rhodium was used as an internal standard to correct instrumental drift during the analysis of the mass spectrometer. Samples were measured on a sector field SF-ICPMS (ThermoFisher Scientific, Element-2) at the Royal NIOZ. Resolutions for the measurements were based on 3 slits, measuring at high resolution: 10000; medium resolution: 4000; low resolution: 300. To fully separate the ^{39}K-signal from ^{38}Ar^{1}H, potassium was measured in high resolution. This strategy was based on the ratio of the mass over the mass difference: ^{39}K has an atomic mass (M) of 38.96371 and ^{38}Ar^{1}H has an M of: 38.97056. Dividing the M of potassium over the difference in M, gives 5688 > 4000, which requires the high-resolution settings of the detector (Supplementary Figure S1). Similarly, measuring in medium resolution is also necessary for ^{32}S due to interference from ^{16}O^{16}O, dividing the M of sulfur over the difference in M gives 479 > 300. ^{11}B, ^{23}Na, ^{25}Mg, ^{43}Ca, ^{88}Sr and ^{103}Rh were all measured in low resolution (Tables 2, 3) and values El/Ca_{sw} (Tables 4, 5).

2.3.2 Foraminiferal element uptake

2.3.2.1 Cleaning procedure for shells from the culture experiments

Even though the foraminifera were all derived from culture experiments in which no sediment was present, all samples were carefully cleaned prior to element analyses. We followed a cleaning procedure based on the protocol from Barker et al. (2003). The foraminifera were not crushed, because the specimens do not contain sedimentary infillings. Crushing or over-crushing can lead to losses of carbonate material (Barker et al., 2003). First organic matter was removed using a 1% H_2O_2 buffered with a NH_4OH solution, adding 250 µL to each 500 µL Eppendorf, which was then transferred to a pre-warmed water-bath at 95°C for 10 minutes and ultrasonicated. Afterwards, the solution was removed with a 0.1 ml pipette. This procedure was repeated twice and the uncrushed foraminifera and buffered H_2O_2 solution probably gave a neglectable loss of carbonate during this organic removal step. After this step, the foraminifera were rinsed three times with ultrapure water (Milli-Q, >18.2 MΩ) by filling the tube fully with ultrapure water and removing after fully settling of the foraminifera. Possible remaining contaminants at the surface of the foraminiferal shells were finally removed by a leaching step with diluted HNO_3 (250µL 0.001 M) and concurrent gentle ultrasonication for 30 seconds. The HNO_3 was removed, and samples were cleaned with ultrapure water. The cleaned foraminifera were dissolved in 0.5 ml 0.1M ultra-pure HNO_3 (two times sub-boiled analytical grade acid in the NIOZ clean lab). To enhance the dissolution, vials were placed in an ultrasonic bath for 15 min and visually inspected to ensure complete dissolution.

2.3.2.2 SF-ICPMS analyses

For all solutions with dissolved calcium carbonate, the [Ca^{2+}] were pre-determined in medium resolution with the SF-ICPMS against a 5-point external calibration line using ^{45}Sc as an internal standard. Based on this data, samples were diluted to obtain a 100 ppm Ca matrix for each sample, minimizing mass bias effects between samples and standards. To determine foraminiferal element to calcium ratios with the SF-ICPMS, a ratio calibration method (de Villiers et al., 2002) was employed using standards with similar matrices as the samples. Samples (between 20-40 individuals per condition) were divided to obtain a minimum weight of 300µg. Samples were measured in triplicate using a low sample flow of 50µl/min (ESI, microFAST). To monitor accuracy, JCp-1 (Geological Survey of Japan, coral; *Porites* sp (Okai et al., 2004), JCt-1 (giant clam), and NFHS-2NP (Boer et al., 2022) were included in the analyses. NFHS-1(NIOZ Foraminifera House Standard; (Mezger et al., 2016) was used as a drift standard. Accuracies are listed in (Supplementary Table S6).

2.4 Statistical analysis

To analyze (potential) correlations between seawater temperature/chemistry and foraminiferal calcite composition, a bootstrap method was applied. This allows calculating confidence intervals for potential correlations through iterative resampling of the dataset generating distinct simulated sub-sets of samples (in this case 1000 iterations were used). The results of these regressions are only shown when p-values< 0.05. Confidence intervals displayed in the figures were taken from the means and standard deviations obtained from the bootstrap analysis. Analyses were performed using a standard package available for Python: scipy.stats (Virtanen et al., 2020).

TABLE 2 Elements in the seawater (mean +/- SD) after mixing with North Sea water and measured with SF-ICPMS in the $[Ca^{2+}]_{sw}$ experiment. Low resolution analysis (LR), Medium resolution analysis (MR), High resolution analysis (HR).

Ca (LR)	K (HR)	B (LR)	Na (LR)	Mg (LR)	Sr (LR)	S (MR)
(mmol/kg)	(mmol/kg)	(µmol/kg)	(mmol/kg)	(mmol/kg)	(µmol/kg)	(mmol/kg)
7.76 ± 0.13	7.98 ± 0.03	408.77 ± 2.5	447.22 ± 0.83	49.81 ± 0.04	94.79 ± 0.45	25.81 ± 0.27
15.33 ± 0.05	8.48 ± 0.09	432.77 ± 2.72	469.86 ± 2.16	52.46 ± 0.08	101.89 ± 0.55	27.44 ± 0.14
17.1 ± 0.13	8.39 ± 0.06	426.83 ± 3.34	452.23 ± 0.63	51.52 ± 0.09	100.56 ± 0.46	27.04 ± 0.14
19.76 ± 0.18	8.74 ± 0.09	443.62 ± 3.89	470.09 ± 4.01	53.89 ± 0.54	105.8 ± 0.47	28.47 ± 0.35

TABLE 3 Elements in the seawater (mean +/- SD) after mixing with North Sea water and measured with SF-ICPMS in the $[Ca^{2+}]_{sw}$ and $[K^{+}]_{sw}$ experiment. Low resolution analysis (LR), Medium resolution analysis (MR), High resolution analysis (HR).

Ca (LR)	K (HR)	B (LR)	Na (LR)	Mg (LR)	Sr (LR)	S (MR)
(mmol/kg)	(mmol/kg)	(µmol/kg)	(mmol/kg)	(mmol/kg)	(µmol/kg)	(mmol/kg)
7.9 ± 0.03	6.81 ± 0.04	418.85 ± 4.93	531.01 ± 3.87	50.98 ± 0.07	91.22 ± 0.44	26.75 ± 0.28
9.88 ± 0.08	8.67 ± 0.07	424.62 ± 2.71	470.25 ± 3.7	51.91 ± 0.55	93.24 ± 0.87	27.5 ± 0.03
11.38 ± 0.16	9.82 ± 0.37	421.17 ± 8.33	461.78 ± 5.28	51.17 ± 0.55	91.72 ± 1.29	26.72 ± 0.41
15.24 ± 0.09	13.67 ± 0.27	421.36 ± 1.05	506.16 ± 1.68	51.35 ± 0.04	93.5 ± 0.05	26.54 ± 0.4

2.5 Element partitioning

The incorporation of elements is often presented as the El/Ca (where El is the element analyzed) or D_{EL}, known as the partition coefficient:

$$[El]_{cc}/[Ca^{2+}]_{cc} = D*([El]_{sw}/[Ca^{2+}]_{sw}$$

When D > 1 the element is more concentrated in the shell than in the seawater and when D< 1 the element is excluded from the shell (Lea, 2003). As it is explained by (Lea, 2003) this relation is not strictly following thermodynamic properties, but also affected by biology. Nevertheless, expressing element incorporation into the calcite in terms of D allows better comparison between different ocean chemistries and also between experiments.

3 Results

3.1 Experiment $[Ca^{2+}]_{sw}$

In the first experiment, both $[K^{+}]_{sw}$ and $[Na^{+}]_{sw}$ were kept constant and therefore variability in foraminiferal calcite composition must be related to changes in $[Ca^{2+}]_{sw}$ (Supplementary Table S7). The K/Ca_{cc} values of the different conditions used are statistically the same. The K/Ca_{cc} at the lowest K/Ca_{sw} appear higher than at higher K/Ca_{sw}, but this is likely caused by the contribution of pre-existing calcite (see also discussion, 4.1). Na/Ca_{cc}, however, increases with increasing Na/Ca_{sw} values (and hence decreasing $[Ca^{2+}]_{sw}$) with a significant offset between the lower and the higher Na/Ca_{cc} conditions used in the experiments (Figure 1B; bootstrap analysis, $p<0.05$). Also clear from these figures is that the partitioning coefficients does not remain constant with changing $[Ca^{2+}]_{sw}$, for both K and Na incorporation.

3.2 Experiment $[Ca^{2+}]_{sw}$ and $[K^{+}]_{sw}$

When varying both $[K^{+}]_{sw}$ and $[Ca^{2+}]_{sw}$ and keeping K/Ca_{sw} constant, K/Ca_{cc} increases linearly (Figure 2A). In the same cultured foraminifera, the Na/Ca_{cc} also increases significantly with higher seawater Na/Ca ratios (Figure 2B). When directly comparing these results with those from the first experimental set, it is clear that K-incorporation depends not on $[Ca^{2+}]$ but does respond when both $[K^{+}]$ and $[Ca^{2+}]$ are varied (Figure 2C). Na-incorporation, on the other hand, does react to changes in $[Ca^{2+}]_{sw}$, irrespective of changes in $[K^{+}]$ (Figure 2, Supplementary Table S8).

TABLE 4 El/Ca in the seawater after mixing with North Sea water and measured with SF-ICPMS in the $[Ca^{2+}]_{sw}$ experiment.

K/Ca	B/Ca	Na/Ca	Mg/Ca	Sr/Ca	S/Ca
(mol/mol)	(mol/mol)	(mol/mol)	(mol/mol)	(mol/mol)	(mol/mol)
1.01	0.05	56.78	6.31	12.07	3.31
1.05	0.05	58.52	6.53	12.37	3.35
0.56	0.03	30.66	3.41	6.66	1.79
0.56	0.03	30.66	3.41	6.66	1.79
0.54	0.03	30.55	3.43	6.64	1.78
0.56	0.03	30.68	3.43	6.62	1.80
0.49	0.02	26.11	2.99	5.85	1.58
0.49	0.03	26.61	3.02	5.89	1.58
0.49	0.03	26.61	3.02	5.89	1.58
0.44	0.02	23.79	2.73	5.33	1.45
0.44	0.02	23.80	2.72	5.38	1.44

TABLE 5 El/Ca in the seawater (mean +/- SD) after mixing with North Sea water and measured with SF-ICPMS in the $[Ca^{2+}]_{sw}$ and $[K^{+}]_{sw}$ experiment.

K/Ca (mol/mol)	B/Ca (mol/mol)	Na/Ca (mol/mol)	Mg/Ca (mol/mol)	Sr/Ca (mol/mol)	S/Ca (mol/mol)
0.86	0.05	67.22	6.44	11.43	3.44
0.88	0.05	66.80	6.48	11.69	3.40
0.86	0.05	67.47	6.45	11.55	3.35
0.86	0.05	67.47	6.45	11.55	3.35
0.86	0.04	47.62	5.28	9.33	2.76
0.88	0.04	47.65	5.26	9.52	2.79
0.88	0.04	47.65	5.26	9.52	2.79
0.88	0.04	47.61	5.24	9.40	2.81
0.86	0.04	40.22	4.45	8.03	2.36
0.89	0.04	40.80	4.52	8.09	2.34
0.83	0.04	40.69	4.51	8.05	2.35
0.86	0.03	33.10	3.35	6.09	1.76
0.91	0.03	33.26	3.38	6.16	1.73
0.91	0.03	33.26	3.38	6.16	1.73

3.3 Temperature experiment

Both K/Ca_{cc} and Na/Ca_{cc} of the cultured *A. lessonii* do not show consistent changes with varying temperature (Figures 3A, B), although the average K/Ca_{cc} was slightly higher at the lowest temperature (0.21 +/- 0.06 mmol/mol) (Supplementary Table S9). Variability observed for K/Ca_{cc} was higher than that of Na/Ca_{cc} but does not change consistently between the four temperature conditions using a regression analysis giving for both plots (Figure 3) p-values > 0.05.

3.4 K/Ca_{cc} versus Na/Ca_{cc}

Combining all data, Na/Ca_{cc} and K/Ca_{cc} of the cultured *A. lessonii* do not correlate with each other (Figure 4) when varying temperature or changing only $[Ca^{2+}]$. However, when considering the experiments in which both $[K^{+}]$ and $[Ca^{2+}]$ varied with a constant K/Ca_{sw} K- and Na-incorporation were negatively correlated, this correlation is due to the difference in $[Ca^{2+}]_{sw}$ that changes the Na incorporated, and not because of a Na^{+} and K^{+} compete for the same spot in the calcite crystal lattice during incorporation.

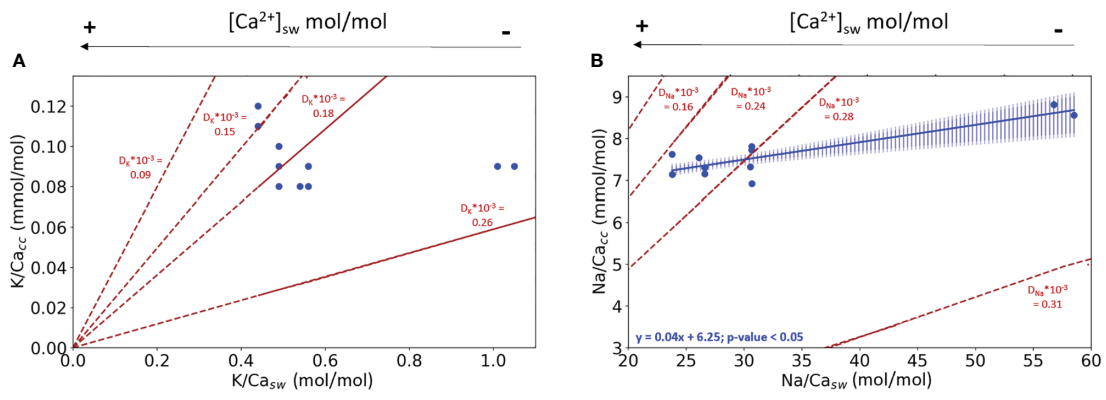

FIGURE 1
(A) K/Ca_{cc} in cultured *A. lessonii* versus K/Ca_{sw} from the experiment with varying $[Ca^{2+}]$, keeping $[K^{+}]$ constant; **(B)** Na/Ca_{cc} from the same specimens versus Na/Ca_{sw}, keeping $[Na^{+}]_{sw}$ constant. Blue dots are the measured El/Ca_{cc}, the blue line in **(B)** indicates the linear correlation between Na/Ca in the culture media and the foraminiferal calcite. The shading surrounding this correlation represents the confidence interval (0.99 darker blue and 0.95 lighter shade of blue) based on a bootstrap analysis (1000 iterations). In both plots, lines with constant partition coefficients (D_K and D_{Na}) are plotted (dashed red lines) to facilitate interpretation of the observed changes in the relative incorporation of elements. The standard deviation for every replicate using the internal error from the SF-ICPMS was very small making it imperceptible in the plotted data (Supplementary Table S10).

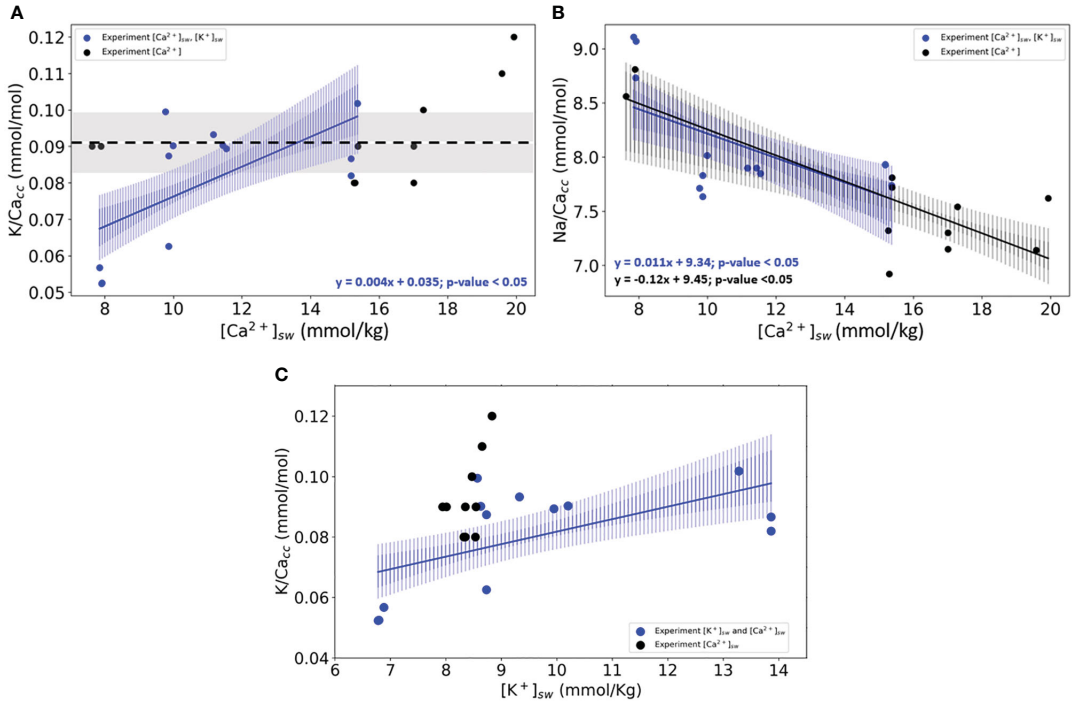

FIGURE 2
(A) K/Ca$_{cc}$ in cultured specimens of **(A)** lessonii as a function of the culture's media [Ca^{2+}]$_{sw}$. **(B)** Na/Ca$_{cc}$ of the same specimens versus [Ca^{2+}]$_{sw}$. **(C)** K/Ca$_{cc}$ versus [K^{+}]$_{sw}$. In panels **(A, B)**, blue dots and lines are the results from the experiment in which both [Ca^{2+}] and [K^{+}] were varied. In black are the results from the experiments (Figure 1) where only [Ca^{2+}] was varied. Lines indicate the linear correlations (both with p-values<0.05) based on the bootstrap analysis, for which the confidence intervals are added as envelopes (0.99 darker blue and 0.95 lighter shade of blue). The standard deviation for every replicate using the internal error from the SF-ICPMS was very small making it imperceptible in the plotted data (Supplementary Table S10). Panel **(C)** shows the same statistical analysis for both experiments axys X changes, and instead of [Ca^{2+}]$_{sw}$, the results are plotted against [K^{+}]$_{sw}$.

4 Discussion

4.1 Consistency of the data, the effect of temperature and the proxy value of K/Ca and Na/Ca

The K/Ca$_{cc}$ values obtained for *A. lessonii* in all experiments ranged between 0.05 and 0.26 mmol/mol (Supplementary Table S9), without a noticeable effect of temperature (Figure 3A). The total amount of calcite added per treatment, either when changing [Ca^{2+}]$_{sw}$ or temperature did not correlate to K/Ca$_{cc}$ (Supplementary Figures S2 and S3, respectively). This means that the average K/Ca$_{cc}$ does not depend on growth rate and changes therein reflect directly the effects of temperature or seawater chemistry. The relatively high variability observed for K/Ca$_{cc}$ at the lowest temperature (Figure 3A) may be explained by uneven growth of foraminiferal specimens across temperatures. At the lowest temperature (18°C) on average fewer chambers were added per specimen than at higher temperatures (Supplementary Tables S13, S14). As this increases the relative contribution of pre-existing carbonate (i.e. from before the actual

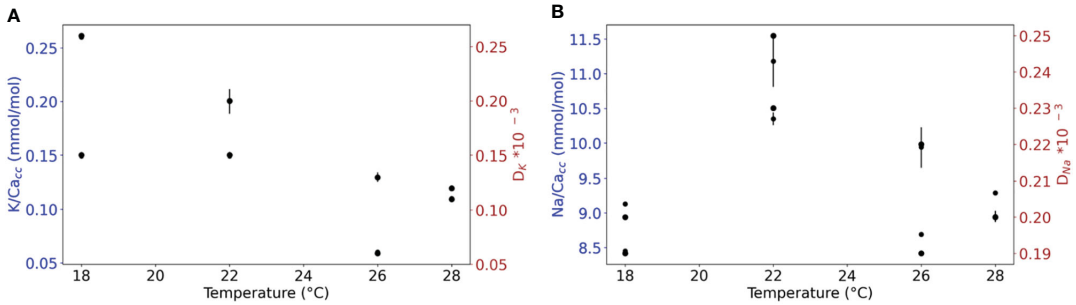

FIGURE 3
(A) K/Ca$_{cc}$ and D$_K$ versus temperature. **(B)** Na/Ca$_{cc}$ and D$_{Na}$ versus temperature. The RSD for every replicate using the internal error from the SF-ICPMS are plotted with black lines (Supplementary Table S11). For either of the elements, a regression analysis shows no significant correlation between El/Ca$_{cc}$ and temperature (p< 0.05).

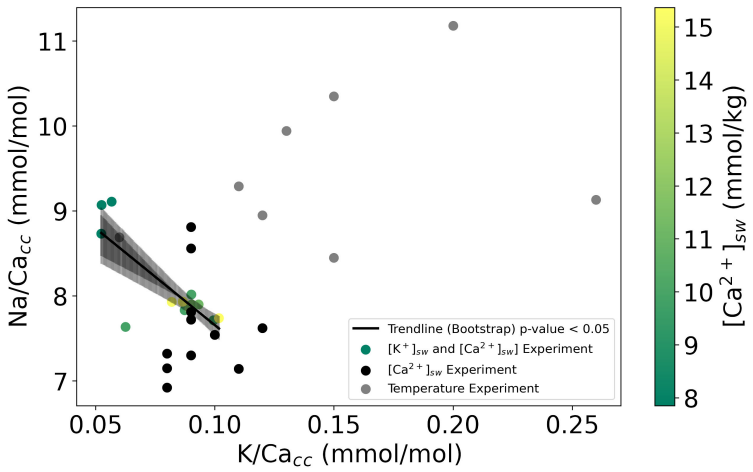

FIGURE 4
Na/Ca$_{cc}$ versus K/Ca$_{cc}$ for the three experiments. Solid lines indicate the linear correlations (both with p-values<0.05) based on the bootstrap analysis, for which the confidence intervals (0.99 darker black and 0.95 lighter black) are added as shading. The color-scale in experiment [K$^+$]$_{sw}$ and [Ca^{2+}]$_{sw}$ shows the [Ca^{2+}]$_{sw}$ from green (higher [Ca^{2+}]$_{sw}$ to yellow (lower [Ca^{2+}]$_{sw}$).

experiment) this would add to the variability in the data. The contribution of chambers formed before start of the incubation may have also biased average K/Ca and Na/Ca values, with a larger impact for specimens that added less chambers during the experiment.

The potassium-to-calcium ratio in *A. lessonii* (0.10 – 0.26; Figure 1A) overlap with those established for inorganically precipitated calcites (Ishikawa and Ichikuni, 1984); K/Ca$_{cc}$: 0.01-0.1 and (Okumura and Kitano, 1986). Still, it is challenging to compare these coefficients directly as the overall composition of the culture media (artificial seawater) in our experiment differed considerably from that used in the inorganic precipitation experiments, which only contained few elements.

The only other report on foraminiferal K/Ca$_{cc}$ indicated similar ratios for the benthic *O. ammonoides* (0.12-0.30; Nambiar et al., 2023), as those reported here (Supplementary Tables S10, S11). The small offset in the average ratios could be caused by differences in culturing conditions or by inter-species differences in El/Ca values as observed for many elements (Bentov and Erez, 2006). Although we used a slightly different analytical approach (higher mass resolution) this is unlikely to have resulted in appreciable offsets between studies (methods and Supplementary Figure S1).

The average and range in Na/Ca$_{cc}$ of cultured specimens (Supplementary Tables S9-S11) are similar to ratios reported previously for this genus (Geerken et al., 2019; Levi et al., 2019). The Na/Ca$_{cc}$ in specimens cultured from 18 to 28°C vary between 8.8 and 11 mmol/mol (Supplementary Table S9) and are not correlated to temperature, which is in line with previous reports (Allen et al., 2016; Geerken et al., 2019). In the experiment with temperatures ranging from 18 to 28°C (Supplementary Table S9, Figure 3), K/Ca$_{cc}$ values show no significant differences between different temperature conditions, agreeing with the field data from (Nambiar et al., 2023). The absence of an effect of temperature on either K/Ca$_{cc}$ or Na/Ca$_{cc}$ underscores the potential for applying these ratios in reconstructing (long-term) changes in seawater composition.

Element/Ca ratios vary greatly between genera and species and generally show elevated ratios for multiple elements in the same taxon (Evans et al., 2015; Mewes et al., 2015a; Hauzer et al., 2018; Van Dijk et al., 2019; Dämmer et al., 2021). The magnitude by which the different elements vary among species, however, is not constant. For K/Ca$_{cc}$, ratios are on average slightly higher in *O. ammonoides* (Nambiar et al., 2023) than in *A. lessonii*. (Figures 1–3), which is in line with the observed difference in Mg/Ca$_{cc}$ between these species. Mg/Ca$_{cc}$ is approximately 140 mmol/mol for *O. ammonoides* (Evans et al., 2015) and varies between 25 and 30 mmol/mol for *Amphistegina* sp (De Nooijer et al., 2017). Similarly, Na/Ca$_{cc}$ in *A. lessonii* varies between 7 and 11 mmol/mol (Figures 1B, 2B and 3B; (Van Dijk et al., 2017c) and around 20 - 25 mmol/mol in *O. ammonoides* (Hauzer et al., 2018). In contrast, interspecific differences in Sr/Ca are relatively small [~1.7 versus ~2.6 mmol/mol for *Amphistegina* and *Operculina*, respectively; (Geerken et al., 2019; Hauzer et al., 2021)], but still, as for the other elements, they are all higher in *Operculina* than in *Amphistegina*. The consistent offsets, albeit with different magnitudes, suggest that differences in biomineralization pathways, e.g. Ca^{2+} pumping rate, between genera and species are reflected in element incorporation (De Nooijer et al., 2023). These inter-specific differences in element uptake are consistent with the reported relatively low K/Ca$_{cc}$ values for planktonic foraminiferal species [0.06-0.12 mmol/mol; (Li et al., 2021)], as these are also known to have low values for Mg/Ca (1-5 mmol/mol; (Nürnberg et al., 1996; Anand et al., 2003) compared to *Amphistegina* and *O. ammonoides* (Figure 5). More recently (Nambiar et al., 2023), however, showed ratios (about 0.25 mmol/mol) for *G. ruber* comparable to those reported here and for *A. lessonii* (Nambiar et al., 2023).

Recently, foraminiferal Na/Ca$_{cc}$ was suggested to act as a proxy for seawater [Ca^{2+}] (Hauzer et al., 2018) in addition to its potential

to reconstruct salinity (Wit et al., 2013; Mezger et al., 2019). Our results confirm that foraminiferal Na/Ca_{cc} is responsive to changes in $[Ca^{2+}]$ (Figures 1, 2) and the salinity range in Tables 2 and 4 in this case, show no significant effect in the Na or K incorporation, due to $[Ca^{2+}]_{sw}$ differences act as the main driver where they are incorporated. Here we show that foraminiferal K/Ca_{cc} may be used to reconstruct past seawater $[K^+]$, adding to our understanding of the long-term cycling of the oceans' major ions as was suggested by Nambiar et al., 2023). For seawater potassium concentrations, such a reconstruction may indicate rates of continental weathering (Kronberg, 1985; Sun et al., 2016) and indirectly, may reflect long-term changes in total alkalinity. Alternatively, seawater potassium concentrations may reflect rates of oceanic crust formation due to the difference between seawater and the mantle (Bloch and Bischoff, 1979).

4.2 Incorporation of potassium in foraminiferal calcite

K/Ca_{cc} in *A. lessonii* does not vary consistently with $[Ca^{2+}]_{sw}$ (and hence K/Ca_{sw}; Figure 1A). Conversely, K/Ca_{cc} increases when $[Ca^{2+}]$ and $[K^+]$ both increase (and K/Ca_{sw} remains similar; Figure 2A). The absence of an effect of seawater Ca^{2+} and a positive effect of the combined K^+ and Ca^{2+} elevation suggests that seawater $[K^+]$ is the main driver of K-incorporation into foraminiferal calcite (Figure 2C), whereas it is not affected by $[Ca^{2+}]$. This resembles results from inorganic experiments in which K-incorporation was found to depend on solution $[K^+]$ (Ishikawa and Ichikuni, 1984; Okumura and Kitano, 1986). Such a dependency is hence fundamentally different from that observed for many divalent cations like Ba^{2+}, Mn^{2+}, Mg^{2+}, or Sr^{2+}, for which the concentration in seawater relative to $[Ca^{2+}]_{sw}$ directly translates into a calcitic El/Ca ratio (Okumura and Kitano, 1986; Alkhatib et al., 2022). Such an incorporation pattern is caused by the competition of these ions with Ca^{2+} for a place in the calcite crystal lattice: for the monovalent cation incorporation is not governed by competition with Ca^{2+}. However, incorporation of monovalent ions (Li^+, Na^+, K^+, etc.) may be affected by different processes such as crystal surface sorption, speciation, and crystal growth rate, which complicates a straightforward interpretation of the environmental controls on element partitioning during calcification. Most likely a combination of all these effects impacts the uptake of monovalent cations.

More precisely, incorporation of an element into foraminiferal calcite is at least a two-step process (Figure 6; Bentov and Erez, 2006). There is the biological activity that configures the size and shape of the calcifying space and sets the composition of the fluid from which $CaCO_3$ precipitates (Erez, 2003; Bentov and Erez, 2006; Bentov et al., 2009; De Nooijer et al., 2014). The exact controls are only partly characterized and may vary between species, but include selective ion transport (Nehrke et al., 2013; Toyofuku et al., 2017), pH manipulation (Bentov et al., 2009; De Nooijer et al., 2009; Glas et al., 2012) and production of organic templates (Branson et al., 2016; Tyszka et al., 2019). Secondly, there are various (physico-) chemical processes that operate within the calcifying space that determine how much of each ion in the fluid is incorporated into the shell. Relevant processes include Rayleigh fractionation (Elderfield et al., 1996; Evans et al., 2018), kinetics (Uchikawa and Zeebe, 2012; Devriendt et al., 2021), $CaCO_3$ phase-transformations (Gray and Evans, 2019), chemical speciation (Van Dijk et al., 2017b) and configuration of ions within the crystal lattice (Branson et al., 2015) (Figure 6). For K one would expect a different trend as K uptake does not depend on Ca concentration (Figures 1, 2), but should reflect K concentration at the site of calcification (SOC). Nambiar et al. (2023), however, suggested an effect of $[Ca^{2+}]$ on K-incorporation, as was observed in corals (Ram and Erez, 2021). The within chamber wall K profiles of Geerken

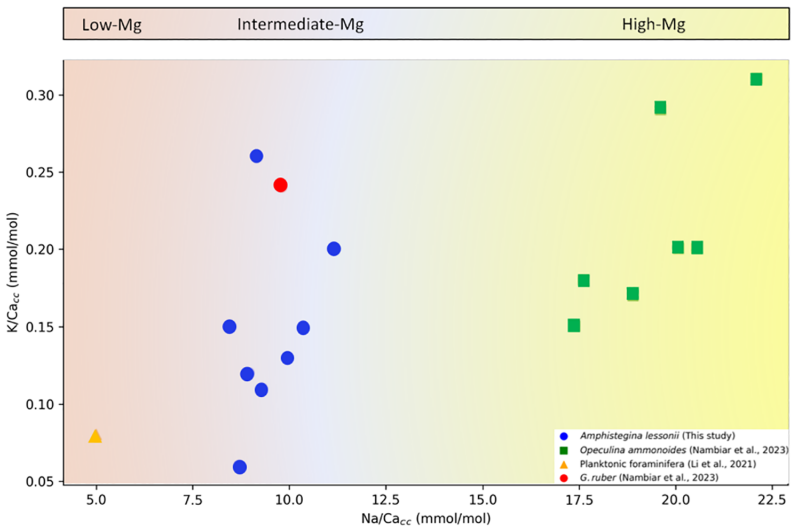

FIGURE 5
K/Ca_{cc} versus Na/Ca_{cc} for groups with different average Mg/Ca_{cc}. Low-Mg/Ca (<40 mmol/mol), Intermediate-Mg/Ca (40 – 100 mmol/mol) and High-Mg/Ca (>100 mmol/mol) (Blackmon and Todd, 1959).

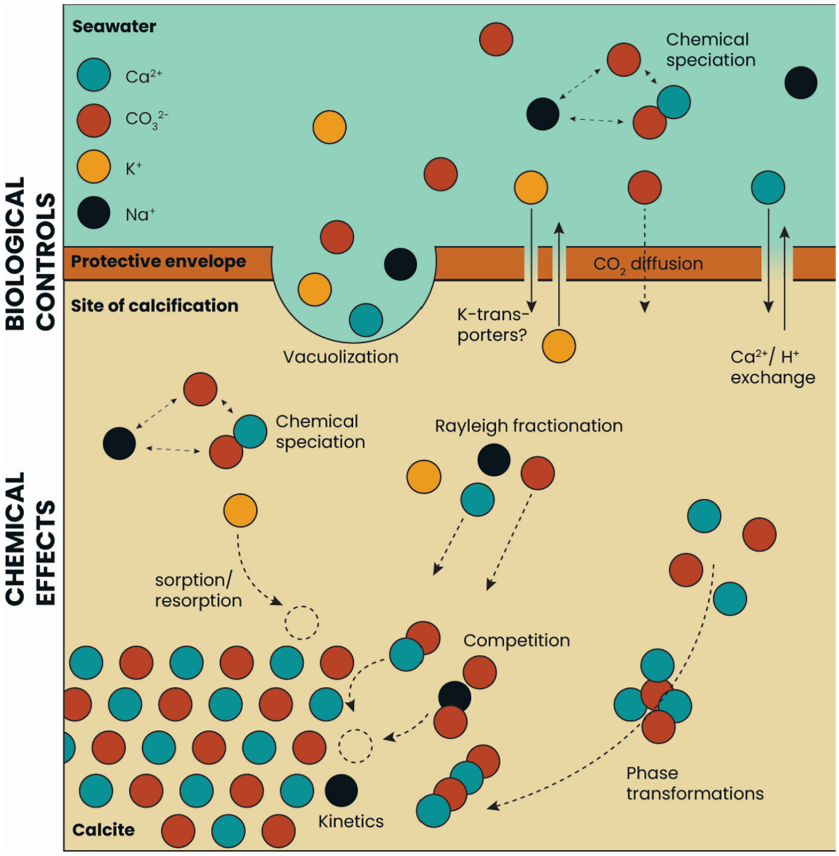

FIGURE 6
Simplified calcification scheme for rotaliid foraminifera. Biological and chemical processes at the site of calcification are presented, with a focus on the differences between Na^+ and K^+ incorporation into the calcite.

et al. (2019) actually show a gradual increase towards the end of a low concentration band (i.e. towards the outer surface of the shell wall). Other studies, however, have shown a tight correlation between the alternating high- and low-K bands with those of other elements (e.g. Mg) in *Amphistegina lobifera* and *A. lessonii* (Levi et al., 2019), which hints at a similarity in their incorporation dynamics. In addition, phosphorus is present in relatively narrow bands, similar to those of potassium, which hints to a coupling in their incorporation mode.

The observed relation between a solution's El/Ca and the calcitic El/Ca is likely affected by both biological and 'chemical' steps during foraminiferal biomineralization. Transport of K-ions over a cell membrane is not likely facilitated by Ca-transporters, while an occasional Mg-ion may well pass a Ca-pump (e.g. Dudev and Lim, 2013). For the precipitation dynamics, the monovalent K ion may occupy the interstitial sites in the calcite lattice (Ishikawa and Ichikuni, 1984), in the organic phases, or be incorporated in amorphous K_2CO_3 (Li et al., 2021). It is likely that all or most of these processes together determine the eventual K/Ca_{cc} and Na/Ca_{cc} of the foraminiferal calcite (Figure 6).

Our results show that the seawater's $[K^+]$, rather than $[Ca^{2+}]$ is the main driver for K partitioning. This is in line with free K^+ being the main species present in seawater (Johnson and Pytkowicz, 1979), with K sorption at the crystal lattice being the primary way K is incorporated. It should be noted however, that the chemical speciation of potassium in the calcifying fluid may differ from that in seawater due to the foraminfer's biological control on that fluid's composition (Erez, 2003; Bentov and Erez, 2006; De Nooijer et al., 2014) In contrast, for Na-incorporation, our results, and the dependence of Na/Ca_{cc} on the solution's Na/Ca (Figure 2) suggest that sodium and calcium compete for the same place in the crystal lattice. This would imply that sodium incorporation substitutes by replacement of two Na ions for one Ca ion (Devriendt et al., 2021) in the calcite and form a quadratic relationship. Since we do not observe this, alternatives including lattice vacancies can be filled by other divalent elements such as Mg^{2+} or Sr^{2+} may also play a role in the calcite's El/Ca.

Although our results cannot exclude that K-incorporation at interstitial sites is responsible for a (minor) part of the foraminiferal K/Ca_{cc}, (Nambiar et al., 2023) showed an increasing K/Ca_{cc} with K/Ca_{sw} for *O. ammonoides* with similar conditions as the one show in the $[Ca^{2+}]_{sw}$ experiment from this study. This may indicate that the crystallographic orientation of potassium differs between foraminiferal species but may also indicate that biological uptake of potassium ions varies among species. The presence of specialized K-transporters in addition to Ca-transporters (Toyofuku et al., 2017) promoting K-incorporation into the shell would imply an advantage of higher K/Ca, which is not immediately apparent. Alternatively,

inward K-transport into the site of calcification may result from the organismal need to accompany inward transport of a negatively charged ions and/or to counter the outward transport of another positively charged ion in the calcifying fluid. Major anions are SO_4^{2-}, Cl^-, but both do not seem to be enriched in foraminiferal calcite compared to seawater and inorganically precipitated calcite (Kontrec et al., 2004; Van Dijk et al., 2017b; Roepert et al., 2020). Cations that are pumped out during calcification include H^+ (Glas et al., 2012) and are hypothesized to be coupled to an inward Ca^{2+} pumping (De Nooijer et al., 2017). The outward pumping of H^+ may sometimes also affect Na^+- and/or K^+-transport. With it is considerably larger ionic radius K^+ (152 pm) is less likely to be 'accidentally' transported through a transporter designed for H^+ (ionic radius of 66 pm) compared to Na^+ (116 pm).

When pumping of K^+ by the foraminifer is somehow affecting the K/Ca at the site of calcification incorporation of potassium in foraminiferal calcite may be impacted by an intracellular role of $[K^+]$. Potassium is often used as an agent to regulate osmosis and is found in cells at $[K^+]/[Na^+]$ ratios in the 0.1–1.0 range (Dibrova et al., 2015). Sodium ions form relatively strong hydrogen bonds, therefore attract water, and disrupt intracellular processes. For this reason, many (marine) cells have $[K^+]/[Na^+]$ antiporters (Nakamura et al., 1992; Shabala et al., 2009). Such a transport mechanism may (partly) explain the observed difference in Na/Ca and K/Ca in foraminifera when compared to inorganically precipitated calcite. The partition coefficients for potassium are relatively similar between inorganic and foraminifera calcite, while the partition coefficients for sodium are much lower in inorganically precipitated calcite (compared to foraminiferal shells). Overall, this makes K uptake in foraminiferal calcite a much more reliable proxy for reconstructing past sea water major ion composition.

5 Conclusions

Potassium in the shells of the benthic foraminifera *A. lessonii* was found at concentrations of 0.05-0.26 mmol/mol Ca. The incorporation of potassium was found not to depend on temperature, nor on seawater $[Ca^{2+}]$. This also implies a fundamental difference in uptake compared to that of Na, the other major monovalent cation in sea water. Experiments in which $[K^+]$ and $[Ca^{2+}]$ varied simultaneously, resulted in a change in the foraminifer's K/Ca, indicating the direct and unique effect of seawater $[K^+]$ on potassium partitioning during calcification. This implies that fossil foraminiferal K/Ca may directly reflect changes in seawater $[K^+]$, without being affected by changes in $[Ca^{2+}]$. We did find an effect of $[Ca^{2+}]_{sw}$ on Na- incorporation, highlighting the potential to use these two elements combined to reconstruct both seawater potassium and calcium concentrations.

Data availability statement

The original contributions presented in the study are included in the article/Supplementary Material. Further inquiries can be directed to the corresponding authors.

Ethics statement

The manuscript presents research on animals that do not require ethical approval for their study.

Author contributions

LP: Conceptualization, Data curation, Formal Analysis, Investigation, Writing – original draft, Writing – review & editing. LD: Conceptualization, Formal Analysis, Methodology, Project administration, Supervision, Writing – original draft, Writing – review & editing. WB: Data curation, Methodology, Writing – original draft, Writing – review & editing. G-JR: Conceptualization, Formal Analysis, Funding acquisition, Investigation, Methodology, Project administration, Supervision, Writing – original draft, Writing – review & editing.

Funding

The author(s) declare financial support was received for the research, authorship, and/or publication of this article. This work was carried out under the program of the Netherlands Earth System Science Centre (NESSC), financially supported by the Ministry of Education Culture and Science (OCW).

Acknowledgments

To Patrick Laan for the SF-ICP-MS analyses for the seawater, and to Karel Baker for the DIC and TA analyses. To Joji Uchikawa for the helpful discussion during the experimental work.

Conflict of interest

The authors declare that the research was conducted in the absence of any commercial or financial relationships that could be construed as a potential conflict of interest.

Publisher's note

Supplementary material

The Supplementary Material for this article can be found online at: https://www.frontiersin.org/articles/10.3389/fmars.2024.1385347/full#supplementary-material

References

Alkhatib, M., Qutob, M., Alkhatib, S., and Eisenhauer, A. (2022). Influence of precipitation rate and temperature on the partitioning of magnesium and strontium in calcite overgrowths. *Chem. Geol.* 599, 120841. doi: 10.1016/j.chemgeo.2022.120841

Allen, K. A., Eggins, S. M., Haynes, L. L., Rosenthal, Y., and Yu, J. (2016). Trace element proxies for surface ocean conditions: A synthesis of culture calibrations with planktic foraminifera. *Geochim. Cosmochim. Acta* 193, 197–221. doi: 10.1016/j.gca.2016.08.015

Anand, P., Elderfield, H., and Conte, M. H. (2003). Calibration of Mg/Ca thermometry in planktonic foraminifera from a sediment trap time series. *Paleoceanography* 18, 1050. doi: 10.1029/2002pa000846

Barker, S., Greaves, M., and Elderfield, H. (2003). A study of cleaning procedures used for foraminiferal Mg/Ca paleothermometry. *Geochem. Geophys. Geosyst.* 4, 1–20. doi: 10.1016/j.quascirev.2004.07.016

Bentov, S., and Erez, J. (2006). Impact of biomineralization processes on the Mg content of foraminiferal shells: A biological perspective. *Geochem. Geophys. Geosyst.* 7, Q01P08. doi: 10.1029/2005GC001015

Bentov, S., Brownlee, C., and Erez, J. (2009). The role of seawater endocytosis in the biomineralization process in calcareous foraminifera. *Proc. Nat. Acad. Sci.* 106 (51), 21500–21504. doi: 10.1073/pnas.0906636106

Blackmon, P. D., and Todd, R. (1959). Mineralogy of some foraminifera as related to their classification and ecology. *J. Paleontol.* 33, 1–15. Available at: http://www.jstor.org/stable/1300802

Bloch, S., and Bischoff, J. L. (1979). The effect of low-temperature alteration of basalt on the oceanic budget of potassium. *Geology* 7, 193–196. https://doi.org/10.1130/0091-7613(1979)7<193:TEOLAO>2.0.CO;2

Boer, W., Weber, M., Mertz-Kraus, R., Hönisch, B., Bijma, J., Raitzsch, M., et al. (2022). New calcium carbonate nano-particulate pressed powder pellet (NFHS-2-NP) for LA-ICP-OES, LA-(MC)-ICP-MS and µXRF. *Geostandards. Geoanalytical. Res.* 46, 411–432. doi: 10.1111/ggr.12425

Branson, O., Bonnin, E. A., Perea, D. E., and Gagnon, A. C. (2016). Nanometer-scale chemistry of a calcite biomineralization template: implications for skeletal composition and nucleation. *Proc. Natl. Acad. Sci. United. States America* 113, 12934–12939. doi: 10.1073/pnas.1522864113

Branson, O., Kaczmarek, K., Redfern, S. A. T., Misra, S., Langer, G., Tyliszczak, T., et al. (2015). The coordination and distribution of B in foraminiferal calcite. *Earth Planet. Sci. Lett.* 416, 67–72. doi: 10.1016/j.epsl.2015.02.006

Culkin, F., and Cox, R. A. (1966). Sodium, potassium, magnesium, calcium and strontium in sea water. *Deep. Sea. Res. Oceanographic. Abstracts.* 13, 789–804. doi: 10.1016/0011-7471(76)90905-0

Dämmer, L. K., Van Dijk, I., Nooijer, L. J., van der Wagt, B., Wilckens, F. W., Zoetemelk, B., et al. (2021). Temperature impact on magnesium isotope fractionation in cultured foraminifera. *Front. Earth Sci.* 9. doi: 10.3389/feart.2021.642256

De Goeyse, S., Webb, A. E., Reichart, G.-J., and De Nooijer, L. J. (2021). Carbonic anhydrase is involved in calcification by the benthic foraminifer *Amphistegina lessonii*. *Biogeosciences* 18, 393–401. doi: 10.5194/bg-18-393-2021

De Nooijer, L. J., Hathorne, E. C., Reichart, G. J., Langer, G., and Bijma, J. (2014). Biomineralization in perforate foraminifera. *Earth-Sci. Rev.* 135, 48–58. doi: 10.1016/j.earscirev.2014.03.013

De Nooijer, L. J., Pacho Sampedro, L., Jorissen, F. J., Pawlowski, J., Rosenthal, Y., Dissard, D., et al. (2023). 500 million years of foraminiferal calcification. *Earth-Sci. Rev.* 243, 104484. doi: 10.1016/j.earscirev.2023.104484

De Nooijer, L. J., Toyofuku, T., and Kitazato, H. (2009). Foraminifera promote calcification by elevating their intracellular pH. *Proc. Natl. Acad. Sci. United. States America* 106, 15374–15378. doi: 10.1073/pnas.0904306106

De Nooijer, L. J., Van Dijk, I., Toyofuku, T., and Reichart, G. J. (2017). The impacts of seawater mg/ca and temperature on element incorporation in benthic foraminiferal calcite. *Geochem. Geophys. Geosyst.* 18, 3617–3630. doi: 10.1002/2017GC007183

de Villiers, S., Greaves, M., and Elderfield, H. (2002). 'An intensity ratio calibration method for the accurate determination of Mg/Ca and Sr/Ca of marine carbonates by ICP-AES'. *Geochem. Geophys. Geosyst.* 3, 1001. doi: 10.1029/2001gc000169

Devriendt, L. S., Mezguer, E. M., Olsen, E. K., Watkins, J. M., Kaczmarek, K., Nehrke, G., et al. (2021). Sodium incorporation into inorganic $CaCO_3$ and implications for biogenic carbonates. *Geochim. Cosmochim. Acta* 314, 294–312. doi: 10.1016/j.gca.2021.07.024

Dibrova, D. V., Galperin, M. Y., Koonin, E. V., and Mulkidjanian, A. Y. (2015). Ancient systems of sodium/potassium homeostasis as predecessors of membrane bioenergetics. *Biochem. (Moscow).* 80, 495–516. doi: 10.1134/S0006297915050016

Dudev, T., and Lim, C. (2013). Importance of metal hydration on the selectivity of Mg^{2+} versus Ca^{2+} in magnesium ion channels. *J. Am. Chem. Soc.* 135, 17200–17208. doi: 10.1021/ja4087769

Dueñas-Bohórquez, A., Raitzsch, M., De Nooijer, L. J., and Reichart, G. J. (2011). Independent impacts of calcium and carbonate ion concentration on Mg and Sr incorporation in cultured benthic foraminifera. *Mar. Micropaleontol.* 81, 122–130. doi: 10.1016/j.marmicro.2011.08.002

Duxbury, A. C., Mackenzie, F. T., and Byrne, R. H. (2024). "seawater". Encyclopedia britannica. Available online at: https://www.britannica.com/science/seawater (Accessed 9 February 2024).

Elderfield, H., Bertram, C. J., and Erez, J. (1996). A biomineralization model for the incorporation of trace elements into foraminiferal calcium carbonate. *Earth Planet. Sci. Lett.* 142, 409–423. doi: 10.1016/0012-821x(96)00105-7

Erez, J. (2003). The source of ions for biomineralization in foraminifera and their implications for paleoceanographic proxies. *Rev. Mineral. Geochem.* 54, 115–149. https://doi.org/10.2113/0540115

Ernst, S., Janse, M., Renema, W., Kouwenhoven, T., Goudeau, M.-L., and Reichart, G. J. (2011). Benthic foraminifera in a large Indo-Pacific coral reef aquarium. *J. Foraminiferal. Res.* 41, 101–113. doi: 10.2113/gsjfr.41.2.101

Evans, D., Erez, J., Oron, S., and Müller, W. (2015). Mg/Ca-temperature and seawater-test chemistry relationships in the shallow-dwelling large benthic foraminifera *Operculina ammonoides*. *Geochim. Cosmochim. Acta* 148, 325–342. doi: 10.1016/j.gca.2014.09.039

Evans, D., Müller, W., and Erez, J. (2018). Assessing foraminifera biomineralisation models through trace element data of cultures under variable seawater chemistry. *Geochim. Cosmochim. Acta* 236, 198–217. doi: 10.1016/j.gca.2018.02.048

Fantle, M. S., and DePaolo, D. J. (2005). Variations in the marine Ca cycle over the past 20 million years. *Earth Planet. Sci. Lett.* 237, 102–117. doi: 10.1016/j.epsl.2005.06.024

Fehrenbacher, J. S., Russell, A. D., Davis, C. V., Gagnon, A. C., Spero, H., Cliff, J. B., et al. (2017). Link between light-triggered Mg-banding and chamber formation in the planktic foraminifera *Neogloboquadrina dutertrei*. *Nat. Commun.* 8, 15441. doi: 10.1038/ncomms15441

Geerken, E., De Nooijer, L. J., Roepert, A., Polerecky, L., King, H. E., and Reichart, G. J. (2019). Element banding and organic linings within chamber walls of two benthic foraminifera. *Sci. Rep.* 9, 3598. doi: 10.1038/s41598-019-40298-y

Geerken, E., De Nooijer, L. J., Van Dijk, I., and Reichart, G. J. (2018). Impact of salinity on element incorporation in two benthic foraminiferal species with contrasting magnesium contents. *Biogeosciences* 15, 2205–2218. doi: 10.5194/bg-15-2205-2018

Glas, M. S., Langer, G., and Keul, N. (2012). Calcification acidifies the microenvironment of a benthic foraminifer (*Ammonia* sp.). *J. Exp. Mar. Biol. Ecol.*, 424-425, 424–425. doi: 10.1016/j.jembe.2012.05.006

Gray, W. R., and Evans, D. (2019). Nonthermal influences on mg/ca in planktonic foraminifera: A review of culture studies and application to the last glacial maximum. *Paleoceanogr. Paleoclimatol.* 34, 306–315. doi: 10.1029/2018PA003517

Hardie, L. A. (1996). Secular variation in seawater chemistry: An explanation for the coupled secular variation in the mineralogies of marine limestones and potash evaporites over the past 600 m.y. Available online at: http://pubs.geoscienceworld.org/gsa/geology/article-pdf/24/3/279/3516554/i0091-7613-24-3-279.pdf.

Hauzer, H., Evans, D., Müller, W., Rosenthal, Y., and Erez, J. (2018). Calibration of Na partitioning in the calcitic foraminifer *Operculina ammonoides* under variable Ca concentration: Toward reconstructing past seawater composition. *Earth Planet. Sci. Lett.* 497, 80–91. doi: 10.1016/j.epsl.2018.06.004

Hauzer, H., Evans, D., Müller, W., Rosenthal, Y., and Erez, J. (2021). Salinity effect on trace element incorporation in cultured shells of the large benthic foraminifer *operculina ammonoides*. *Paleoceanogr. Paleoclimatol.* 36, e2021PA004218. doi: 10.1029/2021PA004218

Holland, K., Branson, O., Haynes, L. L., Hönisch, B., Allen, K. A., Russell, A. D., et al. (2020). Constraining multiple controls on planktic foraminifera Mg/Ca. *Geochim. Cosmochim. Acta* 273, 116–136. doi: 10.1016/j.gca.2020.01.015

Horibe, Y., Endo, K., and Tsubota, H. (1974). Calcium in the South Pacific, and its correlation with carbonate alkalinity. *Earth Planet. Sci. Lett.* 23, 136–140. doi: 10.1016/0012-821X(74)90040-5

Horita, J., Zimmermann, H., and Holland, H. D. (2002). Chemical evolution of seawater during the Phanerozoic: Implications from the record of marine evaporites. *Geochim. Cosmochim. Acta* 66, 3733–3756. doi: 10.1016/S0016-7037(01)00884-5

Humphreys, M. P., Lewis, E. R., Sharp, J. D., and Pierrot, D. (2022). PyCO2SYS v1.8: Marine carbonate system calculations in Python. *Geosci. Model. Dev.* 15, 15–43. doi: 10.5194/gmd-15-15-2022

Ishikawa, M., and Ichikuni, M. (1984). Uptake of sodium and potassium by calcite. *Chem. Geol.* 42, 137–146. doi: 10.1016/0009-2541(84)90010-X

Johnson, K. S., and Pytkowicz, R. M. (1979). Ion association of chloride and sulphate with sodium, potassium, magnesium and calcium in seawater at 25°C. *Mar. Chem.* 8, 87–93. doi: 10.1016/0304-4203(79)90034-3

Kester, D. R. (1967). Preparation of artificial seawater 1. *Limnol. Oceanogr.* 12, 176–179. doi: 10.4319/lo.1967.12.1.0176

Kontrec, J., Kralj, D., Brecevic, L., Falini, G., Fermani, S., Noethig-Laslo, V., et al. (2004). Incorporation of inorganic anions in calcite. *Eur. J. Inorganic. Chem.* 23, 4579–4585. doi: 10.1002/ejic.200400268

Kronberg, B. I. (1985). Weathering dynamics and geosphere mixing with reference to the potassium cycle. *Phys. Earth Planet. Interiors.* 41, 125–132. doi: 10.1016/0031-9201(85)90027-5

Kunioka, D., Toyofuku, T., and Ujiie, Y. (2006). Microdistribution of Mg/Ca, Sr/Ca, and Ba/Ca ratios in *Pulleniatina obliquiloculata* test by using a NanoSIMS: Implication for the vital effect mechanism. *Geochem. Geophys. Geosyst.* 7, Q12P20. doi: 10.1029/2006GC001280

Lea, D. W. (2003). "Trace elements in foraminiferal calcite," in *Modern foraminifera*. Ed. B. K. Sen Gupta (Springer Netherlands, Dordrecht), 259–277. doi: 10.1007/0-306-48104-9_15

Lécuyer, C. (2016). Seawater Residence times of some elements of geochemical interest and the salinity of the oceans. *Bull. la Soc. Geol. France.* 187, 245–260. doi: 10.2113/gssgfbull.187.6.245

Levi, A., Müller, W., and Erez, J. (2019). Intrashell variability of trace elements in benthic foraminifera grown under high CO_2 levels. *Front. Earth Sci.* 7. doi: 10.3389/feart.2019.00247

Li, W., Liu, X. M., Wang, K., Fodrie, F. J., Yoshimura, T., and Hu, Y. F. (2021). Potassium phases and isotopic composition in modern marine biogenic carbonates. *Geochim. Cosmochim. Acta* 304, 364–380. doi: 10.1016/j.gca.2021.04.018

Mewes, A., Langer, G., Thoms, S., Nehrke, G., Reichart, G. J., De Nooijer, L. J., and Bijm, J.. (2015a). 'Impact of seawater [Ca2+] on the calcification and calcite Mg/Ca of Amphistegina lessonii' *Biogeosciences*, 12(7), 2153–2162. doi: 10.5194/bg-12-2153-2015

Mewes, A., Langer, G., Reichart, G. J., De Nooijer, L. G., Nehrke, G., and Bijma, J.. (2015b). 'The impact of Mg contents on Sr partitioning in benthic foraminifers' *Chemical Geology*, 412, pp. 92–98. doi: 10.1016/j.chemgeo.2015.06.026

Mezger, E. M., De Nooijer, L. J., Bertlich, J., Bijma, J., Nürnberg, D., and Reichart, G. J. (2019). Planktonic foraminiferal spine versus shell carbonate Na incorporation in relation to salinity. *Biogeosciences* 16, 1147–1165. doi: 10.5194/bg-16-1147-2019

Mezger, E. M., De Nooijer, L. J., Boer, W., Brummer, G. J. A., and Reichart, G. J. (2016). Salinity controls on Na incorporation in Red Sea planktonic foraminifera. *Paleoceanography* 31, 1562–1582. doi: 10.1002/2016PA003052

Mitsuguchi, T., and Kawakami, T. (2012). 'Potassium and other minor elements in *Porites* corals: Implications for skeletal geochemistry and paleoenvironmental reconstruction'. *Coral. Reefs.* 31, 671–681. doi: 10.1007/s00338-012-0902-3

Nakamura, T., Kawasaki, S., and Unemoto, T. (1992). Roles of K^+ and Na^+ in pH homeostasis and growth of the marine bacterium Vibrio alginolyticus. *J. Gen. Microbiol.* 138, 1271–1276. doi: 10.1099/00221287-138-6-1271

Nambiar, R., Hauzer, H., Gray, W. R., Henehan, M. J., Cotton, L., Erez, J., et al. (2023). Controls on potassium incorporation in foraminifera and other marine calcifying organisms. *Geochim. Cosmochim. Acta* 351, 125–138. doi: 10.1016/j.gca.2023.04.020

Nehrke, G., Keul, N., Langer, G., De Nooijer, L. J., Bijma, J., and Meibom, A. (2013). A new model for biomineralization and trace-element signatures of Foraminifera tests. *Biogeosciences* 10, 6759–6767. doi: 10.5194/bg-10-6759-2013

Nürnberg, D., Bijma, J., and Hemleben, C. (1996). Assessing the reliability of magnesium in foraminiferal calcite as a proxy for water mass temperatures. *Geochim. Cosmochim. Acta* 60, 803–814. doi: 10.1016/0016-7037(95)00446-7

Okai, T., Suzuki, A., Terashima, S., Mayuri, I., Nohara, M., Kawahata, H., et al. (2004). Collaborative analysis of GSJ/AIST geochemical reference materials JCp-1 (Coral) and JCt-1 (Giant Clam). *Chikyukagaku. (Geochemistry).* 38, 281–286.

Okumura, M., and Kitano, Y. (1986). Coprecipitation of alkali metal ions with calcium carbonate. *Geochim. Cosmochim. Acta* 50, 49–58. doi: 10.1016/0016-7037(86)90047-5

Ram, S., and Erez, J. (2021). The distribution coefficients of major and minor elements in coral skeletons under variable calcium seawater concentrations. *Front. Earth Sci.* 9. doi: 10.3389/feart.2021.657176

Roepert, A., Polerecky, L., Geerken, E., Reichart, G. J., and Middelburg, J. J. (2020). 'Distribution of chlorine and fluorine in benthic foraminifera'. *Biogeosciences* 17, 4727–4743. doi: 10.5194/bg-17-4727-2020

Sadekov, A. Y., Darling, K. F., Ishimura, T., Wade, C. M., Kimoto, K., Singh, A. D., et al. (2016). 'Geochemical imprints of genotypic variants of *Globigerina bulloides* in the Arabian Sea'. *Paleoceanography* 31, 1440–1452. doi: 10.1002/2016PA002947

Sanyal, A., Hemming, N. G., Hanson, G. N., and Broecker, W. S. (1995). 'Evidence for a higher pH in the glacial ocean from boron isotopes in foraminifera'. *Nature* 373, 234–236. doi: 10.1038/373234a0

Sarazin, G., Michard, G., and Prevot, F. (1999). 'A rapid and accurate spectroscopic method for alkalinity measurements in sea water samples'. *Water Res.* 33, 290–294. doi: 10.1016/S0043-1354(98)00168-7

Schmidt, C., Titelboim, D., Brandt, J., Herut, B., Abramovich, S., Almogi-Labin, A., et al. (2016). 'Extremely heat tolerant photo-symbiosis in a shallow marine benthic foraminifera'. *Sci. Rep.* 6, 1–9. doi: 10.1038/srep30930

Segev, E., and Erez, J. (2006). 'Effect of Mg/Ca ratio in seawater on shell composition in shallow benthic foraminifera'. *Geochem. Geophys. Geosyst.* 7, 1–8. doi: 10.1029/2005GC000969

Shabala, L., McMeekin, T., and Shabala, S. (2009). 'Osmotic adjustment and requirement for sodium in marine protist thraustochytrid'. *Environ. Microbiol.* 11, 1835–1843. doi: 10.1111/j.1462-2920.2009.01908.x

Sun, X., Higgins, J., and Turchyn, A. V. (2016). 'Diffusive cation fluxes in deep-sea sediments and insight into the global geochemical cycles of calcium, magnesium, sodium and potassium'. *Mar. Geol.* 373, 64–77. doi: 10.1016/j.margeo.2015.12.011

Toyofuku, T., Matsuo, M. Y., De Nooijer, L. J., Nagai, Y., Kawada, S., Fujita, K., et al. (2017). 'Proton pumping accompanies calcification in foraminifera'. *Nat. Commun.* 8, 1–6. doi: 10.1038/ncomms14145

Tyszka, J., Bickmeyer, U., Raitzsch, M., Bijma, J., Kaczmarek, K., Mewes, A., et al. (2019). 'Form and function of F-actin during biomineralization revealed from live experiments on foraminifera'. *Proc. Natl. Acad. Sci. United. States America* 116, 4111–4116. doi: 10.1073/pnas.1810394116

Uchikawa, J., and Zeebe, R. E. (2012). 'The effect of carbonic anhydrase on the kinetics and equilibrium of the oxygen isotope exchange in the CO_2-H_2O system: Implications for $\delta^{18}O$ vital effects in biogenic carbonates'. *Geochim. Cosmochim. Acta* 95, 15–34. doi: 10.1016/j.gca.2012.07.022

Van Dijk, I., De Nooijer, L. J., Boer, W., and Reichart, G. J. (2017b). Sulfur in foraminiferal calcite as a potential proxy for seawater carbonate ion concentration. *Earth Planet. Sci. Lett.* 470, 64–72. doi: 10.1016/j.epsl.2017.04.031

Van Dijk, I., De Nooijer, L. J., and Reichart, G. J. (2017c). Trends in element incorporation in hyaline and porcelaneous foraminifera as a function of pCO_2. *Biogeosciences* 14, 497–510. doi: 10.5194/bg-14-497-2017

Van Dijk, I., De Nooijer, L. J., Wolthers, M., and Reichart, G. J. (2017a). Impacts of pH and $[CO_3^{2-}]$ on the incorporation of Zn in foraminiferal calcite. *Geochim. Cosmochim. Acta* 197, 263–277. doi: 10.1016/j.gca.2016.10.031

Van Dijk, I., Mouret, A., Cotte, M., Le Houedec, S., Oron, S., Reichart, G. J., et al. (2019). Chemical heterogeneity of mg, mn, na, S, and sr in benthic foraminiferal calcite. *Front. Earth Sci.* 7. doi: 10.3389/feart.2019.00281

Virtanen, P., Gommers, R., Oliphant, T.-E., Reddy, T., Cournapeau, D., Burovski, E., et al. (2020). '{SciPy} 1.0: fundamental algorithms for scientific computing in python'. *Nat. Methods* 17, 261–272. doi: 10.1038/s41592-019-0686-2

Wang, K., Close, H.-G., Tuller-Ross, B., and Chen, H. (2020). 'Global average potassium isotope composition of modern seawater'. *ACS Earth Space. Chem.* 4, 1010–1017. doi: 10.1021/acsearthspacechem.0c00047

Wit, J. C., De Nooijer, L. J., Wolthers, M., and Reichart, G. J. (2013). 'A novel salinity proxy based on Na incorporation into foraminiferal calcite'. *Biogeosciences* 10, 6375–6387. doi: 10.5194/bg-10-6375-2013

Zeebe, R. E., and Tyrrell, T. (2018). 'Comment on "The Effects of Secular Calcium and Magnesium Concentration Changes on the Thermodynamics of Seawater Acid/Base Chemistry: Implications for Eocene and Cretaceous Ocean Carbon Chemistry and Buffering" by Hain et al., (2015)'. *Global Biogeochem. Cycles.* 32, 895–897. doi: 10.1002/2017GB005786

frontiers | Frontiers in Marine Science

TYPE Original Research
PUBLISHED 15 October 2024
DOI 10.3389/fmars.2024.1321254

OPEN ACCESS

EDITED BY
Johan Schijf,
University of Maryland, College Park,
United States

REVIEWED BY
Kaustubh Thirumalai,
University of Arizona, United States
Ed Hathorne,
Helmholtz Association of German Research
Centres (HZ), Germany

*CORRESPONDENCE
Casey Saenger
saengec@wwu.edu

RECEIVED 13 October 2023
ACCEPTED 20 September 2024
PUBLISHED 15 October 2024

CITATION
Saenger C, Jimenez-Diaz C, Gagnon A, Mix A, Ross A and Xu T (2024) A framework for reconstructing marine heatwaves from individual foraminifera in sedimentary archives.
Front. Mar. Sci. 11:1321254.
doi: 10.3389/fmars.2024.1321254

A framework for reconstructing marine heatwaves from individual foraminifera in sedimentary archives

Casey Saenger[1]*, Carlos Jimenez-Diaz[1], Alexander Gagnon[2], Alan Mix[3], Andrew Ross[3] and Tongtong Xu[4]

[1]Department of Geology and Program in Marine and Coastal Science, Western Washington University, Bellingham, WA, United States, [2]School of Oceanography, University of Washington, Seattle, WA, United States, [3]College of Earth, Ocean, and Atmospheric Sciences, Oregon State University, Corvallis, OR, United States, [4]National Oceanographic and Atmospheric Administration, Physical Sciences Laboratory, Boulder, CO, United States

Marine heatwaves (MHWs) are warm sea surface temperature (SST) anomalies with substantial ecological and economic consequences. Observations of MHWs are based on relatively short instrumental records, which limit the ability to forecast these events on decadal and longer timescales. Paleoclimate reconstructions can extend the observational record and help to evaluate model performance under near future conditions, but paleo-MHW reconstructions have received little attention, primarily because marine sediments lack the temporal resolution to record short-lived events. Individual foraminifera analysis (IFA) of paleotemperature proxies presents an intriguing opportunity to reconstruct past MHW variability if strong relationships exist between SST distributions and MHW metrics. Here, we describe a method to test this idea by systematically evaluating relationships between MHW metrics and SST distributions that mimic IFA data using a 2000-member linear inverse model (LIM) ensemble. Our approach is adaptable and allows users to define MHWs based on multiple duration and intensity thresholds and to model seasonal biases in five different foraminifera species. It also allows uncertainty in MHW reconstructions to be calculated for a given number of IFA measurements. An example application of our method at 12 north Pacific locations suggests that the cumulative intensity of short-duration, low-intensity MHWs is the strongest target for reconstruction, but that the error on reconstructions will rely heavily on sedimentation rate and the number of foraminifera analyzed. This is evident when a robust transfer function is applied to new core-top oxygen isotope data from 37 individual *Globigerina bulloides* at a site with typical marine sedimentation rates. In this example application, paleo-MHW reconstructions have large uncertainties that hamper comparisons to observational data. However, additional tests demonstrate that our approach has considerable potential to reconstruct past MHW variability at high sedimentation rate sites where hundreds of foraminifera can be analyzed.

KEYWORDS

marine heatwaves, paleoclimate, paleoceanography, planktic foraminifera, individual foraminifera analysis, linear inverse model, north Pacific

1 Introduction

Marine heatwaves (MHWs) are prolonged periods of anomalously warm ocean temperature relative to local climatologies that can have considerable socioeconomic impacts (von Biela et al., 2019; Free et al., 2023; Leggat et al., 2019; Oliver et al., 2021; Rogers-Bennett and Catton, 2019; Smith et al., 2023, 2021). MHWs can occur throughout the global ocean as evidenced by recent events in the northeast Pacific, East China Sea, Tasman Sea, Mediterranean Sea, northwest Atlantic, southwest Atlantic and Benguela current region (Oliver et al., 2021). Observational data suggest that MHW frequency, duration and spatial extent have increased in recent decades (Frölicher et al., 2018; Holbrook et al., 2020; Oliver et al., 2018; Yao et al., 2022), and a prominent north Pacific event from 2014-2016 may be the most ecologically and economically impactful ever recorded (Bond et al., 2015; Cheung and Frölicher, 2020; Di Lorenzo and Mantua, 2016). Nicknamed the "Blob," this event caused major shifts in the geographic range of organisms from copepods to sunfish, closed commercially-important fisheries, initiated an unprecedented harmful algal bloom and contributed to mass strandings of birds and marine mammals (Cavole et al., 2016; Jones et al., 2018; McCabe et al., 2016). Recent trends in MHW behavior are due at least in part to anthropogenic global warming (Barkhordarian et al., 2022; Laufkötter et al., 2020), and forecasts based on general circulation model (GCM) ensembles such as phases 5 and 6 of the Coupled Model Intercomparison Project (i.e. CMIP5 and CMIP6, Eyring et al., 2016; Taylor et al., 2012) generally predict these trends will continue (Frölicher et al., 2018; Oliver et al., 2019). However, comparisons of these GCM ensembles to observed MHWs show significant biases that can both overestimate and underestimate various measures of MHW behavior (Hirsch et al., 2021; Plecha et al., 2021), thereby raising concern regarding the accuracy of decadal to centennial forecasts.

MHW variability reflects the combined influence of temperature changes due to external radiative forcing and internal modes (Holbrook et al., 2019; Oliver et al., 2021). Both internal and external forcings operate on decadal timescales that are relatively well captured by instrumental data, and longer centennial to millennial timescales that are not resolved by observations. Accordingly, MHW forecasts exhibit considerable skill on sub-annual timescales (Holbrook et al., 2020; Jacox et al., 2022), but not on longer timescales over which the models are uncalibrated and unvalidated. Furthermore, observational data reflect the recent, relatively low CO_2 climate, which may not accurately record the breadth and magnitude of feedbacks expected in the high CO_2 climate of future centuries (Tierney et al., 2020). Both processes likely contribute to the biases in CMIP forecasts of future MHW activity, and point to a need for new strategies to validate MHW behavior in models over a larger dynamic range.

Paleoclimate data offer the potential to extend the observational record and thus evaluate model performance under boundary conditions different than those recorded during the observational era. For example, climates such as those of the Pliocene and Eocene have been identified as good analogs for future warming (Burke et al., 2018), and can serve as benchmarks against which to calibrate and validate models. Despite this, few studies have approached MHWs from a paleoclimate perspective, likely because most paleoceanographic archives lack the high temporal resolution necessary to characterize individual MHWs. Massive hermatypic corals may be an exception (Zinke et al., 2015), but this archive is primarily limited to low-latitude ocean regions during the latest Quaternary period. In contrast, marine sediments can record ocean variability across millions of years in diverse oceanographic settings, and preserve proxies like foraminifera that are sensitive to MHWs (Lane et al., 2023). Unfortunately, most marine sedimentary archives have low sediment accumulation rates and experience bioturbation, which leads to temporal resolutions of centuries to millennia that are far too coarse to record monthly to annual MHWs.

Individual foraminifera analysis (IFA) offers a potential solution to this temporal averaging problem in marine sediments. Unlike traditional paleoceanographic applications of foraminifera, which pool individuals to estimate mean conditions, IFA measures geochemical proxies in many single foraminifera and then interprets the shape of the resulting distribution (Ford et al., 2018, 2015; Groeneveld et al., 2019; Khider et al., 2011; Koutavas et al., 2006; Koutavas and Joanides, 2012; Leduc et al., 2009; Rongstad et al., 2020; Rustic et al., 2020; Thirumalai et al., 2019; White et al., 2018). Given the ~4 week lifespan of most mixed layer planktonic foraminifera (Spero, 1998) due to a lunar-pacing of reproduction (Erez et al., 1991; Jonkers et al., 2015), each measured shell approximates a monthly snapshot of ocean conditions. The collective distribution of these snapshots then represents changes in the statistical properties of both mean climate and extremes over a time interval that is dictated by sedimentation rate, bioturbation and sampling interval. For example, IFA has been used to reconstruct the El Niño Southern Oscillation (ENSO) in the tropical Pacific based on the expectation that increased ENSO variability will broaden the distribution of reconstructed SST relative to the seasonal cycle, which manifests itself as an increase in standard deviation (Ford et al., 2015; Khider et al., 2011; Koutavas et al., 2006; Koutavas and Joanides, 2012; Rustic et al., 2020; White et al., 2018). Like ENSO variability, MHWs are also characterized by relatively short-lived sea surface temperature (SST) anomalies, and changes in their mean behavior between time periods could produce distinct changes in IFA-based SST distributions.

In practice, there are a number of complications that make it challenging to identify how an IFA-based SST distribution might be altered by changes in MHWs. For example, traditional approaches to calibrating foraminifera proxies using global core-top sediment (Elderfield and Ganssen, 2000; Malevich et al., 2019; Saenger and Evans, 2019; Tierney et al., 2019) or sediment traps (Anand et al., 2003; Gray et al., 2018; Huang et al., 2008) would be extremely costly because orders of magnitude more analyses would be necessary to generate IFA-based SST distributions for each site or time interval. Furthermore, it is not yet obvious how the accuracy of IFA-based SST distributions vary with the number of geochemical proxy measurements made, which makes it difficult to know how many foraminifera would need to be sampled to make meaningful MHW reconstructions. Variations in the seasonality of different

foraminifera species is also a complicating factor, and it is likely that relationships between IFA-based SST distributions and MHWs are specific to both individual species and sites. Finally, the numerous ways of describing both MHWs and SST distributions create a large pool of potential relationships, which may make it challenging to identify those that are most useful.

In light of these complications, it is attractive to evaluate relationships between IFA-based SST distributions and MHWs in a pseudoproxy framework. Pseudoproxies (Mann and Rutherford, 2002) are realistic approximations of actual proxy data that are generated by passing the output of physically consistent climate simulations through a proxy system model (Dee et al., 2016; Evans et al., 2013) that mimics complicating factors such as variations in seasonality. This approach obviously avoids the cost and labor of true geochemical proxy measurements and allows relationships between IFA-based SST distributions and MHWs to be explored quickly and efficiently. Furthermore, generating pseudoproxies from large ensembles of climate model simulations allows many realistic climate states to be sampled, thereby providing the large sample size necessary for robust measures of skill and error. Because pseudoproxies are generated from a known signal, they also provide valuable opportunities for validation and a testbed for evaluating how the accuracy of a relationship might change due to choices such as the MHW definition assumed, the foraminifera species considered, the sedimentation rate at a site or the number of proxy measurements used to generate an IFA-based SST distribution. Finally, because climate model simulations are spatially complete, a pseudoproxy approach allows relationships to be compared across large regions to identify sites where they have the greatest potential to generate meaningful MHW reconstructions.

Here we describe a method for evaluating quantitative relationships between SST distributions similar to those that could be generated via IFA and various measures of MHW variability with the goal of identifying which have the greatest potential to yield paleo-MHW reconstructions. We adopt a pseudoproxy approach in which a 2000-member linear inverse model (LIM) ensemble is used to compare MHW behavior to SST distribution statistics that mimic IFA measurements. Our approach is adaptable and allows users to evaluate five different foraminifera species, numerous MHW definitions and a number of realistic complications. While we are motivated by the desire to eventually reconstruct paleo-MHWs, the goal of this study is simply to define a framework for identifying the most robust quantitative transfer functions between IFA-based SST distributions and MHWs. Below, we first describe the data sources, construction and validation of an algorithm that can evaluate transfer functions based on different foraminifera species and MHW definitions. We then demonstrate the utility of our approach through the example application of identifying the most promising targets for paleo-MHW reconstructions in the northeast Pacific. Finally, we demonstrate how our approach can be integrated with IFA data using new high-precision oxygen isotope ($\delta^{18}O$) analyses of individual *Globigerina bulloides* from core-top sediments. We focus on the northeast Pacific domain with the goal of generating transfer functions that could eventually be used to generate paleo-MHW reconstructions that place events like the 2014-2016 "Blob" MHW (Bond et al., 2015) into context. However, the approach we describe is also valid for other species and ocean regions, thereby providing a framework for developing additional transfer functions and paving the way toward an improved understanding of the spatiotemporal behavior of MHWs.

2 Methods

2.1 Overview of the algorithm design

A simplified design of our method and its basic order of operations are summarized in Figure 1, while more specific information is presented in later subsections. The primary input to our algorithm is an ensemble of monthly SST timeseries. Monthly data is required since this is the approximate lifespan of an individual foraminifera (Spero, 1998), and each SST value can be considered analogous to what might be reconstructed from the measurement of a paleotemperature proxy in a single foraminifer. Multiple timeseries are required because each timeseries is ultimately reduced to a single SST distribution, and thus effectively contributes only a single data point to a given transfer function. We note that we use the phrase "transfer function" throughout the remainder of the text to describe the quantitative relationships between IFA pseudoproxy SST distributions and MHWs.

The algorithm then allows a user to specify how a MHW is defined and this information is used to calculate MHWs for each SST timeseries within the ensemble. One of five foraminifera species (*Neogloboquadrina pachyderma, Neogloboquadrina incompta, Globigerina bulloides, Trilobatus sacculifer* or *Globigerinoides ruber*) is also specified, and used to weight the monthly SST timeseries based on the seasonal concentration of that species as calculated by the proxy system model of Kretschmer et al. (2018). Statistics that summarize the shape of weighted SST distributions are then regressed against MHW measures using partial least squares regression (Mehmood et al., 2012) to develop initial transfer functions. If regression statistics and comparisons to observed MHWs suggest that a transfer function is promising, the user can perform additional cross validation to evaluate how a transfer function might perform in a paleoclimate context. For example, realistic sedimentation rates and sampling intervals can be specified to estimate how many foraminifera will be required to achieve a desired accuracy in a MHW reconstruction. This can be compared against the number of foraminifera actually present or the analytical budget available to provide a feasibility check before committing to a laborious and costly study.

2.2 Monthly SST from a linear inverse model (LIM) ensemble and observations

As noted previously, implementing our method requires an ensemble of monthly SST data. For the purposes of calibration, data should span a wide range of MHW states while still being physically realistic. Here, we achieve this using a 2,000 member LIM ensemble that has previously been used to explore Pacific MHWs (Xu et al., 2021).

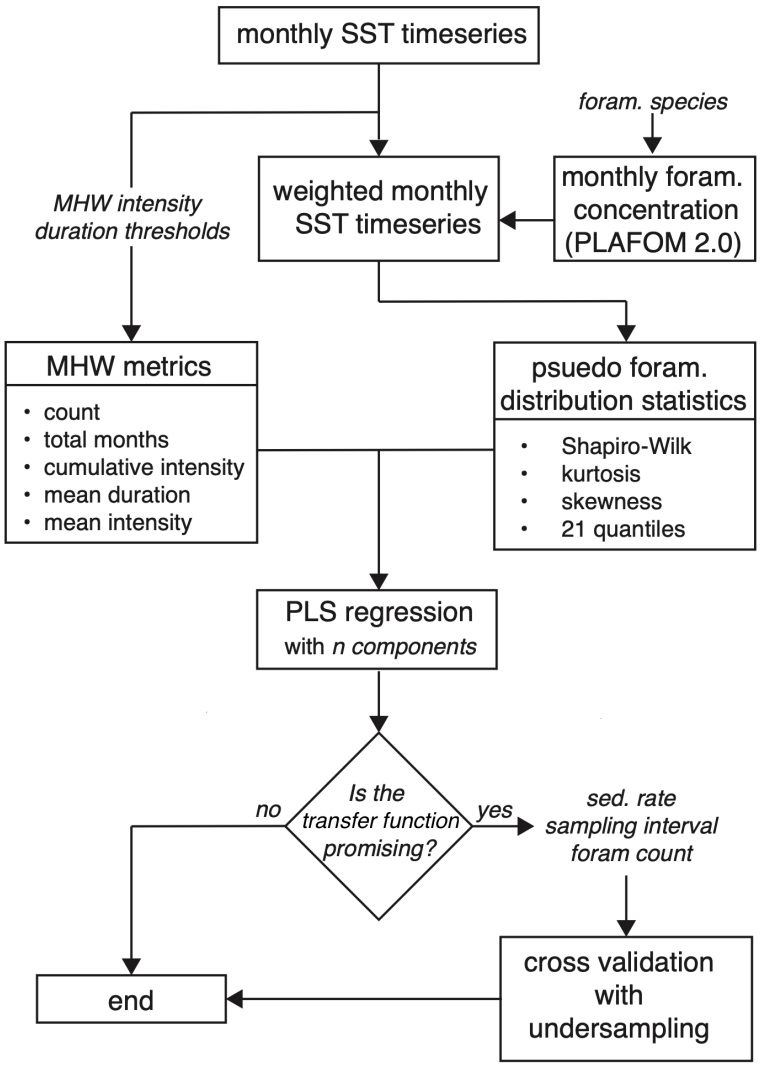

FIGURE 1
Schematic of our workflow for generating transfer functions between pseudoproxy SST distribution statistics and MHW metrics, and evaluating their skill. Italicized text indicates a user-defined choice. Monthly SST timeseries derive from COBEv2, ERSSTv5, HadISST or the LIM ensemble. MHW intensity and duration thresholds refer to the minimum intensity and duration necessary for a warm anomaly to be defined as a MHW, and metrics represent various measures of these MHWs. Monthly foraminifera concentrations, based on the PLAFOM2.0 model of Kretschmer et al. (2018), are used to generate a weighted monthly SST timeseries that represents the seasonal bias of a defined species. Distribution statistics summarize these seasonally-weighted pseudoproxy SST timeseries. Partial least squares (PLS) regression is used to develop transfer functions between distribution statistics and MHW metrics. If a user chooses to do so, the error on a reconstruction for a given number of individual foraminifera can be evaluated.

LIMs are stochastically-forced linear dynamical models that are empirically determined. That is, the predictable dynamics of the climate system are inferred from auto covariance and lagged covariance of the coarse-grained climate variables, whereas the remaining unresolved fast-decaying and rapid nonlinear processes associated with weather are parameterized as spatially-coherent Gaussian white noise. The underlying assumption of a LIM construction is that the coarse-grained climate evolution acts as an integrated response to the rapid weather variability (Hasselmann, 1976), resulting in a system in which its predictable dynamics can be represented to a reasonable approximation linearly and deterministically. The unpredictable stochastic forcing, on the other hand, contributes to energizing the climate system. A LIM simulation obtained by integrating the stochastic forcing forward in time thus represents a climate system that can be diagnosed in the same manner as simulations from coupled GCMs, but with the advantage that many realizations of the simulated timeseries can be generated relatively easily (e.g. Ault et al., 2013; Newman et al., 2011). This general approach has been used extensively to explore Pacific SST on sub-annual to multidecadal timescales using LIMs (Alexander et al., 2008; Capotondi et al., 2022; Penland and Matrosova, 1994; Penland and Sardeshmukh, 1995; Xu et al., 2022, 2021).

The LIM ensemble in this study is based on Extended Reconstructed Sea Surface Temperature data set version 3 (ERSSTv3; Smith et al., 2008) in the tropical and north Pacific (110° E–60°W and 20°S–60°N) from 1950-2019 (Xu et al., 2021). It is gridded at 2° x 2° and consists of 2,000 physically-realistic timeseries of monthly SST that are 70 years each. This ensemble represents a large number of

"alternate histories" of north Pacific SST that drastically increases the data available for generating transfer functions and allows for the large sample size necessary for robust statistics. Furthermore, this large ensemble is more likely to span the range of variability that could have existed in the geologic past, thereby making our transfer functions more relevant to paleo-MHW reconstructions.

To validate LIM-based transfer functions, we also evaluate MHWs in monthly SST timeseries from three additional gridded observational products. ERSST version 5 (ERSSTv5) is gridded at 2° x 2° and was analyzed for the period from 1854-2023 A.D (Huang et al., 2017). Version two of the Centennial *in situ* Observation-Based Estimates of SST (COBEv2) is gridded at 1° x 1° and was analyzed for the period from 1850-2023 (Hirahara et al., 2014). Finally, the Hadley Centre Sea Ice and Sea Surface Temperature data set HadISST is gridded at 1° x 1° and was analyzed for the period from 1870-2022 (Rayner et al., 2003).

2.3 MHW definitions and their detection in observations and LIMs

While MHWs are broadly defined as periods when SSTs exceed climatology by some amount for some period of time, there is no strict consensus on these values. For example, observational studies based on daily satellite SST data commonly define a MHW to be a thermal anomaly that exceeds the 90th percentile for at least five days (Hobday et al., 2016), but model-based studies have considered intervals that exceed climatological SST by at least one standard deviation for at least five months to be MHWs (Xu et al., 2021). While the daily MHW definition is clearly outside the bounds of what our approach can resolve, we see no need to make further *a priori* assumptions about what magnitude of warming or duration constitutes a MHWs. We therefore allow the user to define an intensity threshold and duration for considering a warm anomaly to be a MHW. Intensity thresholds are formulated in terms of the number of standard deviations above monthly climatology (e.g. across all Januarys) within a single timeseries. Duration thresholds are simply an integer number of consecutive months. We use the term "definition" throughout the remainder of the text to refer to these various ways of defining MHWs. For example, a low intensity, short duration definition may specify MHWs to be times when monthly SST exceeds the climatological value by at least one standard deviation for at least one month, while a high intensity, long duration definition might require SST to exceed climatology by at least two standard deviations for at least four months.

For a given definition, MHWs are calculated across the entire length of a SST timeseries, but each monthly timeseries in the ensemble is considered separately. In the case of LIM data, this means MHWs are identified within each 70-year realization, but the 2,000 ensemble members are considered independently. Thus, the LIM ensemble provides 2,000 separate estimates of MHW behavior for each definition considered.

To account for global warming trends, a 30-year high pass filter is applied to ERSSTv5, COBEv2 and HadISST timeseries prior to calculating climatologies (Figure 2A). This is equivalent to a shifting (as opposed to fixed) baseline approach and is consistent with the idea that a MHW should be an exceptional event above a background state that is distinct from lower frequency anthropogenic warming (Amaya et al., 2023). LIM simulations do not have a global warming trend so do not require filtering.

Once MHWs are identified, they are further characterized based on five metrics (Figure 2). In some cases metrics are normalized to a decade to account for the different lengths of ERSSTv5, COBEv2, HadISST and LIM timeseries. We use the term "metric" throughout the remainder of the text to refer to the following five ways of characterizing MHW behavior:

- Count (n/decade): Total MHW events, normalized to a decade
- Total months (n/decade): Total number of months in a timeseries that meet the assigned MHW definition, normalized to a decade.
- Cumulative intensity (°C/decade): Sum of monthly intensities in a timeseries that meet the assigned MHW definition, normalized to a decade.
- Mean duration (months): Average length of all MHWs in a timeseries
- Mean intensity (°C): Average intensity of all MHWs in a timeseries.

The values for these metrics can vary considerably with the choice of MHW definition, and increases or decreases in one metric do not necessarily cause equivalent changes in other metrics. An example using COBEv2 data from the northeast Pacific gridbox closest to Deep Sea Drilling Project (DSDP) Site 36 (Table 1) and spanning the 2012-2018 interval that includes the "Blob" MHW is shown in Figure 2. Using one standard deviation and one month as intensity and duration thresholds, respectively, four MHW events are identified (Figure 2C). Two events have a duration of a single month and intensities of 0.89°C and 0.75°C, respectively, which both exceed one standard deviation (0.51°C), but not two (1.02°C). Because these events are a single month, their cumulative intensities are identical to their mean intensities. A third event has a duration of three months, a mean intensity of 0.91°C and a cumulative intensity of 2.73°C. A fourth event represents the "Blob" event and has a duration of 24 months, a mean intensity of 1.12° C and cumulative intensity of 26.87°C. If the MHW definition is changed to have a duration threshold of five months, the three shorter events are no longer considered MHWs and only the "Blob" event remains with identical metrics (Figure 2D). Using two standard deviations and one month thresholds to define MHWs excludes most of the three shorter events, but also splits the "Blob" event into four (Figure 2E). Thus, the count of MHWs actually increases to five, which have durations of one to six months and mean intensities of 1.09 to 1.50°C. Using two standard deviations and five month thresholds, eliminates all but one high intensity MHW that represents the most intense portion of the "Blob" event (Figure 2F).

2.4 Accounting for seasonality in foraminifera abundance

Planktonic foraminifera live in near-surface ocean environments around the globe and have long been recognized as valuable tools for

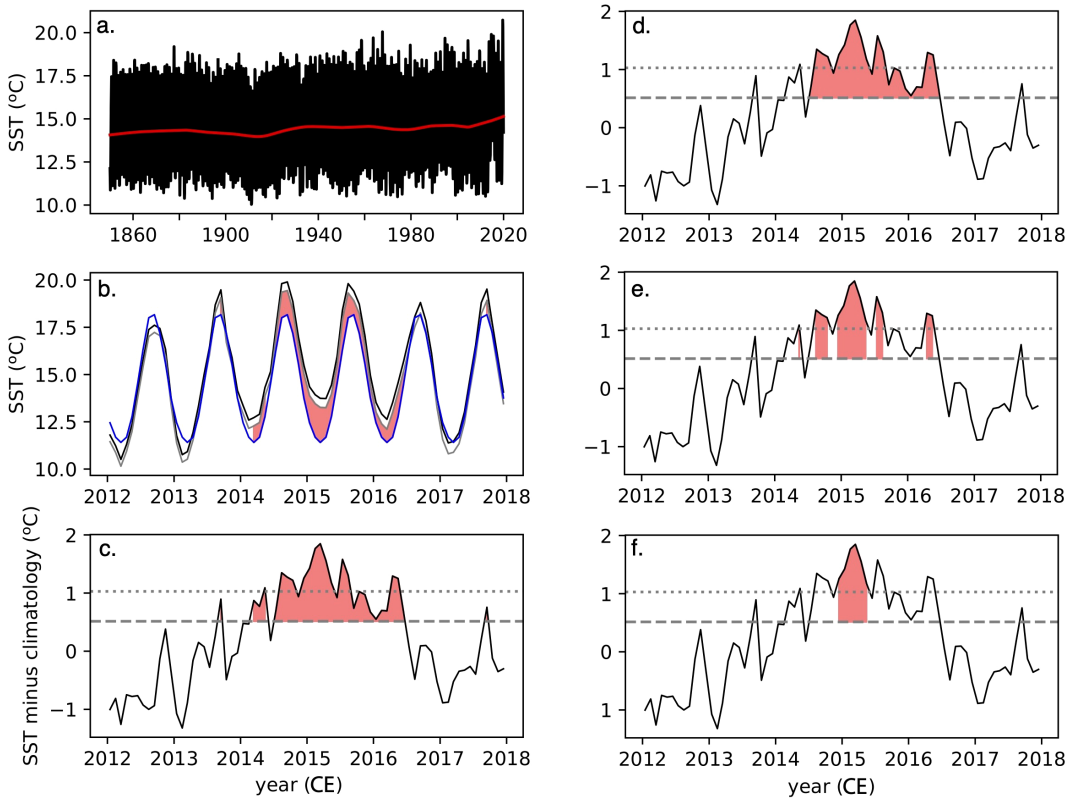

FIGURE 2
(A) COBEv2 SST at DSDP Site 36 (black) and the low frequency trend associated with the 30-year high pass filter (red). This filter is used to remove the global warming trend from observational data when calculating MHW metrics **(B)** Subset of COBEv2 SST for the years from 2012-2018 spanning the "Blob" MHW (black) and the same signal after removing the low frequency trend (grey). The climatology plus one standard deviation (blue) marks a threshold above which a MHW could be defined (red shading) **(C)** SST with the low frequency trend and climatology removed (black) relative to the upper bound of one standard deviation (grey dashed line) and two standard deviations (grey dotted line). Times exceeding one standard deviation provide an equivalent definition (red shading) that are identical to panel **(B)**. **(D)** As in panel **(C)** for intensity and duration thresholds of one standard deviation and five months **(E)** As in panel **(C)** for intensity and duration thresholds of two standard deviations and one month **(F)** As in panel **(C)** for intensity and duration thresholds of two standard deviations and five months.

TABLE 1 Locations and sedimentation rates of north Pacific sites.

site	latitude	longitude	sedimentation rate (cm/kyr)	sedimentation rate reference
ODP 887	54.3654	-148.446	7	Galbraith et al., 2007; Rea, 1994
DSDP 36	40.9847	-130.11	2.4	Brennan et al., 2022; McManus et al., 1970
DSDP 183	52.52	-161.2055	0.92	Costa et al., 2024
DSDP 179	56.409	-145.9887	6.95	Jaeger et al., 2014; Opdyke and Foster, 1970
DSDP 37	40.979	-140.7185	0.26	Opdyke and Foster, 1970
DSDP 177	50.4697	-130.205	2	approximated from Costa et al., 2024
ODP 1023	47.9173	-128.792	2	approximated from Costa et al., 2024
A	55	-140	1	approximated from Costa et al., 2024
B	50	-150	0.23	Costa et al., 2024; Kemnitz et al., 2023
C	50	-140	0.14	Costa et al., 2024
D	45	-150	0.48	Donahue, 1970; Opdyke and Foster, 1970
E	45	-140	0.22	Opdyke and Foster, 1970

reconstructing past SST (Anand et al., 2003; Bemis et al., 1998; Elderfield and Ganssen, 2000; Emiliani, 1955; Lea et al., 2000, 1999). Given their lifespan, measuring established paleotemperature proxies such as $\delta^{18}O$ (Bemis et al., 1998) or magnesium to calcium ratios (Mg/Ca; Lea et al., 1999) in individual foraminifera allows for distributions of monthly SST to be generated (Ford et al., 2015; Koutavas et al., 2006; Rongstad et al., 2020; Rustic et al., 2020). These distributions are approximately equivalent to those based on monthly LIM and observational SST data, and therefore provide a means to use LIM-based transfer functions to reconstruct past MHW behavior.

However, planktonic foraminifera preferentially live at depths and during seasons when optimal growth conditions exist, and are therefore seasonally-biased recorders of SST (Jonkers et al., 2013, 2010; Jonkers and Kučera, 2015; Ortiz et al., 1995; Sautter and Thunell, 1989; Taylor et al., 2018; Tolderlund et al., 1971). To account for seasonality, monthly LIM ensemble data must be weighted to generate pseudoproxy SST timeseries that mimic the information that can be reconstructed from IFA. We achieve this using an existing planktonic foraminifera proxy system model (PLAFOM2.0), which is a global model of foraminifera abundance that predicts the monthly concentration (in mmol C m^{-3}) of five species: *N. pachyderma, N. incompta, G. bulloides, T. sacculifer* and *G. ruber* (Fraile et al., 2008; Kretschmer et al., 2018). PLAFOM2.0 uses a marine ecosystem model that predicts foraminifera food sources (Moore et al., 2001) to calculate species-specific rates of growth and mortality (Fraile et al., 2008). PLAFOM2.0 has recently been integrated with the biogeochemically-active ocean component of the Community Earth System Model (Hurrell et al., 2013) to calculate global estimates of foraminifera concentration in each month of the year and at 24 vertical levels between 0 and 250 meters (Kretschmer et al., 2018).

Our approach extracts PLAFOM2.0 concentrations for the user-defined foraminifera species from the grid-box closest to monthly SST data. Monthly foraminifer concentrations are summed across the model's entire 250 m depth domain, thereby removing the user from *a priori* assumptions regarding depth habitat. The total annual foraminifer concentration is then used to convert monthly concentrations into proportions. Values greater than 0.083 (i.e. 1/12) reflect some degree of foraminifera seasonal preference. An example based on *G. bulloides* from DSDP Site 36 is shown in Figure 3. Monthly proportions are used as weights to resample the original SST timeseries and generate a new SST record that mimics the seasonal bias of the selected foraminifera species.

2.5 Summary statistics of SST distributions

A number of statistical values have been developed to summarize the shape of a distribution. These statistics are attractive for establishing transfer functions because they condense the large amount of data in a SST distribution into a single value. For each of the monthly-weighted SST timeseries described above, we calculate a series of statistics that summarize the shape of their distributions. We use the term "statistic" throughout the remainder of the text to refer to the following measures of distributions that are plausible predictors of MHW metrics:

- Shapiro-Wilk test: A statistical test evaluating the null hypothesis that data are Gaussian (Shapiro and Wilk, 1965). Test statistic values range from 0 to 1, with higher values representing closer agreement with a Gaussian distribution.
- Kurtosis: A measure of how often outliers occur or the "tailedness" of a distribution
- Skewness: A measure of a distribution's asymmetry
- Quantiles 1-21: Values dividing a distribution into 21 continuous intervals of equal probability.

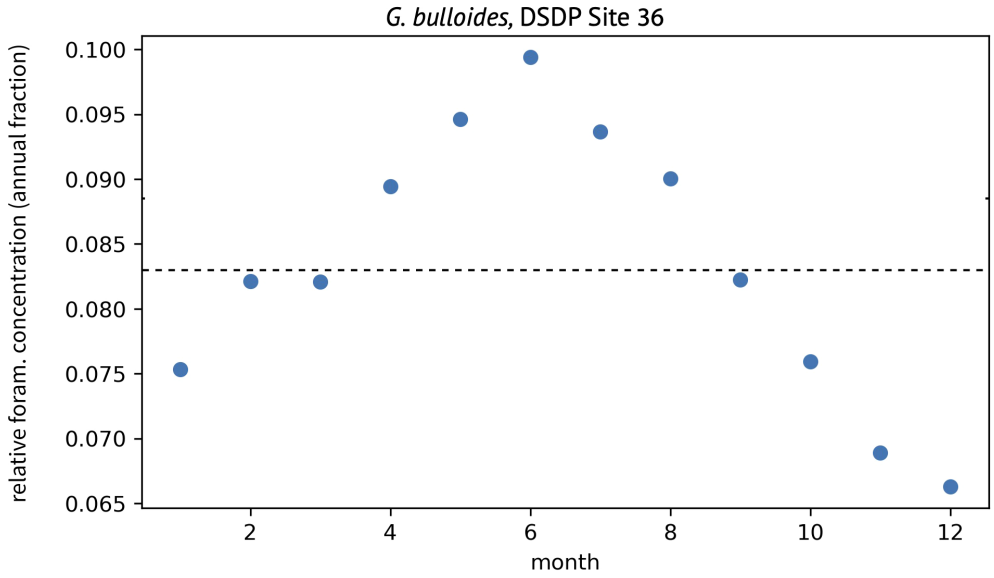

FIGURE 3
Example of the modeled seasonal change in the relative concentration of *G. bulloides* at DSDP Site 36. Values greater than 0.083 (dashed line) represent some degree of seasonal preference.

Statistics are calculated from standardized SST anomalies by subtracting means and dividing by standard deviations, and after 30-year high pass filtering in the case of ERSSTv5, COBEv2 and HadISST. Standardizing has no effect on Shapiro-Wilk, kurtosis and skewness values, and changes quantiles by a fixed proportion that varies between sites. The latter is helpful when comparing sites with different amplitude climatologies as it forces the total range of quantiles to be approximately equal. Standardizing also eliminates the need to select a specific proxy-temperature calibration for cases that calibrations are linear. That is, if $\delta^{18}O$ values of foraminifera were used to estimate SST using a linear calibration (e.g. Bemis et al., 1998), the standardized anomalies of those $\delta^{18}O$ values would have the same distribution statistics as $\delta^{18}O$-based SST estimates (for some statistics, the inverse relationship between $\delta^{18}O$ and temperature would need to be accounted for by multiplying by -1).

2.6 Constructing transfer functions between pseudoproxy SST distribution statistics and MHW metrics

Our method next uses partial least squares regression (PLSR) to evaluate if pseudoproxy SST distribution statistics (section 2.5) are useful predictors of any MHW metric (section 2.3). PLSR is an attractive alternative to more traditional ordinary least squares regression for this application because it allows information from all distribution statistics to contribute to a transfer function despite considerable collinearity among them (Mehmood et al., 2012). Pseudoproxy SST distribution statistics are transformed into a new set of orthogonal components and a transfer function is generated using only a subset of these components. The dimensionality reduction of PLSR is therefore similar to principal components regression (PCR) with the difference that PLSR maximizes covariance between independent and dependent variables when selecting components while PCR only considers the variance of independent variables. Thus, PCR can inadvertently eliminate components with considerable predictive power if they have low variance, while PLSR is less prone to this effect.

We implement PLSR separately for each of the five MHW metrics using the scikit-learn Python module (Pedregosa et al., 2011). The number of components to include in the PLSR is chosen by first randomly selecting 30 pseudoproxy SST timeseries from the ensemble along with their corresponding MHW metrics. Subsets of 70% of each pseudoproxy SST timeseries are then used to generate PLSR-based transfer functions with 1 to 10 components that are each capable of predicting a MHW metric. Applying each transfer function to the withheld 30% of data allows the differences between the predicted and observed MHW metrics to be used to calculate root mean square errors (RMSE):

$$\mathrm{RMSE} = \sqrt{\frac{\sum_i^N (MHW_i - \widehat{MHW}_i)^2}{N}}$$

where MHW_i-hat is the predicted MHW metric for ensemble member i, MHW_i is the true MHW metric for that ensemble member and N is the number of ensemble members considered. The change in RMSE with additional components allows the user to identify an appropriate number of components to include in the PLSR (Figure 4). To guide users toward transfer functions that balance lower RMSE with complexity, we highlight two values: 1) the number of components that yield the overall lowest RMSE and 2) the number of components at which RMSE ceases to improve by at least 1%. After the user selects a number of components, a new PLSR transfer function is generated using all pseudoproxy SST timeseries within the ensemble.

The performance of a transfer function is initially evaluated using its correlation coefficient (r^2), the standard deviation of regression residuals ($RMSE_{reg}$) and the RMSE relative to observations ($RMSE_{obs}$). The latter value is calculated by applying the distribution statistics for ERSSTv5, COBEv2 and HadISST monthly SST data to the LIM-based transfer function and comparing the calculated MHW metric to each record's true value (Figure 5). This out of sample validation provides an important check on how well a LIM-based transfer function reflects reality. If the user deems a transfer function to be sufficiently promising, the influence of under-sampling can then be evaluated.

In practice, IFA will always under-sample past SST because only tens or hundreds of monthly values will be reconstructed from foraminifera within a sedimentary interval that represents decades to millennia. To evaluate how sensitive transfer functions are to this effect, our approach considers a series of scenarios in which 50 to 800 foraminifera tests are picked from a sedimentary interval. Because the number of foraminifera measured is equivalent to the number of months sampled, the amount of time represented in a sedimentary interval (derived from sedimentation rate) can be used to calculate what fraction of all months will be recorded by a given number of IFA measurements. For example, if 200 foraminifera are measured from a sedimentary interval representing 500 years (equivalent to 6,000 months), 3.3% of all months are sampled. Using a randomly selected ensemble member, we randomly draw the fraction of values equivalent to each number of picked foraminifera. This yields an under-sampled pseudoproxy SST record that mimics what would be generated from IFA in marine sediments. The distribution statistics from the under-sampled, pseudoproxy IFA data are then applied to the transfer function and the resulting reconstructed MHW metric is compared with the true value. This is repeated 500 times to quantify the RMSE associated with sampling each number of foraminifera ($RMSE_{samp}$). A fit through a range of possible IFA measurements gives an estimate of $RMSE_{samp}$ for any number of foraminifera (Figure 6) and is valuable for evaluating what level of accuracy can be expected from a sample prior to geochemical analyses.

A disadvantage of PLSR is that the transformation of distribution statistics into new orthogonal variables can complicate the interpretation of regression coefficients in terms of actual physical properties. Our algorithm produces two resources that give some insight into how distribution statistics vary with changes in a MHW metric. The first gives the loadings for each distribution statistic and component (Figure 7A). Larger loadings indicate that a particular distribution statistic has a greater influence on a given component, while loadings of the same sign indicate

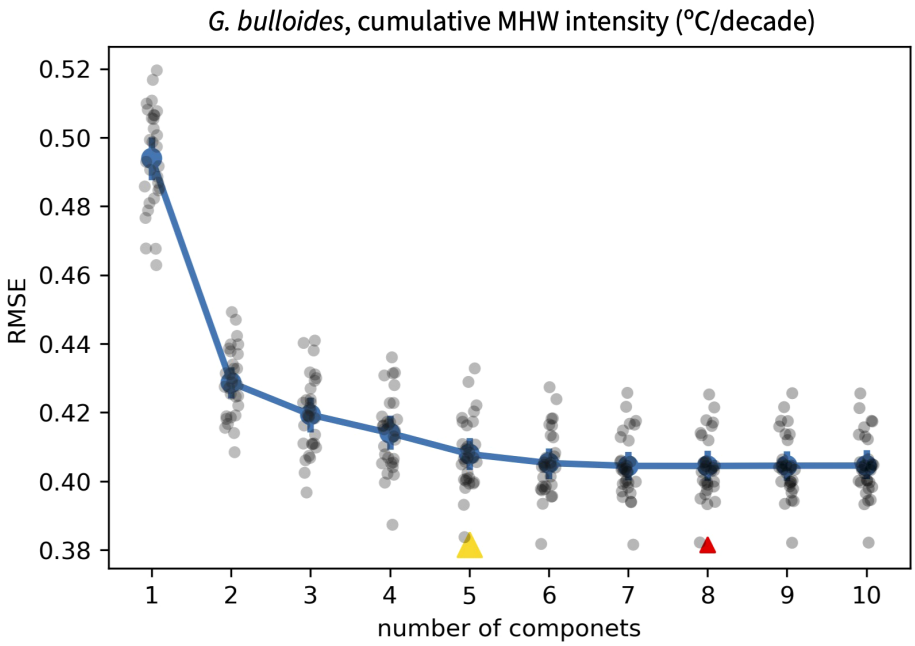

FIGURE 4
Example of how regression RMSE ($RMSE_{reg}$) changes with the number of components included in the partial least squares regression. In this case, the cumulative intensity of MHWs, defined using intensity and duration thresholds of one standard deviation and one month, are related to the statistics of a pseudoproxy SST distribution based on *G. bulloides* seasonality at DSDP Site 36. While the user is ultimately left to select the number of components to use in a PLSR, the values at which $RMSE_{reg}$ is at its minimum (red triangle) and ceases to improve by at least 1% (yellow triangle) are provided to inform this choice.

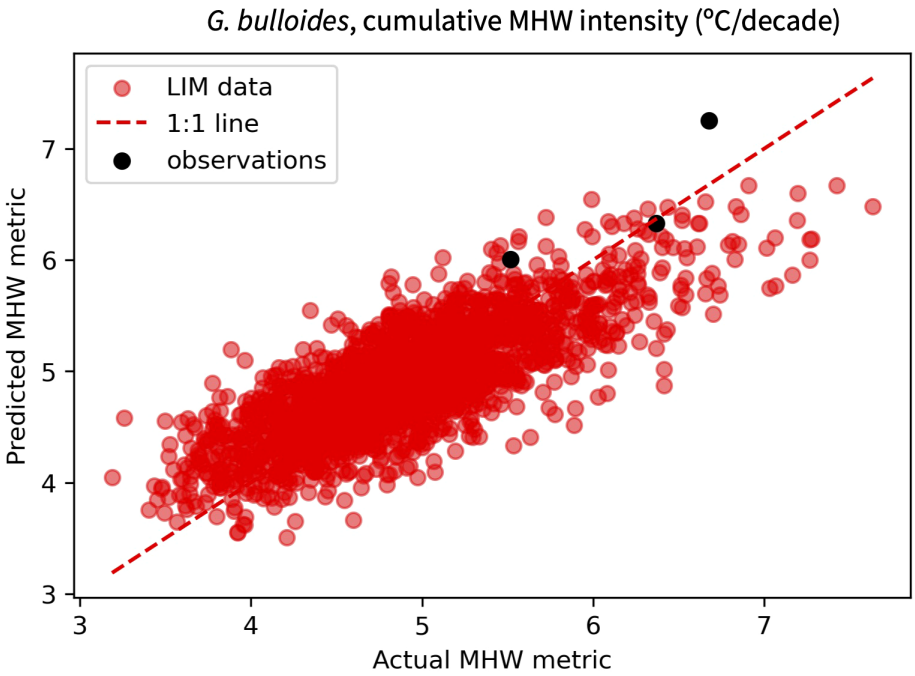

FIGURE 5
Example comparison of MHW cumulative intensity at DSDP Site 36 predicted from a PLSR-based transfer function versus that observed in the LIM ensemble (red) or observational SST products (black). MHWs are defined using intensity and duration thresholds of one standard deviation and one month and distribution statistics derive from a pseudoproxy SST distribution that is based on *G. bulloides* seasonality at DSDP Site 36. The consistency with which the LIM-based transfer function estimates independent observations supports the validity of our approach.

which distribution statistics covary in the same direction. The second resource presents the difference in distribution statistics between ensemble members with the highest and lowest 10% of a MHW metric (Figure 7B). This allows the user to see which distribution statistics change the most between extreme values of MHW metrics.

2.7 Example application at northeast Pacific sites

To demonstrate a potential application of our method we apply it at 12 northeast Pacific locations (Figure 8; Table 1) with the goal of identifying sites where IFA-based SST distributions have the greatest potential to reconstruct paleo-MHW variability. We consider a domain from about 40-60°N and 130-160°W that approximates the area influenced by the 2014-2016 "Blob" MHW (Bond et al., 2015). Of the 12 sites, seven locations (noted with site numbers from the Deep Sea Drilling Program or Ocean Drilling Program (ODP)) represent sediment cores that have been recovered, while the remaining five locations (labeled A-E) represent locations at which cores could potentially be collected in the future. These five sites are exemplary, and selected only to fill gaps in the spatial distribution of existing cores without considering the type or thickness of sediment at specific coordinates. Sedimentation rates at each site are taken from previously published age models when possible, and estimated from adjacent cores (Costa et al., 2024) when such data is unavailable (Table 1).

At each site we consider a series of MHW definitions that include duration thresholds of 1, 2 and 4 months and intensity thresholds of 1 or 2 standard deviations. We model the seasonal abundance of *G. bulloides* and *N. incompta* since they are common in the modern northeast Pacific (Ortiz and Mix, 1992; Sautter and Thunell, 1989; Taylor et al., 2018) and in sediment cores (Davies et al., 2011; Praetorius et al., 2015; Taylor et al., 2014). We consistently select the number of components included in the PLSR based on the value at which RMSE ceases to improve by at least 1% (section 2.6; Figure 4). We perform additional evaluation of under-sampling only when a transfer function's correlation coefficient exceeds 0.5. This value is selected somewhat arbitrarily to increase efficiency by not considering the influence of under-sampling for transfer functions with seemingly little promise. Other users may make alternative decisions. When under-sampling is evaluated, we use our best-estimates of sedimentation rate at each site (Table 1) and assume a 1 cm sampling interval. In total we evaluate 60 potential transfer functions at each of the 12 sites to identify which MHW metrics, based on which MHW definitions, are mostly likely to be reconstructed by which foraminifera species at each location.

2.8 Stable isotope analyses of individual *G. bulloides*

To demonstrate how a transfer function may be applied to actual IFA data to reconstruct paleo-MHWs we also measured $\delta^{18}O$

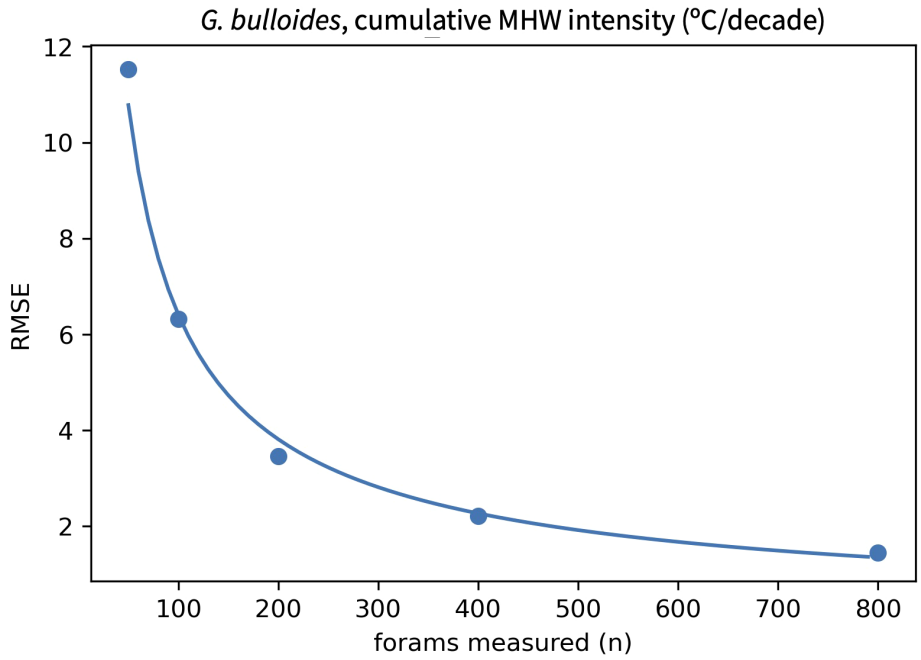

FIGURE 6
Example result demonstrating how the RMSE of a reconstructed MHW metric will vary with the number of foraminifera measured. Results vary based on the strength of a transfer function's fit and the sedimentation rate at a site. Here, the transfer function in Figure 5 is applied to scenarios in which 50, 100, 200, 400 or 800 *G. bulloides* are measured at DSDP site 36. This suggests that the cumulative intensity of MHWs at this site would be reconstructed with an error of approximately ±6°C/decade if 100 *G. bulloides* were measured. A fit through the five points allows $RMSE_{samp}$ to be calculated for any number of foraminifera, which in this case is: $\ln(RMSE_{samp}) = 5.385 - 0.753 * \ln(n\ forams)$.

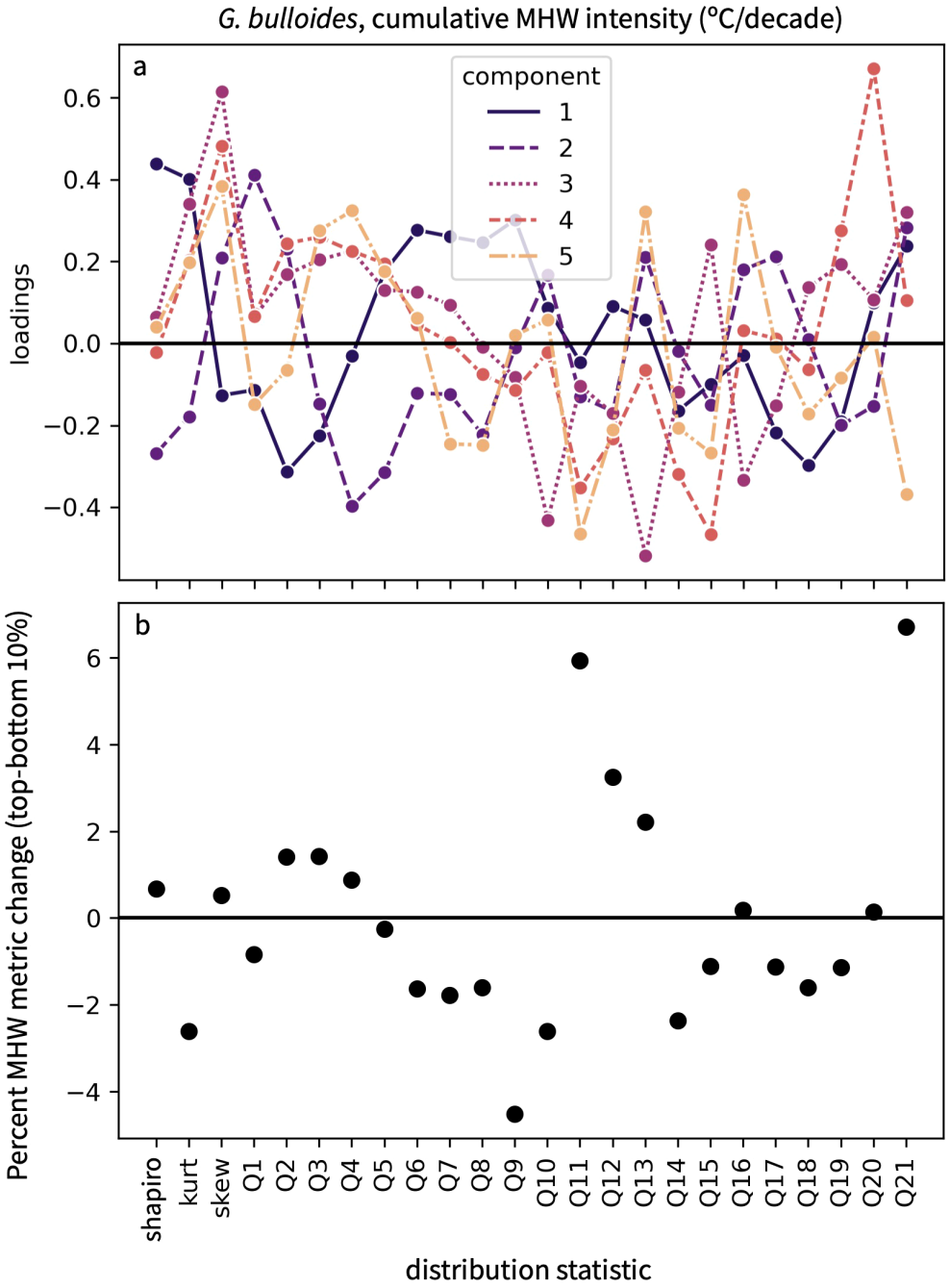

FIGURE 7
Information to aid in the physical interpretation of a transfer function **(A)** The loadings on each component of the PLSR allow the user to visualize how distribution statistics vary relative to one another. **(B)** The percent difference in each distribution statistic between the LIM ensemble members with the highest and lowest 10% of a MHW metric. This example uses the regression from Figure 5 to plot the difference between LIM ensemble members at DSDP Site 36 with the highest and lowest cumulative intensities.

in individual *G. bulloides* from core-top (0-1 cm) sediments at DSDP Site 36. Core-top sediments are commonly assumed to approximate recent oceanographic conditions, and have been widely used to calibrate and validate paleoceanographic proxies (Quintana Krupinski et al., 2017; Rongstad et al., 2020; Saenger and Evans, 2019; Tierney et al., 2019). Core-top sediments were first wet sieved at 63 µm and dried. All *G. bulloides* were then picked from the 150-250 µm and >250 µm size fractions. Forty-five individuals from the larger size fraction were briefly sonicated in water and methanol before being transferred to Kiel device vials. $\delta^{18}O$ was measured at the Oregon State University Stable Isotope Laboratory using a Thermo-Fisher Kiel IV carbonate device coupled to a custom Thermo-Fisher MAT253+ isotope ratio mass spectrometer that has been optimized to analyze small volumes of carbon dioxide. For example, each ion beam has a factor of ~3 greater than stock amplification for m/z 44, 45, and 46, and a

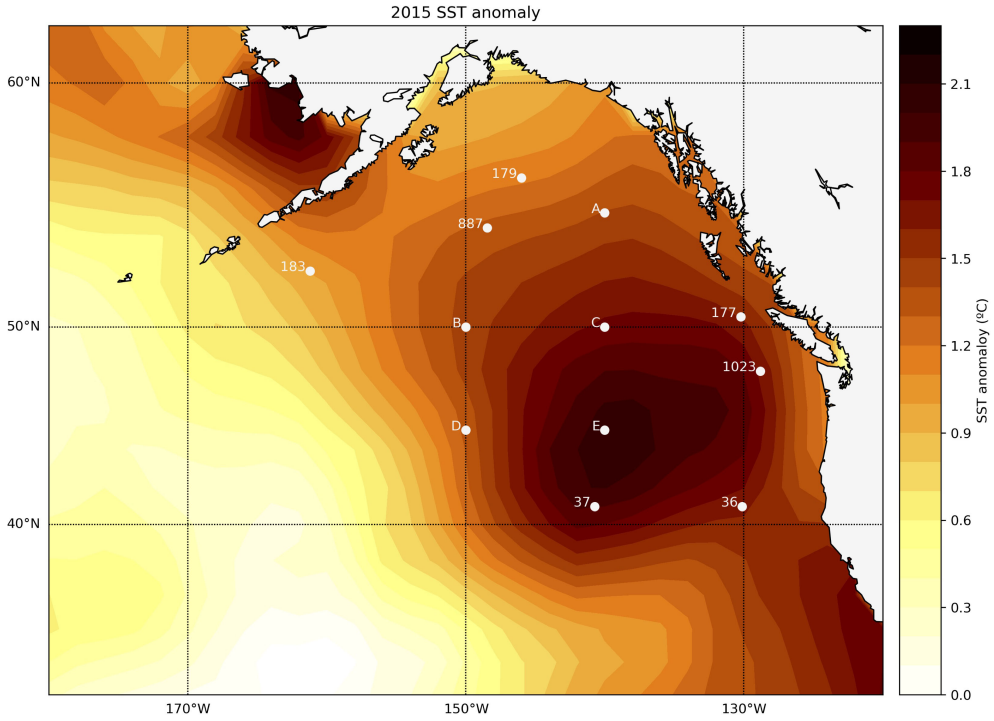

FIGURE 8
Locations of the northeast Pacific sites considered in this study relative to the 2015 SST anomaly associated with the "Blob" MHW. Numeric values represent the locations of existing DSDP and ODP marine sediment cores. Letters represent hypothetical locations at which cores could be collected within the geographic range of the 2015 MHW event.

modified pressure-adjust routine that minimizes sample versus standard pressure imbalances in small samples. This roughly doubles the instrument's signal to noise ratio at low beam intensities (typically near 1000 mV with the greater amplification; Supplementary Table S3), at the cost of a slight increase in nonlinearity with sample size. Modifications prevent running high mass samples without saturating the detectors, or requiring expansions, which can be problematic with such small amounts of CO_2 gas. Loading small volumes of reference gas reproducibly can also be a challenge, and requires extra analyses of carbonate standards for the purpose of isotope calibration relative to Vienna Pee Dee Belemnite (VPDB). In this study, small (up to 0.1 to 0.2 permil) linear corrections were made for source nonlinearity as a function of major beam intensity. Specifically, 8-9 analyses of an in-house standard (Wiley Marble) within each run were used to constrain linear relationships for raw $\delta^{18}O$ and $\delta^{13}C$ versus m/z 44, and then used to correct source nonlinearity in all other analyses from that run using their measured m/z 44 intensity. An additional small correction for reference gas depletion during each run was applied based on trends in the same Wiley Marble standards versus analysis time. This gas depletion correction has since been eliminated by increasing the size of the reference gas reservoir. The weights of the individual shells were calculated from the relationship between initial gas pressures (the Kiel VM1 gauge) and measured weights of standards ranging from about 3 to 17 µg, measured on a Sartorius SE2 ultramicrobalance (Supplementary Table S3). The uncertainty in the calcite weight associated with each shell analysis estimated from initial gas pressures is about 1 µg. Comparing measured to calculated mass for standards in this study yields a RMSE of 2 µg (Supplementary Table S3). Multiple analyses of NBS19 bracketed samples to evaluate precision and normalized data to the VPDB scale.

3 Results

The primary result of this work is the methodology described above, which identifies and quantifies robust transfer functions between pseudoproxy IFA-based SST distributions and MHW metrics. However, our application of it in the northeast Pacific provides an important example of the information it generates, how those results might be used, and the characteristics of sites with the greatest potential to reconstruct MHWs.

3.1 Locations and characteristics of the best transfer functions

Transfer function correlation coefficients vary significantly depending on site, MHW metric and MHW definition. The best fits occur at proposed locations B and C in the central part of the domain (50°N, 140-150°W) where r^2 values can exceed 0.8 (Figure 9A). Robust transfer functions with r^2 >0.7 are still found at many other locations including ODP Site 887, DSDP Site 183, ODP Site 1023 and proposed location E, but sites further south and west (e.g. DSDP Site 37 and proposed location D) have weaker best fits with maximum r^2 values below 0.6. Best fits consistently come from transfer functions that target the cumulative intensity of

10.3389/fmars.2024.1321254

MHWs, while transfer functions that target other MHW metrics rarely have correlation coefficients above 0.5 (Figure 9B). Fits are typically best when MHWs are defined based on a duration of one month, but the decline in r^2 values for duration thresholds of two and four months is modest (Figure 9C). Fits are also highest when MHWs are defined using an intensity threshold of one standard deviation, but often decrease considerably when the threshold is changed to two standard deviations (Figure 9D). In comparison, differences between species are minor and transfer functions based on *G. bulloides* are often similar to those based on *N. incompta* without evidence for once species consistently outperforming the other.

However, high correlation coefficients do not guarantee a transfer function can accurately reconstruct MHWs. While our evaluation of under-sampling does show that $RMSE_{samp}$ decreases in transfer functions with higher r^2 values (Figure 10A), sedimentation rate appears to be a more important control on accuracy (Figure 10B). For example, a transfer function that targets the cumulative intensity of short duration, low intensity MHWs using *G. bulloides* at proposed location C has a very high correlation coefficient of 0.81, but applying this transfer function to a SST distribution based on 200 foraminifera would reconstruct MHW cumulative intensity with an error of ±351% due to the location's low sedimentation rate of 0.14 cm/kyr. In contrast, applying transfer functions with weaker fits (r^2 0.66-0.71) to SST distributions based on 200 foraminifera at sites with higher sedimentation rates of ~7 cm/kyr (i.e. ODP Site 887, DSDP Site 179) would reconstruct MHW cumulative intensity with an error of only about ±45% (Figure 10B).

3.2 Individual *G. bulloides* stable isotopes

Of the 45 individual foraminifera analyzed from site DSDP Site 36, 37 were large enough (calcite weight 3-15 µg) for the dual inlet pressure adjustment required for high precision analysis

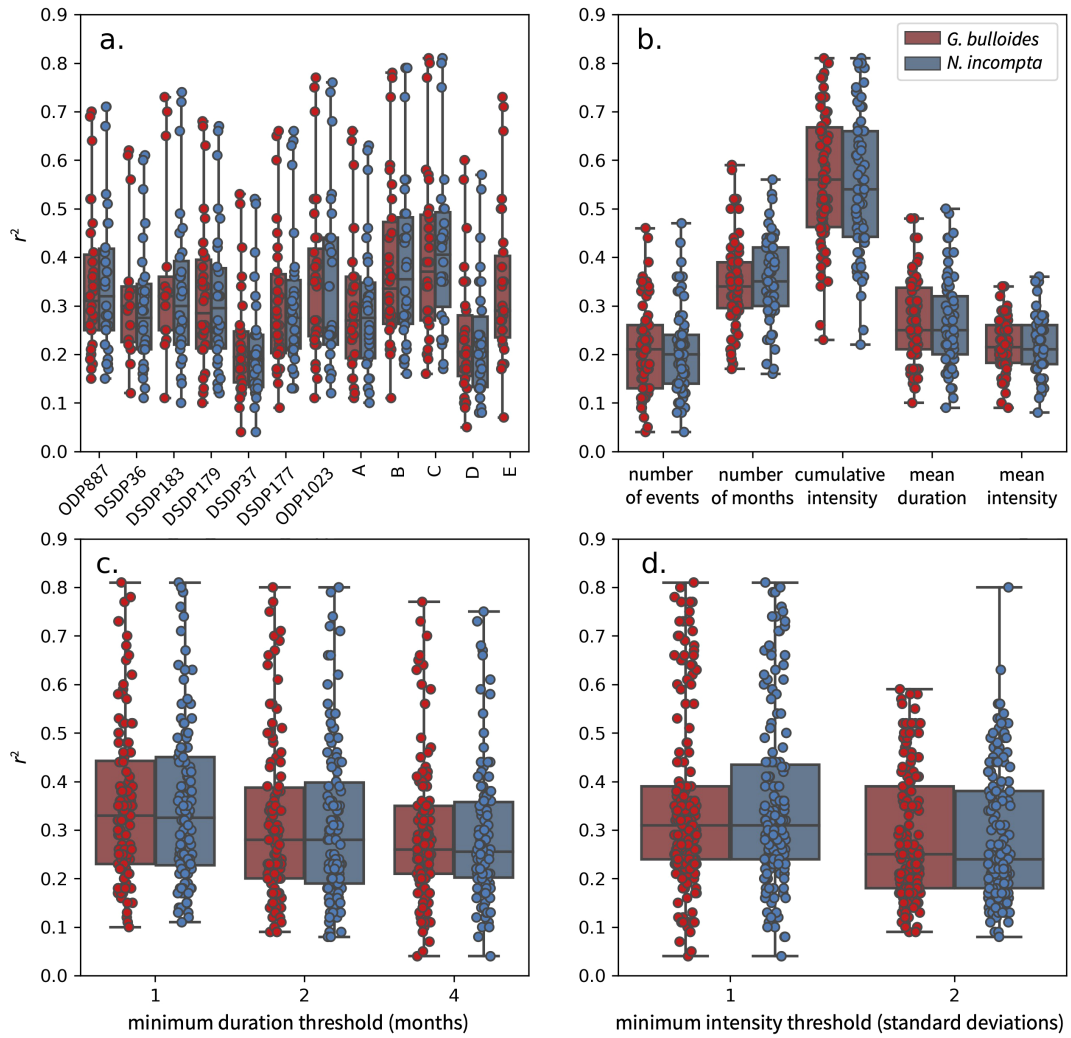

FIGURE 9
Summary of correlation coefficients for all 720 transfer functions considered. **(A)** differences between transfer functions based on *G. bulloides* (red) and *N. incompta* (blue) at the 12 northeast Pacific sites **(B)** differences between transfer functions targeting each of the five MHW metrics **(C)** differences between transfer functions for each of the three duration thresholds considered when defining MHWs **(D)** differences between transfer functions for the two intensity thresholds considered when defining MHWs.

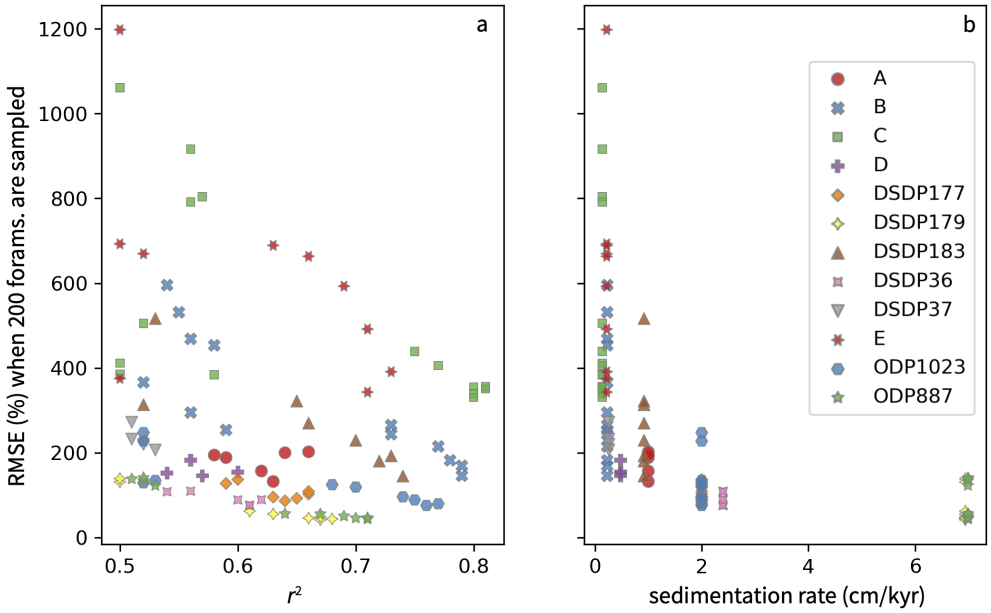

FIGURE 10
The RMSE expected for MHW reconstructions when only 200 foraminifera are measured. **(A)** versus the correlation coefficient of the transfer function and **(B)** versus the sedimentation rate of each site. The lowest RMSE values occur at the highest sedimentation rates, not the highest correlation coefficients. RMSE is expressed as a percent of the LIM ensemble mean to accommodate the differing units of MHW metrics. Undersampling was only evaluated in transfer functions with a $r^2 > 0.5$.

(Supplementary Table S3). External precision was 0.03‰ and 0.09‰ for NBS19 $\delta^{13}C$ and $\delta^{18}O$, respectively (1σ, n = 6) and 0.02‰ and 0.07‰ for in-house standard Wiley Marble (1σ, n = 13). Average $\delta^{18}O$ internal precision for standards with masses >3 µg was 0.05‰ (0.03‰ for masses 10-15 µg, 0.04‰ for 6-10 µg, and 0.07‰ for 3-6 µg). Average $\delta^{18}O$ for all *G. bulloides* was 1.84 ± 0.78‰ with a total range of 0.39 - 3.15‰. While *G. bulloides* with masses of 3-6 µg had a somewhat higher mean $\delta^{18}O$ of 2.1 ± 0.76 (n=14) than those with masses of 6-10 µg ($\delta^{18}O$ = 1.66 ± 0.71; n=11) and 10-15 µg ($\delta^{18}O$ = 1.69 ± 0.83; n=12), the slope of -0.06‰/µg observed for all data was not significant (p = 0.06) and we treated the data as a single population. The standard deviation of the individual shell data is a factor of 20 greater than internal precision, and a factor of 10 greater than external analytical precision, so the variability in foraminiferal data can reliably be interpreted to reflect the environment of their habitat. The distribution of proxy data is shown in Figure 11 and complete distribution statistics are given in Supplementary Table S4, acknowledging that the relatively small number of foraminifera analyzed may not accurately capture the true underlying distribution.

We applied these IFA-based distribution statistics to a transfer function that predicts the cumulative intensity of MHWs at DSDP Site 36. The transfer function accounts for the seasonal ecology of *G. bulloides*, and defines MHWs using intensity and duration thresholds of one standard deviation and one month, respectively. Applying a transfer function that defines MHWs using a two month duration threshold yielded similar results (not shown). IFA-based distribution statistics calculated a cumulative intensity of 10.63°C/decade in core-top sediments, which is appreciably higher than values of 6.68°C/decade, 6.37°C/decade and 5.52°C/decade in ERSSTv5, COBEv2 and HadISST data, respectively. However, because only 37 individuals are measured, the influence of undersampling is severe and we calculate the error on reconstructed cumulative intensity to be ±14.38°C/decade.

4 Discussion

This study provides a framework for developing transfer functions that can reconstruct past MHW variability from IFA paleotemperature distributions. Our systematic application of this approach at a series of northeast Pacific sites suggests that promising transfer functions can be generated from multiple species in most regions, and that the cumulative intensity of short duration, low intensity MHWs is the metric that can be reconstructed with the greatest skill. It is not immediately clear why transfer functions that target cumulative intensity consistently outperform others, but we speculate that it may relate to the metric's reliance on both duration and intensity. That is, variations in MHW duration or intensity alone may cause only modest changes to a SST distribution, while their combined influence in the cumulative intensity metric may be larger and more detectable. Similarly, we speculate that using duration and intensity thresholds of one month and one standard deviation, respectively, to define MHWs yields stronger transfer functions

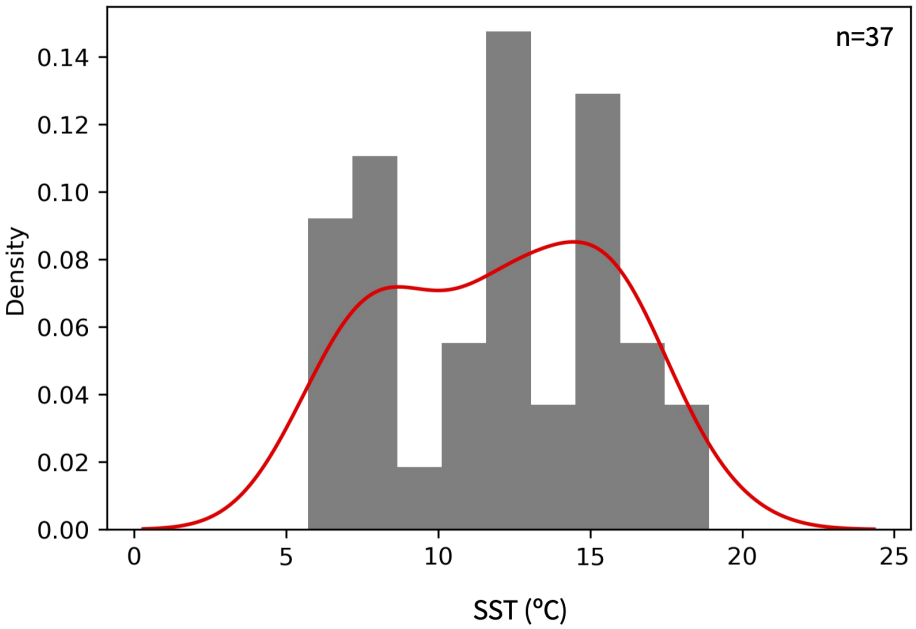

FIGURE 11
Histogram of SST estimates based on the $\delta^{18}O$ of 37 individual *G. bulloides* (grey) and the kernel density estimation of the population (red). Oxygen isotopic values were converted to temperature using the calibration of Bemis et al. (1998). The Shapiro-Wilk statistic, kurtosis and skewness of the distribution are 0.95, -1.18 and -0.075, respectively. Complete statistics are given in Supplementary Table S4.

because of the greater number of these low intensity, short duration events within each LIM ensemble member. A thorough evaluation of the mechanisms responsible for these observations and the degree to which they occur outside the north Pacific domain is left for future work.

In contrast, the relationship between transfer function skill and sedimentation rate is more straightforward. One centimeter of marine sediment in the central gyres can typically reflect many thousand years of time for sedimentation rates <0.25 cm/kyr (Table 1). Transfer function correlation coefficients at proposed location C are the highest of any location we consider, but one centimeter of sediment corresponds to about 7,000 years, or equivalently, 84,000 months. In this case, 200 foraminifera only represent about 0.25% of all months, leading to a severely under-sampled SST distribution and MHW reconstructions with errors exceeding ±350% (Figure 10B). Despite a higher sedimentation rate at DSDP Site 36, the influence of under-sampling on the individual foraminifera $\delta^{18}O$ data we generate is similar. Our 37 analyses represent only about 0.75% of the approximately 5000 months recorded by a centimeter of sediment at the site, making it unlikely that the resulting SST distribution (Figure 11) is representative of the larger population. While it is possible to generate a cumulative intensity estimate from these 37 analyses, the error on this value is too large to compare to observed modern values in a meaningful way. It is regrettable that our $\delta^{18}O$ data was generated in parallel with the development of our method, and we therefore missed an opportunity to evaluate how the relative paucity of *G. bulloides* at DSDP Site 36 would impact the accuracy of MHW reconstructions. Fortunately, similar situations should be avoidable in the future by using our method to calculate the expected accuracy of a MHW reconstruction prior to conducting geochemical analyses.

Given the sensitivity of our method to sedimentation rate, it is not surprising that the most accurate MHW reconstructions occur at ODP Site 887 and DSDP Site 179 where sedimentation rates are ~7 cm/kyr. At these locations, one centimeter of sediment reflects about 150 years, or 1800 months, and measuring 200 foraminifera would represent about 11% of all months. In these cases, the SST distribution is less dramatically under-sampled and $RMSE_{samp}$ decreases to about ±45%. While obviously an improvement, it seems likely that errors of this magnitude would still limit the practical application of our approach to only major shifts in MHW behavior.

The best path to reducing uncertainty in MHW reconstructions when applying our approach is to minimize the degree of under-sampling, which can be achieved in two ways. First, more foraminifera can be measured to increase the fraction of all months sampled. For example, we calculate that the error on MHW cumulative intensity reconstructed from *N. incompta* at DSDP Site 179 can be reduced from ±42% when 200 foraminifera are sampled to ±21% when 800 are sampled. These sample sizes may seem unreasonably large given that IFA studies typically measure only 50-100 individuals (Ford et al., 2015; Koutavas et al., 2006; Rongstad et al., 2020; Rustic et al., 2020). However, previous studies have not rigorously evaluated the sensitivity of their results to under-sampling and may have similar sample requirements. The likelihood that large sample requirements will be necessary to address many hypotheses will favor analytical approaches that achieve high throughput measurements of

geochemical proxies without significantly sacrificing analytical precision. Even with analytical advances, the degree to which errors can be reduced by increasing sample sizes will ultimately be determined by the number of foraminifera present in a sample, and it may not always be possible to achieve a desired level of skill simply by making more measurements.

A second way to decrease the errors caused by under-sampling is to reduce the number of months recorded in a sampling interval by targeting high sedimentation rate sites. Continental margins sites, such as those in the Gulf of Alaska (Walczak et al., 2020) or the Santa Barbara Basin (Hendy et al., 2002), can have sedimentation rates in excess of 100 cm/kyr and minimal bioturbation, which allow a 1 cm sample to achieve near decadal resolution. Application of our method at these locations shows strong transfer functions similar to other north Pacific sites (not shown), and can reconstruct MHW cumulative intensity with an error below ±20% when 100 foraminifera are sampled, and below ±15% when 200 are analyzed. In comparison to reducing errors by increasing sample sizes, targeting high sedimentation rate sites has the advantage of improving accuracy while also minimizing analytical time and expense. These variables are obviously not exclusive however, and sites with both high sedimentation rates and abundant foraminifera are currently the best candidates for applying our method to generate paleo-MHW reconstructions.

Such reconstructions have the potential to significantly expand upon existing paleo-MHW research, which, to our knowledge, consists only of a single study of bi-monthly to annual coral data in western Australia (Zinke et al., 2015). Evidence that foraminifera assemblages vary with MHWs on short timescales (Lane et al., 2023) is an important result, but it will be difficult to attribute assemblage changes to past MHW variability as opposed to changes in the mean state. Additionally, it is not yet clear if changes in assemblages primarily reflect a response to MHW duration, frequency, intensity or some combination of these metrics. On the other hand, our transfer functions target specific MHW metrics in a quantitative way that facilitates statistical analyses and comparisons to independent model simulations. While we highlight a northeast Pacific application, the framework we describe can be applied to other foraminifera species in other ocean domains to significantly advance knowledge of spatiotemporal MHW variability.

Despite promise, the accuracy with which MHWs can be reconstructed using our approach relies on a number of assumptions that should be carefully considered when interpreting results. In many cases these same assumptions also apply to traditional foraminifera-based reconstructions and are an inherent complication of paleoceanography. For example, changes in the seasonality of *G. bulloides* or *N. incompta* growth have the potential to alter mean SST reconstructions (Jonkers and Kučera, 2015), but would also likely change paleotemperature distributions independently of MHW behavior. Applying our transfer functions in the distant past would therefore require demonstrating that seasonality had not changed significantly, or generating new transfer functions with alternate modeled seasonalities that account for any changes. These alternate seasonalities could be generated for modern species by rerunning foraminifera ecology models (Fraile et al., 2008; Kretschmer et al., 2018; Moore et al., 2001) under the boundary conditions of past climates, but may be challenging for extinct species.

It may also be important that PLAFOM2.0 (Kretschmer et al., 2018) calculates seasonal trends in foraminifera *concentrations*, which could differ from trends in calcification. The rate of planktic foraminifera chamber formation and calcification is known to vary throughout their life (de Nooijer et al., 2014; Lea et al., 1995; Ter Kuile and Erez, 1984), causing geochemical proxies such as Mg/Ca or $\delta^{18}O$ to vary with shell size (Elderfield et al., 2002). To minimize this effect, paleoceanographic reconstructions typically target foraminifer tests within narrow size fractions. However, seasonal biases can also differ between size fractions (Jonkers et al., 2013; Thunell et al., 1983) and aren't accounted for by PLAFOM2.0. This could cause the true seasonal bias of actual IFA data to differ from that modeled in IFA pseudoproxies when only narrow size fractions are considered. While additional work is necessary to characterize the scope of this potential complication, solutions seem possible if it proves to be a concern. For example, seasonal biases of specific size fractions could be incorporated into proxy system models like PLAFOM2.0 or shell size could be added as an independent variable when predicting paleotemperatures, thereby allowing all foraminifera to be measured regardless of size fraction.

It is also plausible that the seasonal distributions generated by PLAFOAM2.0 (Kretschmer et al., 2018) do not account for ecological responses that are unique to MHWs. For example, stratification during a MHW could isolate foraminifera from the nutrient-rich subsurface, possibly ending their growing season and ability to record MHWs if they could not alter their habitat depth. While this possibility will ultimately have to be evaluated on a case by case basis, the best data available to evaluate it in the north Pacific is the 4-year sediment trap study of Sautter and Thunell (1989). These data overlap with multiple MHWs, with the initial 2 years being characterized by a long duration, low intensity MHW associated with the 1982/83 El Niño, and a shorter duration MHW occurring during the winter of 1984-85. During this interval *G. bulloides* exhibited a seasonal flux from March-July, while *N. incompta* was most abundant from August-November. Both trends agree with the modeled distributions of Kretschmer et al. (2018), but are inconsistent with the possibility that the growing season of either species ends abruptly with the onset of a MHW. Support for this comes from the observation that *G. bulloides* were found in Santa Barbara Basin sediment traps throughout the 2014-2016 "Blob" MHW (Cherry et al., 2023), although these organisms may be a distinct genotype from those in more subpolar environments and therefore may respond to MHWs differently. Additional monitoring of how foraminifera assemblages and abundance change across a range of MHW intensities and durations (e.g. Lane et al., 2023) is certainly warranted since available data are limited, but current knowledge suggests that *G. bulloides* and *N. incompta* remain present and with similar seasonality during many MHWs.

If future work should demonstrate that certain species exhibit ecological biases that make them unsuitable for MHW

reconstructions, it is encouraging that our method predicts robust transfer functions across multiple species. The framework we describe accommodates five different foraminifera species, and will allow reconstructions to target only the species whose ecology is minimally impacted by MHWs. Alternatively, if multiple species are found to have uncorrelated ecological biases, it may be advantageous to generate multiple independent MHW reconstructions from different species in the same sedimentary interval. These reconstructions could then be combined to maximize their mutual MHW information and minimize species-specific effects.

Moving forward, our approach could be improved by further refining our proxy system model, which could consider bioturbation more realistically. When calculating the fraction of months sampled by a given number of IFA measurements, we currently assume that sedimentation rate is the only variable determining the amount of time represented by one centimeter of sediment. While this assumption may be valid at sites with anoxic bottom waters void of benthic organisms, bioturbation could significantly increase the amount of time represented in a sedimentary interval because of mixing over depths of 10 or more centimeters (Dolman et al., 2021). Fortunately, tools exist to rigorously evaluate bioturbation in sedimentary archives (Dolman and Laepple, 2018) and can be incorporated into future versions of our algorithm.

Species specific paleotemperature calibrations will not be a major concern as long as they are linear, which is often true for $\delta^{18}O$ (Bemis et al., 1998; Mulitza et al., 2003). In these cases, transformations do not change the distribution statistics between raw geochemical data and reconstructed temperature. The same is not true for exponential paleotemperature calibrations (Anand et al., 2003; Lea et al., 1999; Saenger and Evans, 2019), and Mg/Ca data would need to be transformed to temperature to apply our transfer functions. In either case, changes in the $\delta^{18}O$ or Mg/Ca of seawater between time intervals would not influence distributions as long as these values remained relatively constant within each IFA time interval.

Finally, we stress that any paleo-MHW reconstructions based on our approach should be interpreted only in the context within which they are calibrated. Reconstructed MHWs will follow the definition in Section 2.3, and will not necessarily reflect trends based on the daily definitions commonly used when studying modern MHWs. Furthermore, changes in one metric should not be assumed to be representative of other metrics or MHW definitions. That is, a reconstructed increase in MHW cumulative intensity should not be taken to mean there were also increases in the number or duration of events. Similarly, a transfer function based on short duration, low intensity MHWs should not be used to suggest changes in higher intensity or longer duration events. While there are undoubtedly other ways to generate transfer functions between IFA distributions and MHW metrics, reconstructions from this study should only be interpreted for the region, metric and definition for which they are calibrated and validated.

5 Conclusions

We describe a framework to evaluate how well SST distributions can predict MHW metrics, with the goal of generating transfer functions that can be applied to monthly paleotemperature distributions derived from IFA. Results reveal that the cumulative intensity of short duration, low intensity MHWs is the most promising target for reconstruction, and can likely be calculated with an error of less than 15% at continental margin sites with sedimentation rates in excess of 100 cm/kyr. Our approach is a major advance in the nascent field of paleo-MHW research that allows specific MHW metrics and their uncertainty to be quantified from individual foraminifera in marine sediments. While we present an example application from the northeast Pacific, our approach is valid in other ocean domains and for other foraminifera species. Application of our method in broader contexts therefore has considerable potential to advance knowledge surrounding the spatiotemporal variability of MHWs prior to the observational era. Future paleo-MHW reconstructions will provide valuable context for interpreting modern trends as well as out-of-sample validation targets for climate models, both of which should help improve forecasts of MHW behavior on decadal-centennial timescales.

Data availability statement

The datasets presented in this study can be found online at https://github.com/caseysaengerWWU/mhw_calibration.

Author contributions

CS: Conceptualization, Data curation, Formal analysis, Funding acquisition, Investigation, Methodology, Validation, Visualization, Writing – original draft, Writing – review & editing. CJ-D: Investigation, Writing – review & editing. AG: Funding acquisition, Writing – review & editing. AM: Investigation, Methodology, Writing – review & editing. AR: Methodology, Writing – review & editing. TX: Writing – original draft.

Funding

The author(s) declare financial support was received for the research, authorship, and/or publication of this article. We thank the National Science Foundation Division of Ocean Sciences for funding this work through Marine Geology and Geophysics award 2202543 to CS, AG and CJ-D. AM also acknowledges support from Oregon State University, and from NSF Marine Geology and Geophysics awards 1850083 and 2149564.

Acknowledgments

We thank Jennifer Fehrenbacher for valuable discussion of foraminifera ecology and Mike Evans and Andy Bunn for insight regarding regression techniques. We also acknowledge the support of Jennifer McKay for her oversight of OSU's Stable Isotope Laboratory. We thank Johan Schijf and Edmund Hathorne for editorial oversight, the reviewers named on the cover page for thoughtful feedback and additional comments from reviewers.

Conflict of interest

The authors declare that the research was conducted in the absence of any commercial or financial relationships that could be construed as a potential conflict of interest.

Publisher's note

Supplementary material

The Supplementary Material for this article can be found online at: https://www.frontiersin.org/articles/10.3389/fmars.2024.1321254/full#supplementary-material

References

Alexander, M. A., Matrosova, L., Penland, C., Scott, J. D., and Chang, P. (2008). Forecasting pacific SSTs: linear inverse model predictions of the PDO. *J. Clim.* 21, 385–402. doi: 10.1175/2007JCLI1849.1

Amaya, D. J., Jacox, M. G., Fewings, M. R., Saba, V. S., Stuecker, M. F., Rykaczewski, R. R., et al. (2023). Marine heatwaves need clear definitions so coastal communities can adapt. *Nature* 616, 29–32. doi: 10.1038/d41586-023-00924-2

Anand, P., Elderfield, H., and Conte, M. H. (2003). Calibration of Mg/Ca thermometry in planktonic foraminifera from a sediment trap time series. *Paleoceanography* 18. doi: 10.1029/2002PA000846

Ault, T. R., Deser, C., Newman, M., and Emile-Geay, J. (2013). Characterizing decadal to centennial variability in the equatorial Pacific during the last millennium. *Geophys. Res. Lett.* 40, 3450–3456. doi: 10.1002/grl.50647

Barkhordarian, A., Nielsen, D. M., and Baehr, J. (2022). Recent marine heatwaves in the North Pacific warming pool can be attributed to rising atmospheric levels of greenhouse gases. *Commun. Earth Environ.* 3, 1–12. doi: 10.1038/s43247-022-00461-2

Bemis, B. E., Spero, H. J., Bijma, J., and Lea, D. W. (1998). Reevaluation of the oxygen isotopic composition of planktonic foraminifera: Experimental results and revised paleotemperature equations. *Paleoceanography* 13, 150–160. doi: 10.1029/98PA00070

Bond, N. A., Cronin, M. F., Freeland, H., and Mantua, N. (2015). Causes and impacts of the 2014 warm anomaly in the NE Pacific. *Geophys. Res. Lett.* 42, 3414–3420. doi: 10.1002/2015GL063306

Brennan, P. R., Bhattacharya, T., Feng, R., Tierney, J. E., and Jorgensen, E. M. (2022). Patterns and mechanisms of northeast pacific temperature response to pliocene boundary conditions. *Paleoceanogr. Paleoclimatology* 37, e2021PA004370. doi: 10.1029/2021PA004370

Burke, K. D., Williams, J. W., Chandler, M. A., Haywood, A. M., Lunt, D. J., and Otto-Bliesner, B. L. (2018). Pliocene and Eocene provide best analogs for near-future climates. *Proc. Natl. Acad. Sci.* 115, 13288–13293. doi: 10.1073/pnas.1809600115

Capotondi, A., Newman, M., Xu, T., and Di Lorenzo, E. (2022). An optimal precursor of northeast pacific marine heatwaves and central pacific el niño events. *Geophys. Res. Lett.* 49, e2021GL097350. doi: 10.1029/2021GL097350

Cavole, L. M., Demko, A. M., Diner, R. E., Giddings, A., and Koester, I. (2016). Biological impacts of the 2013–2015 warm-water anomaly in the northeast pacific: winners, losers, and the future. *Oceanography* 29, 273–285. doi: 10.5670/oceanog.2016.32

Cherry, K., Havard, E., Benitez-Nelson, C., Tappa, E., and Davis, C. V. (2023). *Planktic Foraminiferal Response to the 2014-2015 Marine Heatwave in the Santa Barbara Basin* (San Francisco: Presented at the AGU Fall Meeting).

Cheung, W. W. L., and Frölicher, T. L. (2020). Marine heatwaves exacerbate climate change impacts for fisheries in the northeast Pacific. *Sci. Rep.* 10, 6678. doi: 10.1038/s41598-020-63650-z

Costa, K. M., Pavia, F. J., Piecuch, C. G., McManus, J. F., and Weinstein, G. A. (2024). Pelagic sedimentation rates in the North Pacific using Thorium-230 depth profiling. *Geochim. Cosmochim. Acta* 369, 126–140. doi: 10.1016/j.gca.2023.11.020

Davies, M. H., Mix, A. C., Stoner, J. S., Addison, J. A., Jaeger, J., Finney, B., et al. (2011). The deglacial transition on the southeastern Alaska Margin: Meltwater input, sea level rise, marine productivity, and sedimentary anoxia. *Paleoceanography* 26. doi: 10.1029/2010PA002051

Dee, S. G., Steiger, N. J., Emile-Geay, J., and Hakim, G. J. (2016). On the utility of proxy system models for estimating climate states over the common era. *J. Adv. Model. Earth Syst.* 8, 1164–1179. doi: 10.1002/2016MS000677

de Nooijer, L. J., Spero, H. J., Erez, J., Bijma, J., and Reichart, G. J. (2014). Biomineralization in perforate foraminifera. *Earth-Sci. Rev.* 135, 48–58. doi: 10.1016/j.earscirev.2014.03.013

Di Lorenzo, E., and Mantua, N. (2016). Multi-year persistence of the 2014/15 North Pacific marine heatwave. *Nat. Clim. Change* 6, 1042–1047. doi: 10.1038/nclimate3082

Dolman, A. M., Groeneveld, J., Mollenhauer, G., Ho, S. L., and Laepple, T. (2021). Estimating bioturbation from replicated small-sample radiocarbon ages. *Paleoceanogr. Paleoclimatology* 36, e2020PA004142. doi: 10.1029/2020PA004142

Dolman, A. M., and Laepple, T. (2018). Sedproxy: a forward model for sediment-archived climate proxies. *Clim. Past* 14, 1851–1868. doi: 10.5194/cp-14-1851-2018

Donahue, J. G. (1970). "Pleistocene diatoms as climatic indicators in North Pacific sediments," in *Geological Investigations of the North Pacific*. Ed. J. D. Hays (Boulder, Colorado: Geological Society of America). doi: 10.1130/MEM126-p121

Elderfield, H., and Ganssen, G. (2000). Past temperature and δ18O of surface ocean waters inferred from foraminiferal Mg/Ca ratios. *Nature* 405, 442–445. doi: 10.1038/35013033

Elderfield, H., Vautravers, M., and Cooper, M. (2002). The relationship between shell size and Mg/Ca, Sr/Ca, δ18O, and δ13C of species of planktonic foraminifera. *Geochem. Geophys. Geosystems* 3, 1–13. doi: 10.1029/2001GC000194

Emiliani, C. (1955). Pleistocene temperatures. *J. Geol.* 63, 538–578. doi: 10.1086/626295

Erez, J., Almogi-Labin, A., and Avraham, S. (1991). On the life history of planktonic foraminifera: lunar reproduction cycle in globigerinoides sacculifer (Brady). *Paleoceanography* 6, 295–306. doi: 10.1029/90PA02731

Evans, M. N., Tolwinski-Ward, S. E., Thompson, D. M., and Anchukaitis, K. J. (2013). Applications of proxy system modeling in high resolution paleoclimatology. *Quat. Sci. Rev.* 76, 16–28. doi: 10.1016/j.quascirev.2013.05.024

Eyring, V., Bony, S., Meehl, G. A., Senior, C. A., Stevens, B., Stouffer, R. J., et al. (2016). Overview of the Coupled Model Intercomparison Project Phase 6 (CMIP6) experimental design and organization. *Geosci. Model. Dev.* 9, 1937–1958. doi: 10.5194/gmd-9-1937-2016

Ford, H. L., McChesney, C. L., Hertzberg, J. E., and McManus, J. F. (2018). A deep eastern equatorial pacific thermocline during the last glacial maximum. *Geophys. Res. Lett.* 45, 11,806–11,816. doi: 10.1029/2018GL079710

Ford, H. L., Ravelo, A. C., and Polissar, P. J. (2015). Reduced el niño–southern oscillation during the last glacial maximum. *Science* 347, 255–258. doi: 10.1126/science.1258437

Fraile, I., Schulz, M., Mulitza, S., and Kucera, M. (2008). Predicting the global distribution of planktonic foraminifera using a dynamic ecosystem model. *Biogeosciences* 5, 891–911. doi: 10.5194/bg-5-891-2008

Free, C. M., Anderson, S. C., Hellmers, E. A., Muhling, B. A., Navarro, M. O., Richerson, K., et al. (2023). Impact of the 2014–2016 marine heatwave on US and Canada West Coast fisheries: Surprises and lessons from key case studies. *Fish Fish.* 24, 652–674. doi: 10.1111/faf.12753

Frölicher, T. L., Fischer, E. M., and Gruber, N. (2018). Marine heatwaves under global warming. *Nature* 560, 360–364. doi: 10.1038/s41586-018-0383-9

Galbraith, E. D., Jaccard, S. L., Pedersen, T. F., Sigman, D. M., Haug, G. H., Cook, M., et al. (2007). Carbon dioxide release from the North Pacific abyss during the last deglaciation. *Nature* 449, 890–893. doi: 10.1038/nature06227

Gray, W. R., Weldeab, S., Lea, D. W., Rosenthal, Y., Gruber, N., Donner, B., et al. (2018). The effects of temperature, salinity, and the carbonate system on Mg/Ca in *Globigerinoides ruber* (white): A global sediment trap calibration. *Earth Planet. Sci. Lett.* 482, 607–620. doi: 10.1016/j.epsl.2017.11.026

Groeneveld, J., Ho, S. L., Mackensen, A., Mohtadi, M., and Laepple, T. (2019). Deciphering the variability in mg/ca and stable oxygen isotopes of individual foraminifera. *Paleoceanogr. Paleoclimatology* 34, 755–773. doi: 10.1029/2018PA003533

Hasselmann, K. (1976). Stochastic climate models Part I. *Theory. Tellus* 28, 473–485. doi: 10.1111/j.2153-3490.1976.tb00696.x

Hendy, I. L., Kennett, J. P., Roark, E. B., and Ingram, B. L. (2002). Apparent synchroneity of submillennial scale climate events between Greenland and Santa Barbara Basin, California from 30–10ka. *Quat. Sci. Rev.* 21, 1167–1184. doi: 10.1016/S0277-3791(01)00138-X

Hirahara, S., Ishii, M., and Fukuda, Y. (2014). Centennial-scale sea surface temperature analysis and its uncertainty. *J. Clim.* 27, 57–75. doi: 10.1175/JCLI-D-12-00837.1

Hirsch, A. L., Ridder, N. N., Perkins-Kirkpatrick, S. E., and Ukkola, A. (2021). CMIP6 multiModel evaluation of present-day heatwave attributes. *Geophys. Res. Lett.* 48, e2021GL095161. doi: 10.1029/2021GL095161

Hobday, A. J., Alexander, L. V., Perkins, S. E., Smale, D. A., Straub, S. C., Oliver, E. C. J., et al. (2016). A hierarchical approach to defining marine heatwaves. *Prog. Oceanogr.* 141, 227–238. doi: 10.1016/j.pocean.2015.12.014

Holbrook, N. J., Scannell, H. A., Sen Gupta, A., Benthuysen, J. A., Feng, M., Oliver, E. C. J., et al. (2019). A global assessment of marine heatwaves and their drivers. *Nat. Commun.* 10, 2624. doi: 10.1038/s41467-019-10206-z

Holbrook, N. J., Sen Gupta, A., Oliver, E. C. J., Hobday, A. J., Benthuysen, J. A., Scannell, H. A., et al. (2020). Keeping pace with marine heatwaves. *Nat. Rev. Earth Environ.* 1, 482–493. doi: 10.1038/s43017-020-0068-4

Huang, B., Thorne, P. W., Banzon, V. F., Boyer, T., Chepurin, G., Lawrimore, J. H., et al. (2017). *NOAA extended reconstructed sea surface temperature (ERSST), version 5*. doi: 10.7289/V5T72FNM

Huang, K.-F., You, C.-F., Lin, H.-L., and Shieh, Y.-T. (2008). *In situ* calibration of Mg/Ca ratio in planktonic foraminiferal shell using time series sediment trap: A case study of intense dissolution artifact in the South China Sea. *Geochem. Geophys. Geosystems* 9. Available at: https://psl.noaa.gov/data/gridded/data.noaa.ersst.v5.html.

Hurrell, J. W., Holland, M. M., Gent, P. R., Ghan, S., Kay, J. E., Kushner, P. J., et al. (2013). The community earth system model: A framework for collaborative research. *Bull. Am. Meteorol. Soc* 94, 1339–1360. doi: 10.1175/BAMS-D-12-00121.1

Jacox, M. G., Alexander, M. A., Amaya, D., Becker, E., Bograd, S. J., Brodie, S., et al. (2022). Global seasonal forecasts of marine heatwaves. *Nature* 604, 486–490. doi: 10.1038/s41586-022-04573-9

Jaeger, J. M., Gulick, S. P. S., LeVay, L. J., Asahi, H., Bahlburg, H., Belanger, C. L., et al. (2014). *Proceedings of the Integrated Ocean Drilling Program Vol. 341: Expedition reports Southern Alaska margin (Technical Report)* (College Station, Texas: Integrated Ocean Drilling Program).

Jones, T., Parrish, J. K., Peterson, W. T., Bjorkstedt, E. P., Bond, N. A., Ballance, L. T., et al. (2018). Massive mortality of a planktivorous seabird in response to a marine heatwave. *Geophys. Res. Lett.* 45, 3193–3202. doi: 10.1002/2017GL076164

Jonkers, L., Brummer, G.-J. A., Peeters, F. J. C., Van Aken, H. M., and De Jong, M. F. (2010). Seasonal stratification, shell flux, and oxygen isotope dynamics of left-coiling *N. pachyderma* and *T. quinqueloba* in the western subpolar North Atlantic: Sseasonal foraminiferal fluxes and δ^{18}O. *Paleoceanography* 25. doi: 10.1029/2009PA001849

Jonkers, L., and Kučera, M. (2015). Global analysis of seasonality in the shell flux of extant planktonic Foraminifera. *Biogeosciences* 12, 2207–2226. doi: 10.5194/bg-12-2207-2015

Jonkers, L., Reynolds, C. E., Richey, J., and Hall, I. R. (2015). Lunar periodicity in the shell flux of planktonic foraminifera in the Gulf of Mexico. *Biogeosciences* 12, 3061–3070. doi: 10.5194/bg-12-3061-2015

Jonkers, L., Van Heuven, S., Zahn, R., and Peeters, F. J. C. (2013). Seasonal patterns of shell flux, δ^{18}O and δ^{13}C of small and large N. pachyderma (s) and *G. bulloides* in the subpolar North Atlantic. *Paleoceanography* 28, 164–174. doi: 10.1002/palo.20018

Kemnitz, N., Hammond, D. E., Henderson, P., Le Roy, E., Charette, M., Moore, W., et al. (2023). Actinium and radium fluxes from the seabed in the northeast Pacific Basin. *Mar. Chem.* 250, 104180. doi: 10.1016/j.marchem.2022.104180

Khider, D., Stott, L. D., Emile-Geay, J., Thunell, R., and Hammond, D. E. (2011). Assessing El Niño Southern Oscillation variability during the past millennium. *Paleoceanography* 26. doi: 10.1029/2011PA002139

Koutavas, A., deMenocal, P. B., Olive, G. C., and Lynch-Stieglitz, J. (2006). Mid-Holocene El Niño–Southern Oscillation (ENSO) attenuation revealed by individual foraminifera in eastern tropical Pacific sediments. *Geology* 34, 993–996. doi: 10.1130/G22810A.1

Koutavas, A., and Joanides, S. (2012). El niño–southern oscillation extrema in the holocene and last glacial maximum. *Paleoceanography* 27. doi: 10.1029/2012PA002378

Kretschmer, K., Jonkers, L., Kucera, M., and Schulz, M. (2018). Modeling seasonal and vertical habitats of planktonic foraminifera on a global scale. *Biogeosciences* 15, 4405–4429. doi: 10.5194/bg-15-4405-2018

Lane, M. K., Fehrenbacher, J. S., Fisher, J. L., Fewings, M. R., Crump, B. C., Risien, C. M., et al. (2023). Planktonic foraminiferal assemblages reflect warming during two recent mid-latitude marine heatwaves. *Front. Mar. Sci.* 10. doi: 10.3389/fmars.2023.1155761

Laufkötter, C., Zscheischler, J., and Frölicher, T. L. (2020). High-impact marine heatwaves attributable to human-induced global warming. *Science* 369, 1621–1625. doi: 10.1126/science.aba0690

Lea, D. W., Martin, P. A., Chan, D. A., and Spero, H. J. (1995). Calcium uptake and calcification rate in the planktonic foraminifer Orbulina universa. *J. Foraminifer. Res.* 25, 14–23. doi: 10.2113/gsjfr.25.1.14

Lea, D. W., Mashiotta, T. A., and Spero, H. J. (1999). Controls on magnesium and strontium uptake in planktonic foraminifera determined by live culturing. *Geochim. Cosmochim. Acta* 63, 2369–2379. doi: 10.1016/S0016-7037(99)00197-0

Lea, D. W., Pak, D. K., and Spero, H. J. (2000). Climate impact of late quaternary equatorial pacific sea surface temperature variations. *Science* 289, 1719–1724. doi: 10.1126/science.289.5485.1719

Leduc, G., Vidal, L., Cartapanis, O., and Bard, E. (2009). Modes of eastern equatorial Pacific thermocline variability: Implications for ENSO dynamics over the last glacial period. *Paleoceanography* 24. doi: 10.1029/2008PA001701

Leggat, W. P., Camp, E. F., Suggett, D. J., Heron, S. F., Fordyce, A. J., Gardner, S., et al. (2019). Rapid coral decay is associated with marine heatwave mortality events on reefs. *Curr. Biol.* 29, 2723–2730.e4. doi: 10.1016/j.cub.2019.06.077

Malevich, S. B., Vetter, L., and Tierney, J. E. (2019). Global core top calibration of δ18O in planktic foraminifera to sea surface temperature. *Paleoceanogr. Paleoclimatology* 34, 1292–1315. doi: 10.1029/2019PA003576

Mann, M. E., and Rutherford, S. (2002). Climate reconstruction using 'Pseudoproxies.'. *Geophys. Res. Lett.* 29. doi: 10.1029/2001GL014554

McCabe, R. M., Hickey, B. M., Kudela, R. M., Lefebvre, K. A., Adams, N. G., Bill, B. D., et al. (2016). An unprecedented coastwide toxic algal bloom linked to anomalous ocean conditions. *Geophys. Res. Lett.* 43, 10,366–10,376. doi: 10.1002/2016GL070023

McManus, D. A., Burns, R. E., Weser, O., Valuer, T., von der Borch, C. V., Olsson, R. K., et al. (1970). "Initial reports of the deep sea drilling project, 5," in *Initial Reports of the Deep Sea Drilling Project* (Washington DC: U.S. Government Printing Office). doi: 10.2973/dsdp.proc.5.1970

Mehmood, T., Liland, K. H., Snipen, L., and Sæbø, S. (2012). A review of variable selection methods in Partial Least Squares Regression. *Chemom. Intell. Lab. Syst.* 118, 62–69. doi: 10.1016/j.chemolab.2012.07.010

Moore, J. K., Doney, S. C., Kleypas, J. A., Glover, D. M., and Fung, I. Y. (2001). An intermediate complexity marine ecosystem model for the global domain. *Deep Sea Res. Part II Top. Stud. Oceanogr.* 49, 403–462. doi: 10.1016/S0967-0645(01)00108-4

Mulitza, S., Boltovskoy, D., Donner, B., Meggers, H., Paul, A., and Wefer, G. (2003). Temperature:δ18O relationships of planktonic foraminifera collected from surface waters. *Palaeogeogr. Palaeoclimatol. Palaeoecol.* 202, 143–152. doi: 10.1016/S0031-0182(03)00633-3

Newman, M., Alexander, M. A., and Scott, J. D. (2011). An empirical model of tropical ocean dynamics. *Clim. Dyn.* 37, 1823–1841. doi: 10.1007/s00382-011-1034-0

Oliver, E. C. J., Benthuysen, J. A., Darmaraki, S., Donat, M. G., Hobday, A. J., Holbrook, N. J., et al. (2021). Marine heatwaves. *Annu. Rev. Mar. Sci.* 13, 313–342. doi: 10.1146/annurev-marine-032720-095144

Oliver, E. C. J., Burrows, M. T., Donat, M. G., Sen Gupta, A., Alexander, L. V., Perkins-Kirkpatrick, S. E., et al. (2019). Projected marine heatwaves in the 21st century and the potential for ecological impact. *Front. Mar. Sci.* 6. doi: 10.3389/fmars.2019.00734

Oliver, E. C. J., Donat, M. G., Burrows, M. T., Moore, P. J., Smale, D. A., Alexander, L. V., et al. (2018). Longer and more frequent marine heatwaves over the past century. *Nat. Commun.* 9, 1324. doi: 10.1038/s41467-018-03732-9

Opdyke, N. D., and Foster, J. H. (1970). "Paleomagnetism of cores from the North Pacific," in *Geological Investigations of the North Pacific*. Ed. J. D. Hays (Boulder, Colorado: Geological Society of America). doi: 10.1130/MEM126-p83

Ortiz, J. D., and Mix, A. C. (1992). The spatial distribution and seasonal succession of planktonic foraminifera in the California Current off Oregon, September 1987 – September 1988. *Geol. Soc Lond. Spec. Publ.* 64, 197–213. doi: 10.1144/GSL.SP.1992.064.01.13

Ortiz, J. D., Mix, A. C., and Collier, R. W. (1995). Environmental control of living symbiotic and asymbiotic foraminifera of the California Current. *Paleoceanography* 10, 987–1009. doi: 10.1029/95PA02088

Pedregosa, F., Varoquaux, G., Gramfort, A., Michel, V., Thirion, B., Grisel, O., et al. (2011). Scikit-learn: machine learning in python. *J. Mach. Learn. Res.* 12, 2825–2830. doi: 10.5555/1953048.2078195

Penland, C., and Matrosova, L. (1994). A balance condition for stochastic numerical models with application to the El Niño-Southern Oscillation. *J. Clim.* 7, 1352–1372. doi: 10.1175/1520-0442(1994)007<1352:ABCFSN>2.0.CO;2

Penland, C., and Sardeshmukh, P. D. (1995). The optimal growth of tropical sea surface temperature anomalies. *J. Clim.* 8, 1999–2024. doi: 10.1175/1520-0442(1995)008<1999:TOGOTS>2.0.CO;2

Plecha, S. M., Soares, P. M. M., Silva-Fernandes, S. M., and Cabos, W. (2021). On the uncertainty of future projections of Marine Heatwave events in the North Atlantic Ocean. *Clim. Dyn.* 56, 2027–2056. doi: 10.1007/s00382-020-05529-3

Praetorius, S. K., Mix, A. C., Walczak, M. H., Wolhowe, M. D., Addison, J. A., and Prahl, F. G. (2015). North Pacific deglacial hypoxic events linked to abrupt ocean warming. *Nature* 527, 362–366. doi: 10.1038/nature15753

Quintana Krupinski, N. B., Russell, A. D., Pak, D. K., and Paytan, A. (2017). Core-top calibration of B/Ca in Pacific Ocean Neogloboquadrina incompta and Globigerina bulloides as a surface water carbonate system proxy. *Earth Planet. Sci. Lett.* 466, 139–151. doi: 10.1016/j.epsl.2017.03.007

Rayner, N. A., Parker, D. E., Horton, E. B., Folland, C. K., Alexander, L. V., Rowell, D. P., et al. (2003). Global analyses of sea surface temperature, sea ice, and night marine air temperature since the late nineteenth century. *J. Geophys. Res. Atmospheres* 108, 2002JD002670. doi: 10.1029/2002JD002670

Rea, D. K. (1994). The paleoclimatic record provided by eolian deposition in the deep sea: The geologic history of wind. *Rev. Geophys.* 32, 159–195. doi: 10.1029/93RG03257

Rogers-Bennett, L., and Catton, C. A. (2019). Marine heat wave and multiple stressors tip bull kelp forest to sea urchin barrens. *Sci. Rep.* 9, 15050. doi: 10.1038/s41598-019-51114-y

Rongstad, B. L., Marchitto, T. M., Serrato Marks, G., Koutavas, A., Mekik, F., and Ravelo, A. C. (2020). Investigating ENSO-related temperature variability in equatorial pacific core-tops using mg/ca in individual planktic foraminifera. *Paleoceanogr. Paleoclimatology* 35, e2019PA003774. doi: 10.1029/2019PA003774

Rustic, G. T., Polissar, P. J., Ravelo, A. C., and White, S. M. (2020). Modulation of late Pleistocene ENSO strength by the tropical Pacific thermocline. *Nat. Commun.* 11, 5377. doi: 10.1038/s41467-020-19161-6

Saenger, C. P., and Evans, M. N. (2019). Calibration and validation of environmental controls on planktic foraminifera mg/ca using global core-top data. *Paleoceanogr. Paleoclimatology* 34, 1249–1270. doi: 10.1029/2018PA003507

Sautter, L. R., and Thunell, R. C. (1989). Seasonal succession of planktonic foraminifera; results from a four-year time-series sediment trap experiment in the Northeast Pacific. *J. Foraminifer. Res.* 19, 253–267. doi: 10.2113/gsjfr.19.4.253

Shapiro, S. S., and Wilk, M. B. (1965). An analysis of variance test for normality (complete samples)†. *Biometrika* 52, 591–611. doi: 10.1093/biomet/52.3-4.591

Smith, K. E., Burrows, M. T., Hobday, A. J., King, N. G., Moore, P. J., Sen Gupta, A., et al. (2023). Biological impacts of marine heatwaves. *Annu. Rev. Mar. Sci.* 15, 119–145. doi: 10.1146/annurev-marine-032122-121437

Smith, K. E., Burrows, M. T., Hobday, A. J., Sen Gupta, A., Moore, P. J., Thomsen, M., et al. (2021). Socioeconomic impacts of marine heatwaves: Global issues and opportunities. *Science* 374, eabj3593. doi: 10.1126/science.abj3593

Smith, T. M., Reynolds, R. W., Peterson, T. C., and Lawrimore, J. (2008). Improvements to NOAA's historical merged land–ocean surface temperature analysis, (1880–2006). *J. Clim.* 21, 2283–2296. doi: 10.1175/2007JCLI2100.1

Spero, H. J. (1998). Life history and stable isotope geochemistry of planktonic foraminifera. *Paleontol. Soc Pap.* 4, 7–36. doi: 10.1017/S1089332600000383

Taylor, M. A., Hendy, I. L., and Pak, D. K. (2014). Deglacial ocean warming and marine margin retreat of the Cordilleran Ice Sheet in the North Pacific Ocean. *Earth Planet. Sci. Lett.* 403, 89–98. doi: 10.1016/j.epsl.2014.06.026

Taylor, B. J., Rae, J. W. B., Gray, W. R., Darling, K. F., Burke, A., Gersonde, R., et al. (2018). Distribution and ecology of planktic foraminifera in the North Pacific: Implications for paleo-reconstructions. *Quat. Sci. Rev.* 191, 256–274. doi: 10.1016/j.quascirev.2018.05.006

Taylor, K. E., Stouffer, R. J., and Meehl, G. A. (2012). An overview of CMIP5 and the experiment design. *Bull. Am. Meteorol. Soc* 93, 485–498. doi: 10.1175/BAMS-D-11-00094.1

Ter Kuile, B., and Erez, J. (1984). *In situ* growth rate experiments on the symbiont-bearing foraminifera Amphistegina lobifera and Amphisorus hemprichii. *J. Foraminifer. Res.* 14, 262–276. doi: 10.2113/gsjfr.14.4.262

Thirumalai, K., DiNezio, P. N., Tierney, J. E., Puy, M., and Mohtadi, M. (2019). An el niño mode in the glacial Indian Ocean? *Paleoceanogr. Paleoclimatology* 34, 1316–1327. doi: 10.1029/2019PA003669

Thunell, R. C., Curry, W. B., and Honjo, S. (1983). Seasonal variation in the flux of planktonic foraminifera: time series sediment trap results from the Panama Basin. *Earth Planet. Sci. Lett.* 64, 44–55. doi: 10.1016/0012-821X(83)90051-1

Tierney, J. E., Malevich, S. B., Gray, W., Vetter, L., and Thirumalai, K. (2019). Bayesian calibration of the mg/ca paleothermometer in planktic foraminifera. *Paleoceanogr. Paleoclimatology* 34, 2005–2030. doi: 10.1029/2019PA003744

Tierney, J. E., Poulsen, C. J., Montañez, I. P., Bhattacharya, T., Feng, R., Ford, H. L., et al. (2020). Past climates inform our future. *Science* 370, eaay3701. doi: 10.1126/science.aay3701

Tolderlund, D. S., Bé, A. W. H., and Be, A. W. H. (1971). Seasonal distribution of planktonic foraminifera in the Western North Atlantic. *Micropaleontology* 17, 297. doi: 10.2307/1485143

von Biela, V. R., Arimitsu, M. L., Piatt, J. F., Heflin, B., Schoen, S. K., Trowbridge, J. L., et al. (2019). Extreme reduction in nutritional value of a key forage fish during the Pacific marine heatwave of 2014-2016. *Mar. Ecol. Prog. Ser.* 613, 171–182. doi: 10.3354/meps12891

Walczak, M. H., Mix, A. C., Cowan, E. A., Fallon, S., Fifield, L. K., Alder, J. R., et al. (2020). Phasing of millennial-scale climate variability in the Pacific and Atlantic Oceans. *Science* 370, 716–720. doi: 10.1126/science.aba7096

White, S. M., Ravelo, A. C., and Polissar, P. J. (2018). Dampened El Niño in the early and mid-holocene due to insolation-forced warming/deepening of the thermocline. *Geophys. Res. Lett.* 45, 316–326. doi: 10.1002/2017GL075433

Xu, T., Newman, M., Capotondi, A., and Di Lorenzo, E. (2021). The continuum of northeast pacific marine heatwaves and their relationship to the tropical pacific. *Geophys. Res. Lett.* 48, 2020GL090661. doi: 10.1029/2020GL090661

Xu, T., Newman, M., Capotondi, A., Stevenson, S., Di Lorenzo, E., and Alexander, M. A. (2022). An increase in marine heatwaves without significant changes in surface ocean temperature variability. *Nat. Commun.* 13, 7396. doi: 10.1038/s41467-022-34934-x

Yao, Y., Wang, C., and Fu, Y. (2022). Global marine heatwaves and cold-spells in present climate to future projections. *Earths Future* 10, e2022EF002787. doi: 10.1029/2022EF002787

Zinke, J., Hoell, A., Lough, J. M., Feng, M., Kuret, A. J., Clarke, H., et al. (2015). Coral record of southeast Indian Ocean marine heatwaves with intensified Western Pacific temperature gradient. *Nat. Commun.* 6, 8562. doi: 10.1038/ncomms9562

Frontiers in Marine Science

Explores ocean-based solutions for emerging global challenges

The third most-cited marine and freshwater biology journal, advancing our understanding of marine systems and addressing global challenges including overfishing, pollution, and climate change.

Discover the latest Research Topics

See more →

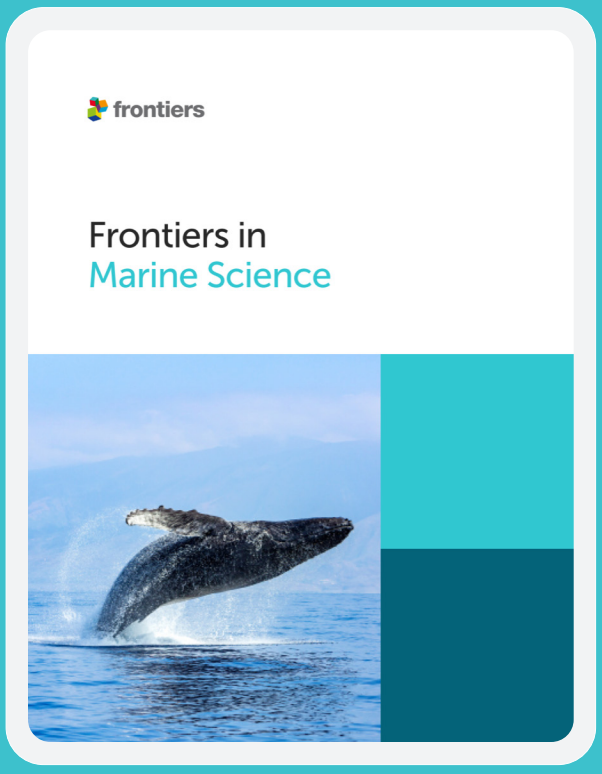

Frontiers

Avenue du Tribunal-Fédéral 34
1005 Lausanne, Switzerland
frontiersin.org

Contact us

+41 (0)21 510 17 00
frontiersin.org/about/contact